Low-Lying Electronic States of the Molecules AB_n ($A =$ Sc-Ni, $B =$ Cu/Ag/Au, $n = 1, 2$)

Inaugural-Dissertation

to obtain the academic degree
Doctor rerum naturalium (Dr rer. nat.)

submitted to
the Department of Biology, Chemistry, and Pharmacy
of Freie Universität Berlin

by
Davood Alizadeh Sanati
from Mashhad, Iran
2019

This work was prepared under supervision of
PD Dr Dirk Andrae (Freie Universität Berlin)
from October 2015 until July 2019.

1. reviewer:	PD Dr Dirk Andrae
2. reviewer:	Prof. Dr Beate Paulus
Date of defence:	19.09.2019

to my beloved mother Nahid and my devoted father Mahdi

Acknowledgement

I would like to, first of all, express my heartfelt gratitude to my supervisor PD Dr Dirk Andrae who (a) continuously supported my PhD studies, (b) patiently taught me how to do research, and (c) showed me the way to understand molecular quantum mechanics. I would like to acknowledge with many thanks Prof. Dr Beate Paulus for reviewing the present dissertation as well as for providing an excellent working environment at the Freie Universität Berlin. I gratefully acknowledge research support from the German Academic Exchange Service (DAAD) under Grant ID 57129429. I formally acknowledge the support by the High-Performance Computing (HPC) facilities at the Freie Universität Berlin (ZEDAT), in particular by Dr Boris Proppe and Dr Loris Bennett. I would like to show my appreciation to professors, postdoctoral researchers, and students in AG Kaghazchi, AG Keller, AG Tremblay, as well as to our respected secretary Mrs. Julija Djordjevic for providing a cordial workplace. I, finally, like to say thank you also to Lukas, Pouya, Sara, Marcel, Matthias, Edoardo, Chrsitian, Kai, and to many others for being dear friends and trusted colleagues.

Contents

1 Introduction **19**

2 Theory and Computations **23**

2.1 Some Remarks on Methodology 23

2.2 Assessment of the Results 27

2.3 Computations: Douglas-Kroll-Hess Framework 28

2.4 Computations: Exact 2-Component Framework 31

3 Results **33**

3.1 The Diatomic Molecules AB 33

3.1.1 Overview 33

3.1.2 BB' 35

3.1.3 FeB 38

3.1.4 CrB, CoB, and NiB 42

3.1.5 The Role of Spin-Orbit Coupling 44

3.1.6 Overall Trends 45

3.2 The Triatomic Molecules AB_2 48

3.2.1 Overview 48

3.2.2 ScB_2 50

3.2.3 TiB_2 59

3.2.4 VB_2 59

3.2.5 CrB_2 61

3.2.6 Overall Trends 64

4 Synopsis and Conclusion **65**

Appendices **81**

A Theory **83**

B Tables and Figures **87**

List of Tables

B.1 Experimental Data on the Diatomic Molecules AB (A=Sc-Ni, B=Cu/Ag/Au) 87

B.2 Energy Levels of the Metal Atoms A and B (Experiment $v.$ Theory) 88

B.3 Correlation between Atomic and Diatomic Molecular Terms of:

I - ScB: ${}^2\mathrm{D} + {}^2\mathrm{S}$; ${}^{1,3}\{\Sigma^+ \oplus \Pi \oplus \Delta\}$ 93

B.4 II - TiB: ${}^3\mathrm{F} + {}^2\mathrm{S}$ and ${}^5\mathrm{F} + {}^2\mathrm{S}$; ${}^{2,4(2),6}\{\Sigma^- \oplus \Pi \oplus \Delta \oplus \Phi\}$ 93

B.5 III - VB: ${}^4\mathrm{F} + {}^2\mathrm{S}$ and ${}^6\mathrm{D} + {}^2\mathrm{S}$; ${}^{3,5}\{\Sigma^- \oplus \Pi \oplus \Delta \oplus \Phi\}$ and ${}^{5,7}\{\Sigma^+ \oplus \Pi \oplus \Delta\}$ 94

B.6 IV - CrB: ${}^7\mathrm{S} + {}^2\mathrm{S}$ and ${}^5\mathrm{S} + {}^2\mathrm{S}$; ${}^{6,8}\Sigma^+$ and ${}^{4,6}\Sigma^+$ 94

B.7 V - MnB: ${}^6\mathrm{S} + {}^2\mathrm{S}$ and ${}^6\mathrm{D} + {}^2\mathrm{S}$; ${}^{5,7}\Sigma^+$ and ${}^{5,7}\{\Sigma^+ \oplus \Pi \oplus \Delta\}$ 95

B.8 VI - FeB: ${}^5\mathrm{D} + {}^2\mathrm{S}$ and ${}^5\mathrm{F} + {}^2\mathrm{S}$; ${}^{4,6}\{\Sigma^+ \oplus \Pi \oplus \Delta\}$ and ${}^{4,6}\{\Sigma^- \oplus \Pi \oplus \Delta \oplus \Phi\}$ 95

B.9 VII - CoB: ${}^4\mathrm{F} + {}^2\mathrm{S}$; ${}^{3,5}\{\Sigma^- \oplus \Pi \oplus \Delta \oplus \Phi\}$ 96

B.10 VIII - NiB: ${}^3\mathrm{D} + {}^2\mathrm{S}$ and ${}^3\mathrm{F} + {}^2\mathrm{S}$ and ${}^1\mathrm{D} + {}^2\mathrm{S}$; ${}^{2,4}\Lambda^{(\pm)}$ 96

B.11 (Λ,S) Spectroscopic Constants for Ground and Low-Lying States of:

I - ScCu: $X^3\Delta < {}^1\Sigma^+ < {}^3\Pi < {}^3\Sigma^+ < {}^1\Delta < {}^1\Pi(0.39\ \mathrm{eV})$ 97

B.12 II - ScAg: $X^3\Delta < {}^1\Sigma^+ < {}^3\Pi < {}^1\Delta < {}^3\Sigma^+ < {}^1\Pi(0.30\ \mathrm{eV})$ 97

B.13 III - ScAu: $X^3\Delta < {}^1\Sigma^+ < {}^3\Pi < {}^1\Delta < {}^3\Sigma^+ < {}^1\Pi(0.50\ \mathrm{eV})$ 97

B.14 IV - TiCu: $X^4\Phi < 1^4\Sigma^- < 1^4\Pi < 1^4\Delta < {}^2\Delta < {}^2\Phi \cdots < 2^4\Phi(0.90\ \mathrm{eV})$ 98

B.15 V - TiAg: $X^4\Phi < 1^4\Sigma^- < 1^4\Pi < 1^4\Delta < {}^2\Delta < {}^2\Phi \cdots < 2^4\Phi(0.81\ \mathrm{eV})$ 99

B.16 VI - TiAu: $X^4\Phi < {}^4\Sigma^- < {}^4\Pi < {}^4\Delta < {}^2\Delta < {}^2\Phi < {}^2\Pi < {}^2\Sigma^-(0.54\ \mathrm{eV})$ 99

B.17 VII - VCu: $X^5\Delta < 1^5\Pi < {}^5\Sigma^- < {}^5\Sigma^+ < {}^5\Phi < 2^5\Pi \cdots < 2^5\Delta(0.92\ \mathrm{eV})$ 100

B.18 VIII - VAg: $X^5\Delta < 1^5\Pi < {}^5\Sigma^+ < {}^5\Sigma^- < {}^5\Phi < 2^5\Pi \cdots < {}^3\Phi(0.56\ \mathrm{eV})$ 100

B.19 IX - VAu: $X^5\Delta < {}^5\Pi < {}^5\Sigma^- < {}^5\Phi < {}^3\Sigma^- < {}^3\Pi < {}^3\Delta < {}^3\Phi(0.60\ \mathrm{eV})$ 101

B.20 X - CrCu: $X^6\Sigma^+ < {}^8\Sigma^+(1.19\ \mathrm{eV}) < 2^6\Sigma^+ < {}^4\Sigma^+$ 102

B.21 XI - CrAg: $X^6\Sigma^+ < {}^8\Sigma^+(1.12\ \mathrm{eV}) < 2^6\Sigma^+ < {}^4\Sigma^+$ 102

B.22 XII - CrAu: $X^6\Sigma^+ < {}^8\Sigma^+(1.95\ \mathrm{eV})$ 103

B.23 XIII - MnCu: $X^7\Sigma^+ < 1^5\Sigma^+(0.27\ \mathrm{eV}) < {}^5\Pi < 2^5\Sigma^+ < {}^5\Delta$ 103

B.24 XIV - MnAg: $X^7\Sigma^+ < 1^5\Sigma^+(0.31\ \mathrm{eV}) < {}^5\Pi < 2^5\Sigma^+ < {}^5\Delta$ 104

B.25 XV - MnAu: $X^7\Sigma^+ < {}^5\Sigma^+(0.66\ \mathrm{eV})$ 104

B.26 XVI - FeCu: $X^6\Delta < 1^4\Delta < 1^6\Pi < {}^6\Sigma^+ < 1^4\Pi < {}^4\Sigma^- \cdots < 2^4\Delta(0.53\ \mathrm{eV})$ 105

B.27 XVII - FeAg: $X^6\Delta < 1^4\Delta < 1^6\Pi < {}^6\Sigma^+ < 1^4\Pi < {}^4\Sigma^- \cdots < 2^4\Delta(0.50\ \mathrm{eV})$ 106

B.28 XVIII - FeAu: $X^6\Delta < {}^6\Pi < {}^6\Sigma^+ < {}^4\Delta < {}^4\Pi < {}^4\Sigma^+(0.79\ \mathrm{eV})$ 107

B.29 XIX - CoCu: $X^3\Phi < {}^3\Delta < {}^3\Sigma^- < {}^3\Pi(0.07\ \mathrm{eV}) < {}^5\Phi < {}^5\Sigma^- < {}^5\Pi < {}^5\Delta$ 108

B.30 XX - CoAg: $X^3\Phi < {}^3\Sigma^- < {}^3\Delta < {}^3\Pi(0.06\ \text{eV}) < {}^5\Phi < {}^5\Sigma^- < {}^5\Pi < {}^5\Delta$. 108
B.31 XXI - CoAu: $X^5\Phi < {}^5\Sigma^- < {}^5\Pi < {}^5\Delta(0.11\ \text{eV}) < {}^3\Phi < {}^3\Sigma^- < {}^3\Pi < {}^3\Delta$ 109
B.32 XXII - NiCu: $X^2\Delta < 1^2\Sigma^+ < 1^2\Pi(0.08\ \text{eV}) < 2^2\Pi < 2^2\Delta < 1^4\Delta < 1^4\Pi$ 110
B.33 XXIII - NiAg: $X^2\Delta < 1^2\Sigma^+ < 1^2\Pi(0.05\ \text{eV}) < 2^2\Pi < 2^2\Delta < 1^4\Delta < 1^4\Pi$ 111
B.34 XXIV - NiAu: $X^2\Delta < {}^2\Pi(0.08\ \text{eV}) < {}^4\Pi < {}^4\Delta < {}^4\Sigma^- < {}^4\Phi < {}^2\Sigma^- < {}^2\Phi$ 112
B.35 Ground State Symmetries (ACu); Exact $v.$ Approximate 2-Component 112
B.36 Ground State Mapping between $A^+({}^{2\mathrm{S}+1}\mathrm{L}_J)$ and $AB(X^{2\mathrm{S}+1}\Lambda_\Omega)$ 113
B.37 Distribution of States of AB_2 among C_1, C_s, C_{2v}, D_{2h}, $C_{\infty v}$, and $D_{\infty h}$ 114
B.38 Ground State Asymptotes $A+2B$, $AB+B$, $A+B_2$ on the PESs of AB_2 . . 115
B.39 $E(\theta, 2.65\ \text{Å}; {}^2\{A_1 \oplus A_2\})$ by $\left[\sin\left(\frac{x}{2}\right)\right]^{-2} \sum_{k=0}^{12} a_{2k} T_{2k}$; Fitting Coefficients . . 120

List of Figures

B.1 Intramolecular Evolution: Low-Lying Electronic States of V, VAg, and $\mathrm{VAg_2}$ 121

B.2 Energy Levels of the B atoms: $^2\mathrm{S} < {}^2\mathrm{D} < {}^2\mathrm{P}^o$(Cu/Au), $^2\mathrm{S} < {}^2\mathrm{P}^o < {}^2\mathrm{D}$(Ag) . 121

B.3 (Λ,S) Potential Energy Curves for Ground and Low-Lying States of AB:

I - DKH-SA-CASSCF; CAS[$(m+1)$E,7O] Space, 3(Sc) $\leq$ m $\leq$ 10(Ni) . 122

B.4 II - DKH-MRCI(+Q); MRCI{[10+$(m+1)$]E,(5+7)O} Valence Space . 126

B.5 Molecular Spin-Orbit Splittings for Ground and Low-Lying States of:

I - ACu; $X^3\Delta_1$, $X^4\Phi_{3/2}$, $X^5\Delta_{0^\pm}$, $X^6\Sigma^+_{1/2}$, $X^7\Sigma^+_3$, $X^6\Delta_{9/2}$, $X^3\Phi_4$, $X^2\Delta_{5/2}$130

B.6 II - AAg; $X^3\Delta_1$, $X^4\Phi_{3/2}$, $X^5\Delta_{0^\pm}$, $X^6\Sigma^+_{1/2}$, $X^7\Sigma^+_3$, $X^6\Delta_{9/2}$, $X^3\Phi_4$, $X^2\Delta_{5/2}$131

B.7 III - AAu; $X^3\Delta_1$, $X^4\Phi_{3/2}$, $X^5\Delta_{0^+}$, $X^6\Sigma^+_{1/2}$, $X^7\Sigma^+_3$, $X^6\Delta_{9/2}$,$X^5\Phi_5$,$X^2\Delta_{5/2}$132

B.8 Ω Potential Energy Curves for Ground and Low-Lying States of:

I - NiCu; Ni($^3\mathrm{F}_4, {}^3\mathrm{F}_3, {}^3\mathrm{D}_3, {}^3\mathrm{F}_2, {}^3\mathrm{D}_2, {}^3\mathrm{D}_1, {}^1\mathrm{D}_2$) + Cu($^2\mathrm{S}_{1/2}$) 133

B.9 II - NiAg; Ni($^3\mathrm{F}_4, {}^3\mathrm{D}_3, {}^3\mathrm{D}_2, {}^3\mathrm{F}_3, {}^3\mathrm{D}_1, {}^3\mathrm{F}_2, {}^1\mathrm{D}_2$) + Ag($^2\mathrm{S}_{1/2}$) 133

B.10 Electronic Energies of the $^{3,5}\Lambda^{(-)}$ States of CoCu against Sommerfeld's Constant134

B.11 Intermolecular Evolution: Mapping Octagons for $A^+(^{2\mathrm{S}+1}\mathrm{L}_J)$ and $AB(^{2\mathrm{S}+1}\Lambda_\Omega)$ 135

B.12 Electronic Configurations $(\mathrm{s}\sigma\mathrm{s}\sigma^*\mathrm{d}\sigma^*\mathrm{d}\pi^*\mathrm{d}\delta^*)^{m+1}$ in AB $^{2\mathrm{S}+1}\Lambda^{(\pm)}$ States . . . 136

B.13 Ground State Spectroscopic Properties as a Function of Atomic Number (AB)

I - r_e; ACu (2.23 Å $\leq r_e \leq$ 2.64 Å) and AAg (2.41 Å $\leq r_e \leq$ 2.75 Å) . . 137

B.14 II - ω_e; ACu ($184 \leq \omega_e \leq 272$ cm^{-1}) and AAu ($226 \leq \omega_e \leq 242$ cm^{-1}) . 137

B.15 III - D_e; ACu ($0.67 \leq D_e \leq 1.81$ eV) and AAu ($1.59 \leq D_e \leq 2.52$ eV) . 138

B.16 Spin-Orbit Splittings for the A $^{2\mathrm{S}+1}\mathrm{L}$ and AB $X^{2\mathrm{S}'+1}\Lambda$ Ground States 138

B.17 The $E(r)$ Potentials for the BAB $^{2\mathrm{S}+1}\Gamma$ and ABB $^{2\mathrm{S}+1}\Lambda$ States of

I - $\mathrm{ScAg_2}$; $D_{\infty h}$: $^2\{\Sigma^+_g, \Sigma^+_u, \Pi_g, \Pi_u, \Delta_g, \Delta_u\}$ and $^4\{\Sigma^+_u, \Pi_u, \Delta_u\}$ 139

B.19 II - $\mathrm{TiAg_2}$; $D_{\infty h}$: $^{3,5}\{\Sigma^-_g, \Sigma^-_u(2), \Pi_g, \Pi_u(2), \Delta_g, \Delta_u(2), \Phi_g, \Phi_u(2)\}$ 142

B.21 III - $\mathrm{VAg_2}$ 145

B.23 IV - $\mathrm{CrAg_2}$ 148

B.25 V - $\mathrm{MnAg_2}$ 151

B.27 VI - $\mathrm{FeAg_2}$ 154

B.29 VII - $\mathrm{CoAg_2}$ 157

B.31 VIII - $\mathrm{NiAg_2}$ 160

B.33 $E(\theta_{BAB}, r_{AB}; {}^{2\mathrm{S}+1}\Gamma)$ ($D_{\infty h}$ & C_{2v})

I - CuScCu 163

B.34 II - AgScAg . . . 164
B.35 III - AuScAu . . . 165
B.36 IV - CuTiCu . . . 167
B.37 V - AgTiAg . . . 168
B.38 VI - AuTiAu . . . 169
B.39 VII - CuVCu . . . 171
B.40 VIII - AgVAg . . . 172
B.41 IX - AuVAu . . . 173
B.42 X - CuCrCu . . . 175
B.43 XI - AgCrAg . . . 176
B.44 XII - AuCrAu . . . 177
B.45 XIII - CuMnCu . . . 179
B.46 XIV - AgMnAg . . . 180
B.47 XV - AuMnAu . . . 181
B.48 XVI - CuFeCu . . . 182
B.49 XVII - AgFeAg . . . 183
B.50 XVIII - AuFeAu . . . 184
B.51 XIX - CuCoCu . . . 187
B.52 XX - AgCoAg . . . 189
B.53 XXI - AuCoAu . . . 191
B.54 XXII - CuNiCu . . . 193
B.55 XXIII - AgNiAg . . . 195
B.56 XXIV - AuNiAu . . . 197
B.58 $E(r_{AB}, r_{BB}; {}^{2\mathrm{S}+1}\Lambda)$ $(C_{\infty v})$
I - ScCuCu . . . 204
B.59 II - ScCuCu 👁 . . . 205
B.60 III - ScAgAg . . . 206
B.61 IV - ScAuAu . . . 207
B.62 V - TiCuCu . . . 208
B.63 VI - TiAgAg . . . 210
B.64 VII - TiAuAu . . . 211
B.65 VIII - VCuCu . . . 212
B.66 IX - VAgAg . . . 214
B.67 X - VAuAu . . . 215
B.68 XI - CrCuCu . . . 216
B.69 XII - CrAgAg . . . 218
B.70 XIII - CrAuAu . . . 219
B.71 XIV - MnCuCu . . . 220
B.72 XV - MnAgAg . . . 221
B.73 XVI - MnAuAu . . . 222

B.74 XVII - FeCuCu . . . 223
B.75 XVIII - FeAgAg . . . 224
B.76 XIX - FeAuAu . . . 226
B.77 XX - CoCuCu . . . 228
B.78 XXI - CoAgAg . . . 230
B.79 XXII - CoAuAu . . . 232
B.80 XXIII - NiCuCu . . . 234
B.81 XXIV - NiAgAg . . . 236
B.82 XXV - NiAuAu . . . 238
B.83 Low-Lying States ($D_{\infty h}$ & C_{2v} & $C_{\infty v}$)
I - $ScCu_2$ . . . 241
B.84 II - $ScAg_2$ . . . 242
B.85 III - $ScAu_2$ . . . 243
B.86 IV - $TiCu_2$ . . . 244
B.87 V - $TiAg_2$ . . . 245
B.88 VI - $TiAu_2$ . . . 246
B.89 VII - VCu_2 . . . 247
B.90 VIII - VAg_2 . . . 248
B.91 IX - VAu_2 . . . 249
B.92 X - $CrCu_2$ . . . 250
B.93 XI - $CrAg_2$ . . . 251
B.94 XII - $CrAu_2$ . . . 252
B.95 XIII - $MnCu_2$ . . . 253
B.96 XIV - $MnAg_2$ . . . 254
B.97 XV - $MnAu_2$ . . . 255
B.98 XVI - $FeCu_2$ . . . 256
B.99 XVII - $FeAg_2$ . . . 257
B.100 XVIII - $FeAu_2$ . . . 258
B.101 XIX - $CoCu_2$ . . . 259
B.102 XX - $CoAg_2$ . . . 260
B.103 XXI - $CoAu_2$ . . . 261
B.104 XXII - $NiCu_2$ . . . 262
B.105 XXIII - $NiAg_2$ . . . 263
B.106 XXIV - $NiAu_2$ . . . 264
B.107 $E(\theta, r \approx r_e; {}^{2S+1}\Gamma)$ . . . 265
B.108 Lowest State(s) Equilibrium A-B and B-B internuclear distances for:
I - Linear $D_{\infty h}$ CuACu; $r_e(A\mathrm{Cu})$: 2.36 Å (NiCu) - 2.67 Å (ScCu) . . . 269
B.109 II - Bent C_{2v} CuACu; $r_e(A\mathrm{Cu})$: 2.43 Å (NiCu) - 2.72 Å (ScCu) . . . 269
B.110 III - Linear $C_{\infty v}$ ACuCu; $r_e(A\mathrm{Cu})$: 2.47 Å (CoCu) - 3.10 Å (ScCu) . . . 270
B.111 IV - Linear $C_{\infty v}$ ACuCu; r_e(CuCu): 2.26 Å ($ScCu_2$) - 2.39 Å ($MnCu_2$) 270

B.112 V - Linear $D_{\infty h}$ AgAAg; $r_e(A\mathrm{Ag})$: 2.50 Å (NiAg) - 2.74 Å (ScAg) . . . 271
B.113 VI - Linear $C_{\infty v}$ AAgAg; $r_e(A\mathrm{Ag})$: 2.62 Å (CoAg) - 2.85 Å (ScAg) . . 271
B.114 VII - Linear $C_{\infty v}$ AAgAg; r_e (AgAg): 2.60 Å (CrAg$_2$) - 2.65 Å (VAg$_2$) 272
B.115 VIII - Linear $D_{\infty h}$ AuAAu; $r_e(A\mathrm{Au})$; 2.36 Å (NiAu) - 2.60 Å (ScAu) . 272
B.116 IX - Linear $C_{\infty v}$ AAuAu; $r_e(A\mathrm{Au})$: 2.43 Å (NiAu) - 2.64 Å (ScAu) . . 273
B.117 X - Linear $C_{\infty v}$ AAuAu; r_e (AuAu): 2.50 Å (CrAu$_2$) - 2.58 Å (MnAu$_2$) 273

Kurzzusammenfassung

Es wurden 561 elektronische Terme von 48 Übergangsmetall Molekülen AB_n (A = Sc-Ni, B = Cu/Ag/Au, n = 1,2) mit der Multireference Configuration Interaction (MRCI) systematisch untersucht. All-Elektron Rechnungen im Valenz quadruple zeta Basissatz wurden einschließlich skalar relativistischer Effekte mittels des Douglas-Kroll-Hess (DKH) Hamiltonian durchgeführt. Für zweiatomige Moleküle wurden vollständige und glatte Potential Energie Kurven auf dem DKH-CASSCF und DKH-MRCI(+Q) Niveau berechnet. Molekulare Eigenschaften—wie internuklearer Gleichgewichtsabstand (r_e), harmonische Frequenz (ω_e), Anharmonizitätskonstante ($\omega_e x_e$), Dissoziationsenergie (D_e), und Dipole Moment (μ_e)—wurden angegeben. Spin-Bahn-Kopplung, Kern Korrelations Effekte, und der Effekt unvollständiger Basissatz wurden für ausgewählte Systeme untersucht. Für die störungstheoretische Behandlung der Spin-Bahn-Kopplung auf dem DKH-MRCI(+SO) Niveau, wurde die Spin-Bahn-Kopplung variationel auf dem Niveau der exakte 2-Komponenten Dirac Gleichung durchgeführt. Im Grundzustand wurde eine binäre Beziehung zwischen dem einatomigen Ion $A^+(^{2\mathrm{S}+1}\mathrm{L}_J)$ und dem zweiatomigen Molekül $AB(X^{2\mathrm{S}+1}\Lambda_\Omega)$ entdeckt. Für dreiatomige Moleküle wurden zwei Sätze von Potential Energie Flächen mittels kubischer Spline Interpolierung konstruiert. Der erste Satz bildet die molekularen $D_{\infty h}$ und C_{2v} Strukturen und ihre Beziehung sind ab, symbolisiert durch $E(\theta_{BAB}, r_{A\text{-}B}; {}^{2\mathrm{S}+1}\Gamma)$. Der zweite Satz, $E(r_{A\text{-}B}, r_{B\text{-}B}; {}^{2\mathrm{S}+1}\Lambda)$, repräsentiert die lineare ABB Form. Sie wurden zunächst bewertet durch Betrachtung der molekularen Stabilität in Bezug auf die Asymptoten $A + B_2$, $AB + B$, und $A + 2B$—alle im Grundzustand. Außerdem wurden Strukturoptimierungen für die niedrigsten Zustände jedes Isomers durchgeführt.

Abstract

A total of 561 electronic terms of 48 transition metal molecules AB_n (A = Sc-Ni, B = Cu/Ag/Au, n = 1,2) were systematically studied using multireference configuration interaction (MRCI) technique. All-electron calculations, employing valence quadruple zeta basis sets, were performed incorporating scalar relativistic effects by means of the Douglas-Kroll-Hess (DKH) Hamiltonian. For diatomic molecules, full and smooth potential energy curves have been constructed at the DKH-CASSCF and DKH-MRCI(+Q) levels of theory, whereby observable molecular properties—such as equilibrium internuclear distance (r_e), harmonic frequency (ω_e), anharmonicity constant ($\omega_e x_e$), dissociation energy (D_e), and dipole moment (μ_e)—have been reported. Spin-orbit coupling, core correlation effects, and basis set incompleteness have been probed for some selected systems. In order to assess the perturbative treatment of spin-orbit coupling at the DKH-MRCI(+SO) level of theory, spin-orbit coupling was dealt with variationally at the exact 2-component level of theory. A ground state binary relation between the atomic ion $A^+({}^{2\mathrm{S}+1}\mathrm{L}_J)$ and the diatomic molecule $AB(X\,{}^{2\mathrm{S}+1}\Lambda_\Omega)$ has been unveiled. For triatomic molecules, two sets of potential energy surfaces have been constructed using spline interpolation. The $D_{\infty h}$ and C_{2v} molecular structures and the connection between them, are pictured by the first set, symbolised by $E(\theta_{BAB}, r_{A\text{-}B}; {}^{2\mathrm{S}+1}\Gamma)$. The second set, $E(r_{A\text{-}B}, r_{B\text{-}B}; {}^{2\mathrm{S}+1}\Lambda)$, represents the linear ABB form. These are assessed, first, by considering the molecular stabilities with respect to the asymptotes $A + B_2$, $AB + B$, and $A + 2B$—all being in ground state. Secondly, structure optimisation calculations have been performed for the lowest states in each isomer.

چکیده

درمجموع، ۵۶۱ جمله الکترونیِ ۴۸ مولکولِ AB_n ـ $A = \text{Sc-Ni}, B = \text{Cu/Ag/Au}, n = 1{,}2$ ـ شامل فلزات واسطه با استفاده از روش برهمکنش آرایشی چندمرجعی (MRCI) شیمی کوانتوم مورد مطالعه و تحلیل قاعده‌مند قرار گرفته‌اند. محاسبات کامپیوتری، با در نظرگرفتن تمامی الکترون‌ها، توسط توابع پایه چهارگانه ظرفیت انجام شده که در آن اثرات نسبیتی اسکالر با هامیلتونی داگلاس‌ـ کرُل‌ـ هِس (DKH) لحاظ شده‌اند. در مورد مولکول‌های دواتمی، منحنی‌های کامل و پیوسته انرژی پتانسیل در سطوح محاسباتی DKH-CASSCF و DKH-MRCI(+Q) بدست آمده که بر اساس آن خصوصیّات مولکولی مشاهده‌پذیر ـ مانند فاصله بین‌هسته‌ای تعادلی (r_e)، فرکانس هماهنگی (ω_e)، ثابت ناهماهنگی ($\omega_e x_e$)، انرژی تفکیک (D_e) و گشتاور دوقطبی (μ_e) ـ گزارش شده‌اند. جفت‌شدگی اسپین‌ـ مدار، تأثیرات همبستگی الکترون‌های درونی و ناکامل‌بودن توابع پایه برای برخی از سیستم‌ها مورد بررسی قرار گرفته‌اند. به منظور ارزیابی لحاظ اختلالی جفت‌شدگی اسپین‌ـ مدار در سطح نظری DKH-MRCI(+SO) این جفت‌شدگی بواسطه نظریه تغییر توسط محاسبات نسبیتی دقیق ۲ـمولفه‌ای نیز محاسبه گردیده‌است. یک ارتباط که تقارن حالت پایه یون اتمی A^+ را به تقارن حالت پایه مولکول دواتمی AB مرتبط می‌کند آشکار شده‌است. برای مولکول‌های سه اتمی، دو مجموعه سطح انرژی پتانسیل توسط درون‌یابی عددی محاسبه شده‌اند. ساختارهای مولکولی $D_{\infty h}$ و C_{2v} ـ بهمراه ارتباط مابین آنها ـ توسط پتانسیل $E(\theta_{BAB}, r_{A\text{–}B}; {}^{2\mathrm{S}+1}\Gamma)$، و ساختار خطی ABB توسط پتانسیل $E(r_{A\text{-}B}, r_{B\text{-}B}; {}^{2\mathrm{S}+1}\Lambda)$ تصویر شده‌اند. ارزیابی این نتایج نظری، در ابتدا، با در نظر گرفتن پایداری های ملکولی نسبت به مجانب‌های حالت پایه $A + B_2$، $AB + B$ و $A + 2B$ میسر و، سپس، محاسبات بهینه سازی ساختاری برای پایین‌ترین حالت‌ها انجام گردید.

Chapter 1

Introduction

The elucidation of electronic structure of transition metal nanoclusters (clusters of a size in the range of 1-100 nm), synthesised and characterised within the specialised areas of nanoscience,[*] has become in the focus of quite many experimental and theoretical workers in the last two decades.[1–25] Heavy budgets allocated in science, engineering, and medicine—resulting in countless number of active researchers working on the field—is an indication of the importance. Numerous practical and basic studies have evinced lively interest in bimetallic nanoclusters, because they are conceptually interesting and technologically important. Furthermore, due to their fascinating and unusual structural, electronic, optical, and magnetic properties, these nanoclusters have proved useful for various applications. These properties differ significantly from those of monometallic species. In former times, also, monometallic copper, silver, and gold were frequently mentioned in aristocratic medieval literature.[26] In recent times, most of the concentration has pointed towards bimetallic nanoclusters containing the late d-block atoms; in particular, the prototypical group 11 elements (Cu/Ag/Au). These clusters constitute the state intermediate between the extended metallic solids and the atoms. Theoretical description of the *smallest* clusters—i.e., di- and triatomic molecules which may be considered as building blocks for the nanoclusters—can be regarded as fundamental to the present-day problem of the evolution of electronic structure from the atoms to the bulk.

The electronic structure of atoms, as they are brought together to form molecules, evolves in time, in space, and in other dimensions (such as spin) according to the time-dependent Schrödinger equation. The question is how does it evolve as one moves from isolated atoms to the solid phase? Low-lying states of metal atoms, on the one hand, can be passably accurately calculated *via* standard techniques in *ab initio* quantum chemistry. Electronic band structure of infinite metallic solids, on the other hand, is (being) fairly understood using methods of solid state physics. Intermediate size range consisting of finite nanoparticles is discerned to a much lesser extent, and has thereby drawn special notice from many research groups.[27–44]

---

[*] nanomaterials, nanoclusters, nanoelectronics, nanophotonics, nanomagnetism, nanochemistry, nanophysics, nanobiotechnology, nanobiology, nanomedicine, nanodrug delivery, nanotribology, nanoelectromechanical systems, nanosensors, nanomaterials for energy, nanopolymers, nanocomposites, nanometals and plasmonics, nanocarbon materials, nanocatalysts, etc.

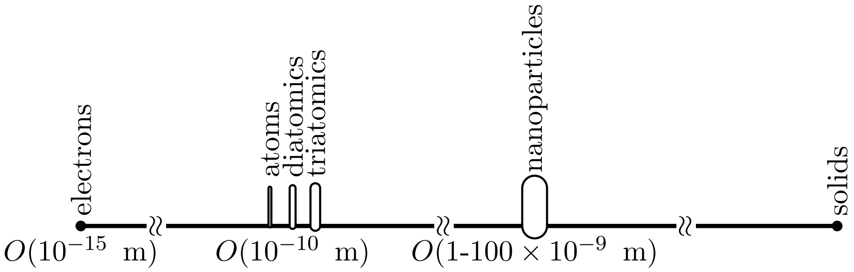

Figure 1.1: Atoms, diatomics, triatomics, and nanoparticles and their relative sizes.

Transition metal nanoparticles (figure 1.1), themselves, consist of *smaller* building blocks: di- and triatomic molecules the understanding of physical and chemical properties of which is of major importance and still remains a significant issue. As it appears that “the particle“ is a continuous distribution of energy through space,[45] and accordingly one can assume there is no end to this breaking the particles into building blocks, the present work concentrates on the di- and triatomic molecules. The work, which elaborates on three homologous sequences of diatomic molecules AB ($A =$ Sc-Ni, $B =$ Cu/Ag/Au) and on three homologous sequences of triatomic molecules AB_2, retrieves fundamental information about these systems, tracing, for the first time, the evolution of electronic structure as a function of size: atoms → diatomics → triatomics. Upon the formation of a triatomic molecule, the electronic states of the reactant system(s), of the intermediate species, and of the product(s) are, according to the theory of potential energy hyper-surface, correlated. This correlation, which has been an important long-standing concept in physics and chemistry, can be described in terms of an *intramolecular* evolution of the electronic structure from separated atoms to the assembled molecules. As an indication of this intramolecular evolution, figure 1.2 shows how the electronic energy levels evolve as one moves from the atom V *via* the diatomic molecule VAg to the triatomic molecule VAg_2; in ideal picture, however, the energy of any state would change continuously and smoothly for $V{+}2Ag \rightleftharpoons VAg{+}Ag \rightleftharpoons VAg_2$. A revelation of direct ground state mappings, unveiling the relationship between the AB and $A'B$ molecules, would provide evidence that electronic structure can unfold also through *intermolecular* evolution. The present work will therefore make a (humble) contribution towards answering the above question, being still a major unsettled interrogation in physical chemistry.

To what extent do the d orbitals take part in the chemical bond of transition metal compounds, and how does the extent of their participation vary as one moves through the Periodic Table?[46] A realistic appreciation of the nature of the bond in a *complete* set of compounds is of paramount importance for both basic science and applications. This work illuminates the cardinal aspects of the class of molecules AB_n ($n = 1, 2$) built from one challenging atom A, and one (two) B atoms with a so-called hydrogen-like electronic configuration. The group 11 elements are thereby relatively more obedient in terms of electron correlation, but unruly in terms of their own complexities including relativity. Since the molecules in question are

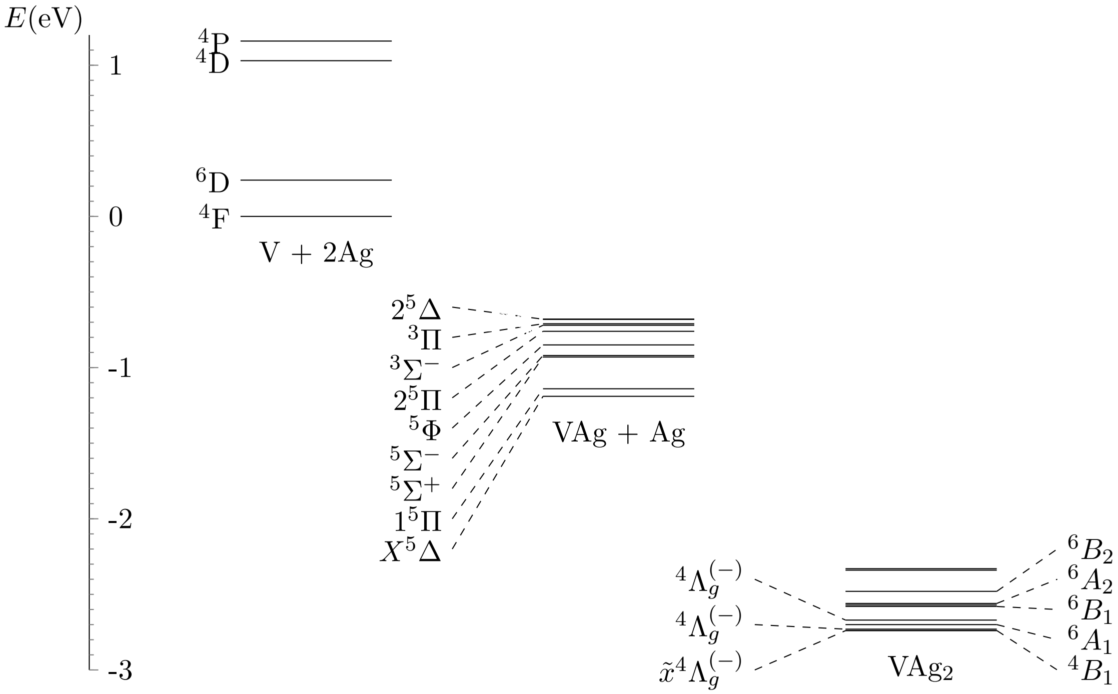

Figure 1.2: Low-lying energy levels for V (experimental J-averaged values), VAg (theoretical), and VAg$_2$ (theoretical).

expected to exhibit similar features, illustrative trends will undoubtedly pop up as one moves horizontally through the 3d series and vertically over the coinage metal set, while indeed treating the entire class uniformly. As A varies (horizontal movement), the general findings, for instance, will indicate how the observable molecular properties, such as the equilibrium A-B internuclear distances and the bond strengths, alter. As B varies (vertical movement), it shall be shown that the bond strengths of Cu systems are slightly less than those of Ag, whereas the molecules containing gold are anomalously more bound. Therefore, some general features of the chemical bonding in the AB_n molecules will be established.

The number of transition metal di- and triatomic molecules, whose spectroscopic information is sufficiently accurately known from experiment, is rather *small.* Previous studies reported on some of the diatomic molecules AB, to the best of one's knowledge, are in detail discussed in subsection 3.1.1; they are less than sufficient. The situation is even worse for the triatomic molecules AB_2; no experimental, nor theoretical, results are procurable for these perplexing particles.

The author of the present contribution commenced doing electronic structure calculations at the university of Tehran, Iran, as early as 2012. He started to work on the ground and low-lying excited states of the heteronuclear diatomic molecules AgAu, CuAg, and CuAu solely embracing the multireference configuration interaction method. The work thereof was published in some international journals[47–49] and, more importantly, provided the prerequisite stepping stones for the present work addressing itself to the problem of obtaining reliable and global description of the ground and low-lying excited states of 24 diatomic molecules

AB and of 24 triatomic molecules AB_2 by pursuing systematic theoretical investigations and by considering a multitude of quasi-degenerate states arising from the ground and low-lying separated atom limits. In the light of the above questions concerning the electronic structure of the AB_n molecules, the present investigation has begun in order to determine or predict spectroscopic constants for the ground and low-lying excited states.

The inaugural aim of the current theoretical research was to unravel the electronic structure and how it evolves for the electronic symmetry species; when two or three transition metal atoms are brought together to form a di- or triatomic molecule. Towards this end, full and smooth potential energy curves have been calculated for the diatomic molecules AB, and spectroscopic constants have been thereby reported in the ΛS representation. Spin-orbit coupling, core-correlation effects, and basis set incompleteness have been investigated for some selected systems. For the triatomic molecules AB_2, the linear BAB, the bent BAB, and the linear ABB structures were examined. Potential energy surfaces were constructed by means of which spectroscopic properties were extracted. These were uniformly assessed by an immense number of subsequent structure optimisation calculations.

Chapter 2 briefly remarks on quantum chemical methodology which has been employed. This chapter also provides details on the computations. In chapter 3 a selection of the results is discussed. Section 3.1 is devoted to the diatomic molecules, and section 3.2 is devoted to the triatomic molecules. Chapter 4 summarises the findings. Finally, the full set of data, with many tables and figures, for all 48 systems (diatomic AB and triatomic AB_2), are provided in the appendices.

Chapter 2

Theory and Computations

In the first part of this chapter basic concepts of the nonrelativistic (or approximate 2-component) and relativistic (or exact 2-component) quantum chemistry—used in the present project for describing the electronic structure of the AB_n molecules—are presented. The configuration interaction model remains a cornerstone of the formalism employed throughout this work; multiconfigurational self-consistent field (MCSCF), complete active space self-consistent field (CASSCF), multireference configuration interaction (MRCI), Kramers-restricted configuration interaction (KRCI), and diagonalising the spin-orbit matrix in a multistate basis are all founded on this model. Although this part of the dissertation is theoretical in scope, due to time limitations, no attempt is made as to theoretical completeness or rigorousness; for further details see refs. 50–64. In the second part of this chapter the necessity of assessing the theoretical results presented on transition metal di- and triatomic molecules and how the assessment was undertaken are discussed. Finally, computational details, within the approximate and exact 2-component relativistic frameworks, are given at the end of this chapter.

2.1 Some Remarks on Methodology

A wide range of experimental observations of some microphysical phenomena and the corresponding theoretical explanations provided the underlying physical ideas based on which a number of postulates were developed in quantum mechanics. The inferential theory, built upon the postulates, leads to the following assumptions whose validity is upheld by its penetrating qualitative as well as quantitative predictive power. The theory assumes that an abstract mathematical entity—a wave function in Schrödinger's formulation, an eigenvector in Heisenberg's matrix approach, and a ket in Dirac's general formalism $|\psi(t)\rangle$—is conceivably assigned to any microphysical system. The time dependent statevector, $|\psi(t)\rangle$, belongs to a Hilbert space and contains all the information about the system and can therefore represent it completely. A mathematical rule (a linear[*] Hermitian[†] operator) is defined in accord with this entity. Upon the application of the operator on $|\psi(t)\rangle$, the statevector is transformed into itself multiplied by a proportionality constant (complex number); $\hat{A}\,|\psi(t)\rangle = \alpha\,|\psi(t)\rangle$. The theory assumes that any dynamical variable—e.g., $\vec{r}(t)$ and $\vec{p}(t)$—corresponds to a linear Hermitian operator whose eigenvectors form a complete basis set.[‡]

The Schrödinger Equation. The time evolution of the state vector $|\psi(t)\rangle$ of the system is unfold by the time-dependent Schrödinger equation $i\hbar\partial\,|\psi(t)\rangle\,/\partial t = \hat{H}\,|\psi(t)\rangle$, where $\hat{H}$ is the Hamiltonian operator corresponding to the total energy of the system. In quantum chemistry, the customary interest is the time-independent Schrödinger equation for systems which possess stationary states, i.e., the potential is independent of time. The physical state of any molecule, containing N electrons—to which electric charge (e), intrinsic spin momentum ($\hat{s}$), and rest mass (m_e) are assigned—and M nuclei, can be quantitatively described by the nonrelativistic time-independent Schrödinger equation. In position representation (red), this equation reads

$$\begin{aligned}\Bigg[&-\sum_{A=1}^{M}\frac{\hbar^2}{2M_A}\nabla^2_{R_A}-\sum_{i=1}^{N}\frac{\hbar^2}{2m_e}\nabla^2_{r_i}-\sum_{A,i}^{M,N}\frac{Z_Ae^2}{|\vec{r}_i-\vec{R}_A|}+\sum_{A>B}\frac{Z_AZ_Be^2}{|\vec{R}_A-\vec{R}_B|}\\&+\sum_{i>j}\frac{e^2}{|\vec{r}_i-\vec{r}_j|}\Bigg]\Psi(\vec{R}_1,\ldots,\vec{R}_M,\vec{r}_1,\ldots,\vec{r}_N)=E\Psi(\vec{R}_1,\ldots,\vec{R}_M,\vec{r}_1,\ldots,\vec{r}_N).\end{aligned} \tag{2.1}$$

See appendix A for the derivation of this equation and for the definitions of the quantities. Within the framework of the so-called clamped nuclei approximation, the nuclei are considered to be fixed because $m_p/m_e \approx 1836$, m_p being the rest mass of proton. Thus, the first term in equation (2.1)—i.e., the kinetic energy of the nuclei—vanishes and the nucleus-nucleus repulsion, $\sum_{A>B} Z_AZ_Be^2/|\vec{R}_A-\vec{R}_B|$, turns into a constant which, from the linearity of Hamiltonian operator, can be transferred into the eigenvalue. This results in the electronic Hamiltonian,

$$\hat{H}_{\text{el}} = -\sum_{i=1}^{N}\frac{\hbar^2}{2m_e}\nabla^2_{r_i}-\sum_{i,A}^{N,M}\frac{Z_Ae^2}{|\vec{r}_i-\vec{R}_A|}+\sum_{i>j}\frac{e^2}{|\vec{r}_i-\vec{r}_j|}, \tag{2.2}$$

which describes the dynamics of N spinless electrons in the electrostatic field of M point charges.[§] The solution of the corresponding Schrödinger equation, $\hat{H}_{\text{el}}\psi_{\text{el}}(\{\vec{r}_i\},\{\vec{R}_A\}) = E_{\text{el}}\psi_{\text{el}}(\{\vec{r}_i\},\{\vec{R}_A\})$, gives electronic energies which parametrically depend on the spatial coordinates of the nuclei, i.e., $E_{\text{el}}(\{\vec{R}_A\})$.

The Spin of Electron. The spin-free Hamiltonian shown in equation (2.2) depends exclusively on the space coordinates of the electrons and nuclei (not on the spin coordinates). However, electrons do possess intrinsic spin[66] which does not correspond closely to anything in classical mechanics. It is assumed that the theory of spin can be built upon a general formalism of the angular momentum (see appendix A), which, in the matrix representation, would lead to $\hat{\vec{J}}^2 \left|j, m_j\right\rangle = \hbar^2 j(j+1) \left|j, m_j\right\rangle$ and $\hat{J}_z \left|j, m_j\right\rangle = \hbar m_j \left|j, m_j\right\rangle$. For the N-electron molecule in question, according to the Russel-Saunders coupling scheme, the total spin operator $\hat{\vec{S}}$ reads $\hat{\vec{S}} = \sum_{i=1}^{N} \hat{\vec{s}}(i)$, where $\hat{\vec{s}}(i)$ is the spin operator corresponding to electron i; $\hat{\vec{s}}^2 \left|1/2, \pm 1/2\right\rangle = \hbar^2 (3/4) \left|1/2, \pm 1/2\right\rangle$, and $\hat{s}_z \left|1/2, \pm 1/2\right\rangle = \pm\hbar(1/2) \left|1/2, \pm 1/2\right\rangle$.

---

[*] For a linear operator $\hat{A}(a\,|\psi\rangle + b\,|\phi\rangle) = a\hat{A}\,|\psi\rangle + b\hat{A}\,|\phi\rangle$. See appendix A for some properties of operators.

[†] For a Hermitian operator $\hat{A}^\dagger = \hat{A}$ where $\langle\psi|\hat{A}^\dagger|\phi\rangle = \langle\phi|\hat{A}|\psi\rangle^*$.

[‡] For a complete basis $\sum_{n=1}^{\infty}|\phi_n\rangle\langle\phi_n| = \hat{I}$.

[§] However, real nuclei have spatial distribution (ref. 65).

The world in which the electrons live is a 5-space; with the coordinates x_1, x_2, x_3, t, and ω. This space corresponds to points whose first four coordinates (x_1, x_2, x_3, t) are expressed in continuous representations. The fifth coordinate ω is an unspecified spin variable which should be dealt with according to the angular momentum algebra; $[\hat{J}_l, \hat{J}_m] = i\hbar\epsilon_{lmn}\hat{J}_n$, and $[\hat{\vec{J}}^2, \hat{J}_l] = 0$. Since the spectra of these operators are discrete (see appendix A), ω should, in principle, be expressed as discrete variable. Within the LS, ΛS, and ΓS coupling schemes ω can be integrated out. In the context of nonrelativistic time-independent formalism, the x_1, x_2, x_3 coordinates are included in the Hamiltonian, while the wave function collectively depends on x_1, x_2, x_3, and ω.[*]

The Construction of Wave Function. In the light of the spin-free electronic Hamiltonian shown in equation (2.2), one can write $[\hat{H}_{\text{el}}, \hat{\vec{S}}^2] = 0$; hence, for the 1-electron system the wave function can be written as $\left|1/2, \pm 1/2\right\rangle \otimes \left|\psi(\vec{r})\right\rangle$. This can be rewritten as $\phi(\boldsymbol{\tau}_i) = f(\omega_i)\psi(\vec{r}_i)$, where $\phi(\boldsymbol{\tau}_i)$ is dubbed spin orbital. The spatial orbital $\psi(\vec{r}_i)$, using the spherical Coulomb potential and in the spherical polar coordinate system, reads $\psi(r_i, \theta_i, \varphi_i) = R_{nl}(r_i) Y_{lm_l}(\theta_i, \varphi_i)$. These spin orbitals ($\left|\phi\right\rangle$) constitute the 1-electron basis for the construction of N-electron wave function ($\left|\Phi\right\rangle$) which—according to the antisymmetry axiom, which is a general form of the Pauli exclusion principle—must by antisymmetric with respect to interchange of the coordinates of any two electrons. This means that $\hat{P}_{ij} \left|\Phi\right\rangle = -\left|\Phi\right\rangle$, or, equivalently,

$$\Phi(\boldsymbol{\tau}_1, \ldots, \boldsymbol{\tau}_i, \ldots, \boldsymbol{\tau}_j, \ldots, \boldsymbol{\tau}_N) = -\Phi(\boldsymbol{\tau}_1, \ldots, \boldsymbol{\tau}_j, \ldots, \boldsymbol{\tau}_i, \ldots, \boldsymbol{\tau}_N), \tag{2.3}$$

where $\boldsymbol{\tau}_i$ denotes both spin (ω) and space (x_1, x_2, x_3) coordinates of electrons, and not time. Equation (2.2), due to the existence of the $\sum_{i,j} e^2/|\vec{r}_i - \vec{r}_j|$ term, does not allow one to write $\Phi(\{\boldsymbol{\tau}_i\})$ as the product of $\phi_i(\boldsymbol{\tau}_1)\phi_j(\boldsymbol{\tau}_2)\ldots\phi_k(\boldsymbol{\tau}_N)$ or in terms of a properly antisymmetrised linear combination of them. The Hartree-Fock theory reduces $\sum_{i,j} e^2/|\vec{r}_i - \vec{r}_j|$ to an effective one electron operator such that $\Phi(\{\boldsymbol{\tau}_i\})$ is separable; the resulting approximate wave function can be expressed as a Slater determinant which, on a basis of K spin orbital, reads $\Phi(\{\boldsymbol{\tau}_i\}) = (N!)^{-1/2} \sum_{n=1}^{N!} (-1)^{P_n} \hat{P}_n \{\phi_i(\boldsymbol{\tau}_1)\phi_j(\boldsymbol{\tau}_2)\ldots\phi_k(\boldsymbol{\tau}_N)\}$.

The introduction of the post Hartree-Fock methods was prompted by the failure of this model in correctly describing some properties such as dissociation of molecules. The configuration interaction method is the first, and perhaps conceptually the simplest, approach that incorporates electron correlation, which is defined as the difference between the exact nonrelativistic energy of the system ($\mathcal{E}_0$) and the Hartree-Fock energy (E_0) obtained in the limit of complete basis set $E_{\text{corr}} = \mathcal{E}_0 - E_0$. The interference phenomenon observed in the double-slit experiment is mathematically formulated by the principle of superposition.[51,67] Ado(a)pting this principle to account for electron correlation leads to an exact wave function that can be written as a linear combination of an *infinite* number of Slater determinants (N-electron basis functions) formed from a *complete* set of spin orbitals (1-electron basis functions). The resulting wave function, therefore, consists of a reference Hartree-Fock determinant which, *via* electronic excitations, can generate the N-electron basis functions. In practice, one has to work with a finite set of spin orbitals, and accordingly with the resultant determinants which are no longer complete. In the full configuration interaction method, the Hamiltonian matrix is diagonalised in the basis of this truncated space which constitutes the reference determinant, the singly excited determinants, etc., up to and including the N-tuply excited determinants. Even for *small* systems and moderately sized 1-electron basis sets, the number of excited determinants is extremely large. Although, neglecting spin-orbit coupling, using spin- and space-adaptation of the wave function one can eliminate a significant number of N-electron basis sets, in most cases the elimination is not enough to make the space parcticable.

---

[*] Based on the unrivalled experience of this work on open-shell transition metal systems, it is thought that it is not enough to incoherently introduce the spin of electrons in an *ad hoc* fashion, i.e., employing a spin-free Hamiltonian operator and thrusting the spin of electrons into the wave function. However—as it is typically undertaken in the contemporary electronic structure theory—the electronic Hamiltonian, for the moment, remains spin-free within the wave function formalism that is touched here.

The Dirac Equation. It is nowadays well-known that in order to correctly describe the chemistry of heavy elements one needs to consider the so-called relativistic effects—i.e., the deviation(s) of results obtained in a theoretical framework which is in accordance with Dirac quantum mechanics, which is formulated in the light of Einstein's theory of special relativity, from those obtained according to Schrödinger quantum mechanics. The continuing development of relativistic molecular orbital (MO) theory is reaching rows of the Periodic Table that are nearly impossible to treat with nonrelativistic approaches. The 1-electron Dirac Hamiltonian is written as

$$\boldsymbol{H}_{\text{D}} = c\boldsymbol{\alpha}\cdot(\boldsymbol{p}+e\boldsymbol{A}) + \boldsymbol{\beta}mc^2 - e\phi\boldsymbol{I}, \tag{2.4}$$

where c is the speed of light, $\boldsymbol{p}(= -i\hbar\boldsymbol{\nabla})$ is the momentum operator, $\boldsymbol{A}$ is the vector potential, and ϕ is the scalar potential. The 4×4 Dirac matrices $\boldsymbol{\alpha}$ and $\boldsymbol{\beta}$ are given by

$$\boldsymbol{\alpha}_t \equiv \begin{pmatrix} \boldsymbol{0}_2 & \boldsymbol{\sigma}_t \\ \boldsymbol{\sigma}_t & \boldsymbol{0}_2 \end{pmatrix}, \ t = (x, y, z), \quad \boldsymbol{\beta} \equiv \begin{pmatrix} \boldsymbol{I}_2 & \boldsymbol{0}_2 \\ \boldsymbol{0}_2 & -\boldsymbol{I}_2 \end{pmatrix}, \tag{2.5}$$

where $\boldsymbol{\sigma}_t$ represents 2×2 Pauli spin matrices comprising

$$\boldsymbol{\sigma}_x \equiv \begin{pmatrix} 0 & 1 \\ 1 & 0 \end{pmatrix}, \boldsymbol{\sigma}_y \equiv \begin{pmatrix} 0 & -i \\ i & 0 \end{pmatrix}, \boldsymbol{\sigma}_z \equiv \begin{pmatrix} 1 & 0 \\ 0 & -1 \end{pmatrix}. \tag{2.6}$$

Since the Dirac equation is only valid for 1-electron systems, the Dirac Hamiltonain has to be extended to an N-electron Hamiltonain to treat the chemically interesting systems. A straightforward way to construct the relativistic N-electron Hamiltonian is to augment the 1-electron Dirac operator, equation 2.4, with a Coulomb or Breit (or its approximate Gaunt) operator or both as a 2-electron term to yield Dirac-Coulomb (DC) or Dirac-Coulomb-Breit (DCB) Hamiltonians.[57,68]

Douglas-Kroll Transformation. In a static potential V, such as that provided by the clamped nuclei approximation, where the vector potential $\boldsymbol{A}$ is zero, the 1-electron Dirac equation can be written as

$$\boldsymbol{H}_{\mathrm{D}} \begin{pmatrix} \Psi^{\mathrm{L}} \\ \Psi^{\mathrm{S}} \end{pmatrix} = \begin{pmatrix} V + mc^2 & c\boldsymbol{\sigma} \cdot \boldsymbol{p} \\ c\boldsymbol{\sigma} \cdot \boldsymbol{p} & V - mc^2 \end{pmatrix} \begin{pmatrix} \Psi^{\mathrm{L}} \\ \Psi^{\mathrm{S}} \end{pmatrix} = E \begin{pmatrix} \Psi^{\mathrm{L}} \\ \Psi^{\mathrm{S}} \end{pmatrix}, \tag{2.7}$$

where Ψ^{L} and Ψ^{S} are the large and small components and E is the energy of the particle. The 2-component relativistic approach can be obtained by block-diagonalisation of the Dirac Hamiltonian with a suitable unitary operator, $\boldsymbol{U}$, that removes the off-diagonal blocks as follows:

$$\boldsymbol{U}\boldsymbol{H}_{\mathrm{D}}\boldsymbol{U}^{\dagger} = \begin{pmatrix} H_{+} & 0 \\ 0 & H_{-} \end{pmatrix}. \tag{2.8}$$

Consequently, the 2-component equation can be solved as $H_{+}\Phi = E\Phi$, which gives the eigenvalues for the electronic solution of the original Dirac equation. Douglas and Kroll[69] proposed a procedure to decompose the overall transformation, $\boldsymbol{U}$, into a sequence of simpler unitary transformations, $\boldsymbol{U} = \ldots \boldsymbol{U}_3\boldsymbol{U}_2\boldsymbol{U}_1\boldsymbol{U}_0$. The Douglas-Kroll transformation correct to second order in the external potential has been extensively studied by Hess and co-workers[70,71] and has become one of the most familiar quasi-relativistic approaches. The Douglas-Kroll-Hess (DKH) method is another term frequently used for the DK method in honour of the pioneering work of Hess.[68]

2.2 Assessment of the Results

Method-inherent errors, which are arisen form the approximations invoked through the history of quantum chemistry, do not allow one to warrant that theoretical results can be assessed independently of experimental inputs. On the other hand, the apparent lack of experimental data on the AB_n molecules shows that the theoretical output of the present work cannot be evaluated on the basis of comparison with dependable experimental information. In the present work, for the diatomic systems, comparison is made between the theoretical results and the experimental data limitedly available for some of the diatomic systems. For the triatomic molecules, none of which has been experimentally characterised, absolute accuracy has been attempted to be evaluated by devising a computational strategy which, with the aim of self-consistency, undertakes self-assessment. This strategy has provided unique, uniform, and universal representations of the low-lying electronic states of the AB_2 molecules using two sets of potential energy surfaces, a series of structure optimisation calculations, and a multitude of additional single point calculations. It is therefore fervently hoped that, in the light of globally reliable picture of the AB_2 molecules which is thoroughly assessed, the path for experimental observation of these molecules has been cleared out. Just like the $\mathrm{BeH_2}$ molecule that had been long the subject of theoretical studies (ref. 72 and refs. therein), and afterwards, it was observed in the gas phase in the work of Bernath *et al.* in 2002.[73]

Consistent conception conceived from theory to
consonant conceptualisation concocted from experiment

It has long been recognised that a reliable quantitative description of the electronic structure requires *ab initio* methods which are capable of sufficiently incorporating electron correlation and relativistic effects. In comparison to main group chemistry, the involvement of transition metal atoms (A = Sc-Ni) in the molecule will definitely complicate the calculations due primarily to their d-type open-shell nature. The molecule—built from transition metal atoms A having electronic configurations $\mathrm{3d}^{m-2}\mathrm{4s}^2/\mathrm{3d}^{m-1}\mathrm{4s}^1$, where $m = 3$(Sc)-10(Ni)—will inherit the open-shell nature in such a way that the complexity of electronic structure is substantially amplified. This is, firstly, because of the fact that the interaction of electrons in molecules is more difficult to describe than in atoms; due to the external field imposed by the bounded atoms, symmetry is degraded and, in turn, the electronic states split into the corresponding irreducible representations of the resulting low-order point group. For example, the combination of 4 (10) atomic terms in Hund's case a (c) leads to 56 (224) ΓS (spin-orbit coupled) molecular states which, in point group $C_{\infty v}$, are termed: ${}^3\mathrm{F}_{\mathrm{Ti}}\oplus{}^2\mathrm{S}_B(2)$ and ${}^5\mathrm{F}_{\mathrm{Ti}}\oplus{}^2\mathrm{S}_B(2) \longrightarrow {}^1\Sigma^-\oplus{}^1\Pi\oplus{}^1\Delta\oplus{}^1\Phi\oplus{}^3\Sigma^-(3)\oplus{}^3\Pi(3)\oplus{}^3\Delta(3)\oplus{}^3\Phi(3)\oplus{}^5\Sigma^-(3)\oplus{}^5\Pi(3)\oplus{}^5\Delta(3)\oplus{}^5\Phi(3)\oplus{}^7\Sigma^-\oplus{}^7\Pi\oplus{}^7\Delta\oplus{}^7\Phi$. Secondly, since the atomic states of the metal centre mix heavily as the chemical bond is formed, the number of electronic configurations dominating the low-lying wave functions increases dramatically. Thirdly—as this work will illustrate—the degree of mixing depends on the molecular structures on which the electronic state exhibits minimum. Thus, globally tried-and-true determination of potential energy hyper-surfaces requires unbiased flexibility in the configuration mixing and orbital optimisation. This is to be achieved in such a way that smoothness of connection between two arbitrary points on $E(x_1, x_2, x_3; {}^{2\mathrm{S}+1}\Gamma)$—$(x_1, x_2, x_3)$ being a triple representing 3 degrees of freedom in a triatomic molecule and ${}^{2\mathrm{S}+1}\Gamma$ being the electronic state under consideration—is fully guaranteed.

Table 2.1 compiles a list containing some of the programmes which were used in this work in order to acquire, to process, to visualise, to analyse, and to interpret the theoretical data.

2.3 Computations: Douglas-Kroll-Hess Framework

Scalar relativistic effects were taken into account by means of the Douglas-Kroll-Hess (DKH) method.[68–71] The all-electron valence quadruple-ζ Gaussian basis sets (dubbed def2-QZVPP) were employed for the 3d metal atoms Sc-Cu.[80] The segmented all-electron relativistically contracted (SARC) Gaussian basis sets, again of valence quadruple-ζ quality, were used for

Table 2.1: List of main programmes used in this work

programme	task	diatomic[a]	triatomic	reference
MOLPRO	*ab initio*	✓	✓	74,75
ORCA	*ab initio*	✓	✗	76,77
DIRAC	relativistic *ab initio*	✓	✗	78
LEVEL	spectroscopic constants	✓	✗	79
Gnuplot	potential energy surfaces	✗	✓	-
Veusz	potential energy curves	✓	✗	-
LaTeX	typesetting	✓	✓	-

[a] Marks (✓and ✗) indicate whether the programme was used or not.

Ag and Au.[81] Guided by the previous work on the heteronuclear diatomic molecules,[47–49] the Au basis set was augmented with two g functions taken from the def2-QZVPP basis.[80] However, it was ascertained that augmenting the Ag basis does not improve the accuracy of the results with respect to the experiment.[47,48] Even though the Ag basis might convey an impression of being "small",[*] noticeable improvement was not witnessed with addition of f and g functions. Hence, the generally contracted basis sets finally used comprise

$$\begin{array}{l} \\ \text{Sc-Cr} \\ \text{Mn-Cu} \\ \text{Ag} \\ \text{Au} \end{array}
\begin{array}{c} \begin{array}{ccccc} \text{s} & \text{p} & \text{d} & \text{f} & \text{g} \end{array} \\ \begin{pmatrix} 24 & 18 & 9 & 3 & 2 \\ 24 & 18 & 10 & 4 & 2 \\ 19 & 14 & 9 & - & - \\ 22 & 15 & 11 & 6 & 2 \end{pmatrix} \end{array}
\rightarrow
\begin{array}{c} \begin{array}{ccccc} \text{s} & \text{p} & \text{d} & \text{f} & \text{g} \end{array} \\ \begin{bmatrix} 11 & 6 & 5 & 3 & 2 \\ 11 & 6 & 5 & 4 & 2 \\ 12 & 9 & 5 & - & - \\ 17 & 11 & 8 & 2 & 2 \end{bmatrix} \end{array}.$$

For the ground state of NiCu, a sequence of aug-cc-pVnZ-DK basis sets (n = T, Q, and 5) was used to estimate the complete basis set (CBS) limit by extrapolation of total energies *via* the formula $E_n(r) = E_{\text{CBS}}(r) + A(r)e^{-(n-1)} + B(r)e^{-(n-1)^2}$, where r is the internuclear distance, E_{CBS} is the energy when basis set approaches completeness, and A and B—both depending on r—are the unknowns.[82]

In order to incorporate both static and dynamic electron correlation at the scalar relativistic level of theory, complete active space self-consistent field followed by multireference configuration interaction were employed—CASSCF + 1 + 2 = MRCI. As zeroth-order ansatz, a wave function of CASSCF type was used where the orbitals 3d4s(A) + ks(B), k=4(Cu), 5(Ag), 6(Au) were included in the correlation treatment. Wave functions for the terms arising from the lowest asymptotes $A(^{2\text{S}+1}\text{L}) + nB(^2\text{S})$, $n = 1, 2$, were calculated using the state-averaged CASSCF (SA-CASSCF) method.[83–86] Therefore, the outer-valence orbitals were correlated, and the filled and highly contracted inner-valence orbitals—i.e., the molecular counterparts of the d orbitals of the B atoms—were, in most cases, constrained to be doubly occupied. For NiCu, for instance, the molecular counterparts of the 3d4s (Ni) and 4s (Cu) orbitals were chosen yielding CAS(11,7). All states having doublet spin multiplicity, i.e., $^2\Lambda^{(\pm)}, \Lambda = \Sigma^+, \Sigma^-, \Pi, \Delta, \Phi, \ldots$, and dissociating to the first six separated atom limits at the CASSCF level (not the experimentally lowest limits), i.e., Ni $3d^84s^2(^3F \oplus {}^1D \oplus {}^3P \oplus {}^1G)$ + Cu $4s^1(^2S)$ and Ni $3d^94s^1(^3D \oplus {}^1D)$ + Cu $4s^1(^2S)$, were computed. The orbitals thus obtained were utilised for the CASSCF calculations of the quartet states, and for the subsequent MRCI jobs.

---

[*] Although the relative *size* of basis sets is typically a heated debate among authors and peer-reviewers, whence many are idling to justify whether a basis is *big* or *small*, "So long as big and small are merely relative concepts, it is no help to explain the big in terms of the small. It is therefore necessary to modify classical ideas in such a way as to give an absolute meaning to size." P.A.M Dirac in ref. 50.

The internally contracted variant of the MRCI approach,[87,88] as implemented in MOLPRO, and the individually selecting MRCI procedure,[86] as implemented in ORCA, were cooperatively employed in order to study the low-lying electronic states of the set of diatomic molecules AB (A = Sc-Ni, B = Cu/Ag/Au). The molecules TiCu, TiAg, VCu, VAg, CrCu, CrAg, MnCu, MnAg, FeCu, FeAg, CoCu, CoAg, and NiAu were studied using the individually selecting MRCI, while the molecules ScB, TiAu, VAu, CrAu, MnAu, FeAu, CoAu, NiCu, and NiAg were investigated using the internally contracted MRCI. All of the triatomic molecules were treated with the internally contracted MRCI. These are written here as MRCI[$(m'$+$m'')$E,$(n'$+$n'')$O]; where $'$ denotes the involvement of electron or orbital at the CAS reference wave functions while $''$ denotes the involvement of electron or orbital at the MRCI promotions. For NiCu, MRCI[(10+11)E,(5+7)O] means that the d (Cu) orbitals were correlated at the MRCI level whereas the d(Ni) + s(Ni) + s(Cu) orbitals were taken into account in the reference as well as the MRCI promotions. The simplest and most widely used correction to the MRCI energy, i.e., the Davidson method, was used to partly rectify the size-consistency errors.[89]

For the diatomic molecules, the outer-core correlation effects on the ground state spectroscopic constants were investigated (cMRCI). The orbitals which were included in the MRCI excitations consist of 3s3p3s3p (ACu), 3s3p4s4p (AAg), 3p5p (TiAu and VAu), and 3s3p5s5p4f (the rest of AAu molecules). For the $^3\Delta$ state ($^3A_1$ state) of VAu, the MRCI expansions contain approximately 5.5×10^6 for the [(10+6)E,(5+8)O] space and 22.5×10^6 contracted configurations for the [(22+6)E,(11+8)O] space. For the *ab initio* calculations it was highly favourable to employ full symmetry ($C_{\infty v}, D_{\infty h}$) for linear species (diatomic molecules and linear triatomic structures). The quantum chemical tools which were used, however, are limited to abelian point groups (D_{2h} and its subgroups). There, nevertheless, exists some tools in which the symmetry is fully utilised; the diatomic problem of Ti_2 was addressed in an MRCI study (ref. 90) where the $D_{\infty h}$ symmetry was utilised in the calculations.

Spin-orbit matrix[91] was diagonalised in the basis of SA-CASSCF or MRCI wave functions. The diagonal elements of the resulting Hamiltonian were replaced by the Davidson corrected DKH-MRCI energies. In addition to the DKH-MRCI-(SO) level, where spin-orbit coupling was calculated *a posteriori*, an independent relativistic method was employed for the atoms and diatomic molecules ACu in order to assess the reliability of the scalar results. Despite the fact that relativistic effects are expected to be larger for silver- and gold-containing molecules attempts to relativistically describe these systems were not successful, primarily due to the expensive calculations.

2.4 Computations: Exact 2-Component Framework

In the exact 2-component (X2C) calculations, the uncontracted triple-ζ basis sets (dyall-v3z) were used for the atomic calculations except Au. For the gold atom and the diatomic molecules ACu, due to the expensiveness, the size of basis sets was reduced even further; namely, dyall-v2z. The large components of dyall-v3z consist of

$$\begin{array}{l c} & \begin{array}{ccccc} \mathrm{s} & \mathrm{p} & \mathrm{d} & \mathrm{f} & \mathrm{g} \end{array} \\ \begin{array}{l} \mathrm{Sc} \\ \mathrm{Ti\text{-}Cu} \\ \mathrm{Ag} \end{array} & \begin{pmatrix} 23 & 16 & 9 & 4 & 2 \\ 23 & 16 & 9 & 3 & 2 \\ 28 & 20 & 13 & 3 & 2 \end{pmatrix}, \end{array}$$

and the large components of dyall-v2z consist of (15s11p6d2f) for Sc, Ti, V, Fe, Co, Ni, Cu, and (24s19p12d9f) for Au.[92–95]

The molecular spinors were optimised using the average-of-configuration Dirac-Hartree-Fock (AC-DHF).[96] For the atomic calculations, m valence electrons, $3 \leq m \leq 11$, were allotted among six Kramers pairs originating from $(k-1)$d+ks; written here as AC-DHF($m|6$). The Kramers-restricted configuration interaction (KRCI) approach[97] was employed on top. In the case of ScCu, for example, the generalised active space (GAS) was subdivided into three parts; SD10E(4in7)SD20KPs. Within the inner-valence spinors ($\mathrm{d_{Cu}}$) two holes were allowed. In (4in7), four electrons were distributed among $\mathrm{3d_{Sc}4s_{Sc}}$ and $\mathrm{4s_{Cu}}$. And, the virtual space—SD20KPs—consisted of 20 Kramers pairs to which excitations took place.

Chapter 3

Results

This work has constructed a plethora of potential energy curves, surfaces, and hyper-surfaces for low-lying electronic states of the molecules AB_n correlating to the separated atom limits

$$A(3\mathrm{d}^{m-2}4\mathrm{s}^2/3\mathrm{d}^{m-1}4\mathrm{s}^1\ {}^{2\mathrm{S}+1}\mathrm{L}) + nB\Big[(k-1)\mathrm{d}^{10}k\mathrm{s}^1\ {}^2\mathrm{S}\Big],$$

where $A = $ Sc-Ni, $B = $ Cu/Ag/Au, $n = 1$ or 2, $2\mathrm{S}+1$ ranges from 1 to 7, L is either S, or D, or F, $m = 3$(Sc)-10(Ni), and $k = 4$(Cu), 5(Ag), or 6(Au).

The first part of this chapter is devoted to the diatomic molecules AB, and the second part is devoted to the triatomic molecules AB_2. Since the number of electronic states considered in the present project is truly immense, the in detail discussion is, unfortunately, limited to some selected systems; the electronic structures of the diatomic molecule FeCu and of the triatomic molecule $\mathrm{ScCu_2}$ are discussed individually. The isovalent species—FeAg, FeAu, $\mathrm{ScAg_2}$, and $\mathrm{ScAu_2}$—are very briefly touched at the appropriate places. Some illustrative comments on CrB, CoB, NiB, TiB_2, VB_2, and CrB_2 are also made. Attentive reader is recommended to peer at the appendices for a complete survey. The selection is, nevertheless, carefully made in order that the fascinating physics of the triatomic molecules AB_2, and of course the atomic and diatomic constituents, are unveiled within an integrated body.

3.1 The Diatomic Molecules *AB*

3.1.1 Overview

In what follows the previous scrutiny on the diatomic molecules AB is given. Then, tabular and graphical collections which are presented in the appendices are introduced.

Several experimental[98–112] and theoretical[113–115] investigations have been reported for some of the diatomic molecules AB ($A = $ Sc-Ni, $B = $ Cu/Ag/Au) and their ions. The experimental dissociation energies of homo- and heteronuclear diatomic molecules built from transition metal atoms were discussed in a review.[98] The diatomic molecules XAu ($X = $ Ni,Co,Fe) were shown to exist in the vapour phase over liquid solutions of gold and transition metals at temperatures above 1800 K.[99] Gaseous VAu was observed by high-temperature mass spectrometry and its dissociation energy was determined.[100] The CrCu molecule was, however, quite challenging.[103–105] Initially, CrCu was formed in a krypton matrix at 4 K and it was indicated that the molecule has a ground state of $^6\Sigma$ symmetry.[103] Shortly afterwards, an erratum was added in which the authors drew the conclusion that CrCu most probably has an $^8\Sigma$ ground state term.[104] Then, two years later, CrCu, CrAg, and CrAu were observed in solid rare-gas matrices at 4 K and a $^4\Sigma$ ground state was assigned to CrCu.[105]

The MnAg molecule was trapped in rare-gas matrices at 4 K, and, using electron spin resonance spectroscopy, a $^7\Sigma$ ground state term was determined.[101] The dissociation energy of MnAu was measured using mass spectrometric studies. By analogy with the MnH hydride, a $^7\Sigma$ ground state term was assumed also for MnAu.[102] Resonant two-photon ionisation spectroscopy was applied, firstly, to identify six band systems of NiCu and to determine the ground state ($X^2\Delta_{5/2}$),[106] and then, subsequently, to analyse and rotationally resolve a total of nine band systems connecting the $3\mathrm{d}^9_{\mathrm{Ni}}3\mathrm{d}^{10}_{\mathrm{Cu}}\sigma^2\ ^2\Delta$ ground state to the $3\mathrm{d}^8_{\mathrm{Ni}}3\mathrm{d}^{10}_{\mathrm{Cu}}\sigma^2\sigma^{*1}$ manifold of states.[107] Having obtained detailed spectroscopic analysis of NiCu in refs. 106 and 107, the authors developed a ligand-field theory for transition metal diatomic molecules having electronic configurations of $\mathrm{d}^9_A\mathrm{d}^{10}_B\sigma^2$, $\mathrm{d}^9_A\mathrm{d}^9_B\sigma^2$, and $\mathrm{d}^8_A(^3\mathrm{F})\mathrm{d}^{10}_B\sigma^2\sigma^{*1}$. Applying their model to the $\mathrm{d}^9_{\mathrm{Ni}}\mathrm{d}^{10}_{\mathrm{Cu}}\sigma^2$ manifold of states in NiCu and to other systems, they demonstrated that their ligand-field model[*] has some validity for diatomic molecules containing nickel.[108] Using dispersed fluorescence, low-lying electronic terms of NiCu were investigated and four out of the five terms from the $3\mathrm{d}^9_{\mathrm{Ni}}3\mathrm{d}^{10}_{\mathrm{Cu}}\sigma^2$ manifold were observed.[109] Spectroscopic investigations showed that NiAu possesses a $^2\Delta_{5/2}$ ground state term, and is in this respect analogous to the isovalent molecule NiCu.[110] A further dispersed fluorescence study provided spectroscopic information about the ground and low-lying excited terms of NiAu.[111] On the theoretical side, full potential energy curves were obtained for the ground and low-lying terms of CrCu using the multireference configuration interaction approach.[113]

Table B.2—containing 5 pages and being compiled in the appendices—lists a multitude of energy levels of the metal atoms A and B together with the theoretical errors associated with various levels of theory employed in the present work. Necessary group theoretical analyses to switch from atomic terms to molecular terms and from (Λ,S) representation to Ω representation are given in tables B.3 (ScB), B.4 (TiB), B.5 (VB), B.6 (CrB), B.7 (MnB), B.8 (FeB), B.9 (CoB), and B.10 (NiB).

Figures B.3 and B.4 display the potential energy curves for the ground and low-lying (Λ,S) states of the diatomic molecules AB obtained at the DKH-CASSCF and DKH-MRCI(+Q) levels of theory. Notice that, except for NiAu, the inner-valence orbitals, i.e., the d orbitals of the B atoms, were not correlated at the DKH-CASSCF level. These potential curves have allowed to detail the spectroscopic information associated with the ΛS terms. The spectroscopic constants—including equilibrium internuclear distance (r_e), harmonic frequency (ω_e), first anharmonicity constant ($\omega_e x_e$), dissociation energy (D_e), dipole moment (μ_e), and main configuration weight (MCW)—were extracted from the DKH-MRCI(+Q) potential energy curves and are gathered in tables B.11 (ScCu), B.12 (ScAg), B.13 (ScAu), B.14 (TiCu), B.15 (TiAg), B.16 (TiAu), B.17 (VCu), B.18 (VAg), B.19 (VAu), B.20 (CrCu), B.21 (CrAg), B.22 (CrAu), B.23 (MnCu), B.24 (MnAg), B.25 (MnAu), B.26 (FeCu), B.27 (FeAg), B.28 (FeAu), B.29 (CoCu), B.30 (CoAg), B.31 (CoAu), B.32 (NiCu), B.33 (NiAg), and B.34 (NiAu). The preliminary stage towards the current project on the AB_n molecules was passed through by elaborately describing the ground and low-lying excited states of (in chronological order) AgAu, CuAg, and CuAu. The theoretical characterisation thereof provided a couple of *small* pieces enriching the experimental authoritative masterpiece written on the perplexing puzzle of the electronic structure of these species by Bishea and co-workers.[46,116,117] Heteronuclear coinage metal diatomic molecules possess a closed-shell ground state of $^1\Sigma^+$ symmetry that is relatively *simple*. The ground state properties have been therefore reported in many studies. In the excited states, however, the electronic structure becomes complicated due mainly to the involvement of open-shell D-type states. Reliable theoretical description of the excited states requires one to understand the difficulties arisen from the open-shell nature that was briefly reviewed in the previous chapter. Furthermore, *relativity* and the large spin-orbit splitting of the ^{2}D term of gold causes *special* issues that need to be *generally* considered. This work, at this point, reminds itself of the key findings on these compounds, in both ΛS and Ω representations. For more details see refs. 47 (AgAu), 48 (CuAg), and 49 (CuAu).

---

[*] Further evidence will be accumulated in this study that this model holds also for the ground states of the diatomic molecules AB.

3.1.2 The Diatomic Molecules BB'

The B atoms. The coinage metal atoms B (Cu,Ag,Au) uniformly possess a ^{2}S ground state term that derives from the electronic configuration $(k-1)\mathrm{d}^{10}k\mathrm{s}^1$. In the absence of spin-orbit coupling, the experimental separation energies for the transitions $(k-1)\mathrm{d}^9k\mathrm{s}^2\ ^2\mathrm{D} \leftarrow (k-1)\mathrm{d}^{10}k\mathrm{s}^1\ ^2\mathrm{S}$ are 1.49 eV (Cu), 3.97 eV (Ag), and 1.74 eV for Au (J-averaged energies). For the transitions $(k-1)\mathrm{d}^{10}k\mathrm{p}^1\ ^2\mathrm{P}^o \leftarrow (k-1)\mathrm{d}^{10}k\mathrm{s}^1\ ^2\mathrm{S}$, the separation energies (see figure B.2) are 3.81 eV (Cu), 3.74 eV (Ag), and 4.95 eV (Au).[118] Notice, firstly, that in the case of Ag, the excited state $^2\mathrm{P}^\mathrm{o}(4\mathrm{d}^{10}5\mathrm{p}^1)$ lies below $^2\mathrm{D}(4\mathrm{d}^9 5\mathrm{s}^1)$: $E(^2\mathrm{P}^\mathrm{o}) = 3.74$ eV and $E(^2\mathrm{D}) = 3.97$ eV. From this one may assume that the electronic intricacy in silver containing systems ($A\mathrm{Ag}_n$) is substantially less than the electronic intricacy in copper and gold homologs. Moreover, concerning the Au atom, one important point that one must bear in mind is that the 5s and 5p electrons are in the same region of space as the 5d electrons (ref. 119). Therefore, in addition to the valence 5d6s orbitals, the 5s5p orbitals should be included in the correlation treatment.[*] The differential 5p-5d correlation was shown to decrease the $^2\mathrm{D} \leftarrow {}^2\mathrm{S}$ separation energy.[120,121] Secondly, in the case of the third-row transition metal atoms (including Au) the J-averaging method is considered to be rather controversial. However, because the LS terms $5\mathrm{d}^{10}6\mathrm{s}^1\ ^2\mathrm{S}$ ($E = 0$), $5\mathrm{d}^9 6\mathrm{s}^2\ ^2\mathrm{D}$ ($E_{J\text{-avg.}} = 1.74$ eV), and $5\mathrm{d}^{10}6\mathrm{p}^1\ ^2\mathrm{P}^o$ ($E_{J\text{-avg.}} = 4.95$ eV) are energetically well separated from each other as compared to the spin-orbit splittings—i.e.,

---

[*] This argument has also some validity, but to a much lesser extent, in Cu (3s,3p,3d) and Ag (4s,4p,4d).

1.52 eV for ^{2}D : $J' = 3/2 \leftarrow J'' = 5/2$ and 0.47 eV for ^{2}P^o : $J' = 3/2 \leftarrow J'' = 1/2$—the J-averaging approximation might still be of some validity for the Au atom. On the other hand, for the Ni atom, the ^{3}D and ^{3}F terms are much close to each other ($\Delta E = 0.03$ eV) than their individual spin-orbit splittings, i.e., 0.19 eV for ^{3}D : $J' = 1 \leftarrow J'' = 3$ and 0.27 eV for ^{3}F : $J' = 2 \leftarrow J'' = 4$.[118]

BB′. As compared with the homonuclear diatomic molecules (Cu$_2$/Ag$_2$/Au$_2$), there has been experimentally little attention on heteronuclear molecules; especially because of difficulties in their synthesis. As zeroth-order ansatz, a wave function of CASSCF type was uniformly used, constructed by allotting 22 valence electrons to a total of 12 molecular orbitals transforming as the set of $(k-1)\mathrm{d}_B \oplus k\mathrm{s}_B \oplus (k-1)\mathrm{d}_{B'} \oplus k\mathrm{s}_{B'}$ atomic orbitals at the separated atom limit. The inclusion of merely s and d orbitals is an optimal choice which simultaneously allows feasibility and acceptability. The CASSCF wave functions for 8 (44) electronic terms of CuAg and AgAu (CuAu), arising from the interactions $B(^2\mathrm{S}) + B'(^2\mathrm{S}) \longrightarrow {}^{1,3}\Sigma^+ B(^2\mathrm{S}) + B'(^2\mathrm{D}) \longrightarrow {}^{1,3}\{\Sigma^+ \oplus \Pi \oplus \Delta\} B(^2\mathrm{D}) + B'(^2\mathrm{D}) \longrightarrow {}^{1,3}\{\Sigma^+(3) \oplus \Sigma^-(2) \oplus \Pi(4) \oplus \Delta(3) \oplus \Phi(2) \oplus \Gamma\}$ were taken into consideration. Based on the DKH-MRCI(+Q) calculations, BB' possesses a $X^1\Sigma^+(X0^+)$ ground state which is dominated by the configuration $|\psi_{^1\Sigma^+}\rangle = |\mathrm{d}_B^{10}\mathrm{d}_{B'}^{10}\mathrm{s}\sigma^2\mathrm{s}\sigma^{*0}\rangle$. This notation suggests that the d orbitals of both parental atoms do not contribute to the bonding and remain in the nature of atomic orbitals. The ground state ket can also be written in the form $|\psi_{^1\Sigma^+}\rangle = |\mathrm{d}\sigma^2\mathrm{d}\pi^4\mathrm{d}\delta^4\mathrm{d}\delta^{*4}\mathrm{d}\pi^{*4}\mathrm{d}\sigma^{*2}\mathrm{s}\sigma^2\mathrm{s}\sigma^{*0}\rangle$. This notation indicates that the ΛS excitations from the d-type orbitals to sσ^* will follow the same trend as that of the molecular orbitals. This is confirmed by the energy ordering obtained: $2^3\Sigma^+ < 1^3\Pi < 1^3\Delta$. Nevertheless, due to multireference character, a different order is seen for singlet states.

At the DKH-MRCI(+Q) level, the $X^1\Sigma^+$ ground state dissociates to $B(^2\mathrm{S}) + B'(^2\mathrm{S})$ with D_e of 1.65 eV (ref. 48), 2.05 eV (ref. 47), and 2.24 eV (ref. 49) for CuAg, AgAu, and CuAu, respectively. As intuitively expected for the hydrogen-like systems, the ground state bonding (sσ orbital) arises mainly from the overlap of the s atomic orbitals. The bonding molecular orbital of BB' is of σ symmetry; at $r = r_e$ the σ molecular orbital consists of $\mathrm{s}(B) + \mathrm{d}_{z^2}(B) + \mathrm{s}(B') + \mathrm{d}_{z^2}(B')$ and at $r \to \infty$ the σ orbital corresponds to $\mathrm{s}(B) + \mathrm{s}(B')$. Spin-orbit coupling has practically no influence on the $X^1\Sigma^+$ ground state of BB'. This can be explained, first, by the closed-shell character of $X^1\Sigma^+$. Second, the ground state is not asymptotically influenced by spin-orbit coupling, because it correlates to $B(^2\mathrm{S}_{1/2}) + B'(^2\mathrm{S}_{1/2})$. For excited states, however, spin-orbit coupling can affect the spectroscopic constants substantially. The excited states of the coinage metal dimers with $\Omega' = 0^+$ all tend to have some ion-pair character. This character derives from the separated ion limit

$$B^+\Big[(k-1)\mathrm{d}^{10}k\mathrm{s}^0\ {}^1\mathrm{S}\Big] + B'^-\Big[(k-1)\mathrm{d}^{10}k\mathrm{s}^2\ {}^1\mathrm{S}\Big],$$

from which only one 0^+ state arises. The transition from the $X0^+$ ground state to the 0^+ ion-pair state is a charge transfer transition and should be extremely intense. The ion-pair 0^+ state experiences a long-range Coulomb attraction that will certainly pull it into the energy subspace considered in this project. However, at and around r_e, the 0^+ states arisen from the ion-pair and the valence separated atom limts mix heavily resulting in polarised orbitals whose appearance would differ fundamentally from the atomic orbitals at $r \to \infty$.

AgAu. The spectroscopic constants of the $X^1\Sigma^+$ ground state* were calculated to be $r_e = 2.56$ Å, $\omega_e = 183.0$ cm^{-1}, $\omega_e x_e = 0.56$ cm^{-1}, and $D_e = 2.05$ eV. The vibrational constants show fair agreement with the experimental values: $\omega_e'' = 198.22 \pm 0.11$ cm^{-1} and $\omega_e x_e'' = 0.512 \pm 0.002$ cm^{-1} (refs. 116,122).[47] The spin-orbit eigenstates, arising from the interactions Ag(^{2}S$_{1/2}$) + Au(^{2}S$_{1/2}$), Ag(^{2}S$_{1/2}$) + Au(^{2}D$_{5/2}$), and Ag(^{2}S$_{1/2}$) + Au(^{2}D$_{3/2}$) were calculated *via* diagonalisation of the Breit-Pauli Hamiltonian matrix represented in the basis of the ΛS wave functions. On the basis of the eigenstates—which are linear combinations of the unperturbed ΛS states (configurations)—the excited $A0^+$ and $B1$ states are composed mainly of $^1\Sigma^+$(64%) and $^1\Pi$(48%) configurations. Therefore, in accordance with the selection rules in the standard ΛS coupling notation[52] ($\Sigma^+ \leftrightarrow \Sigma^+$, $\Sigma^+ \leftrightarrow \Pi$, $\Delta S = 0$), within the energy range of interest the $A0^+$ and $B1$ levels can be excited *via* electric dipole transitions, while most of the other transitions in this range are electric-dipole forbidden and cannot be readily observed. The associated spectroscopic constants were obtained with fair accuracy at the DKH-MRCI(Q)-SO level of theory. For the $A0^+$ state they were calculated as (experimental values in parentheses): $\omega_e = 100(115.7)$ cm^{-1}, $\omega_e x_e = 0.71(0.74)$ cm^{-1}. For the $B1$ state $\omega_e = 75.5(92.6)$ cm^{-1}, $\omega_e x_e = 0.92(1.06)$ cm^{-1}.[47,116,122] The $A0^+$ state shows a multireference character with two dominant configurations involving the promotions s$\sigma^* \leftarrow$ dσ^*; $^1\Sigma^+$(64%) and s$\sigma^* \leftarrow$ dπ^*; $^3\Pi$(16%). Since, upon inclusion of spin-orbit coupling, the $^3\Pi$ state splits to the 0^+, 0^-, 1, and 2 components, and the $^1\Sigma^+$ state splits to 0^+, the experimental assignment of $\Omega = 0^+$ for the A state is exquisitely confirmed. It is interesting to perceptively observe how spin-orbit coupling influences $\omega_e x_e$ and D_e for the $A0^+$ state. The degree of spin-orbit stabilisation is shown to vary as a function of the internuclear separation. The greater stabilisation at the separated atom limit relative to the equilibrium position decreases the well depth, leading to a larger anharmonicity and *smaller* dissociation energy for the $A0^+$ state as compared to the parental $A^1\Sigma^+$ state.

CuAg. This diatomic molecule was the second one that was extensively investigated. In addition to the $^{1,3}\{\Sigma^+(2)\oplus\Pi\oplus\Delta\}$ states, deriving from Cu(^{2}S)+Ag(^{2}S) and Cu(^{2}D)+Ag(^{2}S), a $^1\Sigma^+$ state was initially found to lie low in energy showing significant contribution from the Cu$^+$Ag$^-$ ion-pair state. The strongest evidence that the $^1\Sigma^+(0^+)$ state of CuAg is dominated by the ion-pair Cu^+Ag^- is the close correspondence of the potential energy curve of the CuAg $^1\Sigma^+(0^+)$ state with the ion-pair curve of the Cu^+Ag^- $^1\Sigma^+(0^+)$ state obtained from the $-e^2/r$ attractive potential. Furthermore, the dipole moment and the wave function composition of the CuAg $^1\Sigma^+(0^+)$ state were both suggestive of considerable mixing with Cu^+Ag^- (for further details see ref. 48). Scalar relativistic effects were also probed for CuAg. Thus, potential energy curves at three levels of theory were calculated: MRCI(+Q), DKH-MRCI(+Q), and DKH-MRCI+(SO). Scalar relativistic effects are shown to increase the binding strengths for the excited states; for example for the $^3\Pi$ state $\omega_e(\text{rel.}) - \omega_e(\text{nonrel.}) = 25.4\ \text{cm}^{-1}$ and $D_e(\text{rel.}) - D_e(\text{nonrel.}) = 0.16$ eV. Furthermore, they stabilise the excited states $2^1\Sigma^+$ and $^1\Pi$ by 0.32 eV and 0.60 eV. This is due to the well-known relativistic stabilisation of the ns orbitals and the relativistic destabilisation of the $(n-1)$d orbitals.[48]

---

*It should be stressed that there has been no experimental measurement for the ground state bond length of AgAu, which might be simplistically dubbed as "a simple" or "a well-known" diatomic molecule. In general, the electronic structure of a diatomic molecule depends on the energy levels, the spin, and the spatial symmetries (in the LS scheme) of the constituent atoms. Without having gained adequate insight into the situation at separated atom limits, it is impossible to provide global survey of the low-lying molecular states. H_2, C_2, Pt_2, and U_2 are all "just" diatomic molecules. Reliable theoretical elucidation of electronic structure—e.g., determination of full ΛS and Ω potential energy curves and the assessment of the absolute accuracy—in the latter cases is predicted to be far beyond what standard tools nowadays can handle. It can be therefore asserted that, despite highly developed modern software, before studying the molecular properties of diuranium the atomic situation should be known. In a same manner, the electronic states of d- and f- block diatomic molecules need be thoroughly described prior to the study of larger clusters.

CuAu. For the ground state, at the DKH-MRCI (DKH-cMRCI) level, the spectroscopic constants are $r_e = 2.35$ Å(2.34 Å) and $D_e = 2.24$ eV(2.32 eV) with the Davidson correction included. Comparison with available experimental data—i.e., $r_0 = 2.3302 \pm 0.0006$ Å and $D_0^0 = 2.341 \pm 0.095$ eV—reveals that the ΛS results are already in good agreement with experiment. The $X^1\Sigma^+$ ground state has a dipole moment that is oppositely oriented to the one found for the $3^1\Sigma^+$ state: $\mu(X^1\Sigma^+, r_e) = -2.56$ D corresponding to $^{\delta+}$Cu-Au$^{\delta-}$ and $\mu(3^1\Sigma^+, r_e) = +0.12$ D corresponding to $^{\delta-}$Cu-Au$^{\delta+}$. Hence, the $3^1\Sigma^+ \leftarrow X^1\Sigma^+$ transition has a large charge transfer nature and should be very intense. The oscillator strength calculated for this electronic transition is f=0.17.[49]

To summarise, complementing experimental data, affluent characterisation of the ground ($X0^+$) and low-lying exited states of the diatomic molecules BB' ($B = B' =$ Cu/Ag/Au), with and without considering relativistic effects (scalar effects and spin-orbit coupling), has been given in refs. 47 (AgAu), 48 (CuAg), and 49 (CuAu). At the ΛS DKH-MRCI(+Q) level of theory, the theoretical results on the $^1\Lambda^{(+)}$ excited states did not come to agreement with experimental data. In the presence of spin-orbit coupling, however, not only the experimental data were accurately reproduced, but also some tentative arguments on the excited states were verified. Having succeeded[*] in accurately describing the S- and D-type states of the BB' molecules, this work is encouraged to go on. The next aim is to conduct a systematic study of *real* transition metal molecules whose ground state cannot be easily distinguished in terms of energy from the excited states.

3.1.3 The Diatomic Molecules FeB

FeCu. The Fe atom possess a ^{5}D ground state term which derives from the 3d^{6}4s^2 electronic configuration. The excited terms ^{5}F and ^{3}F both arise from the configuration 3d^{7}4s^1 and lie at 0.87 eV and 1.49 eV (J-averaged energies).[118] Table B.2 shows that the energy ordering of ^{5}D < ^{5}F < ^{3}F can be reproduced at the DKH-CASSCF(8E,6O) level of theory; $E(^5\mathrm{F}) = 0.49$ eV and $E(^3\mathrm{F}) = 1.32$ eV. The Cu atom, on the other hand, exhibits a ^{2}S ground term which arises from the 3d^{10}4s^1 configuration. The DKH-CAS(11E,6O) calculations, incorrectly, yield a lowest state of ^{2}D symmetry for Cu. Thus, the atomic results indicate that for the FeCu molecule undertaking a CAS space of (9E,7O)—i.e., correlating the 3d4s orbitals of Fe and the 4s orbital of Cu—will lead to a lowest separated atom limit of Fe(^{5}D) + Cu(^{2}S). However, adding the 3d orbitals of Cu preferentially stabilises the Cu ^{2}D state such that the lowest separated atom limit becomes Fe(^{5}D) + Cu(^{2}D).

---

[*] Note that the definition of "success" is, here, based on classical ideas comprising of reproduction of experimental data. In subsection 3.2.2, this work, lacking of experimental data on $ScCu_2$ and needing for assessment of the results, gives an absolute meaning to "success". There, "success" is not reproducing the experimental data, but invariance of a property regardless of changes in the conditions of quantum chemical calculation.

For transition metal compounds nothing can guarantee that the ground state will necessarily correlate to the ground state separated atom limit, i.e., where the constituent atoms are in their lowest level. In fact, according to recent findings on the iron diatomic molecules TiFe (ref. 123) and Fe$_2$ (ref. 124), one expects the $^5\mathrm{F}_{\mathrm{Fe}}$-type molecular states to play important role in the depiction of the low-energy electronic structure of the FeB molecules. Thus, for the calculations on FeCu, the LS terms ^{5}D (Fe), ^{5}F (Fe), and ^{2}S (Cu) have been considered. The interaction of Fe(^{5}D) + Cu(^{2}S) and Fe(^{5}F) + Cu(^{2}S), in accordance with the Wigner-Witmer rules,[125] gives rise to the ΛS molecular terms $^{4,6}\{\Sigma^+ \oplus \Sigma^- \oplus \Pi(2) \oplus \Delta(2) \oplus \Phi\}$ (see table B.8). These, after inclusion of spin-orbit coupling, lead to the Ω terms $\frac{1}{2}(19)$, $\frac{3}{2}(16)$, $\frac{5}{2}(12)$, $\frac{7}{2}(8)$, $\frac{9}{2}(4)$, $\frac{11}{2}$.

The ΛS potential energy curves for the ground and low-lying excited states of FeCu, based on the DKH scalar relativistic approach obtained at the CASSCF and MRCI levels of theory, are displayed in figures B.3 and B.4. The potential curves were calculated in a pointwise manner by performing single point calculations for 45 internuclear distances in the range from 1.80 Å to 8.00 Å. Although the CASSCF and MRCI curves differ markedly from each other, they both imply that (a) the lowest (but not the most bound) state of FeCu is $X^6\Delta$ which is energetically so close to the excited states, (b) the quartet states arisen from the second separated atom limit Fe(^{5}F) + Cu(^{2}S) are substantially more bound than all of the states arisen from the lowest limit Fe(^{5}D) + Cu(^{2}S), and (c) the sextet states arisen from the second limit are repulsive or at most only very weakly bound.

To quantitatively describe the electronic structure of FeCu, spectroscopic constants were extracted from the potential energy curves and are compiled in table B.26. The $X^6\Delta$ ground state of FeCu arises from the open-shell configuration $\mathrm{d}_{\mathrm{Cu}}^{10}\,\mathrm{s}\sigma^2\,\mathrm{s}\sigma^{*1}\,\mathrm{d}\delta^{*3}\,\mathrm{d}\pi^{*2}\,\mathrm{d}\sigma^{*1}$(88%) and minor contributions from excited configurations. At the DKH-MRCI[(10+9)E,(5+7)O] level, the ground state $X^6\Delta$ corresponds to the molecular properties $r_e = 2.44$ Å, $\omega_e = 193.6$ cm^{-1}, $\omega_e x_e = 1.90$ cm^{-1}, $D_e = 0.67$ eV, and $\mu = 2.24$ D. Correlating the molecular counterparts of the 3s3p orbitals in both atoms—i.e., DKH-MRCI[(26+9)E,(13+7)O], one obtains $r_e = 2.48$ Å and $D_e = 0.58$ eV. Therefore, for the FeCu $X^6\Delta$ ground state, correlation effects elongate the bond length (r_e) by 0.04 Å and decrease the binding strength (D_e) by 0.09 eV.

The first excited state of FeCu is computed to be of $^4\Delta$ symmetry and to lie above $X^6\Delta$ with an electronic energy (T_e) of 0.04 eV. The FeCu $1^4\Delta$ state has a slightly shorter equilibrium bond length of 2.39 Å, a larger harmonic frequency of 209.4 cm^{-1}, and a *smaller* dissociation energy of 0.63 eV, as compared to the ground state. The FeCu $1^4\Delta$ state is more multireference in character than the $X^6\Delta$ ground state and is dominated by the configurations $\mathrm{d}_{\mathrm{Cu}}^{10}\,\mathrm{s}\sigma^2\,\mathrm{s}\sigma^{*2}\,\mathrm{d}\delta^{*3}\,\mathrm{d}\pi^{*2}$ (51%) and $\mathrm{d}_{\mathrm{Cu}}^{10}\,\mathrm{s}\sigma^2\,\mathrm{s}\sigma^{*1}\,\mathrm{d}\delta^{*3}\mathrm{d}\pi^{*2}\,\mathrm{d}\sigma^{*1}$ (33%). The electronic energies of the excited states $1^6\Pi$, $^6\Sigma^+$, and $1^4\Pi$—all of which dissociate to Fe(^{5}D) + Cu(^{2}S)—are obtained to be 0.07 eV, 0.08 eV, and 0.10 eV, respectively. One should note, however, that the electronic energies for the lowest 4 excited states are *smaller* than the norm of error in separation energy for the $^5\mathrm{F} \leftarrow {}^5\mathrm{D}$ transition of iron atom at the DKH-MRCI(+Q) level of theory, i.e., $||E_{\mathrm{Ref}} - E_{\mathrm{Calc}}|| = 0.10$ eV (see table B.2).

The $^4\Sigma^-$ state of FeCu is calculated to lie 0.25 eV above $X^6\Delta$ and to correlate with Fe(^{5}F) + Cu(^{2}S). Hence, it has the largest D_e and ω_e among the (Λ,S) states which were considered; $D_e = 1.39$ eV and $\omega_e = 229.6$ cm^{-1}. In view of the configurations dominating the wave functions—where the spin of electrons is singled out from the spatial coordinates—one can, with many question marks and from a naïve point of view, justify the stronger chemical bond of $^4\Sigma^-$ relativie to $X^6\Delta$ in such a way as to comply with “the simple* picture that chemists carry in their heads”.[53] The singly bonded $X^6\Delta$ state (*vide supra* and figure B.12) has one molecular orbital of σ symmetry that is fully occupied, while the $^4\Sigma^-$ state—primarily associated with the $\mathrm{d}_{\mathrm{Cu}}^{10}\,\mathrm{s}\sigma^2\,\mathrm{s}\sigma^{*1}\,\mathrm{d}\delta^{*2}\mathrm{d}\pi^{*4}$ (66%) triply bonded configuration—has molecular orbitals of σ and π symmetries being completely filled. According to selection rules in the standard ΛS-coupling notation, electronic transitions from the $X^6\Delta$ ground state to $1^6\Pi$, to $2^6\Delta$, and to $2^6\Pi$ are allowed. It is, however, well-known that spin-orbit coupling causes, firstly, splitting of multiplet electronic states which is usually accompanied by (slight) energy stabilisation which is due to the level shift (ΔE) experienced by the lowest component of the ground state $X^{2\mathrm{S}+1}\Lambda^{(\pm)}(X_\Omega)$ through the interaction with some excited $^{2\mathrm{S}'+1}\Lambda^{(\pm)}$ state (ref. 126)

$$\Delta E(X^{2\mathrm{S}+1}\Lambda^{(\pm)}, \Omega = X_\Omega) = \frac{-|\,\langle {}^{2\mathrm{S}'+1}\Lambda'^{(\pm)}(X_\Omega)|\,\hat{H}_{\mathrm{SO}}\,|X^{2\mathrm{S}+1}\Lambda^{(\pm)}(X_\Omega)\rangle\,|^2}{[E({}^{2\mathrm{S}'+1}\Lambda^{(\pm)}) - E(X^{2\mathrm{S}+1}\Lambda^{(\pm)})]}.$$

Secondly, spin-orbit coupling yields symmetry-allowed mixing between states with different spin-space symmetries, destroying the validity of S as a good quantum number.

The spin-orbit matrix was diagonalised in the basis of 14 $^{2\mathrm{S}+1}\Lambda^{(\pm)}$ wave functions and yielded 60 Ω states in Hund’s case (c),[127] 40 of which lie low in energy and are shown in figure B.5. The lowest Ω term is predicted to be $\Omega = \frac{9}{2}$ which lies 0.05 eV below the parental $X^6\Delta$ state. The ground state symmetry of $^6\Delta_{\frac{9}{2}}$, obtained at the DKH-MRCI+(SO) level of theory, is in agreement with $\Omega = \frac{9}{2}$ for the ground state of FeCu from the X2C-KRCI calculations (see table B.35). Table B.8 shows that, among the spin-orbit components of ^{5}D—i.e., $J = 4, 3, 2, 1, 0$—Fe(^{5}D$_4$) + Cu(^{2}S$_{1/2}$) is the only asymptote to which the $X\frac{9}{2}$ ground state can correlate. One should note that, sometimes, the spin-orbit eigenstates are contaminated through minor contributions from intruder states. For example, the third term of $\Omega = \frac{7}{2}$ symmetry is dominated by the $1^6\Pi$ state with a weight of 88%. This $\Omega = \frac{7}{2}$ term lies above the ground $\Omega = \frac{9}{2}$ term with vertical excitation energies of 0.10 eV and is contaminated with the involvement of $^6\Sigma^+$. As can be seen from table B.8, the $^6\Sigma^+$ term can only give rise to the components $\Omega = \frac{1}{2}$ or $\frac{3}{2}$ or $\frac{5}{2}$ (and not $\Omega = \frac{7}{2}$).

---

*or simplistic

FeAg and FeAu. For FeCu and FeAg, all of the 14 (Λ,S) states correlating to the separated atom limits Fe(^{5}D) + B(^{2}S) and Fe(^{5}F) + B(^{2}S) were included in the calculations. In the case of FeAu, however, only the lowest limit Fe(^{5}D) + Au(^{2}S) was considered. Tables B.26, B.27, and B.28 show that the FeB molecules uniformly possess a ground state of $^6\Delta$ symmetry. As it can be seen from figure B.4, the second asymptote Fe(^{5}F) + B(^{2}S) gives rise to two sets of electronic states: the $^4\Lambda$ and $^6\Lambda$ states, where $\Lambda = \Sigma^-$, Π, Δ, Φ. As the internuclear distance decreases from asymptotic values, e.g., $r < 5$ Å, the cluster of quartet states becomes energetically separated from the cluster of sextet states, with the former being considerably lowered in energy. By analogy with the systems Fe(^{5}F) + Cu(^{2}S) and Fe(^{5}F) + Ag(^{2}S), it is predicted that the Fe(^{5}F) + Au(^{2}S) system will lead to quartet states which are strongly bound as compared to the sextets. The sextet states deriving from Fe(^{5}F) + Cu(^{2}S) are bound to a much lesser extent than those from Fe(^{5}F) + Ag(^{2}S); at the DKH-MRCI(+Q) level, for the $2^6\Delta$ state $D_e = 0.04$ eV (FeCu) and $D_e = 0.21$ eV (FeAg). It should be emphasised that the FeB $^4\Lambda$ states correlating to Fe(3d^{7}4s^1 ^{5}F) + B(ks^1 ^{2}S) are more bound than all of the quartet and sextet states resulting from Fe(3d^{6}4s^2 ^{5}D)+B(ks^1 ^{2}S). In the light of the DKH-MRCI(+Q) results on FeCu and FeAg, one can write

$$\frac{D_e[\mathrm{Fe}B(X^6\Delta)]}{D_e[\mathrm{Fe}B(^4\Sigma^-)]} \approx 50\%.$$

If this relation can be generalised to FeAu, the FeAu $^4\Sigma^-$ state dissociating to Fe(^{5}F)+Au(^{2}S) should have $D_e \simeq 3.7$ eV. This means that, considering the relation $T_e(^6\Delta \leftarrow {}^4\Sigma^-) = D_e(^4\Sigma^-) - D_e(^6\Delta) - T_e(^5\mathrm{F} \leftarrow {}^5\mathrm{D})$, the FeAu $^4\Sigma^-$ state should lie ≈ 1 eV below the $^6\Delta$, which, in this work, is assigned as the ground state of FeAu.

It is interesting to examine the $^4\Lambda$ states originating from Fe(^{5}D) + B(^{2}S) and the $^4\Lambda$ states originating from Fe(^{5}F) + B(^{2}S), B = Cu/Ag. As the internuclear distance decreases and as the quartet states arisen from Fe(^{5}D) + B(^{2}S) become energetically separated from each other, the $1^4\Pi$ and $1^4\Delta$ states descend much further in energy than $^4\Sigma^+$; e.g., for FeCu, at the DKH-MRCI(+Q) level, the electronic energies are $T_e(1^4\Delta) = 0.04$ eV, $T_e(1^4\Pi) = 0.10$ eV, and $T_e(^4\Sigma^+) = 0.34$ eV. The rationale is that the quartet states ($^4\Lambda$) originating from Fe(^{5}F) + B(^{2}S) are strongly bound; i.e., $D_e[\mathrm{Fe}B(^4\Lambda)]$ is calculated to be in the range from 1.11 eV to 1.48 eV. The descent of the quartet states from the second asymptote profoundly influences the quartet states resulting from the first asymptote, provided that the space symmetry of the quartet states is similar. Because of the repulsive interactions $1^4\Delta \leftrightarrow 2^4\Delta$ and $1^4\Pi \leftrightarrow 2^4\Pi$, the $1^4\Delta$ and $1^4\Pi$ states come to lie below $^4\Sigma^+$, for which there are no states of same space symmetry descending from Fe(^{5}F) + B(^{2}S).

The energy ordering of the electronic states in FeCu and FeAg, based on the DKH-MRCI(+Q) calculations, is $X^6\Delta < 1^4\Delta < 1^6\Pi < {}^6\Sigma^+ < 1^4\Pi < {}^4\Sigma^- < {}^4\Phi < {}^4\Sigma^+ < 2^4\Pi < 2^4\Delta$. The highest state of this sequence, $2^4\Delta$, corresponds to $T_e = 0.53$ eV (FeCu) and 0.50 eV (FeAg). Theoretical results indicate that the electronic states of FeAu fall in the energetic order $X^6\Delta < {}^6\Pi < {}^6\Sigma^+ < {}^4\Delta < {}^4\Pi < {}^4\Sigma^+(T_e = 0.79$ eV). At the DKH-MRCI(+Q) level, the ground state dissociation energies of FeB are 0.67 eV (FeCu), 0.77 eV (FeAg), and 1.86 eV (FeAu), respectively. From FeCu to FeAg, the ground state D_e is slightly increased by 15 % while from FeAg to FeAu it shows a drastic increase of 142 %. For the FeCu and FeAg molecules outer-core correlation effects decrease $D_e(X^6\Delta)$ by 0.09 eV and 0.18 eV, and for FeAu they increase $D_e(X^6\Delta)$ by 0.13 eV. The experimental dissociation energy of FeAu, obtained from the Knudsen mass spectrometric method, is available: $D_0^0 = 1.95 \pm 0.22$ eV.[98] Since no electronic term is experimentally assigned, it is presumed that the reported value corresponds to the ground state. The experimental value of D_0^0 agrees well with the theoretical dissociation energy $D_e[\mathrm{FeAu}(X^6\Delta)] = 1.86$ eV and 1.99 eV without and with outer-core correlation effects. One should note, however, that experimental dissociation energies based on the third-law method are prone to error by much more than the published error bounds.[2,128]

3.1.4 The Diatomic Molecules CrB, CoB, and NiB

Cr*B*. With respect to the complexity of electronic structure, the CrB molecules are the simplest cases investigated in this work. They all possess a well isolated $X^6\Sigma^+$ ground state which correlates to the lowest asymptote Cr(^{7}S) + B(^{2}S). At the DKH-MRCI(+Q) level, the lowest excited state of CrB is $^8\Sigma^+$ which has electronic energy of $T_e = 1.19$ eV (CrCu), 1.12 eV (CrAg), and 1.95 eV (CrAu). Low-lying electronic states of CrCu had previously come under an MRCI scrutiny.[113] The investigators utilised a full valence CAS(17,12) as the active space, in contrast to the CAS(7,7) space that was used in the present study. For the $X^6\Sigma^+$ ground state, their DKH-MRCI[17E,12O]/ANO calculations led to $r_e = 2.47$ Å, $\omega_e = 183.6$ cm^{-1}, and $D_e = 1.20$ eV. The present DKH-MRCI[(10+7)E,(5+7)O] study leads to $r_e = 2.47$ Å, $\omega_e = 208.9$ cm^{-1}, and $D_e = 1.21$ eV. Hence, as pointed out in ref. 113, extending the active space from CAS(7,7) to CAS(17,12) has an insignificant or at most *small* influence on spectroscopic constants.[*]

It is worth to mention that the experimental determination of the character of the ground state term of CrCu was quite challenging.[103–105] In chronological order, the $^6\Sigma$,[103] $^8\Sigma$,[104] and $^4\Sigma$[105] symmetries were proposed as correct answers. Note that the symmetry of the most recent proposition of $^4\Sigma$ cannot be derived from the lowest asymptote Cr(^{7}S) + B(^{2}S). Surprisingly, the theoretical result, $X^6\Sigma^+$, predicted in ref. 113 and now confirmed by this

---

[*] In general, although it is necessary to dynamically correlate the filled shell $k\mathrm{d}_B^{10}$ in order to obtain a reliable quantitative description of the low-lying terms of the AB_n species, inclusion of this shell in the CAS calculations is unnecessary. In fact, since none of the diatomic terms (roughly 200 in total) considered in the present study correlates to atomic asymptotes

$$A(^{2\mathrm{S}+1}\mathrm{L}) + B\Big[(k-1)\mathrm{d}^9 k\mathrm{s}^2\ {}^2\mathrm{D})\Big],$$

where d-hole states of the coinage metal atoms B are involved, the inclusion of the $k\mathrm{d}_B^{10}$ shell in the reference space would result in convergence troubles.

work, is in agreement with the earliest proposition made on the basis of experiment.[103]

Co*B*. Unlike other subclasses, the CoB molecules do not exhibit the same ground state term; at the DKH-MRCI(+Q) level, the CoCu and CoAg molecules possess $X^3\Phi$, while the CoAu molecule has $X^5\Phi$. According to potential energy curves of the CoCu $^{3,5}\Lambda$ and the CoAg $^{3,5}\Lambda$ states shown in figure B.4, the cluster of triplet states lies below the cluster of quintet states, whereas for CoAu the situation is reversed. For the CoB $^5\Lambda \leftarrow {}^3\Lambda$ transitions, energy differences are calculated to be in the ranges 1.14-1.52 eV (CoCu), 0.86-1.48 eV (CoAg), and $-$[0.27-0.53] eV (CoAu). On the one hand, due to the comparatively *small* separation energies for the atomic transitions $b^4\mathrm{F} \leftarrow a^4\mathrm{F}$ (0.42 eV) and $a^2\mathrm{F} \leftarrow a^4\mathrm{F}$ (0.88 eV), one expects that some of the $^{3,5}\Lambda$ and $^{1,3}\Lambda$ states resulting from $\mathrm{Co}(b^4\mathrm{F}) + B(^2\mathrm{S})$ and $\mathrm{Co}(a^2\mathrm{F}) + B(^2\mathrm{S})$ play important role in the low-energy terms of the CoB molecules. On the other hand, throughout all molecules AB, the interaction

$$A(3\mathrm{d}^{m-1}4\mathrm{s}^1\ {}^{2\mathrm{S}+1}\mathrm{L}) + B\left[(k-1)\mathrm{d}^{10}k\mathrm{s}^1\ {}^2\mathrm{S}\right]$$

has been shown to be stronger than that of $3\mathrm{d}^{m-2}4\mathrm{s}^2$. Hence, the Co$B$ results are, at best, of qualitative value. As an example, one of the largest discrepancies between the experimental and theoretical dissociation energies is observed for CoAu: $D_0^0 = 2.26 \pm 0.18$ eV[98] versus $D_e = 1.59$ eV. Thus, this work refrains from further interpreting the data on the electronic structure of CoB since they will probably be at odds with future results.

Ni*B*. The ground state term of the nickel atom is $^3\mathrm{D}(3\mathrm{d}^9 4\mathrm{s}^1)$, and the lowest excited terms $^3\mathrm{F}(3\mathrm{d}^8 4\mathrm{s}^2)$ and $^1\mathrm{D}(3\mathrm{d}^9 4\mathrm{s}^1)$ lie at 0.03 eV and 0.33 eV.[118] The data collected in table B.2 show that the ground term of Ni is correctly obtained as $^3\mathrm{D}$ at the DKH-MRCI(+Q) level of theory. According to figure B.4, which displays the ΛS potential energy curves for the low-lying states of NiCu and NiAg, these diatomic molecules exhibit a $X^2\Delta$ ground state which *diabatically* correlates to $\mathrm{Ni}(^3\mathrm{F}) + B(^2\mathrm{S})$. It is interesting to analyse in some depth the mixing between the molecular counterparts of the Ni $^3\mathrm{D}$ and the Ni $^3\mathrm{F}$ states in NiB. The potential curves indicate that the degree of mixing is strong for the molecular terms having $^2\Pi$ and $^2\Delta$ symmetries. As the $1^2\Pi$ and $X^2\Delta$ states descend from $\mathrm{Ni}(^3\mathrm{F}) + B(^2\mathrm{S})$, they heavily perturb the $2^2\Pi$ and $2^2\Delta$ states which originate from $\mathrm{Ni}(^3\mathrm{D}) + B(^2\mathrm{S})$. This perturbation, which is most probably amplified by higher $^2\Pi$ and $^2\Delta$ states, yields avoided crossings through interaction between $X^2\Delta \leftrightarrow 2^2\Delta$ and $1^2\Pi \leftrightarrow 2^2\Pi$. The $^{2,4}\Sigma^\pm$ and $^{2,4}\Phi$ terms remain unperturbed, however. A striking example which supports this argument is provided by the ground state dipole moment of the NiH hydride. It has been established that a $X^2\Delta$ wave function that describes both atomic terms (Ni $^3\mathrm{D}$ and Ni $^3\mathrm{F}$) equally well reproduces the experimental dipole moment of NiH, whereas a wave function which is biased towards Ni $^3\mathrm{D}$ or Ni $^3\mathrm{F}$ yields too large or too *small* dipole moments.[129]

It is remarkable that the electronic states of NiCu and NiAg deriving from the lowest 3 asymptotes—i.e., $\mathrm{Ni}(^1\mathrm{D}) + B(^2\mathrm{S}) \rightarrow {}^2\{\Sigma^+ \oplus \Pi \oplus \Delta\}$, $\mathrm{Ni}(^3\mathrm{F}) + B(^2\mathrm{S}) \rightarrow {}^{2,4}\{\Sigma^- \oplus \Pi \oplus \Delta \oplus \Phi\}$, and $\mathrm{Ni}(^3\mathrm{D}) + B(^2\mathrm{S}) \rightarrow {}^{2,4}\{\Sigma^+ \oplus \Pi \oplus \Delta\}$—were included along the full range of internuclear distances (2-8 Å in case of NiAg). By a comparison between the DKH-CASSCF and DKH-MRCI(+Q) potential energy curves shown in figures B.3 and B.4, one finds that the experimentally lowest separated atom limit, i.e., Ni(^{3}D) + B(^{2}S), happens to be the 5th limit at the static correlated level. At the DKH-CASSCF level, the lowest asymptote Ni(^{3}D) + B(^{2}S) lies higher than the separated atom limits associated with Ni(^{3}F), Ni(^{1}D), Ni(^{3}P), and Ni(^{1}G). It, therefore, appears as if the dynamic correlation downshifts the Ni(^{3}D) + B(^{2}S) limit by $\approx$ 3.1 eV. The lowest asymptote gives rise to the $1^2\Sigma^+$ state which lies below the $X^2\Delta$ ground state at 2.3 Å $\lessapprox r$(NiCu) $\lessapprox$ 3.6 Å and 2.5 Å $\lessapprox r$(NiAg). Analogous behaviour is predicted for NiAu, for which the Ni(^{3}D)+Au(^{2}S) limit, in the basis of the DKH-CASSCF calculations, lies higher in energy than Ni(^{3}F) + Au(^{2}D); this leads to prohibitively large calculations to track down the $^{2,4}\Lambda$ states dissociating to the ground state asymptote. If the colossal calculations could be done in which Ni(^{3}D) + Au(^{2}S) is included along the full range of r, then it is predicted that $E(X^2\Delta) > E(1^2\Sigma^+)$ at $r \gtrapprox 2.35$ Å $+ 0.1$ Å.

3.1.5 The Role of Spin-Orbit Coupling

Approximate 2-component treatment has allowed to schematically illustrate splittings of the (Λ,S) to Ω states in the diatomic molecules AB which are given in figures B.5 (ACu), B.6 (AAg), and B.7 (AAu). At the DKH-MRCI+(SO) level of theory, the ground states are $^3\Delta_1$ (ScB), $^4\Phi_{3/2}$ (TiB), $^5\Delta_{0^+}$ (VB), $^6\Sigma^+_{5/2}$ (CrB), $^7\Sigma^+_3$ (MnB), $^6\Delta_{9/2}$ (FeB), $^3\Phi_4$ (CoB), and $^2\Delta_{5/2}$ (NiB). For CoAu the ground state is of $^5\Phi_5$ symmetry. For the ACu molecules, in addition to the approximate 2-component treatment, spin-orbit coupling was treated *a priori* using the X2C method. Table B.35 is a summary of the ground state terms obtained at the spin-orbit-free DKH-MRCI(+Q) level ($X^{2S+1}\Lambda$), at the DKH-MRCI(+Q) level considering spin-orbit coupling ($X^{2S+1}\Lambda_\Omega$), and at the X2C-KRCI level ($X\Omega$). This table also details the relativistic computations. As can be seen, the ground state terms predicted by the exact and approximate methods are in complete agreement. However, although not reported in this work, the results for the excited Ω terms are not in quantitative agreement.

Figures B.8 and B.9 show the spin-orbit coupled potential energy curves of the Ω states of NiCu and NiAg obtained at the DKH-MRCI(+Q) level. Based on the associated (Λ,S) potential energy curves in NiCu and NiAg, it is already known that the $X^2\Delta$ and $1^2\Pi$ states correlate to the Ni(^{3}F) + B(^{2}S) asymptote, whereas the $1^2\Sigma^+$ state results from the Ni(^{3}D) + B(^{2}S) asymptote. This suggests that the spin-orbit coupled $X^2\Delta_{5/2}$ ground state dissociates to one of the spin-orbit components of Ni(^{3}F), i.e., Ni(^{3}F$_4$) + B(^{2}S$_{1/2}$) or Ni(^{3}F$_3$) + B(^{2}S$_{1/2}$) or Ni(^{3}F$_2$) + B(^{2}S$_{1/2}$), all of which can give rise to $\Omega = 5/2$ (see table B.10). Because of the mixing between the ^{3}D- and ^{3}F-type molecular states, however, this naïve idea is not totally supported by the spin-orbit coupled curves; due to the existence of many perturbations, avoided crossings, and discontinuities the curves appear to be completely shredded, causing some of them to predissociate. For this reason, one cannot ascertain to which asymptotes the low-lying Ω states *diabatically* correlate. Nonetheless, it is suggested that $1^2\Sigma^+_{1/2}$ would derive from Ni(^{3}D$_3$) + B(^{2}S$_{1/2}$), and the separated atom limits Ni(^{3}F$_4$) + B(^{2}S$_{1/2}$), Ni(^{3}F$_3$) +

$B(^2\mathrm{S}_{1/2})$, $\mathrm{Ni}(^3\mathrm{D}_3) + B(^2\mathrm{S}_{1/2})$, and $\mathrm{Ni}(^3\mathrm{D}_2) + B(^2\mathrm{S}_{1/2})$ are plausible candidates to which the terms $X^2\Delta_{5/2}$, $X^2\Delta_{3/2}$, $1^2\Pi_{3/2}$, and $1^2\Pi_{1/2}$ would *diabatically* correlate. Therefore, in the case of NiCu, the ground state dissociation energy calculated with respect to these likely asymptotes are 1.28 eV ($^3\mathrm{F}_4$), 1.44 eV ($^3\mathrm{F}_3$), 1.48 eV ($^3\mathrm{D}_3$), and 1.57 eV ($^3\mathrm{D}_2$).

Figure B.10 displays the low-lying electronic states of CoCu for atomic ($r \geq 5$ Å), intermediate (3 Å $\leq$ r $<$ 5 Å), and molecular (2.1 Å $\leq$ r $<$ 3 Å) regions as a function of the Sommerfeld's constant ($\alpha = 1/c$) calculated at the DKH-CASSCF level. This figure also displays the total energy of the lowest state and how it varies as the speed of light (c) changes. As c increases the excitation energies monotonically decrease for most of the states. At the nonrelativistic limit ($c = 10\,000$ a.u.)—where the scalar relativistic effects and the spin-orbit coupling are simultaneously cancelled out—the excitation energies for the systems $X^3\Phi : \Omega' = 3 \leftarrow \Omega'' = 4$ and $\Omega' = 2 \leftarrow \Omega'' = 4$ expectedly converge to zero. At the separated atom limit, as c decreases the excitation energies increase exponentially until they reach their maximum value at the relativistic limit. The situation is, however, different at the molecular structure ($r = 2.30$ Å), where the Co atomic manifold of states splits due to the external field imposed by the bounded partner atom Cu. At the molecular structure, as c decreases the excitation energies do not increase exponentially; additionally the magnitude of spin-orbit splittings is *smaller* compared to the atomic case. This is most probably because of the interaction with higher-lying states and may rationalise why spin-orbit splitting is usually larger in the free atoms than in the molecules, where it is relatively quenched.[47]

Figure B.16 visualises the spin-orbit splittings for the ground states of the atoms A and of the diatomic molecules AB. There are two illustrative points in this plot. Firstly, the ground state splittings in the AB molecules are equal to or less than those in the free atoms A, with one exception: TiAu. Secondly, since the D-type states of coinage metal atoms B are not involved, the splittings in copper, silver, and gold containing systems are of the same order of magnitude.

3.1.6 Overall Trends

Figures B.13, B.14, and B.15 show the ground state spectroscopic constants r_e, ω_e, and D_e, respectively, and how they vary as one moves from A = Sc to A = Ni for the diatomic molecules AB calculated at the DKH-MRCI(+Q) level of theory. The ground state bond lengths (r_e) are calculated to be in the range 2.23 Å (NiCu) - 2.64 Å (ScCu) for B = Cu, in the range 2.41 Å (NiAg) - 2.75 Å (ScAg) for B = Ag, and in the range 2.35 Å (NiAu) - 2.60 Å (ScAu) for B = Au. The *smallest* r_e within the row is obtained for NiB ($X^2\Delta$) and the largest r_e within the row is obtained for ScB ($X^3\Delta$). The ratio $r_e(A\mathrm{Ag})/r_e(AB)$, corresponding to the ground states of the ACu and AAu diatomic molecules, is predicted to vary in the range of 1.055 ± 0.025. A striking similarity for the triatomic molecules AB_2 will be revealed in subsection 3.2.6.

For a variety of reasons, including the observation of several transition metal oxides and hydrides in the stars and therefore their astrophysical importance, the AH hydrides have received some critical and vast attention.[130–149] Looking for some connection, the ground state symmetries of the atoms A, the monocations A^+, the hydrides AH, and the diatomic molecules AB are compiled in table B.36. For 23 out of the 24 diatomic molecules AB considered in the present work, an interesting binary relation between A^+ and AB has been unveiled. According to this relation, provided that the ground state term of A^+ is known $(^{2\mathrm{S}+1}\mathrm{L}_J)$, one can predict the ground state term of AB being $^{2\mathrm{S}'+1}\Lambda_\Omega$; $\mathrm{S}' = \mathrm{S}$, $\Omega = J$, and $\Lambda = \mathrm{L}$. Notice that the projected orbital angular momentum Λ corresponds to the maximum value of L along the internuclear axis and the projected total angular momentum Ω corresponds to the maximum value of J along the internuclear axis. For example, the ground term of Sc$^+$ and ScB are $^3\mathrm{D}_1$ and $X^3\Delta_1$. In order to see whether the relation between $A^+(^{2\mathrm{S}+1}\mathrm{L}_J)$ and $AB(X^{2\mathrm{S}'+1}\Lambda_\Omega)$ has some validity for the larger class of diatomic molecules MB or not, the scope of the study is slightly broadened from A = Sc-Ni to M = {d-block atoms} (see table B.36). Due to lack of data one can only cast light on the systems YCu, MoB, WB, RuCu, and PtB (B = Cu/Ag/Au). In the cases of YCu$(X^1\Sigma^+)$,[150,151] Mo$B(X^6\Sigma^+_{5/2})$,[152] and Pt$B(X^2\Delta_{5/2})$[111,153,154] the ground state symmetries from literature and those suggested by the mapping from M^+ to MB coincide; this is not the case, however, for WB and RuCu.

It is interesting to discuss a trend which would emerge upon a step-by-step move from ScB (B = Cu/Ag/Au) to NiB from a molecular orbital point of view. For transition metal diatomic molecules AB, one would ordinarily expect the valence s-type and d-type molecular orbitals to fall into the energetic order $\mathrm{d}\sigma_B < \mathrm{d}\pi_B < \mathrm{d}\delta_B < \mathrm{s}\sigma < \mathrm{s}\sigma^* < \mathrm{d}\delta^*_A < \mathrm{d}\pi^*_A < \mathrm{d}\sigma^*_A$.[126,128] Having this ansatz in mind, one can hypothetically invoke a reference closed-shell configuration as $\mathrm{s}\sigma^{*2}\,\mathrm{d}\delta^{*0}\,\mathrm{d}\pi^{*0}\,\mathrm{d}\sigma^{*0}$, where the d_B-type and sσ orbitals are suppressed. Notice that, according to the DKH-MRCI(+Q) results, the $^1\Sigma^+$ state of ScB has significant contribution (24-31%) from this closed-shell configuration—see tables B.11, B.12, B.13. Since the exchange effects are to favour unpairing of the electrons across the quasi-degenerate d_{Sc}-type orbitals, the $\mathrm{s}\sigma^{*2}$ shell cracks open and kicks out one of its electrons to the $\mathrm{d}\delta^*$ orbital, leading to a $\mathrm{s}\sigma^{*1}\,\mathrm{d}\delta^{*1}\,\mathrm{d}\pi^{*0}\,\mathrm{d}\sigma^{*0}$ configuration of $^3\Delta$ symmetry which dominates (89-90 %) the ground state of ScB. Fusing one electron to the resulting $^3\Delta$ configuration one obtains $\mathrm{s}\sigma^{*1}\,\mathrm{d}\delta^{*1}\,\mathrm{d}\pi^{*1}\,\mathrm{d}\sigma^{*0}$, which is the main contribution (84-89 %) of the $X^4\Phi$ ground state of TiB. For the early transition metal atoms it seems that the $k\mathrm{s}_B$ and $3\mathrm{d}_A$ orbitals mix leading to a bonding $\mathrm{s}\sigma^*$ orbital and to an anti-bonding $\mathrm{d}\sigma^*$ orbital; $\mathrm{s}\sigma^*$ is lower in energy and $\mathrm{d}\sigma^*$ is higher in energy to the point that it lies above the $d\delta^*$ and $d\pi^*$ orbitals. Additionally, by analogy with the spin angular momentum, high orbital angular momentum states are favoured over low orbital angular momentum states for the near-degenerate spaces—the $A^+(^{2\mathrm{S}+1}\mathrm{L}_J)$-$AB(X^{2\mathrm{S}+1}\Lambda_\Omega)$ mapping is a strong indication of this proposition.

Therefore, on the basis of the previous $^4\Phi$ configuration, sequentially infusing further a $\mathrm{d}\pi^*$ electron, a $\mathrm{d}\delta^*$ electron, and eventually a $\mathrm{d}\sigma^*$ electron would yield the $\mathrm{s}\sigma^{*1}\,\mathrm{d}\delta^{*1}\,\mathrm{d}\pi^{*2}\,\mathrm{d}\sigma^{*0}$ (79-88 %), $\mathrm{s}\sigma^{*1}\,\mathrm{d}\delta^{*2}\,\mathrm{d}\pi^{*2}\,\mathrm{d}\sigma^{*0}$ (78-84 %), and $\mathrm{s}\sigma^{*1}\,\mathrm{d}\delta^{*2}\,\mathrm{d}\pi^{*2}\,\mathrm{d}\sigma^{*1}$ (84-90 %) configurations dominating the ground states of VB $(X^5\Delta)$, CrB $(X^6\Sigma^+)$, and MnB $(X^7\Sigma^+)$, respectively. One sees here why *spin* should precede *space*; the MnB $X^7\Sigma^+$, $\mathrm{s}\sigma^{*1}\,\mathrm{d}\delta^{*2}\,\mathrm{d}\pi^{*2}\,\mathrm{d}\sigma^{*1}$ configuration with S = 3 and $\Lambda = 0$ is favoured over, for instance, the MnB $^5\Pi$, sσ^{*1} dδ^{*2} dπ^{*3} dσ^{*0} configuration with S = 2 and $\Lambda = 1$. The anti-bonding characteristic of the dσ^* orbital is confirmed by a sudden drop in dissociation energy; $D_e[\mathrm{Cr}B(X^6\Sigma^+)] - D_e[\mathrm{Mn}B(X^7\Sigma^+)]$ = 0.51 eV (B = Cu) and 0.38 eV (B = Ag). For B = Au, however, the dσ^* orbital is not anti-bonding in character which derives from the fact that the relativistic contraction of the 6s$_{\mathrm{Au}}$ orbital and the relativistic expansion of the 5d$_{\mathrm{Au}}$ orbitals significantly decrease the 3d$_A$-6s$_{\mathrm{Au}}$ mixing. For the late transition metal atoms the analysis proceeds similarly; inserting a dδ^* electron and a dπ^* electron, one obtains the sσ^{*1} dδ^{*3} dπ^{*2} dσ^{*1} (88-89 %), $X^6\Delta$ state for the FeB molecules and the sσ^{*2} dδ^{*3} dπ^{*3} dσ^{*0} (87-88 %), $X^3\Phi$ state for the CoCu and CoAg molecules. For the cobalt subclass, inserting a dπ^* electron does not have the same effect on the three molecules. In CoCu and CoAg the insertion causes the sσ^* and dσ^* electrons to pair reflecting tendency towards low-spin states which should be due to energy lowering of the sσ^* orbital leading to a sudden increase in dissociation energy; $D_e[\mathrm{Co}B(X^3\Phi)] - D_e[\mathrm{Fe}B(X^6\Delta)] = 0.86$ eV (B = Cu) and 0.83 eV (B = Ag). In CoAu, the $d\pi^{*1}$ insertion leads to the sσ^{*1} dδ^{*3} dπ^{*3} dσ^{*1} (89 %), $X^5\Phi$ state. Firstly, in comparison to the early transition metal atoms, the 3d orbitals in Co and Ni are quite contracted and are only capable of negligibly overlapping with the ks$_B$ orbital. Secondly, in the case of Co and Ni containing diatomic molecules (CoB and NiB), the number of low-lying states is greatly increased providing the possibility of contribution from the d$_A$ orbital to the bonding. Thirdly, relativistic effects cause the 5d orbitals of the Au atom to expand and therefore to be more available for d$_B$ orbital bonding than the 3d (Cu) and 4d (Ag) orbitals. These suggest that in the case of the CoAu $X^5\Phi$ state the involvement of the 5d^{9}6s^2 ^{2}D state has resulted in a relatively strong d$_{\mathrm{Co}}$-d$_{\mathrm{Au}}$ interaction, which in turn favours the high-spin CoAu $X^5\Phi$ state in comparison to the low-spin $X^3\Phi$ states in CoCu and CoAg. Finally, adding a dπ^* electron to the low-spin configuration of the Co subclass leads to the sσ^{*2} dδ^{*3} dπ^{*4} (59-65 %), $X^2\Delta$ state for the NiB molecules.

Pursuant to the previous paragraph, it is attempted here to describe the bonding character for the ground states of the diatomic molecules AB from a different perspective; the ion-pair $A^+ + B^-$ contribution. Using concentric octagons, figure B.11 represents the ground state terms of the monocations A^+, of the monoanions B^-, and of the diatomic molecules AB together with the corresponding dominant configurations. In this figure the ground state mapping between $A^+(^{2\mathrm{S}+1}\mathrm{L}_J)$ and $AB(X^{2\mathrm{S}+1}\Lambda_\Omega)$ is indicated by straight lines connecting the octagons' vertices. In addition to this intra-vertex mapping, i.e., those from A^+ to AB, there exists also inter-vertex mapping, oppressing the 4s orbitals, between Sc$^+$: 3d^1 ^{3}D and Ni$^+$: 3d^9 ^{2}D (in green), between Ti$^+$: 3d^2 ^{4}F and Co$^+$: 3d^8 ^{3}F (in magenta), between V$^+$: 3d^4 ^{5}D and Fe$^+$: 3d^6 ^{6}D (in brown), and between Cr$^+$: 3d^5 ^{6}S and Mn$^+$: 3d^5 ^{7}S (in violet). This is the inevitable corollary of the connection between electrons and electron holes, according to which the diatomic molecules AB also exhibit mappings (oppressing the inner-most and the outer-most σ orbitals) between ScB: δ^1 $X^3\Delta$ and NiB: $\sigma^2\pi^4\delta^3$ $X^2\Delta$, between TiB: $\pi^1\delta^1$ $X^4\Phi$ and CoB (B = Cu/Ag): $\sigma^2\pi^3\delta^3$ $X^3\Phi$, between VB: $\sigma^1\pi^2\delta^1$ $X^5\Delta$

and FeB: $\sigma^1\pi^2\delta^3$ $X^6\Delta$, and between CrB: $\sigma^1\pi^2\delta^2$ $X^6\Sigma^+$ and MnB: $\sigma^1\pi^2\delta^2$ $X^7\Sigma^+$. Notice that on the basis of the ion-pairs $A^+ + B^-$ the cationic configurations d^3 and d^7 and the corresponding molecular configurations $(\sigma\pi\delta)^3$ and $(\sigma\pi\delta)^7$ do not emerge for the ground states. This suggests, but does not prove, that the ground state bonding is dominated by the electrostatic contributions, most importantly by the ion-pair contribution; the ground state of AB would *diabatically* correlate to the lowest ion-pair separated atom limit $A^+ + B^-$. However, for an abstract ionic bond one would expect, firstly, a large dipole moment of approximately 12 D for internuclear distance (r) around 2.50 Å ($\vec{\mu} = q\vec{r}$). Secondly, the ion-pair term will show up as having dipole moment that linearly increases with respect to internuclear distance. None of these two requirements for pure ionic bonds is fulfilled in the MRCI results of this work.

The electronic configurations which dominate the ground and low-lying states of the diatomic molecules AB, at the DKH-MRCI level, are shown in figure B.12. As it can be seen, for the molecules ScB, TiB, VB, CrB, and MnB, the inner-most sσ orbital is always doubly occupied. The second inner-most orbital, dσ^*, is always empty or singly occupied; therefore, as mentioned above, this orbital should be anti-bonding for the early transition metal molecules. Interestingly, for the excited terms that are weakly bound ($D_e \leq 0.3$ eV), i.e., $^6\Sigma^-, {}^6\Pi, {}^6\Delta, {}^6\Phi$ in TiCu/TiAg, $^7\Sigma^+, {}^7\Pi, {}^7\Delta$ in VCu/VAg, $^8\Sigma^+$ in CrB, and $^7\Pi$ in MnCu/MnAg, the dominant configuration is sσ^1dσ^{*1}. For the excited terms that are strongly bound, i.e., $2^4\Sigma^-$, $2^4\Pi$, $2^4\Delta$, $2^4\Phi$ in TiCu/TiAg, and $^5\Sigma^+$, $2^5\Pi$, $2^5\Delta$ in VCu/VAg the dominant configuration is sσ^2dσ^{*0}. The situation is, however, different in the cases of FeB, CoB, and NiB where the dσ^* orbital is no longer of anti-bonding character.

3.2 The Triatomic Molecules AB_2

3.2.1 Overview

As mentioned in subsection 3.1.2, the electronic complexity in silver containing systems (AAg$_n$) is predicted to be substantially less than that in copper and gold systems. For this reason, as the first step, the (Λ,S) potential energy curves along the A-Ag internuclear distances were constructed for the low-lying states of AAg$_2$ molecules at the DKH-CASSCF level of theory. These potential curves are designated by $E(r; {}^{2S+1}\Gamma)$ and presented in figures B.17 (AgScAg), B.18 (ScAgAg), B.19 (AgTiAg), B.20 (TiAgAg), B.21 (AgVAg), B.22 (VAgAg), B.23 (AgCrAg), B.24 (CrAgAg), B.25 (AgMnAg), B.26 (MnAgAg), B.27 (AgFeAg), B.28 (FeAgAg), B.29 (AgCoAg), B.30 (CoAgAg), B.31 (AgNiAg), and B.32 (NiAgAg). Colours are chosen in such a way that red always corresponds to the states with the lowest spin multiplicity, blue to the next higher multiplicity, magenta to the next, and green to the highest. For instance, in the case of TiAg$_2$, red, blue, magenta, and green pertain to the singlet, triplet, quintet, and septet states, respectively. This choice of colours is conserved for the subsequent dynamically correlated surfaces. For the linear and bent AgAAg structures ($D_{\infty h}$ and C_{2v}), the internuclear distances $r(A$-Ag$)$ were symmetrically varied at each fixed AgAAg bond angle: $\theta = 40°, 50°, \ldots, 180°$. The full range 2 Å $\leq r(A\text{-Ag}) \leq$ 8 Å, where possible, was explored for the discrete AgAAg bond angles. For the linear AAgAg structure ($C_{\infty v}$), one variable was defined (r) simultaneously representing the A-Ag and Ag-Ag distances. Some of the qualitative findings on the electronic states of $A\text{Ag}_2$ at the DKH-CASSCF level were assumed to be generalisable to the $A\text{Cu}_2$ and $A\text{Au}_2$ systems. For example, the doublet, the quartet, the sextet, and the octet states of VAg_2 were investigated at the static correlated level (see figure B.21). It was found that the doublet and octet states, regardless of the space symmetry of the molecule, lie considerably higher in energy than the quartet and sextet states. Therefore, in the subsequent DKH-MRCI(+Q) calculations on the $\text{V}B_2$ molecules, potential energy surfaces for the $^{4,6}\{A_1 \oplus A_2 \oplus B_1 \oplus B_2\}$ states were calculated. In the ΓS calculations, the abelian point group C_{2v} was used.

The C_{2v}-restricted potential energy surfaces were calculated for the low-lying states of the BAB structures (linear and bent) at the DKH-MRCI(+Q) level and using (c)spline interpolation. These potential surfaces are labelled by $E(\theta_{BAB}, r_{AB}; {}^{2\text{S}+1}\Gamma)$ and depicted in figures B.33 (CuScCu), B.34 (AgScAg), B.35 (AuScAu), B.36 (CuTiCu), B.37 (AgTiAg), B.38 (AuTiAu), B.39 (CuVCu), B.40 (AgVAg), B.41 (AuVAu), B.42 (CuCrCu), B.43 (AgCrAg), B.44 (AuCrAu), B.45 (CuMnCu), B.46 (AgMnAg), B.47 (AuMnAu), B.48 (CuFeCu), B.49 (AgFeAg), B.50 (AuFeAu), B.51 (CuCoCu), B.52 (AgCoAg), B.53 (AuCoAu), B.54 (CuNiCu), B.55 (AgNiAg), and B.56 (AuNiAu). The $D_{\infty h}$ and C_{2v} point groups and the connection between them have been examined. The *ab initio* inputs, based on which the ensuing interpolation was carried out, are shown using the black points along the transparent potential surfaces. The coordinate θ is the $\angle BAB$ bond angle, the coordinate r is the A-B distance, and $^{2\text{S}+1}\Gamma$ is the electronic state under consideration, with spin multiplicity 2S+1 and irreducible representation Γ. The distances B-A and A-B were altered symmetrically; accordingly, the C_{2v}-constrained points on the θ_{BAB}-r_{AB} plane have been examined.* The coordinate ranges $40° \leq \theta \leq 180°$ and 2 Å $\leq r \leq$ 3 Å were probed because it was intuitively evident enough that the low-lying minima (including the ground state) would occur in these ranges.

The C_{2v}-restricted potential energy surfaces were constructed for the low-lying states of the linear ABB structures ($C_{\infty v}$). These potential surfaces are denoted by $E(r_{AB}, r_{BB}; {}^{2\text{S}+1}\Lambda)$ and represented in figures B.58 (ScCuCu), B.60 (ScAgAg), B.61 (ScAuAu), B.62 (TiCuCu), B.63 (TiAgAg), B.64 (TiAuAu), B.65 (VCuCu), B.66 (VAgAg), B.67 (VAuAu), B.68 (CrCuCu), B.69 (CrAgAg), B.70 (CrAuAu), B.71 (MnCuCu), B.72 (MnAgAg), B.73 (MnAuAu), B.74 (FeCuCu), B.75 (FeAgAg), B.76 (FeAuAu), B.77 (CoCuCu), B.78 (CoAgAg), B.79 (CoAuAu), B.80 (NiCuCu), B.81 (NiAgAg), and B.82 (NiAuAu). The coordinates r_{AB} and r_{BB} represent the A-B (vertical axis) and B-B (horizontal axis) internuclear distances, with the ranges 2 Å $\leq r_{AB}, r_{BB} \leq$ 3 Å. Notice that the abscissa and the ordinate of a point on the r_{AB}-r_{BB} plane correspond to vertical and horizontal axes.

---

*Although very unlikely, the minimum points obtained from these surfaces might correspond to saddle points and not to true minima since the third coordinate of a triatomic 3-space was untouched.

The potential energy surfaces $E(\theta_{BAB}, r_{AB}; {}^{2S+1}\Gamma)$ and $E(r_{AB}, r_{BB}; {}^{2S+1}\Lambda)$ have provided a global representation of the low-lying states of the triatomic molecules AB_2 in their $D_{\infty h}$, C_{2v}, and $C_{\infty v}$ structures. With the help of this global view, structure optimisation calculations were undertaken around the minima at the same level of theory but using the C_s point group. The optimised minima thus obtained were then compared with the interpolated ones, mutually verifying or refuting the equilibrium structures and the total energies associated with the system in question. The energetics of the ground and low-lying states of the AB_2 molecules are schematically illustrated in figures B.83 ($ScCu_2$), B.84 ($ScAg_2$), B.85 ($ScAu_2$), B.86 ($TiCu_2$), B.87 ($TiAg_2$), B.88 ($TiAu_2$), B.89 (VCu_2), B.90 (VAg_2), B.91 (VAu_2), B.92 ($CrCu_2$), B.93 ($CrAg_2$), B.94 ($CrAu_2$), B.95 ($MnCu_2$), B.96 ($MnAg_2$), B.97 ($MnAu_2$), B.98 ($FeCu_2$), B.99 ($FeAg_2$), B.100 ($FeAu_2$), B.101 ($CoCu_2$), B.102 ($CoAg_2$), B.103 ($CoAu_2$), B.104 ($NiCu_2$), B.105 ($NiAg_2$), and B.106 ($NiAu_2$). In these figures three "axis-like" line segments, tagged with the point groups ($D_{\infty h}$, C_{2v}, $C_{\infty h}$) and the associated coordinates, are drawn. The vertical axis (z) represents the total energy of the states. Parallel lines, affixed with the equilibrium structures of the given state, indicate the same symmetry as the principal line segments. Potential (C_{2v}) and optimised (C_s) minima are shown in black and blue.

3.2.2 The Triatomic Molecules ScB_2

$ScCu_2$.

The Moieties; Sc, Cu, ScCu, and Cu_2. The ground state term of the scandium atom is ^{2}D(3d^{1}4s^2), and the lowest excited terms ^{4}F and ^{2}F—both arising from the 3d^{2}4s^1 configuration—lie at 1.43 eV and 1.85 eV (J-averaged energies derived from experimental data).[118] On the basis of table B.2, the $^4\text{F} \leftarrow {}^2\text{D}$ and $^2\text{F} \leftarrow {}^2\text{D}$ separation energies of Sc, at the DKH-MRCI(+Q) level of theory considering the core correlation effects of the 3s3p orbitals, are calculated to be 0.11 eV(^{4}F) and 0.20 eV(^{2}F) larger than the experimental values. These separation energies are to be compared with another MRCI study where the ^{4}F and ^{2}F terms of Sc were calculated to lie 0.10 eV and 0.09 eV below the experimental levels.[155] The data compiled in table B.2 show two striking considerations as to the outcome of the atomic results obtained at various levels of theory. First, for the LS transition Sc $^4\text{F} \leftarrow$ Sc ^{2}D, the separation energy, at the DKH-CAS(11,10) level, is only 0.09 eV larger than the reference value—i.e., in better agreement with experiment than the dynamically correlated level—which is obviously due to fortuitous cancellation of errors. Second, for the spin-orbit transitions Sc $^4\text{F}_{J'} \leftarrow$ Sc $^2\text{D}_{J''}$, where $J'' = \frac{3}{2}, \frac{5}{2}$ and $J' = \frac{3}{2}, \frac{5}{2}, \frac{7}{2}, \frac{9}{2}$, the errors associated with the X2C-KRCI calculations are *smaller* than those associated with the spin-orbit-free core-correlated DKH-MRCI(+Q) calculations. Including all of the atoms (Sc-Ni, Cu/Ag/Au) and all of the transitions, the overall mean absolute deviations (MAD) from the reference energies at the DKH-c-CASSCF, at the DKH-c-MRCI(+Q), and at the X2C-KRCI levels of theory—coming up to one's expectations—are obtained to be 0.74 eV, 0.06 eV, and 0.11 eV, respectively.

An averaged coupled pair functional (DKH-ACPF) study at the complete basis set (CBS) limit, considering the 3s3p core correlation effects, calculated a very accurate $^4\mathrm{F} \leftarrow {}^2\mathrm{D}$ separation energy for the Sc atom which was about 0.02 eV *smaller* than the experimental value.[82,156,157] This DKH-ACPF study—developing separate basis sets for valence-only correlation, 3d4s, as well as those including the effects of outer-core correlation—yielded a core correlation contribution of -0.32 eV for the $^4\mathrm{F} \leftarrow {}^2\mathrm{D}$ transition of Sc; to be compared with -0.21 eV obtained at the DKH-MRCI(+Q) level in the present work. Overall, including all the 11 atoms, the mean absolute deviation of the core contributions calculated in the present work from those calculated in the DKH-ACPF study is about 0.11 eV. Nonetheless, use of basis sets that even contain special core-polarisation functions is yet highly desirable for the inclusion of the core (or inner-shell) correlation energy. In a previous DKH-CCSD(T) and DKH-CASPT2 study, the effect of adding two h-type functions to the ANO-RCC basis sets for the 3d atoms was investigated and shown to lower the separation energies for the $\mathrm{s}^1\mathrm{d}^{m-1} \leftarrow \mathrm{s}^2\mathrm{d}^{m-2}$ excitations.[158] Before proceeding any further, be reminded that "the state of a microscopic system has a meaning independent of the basis in which it is expanded."[51] For the current work the dependence of the atomic separation energies on the h-type functions would disappointingly mean that the molecular states will become more dense and the energy gap between the clusters of terms will narrow along the potential energy curves/surfaces when large basis sets are used; making it more difficult to record a global portrait of the system under investigation. Another important inferential deduction on the 3d atoms is the double shell effect which accounts for the essence of including an extra d shell in the active space in order to extract accurate separation energies.[158,159] This active space enlargement was out of the question for the current work because, similar to the increase in the size of basis sets, it would have made the molecular calculations unfeasible.

The ground state of the copper atom is $^2\mathrm{S}(3\mathrm{d}^{10}4\mathrm{s}^1)$, and the only d-hole excited state $^2\mathrm{D}(3\mathrm{d}^9 4\mathrm{s}^2)$ lies at 1.49 eV (J-averaged energies).[118] The diatomic molecule Cu_2 possesses the $X^1\Sigma_g^+$ $(3\mathrm{d}^{10}_{\mathrm{Cu}}3\mathrm{d}^{10}_{\mathrm{Cu}}\sigma^2_{\mathrm{g}})$ ground state which is, in energy scale, relatively well separated from the lowest excited state.[160] For the ground state of Cu_2 the experimental values of equilibrium bond length and of dissociation energy are $r_e = 2.220$ Å and $D_0^0 = 2.01 \pm 0.08$ eV.[160] According to table B.11, ScCu has a $X^3\Delta$ (90% $3\mathrm{d}^{10}_{\mathrm{Cu}}\mathrm{s}\sigma^2\mathrm{s}\sigma^{*1}\mathrm{d}\delta^{*1}$) ground state that arises from the $\mathrm{Sc}(^2\mathrm{D}) + \mathrm{Cu}(^2\mathrm{S})$ asymptote (see figure B.4), based on the DKH-MRCI[(10+4)E,(5+7)O] calculations. For this state one finds $r_e = 2.64$ Å and $D_e = 1.17$ eV at the valence correlated level and $r_e = 2.60$ Å and $D_e = 1.14$ eV at the outer-core valence correlated level. In view of the dominant configurations, rearrangements of the d-type electron ($\mathrm{d}\delta^{*1}$) among the quasi-degenerate d-type orbitals lead to the $\mathrm{s}\sigma^2\mathrm{s}\sigma^{*1}\mathrm{d}\sigma^{*1}$(64%) $^1\Sigma^+$ and $\mathrm{s}\sigma^2\mathrm{s}\sigma^{*1}\mathrm{d}\pi^{*1}$(90%) $^3\Pi$ excited states lying 0.12 eV and 0.15 eV above the $X^3\Delta$ ground state. By comparing the ScCu $X^3\Delta$ state with the Cu_2 $X^1\Sigma_g^+$ state, one sees the latter system having a substantially *smaller* equilibrium bond length (0.42 Å) and a considerably larger dissociation energy (0.8 eV). For the ground state equilibrium bond lengths of ACu, the ScCu $X^3\Delta$ state is the upper limit and the Cu_2 $X^1\Sigma_g^+$ state is the lower limit—see figure B.13 for an illustration.

Asymptotic Considerations. Interaction of the scandium atom with two copper atoms, Sc(^{2}D) + 2Cu(^{2}S), irrespective of the atoms' orientations, yields 15 electronic states: 10 doublet states and 5 quartet states. Table B.37 shows how the $^{2,4}\Gamma$ states of ScCu$_2$ get distributed over the irreducible representations of the point groups C_1, C_s, C_{2v}, D_{2h}, $C_{\infty v}$, and $D_{\infty h}$. For instance, within the $D_{\infty h}$ point group, corresponding to linear CuScCu structure, the ground state separated atom limit gives rise to the molecular states[125] $^2\{\Sigma_g^+ \oplus \Sigma_u^+ \oplus \Pi_g \oplus \Pi_u \oplus \Delta_g \oplus \Delta_u\}$ and $^4\{\Sigma_u^+ \oplus \Pi_u \oplus \Delta_u\}$. The $C_1 \to C_{\infty v} \to C_{2v}$ correlation for the ScCu$_2$ $^{2,4}\Gamma$ states is schematically illustrated in figure 3.1.

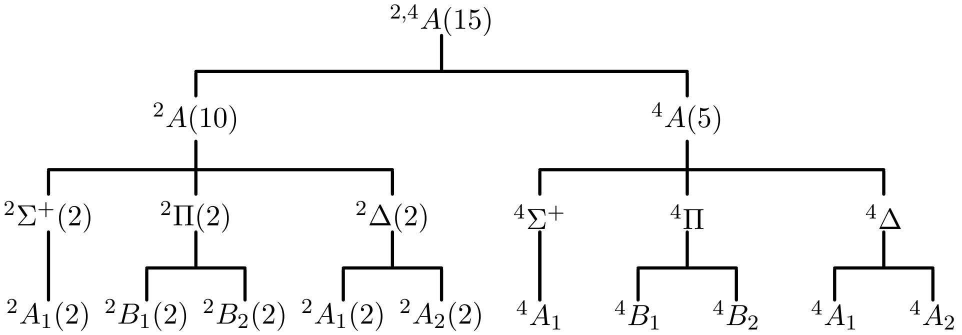

Figure 3.1: Symmetry of the electronic states of ScCu$_2$

Clearly, the Sc(^{2}D) + 2Cu(^{2}S) separated atom limit, associated with three free atoms in their respective ground states, is not the lowest significant asymptote in the ScCu$_2$ triatomic molecule. The ScCu($X^3\Delta$) + Cu(^{2}S) asymptote, associated with the diatomic molecule ScCu and the copper atom, lies 1.11±0.06 eV below the Sc(^{2}D) + 2Cu(^{2}S) separated atom limit. On the one hand, the dissociation energy (D_e) of the ScCu $X^3\Delta$ state, obtained at the DKH-MRCI(+Q) level of theory, is 1.17 eV and 1.14 eV without and with the outer-core correlation effects (table B.11). On the other hand, on the basis of the $E(r_{\text{ScCu}}, r_{\text{CuCu}}; {}^{2,4}\Lambda)$ potential energy surfaces, the energy difference between a point corresponding to the ground state Sc + 2Cu asymptote and a point corresponding to the ground state ScCu + Cu asymptote, i.e.,

$$E\Big(\infty, \infty; {}^4\{A_1(2) \oplus B_1 \oplus B_2 \oplus A_2\}\Big) - E\Big(2.64\ \text{Å}, \infty; {}^{2,4}\{A_1 \oplus A_2\}\Big),$$

is 1.05 eV at the DKH-MRCI[(20+5)E,(10+8)O] level (see table B.38). These theoretical dissociation energies for the ScCu $X^3\Delta$ state, or equivalently stated, the energy differences (ΔE) between the asymptotes Sc(^{2}D) + 2Cu(^{2}S) and ScCu($X^3\Delta$) + Cu(^{2}S)—i.e., 1.17 eV, 1.14 eV, and 1.05 eV—can be combined in such a way as to comply with experimental uncertainties; $\Delta E = 1.11 \pm 0.06$ eV.

Now, the third important asymptote, Sc(^{2}D) + Cu$_2$($X^1\Sigma_\text{g}^+$), is being discussed which positively lies below the ScCu($X^3\Delta$) + Cu(^{2}S) asymptote. It is crucial that this statement be quantified, if one is to adequately understand the electronic structure of the ScCu$_2$ molecule. In oder to do so, the corresponding energy difference (ΔE) between these two asymptotes are estimated in what follows, despite the probable controversies which would arouse. In order to predict ΔE between these two asymptotes some of the experimental and theoretical dissociation energies which are reported in literature for the Cu_2 $X^1\Sigma_g^+$ state are collected in table B.38. Considering the experimental dissociation energy $D_0^0 = 2.01 \pm 0.08$ eV for the Cu_2 $X^1\Sigma_g^+$ state (ref. 160), and combining it with the theoretical dissociation energy $D_e = 1.11 \pm 0.06$ eV for the ScCu $X^3\Delta$ state derived in the preceding paragraph,* one can express this ΔE in the form

$$E\Big(2.64\ \text{Å}, \infty; {}^{2,4}\{A_1 \oplus A_2\}\Big) - E\Big(\infty, 2.22\ \text{Å}; {}^2\{A_1(2) \oplus B_1 \oplus B_2 \oplus A_2\}\Big) = 0.90 \pm 0.14\ \text{eV}.$$

Notice that the first term must correspond to a 4-fold degeneracy due to the $X^3\Delta + {}^2\text{S}$ interaction and the second term must correspond to a 5-fold degeneracy due to the ${}^2\text{D} + X^1\Sigma_g^+$ interaction. According to the $E(r_{\text{ScCu}}, r_{\text{CuCu}}; {}^{2,4}\Lambda)$ potentials, calculated at the DKH-MRCI[(20+5)E,(10+8)O] level of theory, $\Delta E = 0.62$ eV; with the $\text{Sc}({}^2\text{D}) + \text{Cu}_2(X^1\Sigma_\text{g}^+)$ asymptote being lower in energy. In a single reference coupled pair functional (CPF) study—employing a basis of the size (16s,11p,6d,3f)/[10s,7p,4d,3f], in a modified CPF study—utilising a basis of the size (16s,12p,7d,4f)/[6s5p3d2f], and in a second CPF study—using a basis of the size [9s,7p,4d,3f,1g], the dissociation energy (D_e) of the Cu_2 $X^1\Sigma_g^+$ state was calculated to be 1.84 eV (ref. 161), 1.74 eV (ref. 162), and 1.81 eV (ref. 119). Considering these dissociation energies, and combining them with $D_e[\text{ScCu}(X^3\Delta)] = 1.11 \pm 0.06$ eV one obtains the $\text{Sc}({}^2\text{D}) + \text{Cu}_2(X^1\Sigma_\text{g}^+)$ asymptote lying 0.73(6) eV, 0.63(6) eV, and 0.70(6) eV, respectively, below the $\text{ScCu}(X^3\Delta) + \text{Cu}({}^2\text{S})$ asymptote. Notice, finally, that the experimental dissociation energy of the Cu_2 $X^1\Sigma_g^+$ state is overestimated in comparison with all theoretical values collected and calculated here.

The ground state asymptote $\text{Sc}({}^2\text{D}) + \text{Cu}_2(X^1\Sigma_\text{g}^+)$ is therefore proved to lie, energetically, below the $\text{ScCu}(X^3\Delta) + \text{Cu}({}^2\text{S})$ asymptote. Group theory, on the other hand, tells one that the $\text{Sc}({}^2\text{D}) + \text{Cu}_2(X^1\Sigma_g^+)$ interaction through the $C_{\infty v}$- and C_{2v}-restricted reaction channels gives rise to the triatomic molecular terms ${}^2\{\Sigma^+ \oplus \Pi \oplus \Delta\}$ and ${}^2\{A_1(2) \oplus B_1 \oplus B_2 \oplus A_2\}$.[125] Nothing prevents one from decreeing that these terms transform to ${}^2\{\Sigma_g^+ \oplus \Pi_g \oplus \Delta_g\}$ through the $D_{\infty h}$-constrained channel. It therefore seems reasonable to postulate that the Sc ^{2}D atomic state has, due to the interaction with the Cu_2 $X^1\Sigma_g^+$ state, converted into a ${}^2\Gamma$ cluster which consists of 5 D-based states being energetically well separated from the excited states. In what follows it will be shown that this proposition holds for the linear structures ($D_{\infty h}$ and $C_{\infty v}$) but not for the bent form (C_{2v}).

The $D_{\infty h}$ Structure. According to figure B.83, which schematically illustrates the low-lying electronic states of the $ScCu_2$ molecule obtained at the spin-orbit-free DKH-MRCI valence level of correlation, this triatomic molecule possesses a doublet (orbitally degenerate) ground state that belongs to the linear CuScCu form.† The equilibrium Sc-Cu internuclear

---

[*] Zero-point energy corrections for both states are neglected.

[†] Notice that a ground state of $D_{\infty h}$ space symmetry, i.e., the linear BAB structure, is compatible with the way an inorganic chemist would presume the structural model in transition metal complexes: one metal centre (atom A) surrounded by well-structured ligands (B atoms) in such a way that symmetry is degraded as less as possible—e.g., from spherical symmetry to linear $D_{\infty h}$.

distance is calculated to be 2.666 Å and 2.672 Å based on the interpolated potential energy surfaces and the structure optimisation calculations. Rounding these values, one obtains $r_e(\text{ScCu}) = 2.67$ Å for the ground state of the ScCu_2 molecule, which shows a slight elongation as compared to the bond length of the diatomic molecule ScCu; $r_e(X^3\Delta) = 2.64$ Å at the DKH-MRCI(+Q) level and 2.60 Å at the DKH-cMRCI(+Q) level (see table B.11). A triple computation, i.e., three single point calculations employing the C_s, C_{2v}, and D_{2h} point groups, undertaken at the $D_{\infty h}$ equilibrium point of $(180°, 2.67$ Å$)$ belonging to the θ(CuScCu)-r(ScCu) plane, shows that the ground state of the ScCu_2 molecule is of $^2\Delta_g$ symmetry. For the simplicity of language this is written as $(180°, 2.67$ Å$; \tilde{X}^2\Delta_g)$. The DKH-MRCI wave functions show that the $\tilde{X}^2\Delta_g$ ground state has the dominant electronic configuration $\mathrm{d}^{10}_{\mathrm{Cu},1}\,\mathrm{d}^{10}_{\mathrm{Cu},2}\,\mathrm{s}\sigma^2_{\mathrm{g}}\,\mathrm{s}\sigma^2_{\mathrm{u}}\mathrm{d}\delta^1_{\mathrm{g}}(86\%)$ where the core orbitals have been suppressed and other open-shell configurations with minor contributions are omitted. Notice that, similar to the diatomic molecule ScCu, the Cu d orbitals do not contribute to bonding of the ground state of ScCu_2 and remain in the nature of non-bonding atomic orbitals.

An excited $^2\Sigma^+_g$ state is calculated to occur above the $\tilde{X}^2\Delta_g$ ground state of ScCu_2 with vertical excitation energies of 0.116 eV (if one employs the C_s and the D_{2h} point groups) or of 0.117 eV (if one employs the C_{2v} point group). Since one of the components of the $\tilde{X}^2\Delta_g$ state and the $^2\Sigma^+_g$ state both transform to the $^2A_1$ irreducible representation of the C_{2v} point group, i.e., $^2\Sigma^+_g \to {}^2A_1$ and $X^2\Delta_g \to {}^2A_1 \oplus {}^2A_2$, and since the sole lowest $^2A_1$ state was calculated in the potential surfaces, the $^2\Sigma^+_g$ excited state is not displayed in figure B.83. A second excited state, being of $^2\Pi_g$ symmetry, is computed to vertically lie at 0.215 eV (C_s and D_{2h}) or 0.216 eV (C_{2v}) and to exhibit its potential minimum at the $D_{\infty h}$ point of $(180°, 2.65$ Å$)$. The *small* vertical excitation energies for the $^2\Sigma^+_g \leftarrow \tilde{X}^2\Delta_g$ ($\Delta E = 0.12$ eV) and the $^2\Pi_g \leftarrow \tilde{X}^2\Delta_g$ ($\Delta E = 0.22$ eV) transitions are suggestive of the near-degeneracy of the $\mathrm{d_{Sc}}$-type molecular orbitals in the ScCu_2 molecule and imply that the $^2\Sigma^+_g$ state should be generated from the one-electron $d\sigma_g \leftarrow d\delta_g$ excitation and correspond to the $\mathrm{s}\sigma^2_{\mathrm{g}}\,\mathrm{s}\sigma^2_{\mathrm{u}}\,\mathrm{d}\sigma^1_{\mathrm{g}}$ configuration, while the $^2\Pi_g$ state should be generated from $\mathrm{d}\pi_{\mathrm{g}} \leftarrow \mathrm{d}\delta_{\mathrm{g}}$ and correspond to $\mathrm{s}\sigma^2_{\mathrm{g}}\,\mathrm{s}\sigma^2_{\mathrm{u}}\,\mathrm{d}\pi^1_{\mathrm{g}}$.

According to figure B.33 the $D_{\infty h}$ $^4\Lambda$ states, lying in the range 2.2-2.3 eV above the $\tilde{X}^2\Delta_g$ ground state, do not exhibit $D_{\infty h}$ minima, and the linear CuScCu molecule, having a quartet spin symmetry, will thereby transform into one of the C_{2v} minima. With the quality of agreement between the high level *ab initio* calculations—i.e., potential energy surface, structure optimisation, and single point calculations—there can be little doubt that the ground state of ScCu_2 is $\tilde{X}^2\Delta_g$. It is intriguing to also comment on the invariance of vertical excitation energies for the $^2\Sigma^+_g$ and $^2\Pi_g$ states with respect to the point group used in the calculations. It is believed that the invariance provides evidence that ScCu_2, at least at and around its global minimum, belongs to the subclass of systems which are "successfully" characterised in the present theoretical work. Uttering the word success, in this context, refers to the *absolute* consistency between the theoretical results, and it is independent of the fact that one is, still and unfortunately, suffering from the lack of experimental data on molecules such as $ScCu_2$. As it will be unveiled later on, this success is not notched up for all of the AB_2 molecules. Therefore, although the present work is a good beginning point, it is not sufficient for most of the molecules.

It is important to note how this work can comment on the exo- and endothermicity of the ground state reactions like $AB+B \rightarrow AB_2$ and $A+B_2 \rightarrow AB_2$, the ground state displacement reaction $AB+B \rightarrow A+B_2$ etc. This would be extremely useful for spectroscopists who have to deal with molecular beams containing a vast range of species (e.g., atomic, diatomic, and triatomic) whose relative stabilities should be known/estimated in advance to appropriately target a desired mixed metal molecule, and not some species which are invariably present in the molecular beam. According to table B.38, considering the dissociation energy for the $X^3\Delta$ ground state of the ScCu molecule one can write

$$\mathrm{ScCu}(X^3\Delta) \longrightarrow \mathrm{Sc}(^2\mathrm{D}) + \mathrm{Cu}(^2\mathrm{S}) \qquad \Delta E = 1.11 \pm 0.06 \text{ eV}. \tag{†}$$

Additionally, considering the atomisation energy for the $\tilde{X}^2\Delta_g$ ground state of the $ScCu_2$ molecule one can write

$$\mathrm{Sc}(^2\mathrm{D}) + 2\mathrm{Cu}(^2\mathrm{S}) \longrightarrow \mathrm{ScCu_2}(\tilde{X}^2\Delta_g) \qquad \Delta E = \; -2.93 \text{ eV}. \tag{‡}$$

By first adding a ground state copper atom to both sides of equation (†), and second adding the resulting equation to equation (‡) one can assert that the ground state reaction $\mathrm{ScCu} + \mathrm{Cu} \longrightarrow \mathrm{ScCu_2}$ is exothermic, with $\Delta E = -1.82 \pm 0.06$ eV.

The C_{2v} Structure. In contrast to the $D_{\infty h}$ CuScCu and the $C_{\infty v}$ ScCuCu structures where the doublet states were found to be energetically well separated from the quartet states, the C_{2v} CuScCu structure (figure 3.2) exhibits a complex electronic structure where the doublet and quartet states, energetically and spatially, lie close to each other. These quartet C_{2v} states are most probably originated from the ^{4}F state of atomic scandium that lies 1.43 eV above ^{2}D (J-averaged experimental energies).[118]

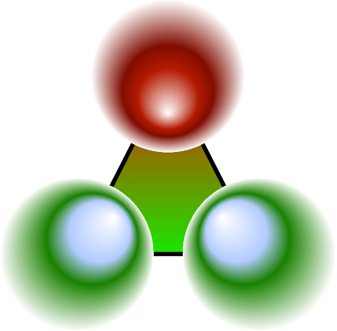
Figure 3.2: C_{2v} $ScCu_2$

Based on the interpolated potential energy surfaces, the bent CuScCu form possesses a lowest $^2A_1$ state which lies 0.46 eV above the $\tilde{X}^2\Delta_g$ ground state and which exhibits its minimum where $\theta_e(\mathrm{CuScCu}) = 54°$ and $r_e(\mathrm{ScCu}) = 2.646$ Å. Thus, the bent form in its lowest $^2A_1$ state has an equilibrium Sc-Cu bond length which is slightly shorter than the bond length in the linear CuScCu structure in its ground $\tilde{X}^2\Delta_g$ state, i.e., $r_e(\tilde{X}^2\Delta_g) - r_e(^2A_1) = 0.02$ Å. The copper-copper distance is obtained as $r_e(\mathrm{CuCu}) = 2.404$ Å for the C_{2v} CuScCu $^2A_1$ state; being 0.18 Å longer than r_e in the Cu_2 $X^1\Sigma_g^+$ state. In the light of interpolated surfaces, for the energy ordering of the C_{2v} CuScCu $^{2,4}\Gamma$ states one can write $^2A_1(0.46) < {}^4B_2 < {}^4B_1 < {}^4A_2 < {}^2B_2 < {}^2A_2 < {}^2B_1 < {}^4A_1(0.91)$, where the electronic energies T_e (in eV) are given in parentheses. For these states, outside of the $^2A_1$ state, the Sc-Cu bond length lies in the range of 2.69-2.72 Å, and the equilibrium CuScCu bond angle is $\theta_e = 53°$. Structure optimisation calculations (employing the C_s point group) agree well with the interpolated surfaces in this case and imply that the lowest state of the C_{2v} CuScCu structure is of doublet spin symmetry ($^2A'$). However, for the electronic energies T_e, for the bond angles θ_e(CuScCu), and for the bond lengths r_e(ScCu) the differences are obtained to be $T_e[^2A'(\text{optimised})] - T_e[^2A_1(\text{interpolated})] = +0.15$ eV, $\theta_e[^2A'(\text{opt.})] - \theta_e[^2A_1(\text{int.})] = +1°$, and $r_e[^2A'(\text{opt.})] - r_e[^2A_1(\text{int.})] = +0.01$ Å at the DKH-MRCI level. Hereafter, electronic energies (T_e) are relative to the ground state ($\tilde{X}$) of the triatomic molecule in question.

It is interesting to mathematically describe the $E(\theta, 2.65\text{ Å}; {}^2A_1 \oplus {}^2A_2)$ potentials for the two components of the $\tilde{X}^2\Delta_g$ ground state (the $^2A_1$ and $^2A_2$ states) of the ScCu$_2$ molecule using a least-squares fit. Shown in figure 3.3 are the electronic energies of the $^2A_1$ and $^2A_2$ states interpolated from the cspline technique against x, that is a variable to which the θ(CuScCu) bond angle has been mapped *via* the relation $x = -1 + \theta/\pi$. The interpolated energies of the $D_{\infty h}$ and the C_{2v} CuScCu $^2A_1/^2A_2$ states have been considered and fitted to an expansion in terms of the Chebyshev polynomials $T_{2k}(x)$ of even order:

$$V(x) = [\sin(\frac{x}{2})]^{-2} \sum_{k=0}^{12} a_{2k} T_{2k} \quad (-1 \leq x \leq 1), \quad x = -1 + \frac{\theta}{\pi},$$

where a_{2k} are fitting coefficients (table B.39), $T_0(x) = 1$, $T_1(x) = x$, and $T_{k+1}(x) = 2xT_k(x) - T_{k-1}(x)$. The sine factor $[\sin^2(x/2)]^{-1}$ guarantees that $V(x)$ has singularities at the left ($\theta = 0°$) and the right ($\theta = 360°$) interval ends. Notice that the electronic energies should not change when reflected over the $x = 0$ axis which implies that $V(x) = V(-x)$ or, equivalently stated, $V(\pi + \Delta\theta) = V(\pi - \Delta\theta)$. This one-dimensional fit suggests that future higher-dimensional studies are likely to succeed in simulating the rovibronic spectroscopy of the AB_2 systems.

For the $^2A_1$ state of the triatomic molecule ScCu$_2$, the MRCI[(20+5)E,(10+8)O] expansion—i.e., correlating all valence electrons—contains approximately 21 million contracted configurations. In total, for the 8 $^{2,4}\Gamma$ states of ScCu$_2$,* roughly 160 million configurations were optimised at each *ab initio* point, based on which the subsequent interpolation was carried out. In order to estimate the "interpolation error" introduced due to the use of (c)spline technique, three single point calculations were performed for the ScCu$_2$ $^2A_1$ state at the $(180°, 2.666\text{ Å})$ and at the $(54.05°, 2.646\text{ Å})$ points, which belong to the r(ScCu)-θ(CuScCu) plane ($D_{\infty h}$ and C_{2v}), and at the $(3.099\text{ Å}, 2.274\text{ Å})$ point which belongs to the r(ScCu)-r(CuCu) plane ($C_{\infty v}$). The resultant energy differences $E[^2A_1(\text{opt.})] - E[^2A_1(\text{int.})]$ were calculated to be 0.001 eV ($D_{\infty h}$), 0.167 eV (C_{2v}), and 0.003 eV ($C_{\infty v}$); with the interpolated energies being lower than those of *ab initio* calculations. The larger C_{2v} energy difference, $\Delta E(C_{2v}) = 0.167$ eV, as

---

*$\Gamma = A_1, B_1, B_2, A_2$

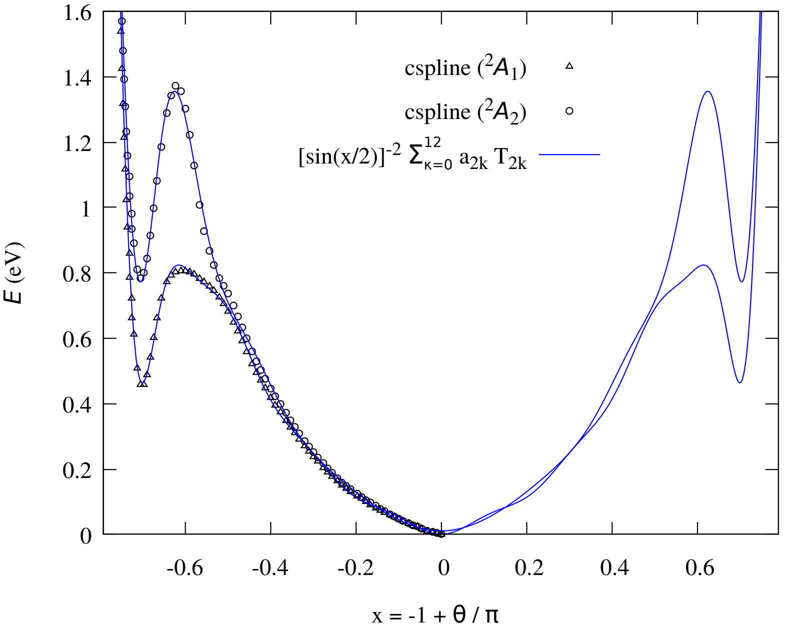

Figure 3.3: The $E(\theta, 2.65\ \text{Å}; {}^2\{A_1 \oplus A_2\})$ potential of the $D_{\infty h}$ and the C_{2v} CuScCu structures obtained at the DKH-MRCI(+Q) level of theory

compared with the $D_{\infty h}$ energy difference, $\Delta E(D_{\infty h}) = 0.001$ eV, can be rationalised on the basis of the slopes of the $V(x)$ functions around the respective $D_{\infty h}$ and C_{2v} minima (see figure 3.3), i.e.,

$$\left.\frac{\partial V(x)}{\partial x}\right|_{x\to 0^{\pm}} << \left.\frac{\partial V(x)}{\partial x}\right|_{x\to 0.7^{\pm}\ \text{or}\ -0.7^{\pm}}.$$

Rectification of this error would, of necessity, require more *ab initio* inputs for the ensuing interpolation, which were prohibitively expensive. The shortcoming due to the interpolation noise—that can be to more or less extent generalised to other systems—exposes that for those portions of potential energy surfaces where the bent C_{2v} forms are involved, the situation becomes flawed and, interpolated and optimised results are predicted to disagree sharply, leaving the corresponding results to be of uncertain reliability. As another example, for the lowest $^5\Gamma$ state of the bent C_{2v} AuTiAu structure $T_e(^5\Gamma_{\text{opt.}}) - T_e(^5\Gamma_{\text{int.}}) = 0.80$ eV, which is indeed disappointing.

The $C_{\infty v}$ Structure. On the basis of figure B.83, the linear ScCuCu structure, at the DKH-MRCI(+Q) level, has a lowest $^2\Delta$ state whose electronic energy (T_e) is 0.74 eV, whose Sc-Cu bond length is 3.099 Å (3.074 Å), and whose Cu-Cu bond length is 2.274 Å (2.259 Å) in the light of interpolated (optimised) results. Potential energy surfaces have also located a $^2\Pi$ state which lies 0.81 eV above the $\tilde{X}^2\Delta_g$ ground state and which exhibits its minimum at $r_e(\text{ScCu}) = 3.096$ Å and $r_e(\text{CuCu}) = 2.274$ Å. According to figure B.58[*] which shows the iso-energy contours for the $^{2,4}\Lambda^{(+)}$ states of the $C_{\infty v}$ ScCuCu structure, the $^2\Delta$ and $^2\Pi$ states possess two minima on the r(ScCu)-r(CuCu) plane under investigation. For example, for the $^2A_1$ and $^2A_2$ states of ScCuCu, which are most likely the two components of a $^2\Delta$ state, the contours have one minimum at $(3.099\ \text{Å}, 2.274\ \text{Å})$ and another one around $(2.83\ \text{Å}, 2.27\ \text{Å})$. Notice that the iso-energy contours are overall drawn with the incremental level of 0.02 eV, one in every three levels is tagged with energies. One can therefore, darting a glance over the levels, approximately locate the minima and their electronic energies with respect to the ground state of the given system.

---

[*] A closer depiction of figure B.58 (interpolation grid of 100 × 100) is given by figure B.59 (interpolation grid of 200 × 200).

$ScAg_2$ and $ScAu_2$. Similar to the $ScCu_2$ molecule, the $ScAg_2$ and $ScAu_2$ molecules possess a $\tilde{X}^2\Delta_g$ ground state, for which potential energy surfaces and structure optimisation calculations agree perfectly with each other, implying that the equilibrium bond lengths r_e(Sc-B) are 2.743 Å ($ScAg_2$) and 2.604 Å ($ScAu_2$).

Figure B.17 displays the potential energy curves along the Sc-Ag internuclear distance for the triatomic molecule $ScAg_2$ obtained at the DKH-CASSCF level of theory. As it can be seen, at $\theta(\text{AgScAg}) = 180°$ which corresponds to the linear $D_{\infty h}$ AgScAg structure, the lowest states are $^2A_1$ and $^2A_2$ ($\tilde{X}^2\Delta_g$) because in the CASSCF calculations the principal (internuclear) axis was the z axis. However, in the DKH-MRCI(+Q) potential energy surfaces shown in figure B.33 the principal axis was the y axis, leading to the C_{2v} components of $^2A_1$ and $^2B_1$ for the $ScAg_2$ $\tilde{X}^2\Delta_g$ ground state. On the basis of figure B.17, for the linear $D_{\infty h}$ AgScAg structure, electronic states which derive from the second separated atom limit Sc(^{4}F) + 2Ag(^{2}S), including the sextet states, do not contribute to the low-energy regime. This justifies the absence of sextet states in the eventual DKH-MRCI(+Q) potential energy surfaces of the ScB_2 molecules. Note, however, that the more one moves to the right of the 3d atoms—with a pragmatic borderline between Mn and Fe—the less reliable become the DKH-CASSCF potential energy curves; obviously it is because the less electron correlation is recovered since the active orbitals are almost filled in the case of the molecules FeB_n, CoB_n, and NiB_n ($n = 1, 2$).

It is explained now how the full $D_{\infty h}$ symmetry assignment was made for the $\tilde{X}^2\Delta_g$ ground state of $ScAg_2$ (and likewise for other triatomic species). Having found the location of the global minimum of the potential energy surfaces $(D_{\infty h}, C_{2v}, C_{\infty v})$ of the $ScAg_2$ states of interest, three single point calculations were performed at the $D_{\infty h}$ equilibrium point of $(180°, 2.743\ \text{Å})$ employing the C_{2v}, the C_s, and the D_{2h} abelian point groups. In the C_{2v} calculation, it was indicated that the lowest state is of $^2\Delta$ ($^2A_1$ and $^2B_1$) symmetry and that the $^2\Sigma^+$ ($^2A_1$) and $^2\Pi$ ($^2A_2$ and $^2B_2$) excited states vertically lie at 0.132 eV and 0.23 eV. The C_s calculation implied that the lowest state is of $^2\Delta$ ($^2A'$ and $^2A''$) symmetry and that the $^2\Sigma$ ($^2A'$) and $^2\Pi$ ($^2A'$ and $^2A''$) excited states vertically lie at 0.131 eV and 0.229 eV. In the D_{2h} calculation, it was found that the lowest state is of $^2\Delta_g$ (^2A_g and $^2B_{1g}$) symmetry and that the $^2\Sigma_g^+$ (^2A_g) and $^2\Pi_g$ ($^2B_{2g}$ and $^2B_{3g}$) excited states vertically lie at 0.131 eV and 0.228 eV. This triple computation therefore indicates that the ground state term of the $ScAg_2$ molecule belongs to the $D_{\infty h}$ AgScAg structure which occurs at $(180°, 2.743\ \text{Å})$ and is of $^2\Delta_g$ symmetry. For some of the triatomic species, such as the VB_2 and NiB_2 molecules (see table

B.38), the lowest states of $D_{\infty h}$ space symmetry were not successfully assigned, because the energy ordering of the low-lying states was not invariant with respect to the conditions of calculations.

3.2.3 The Triatomic Molecules TiB_2

Of the 24 triatomic molecules considered in this study, $TiCu_2$ is the only molecule whose linear $D_{\infty h}$ CuTiCu form does not exhibit any bound electronic state (see figure B.86), and $TiAu_2$ is the only molecule whose linear $C_{\infty v}$ TiAuAu form does not exhibit any bound electronic state (see figure B.88). It is, by figures B.36, B.88, and B.107, evidenced that the triplet states of the linear CuTiCu form are subject to a sort of distortion that breaks the $D_{\infty h}$ space symmetry into C_{2v} such that the global minimum of the potential energy surfaces obtained at the DKH-MRCI(+Q) level of theory occurs at an unusual equilibrium bond angle of $\theta(\text{CuTiCu}) = 167°$ belonging to a ${}^3A_1$ state. The structure optimisation calculations, likewise, suggest that the $TiCu_2$ molecule possesses a triplet ground state which corresponds to a C_{2v} minimum of $(177.5°, 2.570$ Å$)$ which is slightly deviated from linearity. The force causing this distortion is in nature analogous to the one in homonuclear coinage metal trimers B_3 which breaks the $\tilde{X}^2E$ ground state in D_{3h} symmetry into ${}^2A_1$ and ${}^2B_2$ in C_{2v}.[27] In contrast to $TiCu_2$, the $TiAg_2$ and $TiAu_2$ molecules both possess a $\tilde{X}^3\Phi_g$ ground state which, according to optimised results, corresponds to $r_e(\text{TiAg}) = 2.633$ Å ($TiAg_2$) and $r_e(\text{TiAu}) = 2.514$ Å ($TiAu_2$), see figures B.87 and B.88 for further details.

It is worth to consider the relation $A_e[\text{Ti}B_2(\tilde{X}^3\Phi_g)]/D_e[\text{Ti}B(X^4\Phi)]$ where D_e is the dissociation energy of the diatomic molecule TiB and A_e is the atomisation energy of the triatomic molecule TiB_2. According to the DKH-MRCI(+Q) calculations without considering outer-core correlation effects, this ratio is obtained to be 2.2 for $B =$ Cu, 2.5 for $B =$ Ag, and 2.3 for $B =$ Au. Using the ratio of 2.3 for $B =$ Au, and considering $D_e[\text{TiAu}(X^4\Phi)] = 2.50$ eV at the core correlated level of MRCI[(22+5)E,(11+7)O], one can predict an atomisation energy of ≈ 5.8 eV for the $\tilde{X}^3\Phi_g$ ground state of $TiAu_2$ at the MRCI[(38+6)E,(19+8)O] level of theory, as compared to the $A_e[\text{TiAu}_2(\tilde{X}^3\Phi_g)] = 5.57$ eV obtained at the MRCI[(20+6)E,(10+8)O] level of theory.

3.2.4 The Triatomic Molecules VB_2

VCu_2. It is, from figure B.89, indicated that the VCu_2 molecule (and likewise the VAg_2 molecule) takes on a congested electronic structure in that the $D_{\infty h}$, the C_{2v}, and the $C_{\infty v}$ isomers lie, in energy, so close to each other; that is, relative to the $ScCu_2$ molecule one can write

$$E\,(C_{2v}\ \text{CuScCu}\ \tilde{x}^2A_1) - E\,(D_{\infty h}\ \text{CuScCu}\ \tilde{X}^2\Delta_g) = 0.46\ \text{eV},$$
$$E\,(C_{2v}\ \text{CuVCu}\ \tilde{x}^6A_1) - E\,(D_{\infty h}\ \text{CuVCu}\ \tilde{x}^4\Lambda_g) = -0.06\ \text{eV},$$

where $\tilde{x}$ denotes the lowest electronic state of the given isomer, but not necessarily the ground state ($\tilde{X}$). Thus, this work does not determine the ground state of the VCu_2 and VAg_2 molecules, it instead suggests two candidates: the linear $D_{\infty h}$ BVB structure being of quartet spin symmetry and the bent C_{2v} BVB structure being of sextet spin symmetry. These two candidates are, within the accuracy of the present study, indistinguishable from each other. Potential energy surfaces and structure optimisation calculations, performed at the DKH-MRCI(+Q) level of theory, both imply that the linear $D_{\infty h}$ CuVCu structure possesses a $\tilde{x}^4\Lambda_g$ state which can be orbitally degenerate. It is agreeable that these two methods lead also to the same equilibrium V-Cu internuclear distance; $r_e[\text{V-Cu}(\tilde{x}^4\Lambda_g)] = 2.522$ Å. This $D_{\infty h}$ bond length may be compared with that of the diatomic molecule VCu: $r_e[\text{V-Cu}(X^5\Delta)] = 2.47$ Å (table B.17). A single point calculation performed at the $D_{\infty h}$ equilibrium point of $(180°, 2.522\ \text{Å})$, employing the C_s point group in the calculation, leads to energy ordering of ${}^4\Sigma_g^- < {}^4\Pi_g(0.01\ \text{eV}) < {}^4\Delta_g(0.03\ \text{eV})$, where vertical excitation energies are given in parentheses. Employing the C_{2v} and D_{2h} point groups, however, yields ${}^4\Pi_\text{g} < {}^4\Sigma_\text{g}^-(0.01\ \text{eV}) < {}^4\Delta_\text{g}(0.03\ \text{eV}) < {}^4\Phi_\text{g}(0.15\ \text{eV})$. Therefore, the full spatial symmetry of the lowest state of the $D_{\infty h}$ CuVCu isomer cannot be fully assigned.

Figure B.107 shows that at $\theta = \pi \pm \delta\theta$ the ${}^4\Delta_g$ state in $D_{\infty h}$ splits into the ${}^4A_1$ and ${}^4B_1$ states in C_{2v}. Similar to the $D_{\infty h}$ CuTiCu ${}^3\Lambda_g$ states, the $D_{\infty h}$ CuVCu ${}^4\Delta_g$ state is subject to the distortion, leading to a *small* distortion stabilisation in the electronic energy of the ${}^4B_1$ component. The distortion lowers the energy of the ${}^4B_1$ state—not the partner ${}^4A_1$ state—but the energy lowering is not enough to bring the ${}^4B_1$ state below the ${}^4\Sigma_g^-$ or ${}^4\Pi_g$ states. On the basis of table B.38, for the atomisation energy of VCu_2 one can write

$$\text{VCu}_2\left[\tilde{\text{x}}^4\Lambda_\text{g}\right] \longrightarrow \text{V}(^4\text{F}) + 2\text{Cu}(^2\text{S}) \qquad \Delta E = +\,2.48\ \text{eV}.$$

This means that, if one chooses $D_0^0 = 2.01 \pm 0.08$ eV as the dissociation energy of the Cu_2 $X^1\Sigma_g^+$ state,[160] the relative stability of the linear $D_{\infty h}$ CuVCu structure is only 0.47 ± 0.08 eV. In the C_{2v} form, VCu_2 has a lowest sextet state that corresponds to the molecular structure $(53.8°, 2.604\ \text{Å})$ or $(54°, 2.584\ \text{Å})$ based on optimised and interpolated results. The former equilibrium point results in $r_e[\text{Cu-Cu}(\tilde{x}^6A_1)] = 2.36$ Å, and the latter equilibrium point gives $r_e[\text{Cu-Cu}(\tilde{x}^6A_1)] = 2.35$ Å. These are to be compared with the experimental Cu-Cu bond length in the diatomic molecule Cu_2; $r_e(X^1\Sigma_g^+) = 2.2195$ Å,[160] that is $\Delta r_e(\text{Cu-Cu}) = 0.14(3)$ Å increase upon formation of C_{2v} CuVCu according to $\text{Cu}_2(X^1\Sigma_\text{g}^+) + \text{V}(^4\text{F}) \longrightarrow \text{VCu}_2(^6\text{A}_1)$.

VAg₂. The linear $D_{\infty h}$ AgVAg structure has a tentative lowest ${}^4\Sigma_g^-$ term that, according to the DKH-MRCI(+Q) calculations, corresponds to a V-Ag bond length of 2.611 Å (optimised) or 2.616 Å (interpolated). Single point calculations performed at the $D_{\infty h}$ equilibrium, employing the C_{2v} and D_{2h} point groups, result in the energy ordering of ${}^4\Sigma_g^- < {}^4\Pi_g(0.01) < {}^4\Delta_g(0.07) < {}^4\Phi_g(0.17)$, where vertical excitation energies (eV) are given in parentheses. Employing the C_s point group, however, one obtains ${}^4\Sigma_g^- \simeq {}^4\Pi_g \simeq {}^4\Delta_g < {}^4\Phi_g(0.09\ \text{eV})$.

Figure B.21 shows that, at the DKH-CASSCF level of theory, the cluster of the even states $^4\{\Sigma_g^- \oplus \Pi_g \oplus \Delta_g \oplus \Phi_g\}$, which lies considerably below the odd counterpart, i.e., the $^4\Lambda_u$ $(\Lambda = \Sigma^-, \Pi, \Delta, \Phi)$ states, correlates to the second separated atom limit V(^{4}F) + 2Ag(^{2}S), which is experimentally the lowest separated atom limit.

It is remarkable that, similar to the $D_{\infty h}$ CuVCu $^4\Delta_g$ state, as the linear AgVAg isomer bends the $^4\Delta_g$ state splits into the $^4A_1$ and $^4B_1$ states; the $^4B_1$ state is subject to the distortion, while the partner $^4A_1$ state is not. The distortion stabilisation of the AgVAg $^4B_1$ state is, however, larger than that of the CuVCu $^4B_1$ state such that it lowers the AgVAg $^4B_1$ state more, leading to the detection of a stationary point at $(170°, 2.600$ Å) which is, according to figure B.90, isoenergetic with the lowest $D_{\infty h}$ state(s) ($^4\Sigma_g^-$ and $^4\Pi_g$). Hence, the AgVAg $^4B_1$ state exhibits two extrema which are energetically and spatially so close to each other: a $D_{\infty h}$ extremum (presumably a saddle point) at $[180°, 2.62(3)$ Å], and a C_{2v} extremum (presumably a true minimum) at $(170°, 2.600$ Å). For the bent AgVAg structure, the interpolated and optimised calculations agree that the lowest state is of sextet spin symmetry (C_{2v} $\tilde{x}^6\Gamma$). They, however, disagree on the equilibrium molecular structure and on the relative energy of the lowest C_{2v} $\tilde{x}^6\Gamma$ state. Interpolated potential surfaces lead to $r_e[\mathrm{VAg}(\tilde{x}^6A_1)] = 2.680$ Å, while optimised results yield $r_e(\mathrm{VAg}) = 2.720$ Å for the $\tilde{x}^6\Gamma$ state of the bent AgVAg. For the AgVAg bond angle and for electronic energies associated with the linear-to-bent transition $\tilde{x}^6\Gamma(C_{2v}) \leftarrow \tilde{x}^4\Sigma_g^-(D_{\infty h})$, the discrepancies are $\theta_\mathrm{e}(\mathrm{opt.}) - \theta_\mathrm{e}(\mathrm{int.}) = -3°$, and $T_\mathrm{e}(\mathrm{opt.}) - T_\mathrm{e}(\mathrm{int.}) = 0.31$ eV. One can, from table B.38, state that adding one silver atom to vanadium leads to stabilisation energy of 1.19 ± 0.05 eV

$$\mathrm{V}(^4\mathrm{F}) + \mathrm{Ag}(^2\mathrm{S}) \longrightarrow \mathrm{VAg}(X^5\Delta) \qquad \Delta E = -\,1.19 \pm 0.05 \text{ eV}.$$

However, addition of two silver atoms gives

$$\mathrm{V}(^4\mathrm{F}) + 2\mathrm{Ag}(^2\mathrm{S}) \longrightarrow \mathrm{VAg_2}(\tilde{\mathrm{x}}^4\Sigma_\mathrm{g}^-) \qquad \Delta E = -\,2.74 \text{ eV}.$$

Since addition of two Ag atoms stabilises the system by more than twice the amount one Ag atom does, it may reflect the tendency of the cluster to grow further and further.[163]

VAu$_2$. According to the DKH-MRCI(+Q) results, this molecule is predicted to possess a $\tilde{X}^4\Lambda_g$ ground state having its equilibrium structure at $r_e(\mathrm{VAu})$ of 2.475 Å (interpolated) or 2.488 Å (optimised). Similar to the VCu$_2$ and VAg$_2$ molecules, spatial symmetry of the ground state of VAu$_2$ was not fully assigned because equilibrium single point calculations, employing the C_{2v} and D_{2h} point groups, led to the energy sequence $^4\Sigma_g^- < {}^4\Pi_g(0.02) < {}^4\Delta_g(0.2) < {}^4\Phi_g(0.30)$, with vertical excitation energies (eV) given in parentheses. Employing the C_s point group, however, yields $^4\Pi_g < {}^4\Sigma_g^-(0.02 \text{ eV}) < {}^4\Delta_g(0.18 \text{ eV}) < {}^4\Phi_g(0.30 \text{ eV})$.

3.2.5 The Triatomic Molecules CrB_2

CrCu$_2$. Based on the DKH-MRCI(+Q) calculations, the lowest states of the linear $D_{\infty h}$ CuCrCu, the bent C_{2v} CuCrCu, and the linear $C_{\infty v}$ CrCuCu structures are practically degenerate within the accuracy of the present work (figure B.92).

In the light of the structure optimisation calculations, the ground state of $CrCu_2$ belongs to the linear $C_{\infty v}$ CrCuCu structure and is of ${}^7\Sigma^+$ symmetry which has its minimum at $r_e(\text{CrCu}) = 2.586$ Å and $r_e(\text{CuCu}) = 2.265$ Å. The data amassed in table B.38 show that the atomisation energy of the ${}^7\Sigma^+$ state of the $CrCu_2$ molecule is only 1.87 eV. This means, being inclined to agree with $D_0^0 = 2.01 \pm 0.08$ eV for the ground state of the diatomic molecule Cu_2, that the $CrCu_2$ molecule is (due to lack of a better word)[*] *unstable* with respect to the asymptote ${}^7\text{S(Cr)} + X^1\Sigma_{\text{g}}^+(\text{Cu}_2)$; a serious tendency to predissociate on a subnanosecond time scale would probably prevent the observation of this molecule. On the other hand, embracing the theoretical dissociation energies of the Cu_2 $X^1\Sigma_g^+$ state—1.74 eV (ref. 162), 1.81 eV (ref. 119), 1.84 eV (ref. 161), and 1.62 eV (potential surfaces)—points to the more logical conclusion that $CrCu_2$ is loose and a metastable intermediate for the reaction

$$\text{CrCu}(X^6\Sigma^+) + \text{Cu}(^2\text{S}) \longrightarrow \text{CrCu}_2(\tilde{x}^7\Sigma^+) \qquad \Delta E = -0.71 \pm 0.05 \text{ eV}$$
$$\text{CrCu}_2(\tilde{x}^7\Sigma^+) \longrightarrow \text{Cr}(^7\text{S}) + \text{Cu}_2(X^1\Sigma_g^+),$$

where for the latter equation ΔE is estimated to be in the range of 0.03-0.25 eV. In general, although it is informative to study loose molecules such as $CrCu_2$, these molecules, irrespective of the electronic states, have low bond strength with respect to the B_2 $X^1\Sigma_g^+$ state and would, most probably predissociate as soon as the energy exceeds the energy of the $A(^{2\text{S}+1}\text{L}) + B_2(X^1\Sigma_{\text{g}}^+)$ asymptote. It is therefore predicted that very special experimental techniques are required to trap and observe molecules like $CrCu_2$, for not only they are floppy but also for the energetic and spatial proximity of the low-lying electronic states.

Potential energy surfaces imply that the linear $C_{\infty v}$ CrCuCu structure has a lowest $\tilde{x}^7\Sigma^+$ state. However, for the lowest $\tilde{x}^7\Sigma^+$ state of the linear $C_{\infty v}$ CrCuCu structure the discrepancies in total energies and in equilibrium molecular properties between the interpolated and optimised results are $E[\tilde{x}^7\Sigma^+(\text{int.})] - E[\tilde{x}^7\Sigma^+(\text{opt.})] = 0.19$ eV, $r_e[\text{CrCu(int.)}] - r_e[\text{CrCu(opt.)}] = 0.05$ Å, and $r_e[\text{CuCu(int.)}] - r_e[\text{CuCu(opt.)}] = 0.09$ Å. For the linear structures ($D_{\infty h}$ and $C_{\infty v}$), where interpolation noise is estimated to be negligibly *small*, sharp disagreements between the interpolated and optimised results, as to electronic energies or equilibrium molecular properties, are warning signals indicating that one of the methods (or both of them) is biased towards some configuration in the CASSCF wave functions, and this bias was not removed in the subsequent MRCI treatment.

It is worth noting that, from the C_{2v} standpoint, the ${}^7A_1$ (^{7}S) and ${}^5A_1$ (^{5}S) states of the Cr atom (table B.2), the X^6A_1 ($X^6\Sigma^+$) and ${}^8A_1$ (${}^8\Sigma^+$) states of the CrCu diatomic molecule (table B.20), and the $\tilde{x}^7A_1$ ($\tilde{x}^7\Sigma^+$) and ${}^5A_1$ (${}^5\Sigma^+$) states of the linear $C_{\infty v}$ CrCuCu structure are all orbitally non-degenerate states.

---

[*] A charming story on the MgH_2 molecule inhibits one from uttering the term *stability* and its word family. In 1975, in the light of theoretical findings, Ahlrichs *et al.* stated: "... we conclude that MgH_2 is not bound with respect to Mg + H_2 and hence not likely to be a stable species." (ref. 164). In 2003, Shayesteh *et al.* reported on the discovery of free gaseous MgH_2 (ref. 165).

In contrast to the structure optimisation calculations which predicted a $C_{\infty v}$ $\tilde{x}^7\Sigma^+$ ground state for the triatomic molecule $CrCu_2$, the interpolated potential energy surfaces indicate that the ground state of $CrCu_2$ belongs to the C_{2v} isomer and is of ${}^7A_1$ symmetry (see figure B.92). A second C_{2v} CuCrCu state of ${}^5B_2$ symmetry has been interpolated to lie energetically close to the $\tilde{x}^7A_1$ state but spatially far away from this state. The energy difference between the ${}^5B_2$ and $\tilde{x}^7A_1$ states, at the interpolated level, is calculated to be $E({}^5B_2) - E(\tilde{x}^7A_1) = 0.01$ eV. The equilibrium structure of the ${}^5B_2$ state is interpolated to be $\theta_e(\text{CuCrCu}) = 121°$ and $r_e(\text{CrCu}) = 2.489$ Å, and the equilibrium structure of the $\tilde{x}^7A_1$ state is found at $(55°, 2.540$ Å$)$. Figure B.107 unveils that the CuCrCu ${}^5B_2$ state, being the C_{2v} component of a quintet doubly-degenerate $D_{\infty h}$ state (presumably a ${}^5\Pi_g$), is subject to the distortion from linearity. However, in contrast to the distortion in the $TiCu_2$, VCu_2, and VAg_2 molecules (*vide supra*), and in analogy with the distortion in the $CrAg_2$ molecule (*vide infra*), the distortion of the CuCrCu ${}^5B_2$ state causes a broad well (figure B.42) for its global minimum which is most probably due to the weak bonding interaction in $CrCu_2$ as compared to the $TiCu_2$ and VCu_2 species. For $TiCu_2$, VCu_2, and $CrCu_2$ the ground state atomisation energies are calculated to be 2.52 eV, 2.48 eV, and 1.87 eV, respectively.

In order to appreciate the complexity of the electronic structure in a molecular system, it is typically proved useful to consider the constituent fragments. The $CrCu_2$ molecule is a good example that the electronic states of the fragments cannot always be uniquely related to those of the molecule. The Cr atom possesses a ground state, ^{7}S, which is well separated from the lowest excited state; ^{5}S ($E = 0.94$ eV). The Cu atom and the Cu_2 molecule have a simple electronic structure, whose ground states are energetically well isolated from the excited states. The CrCu molecule has a ground state, $X^6\Sigma^+$, which is also well separated from the first excited state; ${}^8\Sigma^+$ ($T_e = 1.19$ eV). However, adding a second Cu atom unpredictably complicates the situation in that, within an energy range of 1 eV, the $CrCu_2$ molecule exhibits at least 22 (optimised and interpolated) electronic states, which in turn made this work incapable of predicting its ground state.

$CrAg_2$. According to figure B.93, which displays the low-lying electronic states of the $CrAg_2$ molecule obtained at the DKH-MRCI(+Q) level of theory, $CrAg_2$ possesses a lowest $C_{\infty v}$ $\tilde{x}^7\Sigma^+$ state which is, within the accuracy of the present study, degenerate with a lowest C_{2v} $\tilde{x}^5B_2$ state, i.e., $E[\tilde{x}^7\Sigma^+(\text{int.})] - E[\tilde{x}^5B_2(\text{int.})] = 0.007$ eV and $E[\tilde{x}^7\Sigma^+(\text{opt.})] - E[\tilde{x}^5B_2(\text{opt.})] = 0.010$ eV. Furthermore, in the case of the CrAgAg $\tilde{x}^7\Sigma^+$ and the AgCrAg $\tilde{x}^5B_2$ states the interpolated and optimised levels agree absolutely with each other, i.e., $E[\tilde{x}^7\Sigma^+(\text{opt.})] - E[\tilde{x}^7\Sigma^+(\text{int.})] = 0.000$ eV and $E[\tilde{x}^5B_2(\text{opt.})] - E[\tilde{x}^5B_2(\text{int.})] = 0.003$ eV. At the interpolated (optimised) level, for the $\tilde{x}^7\Sigma^+$ state the Cr-Ag bond length is 2.757 Å (2.758 Å) and the Ag-Ag bond length is 2.602 Å (2.603 Å). According to figure B.23—displaying the DKH-CASSCF potential energy curves along the Cr-Ag internuclear distance—the ${}^9\Sigma^+$ state originating from the Cr(^{7}S) + 2Ag(^{2}S) separated atom limit and the triplet states originating from the Cr(^{5}D) + 2Ag(^{2}S) separated atom limit, irrespective of the molecular structure, are not bound. Notice that the second seprated atom limit of the $CrAg_2$

molecule is, experimentally, Cr(^{5}S) + 2Ag(^{2}S).[118] At the DKH-CASSCF level, however, the second separated atom limit is calculated to be Cr(^{5}D) + 2Ag(^{2}S).

CrAu$_2$. In contrast to the CrCu$_2$ and CrAg$_2$ molecules, CrAu$_2$ possesses a $D_{\infty h}$ AuCrAu $\tilde{X}^5\Sigma_g^+$ ground state which is well separated from the lowest C_{2v} AuCrAu and the $C_{\infty v}$ CrAuAu minima; that is, at the interpolated level, for the linear-to-bent transition $\tilde{x}^7A_1 \longleftarrow \tilde{X}^5\Sigma_g^+$, $T_e = 1.24$ eV, and for the linear-to-linear transition $\tilde{x}^7\Sigma^+ \longleftarrow \tilde{X}^5\Sigma_g^+$, $T_e = 1.52$ eV.

3.2.6 Overall Trends

Figures B.108-B.117 display the A-B (B-B) bond lengths, A = Sc-Ni, B = Cu/Ag/Au, for the lowest state of structures $D_{\infty h}$ BAB, C_{2v} BAB, and $C_{\infty v}$ ABB calculated at the DKH-MRCI(+Q) level of theory. For the $D_{\infty h}$ BAB structures, for example, the lowest state bond lengths $r_e(AB)$ are calculated to be in the range 2.36 Å (NiCu) - 2.67 Å (ScCu) for B = Cu, in the range 2.50 Å (NiAg) - 2.74 Å (ScAg) for B = Ag, and in the range 2.36 Å (NiAu) - 2.60 Å (ScAu) for B = Au. Similar to the ratio $r_e(A\text{Ag})/r_e(AB)$, corresponding to the ground states of the diatomic molecules AB, which was predicted to vary within 1.055 ± 0.025 (see subsection 3.1.6), the ratio $r_e[A\text{Ag}(D_{\infty h})]/r_e[AB(D_{\infty h})]$, corresponding to the lowest states of the linear BAB structures, is calculated to vary within 1.044 ± 0.016. Figure B.108 shows $r_e(A\text{Cu})$ for the lowest and low-lying excited states of the $D_{\infty h}$ CuACu structures along with the linear regression line expressed as $r_e = a\,Z_A + b$, where $a = -0.04$ Å, $b = 3.46$ Å, and Z_A is the atomic number of the atom A. According to this figure, one can predict that the $D_{\infty h}$ CuTiCu $^3\Lambda_g$ states—outside of those states which are subject to the distortion from linearity—would correspond to $r_e(\text{TiCu}) \approx 2.58$ Å. Notice that linear CuTiCu did not show any bound electronic states based on the DKH-MRCI(+Q) results presented in this work.

As one moves through the 3d atoms from Sc to V, the separation energies for the LS excitations 3d^{m-1}4s^1 ← 3d^{m-2}4s^2 decrease; for scandium $\Delta E(^4\text{F} \leftarrow {}^2\text{D}) = 1.43$ eV, for titanium $\Delta E(^5\text{F} \leftarrow {}^3\text{F}) = 0.81$ eV, and for vanadium $\Delta E(^6\text{D} \leftarrow {}^4\text{F}) = 0.24$ eV.[118] In triatomic molecules ScAg$_2$, TiAg$_2$, and VAg$_2$, a trend has emerged for the linear-to-bent transitions which, most probably, relates to this increasing stabilisation of the higher spin A states; at the optimised level for ScAg$_2$ $\Delta E[^4\Gamma(C_{2v}) \leftarrow \tilde{X}^2\Delta_g] = 0.88$ eV, for TiAg$_2$ $\Delta E[^5\Gamma(C_{2v}) \leftarrow \tilde{X}^3\Phi_g] = 0.56$ eV, and for VAg$_2$ $\Delta E[^6\Gamma(C_{2v}) \leftarrow \tilde{x}^4\Sigma_g^-] = 0.35$ eV. This perhaps reflects that the higher-spin states being of C_{2v} space symmetry are heavily influenced by the atomic states deriving from the high-spin A 3d^{m-1}4s^1 states.

Chapter 4

Synopsis and Conclusion

A total of 561 electronic terms of 24 bimetallic transition metal diatomic molecules AB ($A =$ Sc-Ni, $B =$ Cu/Ag/Au) and of 24 bimetallic transition metal triatomic molecules AB_2 were studied, allowing to uniformly determine the complete set of spectroscopic constants for these species. All-electron calculations were undertaken treating scalar relativistic effects on an equal footing with electron correlation which was incorporated using multireference approaches.

For the diatomic molecules, spin-orbit coupling was calculated *a posteriori* based on the CASSCF/MRCI eigenvalues and eigenstates as zeroth-order solutions. Full and smooth potential energy curves were provided for the ground and low-lying states in the (Λ, S) representation, whereby spectroscopic constants were derived. As to the assessment, the theoretical results on diatomic species show good agreement with the experimental data limitedly available for some systems. Exact 2-component relativistic calculations were performed for the atoms and the ACu molecules in order to assess the credibility of the perturbative spin-orbit coupling. Inclusion of outer-core correlation effects has allowed to evaluate the magnitude of its influence on the spectroscopic constants of the ground state.

For the triatomic molecules, two sets of potential energy surfaces have been constructed using spline interpolation, whereby observable molecular properties have been extracted. The first set, $E(\theta_{BAB}, r_{AB}; {}^{2\mathrm{S}+1}\Gamma)$, describes the electronic states corresponding to the linear BAB and the bent BAB structures as well as the smooth connection between them. The second set, $E(r_{AB}, r_{BB}; {}^{2\mathrm{S}+1}\Lambda)$, represents the electronic states corresponding to the linear ABB structure. The potential minima thus obtained have been assessed, first, by considering their relative stabilities with respect to the asymptotes $A + B_2$, $AB + B$, and $A + 2B$—all being in their respective ground states. Secondly, automatic structure optimisation calculations have been applied for the lowest states of each isomer.

For the diatomic molecules AB, at the valence correlated DKH-MRCI-(SO) level of theory, the following electronic ground state terms are found: ${}^3\Delta_1(\mathrm{Sc}B)$, ${}^4\Phi_{3/2}(\mathrm{Ti}B)$, ${}^5\Delta_{0^+}(\mathrm{V}B)$, ${}^6\Sigma^+_{5/2}(\mathrm{Cr}B)$, ${}^7\Sigma^+_3(\mathrm{Mn}B)$, ${}^6\Delta_{9/2}(\mathrm{Fe}B)$, ${}^3\Phi_4(\mathrm{CoCu,CoAg})$, ${}^5\Phi_5(\mathrm{CoAu})$, and ${}^2\Delta_{5/2}(\mathrm{Ni}B)$. These ground state terms could have been predicted by the mapping between the diatomic molecules

AB and the monocations A^+: Sc$^+$ ^{3}D$_1$, Ti$^+$ ^{4}F$_{3/2}$, V$^+$ ^{5}D$_0$, Cr$^+$ ^{6}S$_{5/2}$, Mn$^+$ ^{7}S$_3$, Fe$^+$ ^{6}D$_{9/2}$, Co$^+$ ^{3}F$_4$, and Ni$^+$ ^{2}D$_{5/2}$. The ground state mapping between A^+ and AB, observed in this study, accumulates further evidence as to the ligand field model (see ref. 108) which treats a transition metal diatomic molecule (e.g., AB) as two positively charged cores, (A^+ and B^+), surrounded by a σ^2 cloud. Although the ground state of the AB molecule is predicted to correlate with the separated atom limit $A(3\mathrm{d}^{m-2}4\mathrm{s}^2) + B[(k-1)\mathrm{d}^{10}k\mathrm{s}^1]$ in most cases, the A $3\mathrm{d}^{m-1}4\mathrm{s}^1$ configuration, due to a strong $\sigma(\mathrm{s}_A\text{-}\mathrm{s}_B)$ interaction, results in molecular states which are sometimes more bound than the ground state; e.g., $D_e[\mathrm{Ti}B(2^4\Delta)] - D_e[\mathrm{Ti}B(X^4\Phi)] =$ 0.13 eV($B =$ Cu) and 0.28 eV($B =$ Ag), $D_e[\mathrm{Fe}B(^4\Sigma^-)] - D_e[\mathrm{Fe}B(X^6\Delta)] = 0.72$ eV($B =$ Cu) and 0.71 eV($B =$ Ag). The AAu molecules possess larger ground state dissociation energies than either the ACu or the AAg molecules which could be attributed to relativity;[166,167] 0.67 eV [FeCu($X^6\Delta$)] $\leq D_e \leq$ 1.81 eV [NiCu($X^2\Delta$)], 0.77 eV [FeAg($X^6\Delta$)] $\leq D_e \leq$ 1.68 eV [NiAg($X^2\Delta$)], and 1.59 eV [CoAu($X^5\Phi$)] $\leq D_e \leq$ 2.52 eV [ScAu($X^3\Delta$)].

At the valence correlated DKH-MRCI(+Q) level of theory, the triatomic molecules whose ground states ($\tilde{X}$) belong to the linear $D_{\infty h}$ BAB isomer are ScB_2 ($^2\Delta_g$), TiAg$_2$ ($^3\Phi_g$), TiAu$_2$ ($^3\Phi_g$), VAu$_2$ ($^4\Lambda_g^{(-)}$), CrAu$_2$ ($^5\Sigma_g^+$), MnB_2 ($^6\Sigma_g^+$), FeB_2 ($^5\Delta_g$), CoB_2 ($^4\Phi_g$), and NiB_2 ($^3\Lambda_g^{(-)}$). For the TiCu$_2$ molecule a $\tilde{x}^3A_1$ state, corresponding to a C_{2v} CuTiCu isomer which is slightly distorted from the linear $D_{\infty h}$ CuTiCu form [$\theta = 167°$(int.) and $\theta = 178°$(opt.)], is predicted to be a good ground state candidate. For the VCu$_2$ and VAg$_2$ molecules, the linear $D_{\infty h}$ BVB $\tilde{x}^4\Lambda_g^{(-)}$ state is practically degenerate with the bent C_{2v} BVB $\tilde{x}^6\Gamma$ state within the accuracy of this work—in the case of the VAg$_2$ molecule a distorted C_{2v} AgVAg $\tilde{x}^4B_1$ state is also a good candidate for the ground state. For the CrCu$_2$ and CrAg$_2$ molecules, four spin-space symmetries are predicted for the ground state; a linear $D_{\infty h}$ $B$Cr$B$ $\tilde{x}^5\Sigma_g^+$ state, a linear $C_{\infty v}$ CrBB $\tilde{x}^7\Sigma^+$ state, a bent C_{2v} $B$Cr$B$ $\tilde{x}^7A_1$ state, and a bent C_{2v} $B$Cr$B$ $\tilde{x}^5B_2$—in the case of CrAg$_2$ a linear $D_{\infty h}$ AgCrAg $\tilde{x}^7\Lambda_{(g/u)}^{(\pm)}$ is also a good candidate for the ground state. Due to invariance of the energy ordering of the ground and the low-lying excited states with respect to the change in the conditions of the calculations, it was sometimes possible to unambiguously assign Λ quantum numbers to the $D_{\infty h}$ ground states, and sometimes, due to the quasi-degeneracy of the linear $D_{\infty h}$ BAB states, it was not.

Bibliography

[1] Annamraju Kasi Viswanath. From Clusters to Semiconductor Nanostructures. *Journal of Nanoscience and Nanotechnology*, 14(2):1253–1281, 2014. doi: doi:10.1166/jnn.2014.9009.

[2] Michael D. Morse. Clusters of transition-metal atoms. *Chem. Rev.*, 86(6):1049–1109, 1986. doi: 10.1021/cr00076a005.

[3] J. Jellinek and E. B. Krissinel. *Theory of Atomic and Molecular Clusters*. Springer: Berlin, Germany, 1999.

[4] Pham Vu Nhat and Minh Tho Nguyen. Trends in structural, electronic and energetic properties of bimetallic vanadium-gold clusters Au_nV with n = 1-14. *Phys. Chem. Chem. Phys.*, 13:16254–16264, 2011. doi: 10.1039/C1CP22078K.

[5] Han Myoung Lee, Maofa Ge, B. R. Sahu, P. Tarakeshwar, and Kwang S. Kim. Geometrical and Electronic Structures of Gold, Silver, and Gold-Silver Binary Clusters: Origins of Ductility of Gold and Gold-Silver Alloy Formation. *J. Phys. Chem. B*, 107 (37):9994–10005, 2003. doi: 10.1021/jp034826+.

[6] F. Baletto, C. Mottet, A. Rapallo, G. Rossi, and R. Ferrando. Growth and energetic stability of AgNi core-shell clusters. *Surf. Sci.*, 566-568, Part 1:192–196, 2004. doi: 10.1016/j.susc.2004.05.044. Proceedings of the 22nd European Conference on Surface Science.

[7] Giulia Rossi, Riccardo Ferrando, Arnaldo Rapallo, Alessandro Fortunelli, Benjamin C. Curley, Lesley D. Lloyd, and Roy L. Johnston. Global optimization of bimetallic cluster structures. II. Size-matched Ag-Pd, Ag-Au, and Pd-Pt systems. *J. Chem. Phys.*, 122: 194309, 2005. doi: 10.1063/1.1898224.

[8] R. Ferrando, A. Fortunelli, and G. Rossi. Quantum effects on the structure of pure and binary metallic nanoclusters. *Phys. Rev. B*, 72:085449, 2005. doi: 10.1103/PhysRevB.72.085449.

[9] Natalie Austin and Giannis Mpourmpakis. Understanding the Stability and Electronic and Adsorption Properties of Subnanometer Group XI Monometallic and Bimetallic Catalysts. *J. Phys. Chem. C*, 118:18521–18528, 2014. doi: 10.1021/jp504015a.

[10] Hervé Portales, Lucien Saviot, Eugène Duval, Mélanie Gaudry, Emmanuel Cottancin, Michel Pellarin, Jean Lermé, and Michel Broyer. Resonant Raman scattering by quadrupolar vibrations of Ni-Ag core-shell nanoparticles. *Phys. Rev. B*, 65:165422,

Apr 2002. doi: 10.1103/PhysRevB.65.165422.

[11] M. Moskovits, I. Srnováá-ŠŠloufováá, and B. Vlččkováá. Bimetallic Ag-Au nanoparticles: Extracting meaningful optical constants from the surface-plasmon extinction spectrum. *J. Chem. Phys.*, 116(23):10435–10446, 2002. doi: 10.1063/1.1449943.

[12] M. Gaudry, E. Cottancin, M. Pellarin, J. Lermé, L. Arnaud, J. R. Huntzinger, J. L. Vialle, M. Broyer, J. L. Rousset, M. Treilleux, and P. Mélinon. Size and composition dependence in the optical properties of mixed (transition metal/noble metal) embedded clusters. *Phys. Rev. B*, 67:155409, 2003. doi: 10.1103/PhysRevB.67.155409.

[13] Shouheng Sun, C. B. Murray, Dieter Weller, Liesl Folks, and Andreas Moser. Monodisperse FePt Nanoparticles and Ferromagnetic FePt Nanocrystal Superlattices. *Science*, 287:1989–1992, 2000. doi: 10.1126/science.287.5460.1989.

[14] S. Dennler, J. L. Ricardo-Chavez, J. Morillo, and G. M. Pastor. Density functional calculations on small bimetallic magnetic clusters. *Eur. Phys. J. D*, 24(1-3):237–240, 2003. doi: 10.1140/epjd/e2003-00130-9.

[15] E. Janssens, S. Neukermans, H. M. T. Nguyen, M. T. Nguyen, and P. Lievens. Quenching of the Magnetic Moment of a Transition Metal Dopant in Silver Clusters. *Phys. Rev. Lett.*, 94:113401, Mar 2005. doi: 10.1103/PhysRevLett.94.113401.

[16] Hung Tan Pham, Loc Quang Ngo, My Phuong Pham-Ho, and Minh Tho Nguyen. Theoretical Study of Small Scandium-Doped Silver Clusters ScAg_n with n = 1–7: σ-Aromatic Feature. *J. Phys. Chem. A*, 120:7964–7972, 2016. doi: 10.1021/acs.jpca.6b08080. PMID: 27648673.

[17] Jinyun Yuan, Guowei Li, Baocheng Yang, Jinping Zhang, Zijiong Li, and Houyang Chen. Selective adsorption of ethylene on bimetallic $\mathrm{CuV}_n^{+/0}$ (n = 1–5) clusters: A theoretical study. *Comput. Mater. Sci.*, 111:489–496, 2016. doi: 10.1016/j.commatsci.2015.09.064.

[18] Jinyun Yuan, Baocheng Yang, Guowei Li, Yubing Si, Shuaiwei Wang, Shouren Zhang, and Houyang Chen. Geometries and electronic properties of bimetallic CuV_n (n = 1–5) clusters and their cations: Insight from density functional calculations. *Comput. Mater. Sci.*, 102:213–219, 2015. doi: 10.1016/j.commatsci.2015.02.037.

[19] K. Hirsch, V. Zamudio-Bayer, A. Langenberg, M. Vogel, J. Rittmann, S. Forin, T. Mööller, B. v. Issendorff, and J. T. Lau. Impurity Electron Localization in Early-Transition-Metal-Doped Gold Clusters. *J. Phys. Chem. C*, 119:11184–11192, 2015. doi: 10.1021/jp511927q.

[20] Hui-Fang Li and Huai-Qian Wang. Probing the stability of neutral and anionic transition-metal-doped golden cage nanoclusters: $\mathrm{M@Au}_{16}$ (M = Sc, Ti, V). *Phys. Chem. Chem. Phys.*, 16:244–254, 2014. doi: 10.1039/C3CP53292E.

[21] Die Dong, Xiao-Yu Kuang, Jian-Jun Guo, and Ben-Xia Zheng. Geometries, stabilities, and magnetic properties of $\mathrm{Cr@Au}_n$ ($n = 1-8$) clusters: Density functional theory study. *Physica A: Statistical Mechanics and its Applications*, 389(22):5216–5222, 2010. doi: 10.1016/j.physa.2010.07.019.

[22] Xiaohui Wei, Rulong Zhou, Williams Lefebvre, Kai He, Damien Le Roy, Ralph Skomski, Xingzhong Li, Jeffrey E. Shield, Matthew J. Kramer, Shuang Chen, Xiao Cheng Zeng, and David J. Sellmyer. Structural and Magnetic Evolution of Bimetallic MnAu Clusters Driven by Asymmetric Atomic Migration. *Nano Lett.*, 14:1362–1368, 2014. doi: 10.1021/nl404412w. PMID: 24517293.

[23] Meng Zhang, Hongyu Zhang, Lina Zhao, Yan Li, and Youhua Luo. Low-Energy Isomer Identification, Structural Evolution, and Magnetic Properties in Manganese-Doped Gold Clusters MnAu_n (n = 1–16). *J. Phys. Chem. A*, 116(6):1493–1502, 2012. doi: 10.1021/jp2094406.

[24] Rulong Zhou, Xiaohui Wei, Kai He, Jeffrey E. Shield, David J. Sellmyer, and Xiao Cheng Zeng. Theoretical and Experimental Characterization of Structures of MnAu Nanoclusters in the Size Range of 1–3 nm. *ACS Nano*, 5:9966–9976, 2011. doi: 10.1021/nn203739d. PMID: 22106816.

[25] X. Wei, D. Le Roy, R. Skomski, X. Z. Li, Z. Sun, J. E. Shield, M. J. Kramer, and D. J. Sellmyer. Structure and magnetism of MnAu nanoclusters. *J. Appl. Phys.*, 109:07B523, 2011. doi: 10.1063/1.3559502.

[26] Jacob Grimm and Wilhelm Grimm. *The poor miller's apprentice and the cat (Der arme Müllerbursch und das Kätzchen)*, page 348. Princeton University Press, 2014.

[27] Gregory A. Bishea, Caleb A. Arrington, Jane M. Behm, and Michael D. Morse. Resonant two-photon ionization spectroscopy of coinage metal trimers: $\mathrm{Cu_2Ag}$, $\mathrm{Cu_2Au}$, and CuAgAu. *The Journal of Chemical Physics*, 95(12):8765–8778, 1991. doi: 10.1063/1.461212.

[28] E. Folcke, J. M. Le Breton, W. Lefebvre, J. Bran, R. Lardéé, F. Golkar, and J. E. Shield. Investigation of the magnetic properties of FeAu nanoclusters in a W matrix: Evidence for exchange-bias phenomenon. *J. Appl. Phys.*, 113:183903, 2013. doi: 10.1063/1.4803129.

[29] A. S. Prokhorov, E. S. Zhukova, B. P. Gorshunov, M. B. S. Hesselberth, J. Aarts, G. J. Nieuwenhuys, S. Kaiser, and M. Dressel. Localization of conduction electrons in the ferromagnetic clusters AuFe. *JETP Letters*, 89:466–470, 2009. doi: 10.1134/S0021364009090094.

[30] B. Gorshunov, S. Kaiser, E. S. Zhukova, A. S. Prokhorov, M. B. S. Hesselberth, J. Aarts, G. J. Nieuwenhuys, and M. Dressel. Charge carrier localization due to ferromagnetic clusters in concentrated AuFe alloys. *Phys. Rev. B*, 79:054203, 2009. doi: 10.1103/PhysRevB.79.054203.

[31] Patrick Huang and Emily A. Carter. Ab Initio Explanation of Tunneling Line Shapes for the Kondo Impurity State. *Nano Lett.*, 8:1265–1269, 2008. doi: 10.1021/nl0804203.

[32] J. Tuaillon-Combes, E. Bernstein, O. Boisron, and P. Méélinon. Monitoring the core shell structure in bimetallic clusters: The case of CoAg. *Chem. Phys. Lett.*, 564:65–68, 2013. doi: 10.1016/j.cplett.2013.02.024.

[33] F. Dorfbauer, T. Schrefl, M. Kirschner, G. Hrkac, D. Suess, O. Ertl, and J. Fidler.

Nanostructure calculation of CoAg core-shell clusters. *J. Appl. Phys.*, 99:08G706, 2006. doi: 10.1063/1.2176107.

[34] Mahdieh Aghajani, S. Javad Hashemifar, and Hadi Akbarzadeh. First-principles insights into interaction of Au with small Co clusters. *Physica E: Low-dimensional Systems and Nanostructures*, 62:64–70, 2014. doi: 10.1016/j.physe.2014.04.025.

[35] D. Llamosa Péérez, A. Espinosa, L. Martíínez, E. Romáán, C. Ballesteros, A. Mayoral, M. Garcíía-Hernáández, and Y. Huttel. Thermal Diffusion at Nanoscale: From CoAu Alloy Nanoparticles to Co@Au Core/Shell Structures. *J. Phys. Chem. C*, 117(6):3101–3108, 2013. doi: 10.1021/jp310971f.

[36] Kari Laasonen, Emanuele Panizon, Davide Bochicchio, and Riccardo Ferrando. Competition between Icosahedral Motifs in AgCu, AgNi, and AgCo Nanoalloys: A Combined Atomistic-DFT Study. *J. Phys. Chem. C*, 117(49):26405–26413, 2013. doi: 10.1021/jp410379u.

[37] Davide Bochicchio and Riccardo Ferrando. Size-Dependent Transition to High-Symmetry Chiral Structures in AgCu, AgCo, AgNi, and AuNi Nanoalloys. *Nano Lett.*, 10(10):4211–4216, 2010. doi: 10.1021/nl102588p.

[38] Bethany J. Auten, Benjamin P. Hahn, Ganesh Vijayaraghavan, Keith J. Stevenson, and Bert D. Chandler. Preparation and Characterization of 3 nm Magnetic NiAu Nanoparticles. *J. Phys. Chem. C*, 112(14):5365–5372, 2008. doi: 10.1021/jp076982c.

[39] D. W. Yuan, Yang Wang, and Zhi Zeng. Geometric, electronic, and bonding properties of $\mathrm{Au}_N M$ (N = 1–7, M = Ni, Pd, Pt) clusters. *J. Chem. Phys.*, 122(11):114310, 2005. doi: 10.1063/1.1862239.

[40] Emanuele Panizon, Jimena A. Olmos-Asar, Maria Peressi, and Riccardo Ferrando. Study of structures and thermodynamics of CuNi nanoalloys using a new DFT-fitted atomistic potential. *Phys. Chem. Chem. Phys.*, 17:28068–28075, 2015. doi: 10.1039/C5CP00215J.

[41] P. Quaino, G. Belletti, S. A. Shermukhamedov, D. V. Glukhov, E. Santos, W. Schmickler, and R. Nazmutdinov. Understanding the structure and reactivity of NiCu nanoparticles: an atomistic model. *Phys. Chem. Chem. Phys.*, 19:26812–26820, 2017. doi: 10.1039/C7CP04641C.

[42] Pedro A. Derosa, Jorge M. Seminario, and Perla B. Balbuena. Properties of Small Bimetallic Ni-Cu Clusters. *J. Phys. Chem. A*, 105(33):7917–7925, 2001. doi: 10.1021/jp0104637.

[43] G. Rossi, A. Rapallo, C. Mottet, A. Fortunelli, F. Baletto, and R. Ferrando. Magic Polyicosahedral Core-Shell Clusters. *Phys. Rev. Lett.*, 93:105503, Sep 2004. doi: 10.1103/PhysRevLett.93.105503.

[44] J. L. Rousset, F. J. Cadete Santos Aires, B. R. Sekhar, P. Méélinon, B. Prevel, and M. Pellarin. Comparative X-ray Photoemission Spectroscopy Study of Au, Ni, and AuNi Clusters Produced by Laser Vaporization of Bulk Metals. *J. Phys. Chem. B*, 104 (23):5430–5435, 2000. doi: 10.1021/jp994391j.

[45] M. Hessabi. Continuous particles. *Proceedings of the National Academy of Sciences of the United States of America*, 33(6):189–194, 1947.

[46] Gregory A. Bishea, Jacqueline C. Pinegar, and Michael D. Morse. The ground state and excited d-hole states of CuAu. *The Journal of Chemical Physics*, 95(8):5630–5645, 1991. doi: 10.1063/1.461638.

[47] Davood Alizadeh, Zahra Jamshidi, and Alireza Shayesteh. Spin-orbit and relativistic all-electron potential energy curves for the ground and low-lying excited states of AgAu. *Phys. Chem. Chem. Phys.*, 15:18678–18687, 2013. doi: 10.1039/C3CP52647J.

[48] Davood Alizadeh, Zahra Jamshidi, and Alireza Shayesteh. Potential energy curves for the ground and low-lying excited states of CuAg. *J. Chem. Phys.*, 141(15):154301, 2014. doi: 10.1063/1.4897540.

[49] Davood Alizadeh Sanati and Dirk Andrae. Low-Lying Electronic States of CuAu. *J. Phys. Chem. A*, 120(29):5856–5867, 2016. doi: 10.1021/acs.jpca.6b05522.

[50] P. A. M. Dirac. *The Principles of Quantum Mechanics*. Oxford University Press, fourth (revised) edition, 1957.

[51] N. Zettili. *Quantum Mechanics: Concepts and Applications*. John Wily & and Sons, Ltd, second edition, 2009.

[52] P. F. Bernath. *Spectra of Atoms and Molecules*. Oxford University Press, second edition, 2005.

[53] A. Szabo and N. S. Ostlund. *Modern Quantum Chemistry: Introduction to Advanced Electronic Structure Theory*. Dover Publications, Inc, first edition, 1996.

[54] Charlotte Froese Fischer. *The Hartree-Fock Method for Atoms; a Numerical Approach*. John Wiley & Sons, Inc., 1977.

[55] I. N. Levine. *Quantum Chemistry*. Prentice-Hall, fifth edition, 2000.

[56] F. Jensen. *Introduction to Computational Chemistry*. John Wily & Sons, Ltd, second edition, 2007.

[57] Kenneth G. Dyall and Jr. Knut Fægri. *Introduction to Relativistic Quantum Chemistry*. Oxford University Press, 2007.

[58] Trygve Helgaker, Poul Jørgensen, and Jeppe Olsen. *Molecular Electronic-Structure Theory*. John Wiley & Sons, Ltd., 2000.

[59] Hans Hellmann. *Einführung in die Quantenchemie*. Springer, 2015.

[60] Wenjian Liu, editor. *Handbook of Relativistic Quantum Chemistry*. Springer, 2017.

[61] István Mayer. *Simple Theorems, Proofs, and Derivations in Quantum Chemistry*. Springer Science+Business Media New York, 2003.

[62] Linus Pauling and E. Bright Wilson. *Intoduction to Quantum Mechanics; with Applications to Chemistry*. McGraw-Hill Book Company, Inc., 1935.

[63] Lucjan Piela. *Ideas of Quantum Chemistry*. Elsevier, 2007.

[64] Markus Reiher and Alexander Wolf. *Relativistic Quantum Chemistry*. Wiley-VCH, 2nd edition, 2015.

[65] Dirk Andrae. *Nuclear Charge Density and Magnetization Distributions*, pages 51–81.

Springer Berlin Heidelberg, Berlin, Heidelberg, 2017. ISBN 978-3-642-40766-6. doi: 10.1007/978-3-642-40766-6_23.

[66] Walther Gerlach and Otto Stern. Das magnetische Moment des Silberatoms. *Zeitschrift für Physik*, 9(1):353–355, Dec 1922. ISSN 0044-3328. doi: 10.1007/BF01326984.

[67] E. Merzbacher. *Quantum Mechanics*. John Wily & Sons, Ltd, second and third edition, 1998.

[68] Takahito Nakajima and Kimihiko Hirao. The Douglas-Kroll-Hess Approach. *Chem. Rev.*, 112(1):385–402, 2012. doi: 10.1021/cr200040s.

[69] Marvin Douglas and Norman M Kroll. Quantum Electrodynamical Corrections to the Fine Structure of Helium. *Annals of Physics*, 82(1):89 – 155, 1974. doi: https://doi.org/10.1016/0003-4916(74)90333-9.

[70] Bernd A. Hess. Relativistic electronic-structure calculations employing a two-component no-pair formalism with external-field projection operators. *Phys. Rev. A*, 33:3742–3748, Jun 1986. doi: 10.1103/PhysRevA.33.3742.

[71] Georg Jansen and Bernd A. Hess. Revision of the Douglas-Kroll transformation. *Phys. Rev. A*, 39:6016–6017, Jun 1989. doi: 10.1103/PhysRevA.39.6016.

[72] Hui Li and Robert J. Le Roy. An accurate *ab initio* potential energy surface and calculated spectroscopic constants for BeH_2, BeD_2, and BeHD. *The Journal of Chemical Physics*, 125(4):044307, 2006. doi: 10.1063/1.2212933.

[73] Peter F. Bernath, Alireza Shayesteh, Keith Tereszchuk, and Reginald Colin. The Vibration-Rotation Emission Spectrum of Free BeH_2. *Science*, 297:1323–1324, 2002. doi: 10.1126/science.1074580.

[74] Hans-Joachim Werner, Peter J. Knowles, Gerald Knizia, Frederick R. Manby, and Martin Schütz. Molpro: a general-purpose quantum chemistry program package. *Wiley Interdisciplinary Reviews: Computational Molecular Science*, 2(2):242–253, 2012. doi: 10.1002/wcms.82.

[75] H.-J. Werner; P. J. Knowles; G. Knizia; F. R. Manby; M. Schütz; P. Celani; T. Korona; R. Lindh; A. Mitrushenkov; G. Rauhut; et al. *MOLPRO*, version 2012.1, a package of ab initio programs; 2012.

[76] Frank Neese. The ORCA program system. *Wiley Interdisciplinary Reviews: Computational Molecular Science*, 2(1):73–78, 2012. doi: 10.1002/wcms.81.

[77] F. Neese. *ORCA — An ab Initio, Density Functional and Semiempirical Program Package, versions 3.0.0,3.0.1,3.0.3*; Max-Planck-Institute for Chemical Energy Conversion: Mülheim an der Ruhr, Germany, 2014.

[78] DIRAC, a relativistic ab initio electronic structure program, Release DIRAC15 (2015), written by R. Bast, T. Saue, L. Visscher, and H. J. Aa. Jensen, with contributions from V. Bakken, K. G. Dyall, S. Dubillard, U. Ekström, E. Eliav, T. Enevoldsen, E. Fasshauer, T. Fleig, O. Fossgaard, A. S. P. Gomes, T. Helgaker, J. Henriksson, M. Iliaš, Ch. R. Jacob, S. Knecht, S. Komorovsky, O. Kullie, J. K. Laerdahl, C. V. Larsen, Y. S. Lee, H. S. Nataraj, M. K. Nayak, P. Norman, G. Olejniczak, J. Olsen, Y. C. Park, J.

K. Pedersen, M. Pernpointner, R. Di Remigio, K. Ruud, P. Salek, B. Schimmelpfennig, J. Sikkema, A. J. Thorvaldsen, J. Thyssen, J. van Stralen, S. Villaume, O. Visser, T. Winther, and S. Yamamoto (see http://www.diracprogram.org).).

[79] R. J. Le Roy. *Level 8.0: A Computer Program for Solving the Radial Schrödinger Equation for Bound and Quasibound Levels*; Chemical Physics Research Report CP-663; University of Waterloo: Ontario, Canada, 2007.

[80] Florian Weigend and Reinhart Ahlrichs. Balanced basis sets of split valence, triple zeta valence and quadruple zeta valence quality for H to Rn: Design and assessment of accuracy. *Phys. Chem. Chem. Phys.*, 7:3297–3305, 2005. doi: 10.1039/B508541A.

[81] Dimitrios A. Pantazis, Xian-Yang Chen, Clark R. Landis, and Frank Neese. All-Electron Scalar Relativistic Basis Sets for Third-Row Transition Metal Atoms. *J. Chem. Theory Comput.*, 4(6):908–919, 2008. doi: 10.1021/ct800047t.

[82] Nikolai B. Balabanov and Kirk A. Peterson. Systematically convergent basis sets for transition metals. I. All-electron correlation consistent basis sets for the 3d elements Sc-Zn. *J. Chem. Phys.*, 123:064107, 2005. doi: 10.1063/1.1998907.

[83] Hans-Joachim Werner. *Matrix-Formulated Direct Multiconfiguration Self-Consistent Field and Multiconfiguration Reference Configuration-Interaction Methods*, volume LXIX, pages 1–62. John Wiley & Sons, Inc., 1987. doi: 10.1002/9780470142943.ch1.

[84] Hans-Joachim Werner and Peter J. Knowles. A second order multiconfiguration SCF procedure with optimum convergence. *J. Chem. Phys.*, 82(11):5053–5063, 1985. doi: 10.1063/1.448627.

[85] Peter J. Knowles and Hans-Joachim Werner. An efficient second-order MC SCF method for long configuration expansions. *Chem. Phys. Lett.*, 115(3):259–267, 1985. doi: 10.1016/0009-2614(85)80025-7.

[86] Frank Neese, Taras Petrenko, Dmitry Ganyushin, and Gottfried Olbrich. Advanced aspects of ab initio theoretical optical spectroscopy of transition metal complexes: Multiplets, spin-orbit coupling and resonance Raman intensities. *Coord. Chem. Rev.*, 251 (3-4):288–327, 2007. doi: 10.1016/j.ccr.2006.05.019.

[87] Peter J. Knowles and Hans-Joachim Werner. Internally contracted multiconfiguration-reference configuration interaction calculations for excited states. *Theoretica chimica acta*, 84(1):95–103, 1992. doi: 10.1007/BF01117405.

[88] Hans-Joachim Werner and Ernst-Albrecht Reinsch. The self-consistent electron pairs method for multiconfiguration reference state functions. *J. Chem. Phys.*, 76(6):3144–3156, 1982. doi: 10.1063/1.443357.

[89] Ernest R. Davidson and Donald W. Silver. Size consistency in the dilute helium gas electronic structure. *Chem. Phys. Lett.*, 52(3):403–406, 1977. doi: 10.1016/0009-2614(77)80475-2.

[90] Yoshi-ichi Suzuki and Takeshi Noro and Fukashi Sasaki and Hiroshi Tatewaki. Potential energy curve of the ground state of the titanium dimer. *Journal of Molecular Structure: THEOCHEM*, 461-462:351–357, 1999. doi: 10.1016/S0166-1280(98)00449-7.

[91] G. Breit. Dirac's Equation and the Spin-Spin Interactions of Two Electrons. *Phys. Rev.*, 39:616–624, Feb 1932. doi: 10.1103/PhysRev.39.616.

[92] K. G. Dyall and A. S. P. Gomes. Unpublished.

[93] Kenneth G. Dyall. Relativistic double-zeta, triple-zeta, and quadruple-zeta basis sets for the 4d elements Y-Cd. *Theor. Chem. Acc.*, 117(4):483–489, 2007. doi: 10.1007/s00214-006-0174-5.

[94] Kenneth G. Dyall. Relativistic double-zeta, triple-zeta, and quadruple-zeta basis sets for the 5d elements Hf-Hg. *Theor. Chem. Acc.*, 112(5):403–409, 2004. doi: 10.1007/s00214-004-0607-y.

[95] Kenneth G. Dyall and Andre S. P. Gomes. Revised relativistic basis sets for the 5d elements Hf-Hg. *Theor. Chem. Acc.*, 125(1):97, 2009. doi: 10.1007/s00214-009-0717-7.

[96] J. Thyssen. PhD thesis, University of Southern Denmark (Denmark), 2004.

[97] Timo Fleig, Jeppe Olsen, and Lucas Visscher. The generalized active space concept for the relativistic treatment of electron correlation. II. Large-scale configuration interaction implementation based on relativistic 2- and 4-spinors and its application. *J. Chem. Phys.*, 119(6):2963–2971, 2003. doi: 10.1063/1.1590636.

[98] K. A. Gingerich. Experimental and predicted stability of diatomic metals and metallic clusters. *Faraday Symp. Chem. Soc.*, 14:109–125, 1980. doi: 10.1039/FS9801400109.

[99] Arthur Kant. Mass-Spectrometric Studies of the Gaseous Systems Au-Ni, Au-Co, and Au-Fe, and Dissociation Energies of AuNi, AuCo, and AuFe. *J. Chem. Phys.*, 49(11): 5144–5146, 1968. doi: 10.1063/1.1670012.

[100] S. K. Gupta, M. Pelino, and K. A. Gingerich. Observation and bond dissociation energy of gaseous AuV by high temperature mass spectrometry. *J. Chem. Phys.*, 70 (4):2044–2045, 1979. doi: 10.1063/1.437645.

[101] C. A. Baumann, R. J. Van Zee, and W. Weltner Jr. ESR of bimetallic transition metal molecules. 2. Manganese-silver (MnAg), chromium-zinc (CrZn), and diatomics attempted but not observed. *J. Phys. Chem.*, 88(9):1815–1820, 1984. doi: 10.1021/j150653a029.

[102] S. Smoes and J. Drowart. Mass-spectrometric determination of the dissociation energy of the molecule AuMn. *Chem. Commun. (London)*, -:534–535, 1968. doi: 10.1039/C19680000534.

[103] R. J. Van Zee and W. Weltner Jr. ESR of the $^6\Sigma$ CrCu molecule at 4°K. *J. Chem. Phys.*, 74:4330–4333, 1981. doi: 10.1063/1.441674.

[104] R. J. Van Zee and W. Weltner Jr. Erratum: ESR of the $^6\Sigma$ CrCu molecule at 4°K [J. Chem. Phys. 74, 4330 (1981)]. *J. Chem. Phys.*, 75(5):2484–2484, 1981. doi: 10.1063/1.442668.

[105] C. A. Baumann, R. J. Van Zee, and W. Weltner Jr. ESR of bimetallic transition-metal molecules at 4°K. I. CrCu, CrAg, and CrAu. *J. Chem. Phys.*, 79:5272–5279, 1983. doi: 10.1063/1.445715.

[106] Zhenwen Fu and Michael D. Morse. Spectroscopy and electronic structure of jet-cooled

NiCu. *J. Chem. Phys.*, 90:3417, 1989. doi: 10.1063/1.455850.

[107] Eileen M. Spain and Michael D. Morse. The $3d^8_{\text{Ni}}(^3F)3d^{10}_{\text{Cu}}\sigma^2\sigma^{*1}$ manifold of excited electronic states of NiCu. *J. Chem. Phys.*, 97(7):4633–4640, 1992. doi: 10.1063/1.463866.

[108] Eileen M. Spain and Michael D. Morse. Ligand-field theory applied to diatomic transition metals. Results for the $d^9_A d^9_B \sigma^2$ states of Ni_2, the $d^9_{\text{Ni}} d^{10}_{\text{Cu}} \sigma^2$ states of NiCu, and the $d^8_{\text{Ni}}(^3F)d^{10}_{\text{Cu}}\sigma^2\sigma^{*1}$ excited states of NiCu. *J. Chem. Phys.*, 97(7):4641–4660, 1992. doi: 10.1063/1.463867.

[109] Gretchen K. Rothschopf and Michael D. Morse. Monoligated Monovalent Ni: the $3d^9_{\text{Ni}}$ Manifold of States of NiCu and Comparison to the $3d^9$ States of AlNi, NiH, NiCl, and NiF. *J. Phys. Chem. A*, 109(50):11358–11364, 2005. doi: 10.1021/jp053022m.

[110] Eileen M. Spain and Michael D. Morse. Spectroscopic studies of jet-cooled NiAu and PtCu. *J. Chem. Phys.*, 97:4605, 1992. doi: 10.1063/1.463863.

[111] Jacqueline C. Fabbi, Lars Karlsson, Jon D. Langenberg, Quinton D. Costello, and Michael D. Morse. Dispersed fluorescence spectroscopy of AlNi, NiAu, and PtCu. *J. Chem. Phys.*, 118:9247, 2003. doi: 10.1063/1.1567712.

[112] St. J. Dixon-Warren, R. F. Gunion, and W. C. Lineberger. Photoelectron spectroscopy of mixed metal cluster anions: $NiCu^-$, $NiAg^-$, $NiAg_2^-$, and Ni_2Ag^-. *J. Chem. Phys.*, 104:4902, 1996. doi: 10.1063/1.471123.

[113] M. Wang, B. Wang, and Z. Chen. Magnetic coupling interaction for mixed transition metal dimer: Ab initio MRCI(SD) + Q investigation on CrCu. *Chem. Phys. Lett.*, 435: 5–9, 2007. doi: 10.1016/j.cplett.2006.12.037.

[114] G. L. Gutsev, P. Jena, B. K. Rao, and S. N. Khanna. Electronic structure and chemical bonding of 3d-metal dimers ScX, X=Sc–Zn. *J. Chem. Phys.*, 114:10738, 2001. doi: 10.1063/1.1373693.

[115] G. L. Gutsev, M. D. Mochena, P. Jena, C. W. Bauschlicher Jr., and H. Partridge III. Periodic table of 3d-metal dimers and their ions. *J. Chem. Phys.*, 121(14):6785–6797, 2004. doi: 10.1063/1.1788656.

[116] Gregory A. Bishea and Michael D. Morse. Spectroscopic studies of jet-cooled AgAu and Au_2. *The Journal of Chemical Physics*, 95(8):5646–5659, 1991. doi: 10.1063/1.461639.

[117] Gregory A. Bishea, Ninette Marak, and Michael D. Morse. Spectroscopic studies of jet-cooled CuAg. *The Journal of Chemical Physics*, 95(8):5618–5629, 1991. doi: 10.1063/1.461637.

[118] A. Kramida, Yu. Ralchenko, J. Reader, and NIST ASD Team. NIST Atomic Spectra Database, version 5.3, NIST Standard Reference Database Number 78, National Institute of Standards and Technology: Gaithersburg, MD, 2016. URL `http://physics.nist.gov/asd`.

[119] Stephen P. Walch, Charles W. Bauschlicher, and Stephen R. Langhoff. Theoretical studies of diatomic and triatomic systems containing the group IB atoms Cu, Ag, and Au. *The Journal of Chemical Physics*, 85(10):5900–5907, 1986. doi: 10.1063/1.451501.

[120] Artur Pizlo, Georg Jansen, Bernd Artur Heß, and Wolfgang von Niessen. Ionization potential and electron affinity of the Au atom and the AuH molecule by all-electron relativistic configuration interaction and propagator techniques. *The Journal of Chemical Physics*, 98(5):3945–3951, 1993. doi: 10.1063/1.464021.

[121] Georg Jansen and Bernd A. Hess. Relativistic all-electron configuration interaction calculations on the gold atom. *Chemical Physics Letters*, 160(5):507 – 513, 1989. ISSN 0009-2614. doi: https://doi.org/10.1016/0009-2614(89)80054-5. URL `http://www.sciencedirect.com/science/article/pii/0009261489800545`.

[122] Jacqueline C. Fabbi, Jon D. Langenberg, Quinton D. Costello, Michael D. Morse, and Lars Karlsson. Dispersed fluorescence spectroscopy of jet-cooled AgAu and Pt_2. *The Journal of Chemical Physics*, 115(16):7543–7549, 2001. doi: 10.1063/1.1407273.

[123] Olha Krechkivska, Michael D. Morse, Apostolos Kalemos, and Aristides Mavridis. Electronic spectroscopy and electronic structure of diatomic TiFe. *J. Chem. Phys.*, 137(5): 054302, 2012. doi: 10.1063/1.4738958.

[124] Apostolos Kalemos. Fe_2: As simple as a Herculean labour. Neutral (Fe_2), cationic (Fe_2^+), and anionic (Fe_2^-) species. *J. Chem. Phys.*, 142:244304, 2015. doi: 10.1063/1.4922793.

[125] E. Wigner and E. E. Witmer. Über die Struktur der zweiatomigen Molekelspektren nach der Quantenmechanik. *Zeitschrift für Physik*, 51(11):859–886, Nov 1928. doi: 10.1007/BF01400247.

[126] Eileen M. Spain, Jane M. Behm, and Michael D. Morse. The 846 nm $A'^3\Sigma_u^- \leftarrow X^3\Sigma_g^-$ band system of jet-cooled V_2. *J. Chem. Phys.*, 96(4):2511–2516, 1992. doi: 10.1063/1.462002.

[127] G. Herzberg. *Molecular Spectra and Molecular Structure*. D. VAN NOSTRAD COMPANY, second edition, 1950.

[128] Mats Doverstål, Bo Lindgren, Ulf Sassenberg, Caleb A. Arrington, and Michael D. Morse. The $^3\Pi_{0u} \leftarrow X^3\Delta_{1g}$ band system of jet-cooled Ti_2. *J. Chem. Phys.*, 97(10): 7087–7092, 1992. doi: 10.1063/1.463534.

[129] Charles W. Bauschlicher Jr., Per Siegbahn, and Lars G. M. Pettersson. The atomic states of nickel. *Theoretica chimica acta*, 74(6):479–491, 1988. doi: 10.1007/BF00528018.

[130] R. S. Ram and P. F. Bernath. Fourier transformation emission spectroscopy of the systems $B^1\Pi - X^1\Sigma^+$, $C^1\Sigma^+ - X^1\Sigma^+$, and $G^1\Pi - X^1\Sigma^+$ of ScH and ScD. *J. Chem. Phys.*, 105:2668, 1996. doi: 10.1063/1.472130.

[131] O. Launila and B. Lindgren. Spectroscopy of TiH: Rotational analysis of the $^4\Gamma \rightarrow X^4\Phi$ (0,0) band at 530 nm. *J. Chem. Phys.*, 104(17):6418–6422, 1996. doi: 10.1063/1.471362.

[132] Shiro Koseki, Yohei Ishihara, Dmitri G. Fedorov, Hiroaki Umeda, Michael W. Schmidt, and Mark S. Gordon. Dissociation Potential Curves of Low-Lying States in Transition Metal Hydrides. 2. Hydrides of Groups 3 and 5. *J. Phys. Chem. A*, 108(21):4707–4719, 2004. doi: 10.1021/jp049839h.

[133] Saeyoung Shin, Dale J. Brugh, and Michael D. Morse. Radiative Lifetime of the v =

0, 1 Levels of the $A^6\Sigma^+$ State of CrH. *Astrophys. J.*, 619(1):407, 2005. URL `http://stacks.iop.org/0004-637X/619/i=1/a=407`.

[134] Iouli E. Gordon, Dominique R.T. Appadoo, Alireza Shayesteh, Kaley A. Walker, and Peter F. Bernath. Fourier transform infrared emission spectra of MnH and MnD. *J. Mol. Spectrosc.*, 229(1):145–149, 2005. doi: 10.1016/j.jms.2004.08.010.

[135] R. T. Carter and J. M. Brown. Observation of the $g^6\Phi_{11/2} - X^4\Delta_{7/2}$, $\Delta\Omega = 2$ Subband in FeH. *J. Mol. Spectrosc.*, 166(1):249–250, 1994. doi: 10.1006/jmsp.1994.1190.

[136] Iouli E. Gordon, Robert J. Le Roy, and Peter F. Bernath. Near infrared emission spectra of CoH and CoD. *J. Mol. Spectrosc.*, 237(1):11–18, 2006. doi: 10.1016/j.jms.2006.02.011.

[137] Leah C. O'Brien and James J. O'Brien. Laboratory Measurements of NiH by Intracavity Laser Absorption Spectroscopy. *Astrophys. J.*, 621(1):554, 2005. URL `http://stacks.iop.org/0004-637X/621/i=1/a=554`.

[138] R. S. Ram and P. F. Bernath. Fourier transform emission spectroscopy of new infrared systems of LaH and LaD. *J. Chem. Phys.*, 104(17):6444–6451, 1996. doi: 10.1063/1.471365.

[139] Gongyi Hong, Michael Dolg, and Lemin Li. A comparison of scalar-relativistic ZORA and DKH density functional schemes: monohydrides, monooxides and monofluorides of La, Lu, Ac and Lr. *Chem. Phys. Lett.*, 334(4–6):396–402, 2001. doi: 10.1016/S0009-2614(00)01430-5.

[140] K. Balasubramanian and J. Z. Wang. Spectroscopic properties and potential energy curves of thirty-six electronic states of ZrH. *Chem. Phys. Lett.*, 154(6):525–530, 1989. ISSN 0009-2614. doi: 10.1016/0009-2614(89)87145-3.

[141] R. S. Ram and P. F. Bernath. Fourier transform emission spectroscopy of HfH and HfD. *J. Chem. Phys.*, 101(1):74–79, 1994. doi: 10.1063/1.468130.

[142] Kalyan K. Das and K. Balasubramanian. Spectroscopic properties and potential energy curves of 28 electronic states of NbH. *J. Mol. Spectrosc.*, 144(2):245–256, 1990. doi: 10.1016/0022-2852(90)90212-9.

[143] W. Cheng and K. Balasubramanian. Spectroscopic constants and potential energy curves for TaH. *J. Mol. Spectrosc.*, 149(1):99–108, 1991. ISSN 0022-2852. doi: 10.1016/0022-2852(91)90145-Z.

[144] Jia-Zhen Wang and K. Balasubramanian. Spectroscopic properties and potential energy curves for 27 electronic states of TcH. *J. Mol. Spectrosc.*, 138(1):204–221, 1989. doi: 10.1016/0022-2852(89)90111-2.

[145] D. G. Dai and K. Balasubramanian. Spectroscopic Properties and Potential Energy Curves for 30 Electronic States of ReH. *J. Mol. Spectrosc.*, 158(2):455–467, 1993. doi: 10.1006/jmsp.1993.1089.

[146] D. Andrae, U. Häußermann, M. Dolg, H. Stoll, and H. Preuß. Energy-adjusted ab initio pseudopotentials for the second and third row transition elements: Molecular test for M_2 (M=Ag, Au) and MH (M=Ru, Os). *Theoretica chimica acta*, 78(4):247–266, 1991.

doi: 10.1007/BF01112848.

[147] Walter J. Balfour, Jianying Cao, and Charles X. W. Qian. Characterization of Electronic Spectra of Rhodium Monohydride and Monodeuteride. *J. Mol. Spectrosc.*, 201 (2):244–248, 2000. doi: 10.1006/jmsp.2000.8082.

[148] Dingguo Dai and K. Balasubramanian. Spectroscopic constants and potential energy curves of iridium hydride (IrH). *New J. Chem.*, 15:721–726, 1991.

[149] Michael C. McCarthy and Robert W. Field. Frequency-modulation enhanced magnetic rotation spectroscopy of PdH, PdD, NiH, and CuH. *J. Chem. Phys.*, 100(9):6347–6358, 1994. doi: 10.1063/1.467096.

[150] Caleb A. Arrington, Dale J. Brugh, Michael D. Morse, and Mats Doverstål. Spectroscopy of jet-cooled YCu. *J. Chem. Phys.*, 102(22):8704–8713, 1995. doi: 10.1063/1.468973.

[151] Alessandra Ricca and Charles W. Bauschlicher. The low-lying electronic states of YCu. *Chem. Phys.*, 200(3):337–345, 1995. doi: 10.1016/0301-0104(95)00231-6.

[152] Y. M. Hamrick, R. J. Van Zee, and W. Weltner Jr. ESR of bimetallic transition-metal molecules: Mo and W with Cu, Ag, and Au. *Chem. Phys. Lett.*, 181(2):193–200, 1991. doi: 10.1016/0009-2614(91)90354-C.

[153] Minori Abe, Sayaka Mori, Takahito Nakajima, and Kimihiko Hirao. Electronic structures of PtCu, PtAg, and PtAu molecules: a Dirac four-component relativistic study. *Chem. Phys.*, 311(1-2):129–137, 2005. doi: 10.1016/j.chemphys.2004.09.035.

[154] Dingguo Dai and K. Balasubramanian. Pt_3Au and PtAu clusters: Electronic states and potential energy surfaces. *J. Chem. Phys.*, 100(6):4401–4407, 1994. doi: 10.1063/1.466322.

[155] Lorenzo Lodi, Sergei N. Yurchenko, and Jonathan Tennyson. The calculated rovibronic spectrum of scandium hydride, ScH. *Mol. Phys.*, 113:1998–2011, 2015. doi: 10.1080/00268976.2015.1029996.

[156] Nikolai B. Balabanov and Kirk A. Peterson. Basis set limit electronic excitation energies, ionization potentials, and electron affinities for the 3d transition metal atoms: Coupled cluster and multireference methods. *J. Chem. Phys.*, 125:074110, 2006. doi: 10.1063/1.2335444.

[157] Kirk A. Peterson and Cristina Puzzarini. Systematically convergent basis sets for transition metals. II. Pseudopotential-based correlation consistent basis sets for the group 11 (Cu, Ag, Au) and 12 (Zn, Cd, Hg) elements. *Theor. Chem. Acc.*, 114:283–296, 2005. doi: 10.1007/s00214-005-0681-9.

[158] Juraj Raab and Björn O. Roos. Excitation Energies for Transition Metal Atoms – A Comparison between Coupled Cluster Methods and Second-Order Perturbation Theory. *Adv. Quantum Chem.*, 48:421–433, 2005. doi: 10.1016/S0065-3276(05)48022-3.

[159] Kerstin Andersson and Björn O. Roos. Excitation energies in the nickel atom studied with the complete active space SCF method and second-order perturbation theory. *Chem. Phys. Lett.*, 191(6):507–514, 1992. ISSN 0009-2614. doi: 10.1016/0009-

2614(92)85581-T.

[160] Michael D. Morse. Clusters of transition-metal atoms. *Chem. Rev.*, 86(6):1049–1109, 1986. doi: 10.1021/cr00076a005.

[161] P. Scharf, S. Brode, and R. Ahlrichs. Electronic structure and bonding in the ground state of Cu_2. *Chemical Physics Letters*, 113(5):447–450, 1985. doi: https://doi.org/10.1016/0009-2614(85)80078-6.

[162] Charles W. Bauschlicher, Stephen R. Langhoff, and Peter R. Taylor. Theoretical study of the electron affinities of Cu, Cu_2, and Cu_3. *The Journal of Chemical Physics*, 88(2): 1041–1045, 1988. doi: 10.1063/1.454272.

[163] William H. Blades, Arthur C. Reber, Shiv N. Khanna, Luis López-Sosa, Patrizia Calaminici, and Andreas M. Köster. Evolution of the Spin Magnetic Moments and Atomic Valence of Vanadium in VCu_x^+, VAg_x+, and VAu_x^+ Clusters (x = 3–14). *The Journal of Physical Chemistry A*, 121(15):2990–2999, 2017. doi: 10.1021/acs.jpca.7b01030. URL `https://doi.org/10.1021/acs.jpca.7b01030`. PMID: 28350450.

[164] R. Ahlrichs, F. Keil, H. Lischka, W. Kutzelnigg, and V. Staemmler. Pno—ci (pair natural-orbital configuration interaction) and cepa—pno (coupled electron pair approximation with pair natural orbitals) calculations of molecular systems. iii. the molecules mgh_2, alh_3, sih_4, ph_3 (planar and pyramidal), h_2s, hcl, and the ar atom. *The Journal of Chemical Physics*, 63(1):455–463, 1975. doi: 10.1063/1.431073.

[165] A. Shayesteh, D. R. T. Appadoo, I. Gordon, and P. F. Bernath. The vibration–rotation emission spectrum of MgH_2. *The Journal of Chemical Physics*, 119(15):7785–7788, 2003. doi: 10.1063/1.1609973.

[166] Peter Schwerdtfeger and Michael Dolg. Anomalous high gold-metal bond stabilities: Relativistic configuration-interaction calculations for AuLa and AuLu. *Phys. Rev. A*, 43:1644–1647, Feb 1991. doi: 10.1103/PhysRevA.43.1644.

[167] Ralf Wesendrup, Jon K. Laerdahl, and Peter Schwerdtfeger. Relativistic effects in gold chemistry. VI. Coupled cluster calculations for the isoelectronic series $AuPt^-$, Au_2, and $AuHg^+$. *J. Chem. Phys.*, 110(19):9457–9462, 1999. doi: 10.1063/1.478911.

[168] Dirk Andrae. How to calculate atomic open-shell LS terms with tools designed to treat molecules. URL `http://userpage.fu-berlin.de/~dandrae/openshell/openls/openls.html`.

[169] Zygmunt J. Jakubek, Benoit Simard, and Walter J. Balfour. Disentangling the mystery of green bands of yttrium monohydride with the help of Stark spectroscopy. *Chem. Phys. Lett.*, 351(5-6):365–373, 2002. doi: 10.1016/S0009-2614(01)01398-7.

[170] K. Balasubramanian. The low-lying states of the second-row transition metal hydrides (YH-CdH). *J. Chem. Phys.*, 93(11):8061–8072, 1990. doi: 10.1063/1.459336.

[171] Zhongxin Ma and K. Balasubramanian. Electronic states of WH. *Chem. Phys. Lett.*, 181(5):467–473, 1991. doi: 10.1016/0009-2614(91)90382-J.

[172] K. Balasubramanian and Jia-Zhen Wang. Spectroscopic constants and potential en-

ergy curves of 21 electronic states of RuH. *Chem. Phys.*, 140(2):243–253, 1990. doi: 10.1016/0301-0104(90)87006-W.

[173] M. C. Mccarthy, R. W. Field, R. Engleman, and P. F. Bernath. Laser and Fourier Transform Spectroscopy of PtH and PtD. *J. Mol. Spectrosc.*, 158(1):208–236, 1993. doi: 10.1006/jmsp.1993.1067.

[174] F. Colmenares, A. Ramıírez-Solís, and O Novaro. Theoretical study of the CuRu+H_2 molecular interaction. *Chem. Phys. Lett.*, 345(1-2):111–117, 2001. doi: 10.1016/S0009-2614(01)00829-6.

[175] Qingsheng Ran, Richard W. Schmude, Karl A. Gingerich, Dale W. Wilhite, and Joseph E. Kingcade. Dissociation energy and enthalpy of formation of gaseous silver dimer. *The Journal of Physical Chemistry*, 97(32):8535–8540, 1993. doi: 10.1021/j100134a025.

[176] Eileen M. Spain and Michael D. Morse. Spectroscopic studies of jet-cooled NiAu and PtCu. *J. Chem. Phys.*, 97:4605, 1992. doi: 10.1063/1.463863.

Appendices

Appendix A

Theory

Operators

An operator $\hat{A}$ is a mathematical rule which transforms one state vector into another. For example, here are some operators frequently used in quantum mechanics; the unity operator: $\hat{I}\,|\psi\rangle = |\psi\rangle$, the gradient operator $\hat{\vec{\nabla}}$, the linear momentum operator $\hat{\vec{p}}\psi(\vec{r}) = -i\hbar\hat{\vec{\nabla}}\psi(\vec{r})$, the Laplacian operator $\hat{\nabla}^2$, and the parity operator: $\hat{P}\psi(\vec{r}) = \psi(-\vec{r})$. In the products of operators the order matters in general; $\hat{A}\hat{B} \neq \hat{B}\hat{A}$ or $[\hat{A},\hat{B}] \neq 0$. When the product $\hat{A}\hat{B}$ operates on a state vector $|\psi\rangle$, the operator $\hat{B}$ acts first on the state vector $|\psi\rangle$ and then the operator $\hat{A}$ acts on the state vector $\hat{B}\,|\psi\rangle$; $\hat{A}\hat{B}\,|\psi\rangle = \hat{A}(\hat{B}\,|\psi\rangle)$. If the operator $\hat{A}$ is distributive, $\hat{A}(|\psi\rangle + |\phi\rangle) = \hat{A}\,|\psi\rangle + \hat{A}\,|\phi\rangle$, and if the operator $\hat{A}$ commutes with the complex number a, $[\hat{A},a] = 0$, then $\hat{A}$ is said to be linear operator; $\hat{A}(a\,|\psi\rangle + b\,|\phi\rangle) = a\hat{A}\,|\psi\rangle + b\hat{A}\,|\phi\rangle$. The expectation value or the mean value of an operator $\hat{A}$, $\langle\hat{A}\rangle$, with respect to a state vector $|\psi\rangle$ is given by $\langle\hat{A}\rangle = \langle\psi|\hat{A}|\psi\rangle \,/\, \langle\psi|\psi\rangle$. The Hermitian adjoint or conjugate of a complex number a, $a^\dagger$, is the complex conjugate of the complex number a; $a^\dagger = a^*$. The Hermitian adjoint of an operator $\hat{A}$, $\hat{A}^\dagger$, is defined by the relation $\langle\psi|\hat{A}^\dagger|\phi\rangle = \langle\phi|\hat{A}|\psi\rangle^*$. An operator $\hat{A}$ is said to be Hermitian if it is equal to its adjoint $\hat{A}^\dagger$; $\hat{A} = \hat{A}^\dagger$ or $\langle\psi|\hat{A}|\phi\rangle = \langle\phi|\hat{A}|\psi\rangle^*$.

Spin-Free Schrödinger Equation

In order to quantitatively describe the hydrogen atom—which consists of an electron and a proton to either of which an electric charge, an intrinsic spin momentum, and a rest mass (m_e or m_p) are assigned—the nonrelativistic time-dependent Schrödinger equation for the spinless particles, in position representation (red), reads

$$\Big[-\frac{\hbar^2}{2m_p}\nabla_p^2 - \frac{\hbar^2}{2m_e}\nabla_e^2 + V(\vec{r}_p,\vec{r}_e,t)\Big]\Psi(\vec{r}_p,\vec{r}_e,t) = i\hbar\frac{\partial}{\partial t}\Psi(\vec{r}_p,\vec{r}_e,t). \tag{A.1}$$

Assuming that $V(\vec{r}_p, \vec{r}_e, t) = V(|\vec{r}_p - \vec{r}_e|) = V(r)$, that is the system is stationary and the potential is scalar, the nonrelativistic time-independent Schrödinger equation reads

$$\left[-\frac{\hbar^2}{2m_p}\nabla_p^2 - \frac{\hbar^2}{2m_e}\nabla_e^2 + V(r)\right]\chi(\vec{r}_p, \vec{r}_e) = E\chi(\vec{r}_p, \vec{r}_e). \tag{A.2}$$

Transforming $\vec{r}_p$ and $\vec{r}_e$ to $\vec{R}$ and $\vec{r}$, $\vec{R}$ being the vector which connects the origin of the coordinate system to the center of mass of the system, the nonrelativistic time-independent Schrödinger equation reads

$$\left[-\frac{\hbar^2}{2M}\nabla_R^2 - \frac{\hbar^2}{2\mu}\nabla_r^2 + V(r)\right]\psi(\vec{R}, \vec{r}) = E\psi(\vec{R}, \vec{r}), \tag{A.3}$$

where $M = m_p + m_e$ and $\mu = m_p m_e/(m_p + m_e)$. Generalisation of the dynamics of the hydrogen atom to a neutral atom with atomic number of Z, the nonrelativistic time-independent Schrödinger equation reads

$$\begin{aligned}\Big[-\frac{\hbar^2}{2M}\nabla_R^2 - \sum_{i=1}^{Z}\frac{\hbar^2}{2m_e}\nabla_{r_i}^2 - \sum_{i=1}^{Z}\frac{Ze^2}{|\vec{r}_i - \vec{R}|} + \sum_{i>j}\frac{e^2}{|\vec{r}_i - \vec{r}_j|}\Big]\psi(\vec{R}, \vec{r}_1, \vec{r}_2, \ldots, \vec{r}_Z) \\ = E\psi(\vec{R}, \vec{r}_1, \vec{r}_2, \ldots, \vec{r}_Z),\end{aligned} \tag{A.4}$$

where M is the mass of the nucleus and $\vec{R}$ represents the position of the center of mass of the nucleus. For a molecule containing M nuclei and N electrons[*] the nonrelativistic time-independent Schrödinger equation reads

$$\begin{aligned}\Bigg[-\sum_{A=1}^{M}\frac{\hbar^2}{2M_A}\nabla_{R_A}^2 - \sum_{i=1}^{N}\frac{\hbar^2}{2m_e}\nabla_{r_i}^2 - \sum_{A,i}^{M,N}\frac{Z_A e^2}{|\vec{r}_i - \vec{R}_A|} + \sum_{A>B}\frac{Z_A Z_B e^2}{|\vec{R}_A - \vec{R}_B|} \\ + \sum_{i>j}\frac{e^2}{|\vec{r}_i - \vec{r}_j|}\Bigg]\psi(R_1, \ldots, R_M, r_1, \ldots, r_N) = E\psi(R_1, \ldots, R_M, r_1, \ldots, r_N)\end{aligned} \tag{A.5}$$

Within the framework of the so-called clamped nuclei approximation, the nuclei are considered to be fixed because $m_p/m_e \approx 1836$, m_p and m_e being the rest mass of proton and electron. Thus, the first term in equation (2.1) vanishes and the nucleus-nucleus repulsion, $\sum_{A>B} Z_A Z_B e^2/|\vec{R}_A - \vec{R}_B|$, turns into a constant which, from the linearity of Hamiltonian operator, can be transferred into the eigenvalue. This results in the electronic Hamiltonian which describes the dynamics of N spinless electrons in the electrostatic field of M point charges.

$$\hat{H}_{\text{el}} = -\sum_{i=1}^{N}\frac{\hbar^2}{2m_e}\nabla_{r_i}^2 - \sum_{i,A}^{N,M}\frac{Z_A e^2}{|\vec{r}_i - \vec{R}_A|} + \sum_{i>j}\frac{e^2}{|\vec{r}_i - \vec{r}_j|}. \tag{A.6}$$

---

[*] Since low-energy phenomena are addressed in this work, pair production does not take place (ref. 51) and N is a constant.

The solution of the corresponding nonrelativistic time-independent electronic Schrödinger equation, $H_{\mathrm{el}}\psi_{\mathrm{el}}(\{\vec{r}_i\},\{\vec{R}_A\}) = E_{\mathrm{el}}\psi_{\mathrm{el}}(\{\vec{r}_i\},\{\vec{R}_A\})$, gives electronic energies which explicitly depend on the spatial coordinates of the electrons and parametrically on the spatial coordinates of the nuclei, i.e., $E_{\mathrm{el}}(\{\vec{R}_A\})$.

Orbital Angular Momentum

According to classical physics, for a particle with linear momentum of $\vec{p}$ and position of $\vec{r}$ one can write

$$\vec{L} = \vec{r}\times\vec{p} = \begin{vmatrix} \vec{i} & \vec{j} & \vec{k} \\ x & y & z \\ p_x & p_y & p_z \end{vmatrix} = (yp_z - zp_y)\vec{i} + (zp_x - xp_z)\vec{j} + (xp_y - yp_x)\vec{k}, \tag{A.7}$$

where $\vec{L}$ denotes the angular momentum of the particle. By substituting the dynamical variables $\vec{r}$ and $\vec{p}$ by the corresponding quantum mechanical operators one can write $\hat{\vec{L}} = \hat{\vec{r}}\times\hat{\vec{p}} = -i\hbar\hat{\vec{r}}\times\hat{\vec{\nabla}}$ for the orbital angular momentum, whose Cartesian components read $\hat{L}_x = \hat{y}\hat{p}_z - \hat{z}\hat{p}_y = -i\hbar(\hat{y}\partial/\partial z - \hat{z}\partial/\partial y)$, $\hat{L}_y = \hat{z}\hat{p}_x - \hat{x}\hat{p}_z = -i\hbar(\hat{z}\partial/\partial x - \hat{x}\partial/\partial z)$, and $\hat{L}_z = \hat{x}\hat{p}_y - \hat{y}\hat{p}_x = -i\hbar(\hat{x}\partial/\partial y - \hat{y}\partial/\partial x)$. Since the operators $\hat{x}$, $\hat{y}$, and $\hat{z}$ mutually commute and so do the operators $\hat{p}_x$, $\hat{p}_y$, and $\hat{p}_z$, and since $[\hat{x},\hat{p}_x] = i\hbar$, $[\hat{y},\hat{p}_y] = i\hbar$, and $[\hat{z},\hat{p}_z] = i\hbar$, one can write

$$\begin{aligned}
[\hat{L}_x,\hat{L}_y] &= [\hat{y}\hat{p}_z - \hat{z}\hat{p}_y, \hat{z}\hat{p}_x - \hat{x}\hat{p}_z] \\
&= [\hat{y}\hat{p}_z,\hat{z}\hat{p}_x] - [\hat{y}\hat{p}_z,\hat{x}\hat{p}_z] - [\hat{z}\hat{p}_y,\hat{z}\hat{p}_x] + [\hat{z}\hat{p}_y,\hat{x}\hat{p}_z] \\
&= \hat{y}[\hat{p}_z,\hat{z}]\hat{p}_x + \hat{x}[\hat{z},\hat{p}_z]\hat{p}_y = i\hbar(\hat{x}\hat{p}_y - \hat{y}\hat{p}_x) = i\hbar\hat{L}_z.
\end{aligned} \tag{A.8}$$

For the other two commutations, according to the cyclic permutation $x \to y \to z \to x$, one has $[\hat{L}_y,\hat{L}_z] = i\hbar\hat{L}_x$ and $[\hat{L}_z,\hat{L}_x] = i\hbar\hat{L}_y$. Notice that $[\hat{x},\hat{L}_x] = 0$, $[\hat{x},\hat{L}_y] = i\hbar\hat{z}$, $[\hat{x},\hat{L}_z] = -i\hbar\hat{y}$, $[\hat{p}_x,\hat{L}_x] = 0$, $[\hat{p}_x,\hat{L}_y] = i\hbar\hat{p}_z$, and $[\hat{p}_x,\hat{L}_z] = -i\hbar\hat{p}_y$. Therefore, $[\hat{x},\hat{\vec{L}}^2] = i\hbar(\hat{L}_y\hat{z} + \hat{z}\hat{L}_y - \hat{L}_z\hat{y} - \hat{y}\hat{L}_y)$ and $[\hat{p}_x,\hat{\vec{L}}^2] = i\hbar(\hat{L}_y\hat{p}_z + \hat{p}_z\hat{L}_y - \hat{L}_z\hat{p}_y - \hat{p}_y\hat{L}_y)$.

General Formalism of Angular Momentum

A general angular momentum operator $\hat{\vec{J}}$ can be defined in terms of its components $\hat{J}_x$, $\hat{J}_y$ and $\hat{J}_z$ such that $[\hat{J}_x,\hat{J}_y] = i\hbar\hat{J}_z$, $[\hat{J}_y,\hat{J}_z] = i\hbar\hat{J}_x$, and $[\hat{J}_z,\hat{J}_x] = i\hbar\hat{J}_y$, or equivalently stated

$$\hat{\vec{J}}\times\hat{\vec{J}} = \begin{vmatrix} \vec{i} & \vec{j} & \vec{k} \\ \hat{J}_x & \hat{J}_y & \hat{J}_z \\ \hat{J}_x & \hat{J}_y & \hat{J}_z \end{vmatrix} = i\hbar\hat{\vec{J}}. \tag{A.9}$$

Notice that $[\hat{\vec{J}}^2,\hat{J}_k] = 0$, where k stands for x, y, and z.

For example,

$$\begin{aligned}[\hat{\vec{J}}^2,\hat{J}_x] &= [\hat{J}_x^2+\hat{J}_y^2+\hat{J}_z^2,\hat{J}_x] = [\hat{J}_x^2,\hat{J}_x]+[\hat{J}_y^2,\hat{J}_x]+[\hat{J}_z^2,\hat{J}_x]\\ &= 0+\hat{J}_y[\hat{J}_y,\hat{J}_x]+[\hat{J}_y,\hat{J}_x]\hat{J}_y+\hat{J}_z[\hat{J}_z,\hat{J}_x]+[\hat{J}_z,\hat{J}_x]\hat{J}_z\\ &= i\hbar(\hat{J}_z\hat{J}_y-\hat{J}_z\hat{J}_y+\hat{J}_y\hat{J}_z-\hat{J}_y\hat{J}_z)=0.\end{aligned} \tag{A.10}$$

In the light of the relation $\hat{J}_\pm = \hat{J}_x \pm i\hat{J}_y$, one can write $[\hat{\vec{J}}^2,\hat{J}_\pm]=0$, $[\hat{J}_+,\hat{J}_-]=2\hbar\hat{J}_z$, and $[\hat{J}_z,\hat{J}_\pm]=\pm\hbar\hat{J}_\pm$. It is easy to show that $\hat{J}_\pm\hat{J}_\mp = \hat{\vec{J}}^2-\hat{J}_z^2\pm\hbar\hat{J}_z$ which leads to $\hat{\vec{J}}^2 = (1/2)(\hat{J}_+\hat{J}_- + \hat{J}_-\hat{J}_+)+\hat{J}_z^2$. Considering the relation $\hat{J}_z\left|\alpha,\beta\right\rangle = \hbar\beta\left|\alpha,\beta\right\rangle$, one can write $\hat{J}_z(\hat{J}_\pm\left|\alpha,\beta\right\rangle) = \hbar(\beta\pm1)(\hat{J}_\pm\left|\alpha,\beta\right\rangle)$. So, $\hat{\vec{J}}^2(\hat{J}_\pm\left|\alpha,\beta\right\rangle) = \hbar^2\alpha(\hat{J}_\pm\left|\alpha,\beta\right\rangle)$. Considering the equation $\hat{\vec{J}}^2\left|\alpha,\beta\right\rangle = \hbar^2\alpha\left|\alpha,\beta\right\rangle$, it is easy to verify that $\alpha\geq\beta^2$. It can be shown that $-j\leq m\leq j$. To summarise $\hat{\vec{J}}^2\left|j,m\right\rangle = \hbar^2 j(j+1)\left|j,m\right\rangle$ and $\hat{J}_z\left|j,m\right\rangle = \hbar m\left|j,m\right\rangle$.

The Hydrogen Atom

For the hydrogen atom, equation (A.6), ignoring the kinetic energy of the proton and using the Coulomb potential in CGS system, can be written as

$$\Big(-\frac{\hbar^2}{2\mu}\nabla^2-\frac{e^2}{r}\Big)\psi = E\psi. \tag{A.11}$$

It is unique of the hydrogen atom (hydrogen-like ions) and its spherical potential that the partial differential equation (A.11) can be separated into three ordinary differential equations in the spherical polar coordinate system; $x = r\sin\theta\cos\varphi$, $y = r\sin\theta\sin\varphi$, and $z = r\cos\theta$. So,

$$\begin{aligned}&\left[-\frac{\hbar^2}{2\mu}\left\{\frac{1}{r^2}\frac{\partial}{\partial r}\left[r^2\frac{\partial}{\partial r}\right]+\frac{1}{r^2}\left[\frac{1}{\sin\theta}\frac{\partial}{\partial\theta}\left(\sin\theta\frac{\partial}{\partial\theta}\right)+\frac{1}{\sin^2\theta}\frac{\partial^2}{\partial\varphi^2}\right]\right\}-\frac{e^2}{r}\right]\psi\\ &=\left[-\frac{\hbar^2}{2\mu}\left(\frac{1}{r}\frac{\partial^2}{\partial r^2}r-\frac{1}{\hbar^2 r^2}\vec{L}^2\right)\right]\psi = E\psi.\end{aligned} \tag{A.12}$$

The exact solution of equation (A.12) is therefore a product of two functions; a $R_{nl}(r)$ radial function which is associated with the Laguerre polynomials and a $Y_{lm}(\theta,\varphi)$ spherical harmonic. Boundary conditions lead to quantisation and the principal quantum number $n = 1, 2, \ldots, \infty$, the azimuthal quantum number $l = 0, 1, \ldots, n-1$, and $m = 0, \pm1, \ldots, \pm l$.

Appendix B

Tables and Figures

Table B.1: Available experimental data for the diatomic molecules AB

$\mathrm{Z_A}$ $\mathrm{Z_B}$	21	22	23	24	25	26	27	28	$\mathrm{Z_A}$ $\mathrm{Z_B}$
29	-	-	-	CrCu[c]	-	-	CoCu[i]	NiCu[k]	29
47	-	-	-	CrAg[d]	MnAg[f]	-	-	NiAg[l]	47
79	ScAu[a]	-	VAu[b]	CrAu[e]	MnAu[g]	FeAu[h]	CoAu[j]	NiAu[m]	79

[a] D_0^0 (ref. 98)

[b] D_0^0 (refs. 98,100)

[c] $X^{2\mathrm{S}+1}\Sigma$, $2\mathrm{S}+1=4$ (ref. 105) or 6 (ref. 103) or 8 (ref. 104), D_0^0 (ref. 98)

[d] $X^6\Sigma$ (ref. 105)

[e] $X^6\Sigma$ (ref. 105), D_0^0 (ref. 98)

[f] $X^7\Sigma$ (ref. 101), D_0^0 (refs. 98,101)

[g] D_0^0 (refs. 98,102)

[h] D_0^0 (ref. 98)

[i] D_0^0 (ref. 98)

[j] D_0^0 (ref. 98)

[k] $X^2\Delta_{5/2}, A, B, C, D, E, F,\ D_0, r_e, \omega_e, \omega_e x_e, ...$ (refs. 98,106–108,112)

[l] $X^2\Delta, {}^4\Delta$, ω_e (ref. 112)

[m] $X^2\Delta_{5/2}, \Omega=3/2, \Omega=1/2, \Omega=3/2, \Omega=1/2, [18.4]5/2, [18.5]3/2,\ D_0, r_0, \omega_e, ...$ (refs. 98,110,111)

Table B.2: Errors in excitation energies for the low-lying electronic levels of the metal atoms A (Sc-Ni) and B (Cu/Ag/Au) calculated at various levels of theory (CASSCF, MRCI, KRCI) considering relativistic effects. Table entries are $E_{\text{Ref}} - E_{\text{Calc}}$ (eV), where the reference energies are given in last column. The spin-orbit coupled components (J) are indented relative to the parental ΛS terms.

atom	configuration	term	J	c-CAS[a]	CAS[b]	CAS-v[c]	c-MRCI[d]	MRCI[d]	MRCI-v[d]	KRCI[e]	expt.[i]
Sc	$3d^14s^2$	^{2}D		0.00	0.00	0.00	0.00	0.00	0.00	-	0.000000
			3/2	-	-	-	-	-	0.00	0.00	0.000000
			5/2	-	-	-	-	-	0.00	−0.01	0.020871
	$3d^24s^1$	^{4}F		−0.09	0.68	−0.13	−0.11	−0.32	−0.27	-	1.426944
			3/2	-	-	-	-	-	−0.27	−0.06	1.428297
			5/2	-	-	-	-	-	−0.27	−0.06	1.432971
			7/2	-	-	-	-	-	−0.27	−0.07	1.439491
			9/2	-	-	-	-	-	−0.28	−0.07	1.447811
	$3d^24s^1$	^{2}F		−0.36	0.21	−0.13	−0.20	−0.17	−0.17	-	1.846282
			5/2	-	-	-	-	-	−0.17	−0.09	1.850597
			7/2	-	-	-	-	-	−0.17	−0.09	1.864960
Ti	$3d^24s^2$	^{3}F		0.00	0.00	0.00	0.00	0.00	0.00	-	0.000000
			2	-	-	-	-	-	0.00	0.00	0.000000
			3	-	-	-	-	-	0.00	0.00	0.021094
			4	-	-	-	-	-	0.00	−0.01	0.047966
	$3d^34s^1$	^{5}F		−1.19	−0.15	−1.02	0.05	−0.28	−0.24	-	0.805758
			1	-	-	-	-	-	−0.24	0.03	0.812944
			2	-	-	-	-	-	−0.24	0.03	0.818143
			3	-	-	-	-	-	−0.24	0.03	0.825860
			4	-	-	-	-	-	−0.24	0.03	0.835995
			5	-	-	-	-	-	−0.24	0.03	0.848419
	$3d^24s^2$	^{1}D		−0.15	−0.25	−0.24	−0.05	−0.11	−0.10	-	0.871961
			2	-	-	-	-	-	−0.10	−0.24	0.899549
	$3d^24s^2$	^{3}P		−0.24	−0.29	−0.32	−0.01	−0.12	−0.14	-	1.032141
			0	-	-	-	-	-	−0.14	−0.21	1.046007
			1	-	-	-	-	-	−0.14	−0.21	1.052926

Continued on next page

Table B.2 – *Continued from previous page*

atom	configuration	term	J	c-CAS^a	CAS^b	CAS-v^c	c-MRCI^d	MRCI^d	MRCI-v^d	KRCI^e	expt.^{i}
			2	-	-	-	-	-	−0.14	−0.22	1.066555
V	3d^{3}4s^2	^{4}F		0.00	0.00	0.00	0.00	0.00	0.00	-	0.000000
			3/2	-	-	-	-	-	0.00	0.00	0.000000
			5/2	-	-	-	-	-	0.00	0.00	0.017033
			7/2	-	-	-	-	-	0.00	−0.01	0.040104
			9/2	-	-	-	-	-	0.00	−0.01	0.068558
	3d^{4}4s^1	^{6}D		−0.60	0.09	−0.80	0.07	−0.17	−0.17	-	0.245144
			1/2	-	-	-	-	-	−0.17	0.04	0.261889
			3/2	-	-	-	-	-	−0.17	0.04	0.266964
			5/2	-	-	-	-	-	−0.17	0.04	0.275259
			7/2	-	-	-	-	-	−0.18	0.04	0.286572
			9/2	-	-	-	-	-	−0.18	0.04	0.300634
	3d^{4}4s^1	^{4}D		−0.92	−0.29	−0.84	−0.04	−0.10	−0.14	-	1.026226
			1/2	-	-	-	-	-	−0.15	−0.04	1.043079
			3/2	-	-	-	-	-	−0.15	−0.04	1.050919
			5/2	-	-	-	-	-	−0.15	−0.04	1.063602
			7/2	-	-	-	-	-	−0.15	−0.04	1.080617
	3d^{3}4s^2	^{4}P		−0.21	−0.36	−0.38	0.01	−0.14	−0.15	-	1.164965
			1/2	-	-	-	-	-	−0.15	−0.23	1.183383
			3/2	-	-	-	-	-	−0.15	−0.23	1.194839
			5/2	-	-	-	-	-	−0.15	−0.24	1.218096
Cr	3d^{5}4s^1	^{7}S		−0.56	0.00	−0.75	0.00	0.00	0.00	-	0.000000
			3	-	-	-	-	-	0.00	0.00	0.000000
	3d^{5}4s^1	^{5}S		−0.84	−0.31	−0.74	−0.09	0.07	0.02	-	0.941430
			2	-	-	-	-	-	0.02	−0.11	0.941430
	3d^{4}4s^2	^{5}D		1.00	0.88	1.00	−0.11	0.00	0.03	-	1.003056
			0	-	-	-	-	-	0.03	−0.23	0.960970
			1	-	-	-	-	-	0.03	−0.23	0.968413

Continued on next page

Table B.2 – *Continued from previous page*

atom	configuration	term	J	c-CAS[a]	CAS[b]	CAS-v[c]	c-MRCI[d]	MRCI[d]	MRCI-v[d]	KRCI[e]	expt.[i]
			2	-	-	-	-	-	0.03	−0.23	0.982877
			3	-	-	-	-	-	0.03	−0.23	1.003675
			4	-	-	-	-	-	0.03	−0.24	1.030008
Mn	$3d^5 4s^2$	^{6}S		0.00	0.00	0.00	0.00	0.00	0.00	-	0.000000
			5/2	-	-	-	-	-	0.00	0.00	0.000000
	$3d^6 4s^1$	^{6}D		0.40	0.68	−0.07	0.01	−0.33	−0.36	-	2.145076
			9/2	-	-	-	-	-	−0.36	−0.18	2.114214
			7/2	-	-	-	-	-	−0.36	−0.20	2.142695
			5/2	-	-	-	-	-	−0.36	−0.22	2.163713
			3/2	-	-	-	-	-	−0.37	−0.23	2.178214
			1/2	-	-	-	-	-	−0.37	−0.23	2.186728
Fe	$3d^6 4s^2$	^{5}D		0.00	0.00	0.00	0.00	0.00	0.00	-	0.000000
			4	-	-	-	-	-	0.00	0.00	0.000000
			3	-	-	-	-	-	0.00	0.00	0.051569
			2	-	-	-	-	-	0.01	0.00	0.087286
			1	-	-	-	-	-	0.01	0.00	0.110114
			0	-	-	-	-	-	0.00	0.00	0.121266
	$3d^7 4s^1$	^{5}F		0.10	0.38	0.37	0.13	−0.10	−0.10	-	0.874930
			5	-	-	-	-	-	−0.09	−0.06	0.858996
			4	-	-	-	-	-	−0.09	−0.06	0.914602
			3	-	-	-	-	-	−0.09	−0.06	0.958157
			2	-	-	-	-	-	−0.10	−0.06	0.990111
			1	-	-	-	-	-	−0.10	−0.06	1.011056
	$3d^7 4s^1$	^{3}F		−0.10	0.17	0.16	0.10	−0.07	−0.07	-	1.488361
			4	-	-	-	-	-	−0.07	−0.11	1.484864
			3	-	-	-	-	-	−0.07	−0.11	1.557357
			2	-	-	-	-	-	−0.08	−0.11	1.607896

Continued on next page

Table B.2 – *Continued from previous page*

atom	configuration	term	J	c-CAS[a]	CAS[b]	CAS-v[c]	c-MRCI[d]	MRCI[d]	MRCI-v[d]	KRCI[e]	expt.[i]
Co	3d^{7}4s^2	a^4F		0.00	0.00	0.00	0.00	0.00	0.00	-	0.000000
			9/2	-	-	-	-	-	0.00	0.00	0.000000
			7/2	-	-	-	-	-	0.00	0.00	0.101171
			5/2	-	-	-	-	-	0.00	0.00	0.174426
			3/2	-	-	-	-	-	0.00	0.00	0.224328
	3d^{8}4s^1	b^4F		−2.72	−2.56	−3.30	0.05	−0.01	−0.15	-	0.417152
			9/2	-	-	-	-	-	−0.14	−0.16	0.431815
			7/2	-	-	-	-	-	−0.15	−0.16	0.513624
			5/2	-	-	-	-	-	−0.15	−0.16	0.581508
			3/2	-	-	-	-	-	−0.15	−0.16	0.629323
	3d^{8}4s^1	a^2F		−2.88	−2.73	−3.38	−0.07	−0.09	−0.24	-	0.878525
			7/2	-	-	-	-	-	−0.24	−0.19	0.922741
			5/2	-	-	-	-	-	−0.25	−0.19	1.049007
Ni	3d^{9}4s^1	^{3}D		−3.15	−3.13	−3.83	0.00	0.00	−0.13	-	0.000000
			3	-	-	-	-	-	−0.15	−0.41	0.025390
			2	-	-	-	-	-	−0.16	−0.33	0.109083
			1	-	-	-	-	-	−0.15	−0.32	0.212396
	3d^{8}4s^2	^{3}F		0.03	0.03	0.03	−0.07	−0.02	0.03	-	0.029799
			4	-	-	-	-	-	0.00	0.03	0.000000
			3	-	-	-	-	-	0.00	−0.06	0.165167
			2	-	-	-	-	-	−0.01	−0.08	0.274817
	3d^{9}4s^1	^{1}D		−1.26	−1.58	−1.57	−0.09	−0.06	−0.20	-	0.332089
			2	-	-	-	-	-	−0.25	−0.40	0.422778
Cu	3d^{10}4s^1	^{2}S		−2.79	−2.79	−3.48	0.00	0.00	0.00	-	0.000000
			1/2	-	-	-	-	-	0.00	0.00	0.000000
	3d^{9}4s^2	^{2}D		1.49	1.49	1.49	0.15	0.15	0.38	-	1.490259
			5/2	-	-	-	-	-	0.38	0.43	1.3889476

Continued on next page

Table B.2 – *Continued from previous page*

atom	configuration	term	J	c-CAS[a]	CAS[b]	CAS-v[c]	c-MRCI[d]	MRCI[d]	MRCI-v[d]	KRCI[e]	expt.[i]
			3/2	-	-	-	-	-	0.38	0.41	1.6422256
Ag	$4d^{10}5s^1$	^2S		0.00	0.00	0.00	0.00	0.00	0.00	-	0.000000
			1/2	-	-	-	-	-	0.00	0.00	0.000000
	$4d^{10}5p^1$	$^2P^o$		-	-	-0.01	-	-	-0.29	-	3.740082
			1/2	-	-	-	-	-	-0.26	-	3.663988
			3/2	-	-	-	-	-	-0.31	-	3.778129
	$4d^9 5s^2$	^2D		1.33	1.33	1.32	0.42	0.53	0.51	-	3.971346
			5/2	-	-	-	-	-	0.51	-0.04	3.749567
			3/2	-	-	-	-	-	0.52	-0.05	4.304016
Au	$5d^{10}6s^1$	^2S		0.00	0.00	0.00	0.00	0.00	0.00	-	0.000000
			1/2	-	-	-	-	-	0.00	0.00[g]	0.000000
	$5d^9 6s^2$	^2D		0.52	0.52	1.16	0.02	-0.10	-0.02	-	1.744555
			5/2	-	-	-	-	-	0.04	-0.09[g]	1.135841
			3/2	-	-	-	-	-	-0.10	-0.08[g]	2.657625
…[h]											
MAD[f]				0.74	0.67	0.86	0.06	0.09	0.12	-	0.00
MAD				-	-	-	-	-	0.13	0.11	0.00

[a] SA-CASSCF(n,10), where the number of active electrons n varies from 11 to 18 for the atoms Sc to Ni. $n = 19$ for the atoms B. The 10 active orbitals are $(k-1)$s+$(k-1)$p+$(k-1)$d+ks. $k = 4$ for the atoms A and Cu, $k = 5$ for Ag, and $k = 6$ for Au.

[b] SA-CASSCF(m,6), where the number of valence electrons m varies from 3 to 10 for the atoms Sc to Ni. $m = 11$ for the atoms B. The 6 active orbitals are $(k-1)$d+ks.

[c] SA-CASSCF(m,9). The 9 active orbitals are $(k-1)$d+ks+kp.

[d] MRCI calculations on top of the corresponding SA-CASSCF calculations as defined in the footnotes a, b, and c. Davidson correction has been included in the MRCI energies.

[e] AC-DHF($m|6$) with the subsequent GASCI($m|l$). The 6 Kramers pairs are composed of the $(k-1)$d+ks atomic spinors. l is the number of virtual orbitals which was chosen on a case-by-case basis ($37 \leq l \leq 76$).

[f] MAD stands for mean absolute deviation from the reference energies, $(1/j)\sum_{i=1}^{j} |E_{\mathrm{Ref}}(i) - E_{\mathrm{Calc}}(i)|$, $j = 31$ and $j = 88$ for the ΛS and spin-orbit cases.

[g] In contrast to other atoms for which the dyall-v3z basis (ref. 92) were used in the KRCI calculations, for the Au atom the dyall-v2z basis (ref. 94) was employed.

[h] See also ref. 168 for the LS terms of the configurations s^1, p^{1-5}, d^{1-9}, and f^{1-13} for some further atoms and cations.

[i] Experimental energies for the levels E_J were taken from ref. 118.

Table B.3: Correlation between atomic and molecular terms in ScB. Energies are in eV.

Sc	B	(Λ,S) terms	energy	Sc	B	Ω terms	energy
^{2}D, 3d^{1}4s^2	^{2}S, $(k-1)$d^{10}ks^1	$^{1,3}[\Sigma^+ \oplus \Pi \oplus \Delta]$[a]	0.00	3/2	1/2	$2 \oplus 1(2) \oplus 0^+ \oplus 0^-$	0.00
				5/2	1/2	$3 \oplus 2(2) \oplus 1(2) \oplus 0^+ \oplus 0^-$	0.02

[a] $^1\Sigma^+ \Rightarrow 0^+$ $^1\Pi \Rightarrow 1$ $^1\Delta \Rightarrow 2$ $^3\Sigma^+ \Rightarrow 0^- \oplus 1$ $^3\Pi \Rightarrow 0^+ \oplus 0^- \oplus 1 \oplus 2$ $^3\Delta \Rightarrow 1 \oplus 2 \oplus 3$

Table B.4: Correlation between atomic and molecular terms in TiB. Energies are in eV.

Ti	B	(Λ,S) terms	energy	Ti	B	Ω terms	energy
^{3}F, 3d^{2}4s^2	^{2}S, $(k-1)$d^{10}ks^1	$^{2,4}[\Sigma^- \oplus \Pi \oplus \Delta \oplus \Phi]$[a]	0.00	2	1/2	$\frac{5}{2} \oplus \frac{3}{2}(2) \oplus \frac{1}{2}(2)$	0.00
				3	1/2	$\frac{7}{2} \oplus \frac{5}{2}(2) \oplus \frac{3}{2}(2) \oplus \frac{1}{2}(2)$	0.02
				4	1/2	$\frac{9}{2} \oplus \frac{7}{2}(2) \oplus \frac{5}{2}(2) \oplus \frac{3}{2}(2) \oplus \frac{1}{2}(2)$	0.05
^{5}F, 3d^{3}4s^1	^{2}S, $(k-1)$d^{10}ks^1	$^{4,6}[\Sigma^- \oplus \Pi \oplus \Delta \oplus \Phi]$[a]	0.81	1	1/2	$\frac{3}{2} \oplus \frac{1}{2}(2)$	0.81
				2	1/2	$\frac{5}{2} \oplus \frac{3}{2}(2) \oplus \frac{1}{2}(2)$	0.82
				3	1/2	$\frac{7}{2} \oplus \frac{5}{2}(2) \oplus \frac{3}{2}(2) \oplus \frac{1}{2}(2)$	0.83
				4	1/2	$\frac{9}{2} \oplus \frac{7}{2}(2) \oplus \frac{5}{2}(2) \oplus \frac{3}{2}(2) \oplus \frac{1}{2}(2)$	0.84
				5	1/2	$\frac{11}{2} \oplus \frac{9}{2}(2) \oplus \frac{7}{2}(2) \oplus \frac{5}{2}(2) \oplus \frac{3}{2}(2) \oplus \frac{1}{2}(2)$	0.85

[a] $^2\Sigma^- \Rightarrow 1/2$ $^2\Pi \Rightarrow 1/2 \oplus 3/2$ $^2\Delta \Rightarrow 3/2 \oplus 5/2$ $^2\Phi \Rightarrow 5/2 \oplus 7/2$ $^4\Sigma^- \Rightarrow 1/2 \oplus 3/2$ $^4\Pi \Rightarrow 1/2 \oplus 1/2 \oplus 3/2 \oplus 5/2$ $^4\Delta \Rightarrow 1/2 \oplus 3/2 \oplus 5/2 \oplus 7/2$ $^4\Phi \Rightarrow 3/2 \oplus 5/2 \oplus 7/2 \oplus 9/2$ $^6\Sigma^- \Rightarrow 1/2 \oplus 3/2 \oplus 5/2$ $^6\Pi \Rightarrow 1/2 \oplus 1/2 \oplus 3/2 \oplus 3/2 \oplus 5/2 \oplus 7/2$ $^6\Delta \Rightarrow 1/2 \oplus 1/2 \oplus 3/2 \oplus 5/2 \oplus 7/2 \oplus 9/2$ $^6\Phi \Rightarrow 1/2 \oplus 3/2 \oplus 5/2 \oplus 7/2 \oplus 9/2 \oplus 11/2$

Table B.5: Correlation between atomic and molecular terms in VB. Energies are in eV.

V	B	(Λ,S) terms	energy	V	B	Ω terms	energy
^{4}F, $3d^34s^2$	^{2}S, $(k-1)d^{10}ks^1$	$^{3,5}[\Sigma^- \oplus \Pi \oplus \Delta \oplus \Phi]^a$	0.00	3/2	1/2	$2 \oplus 1(2) \oplus 0^+ \oplus 0^-$	0.00
				5/2	1/2	$3 \oplus 2(2) \oplus 1(2) \oplus 0^+ \oplus 0^-$	0.02
				7/2	1/2	$4 \oplus 3(2) \oplus 2(2) \oplus 1(2) \oplus 0^+ \oplus 0^-$	0.04
				9/2	1/2	$5 \oplus 4(2) \oplus 3(2) \oplus 2(2) \oplus 1(2) \oplus 0^+ \oplus 0^-$	0.07
^{6}D, $3d^44s^1$	^{2}S, $(k-1)d^{10}ks^1$	$^{5,7}[\Sigma^+ \oplus \Pi \oplus \Delta]^a$	0.25	1/2	1/2	$1 \oplus 0^+ \oplus 0^-$	0.26
				3/2	1/2	$2 \oplus 1(2) \oplus 0^+ \oplus 0^-$	0.27
				5/2	1/2	$3 \oplus 2(2) \oplus 1(2) \oplus 0^+ \oplus 0^-$	0.28
				7/2	1/2	$4 \oplus 3(2) \oplus 2(2) \oplus 1(2) \oplus 0^+ \oplus 0^-$	0.29
				9/2	1/2	$5 \oplus 4(2) \oplus 3(2) \oplus 2(2) \oplus 1(2) \oplus 0^+ \oplus 0^-$	0.30

[a] $^3\Sigma^- \Rightarrow 0^+ \oplus 1$ $^3\Pi \Rightarrow 0^+ \oplus 0^- \oplus 1 \oplus 2$ $^3\Delta \Rightarrow 1 \oplus 2 \oplus 3$ $^3\Phi \Rightarrow 2 \oplus 3 \oplus 4$ $^5\Sigma^+ \Rightarrow 0^+ \oplus 1 \oplus 2$ $^5\Sigma^- \Rightarrow 0^- \oplus 1 \oplus 2$ $^5\Pi \Rightarrow 0^+ \oplus 0^- \oplus 1 \oplus 1 \oplus 2 \oplus 3$ $^5\Delta \Rightarrow 0^+ \oplus 0^- \oplus 1 \oplus 2 \oplus 3 \oplus 4$ $^5\Phi \Rightarrow 1 \oplus 2 \oplus 3 \oplus 4 \oplus 5$ $^7\Sigma^+ \Rightarrow 0^- \oplus 1 \oplus 2 \oplus 3$ $^7\Pi \Rightarrow 0^+ \oplus 0^- \oplus 1 \oplus 1 \oplus 2 \oplus 2 \oplus 3 \oplus 4$ $^7\Delta \Rightarrow 0^+ \oplus 0^- \oplus 1 \oplus 1 \oplus 2 \oplus 3 \oplus 4 \oplus 5$

Table B.6: Correlation between atomic and molecular terms in CrB. Energies are in eV.

Cr	B	(Λ,S) terms	energy	Cr	B	Ω terms	energy
^{7}S, $3d^54s^1$	^{2}S, $(k-1)d^{10}ks^1$	$^{6,8}[\Sigma^+]^a$	0.00	3	1/2	$\frac{7}{2} \oplus \frac{5}{2}(2) \oplus \frac{3}{2}(2) \oplus \frac{1}{2}(2)$	0.00
^{5}S, $3d^54s^1$	^{2}S, $(k-1)d^{10}ks^1$	$^{4,6}[\Sigma^+]^a$	0.94	2	1/2	$\frac{5}{2} \oplus \frac{3}{2}(2) \oplus \frac{1}{2}(2)$	0.94

[a] $^6\Sigma^+ \Rightarrow 1/2 \oplus 3/2 \oplus 5/2$ $^8\Sigma^+ \Rightarrow 1/2 \oplus 3/2 \oplus 5/2 \oplus 7/2$ $^4\Sigma^+ \Rightarrow 1/2 \oplus 3/2$

Table B.7: Correlation between atomic and molecular terms in MnB. Energies are in eV.

Mn	B	(Λ,S) terms	energy	Mn	B	Ω terms	energy
^{6}S, 3d^{5}4s^2	^{2}S, $(k-1)$d^{10}ks^1	$^{5,7}[\Sigma^+]^a$	0.00	5/2	1/2	$3 \oplus 2(2) \oplus 1(2) \oplus 0^+ \oplus 0^-$	0.00
^{6}D, 3d^{6}4s^1	^{2}S, $(k-1)$d^{10}ks^1	$^{5,7}[\Sigma^+ \oplus \Pi \oplus \Delta]^a$	2.15	9/2	1/2	$5 \oplus 4(2) \oplus 3(2) \oplus 2(2) \oplus 1(2) \oplus 0^+ \oplus 0^-$	2.11
				7/2	1/2	$4 \oplus 3(2) \oplus 2(2) \oplus 1(2) \oplus 0^+ \oplus 0^-$	2.14
				5/2	1/2	$3 \oplus 2(2) \oplus 1(2) \oplus 0^+ \oplus 0^-$	2.16
				3/2	1/2	$2 \oplus 1(2) \oplus 0^+ \oplus 0^-$	2.18
				1/2	1/2	$1 \oplus 0^+ \oplus 0^-$	2.19

[a] $^5\Sigma^+ \Rightarrow 0^+ \oplus 1 \oplus 2$ $\quad ^5\Pi \Rightarrow 0^+ \oplus 0^- \oplus 1 \oplus 1 \oplus 2 \oplus 3$ $\quad ^5\Delta \Rightarrow 0^+ \oplus 0^- \oplus 1 \oplus 2 \oplus 3 \oplus 4$ $\quad ^7\Sigma^+ \Rightarrow 0^- \oplus 1 \oplus 2 \oplus 3$ $\quad ^7\Pi \Rightarrow 0^+ \oplus 0^- \oplus 1 \oplus 1 \oplus 2 \oplus 2 \oplus 3 \oplus 4$ $\quad ^7\Delta \Rightarrow 0^+ \oplus 0^- \oplus 1 \oplus 1 \oplus 2 \oplus 3 \oplus 4 \oplus 5$

Table B.8: Correlation between atomic and molecular terms in FeB. Energies are in eV.

Fe	B	(Λ,S) terms	energy	Fe	B	Ω terms	energy
^{5}D, 3d^{6}4s^2	^{2}S, $(k-1)$d^{10}ks^1	$^{4,6}[\Sigma^+ \oplus \Pi \oplus \Delta]^a$	0.00	4	1/2	$\frac{9}{2} \oplus \frac{7}{2}(2) \oplus \frac{5}{2}(2) \oplus \frac{3}{2}(2) \oplus \frac{1}{2}(2)$	0.00
				3	1/2	$\frac{7}{2} \oplus \frac{5}{2}(2) \oplus \frac{3}{2}(2) \oplus \frac{1}{2}(2)$	0.05
				2	1/2	$\frac{5}{2} \oplus \frac{3}{2}(2) \oplus \frac{1}{2}(2)$	0.09
				1	1/2	$\frac{3}{2} \oplus \frac{1}{2}(2)$	0.11
				0	1/2	$\frac{1}{2}$	0.12
^{5}F, 3d^{7}4s^1	^{2}S, $(k-1)$d^{10}ks^1	$^{4,6}[\Sigma^- \oplus \Pi \oplus \Delta \oplus \Phi]^a$	0.87	5	1/2	$\frac{11}{2} \oplus \frac{9}{2}(2) \oplus \frac{7}{2}(2) \oplus \frac{5}{2}(2) \oplus \frac{3}{2}(2) \oplus \frac{1}{2}(2)$	0.86
				4	1/2	$\frac{9}{2} \oplus \frac{7}{2}(2) \oplus \frac{5}{2}(2) \oplus \frac{3}{2}(2) \oplus \frac{1}{2}(2)$	0.91
				3	1/2	$\frac{7}{2} \oplus \frac{5}{2}(2) \oplus \frac{3}{2}(2) \oplus \frac{1}{2}(2)$	0.96
				2	1/2	$\frac{5}{2} \oplus \frac{3}{2}(2) \oplus \frac{1}{2}(2)$	0.99
				1	1/2	$\frac{3}{2} \oplus \frac{1}{2}(2)$	1.01

[a] $^4\Sigma^+ \Rightarrow 1/2 \oplus 3/2$ $\quad ^4\Sigma^- \Rightarrow 1/2 \oplus 3/2$ $\quad ^4\Pi \Rightarrow 1/2 \oplus 1/2 \oplus 3/2 \oplus 5/2$ $\quad ^4\Delta \Rightarrow 1/2 \oplus 3/2 \oplus 5/2 \oplus 7/2$ $\quad ^4\Phi \Rightarrow 3/2 \oplus 5/2 \oplus 7/2 \oplus 9/2$ $\quad ^6\Sigma^+ \Rightarrow 1/2 \oplus 3/2 \oplus 5/2$ $\quad ^6\Sigma^- \Rightarrow 1/2 \oplus 3/2 \oplus 5/2$ $\quad ^6\Pi \Rightarrow 1/2 \oplus 1/2 \oplus 3/2 \oplus 3/2 \oplus 5/2 \oplus 7/2$ $\quad ^6\Delta \Rightarrow 1/2 \oplus 1/2 \oplus 3/2 \oplus 5/2 \oplus 7/2 \oplus 9/2$ $\quad ^6\Phi \Rightarrow 1/2 \oplus 3/2 \oplus 5/2 \oplus 7/2 \oplus 9/2 \oplus 11/2$

Table B.9: Correlation between atomic and molecular terms in CoB. Energies are in eV.

Co	B	(Λ,S) terms	energy	Co	B	Ω terms	energy
^{4}F, 3d^{7}4s^2	^{2}S, $(k-1)$d^{10}ks^1	$^{3,5}[\Sigma^- \oplus \Pi \oplus \Delta \oplus \Phi]^a$	0.00	9/2	1/2	$5 \oplus 4(2) \oplus 3(2) \oplus 2(2) \oplus 1(2) \oplus 0^+ \oplus 0^-$	0.00
				7/2	1/2	$4 \oplus 3(2) \oplus 2(2) \oplus 1(2) \oplus 0^+ \oplus 0^-$	0.10
				5/2	1/2	$3 \oplus 2(2) \oplus 1(2) \oplus 0^+ \oplus 0^-$	0.17
				3/2	1/2	$2 \oplus 1(2) \oplus 0^+ \oplus 0^-$	0.22

[a] $^3\Sigma^- \Rightarrow 0^+ \oplus 1$ $^3\Pi \Rightarrow 0^+ \oplus 0^- \oplus 1 \oplus 2$ $^3\Delta \Rightarrow 1 \oplus 2 \oplus 3$ $^3\Phi \Rightarrow 2 \oplus 3 \oplus 4$ $^5\Sigma^- \Rightarrow 0^- \oplus 1 \oplus 2$ $^5\Pi \Rightarrow 0^+ \oplus 0^- \oplus 1 \oplus 1 \oplus 2 \oplus 3$
$^5\Delta \Rightarrow 0^+ \oplus 0^- \oplus 1 \oplus 2 \oplus 3 \oplus 4$ $^5\Phi \Rightarrow 1 \oplus 2 \oplus 3 \oplus 4 \oplus 5$

Table B.10: Correlation between atomic and molecular terms in NiB. Energies are in eV.

Ni	B	(Λ,S) terms	energy	Ni	B	Ω terms	energy
^{3}D, 3d^{9}4s^1	^{2}S, $(k-1)$d^{10}ks^1	$^{2,4}[\Sigma^+ \oplus \Pi \oplus \Delta]^a$	0.00	3	1/2	$\frac{7}{2} \oplus \frac{5}{2}(2) \oplus \frac{3}{2}(2) \oplus \frac{1}{2}(2)$	0.03
				2	1/2	$\frac{5}{2} \oplus \frac{3}{2}(2) \oplus \frac{1}{2}(2)$	0.11
				1	1/2	$\frac{3}{2} \oplus \frac{1}{2}(2)$	0.21
^{3}F, 3d^{8}4s^2	^{2}S, $(k-1)$d^{10}ks^1	$^{2,4}[\Sigma^- \oplus \Pi \oplus \Delta \oplus \Phi]^a$	0.03	4	1/2	$\frac{9}{2} \oplus \frac{7}{2}(2) \oplus \frac{5}{2}(2) \oplus \frac{3}{2}(2) \oplus \frac{1}{2}(2)$	0.00
				3	1/2	$\frac{7}{2} \oplus \frac{5}{2}(2) \oplus \frac{3}{2}(2) \oplus \frac{1}{2}(2)$	0.17
				2	1/2	$\frac{5}{2} \oplus \frac{3}{2}(2) \oplus \frac{1}{2}(2)$	0.27
^{1}D, 3d^{9}4s^1	^{2}S, $(k-1)$d^{10}ks^1	$^2[\Sigma^+ \oplus \Pi \oplus \Delta]^a$	0.33	2	1/2	$\frac{5}{2} \oplus \frac{3}{2}(2) \oplus \frac{1}{2}(2)$	0.42

[a] $^2\Sigma^- \Rightarrow 1/2$ $^2\Sigma^+ \Rightarrow 1/2$ $^2\Pi \Rightarrow 1/2 \oplus 3/2$ $^2\Delta \Rightarrow 3/2 \oplus 5/2$ $^2\Phi \Rightarrow 5/2 \oplus 7/2$ $^4\Sigma^- \Rightarrow 1/2 \oplus 3/2$ $^4\Sigma^+ \Rightarrow 1/2 \oplus 3/2$
$^4\Pi \Rightarrow 1/2 \oplus 1/2 \oplus 3/2 \oplus 5/2$ $^4\Delta \Rightarrow 1/2 \oplus 3/2 \oplus 5/2 \oplus 7/2$ $^4\Phi \Rightarrow 3/2 \oplus 5/2 \oplus 7/2 \oplus 9/2$

Table B.11: Bond length r_e(Å), harmonic frequency and anharmonicity constant $\omega_e, \omega_e x_e$(cm^{-1}), dissociation energy D_e(eV), electronic energy T_e(eV), dipole moment μ(D), and main configuration weight(MCW) of the low-lying states of the diatomic molecule **ScCu** obtained at the DKH-MRCI(+Q) level

No.	Term	r_e	ω_e	$\omega_e x_e$	D_e	T_e	μ^a	MCW^a
1	$X^3\Delta$							
	MRCI^b	2.64	198.6	0.52	1.17	0.00	1.02	90% [24421001]
	cMRCI^c	2.60	202.0	0.65	1.14	0.00	0.95	87% [24421001]
2	$^1\Sigma^+$	2.59	207.1	0.76	1.05	0.12	0.29	64% [24421100] + 25% [24422000]
3	$^3\Pi$	2.63	192.8	0.50	1.02	0.15	0.70	90% [24421010]
4	$^3\Sigma^+$	2.63	194.2	0.52	0.96	0.21	0.42	90% [24421100]
5	$^1\Delta$	2.65	197.2	0.44	0.96	0.21	0.19	88% [24421001]
6	$^1\Pi$	2.65	184.2	0.50	0.78	0.39	0.92	90% [24421010]

[a] Dipole moments (μ) and main configuration weights (MCW) correspond to $r = 2.65$ Å. The occupations of the orbitals $\sigma\pi\delta\sigma\sigma\sigma\pi\delta$ are given in brackets. Weights larger than one-tenth are reported.

[b] MRCI[(10+4)E,(5+7)O] [c] MRCI[(26+4)E,(13+7)O]

Table B.12: Bond length r_e(Å), harmonic frequency and anharmonicity constant $\omega_e, \omega_e x_e$(cm^{-1}), dissociation energy D_e(eV), electronic energy T_e(eV), dipole moment μ(D), and main configuration weight(MCW) of the low-lying states of the diatomic molecule **ScAg** obtained at the DKH-MRCI(+Q) level

No.	Term	r_e	ω_e	$\omega_e x_e$	D_e	T_e	μ^a	MCW^a
1	$X^3\Delta$							
	MRCI^b	2.75	175.4	0.46	1.21	0.00	0.73	89% [24421001]
	cMRCI^c	2.72	173.7	0.38	1.11	0.00	0.72	88% [24421001]
2	$^1\Sigma^+$	2.71	179.8	0.68	1.14	0.07	0.40	65% [24421100] + 24% [24422000]
3	$^3\Pi$	2.74	172.6	0.55	1.11	0.10	0.38	89% [24421010]
4	$^1\Delta$	2.75	172.3	0.53	1.07	0.15	-0.21	87% [24421001]
5	$^3\Sigma^+$	2.75	174.5	0.60	1.04	0.18	0.08	90% [24421100]
6	$^1\Pi$	2.77	163.4	0.78	0.91	0.30	0.73	89% [24421010]

[a] Dipole moments (μ) and main configuration weights (MCW) correspond to $r = 2.75$ Å. The occupations of the orbitals $\sigma\pi\delta\sigma\sigma\sigma\pi\delta$ are given in brackets. Weights larger than one-tenth are reported.

[b] MRCI[(10+4)E,(5+7)O] [c] MRCI[(26+4)E,(13+7)O]

Table B.13: Bond length r_e(Å), harmonic frequency and anharmonicity constant $\omega_e, \omega_e x_e$(cm^{-1}), dissociation energy D_e (eV), electronic energy T_e(eV), dipole moment μ(D), and main configuration weight(MCW) of the low-lying states of the diatomic molecule **ScAu** obtained at the DKH-MRCI(+Q) level

No.	Term	r_e	ω_e	$\omega_e x_e$	D_e	T_e	μ^a	MWC^a
1	$X^3\Delta$							
	MRCI^b	2.60	226.2	0.79	2.52	0.00	2.00	89% [24421001]
	cMRCI^c	2.52	242.7	0.58	2.69	0.00	1.90	87% [24421001]
	expt.	-	-	-	2.87(0.18)^d	-	-	-
2	$^1\Sigma^+$	2.54	240.7	0.73	2.38	0.15	1.76	56% [24421100] + 31% [24422000]
3	$^3\Pi$	2.62	223.2	0.60	2.33	0.19	1.91	89% [24421010]
4	$^1\Delta$	2.59	228.0	0.65	2.29	0.23	1.49	87% [24421001]
5	$^3\Sigma^+$	2.62	224.2	0.65	2.21	0.31	1.64	89% [24421100]
6	$^1\Pi$	2.62	217.3	0.56	2.02	0.50	2.19	88% [24421010]

[a] Dipole moments (μ) and main configuration weights (MCW) correspond to $r = 2.60$ Å. The occupations of the orbitals $\sigma\pi\delta\sigma\sigma\sigma\pi\delta$ are given in brackets. Weights larger than one-tenth are reported.

[b] MRCI[(10+4)E,(5+7)O] [c] MRCI[(40+4)E,(20+7)O]

[d] From ref. 98. The experimental bond strength in ref. 98 is D_0^0. No electronic term was mentioned/assigned in this work. It is presumed that the reported value corresponds to the electronic ground state term calculated in the present work.

Table B.14: Bond length r_e(Å), harmonic frequency and anharmonicity constant $\omega_e, \omega_e x_e$(cm^{-1}), dissociation energy D_e(eV), electronic energy T_e(eV), dipole moment μ(D), and main configuration weight(MCW) of the low-lying states of the diatomic molecule **TiCu** obtained at the DKH-MRCI(+Q) level

No.	Term	r_e	ω_e	$\omega_e x_e$	D_e	T_e	μ^a	MCW^a
1	$X^4\Phi$							
	MRCI^b	2.52	214.6	0.75	1.14	0.00	2.75	84% [24421011]
	cMRCI^c	2.51	212.1	0.71	1.10	-	2.07	83% [24421011]
2	$1^4\Sigma^-$	2.53	230.0	1.07	1.06	0.08	2.68	54% [24421020] + 29% [24421002]
3	$1^4\Pi$	2.53	208.1	0.78	0.99	0.15	2.71	65% [24421011] + 18% [24421110]
4	$1^4\Delta$	2.52	206.8	1.75	0.87	0.27	2.74	89% [24421101]
5	$^2\Delta$	2.54	194.7	1.38	0.77	0.37	1.39	66% [24421101] + 22% [24422001]
6	$^2\Phi$	2.54	193.2	0.96	0.73	0.41	2.08	88% [24421011]
7	$^2\Pi$	2.56	187.9	0.97	0.70	0.44	1.82	54% [24421011] + 26% [24421110]
8	$^2\Sigma^-$	2.56	188.2	1.22	0.67	0.48	2.12	67% [24421020] + 22% [24421002]
9	$2^4\Delta$	2.56	190.4	0.51	1.27	0.76	3.78	81% [24420021]
10	$2^4\Pi$	2.58	187.2	0.83	1.20	0.83	3.55	43% [24420111] + 26% [24420012] + 13% [24421110]
11	$2^4\Sigma^-$	2.58	188.1	1.41	1.20	0.83	3.44	45% [24420102] + 19% [24421020] + 11% [24420120]
12	$2^4\Phi$	2.55	189.1	1.41	1.13	0.90	3.53	78% [24420111]
13	$^6\Delta$	3.26	36.2	2.35	0.04	2.00	1.71	88% [24411021]
14	$^6\Phi$	3.47	12.5	0.06	0.02	2.01	1.51	92% [24411111]
15	$^6\Pi$	4.42	11.7	0.06	0.02	2.02	1.69	63% [24411111] + 27% [24411012]
16	$^6\Sigma^-$	4.71	11.7	0.10	0.01	2.02	1.60	55% [24411102] + 37% [24411120]

[a] Dipole moments (μ) and main configuration weights (MCW) correspond to $r = 2.50$ Å. The occupations of the orbitals $\sigma\pi\delta\sigma\sigma\sigma\pi\delta$ are given in brackets. Weights larger than one-tenth are reported.

[b] MRCI[(10+5)E,(5+7)O] [c] MRCI[(26+5)E,(13+7)O]

Table B.15: Bond length r_e(Å), harmonic frequency and anharmonicity constant $\omega_e, \omega_e x_e$(cm^{-1}), dissociation energy D_e(eV), electronic energy T_e(eV), dipole moment μ(D), and main configuration weight(MCW) of the low-lying states of the diatomic molecule **TiAg** obtained at the DKH-MRCI(+Q) level

No.	Term	r_e	ω_e	$\omega_e x_e$	D_e	T_e	μ^a	MCW^a
1	$X^4\Phi$							
	MRCI^b	2.63	192.6	0.21	1.19	0.00	1.92	85% [24421011]
	cMRCI^c	2.62	189.1	0.94	1.04	0.00	1.60^d	83% [24421011]^d
2	$1^4\Sigma^-$	2.65	190.0	0.17	1.13	0.07	1.13	58% [24421020] + 27% [24421002]
3	$1^4\Pi$	2.65	188.6	0.30	1.08	0.11	1.81	63% [24421011] + 22% [24421110]
4	$1^4\Delta$	2.65	186.2	0.43	1.02	0.18	1.74	88% [24421101]
5	$^2\Delta$	2.65	180.4	0.72	0.90	0.30	0.83	68% [24421101] + 18% [24422001]
6	$^2\Phi$	2.65	180.6	1.26	0.86	0.34	1.27	87% [24421011]
7	$^2\Pi$	2.66	177.9	1.63	0.83	0.37	1.15	53% [24421011] + 27% [24421110]
8	$^2\Sigma^-$	2.68	175.6	1.50	0.79	0.41	1.35	66% [24421020] + 21% [24421002]
9	$2^4\Delta$	2.65	187.3	0.65	1.47	0.73	2.60	81% [24420021]
10	$2^4\Pi$	2.66	185.5	0.76	1.42	0.78	2.53	43% [24420111] + 29% [24420012]
11	$2^4\Sigma^-$	2.66	184.5	0.74	1.41	0.79	2.49	49% [24420102] + 13% [24421020] + 12% [24420120]
12	$2^4\Phi$	2.65	189.2	0.79	1.39	0.81	2.29	77% [24420111]
13	$^6\Delta$	2.95	97.8	1.46	0.30	1.89	1.62	88% [24411021]
14	$^6\Phi$	3.05	83.1	1.05	0.24	1.96	1.49	91% [24411111]
15	$^6\Pi$	3.10	70.8	0.50	0.20	1.99	1.71	59% [24411111] + 31% [24401112]
16	$^6\Sigma^-$	3.19	62.4	0.69	0.17	2.03	1.67	61% [24411102] + 31% [24411120]

[a] Dipole moments (μ) and main configuration weights (MCW) correspond to $r = 2.65$ Å. The occupations of the orbitals $\sigma\pi\delta\sigma\sigma\sigma\pi\delta$ are given in brackets. Weights larger than one-tenth are reported.

[b] MRCI[(10+5)E,(5+7)O] [c] MRCI[(26+5)E,(13+7)O]

[d] These values correspond to $r = 2.60$ Å.

Table B.16: Bond length r_e(Å), harmonic frequency and anharmonicity constant $\omega_e, \omega_e x_e$(cm^{-1}), dissociation energy D_e(eV), electronic energy T_e(eV), dipole moment μ(D), and main configuration weight(MCW) of the low-lying states of the diatomic molecule **TiAu** obtained at the DKH-MRCI(+Q) level

No.	Term	r_e	ω_e	$\omega_e x_e$	D_e	T_e	μ^a	MCW^a
1	$X^4\Phi$							
	MRCI^b	2.54	231.9	0.58	2.41	0.00	1.55	89% [24421011]
	cMRCI^c	2.49	241.4	0.49	2.50	0.00	1.48	88% [24421011]
2	$^4\Sigma^-$	2.55	229.4	0.57	2.30	0.11	1.58	58% [24421020] + 31% [24421002]
3	$^4\Pi$	2.55	228.8	0.61	2.27	0.14	1.51	64% [24421011]
4	$^4\Delta$	2.55	227.3	0.53	2.25	0.16	1.32	89% [24421101]
5	$^2\Delta$	2.52	233.2	0.65	2.00	0.41	1.01	79% [24421101]
6	$^2\Phi$	2.55	230.0	0.52	1.99	0.42	1.27	89% [24421011]
7	$^2\Pi$	2.55	228.5	0.53	1.90	0.51	1.28	46% [24421011] + 19% [24421110]
8	$^2\Sigma^-$	2.56	226.8	0.45	1.87	0.54	1.34	54% [24421020] + 26% [24421002]

[a] Dipole moments (μ) and main configuration weights (MCW) correspond to $r = 2.55$ Å. The occupations of the orbitals $\sigma\pi\delta\sigma\sigma\sigma\pi\delta$ are given in brackets. Weights larger than one-tenth are reported.

[b] MRCI[(10+5)E,(5+7)O] [c] MRCI[(22+5)E,(11+7)O]

Table B.17: Bond length r_e(Å), harmonic frequency and anharmonicity constant $\omega_e, \omega_e x_e$(cm^{-1}), dissociation energy D_e(eV), electronic energy T_e(eV), dipole moment μ(D), and main configuration weight(MCW) of the low-lying states of the diatomic molecule **VCu** obtained at the DKH-MRCI(+Q) level

No.	Term	r_e	ω_e	$\omega_e x_e$	D_e	T_e	μ^a	MCW^a
1	$X^5\Delta$							
	MRCI^b	2.47	226.5	2.37	1.25	0.00	2.32	79% [24421021]
	cMRCI^c	2.47	197.0	−0.64	1.20	-	1.89^d	82% [24421021]^d
2	$1^5\Pi$	2.49	222.7	3.09	1.13	0.12	2.48	55% [24421012]
3	$^5\Sigma^-$	2.50	251.1	8.48	0.87	0.38	2.07	75% [24421102] + 14% [24421120]
4	$^5\Sigma^+$	2.55	189.3	0.63	1.18	0.42	3.41	78% [24420022]
5	$^5\Phi$	2.50	244.8	9.38	0.80	0.45	2.09	90% [24421111]
6	$2^5\Pi$	2.51	215.2	4.39	1.02	0.59	2.85	52% [24420112] + 31% [24421111]
7	$^3\Sigma^-$	2.51	212.7	5.28	0.66	0.60	1.00	48% [24421102] + 21% [24422002]
8	$^3\Pi$	2.51	209.3	4.29	0.65	0.60	1.20	36% [24421012] + 33% [24421111]
9	$^3\Delta$	2.51	206.5	3.77	0.64	0.61	1.52	84% [24421021]
10	$^3\Phi$	2.52	194.3	2.54	0.63	0.62	1.05	57% [24421111] + 27% [24422011]
11	$2^5\Delta$	2.50	222.3	6.56	0.69	0.92	2.77	74% [24420121]
12	$^7\Delta$	3.30	21.6	1.41	0.02	1.58	1.88	91% [24411121]
13	$^7\Sigma^+$	4.26	11.7	0.20	0.01	1.59	2.25	82% [24411022]
14	$^7\Pi$	4.63	11.7	0.27	0.01	1.60	2.11	91% [24411112]

[a] Dipole moments (μ) and main configuration weights (MCW) correspond to $r = 2.45$ Å. The occupations of the orbitals $\sigma\pi\delta\sigma\sigma\sigma\pi\delta$ are given in brackets. Weights larger than one-tenth are reported.

[b] MRCI[(10+6)E,(5+7)O] [c] MRCI[(26+6)E,(13+7)O] [d] These values correspond to $r = 2.50$ Å.

Table B.18: Bond length r_e(Å), harmonic frequency and anharmonicity constant $\omega_e, \omega_e x_e$(cm^{-1}), dissociation energy D_e(eV), electronic energy T_e(eV), dipole moment μ(D), and main configuration weight(MCW) of the low-lying states of the diatomic molecule **VAg** obtained at the DKH-MRCI(+Q) level

No.	Term	r_e	ω_e	$\omega_e x_e$	D_e	T_e	μ^a	MCW^a
1	$X^5\Delta$							
	MRCI^b	2.59	192.3	0.62	1.24	0.00	1.62	75% [24421021]
	cMRCI^c	2.61	183.6	0.59	1.15	-	1.30	79% [24421021]
2	$1^5\Pi$	2.60	186.9	0.55	1.14	0.10	1.81	51% [24421012] + 14% [24420112]
3	$^5\Sigma^+$	2.62	178.8	0.59	1.31	0.31	2.28	77% [24420022] + 10% [24411022]
4	$^5\Sigma^-$	2.63	177.2	0.17	0.92	0.32	1.47	74% [24421102] + 14% [24421120]
5	$^5\Phi$	2.64	173.2	0.17	0.85	0.39	1.37	89% [24421111]
6	$2^5\Pi$	2.64	174.5	0.24	1.15	0.48	1.79	50% [24420112] + 31% [24421111]
7	$^3\Sigma^-$	2.65	162.5	0.12	0.72	0.52	0.48	50% [24421102] + 18% [24422002] + 10% [24421120]
8	$^3\Pi$	2.64	165.0	0.75	0.71	0.53	0.64	36% [24421012] + 35% [24421111]
9	$2^5\Delta$	2.63	174.1	0.06	1.07	0.56	1.62	69% [24420121] + 13% [24421021]
10	$^3\Delta$	2.65	161.7	0.52	0.68	0.56	1.62	84% [24421021]
11	$^3\Phi$	2.65	164.1	1.67	0.68	0.56	0.64	60% [24421111] + 24% [24422011]
12	$^7\Delta$	3.03	81.2	1.34	0.22	1.41	1.51	90% [24411121]
13	$^7\Sigma^+$	3.05	72.2	1.00	0.19	1.44	1.92	83% [24411022]
14	$^7\Pi$	3.22	58.7	1.14	0.14	1.49	1.75	90% [24411112]

[a] Dipole moments (μ) and main configuration weights (MCW) correspond to $r = 2.60$ Å. The occupations of the orbitals $\sigma\pi\delta\sigma\sigma\sigma\pi\delta$ are given in brackets. Weights larger than one-tenth are reported.

[b] MRCI[(10+6)E,(5+7)O] [c] MRCI[(26+6)E,(13+7)O]

Table B.19: Bond length r_e(Å), harmonic frequency and anharmonicity constant $\omega_e, \omega_e x_e$(cm^{-1}), dissociation energy D_e(eV), electronic energy T_e(eV), dipole moment μ(D), and main configuration weight(MCW) of the low-lying states of the diatomic molecule **VAu** obtained at the DKH-MRCI(+Q) level

No.	Term	r_e	ω_e	$\omega_e x_e$	D_e	T_e	μ^a	MCW^a
1	$X^5\Delta$							
	MRCI^b	2.51	235.8	0.58	2.29	0.00	1.57	88% [244210210]
	cMRCI^c	2.49	239.0	−0.62	2.33	0.00	1.52	87% [244210210]
	expt.^{d}	-	-	-	2.47(0.12)	-	-	-
2	$^5\Pi$	2.50	234.7	0.59	2.29	0.00	1.43	47% [244210120] + 42% [244211110]
3	$^5\Sigma^-$	2.50	231.5	0.46	2.24	0.05	1.34	77% [244211020] + 12% [244211200]
4	$^5\Phi$	2.52	229.5	0.60	2.09	0.20	1.40	88% [244211110]
5	$^3\Sigma^-$	2.48	237.7	0.70	1.83	0.46	0.86	50% [244211020] + 18% [244220020]
6	$^3\Pi$	2.49	237.8	0.63	1.81	0.48	1.05	39% [244210120] + 29% [244211110] + 11% [244220110]
7	$^3\Delta$	2.51	235.7	0.66	1.73	0.56	1.41	80% [244210210]
8	$^3\Phi$	2.50	233.2	0.59	1.68	0.60	1.20	57% [244211110] + 23% [244220110]

[a] Dipole moments (μ) and main configuration weights (MCW) correspond to $r = 2.50$ Å. The occupations of the orbitals $\sigma\pi\delta\sigma\sigma\sigma\pi\delta\sigma$ are given in brackets. Weights larger than one-tenth are reported.

[b] MRCI[(10+6)E,(5+8)O] [c] MRCI[(22+6)E,(11+8)O]

[d] D_0^0 from ref. 100. No electronic term was mentioned/assigned in this work. It is presumed that the reported value corresponds to the electronic ground state term calculated in the present work.

Table B.20: Bond length r_e(Å), harmonic frequency and anharmonicity constant $\omega_e, \omega_e x_e$(cm^{-1}), dissociation energy D_e(eV), electronic energy T_e(eV), dipole moment μ(D), and main configuration weight(MCW) of the low-lying states of the diatomic molecule **CrCu** obtained at the DKH-MRCI(+Q) level

No.	Term	r_e	ω_e	$\omega_e x_e$	D_e	T_e	μ[a]	MCW[a]
1	$X^6\Sigma^+$[b]							
	MRCI[c]	2.47	208.9	1.30	1.21	0.00	2.17	78% [24420122]
	cMRCI[d]	2.46	203.3	1.35	1.11	-	1.64[e]	77% [24420122][e]
	MRCI(SD)+Q[f]	2.468	183.6	0.64	1.195	0.00	-	77.4% [24420122]
	expt.	-	-	-	1.61(0.26)[g]	-	-	-
2	$^8\Sigma^+$	3.90	20.1	1.64	0.02	1.19	0.96	92% [24411122]
	MRCI(SD)+Q[f]	-	-	-	-	1.439	-	91.9% [24411122]
3	$2^6\Sigma^+$	2.75	57.7	−0.80	0.33	1.82	0.34	40% [24411122] + 39% [24421022]
4	$^4\Sigma^+$	2.48	188.5	−7.58	0.16	2.00	0.40	44% [24421022] + 19% [24411122] + 16% [24420122]

[a] Dipole moments (μ) and main configuration weights (MCW) correspond to $r = 2.45$ Å. The occupations of the orbitals $\sigma\pi\delta\sigma\sigma\sigma\pi\delta$ are given in brackets. Weights larger than one-tenth are reported.

[b] In ref. 103, the CrCu molecule was formed in a solid krypton at 4 K, and it was indicated that the molecule has a $^6\Sigma$ ground state term. In the very same year (1981), the authors published an erratum in which they drew the conclusion that CrCu most probably has an $^8\Sigma$ ground term—ref. 104. Two years later, however, they observed the molecule in solid rare-gas matrices at 4 K and assigned a $^4\Sigma$ ground term to CrCu—ref. 105.

[c] MRCI[(10+7)E,(5+7)O] [d] MRCI[(26+7)E,(13+7)O]

[e] These values correspond to $r = 2.50$ Å.

[f] From ref. 113. In ref. 113, CAS(17,12) was employed as the active space and as the reference space. The electronic term energy reported in ref. 113 is vertical excitation energy.

[g] D_0^0 from ref. 98. No electronic term was mentioned/assigned in this work. It is presumed that the reported value corresponds to the electronic ground state term calculated in the present work.

Table B.21: Bond length r_e(Å), harmonic frequency and anharmonicity constant $\omega_e, \omega_e x_e$(cm^{-1}), dissociation energy D_e(eV), electronic energy T_e(eV), dipole moment μ(D), and main configuration weight(MCW) of the low-lying states of the diatomic molecule **CrAg** obtained at the DKH-MRCI(+Q) level

No.	Term	r_e	ω_e	$\omega_e x_e$	D_e	T_e	μ[a]	MCW[a]
1	$X^6\Sigma^+$[b]							
	MRCI[c]	2.60	188.6	1.53	1.25	0.00	1.26	81% [24420122]
	cMRCI[d]	2.61	182.5	1.66	1.08	-	0.83	80% [24420122]
2	$^8\Sigma^+$	3.18	54.2	0.67	0.13	1.12	1.26	92% [24411122]
3	$2^6\Sigma^+$	2.85	70.7	−0.08	0.46	1.72	0.26	45% [24411122] + 34% [24421022]
4	$^4\Sigma^+$	2.52	136.9	−0.85	0.31	1.87	0.18	47% [24421022] + 18% [24411122] + 14% [24420122]

[a] Dipole moments (μ) and main configuration weights (MCW) correspond to $r = 2.60$ Å. The occupations of the orbitals $\sigma\pi\delta\sigma\sigma\sigma\pi\delta$ are given in brackets. Weights larger than one-tenth are reported.

[b] Experimental ground state term is $^6\Sigma$ (ref. 105).

[c] MRCI[(10+7)E,(5+7)O] [d] MRCI[(26+7)E,(13+7)O]

Table B.22: Bond length r_e(Å), harmonic frequency and anharmonicity constant $\omega_e, \omega_e x_e$(cm^{-1}), dissociation energy D_e(eV), electronic energy T_e(eV), dipole moment μ(D), and main configuration weight(MCW) of the low-lying states of the diatomic molecule **CrAu** obtained at the DKH-MRCI(+Q) level

No.	Term	r_e	ω_e	$\omega_e x_e$	D_e	T_e	μ^a	MCW^a
1	$X^6\Sigma^{+b}$							
	MRCI^c	2.50	230.9	0.71	2.01	0.00	3.81	84% [24420122]
	cMRCI^d	2.46	238.5	0.86	1.96	0.00	3.55	82% [24420122]
	expt.	-	-	-	2.17(0.18)^e	-	-	-
2	$^8\Sigma^+$	3.21	39.1	1.42	0.05	1.95	-0.21	91% [24411122]

[a] Dipole moments (μ) and main configuration weights (MCW) correspond to r = 2.50 Å. The occupations of the orbitals $\sigma\pi\delta\sigma\sigma\sigma\pi\delta$ are given in brackets. Weights larger than one-tenth are reported.

[b] Experimental ground state term is $^6\Sigma$ (ref. 105).

[c] MRCI[(10+7)E,(5+7)O] [d] MRCI[(40+7)E,(20+7)O]

[e] D_0^0 from ref. 98. No electronic term was mentioned/assigned in this work. It is presumed that the reported value corresponds to the electronic ground state term calculated in the present work.

Table B.23: Bond length r_e(Å), harmonic frequency and anharmonicity constant $\omega_e, \omega_e x_e$(cm^{-1}), dissociation energy D_e(eV), electronic energy T_e(eV), dipole moment μ(D), and main configuration weight (MCW) of the low-lying states of the diatomic molecule **MnCu** obtained at the DKH-MRCI(+Q) level

No.	Term	r_e	ω_e	$\omega_e x_e$	D_e	T_e	μ^a	MCW^a
1	$X^7\Sigma^+$							
	MRCI^b	2.47	184.1	1.29	0.70	0.00	2.53	85% [24421122]
	cMRCI^c	2.52	174.2	2.24	0.57	-	2.45	84% [24421122]
2	$1^5\Sigma^+$	2.53	162.4	2.03	0.42	0.27	1.13	67% [24421122] + 14% [24422022]
3	$^5\Pi$	2.39	218.5	0.51	1.33	1.61	1.76	83% [24421032]
4	$2^5\Sigma^+$	2.40	217.7	0.13	1.33	1.62	2.02	70% [24422022] + 12% [24421122]
5	$^5\Delta$	2.44	205.6	0.84	1.20	1.74	1.98	83% [24421023]
6	$2^7\Sigma^+$	2.79	128.6	0.94	0.38	2.56	0.66	79% [24412122] + 10% [24411222]
7	$^7\Pi$	4.15	12.4	0.36	0.01	2.93	0.06	91% [24411132]

[a] Dipole moments (μ) and main configuration weights (MCW) correspond to r = 2.50 Å. The occupations of the orbitals $\sigma\pi\delta\sigma\sigma\sigma\pi\delta$ are given in brackets. Weights larger than one-tenth are reported.

[b] MRCI[(10+8)E,(5+7)O] [c] MRCI[(26+8)E,(13+7)O]

Table B.24: Bond length r_e(Å), harmonic frequency and anharmonicity constant $\omega_e, \omega_e x_e$(cm^{-1}), dissociation energy D_e(eV), electronic energy T_e(eV), dipole moment μ(D), and main configuration weight (MCW) of the low-lying states of the diatomic molecule **MnAg** obtained at the DKH-MRCI(+Q) level

No.	Term	r_e	ω_e	$\omega_e x_e$	D_e	T_e	μ[a]	MCW[a]
1	$X^7\Sigma^+$							
	MRCI[b]	2.59	169.2	0.26	0.87	0.00	1.71	84% [24421122]
	cMRCI[c]	2.66	147.6	1.42	0.61	0.00	1.84	83% [24421122]
	expt.	-	-	-	0.99(0.22)[d]	-	-	-
2	$1^5\Sigma^+$	2.67	141.9	0.90	0.56	0.31	0.61	69% [24421122]
3	$^5\Pi$	2.53	197.6	0.74	1.46	1.79	0.65	83% [24421032]
4	$2^5\Sigma^+$	2.55	195.6	0.57	1.43	1.82	0.91	74% [24422022]
5	$^5\Delta$	2.56	184.8	0.55	1.33	1.92	0.92	84% [24421023]
6	$^7\Pi$	3.04	65.7	0.63	0.19	3.06	0.32	91% [24411132]

---

[a] Dipole moments (μ) and main configuration weights (MCW) correspond to r = 2.60 Å. The occupations of the orbitals $\sigma\pi\delta\sigma\sigma\sigma\pi\delta$ are given in brackets. Weights larger than one-tenth are reported.

[b] MRCI[(10+8)E,(5+7)O]

[c] MRCI[(26+8)E,(13+7)O]

[d] From ref. 98 (D^0). No electronic term was mentioned/assigned in this work. It is presumed that the reported value corresponds to the electronic ground state term calculated in the present work.

Table B.25: Bond length r_e(Å), harmonic frequency and anharmonicity constant $\omega_e, \omega_e x_e$(cm^{-1}), dissociation energy D_e(eV), electronic energy T_e(eV), dipole moment μ(D), and main configuration weight (MCW) of the low-lying states of the diatomic molecule **MnAu** obtained at the DKH-MRCI(+Q) level

No.	Term	r_e	ω_e	$\omega_e x_e$	D_e	T_e	μ[a]	MCW[a]
1	$X^7\Sigma^+$							
	MRCI[b]	2.48	231.2	0.60	1.93	0.00	1.49	90% [24421122]
	cMRCI[c]	2.45	-	-	2.05	0.00	1.43	89% [24421122]
	expt.[d]	-	-	-	1.88(0.13)	-	-	-
	expt.[e]	-	-	-	1.95(0.13)	-	-	-
2	$^5\Sigma^+$	2.47	230.7	0.69	1.27	0.66	1.26	35% [24422022] + 34% [24421122] + 19% [24420222]

---

[a] Dipole moments (μ) and main configuration weights (MCW) correspond to r = 2.50 Å. The occupations of the orbitals $\sigma\pi\delta\sigma\sigma\sigma\pi\delta$ are given in brackets. Weights larger than one-tenth are reported.

[b] MRCI[(10+8)E,(5+7)O]

[c] MRCI[(40+8)E,(20+7)O]

[d] From ref. 102. In ref. 102, the authors assumed a $^7\Sigma$ electronic ground state term for MnAu by analogy with MnH.

[e] D_0^0 from ref. 98. No electronic term was mentioned/assigned in this work. It is presumed that the reported value corresponds to the electronic ground state term calculated in the present work.

Table B.26: Bond length r_e(Å), harmonic frequency and anharmonicity constant $\omega_e, \omega_e x_e$(cm^{-1}), dissociation energy D_e(eV), electronic energy T_e(eV), dipole moment μ(D), and main configuration weight (MCW) of the low-lying states of the diatomic molecule **FeCu** obtained at the DKH-MRCI(+Q) level

No.	Term	r_e	ω_e	$\omega_e x_e$	D_e	T_e	μ^a	MCW^a
1	$X^6\Delta$							
	MRCI^b	2.44	193.6	1.90	0.67	0.00	2.24	88% [24421123]
	cMRCI^c	2.48	175.5	1.46	0.58	-	2.15^d	87% [24421123]^d
2	$1^4\Delta$	2.39	209.4	2.77	0.63	0.04	0.96	51% [24422023] + 33% [24421123]
3	$1^6\Pi$	2.46	186.3	2.17	0.60	0.07	2.17	88% [24421132]
4	$^6\Sigma^+$	2.46	183.3	1.95	0.59	0.08	1.95	87% [24422122]
5	$1^4\Pi$	2.39	199.5	2.14	0.57	0.10	0.92	43% [24421132] + 30% [24422032] + 10% [24421033]
6	$^4\Sigma^-$	2.35	229.6	1.71	1.39	0.25	1.49	66% [24421042] + 12% [24421024]
7	$^4\Phi$	2.38	220.4	1.52	1.32	0.32	1.63	78% [24421033] + 10% [24411133]
8	$^4\Sigma^+$	2.53	148.8	1.95	0.33	0.34	1.30	84% [24422122]
9	$2^4\Pi$	2.43	202.5	0.48	1.21	0.43	1.76	35% [24421033] + 34% [24421132] + 10% [24422032]
10	$2^4\Delta$	2.45	193.1	1.84	1.11	0.53	2.04	50% [24421123] + 28% [24422023]
11	$2^6\Delta$	3.14	41.3	2.19	0.04	1.60	0.33	89% [24412123]
12	$^6\Sigma^-$	4.60	10.9	0.21	0.01	1.63	0.25	75% [24411142] + 15% [24411124]
13	$2^6\Pi$	4.18	10.3	0.15	0.01	1.63	0.26	46% [24411133] + 43% [24412132]
14	$^6\Phi$	4.62	10.2	0.28	0.01	1.63	0.35	90% [24411133]

[a] Dipole moments (μ) and main configuration weights (MCW) correspond to r = 2.45 Å. The occupations of the orbitals $\sigma\pi\delta\sigma\sigma\sigma\pi\delta$ are given in brackets. Weights larger than one-tenth are reported.

[b] MRCI[(10+9)E,(5+7)O] [c] MRCI[(26+9)E,(13+7)O] [d] At r = 2.50 Å.

Table B.27: Bond length r_e(Å), harmonic frequency and anharmonicity constant $\omega_e, \omega_e x_e$(cm^{-1}), dissociation energy D_e(eV), electronic energy T_e(eV), dipole moment μ(D), and main configuration weight (MCW) of the low-lying states of the diatomic molecule **FeAg** obtained at the DKH-MRCI(+Q) level

No.	Term	r_e	ω_e	$\omega_e x_e$	D_e	T_e	μ[a]	MCW[a]
1	$X^6\Delta$							
	MRCI[b]	2.56	168.9	0.91	0.77	0.00	1.41	88% [24421123]
	cMRCI[c]	2.63	150.5	1.23	0.59	-	1.51[d]	87% [24421123][d]
2	$1^4\Delta$	2.55	182.6	2.11	0.71	0.06	0.12	49% [24422023] + 36% [24421123]
3	$1^6\Pi$	2.60	163.8	1.71	0.69	0.08	1.40	87% [24421132]
4	$^6\Sigma^+$	2.61	160.6	1.28	0.68	0.09	1.31	87% [24422122]
5	$1^4\Pi$	2.55	173.1	2.03	0.65	0.12	0.17	44% [24421132] + 29% [24422032] + 10% [24421033]
6	$^4\Sigma^-$	2.50	203.3	0.99	1.48	0.25	0.38	67% [24421042] + 13% [24421024]
7	$^4\Phi$	2.52	196.8	0.77	1.43	0.31	0.52	80% [24421033]
8	$^4\Sigma^+$	2.67	132.5	1.01	0.45	0.33	0.74	84% [24422122]
9	$2^4\Pi$	2.58	185.9	1.21	1.33	0.41	0.82	33% [24421132] + 36% [24421033] + 10% [24422032] +
10	$2^4\Delta$	2.60	171.8	0.50	1.23	0.50	1.11	47% [24421123] + 32% [24422023]
11	$^6\Sigma^-$	3.05	62.5	1.21	0.15	1.58	0.51	74% [24411142] + 16% [24411124]
12	$2^6\Delta$	2.96	83.8	1.87	0.21	1.52	0.56	89% [24412123]
13	$2^6\Pi$	3.03	70.8	1.15	0.18	1.55	0.50	48% [24411133] + 42% [24412132]
14	$^6\Phi$	3.13	55.4	1.04	0.14	1.60	0.64	48% [24411133]

---

[a] Dipole moments (μ) and main configuration weights (MCW) correspond to r = 2.55 Å. The occupations of the orbitals $\sigma\pi\delta\sigma\sigma\sigma\pi\delta$ are given in brackets. Weights larger than one-tenth are reported.

[b] MRCI[(10+9)E,(5+7)O] [c] MRCI[(26+9)E,(13+7)O] [d] These values correspond to r = 2.60 Å.

Table B.28: Bond length r_e(Å), harmonic frequency and anharmonicity constant $\omega_e, \omega_e x_e$(cm^{-1}), dissociation energy D_e(eV), electronic energy T_e(eV), dipole moment μ(D), and main configuration weight (MCW) of the low-lying states of the diatomic molecule **FeAu** obtained at the DKH-MRCI(+Q) level

No.	Term	r_e	ω_e	$\omega_e x_e$	D_e	T_e	μ^a	MCW^a
1	$X^6\Delta$							
	MRCI^b	2.43	238.8	0.69	1.86	0.00	1.18	89% [24421123]
	cMRCI^c	2.39	249.7	0.68	1.99	0.00	1.18	89% [24421123]
	expt.	-	-	-	1.95(0.22)^d	-	-	-
2	$^6\Pi$	2.45	235.8	1.46	1.64	0.22	1.29	89% [24421132]
3	$^6\Sigma^+$	2.44	236.1	1.43	1.61	0.25	1.17	89% [24422122]
4	$^4\Delta$	2.42	238.0	0.94	1.30	0.56	1.17	49% [24421123] + 27% [24422023] + 13% [24420223]
5	$^4\Pi$	2.44	233.2	1.08	1.19	0.68	1.05	50% [24421132] + 26% [24422032] + 13% [24420232]
6	$^4\Sigma^+$	2.45	227.7	1.04	1.07	0.79	1.04	75% [24422122] + 13% [24421222]

[a] Dipole moments (μ) and main configuration weights (MCW) correspond to $r = 2.45$ Å. The occupations of the orbitals $\sigma\pi\delta\sigma\sigma\sigma\pi\delta$ are given in brackets. Weights larger than one-tenth are reported.

[b] MRCI[(10+9)E,(5+7)O] [c] MRCI[(40+9)E,(20+7)O]

[d] D_0^0 from ref. 98. No electronic term was mentioned/assigned in this work. It is presumed that the reported value corresponds to the electronic ground state term calculated in the present work.

Table B.29: Bond length r_e(Å), harmonic frequency and anharmonicity constant $\omega_e, \omega_e x_e$(cm^{-1}), dissociation energy D_e(eV), electronic energy T_e(eV), dipole moment μ(D), and main configuration weight (MCW) of the low-lying states of the diatomic molecule **CoCu** obtained at the DKH-MRCI(+Q) level

No.	Term	r_e	ω_e	$\omega_e x_e$	D_e	T_e	μ^a	MCW^a
1	$X^3\Phi$							
	MRCI[b]	2.31	239.4	1.27	1.53	0.00	0.54	88% [24422033]
	cMRCI[c]	2.31	235.4	1.37	1.46	-	0.50	87% [24422033]
	expt.	-	-	-	1.69(0.22)[d]	-	-	-
2	$^3\Delta$	2.32	228.6	0.59	1.47	0.06	0.69	72% [24412043] + 15% [24421043]
3	$^3\Sigma^-$	2.33	223.4	-1.01	1.47	0.07	0.65	67% [24422024] + 21% [24422042]
4	$^3\Pi$	2.33	229.1	0.73	1.46	0.07	0.66	57% [24422033] + 26% [24412034]
5	$^5\Phi$	2.38	213.4	0.96	0.32	1.21	1.30	83% [24421133]
6	$^5\Sigma^-$	2.40	172.2	5.22	0.14	1.40	0.93	57% [24421124] + 29% [24421142]
7	$^5\Pi$	4.33	10.8	0.04	0.01	1.52	0.54	65% [24421133] + 23% [24411134]
8	$^5\Delta$	4.33	13.8	0.57	0.01	1.52	0.23	91% [24411143]

[a] Dipole moments (μ) and main configuration weights (MCW) correspond to r = 2.30 Å. The occupations of the orbitals $\sigma\pi\delta\sigma\sigma\sigma\pi\delta$ are given in brackets. Weights larger than one-tenth are reported.

[b] MRCI[(10+10)E,(5+7)O] [c] MRCI[(26+10)E,(13+7)O]

[d] D_0^0 from ref. 98. No electronic term was mentioned/assigned in this work. It is presumed that the reported value corresponds to the electronic ground state term calculated in the present work.

Table B.30: Bond length r_e (Å), harmonic frequency and anharmonicity constant $\omega_e, \omega_e x_e$ (cm^{-1}), dissociation energy D_e (eV), electronic energy T_e(eV), dipole moment μ (D), and main configuration weight (MCW) of the low-lying states of the diatomic molecule **CoAg** obtained at the DKH-MRCI(+Q) level

No.	Term	r_e	ω_e	$\omega_e x_e$	D_e	T_e	μ^a	MCW^a
1	$X^3\Phi$							
	MRCI[b]	2.47	208.8	0.84	1.60	0.00	0.51	87% [24422033]
	cMRCI[c]	2.48	204.4	0.81	1.44	-	0.40[d]	87% [24422033][d]
2	$^3\Sigma^-$	2.47	203.6	1.23	1.56	0.05	0.34	68% [24422024] + 20% [24422042]
3	$^3\Delta$	2.48	208.5	1.24	1.55	0.05	0.37	78% [24412043]
4	$^3\Pi$	2.48	204.6	0.97	1.55	0.06	0.35	56% [24422033] + 29% [24412034]
5	$^5\Phi$	2.45	178.3	6.91	0.68	0.92	1.34	64% [24421133] + 23% [24412133]
6	$^5\Sigma^-$	2.48	204.2	1.33	0.43	1.17	0.92	50% [24421124] + 25% [24421142] + 11% [24412142]
7	$^5\Pi$	2.59	134.5	9.65	0.21	1.40	0.39	59% [24421133] + 24% [24411134]
8	$^5\Delta$	3.06	52.6	0.96	0.13	1.48	0.46	91% [24411143]

[a] Dipole moments (μ) and main configuration weights (MCW) correspond to r = 2.45 Å. The occupations of the orbitals $\sigma\pi\delta\sigma\sigma\sigma\pi\delta$ are given in brackets. Weights larger than one-tenth are reported.

[b] MRCI[(10+10)E,(5+7)O] [c] MRCI[(26+10)E,(13+7)O]

[d] These values correspond to r = 2.50 Å.

Table B.31: Bond length r_e(Å), harmonic frequency and anharmonicity constant $\omega_e, \omega_e x_e$(cm^{-1}), dissociation energy D_e(eV), electronic energy T_e(eV), dipole moment μ(D), and main configuration weight (MCW) of the low-lying states of the diatomic molecule **CoAu** obtained at the DKH-MRCI(+Q) level

No.	Term	r_e	ω_e	$\omega_e x_e$	D_e	T_e	μ^a	MCW^a
1	$X^5\Phi$							
	MRCI^b	2.41	238.2	0.95	1.59	0.00	1.49	89% [24412133]
	cMRCI^c	2.38	248.1	0.87	1.71	0.00	1.56	88% [24412133]
	expt.	-	-	-	2.26(0.18)^d	-	-	-
2	$^5\Sigma^-$	2.41	233.8	0.84	1.52	0.07	1.37	66% [24412142] + 23% [24412124]
3	$^5\Pi$	2.42	233.7	0.91	1.49	0.10	1.48	58% [24412133] + 31% [24422132]
4	$^5\Delta$	2.42	233.0	0.68	1.48	0.11	1.53	89% [24422123]
5	$^3\Phi$	2.40	233.5	1.01	1.21	0.38	1.04	59% [24412133] + 15% [24422033]
6	$^3\Sigma^-$	2.41	230.5	0.97	1.14	0.45	0.99	54% [24412142] + 15% [24412124] + 11% [24422042]
7	$^3\Pi$	2.42	228.2	1.05	1.10	0.48	1.01	44% [24412133] + 31% [24422132]
8	$^3\Delta$	2.42	226.0	1.24	1.06	0.53	1.05	85% [24422123]

[a] Dipole moments (μ) and main configuration weights (MCW) correspond to $r = 2.40$ Å. The occupations of the orbitals $\sigma\pi\delta\sigma\sigma\sigma\pi\delta$ are given in brackets. Weights larger than one-tenth are reported.

[b] MRCI[(10+10)E,(5+7)O]

[c] MRCI[(40+10)E,(20+7)O]

[d] D_0^0 from ref. 98. No electronic term was mentioned/assigned in this work. It is presumed that the reported value corresponds to the electronic ground state term calculated in the present work.

Table B.32: Bond length r_e(Å), harmonic frequency and anharmonicity constant $\omega_e, \omega_e x_e$(cm^{-1}), dissociation energy D_e(eV), electronic energy T_e(eV), dipole moment μ(D), and main configuration weight (MCW) of the low-lying states of the diatomic molecule **NiCu** obtained at the DKH-MRCI(+Q) level

No.	Term	r_e	ω_e	$\omega_e x_e$	D_e	T_e	μ^a	MCW^a
1	$X^2\Delta$							
	MRCI-1[h]	2.33	254.4	0.78	1.81[e]	0.00	−0.20[i]	74% [24420243] + 15% [24411243][i]
	MRCI[b]	2.23	272.3	0.92	1.33[e]	0.00	1.43	59% [24420243] + 15% [24421143] + 13% [24411243]
	$X^2\Delta_{5/2}$							
	MRCI-SO	2.23	278.2	–	†[g]	0.00	1.42	–
	expt.[c]	2.2330	273.01	1.00	2.05	0.00	–	$d^{10}_{\mathrm{Cu}}d^{9}_{\mathrm{Ni}}\sigma^2$
	expt.[k]	–	–	–	2.08	–	–	–
2	$1^2\Sigma^+$	2.31	230.0	0.95	1.48[f]	0.00	2.00	67% [24420144] + 18% [24411144]
3	$1^2\Pi$	2.25	267.0	0.45	1.25	0.08	1.66	59% [24420234] + 16% [24411234]
4	$2^2\Pi$	2.88	166.0	4.54	0.75	0.73	1.00	32% [24421233] + 25% [24421134]
5	$2^2\Delta$	2.69	167.0	5.54	0.69	0.80	1.10	73% [24421143] + 10% [24420243]
6	$1^4\Delta$	2.41	182.0	2.00	0.49	0.84	1.45	90% [24421143]
	expt.[d]				0.11	1.94	–	$d^{10}_{\mathrm{Cu}}d^{9}_{\mathrm{Ni}}\sigma^1\sigma^{*1}$
7	$1^4\Pi$	2.42	176.8	2.01	0.47	0.86	1.21	51% [24421233] + 39% [24421134]
8	$^4\Sigma^-$	2.44	167.2	1.97	0.44	0.89	0.94	72% [24421224] + 17% [24421242]
9	$^4\Phi$	2.45	163.9	2.03	0.42	0.91	0.96	89% [24421233]
10	$^2\Phi$	2.49	145.4	2.20	0.30	1.02	0.68	88% [24421233]
11	$^2\Sigma^-$	2.49	144.1	2.16	0.30	1.03	0.71	70% [24421224] + 14% [24421242]

[a] Dipole moments (μ) and main configuration weights (MCW) correspond to $r = 2.25$ Å. The occupations of the orbitals $\sigma\pi\delta\sigma\sigma\sigma\pi\delta$ are given in brackets. Weights larger than one-tenth are reported.

[b] MRCI[(10+11)E,(5+7)O]

[c] From ref. 106. For the $X^2\Delta_{5/2}$ ground state term experimental values along with errors are: $r_e = 2.2330(0.006)$ Å, $\omega_e = 273.01(1.15)$ cm^{-1}, $\omega_e x_e = 1.00(0.38)$ cm^{-1}, and $D_0 = 2.05(0.10)$ eV.

[d] From ref. 112. Experimental values along with errors: $D_e = 0.11(0.05)$ eV, and $T_e = 1.94(0.02)$ eV.

[e] With respect to the separated atom limit Ni(^{3}F) + Cu(^{2}S).

[f] With respect to the separated atom limit Ni(^{3}D) + Cu(^{2}S).

[g] $D_e = 1.28$, 1.44, 1.48, and 1.57 eV with respect to Ni(^{3}F$_4$) + Cu(^{2}S$_{1/2}$), Ni(^{3}F$_3$) + Cu(^{2}S$_{1/2}$), Ni(^{3}D$_3$) + Cu(^{2}S$_{1/2}$), and Ni(^{3}D$_2$) + Cu(^{2}S$_{1/2}$), respectively.

[h] MRCI[(11)E,(7)O].

[i] These values correspond to $r = 2.35$ Å.

[k] $D_0^0 = 2.08 \pm 0.22$ eV from ref. 98. No electronic term was mentioned/assigned in this work. It is presumed that the reported value corresponds to the electronic ground state term calculated in the present work.

Table B.33: Bond length r_e(Å), harmonic frequency and anharmonicity constant $\omega_e, \omega_e x_e$(cm^{-1}), dissociation energy D_e(eV), electronic energy T_e(eV), dipole moment μ(D), and main configuration weight (MCW) of the low-lying states of the diatomic molecule **NiAg** obtained at the DKH-MRCI(+Q) level

No.	Term	r_e	ω_e	$\omega_e x_e$	D_e	T_e	μ^a	MCW^a
1	$X^2\Delta$							
	MRCI-1^h	2.50	218.0	0.50	1.68^e	0.00	−0.41	72% [24420243] + 72% [24411243]
	MRCI^b	2.41	237.3	0.58	1.68^e	0.00	0.65	64% [24420243] + 14% [24411243]
	$\mathrm{X}^2\Delta_{5/2}$							
	MRCI-SO	2.40	234.1	–	†^{g}	0.00	0.63	–
	expt.^{c}	2.40^d	235	–	1.96^d	0.00	–	$\mathrm{d}^{10}_{\mathrm{Cu}}\mathrm{d}^{9}_{\mathrm{Ni}}\mathrm{s}\sigma^2$
2	$1^2\Sigma^+$	2.44	211.7	0.74	1.64^f	0.02	1.09	68% [24420144] + 17% [24411144]
3	$1^2\Pi$	2.43	226.5	0.48	1.64	0.05	0.85	66% [24420234] + 17% [24411234]
4	$2^2\Pi$	3.31	181.9	4.08	0.63	1.03	0.46	49% [24421233] + 36% [24421134]
5	$2^2\Delta$	3.29	139.1	13.56	0.56	1.10	0.56	80% [24421143]
6	$1^4\Delta$	2.57	155.4	1.47	0.54	1.14	0.87	91% [24421143]
7	$1^4\Pi$	2.58	153.3	0.11	0.54	1.15	0.70	51% [24421233] + 39% [24421134]
8	$^4\Sigma^-$	2.59	148.2	1.43	0.52	1.17	0.70	73% [24421224] + 17% [24421242]
9	$^4\Phi$	2.60	144.6	1.37	0.49	1.19	0.56	90% [24421233]
10	$^2\Phi$	2.64	132.1	1.59	0.40	1.28	0.32	67% [24421233]
11	$^2\Sigma^-$	2.64	131.5	1.58	0.40	1.29	0.32	71% [24421224] + 14% [24421242]

[a] Dipole moments (μ) and main configuration weights (MCW) correspond to $r = 2.40$ Å. The occupations of the orbitals $\sigma\pi\delta\sigma\sigma\sigma\pi\delta$ are given in brackets. Weights larger than one-tenth are reported.

[b] MRCI[(10+11)E,(5+7)O]

[c] From ref. 112. Experimental value along with error is: $\omega_e = 235(25)$ cm^{-1}.

[d] From ref. 112. r_e and D_0 correspond to some Theoretical values published in a private communication by E. Brocławik.

[e] With respect to the separated atom limit Ni(^{3}F) + Ag(^{2}S).

[f] With respect to the separated atom limit Ni(^{3}D) + Ag(^{2}S).

[g] $D_e = 1.63, 1.66, 1.74$, and 1.79 eV with respect to Ni($^3\mathrm{F}_4$) + Ag($^2\mathrm{S}_{1/2}$), Ni($^3\mathrm{D}_3$) + Ag($^2\mathrm{S}_{1/2}$), Ni($^3\mathrm{D}_2$) + Ag($^2\mathrm{S}_{1/2}$), and Ni($^3\mathrm{F}_3$) + Ag($^2\mathrm{S}_{1/2}$).

[h] MRCI[(11)E,(7)O].

Table B.34: Bond length r_e(Å), harmonic frequency and anharmonicity constant $\omega_e, \omega_e x_e$(cm^{-1}), dissociation energy D_e(eV), electronic energy T_e(eV), dipole moment μ(D), and main configuration weight (MCW) of the low-lying states of the diatomic molecule **NiAu** obtained at the DKH-MRCI(+Q) level

No.	Term	r_e	ω_e	$\omega_e x_e$	D_e	T_e	μ^a	MCW^a
1	$X^2\Delta$							
	MRCI^b	2.35	242.3	1.69	2.02	0.00	2.16	65% [24420243] + 12% [24421143]
	cMRCI^c	2.34	259.8	0.46	1.99	–	2.05	66% [24420243] + 10% [24421143]
	expt.^{d}	2.351	259.4	0.72	2.52	0.00	–	$d^{10}_{Au}d^{9}_{Ni}\sigma^2$
	expt.^{e}	–	–	–	2.60	–	–	–
2	$^2\Pi$	2.36	271.3	2.79	1.94	0.08	2.40	54% [24420234] + 15% [24421134]
3	$^4\Pi$	2.36	238.5	1.16	1.32	0.69	2.46	36% [24421134] + 27% [24421233]
4	$^4\Delta$	2.38	206.1	2.42	1.31	0.71	2.56	74% [24421143]
5	$^4\Sigma^-$	2.36	266.0	4.69	1.31	0.71	2.33	45% [24421224] + 16% [24422124]
6	$^4\Phi$	2.39	229.8	1.39	1.19	0.83	2.35	53% [24421233] + 17% [24422133]
7	$^2\Sigma^-$	2.38	214.2	0.31	1.02	1.00	1.95	42% [24421224] + 15% [24422124]
8	$^2\Phi$	2.41	214.1	1.08	0.94	1.08	1.89	49% [24421233] + 17% [24422133] + 11% [14422233] + 10% [24412233]

[a] Dipole moments (μ) and main configuration weights (MCW) correspond to r = 2.40 Å. The occupations of the orbitals $\sigma\pi\delta\sigma\sigma\sigma\pi\delta$ are given in brackets. Weights larger than one-tenth are reported.

[b] MRCI[(21)E,(12)O]. [c] MRCI[(30+21)E,(15+12)O]

[d] From refs. 110 and 111. For the ground state term $X^2\Delta_{5/2}$ experimental values along with errors are: $r_0 = 2.351(1)$ Å, $\omega_e = 259.4 \pm 0.4$ cm^{-1}, $\omega_e x_e = 0.72 \pm 0.03$ cm^{-1}, and $D_0 = 2.52 \pm 0.17$ eV.

[e] $D_0^0 = 2.60 \pm 0.22$ eV from ref. 98. No electronic term was mentioned/assigned in this work. It is presumed that the reported value corresponds to the electronic ground state term calculated in the present work.

Table B.35: ΛS and Ω ground state terms of the ACu (A = Sc-Ni) diatomic molecules obtained at the approximate and exact 2-component levels of theory

ACu	ground state term			details of the 2-c calculations		
	$^{2S+1}\Lambda^a$	$^{2S+1}\Lambda_\Omega{}^b$	Ω^c	AC-DHF	KRCI	considered Ω values
ScCu	$^3\Delta$	$^3\Delta_1$	1	2(1in1,1in5)	SD10E(4in7)SD20KPs	0,1,2,3
TiCu	$^4\Phi$	$^4\Phi_{3/2}$	3/2	1(3in13)	SD10E(5in7)SD14KPs	1/2,3/2,5/2,7/2,9/2
VCu	$^5\Delta$	$^5\Delta_0$	0	1(4in6)	SD10E(6in7)SD12KPs	0,1,2,3,4
CrCu	$^6\Sigma^+$	$^6\Sigma^+_{5/2}$	-	-	-	-
MnCu	$^7\Sigma^+$	$^7\Sigma^+_3$	-	-	-	-
FeCu	$^6\Delta$	$^6\Delta_{9/2}$	9/2	1(9in7)	SD10E(9in7)SD13KPs	1/2,3/2,5/2,7/2,9/2
CoCu	$^3\Phi$	$^3\Phi_4$	4	1(20in15)	SD10E(10in7)SD28KPs	1,2,3,4,5
NiCu	$^2\Delta$	$^2\Delta_{5/2}$	5/2	1(21in12)	SD10E(11in7)SD28KPs	1/2,3/2,5/2,7/2

[a] With the Douglas-Kroll-Hess Hamiltonian method at the multireference configuration interaction level including Davidson corrections, DKH-MRCI(+Q)

[b] At the DKH-MRCI(+Q) level with perturbative treatment of spin-orbit coupling

[c] With the exact 2-component Hamiltonian at the Kramers-restricted configuration interaction level

Table B.36: Ground state terms of the d-block systems M, M^+, MB (B = Cu/Ag/Au), and MH.

	Atom		Molecule			Atom		Molecule	
	M^a	$M^{+\ a,b}$	MB^e	$M\mathrm{H}^c$		M	M^+	MB	$M\mathrm{H}$
Sc	${}^2\mathrm{D}_{3/2}$	${}^3\mathrm{D}_1$	$X^3\Delta_1$	$X^1\Sigma^+$	Mn	${}^6\mathrm{S}_{5/2}$	${}^7\mathrm{S}_3$	$X^7\Sigma_3^+$	$X^7\Sigma^+$
Ti	${}^3\mathrm{F}_2$	${}^4\mathrm{F}_{3/2}$	$X^4\Phi_{3/2}$	$X^4\Phi$	Fe	${}^5\mathrm{D}_4$	${}^6\mathrm{D}_{9/2}$	$X^6\Delta_{9/2}$	$X^4\Delta_{7/2}$
V	${}^4\mathrm{F}_{3/2}$	${}^5\mathrm{D}_0$	$X^5\Delta_0$	$X^5\Delta_{0+}$	Co	${}^4\mathrm{F}_{9/2}$	${}^3\mathrm{F}_4$	$X^3\Phi_4{}^d$	$X^3\Phi_4$
Cr	${}^7\mathrm{S}_3$	${}^6\mathrm{S}_{5/2}$	$X^6\Sigma_{5/2}^+$	$X^6\Sigma^+$	Ni	${}^3\mathrm{F}_4$	${}^2\mathrm{D}_{5/2}$	$X^2\Delta_{5/2}$	$X^2\Delta_{5/2}$
				Pertinent species					
Y	${}^2\mathrm{D}_{3/2}$	${}^1\mathrm{S}$	$X^1\Sigma^+$	$X^1\Sigma^+$	Tc	${}^6\mathrm{S}_{5/2}$	${}^7\mathrm{S}_3$	${}^7\Sigma_3^+$	$X^7\Sigma^+$
Zr	${}^3\mathrm{F}_2$	${}^4\mathrm{F}_{3/2}$	${}^4\Phi_{3/2}$	$X^2\Delta_{3/2}$	Ru	${}^5\mathrm{F}_5$	${}^4\mathrm{F}_{9/2}$	${}^4\Phi_{9/2}$	$X^4\Sigma^-$
Nb	${}^6\mathrm{D}_{1/2}$	${}^5\mathrm{D}_0$	${}^5\Delta_0$	$X^5\Delta$	Rh	${}^4\mathrm{F}_{9/2}$	${}^3\mathrm{F}_4$	${}^3\Phi_4$	$X^3\Delta_3$
Mo	${}^7\mathrm{S}_3$	${}^6\mathrm{S}_{5/2}$	$X^6\Sigma_{5/2}^+$	$X^6\Sigma^+$	Pd	${}^1\mathrm{S}$	${}^2\mathrm{D}_{5/2}$	${}^2\Delta_{5/2}$	$X\Omega = 1/2$
La	${}^2\mathrm{D}_{3/2}$	${}^3\mathrm{F}_2$	${}^3\Phi_2$	$X^1\Sigma^+$	Re	${}^6\mathrm{S}_{5/2}$	${}^7\mathrm{S}_3$	${}^7\Sigma_3^+$	$X^7\Sigma^+$
Hf	${}^3\mathrm{F}_2$	${}^2\mathrm{D}_{3/2}$	${}^2\Delta_{3/2}$	$X^2\Delta_{3/2}$	Os	${}^5\mathrm{D}_4$	${}^6\mathrm{D}_{9/2}$	${}^6\Delta_{9/2}$	$X^4\Pi$
Ta	${}^4\mathrm{F}_{3/2}$	${}^5\mathrm{F}_1$	${}^5\Phi_1$	$X\Omega = 0^+$	Ir	${}^4\mathrm{F}_{9/2}$	${}^5\mathrm{F}_5$	${}^5\Phi_5$	$X\Omega = 0^+$
W	${}^5\mathrm{D}_0$	${}^6\mathrm{D}_{1/2}$	${}^6\Delta_{1/2}$	$X^6\Sigma^+$	Pt	${}^3\mathrm{D}_3$	${}^2\mathrm{D}_{5/2}$	$X^2\Delta_{5/2}$	$X^2\Delta_{5/2}$
Ac	${}^2\mathrm{D}_{3/2}$	${}^1\mathrm{S}$	${}^1\Sigma^+$	$X^1\Sigma^+$	Rf	${}^3\mathrm{F}_2$	${}^2\mathrm{D}_{3/2}$	${}^2\Delta_{3/2}$	-
Db	${}^4\mathrm{F}_{3/2}$	${}^3\mathrm{F}_2$	${}^3\Phi_2$	-	Sg	${}^??_0$	${}^4\mathrm{F}_{3/2}$	${}^4\Phi_{3/2}$	-
Bh	${}^??_{5/2}$	${}^??_0$	${}^??_0$	-	Hs	${}^??_4$	${}^??_{5/2}$	${}^??_{5/2}$	-

[a] From ref. 118. [b] Mapping between the M^+ cations and the diatomic molecules MB is indicated by dotted lines. [c] The ground state terms of hydrides are taken from refs. 130(ScH), 131(TiH), 132(VH), 133(CrH), 134(MnH), 135(FeH), 136(CoH), 137(NiH), 169(YH), 170(MoH), 171(WH), 172(RuH), 173(PtH), 138(LaH), 139(AcH), 140(ZrH), 141(HfH), 142(NbH), 143(TaH), 144(TcH), 145(ReH), 146(OsH), 147(RhH), 148(IrH), and 149(PdH). [d] CoAu has a $X^5\Phi$ ground state. [e] Experimental terms: $X^6\Sigma$(ref. 103) or $X^8\Sigma$(ref. 104) or $X^4\Sigma$(ref. 105) for CrCu, $X^6\Sigma$ for CrAg and CrAu(ref. 105), $X^2\Delta_{5/2}$ for NiCu(ref. 106), $X^2\Delta$ for NiAg(ref. 112), $X^2\Delta_{5/2}$ for NiAu(ref. 111), $X^1\Sigma^+$ for YCu(refs. 150,151), $X^6\Sigma$ for MoCu, MoAg, MoAu, WCu, WAg, and WAu(ref. 152), $X^4\Delta$ (theoretical) for RuCu(ref. 174), $X^2\Delta_{5/2}$ for PtCu(ref. 111), X5/2 (theoretical) for PtAg(ref. 153), $X^2\Delta_{5/2}$ for PtAu(ref. 154).

Table B.37: Distribution of the low-lying electronic states[a] of the triatomic molecules AB_2, A = Sc-Ni and B = Cu/Ag/Au, among the spin-space symmetries. Spin symmetries S $= 0, 0.5, \ldots, 4$ and point groups $C_1, C_s, C_{2v}, D_{2h}, C_{\infty v}$ and $D_{\infty h}$ have been executed.

PG	irrep	ScB_2		TiB_2				VB_2				CrB_2				MnB_2			FeB_2			CoB_2			NiB_2		
		$\frac{1}{2}$	$\frac{3}{2}$	0	1	2	3	$\frac{1}{2}$	$\frac{3}{2}$	$\frac{5}{2}$	$\frac{7}{2}$	1	2	3	4	$\frac{3}{2}$	$\frac{5}{2}$	$\frac{7}{2}$	1	2	3	$\frac{1}{2}$	$\frac{3}{2}$	$\frac{5}{2}$	0	1	2
C_1	A	10	5	7	21	21	7	7	19	17	5	5	11	7	1	6	12	6	12	24	12	7	14	7	7	14	7
C_s	A'	6	3	3	9	9	3	3	9	9	3	3	7	5	1	4	8	4	6	12	6	3	6	3	3	6	3
	A''	4	2	4	12	12	4	4	10	8	2	2	4	2	0	2	4	2	6	12	6	4	8	4	4	8	4
C_{2v}	A_1	3	1	2	5	5	2	2	4	5	1	1	3	2	0	1	4	1	3	6	3	2	3	2	2	3	2
	B_1	2	1	2	6	6	2	2	5	4	1	1	2	1	0	1	2	1	3	6	3	2	4	2	2	4	2
	B_2	3	2	1	4	4	1	1	5	4	2	2	4	3	1	3	4	3	3	6	3	1	3	1	1	3	1
	A_2	2	1	2	6	6	2	2	5	4	1	1	2	1	0	1	2	1	3	6	3	2	4	2	2	4	2
D_{2h}	A_g	2	0	0	1	1	0	0	1	2	0	0	2	1	0	0	3	0	0	3	0	0	1	0	0	1	0
	B_{3u}	1	1	2	4	4	2	2	3	3	1	1	1	1	0	1	1	1	3	3	3	2	2	2	2	2	2
	B_{2u}	1	1	2	4	4	2	2	3	3	1	1	1	1	0	1	1	1	3	3	3	2	2	2	2	2	2
	B_{1g}	1	0	0	2	2	0	0	2	1	0	0	1	0	0	0	1	0	0	3	0	0	2	0	0	2	0
	B_{1u}	2	2	1	2	2	1	1	3	3	2	2	3	3	1	3	3	3	3	3	3	1	1	1	1	1	1
	B_{2g}	1	0	0	2	2	0	0	2	1	0	0	1	0	0	0	1	0	0	3	0	0	2	0	0	2	0
	B_{3g}	1	0	0	2	2	0	0	2	1	0	0	1	0	0	0	1	0	0	3	0	0	2	0	0	2	0
	A_u	1	1	2	4	4	2	2	3	3	1	1	1	1	0	1	1	1	3	3	3	2	2	2	2	2	2
$C_{\infty v}$	Σ^+	2	1	0	0	0	0	0	1	2	1	1	3	3	1	2	4	2	1	2	1	0	0	0	0	0	0
	Σ^-	0	0	1	3	3	1	1	2	1	0	0	0	0	0	0	0	0	1	2	1	1	2	1	1	2	1
	Π	2	1	1	3	3	1	1	3	3	1	1	2	1	0	1	2	1	2	4	2	1	2	1	1	2	1
	Δ	2	1	1	3	3	1	1	3	3	1	1	2	1	0	1	2	1	2	4	2	1	2	1	1	2	1
	Φ	0	0	1	3	3	1	1	2	1	0	0	0	0	0	0	0	0	1	2	1	1	2	1	1	2	1
$D_{\infty h}$	Σ_g^+	1	0	0	0	0	0	0	0	1	0	0	1	1	0	0	2	0	0	1	0	0	0	0	0	0	0
	Σ_u^+	1	1	0	0	0	0	0	1	1	1	1	2	2	1	2	2	2	1	1	1	0	0	0	0	0	0
	Σ_g^-	0	0	0	1	1	0	0	1	0	0	0	0	0	0	0	0	0	0	1	0	0	1	0	0	1	0
	Σ_u^-	0	0	1	2	2	1	1	1	1	0	0	0	0	0	0	0	0	1	1	1	1	1	1	1	1	1
	Π_g	1	0	0	1	1	0	0	1	1	0	0	1	0	0	0	1	0	0	2	0	0	1	0	0	1	0
	Π_u	1	1	1	2	2	1	1	2	2	1	1	1	1	0	1	1	1	2	2	2	1	1	1	1	1	1
	Δ_g	1	0	0	1	1	0	0	1	1	0	0	1	0	0	0	1	0	0	2	0	0	1	0	0	1	0
	Δ_u	1	1	1	2	2	1	1	2	2	1	1	1	1	0	1	1	1	2	2	2	1	1	1	1	1	1
	Φ_g	0	0	0	1	1	0	0	1	0	0	0	0	0	0	0	0	0	0	1	0	0	1	0	0	1	0
	Φ_u	0	0	1	2	2	1	1	1	1	0	0	0	0	0	0	0	0	1	1	1	1	1	1	1	1	1

[a] The combinations $A(^{2S+1}L) + 2B(^2S)$ have been considered where $A(^{2S+1}L)$ is Sc(^{2}D), Ti(^{3}F), Ti(^{5}F), V(^{4}F), V(^{6}D), Cr(^{7}S), Cr(^{5}D), Mn(^{6}S), Mn(^{6}D), Fe(^{5}D), Fe(^{5}F), Co(a^{4}F), and Ni(^{3}F).

Table B.38: Significant points—separated atom limits $A + 2B$, asymptotes $AB + B$, asymptotes $A + B_2$, and the triatomic molecules AB_2, A = Sc-Ni and B = Cu/Ag/Au—on the potential energy hyper-surfaces obtained at the DKH-MRCI(+Q) level.

asymptotes		energy (eV)	level
$A(^{2\mathrm{S}+1}\mathrm{L})$	$2B(^2\mathrm{S})$	0.00	(ref. 118)
$\mathrm{ScCu}(^3\Delta)$	$\mathrm{Cu}(^2\mathrm{S})$	−1.17	MRCI
		−1.14	cMRCI
		−1.05	MRCI[a]
$\mathrm{Sc}(^2\mathrm{D})$	$\mathrm{Cu}_2(^1\Sigma_g^+)$	−1.67	MRCI
		−1.74	MCPF (ref. 162)
		−1.81	CPF (ref. 119)
		−1.84	CPF (ref. 161)
		−2.01(8)	expt. (ref. 160)
$\mathrm{ScCu}_2(\tilde{X}^2\Delta_g)$		−2.93	MRCI
$\mathrm{ScAg}(^3\Delta)$	$\mathrm{Ag}(^2\mathrm{S})$	−1.21	MRCI
		−1.11	cMRCI
		−1.16	MRCI
$\mathrm{Sc}(^2\mathrm{D})$	$\mathrm{Ag}_2(^1\Sigma_g^+)$	−1.46	MRCI
		−1.48	CPF (ref. 119)
		−1.65(3)	expt. (refs. 160,175)
$\mathrm{ScAg}_2(\tilde{X}^2\Delta_g)$		−3.27	MRCI
$\mathrm{ScAu}(^3\Delta)$	$\mathrm{Au}(^2\mathrm{S})$	−2.52	MRCI
		−2.69	cMRCI
		−2.46	MRCI
		−2.87(18)	expt. (ref. 98)
$\mathrm{Sc}(^2\mathrm{D})$	$\mathrm{Au}_2(^1\Sigma_g^+)$	−2.19	MRCI
		−2.290(8)	expt. (ref. 116)
$\mathrm{ScAu}_2(\tilde{X}^2\Delta_g)$		−5.73	MRCI
$\mathrm{TiCu}(^4\Phi)$	$\mathrm{Cu}(^2\mathrm{S})$	−1.14	MRCI
		−1.10	cMRCI
		−0.97	MRCI
$\mathrm{Ti}(^3\mathrm{F})$	$\mathrm{Cu}_2(^1\Sigma_g^+)$	−1.86	MRCI
$\mathrm{TiCu}_2(\tilde{X}^3\Gamma)$		−2.52	MRCI
$\mathrm{TiAg}(^4\Phi)$	$\mathrm{Ag}(^2\mathrm{S})$	−1.19	MRCI
		−1.04	cMRCI
		−0.96	MRCI
$\mathrm{Ti}(^3\mathrm{F})$	$\mathrm{Ag}_2(^1\Sigma_g^+)$	−1.50	MRCI
$\mathrm{TiAg}_2(\tilde{X}^3\Phi_g)$		−2.97	MRCI
$\mathrm{TiAu}(^4\Phi)$	$\mathrm{Au}(^2\mathrm{S})$	−2.41	MRCI

Continued on next page

Table B.38 – *Continued from previous page*

asymptotes		energy (eV)	level
		−2.50	cMRCI
		−2.03	MRCI
Ti(^{3}F)	Au$_2$($^1\Sigma_g^+$)	−2.52	MRCI
TiAu$_2$($\tilde{X}^3\Phi_g$)		−5.57	MRCI
VCu($^5\Delta$)	Cu(^{2}S)	−1.25	MRCI
		−1.20	cMRCI
		−1.17	MRCI
V(^{4}F)	Cu$_2$($^1\Sigma_g^+$)	−1.57	MRCI
VCu$_2$($\tilde{x}^4\Lambda_g^{(-)}$)		−2.48	MRCI
VAg($^5\Delta$)	Ag(^{2}S)	−1.24	MRCI
		−1.15	cMRCI
		−1.14	MRCI
V(^{4}F)	Ag$_2$($^1\Sigma_g^+$)	−1.48	MRCI
VAg$_2$($\tilde{x}^4B_1$)		−2.74	MRCI
VAu($^5\Delta$)	Au(^{2}S)	−2.29	MRCI
		−2.33	cMRCI
		−2.37	MRCI
		−2.47(12)	expt. (ref. 100)
V(^{4}F)	Au$_2$($^1\Sigma_g^+$)	−2.24	MRCI
VAu$_2$($\tilde{X}^4\Lambda_g^{(-)}$)		−5.14	MRCI
CrCu($^6\Sigma^+$)	Cu(^{2}S)	−1.21	MRCI
		−1.11	cMRCI
		−1.20	MRCI (ref. 113)
		−0.51	MRCI
		−1.61(26)	expt. (ref. 98)
Cr(^{7}S)	Cu$_2$($^1\Sigma_g^+$)	−1.62	MRCI
CrCu$_2$($\tilde{x}^7\Sigma^+$)		−1.87	MRCI
CrAg($^6\Sigma^+$)	Ag(^{2}S)	−1.25	MRCI
		−1.08	cMRCI
		−0.46	MRCI
Cr(^{7}S)	Ag$_2$($^1\Sigma_g^+$)	−1.29	MRCI
CrAg$_2$($\tilde{x}^7\Sigma^+$)		−1.81	MRCI
CrAu($^6\Sigma^+$)	Au(^{2}S)	−2.01	MRCI
		−1.96	cMRCI
		−1.55	MRCI
		−2.17(18)	expt. (ref. 98)

Continued on next page

Table B.38 – *Continued from previous page*

asymptotes		energy (eV)	level
Cr(^{7}S)	Au$_2$($^1\Sigma_g^+$)	−2.28	MRCI
CrAu$_2$($\tilde{X}^5\Sigma_g^+$)		−4.13	MRCI
MnCu($^7\Sigma^+$)	Cu(^{2}S)	−0.70	MRCI
		−0.57	cMRCI
		−0.76	MRCI
Mn(^{6}S)	Cu$_2$($^1\Sigma_g^+$)	−1.63	MRCI
MnCu$_2$($\tilde{X}^6\Sigma_g^+$)		−2.49	MRCI
MnAg($^7\Sigma^+$)	Ag(^{2}S)	−0.87	MRCI
		−0.61	cMRCI
		−0.60	MRCI
		−0.99(22)	expt. (ref. 98)
Mn(^{6}S)	Ag$_2$($^1\Sigma_g^+$)	−1.31	MRCI
MnAg$_2$($\tilde{X}^6\Sigma_g^+$)		−2.38	MRCI
MnAu($^7\Sigma^+$)	Au(^{2}S)	−1.93	MRCI
		−2.05	cMRCI
		−2.02	MRCI
		−1.88(13)	expt. (ref. 102)
		−1.95(13)	expt. (ref. 98)
Mn(^{6}S)	Au$_2$($^1\Sigma_g^+$)	−2.25	MRCI
MnAu$_2$($\tilde{X}^6\Sigma_g^+$)		−4.83	MRCI
FeCu($^6\Delta$)	Cu(^{2}S)	−0.67	MRCI
		−0.58	cMRCI
		−0.70	MRCI
Fe(^{5}D)	Cu$_2$($^1\Sigma_g^+$)	−1.62	MRCI
FeCu$_2$($\tilde{X}^5\Delta_g$)		−2.47	MRCI
FeAg($^6\Delta$)	Ag(^{2}S)	−0.77	MRCI
		−0.59	cMRCI
		−0.93	MRCI
Fe(^{5}D)	Ag$_2$($^1\Sigma_g^+$)	−1.55	MRCI
FeAg$_2$($\tilde{X}^5\Delta_g$)		−2.75	MRCI
FeAu($^6\Delta$)	Au(^{2}S)	−1.86	MRCI
		−1.99	cMRCI
		−1.81	MRCI
		−1.95(22)	expt. (ref. 98)
Fe(^{5}D)	Au$_2$($^1\Sigma_g^+$)	−2.10	MRCI
FeAu$_2$($\tilde{X}^5\Delta_g$)		−4.68	MRCI

Continued on next page

Table B.38 – *Continued from previous page*

asymptotes		energy (eV)	level
CoCu($^3\Phi$)	Cu(^{2}S)	−1.53	MRCI
		−1.46	cMRCI
		−0.60	MRCI
		−1.69(22)	expt. (ref. 98)
Co(a^{4}F)	Cu$_2$($^1\Sigma_\mathrm{g}^+$)	−1.98	MRCI
CoCu$_2$($\tilde{X}^4\Phi_g$)		−2.61	MRCI
CoAg($^3\Phi$)	Ag(^{2}S)	−1.60	MRCI
		−1.44	cMRCI
		−1.82	MRCI
Co(a^{4}F)	Ag$_2$($^1\Sigma_\mathrm{g}^+$)	−2.77	MRCI
CoAg$_2$($\tilde{X}^4\Phi_g$)		−3.77	MRCI
CoAu($^5\Phi$)	Au(^{2}S)	−1.59	MRCI
		−1.71	cMRCI
		−1.52	MRCI
		−2.26(18)	expt. (ref. 98)
Co(a^{4}F)	Au$_2$($^1\Sigma_\mathrm{g}^+$)	−2.09	MRCI
CoAu$_2$($\tilde{X}^4\Phi_g$)		−4.29	MRCI
NiCu($^2\Delta$)	Cu(^{2}S)	−1.33	MRCI
		−1.81	MRCI-1
		−0.20	MRCI
		−2.05(10)	expt. (ref. 106)
		−2.08(22)	expt. (ref. 98)
Ni(^{3}F)	Cu$_2$($^1\Sigma_\mathrm{g}^+$)	−1.62	MRCI
NiCu$_2$($\tilde{X}^3\Lambda_g^{(-)}$)		−2.19	MRCI
NiAg($^2\Delta$)	Ag(^{2}S)	−1.68	MRCI
		−1.68	MRCI-1
		−1.51	MRCI
Ni(^{3}F)	Ag$_2$($^1\Sigma_\mathrm{g}^+$)	−2.70	MRCI
NiAg$_2$($\tilde{X}^3\Lambda_g^{(-)}$)		−3.52	MRCI
NiAu($^2\Delta$)	Au(^{2}S)	−2.02	MRCI
		−1.99	cMRCI
		−1.03	MRCI
		−2.52(17)	expt. (ref. 176)
		−2.60(22)	expt. (ref. 98)
Ni(^{3}F)	Au$_2$($^1\Sigma_\mathrm{g}^+$)	−2.08	MRCI
NiAu$_2$($\tilde{X}^3\Lambda_g^{(-)}$)		−4.16	MRCI

Continued on next page

Table B.38 – *Continued from previous page*

asymptotes	energy (eV)	level

[a] For the diatomic molecules AB two MRCI levels of theory are given: one (first) corresponding to the diatomic potential energy curves and one (second) corresponding to the triatomic potential energy surfaces, i.e., the respective asymptotes.

Table B.39: Fitting coefficients (eV) corresponding to the $E(\theta, 2.65\ \text{Å}; {}^2\{A_1 \oplus A_2\})$ potentials of $ScCu_2$

coefficients	${}^2A_1$	${}^2A_2$
a_0	3504.97	3726.92
a_2	6677.19	7087.39
a_4	5765.94	6087.23
a_6	4501.92	4709.39
a_8	3163.12	3265.36
a_{10}	1985.33	2013.36
a_{12}	1101.09	1091.24
a_{14}	531.08	511.132
a_{16}	217.539	201.697
a_{18}	72.9551	64.4592
a_{20}	18.8526	15.6334
a_{22}	3.34722	2.5508
a_{24}	0.306674	0.208975

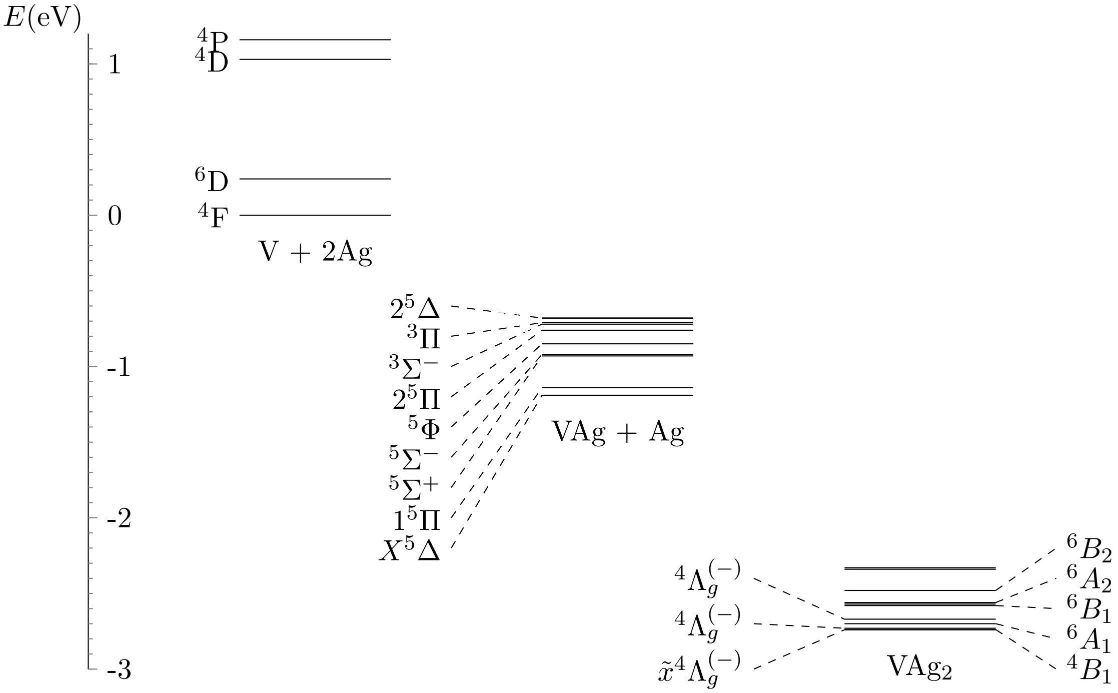

E(eV)
1
0
-1
-2
-3
^{4}P
^{4}D
^{6}D
^{4}F
V + 2Ag
$2^5\Delta$
$^3\Pi$
$^3\Sigma^-$
$2^5\Pi$
$^5\Phi$
$^5\Sigma^-$
$^5\Sigma^+$
$1^5\Pi$
$X^5\Delta$
VAg + Ag
$^4\Lambda_g^{(-)}$
$^4\Lambda_g^{(-)}$
$\tilde{x}^4\Lambda_g^{(-)}$
VAg$_2$
$^6B_2$
$^6A_2$
$^6B_1$
$^6A_1$
$^4B_1$

Figure B.1: Low-lying energy levels for V (experimental J-averaged values), VAg (theoretical), and VAg$_2$ (theoretical).

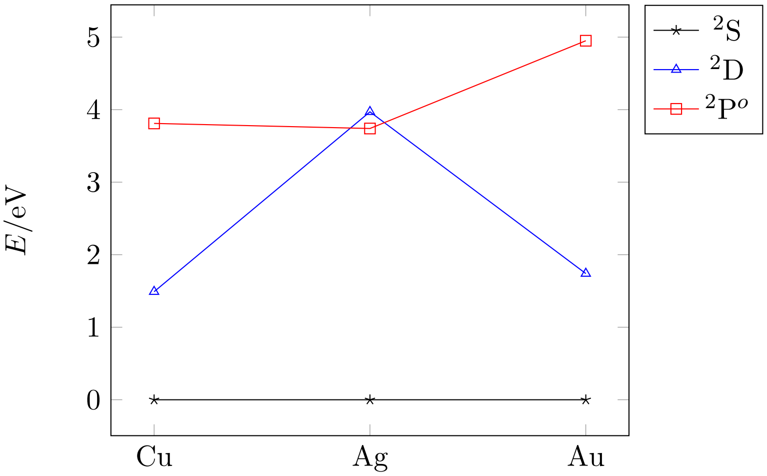

Figure B.2: The experimental energy levels for the B (Cu/Ag/Au) atoms. The source is the NIST website.

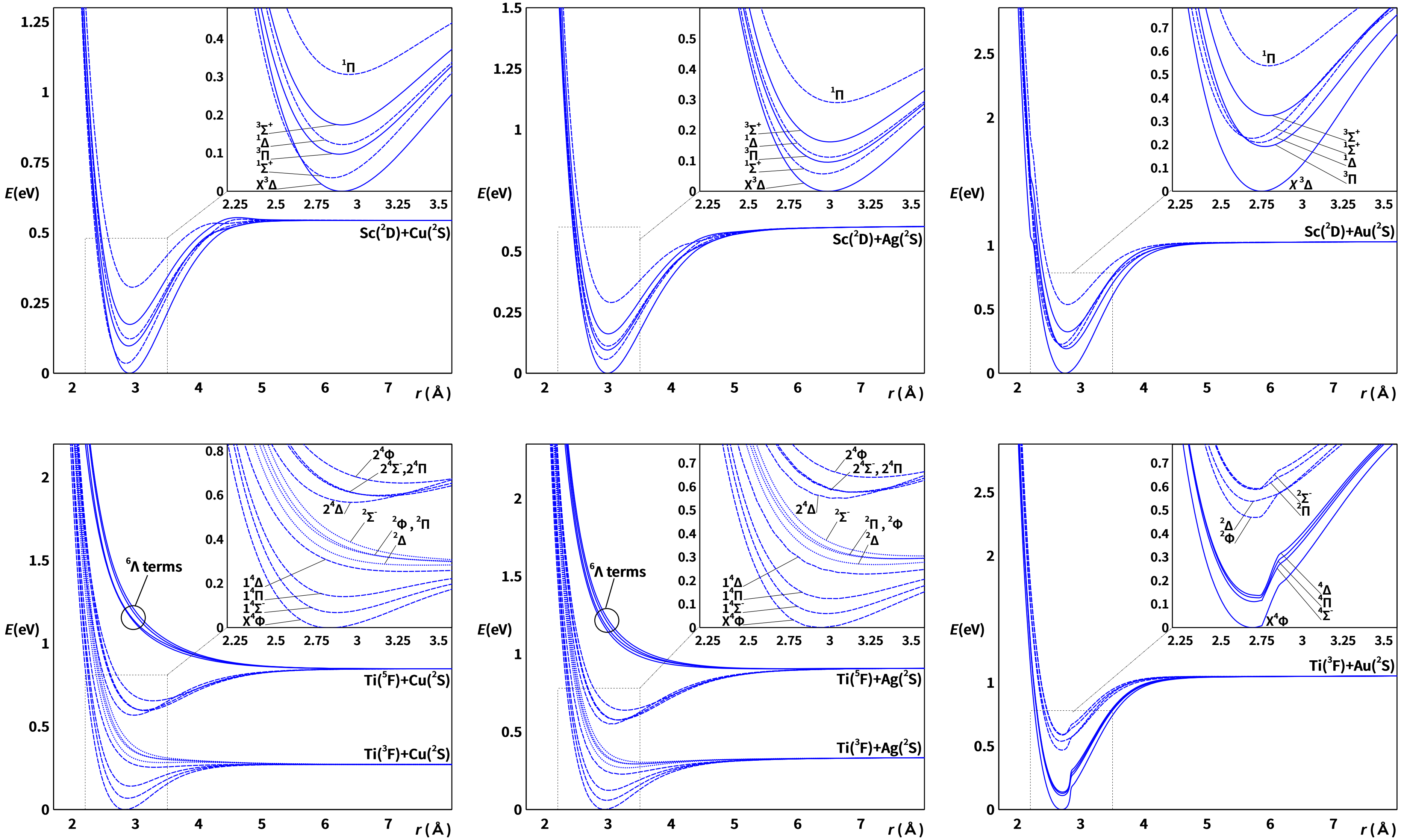

Figure B.3: Potential energy curves of the ground and low-lying excited ΛS terms of the diatomic molecules AB (A = Sc-Ni, B = Cu/Ag/Au) obtained at the DKH-CASSCF level of theory.

Continued on next page

Continued from previous page

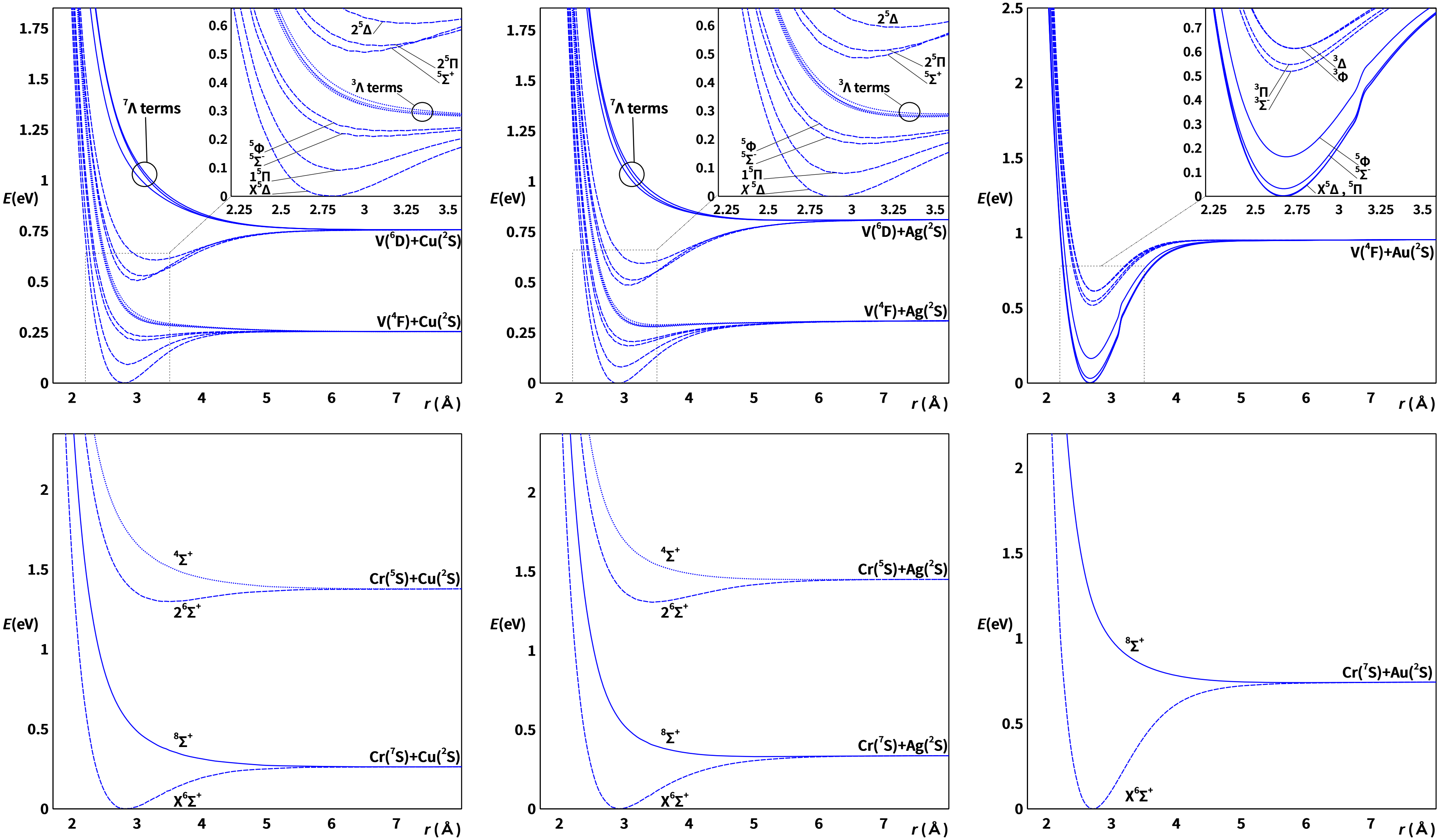

Continued on next page

Continued from previous page

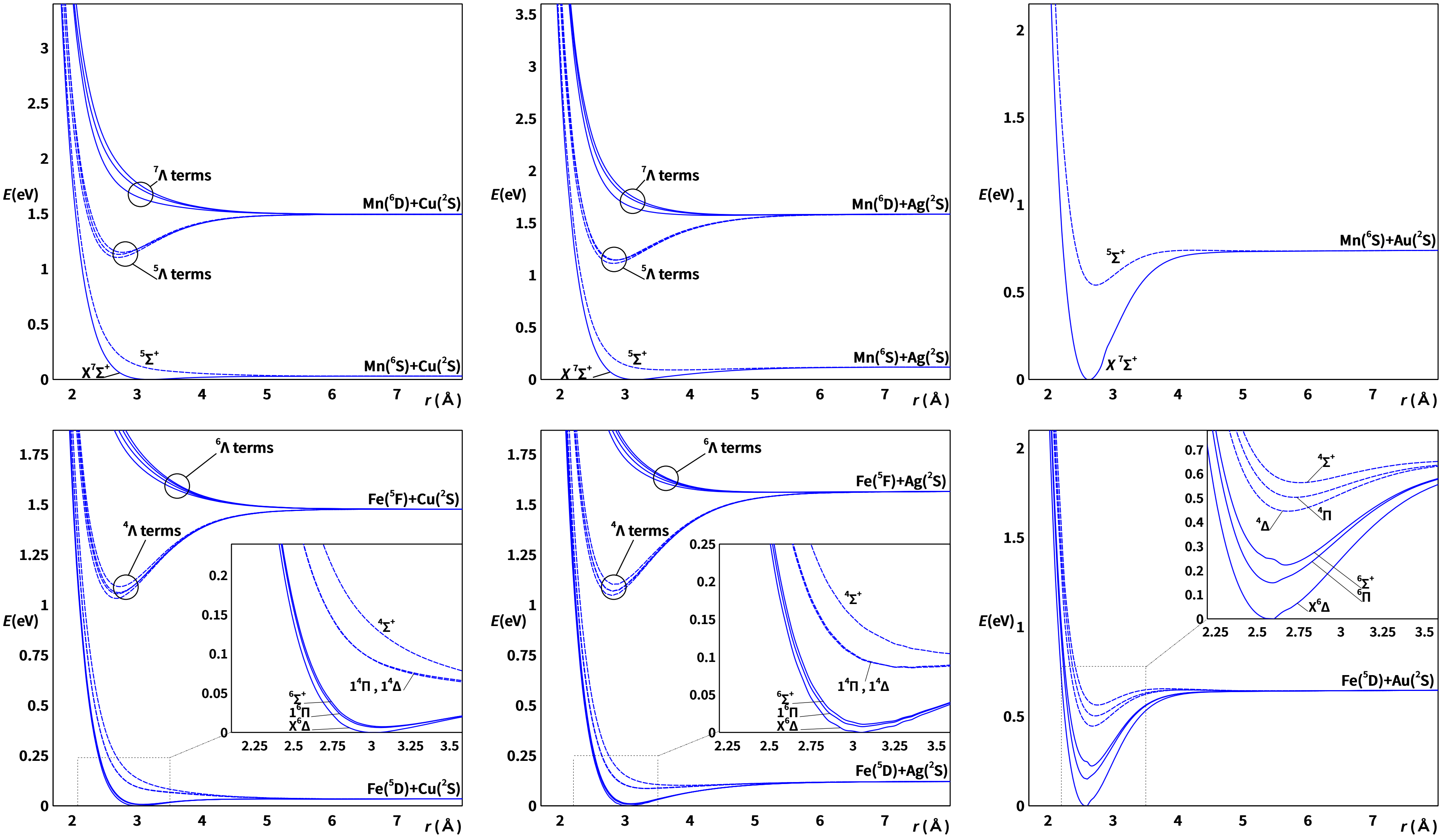

Continued on next page

Continued from previous page

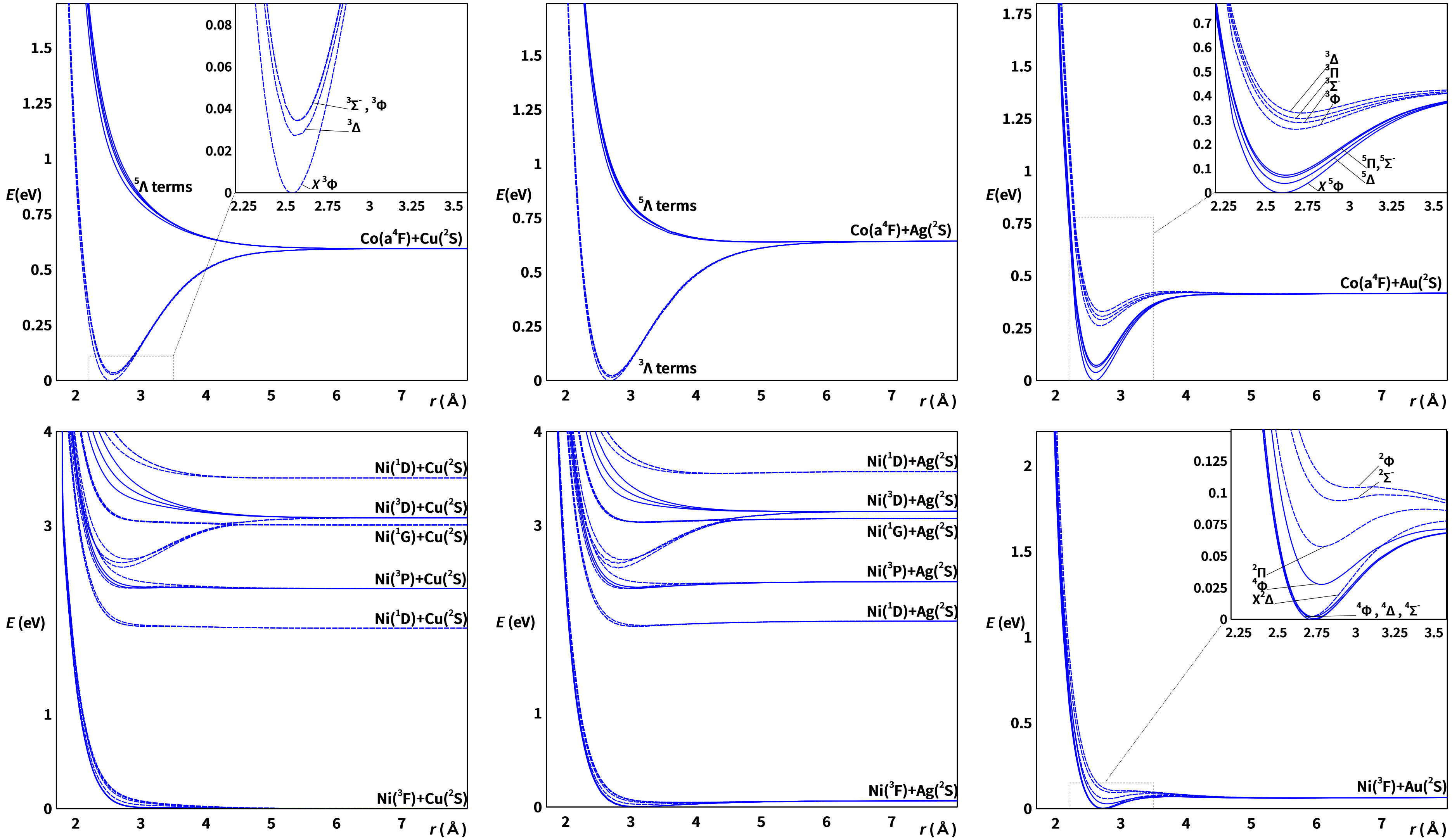

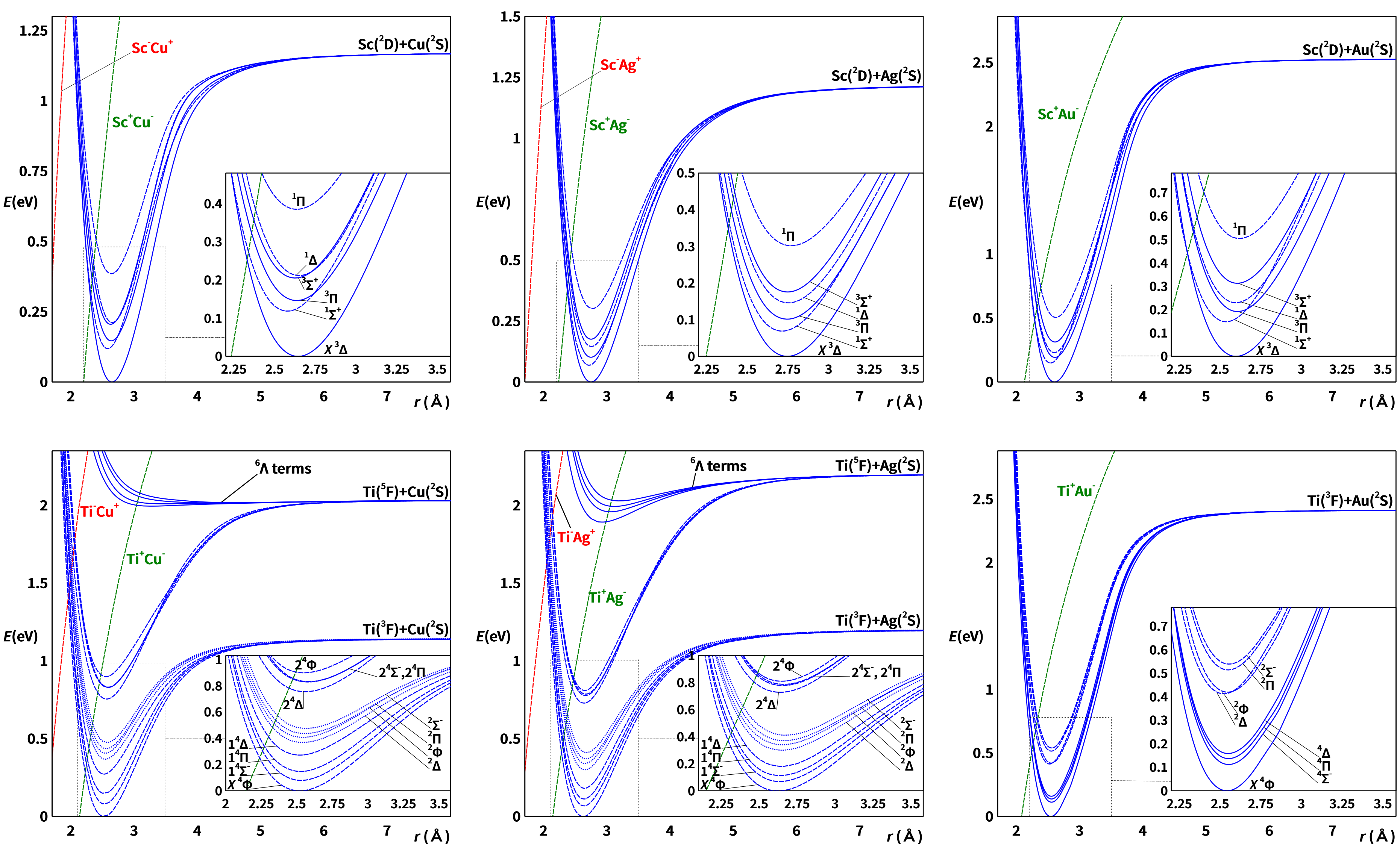

Figure B.4: Potential energy curves of the ground and low-lying excited ΛS terms of the diatomic molecules AB (A = Sc-Ni, B = Cu/Ag/Au) obtained at the DKH-MRCI(+Q) level of theory. The ion-pair curves for A^+B^- (in green) and A^-B^+ (in red) are displayed and are extrapolated from the separated ion limits $A^+ + B^-$ ($A^- + B^+$) using a $-e^2/r$ attractive potential. Since the manganese atom does not bind electrons,[82] the Mn$^-B^+$ ion-pair curves have not been plotted. Due to the high ionisation potential of the gold atom (9.23 eV),[82] the (A^- + Au$^+$) curves lie so high in energy and they are not visible in some of the plots.

Continued on next page

Continued from previous page

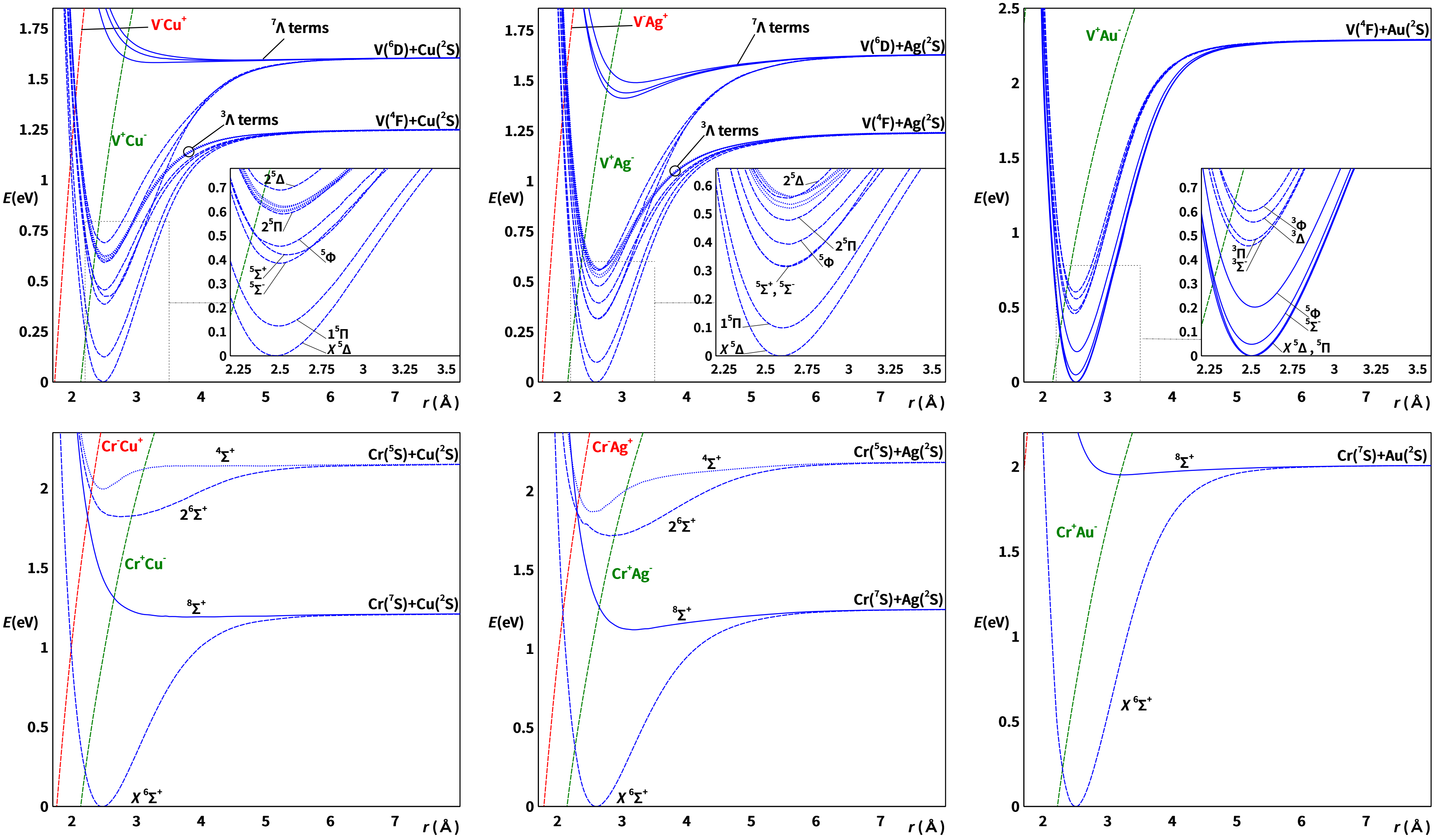

Continued on next page

Continued from previous page

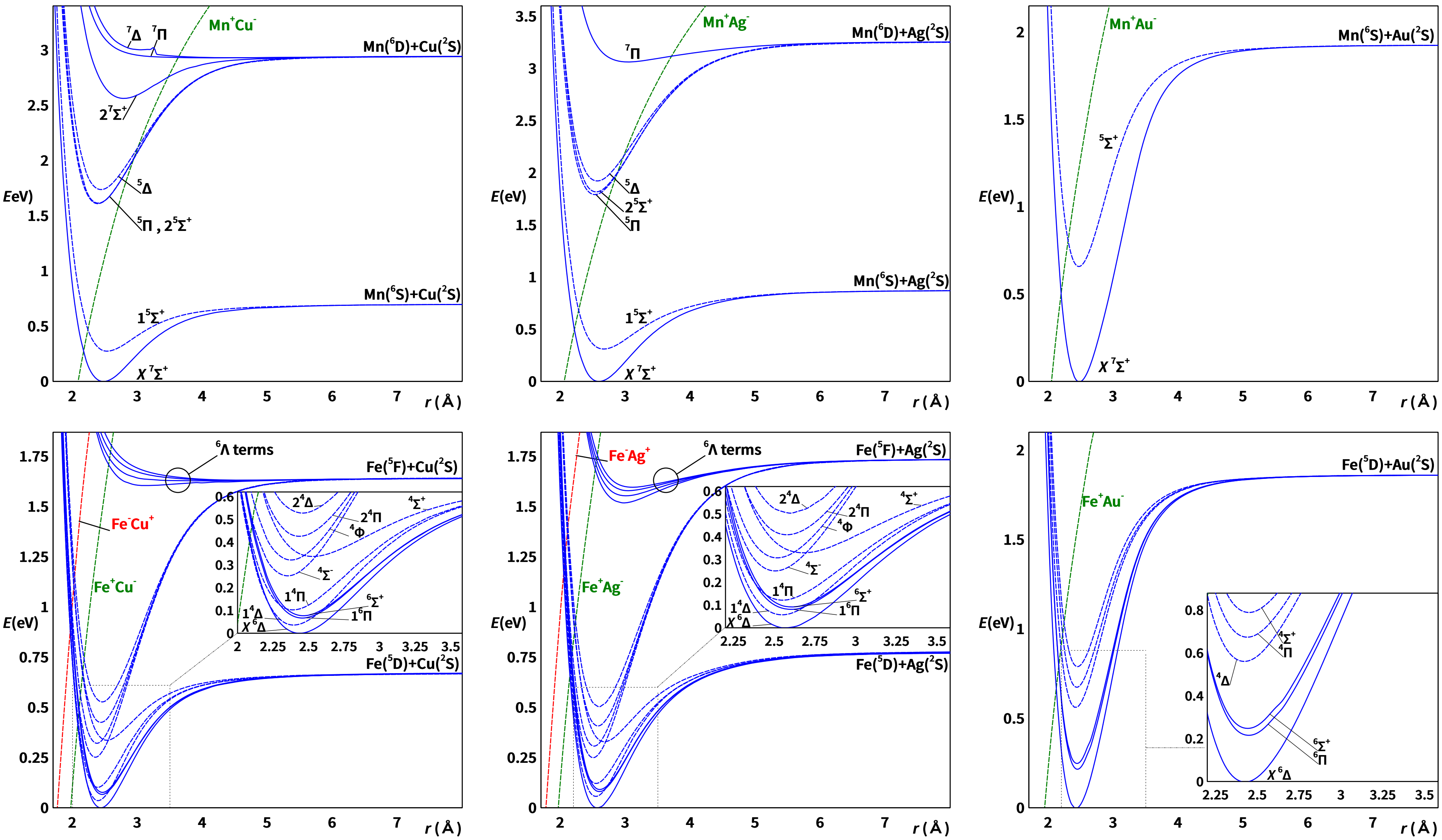

Continued on next page

Continued from previous page

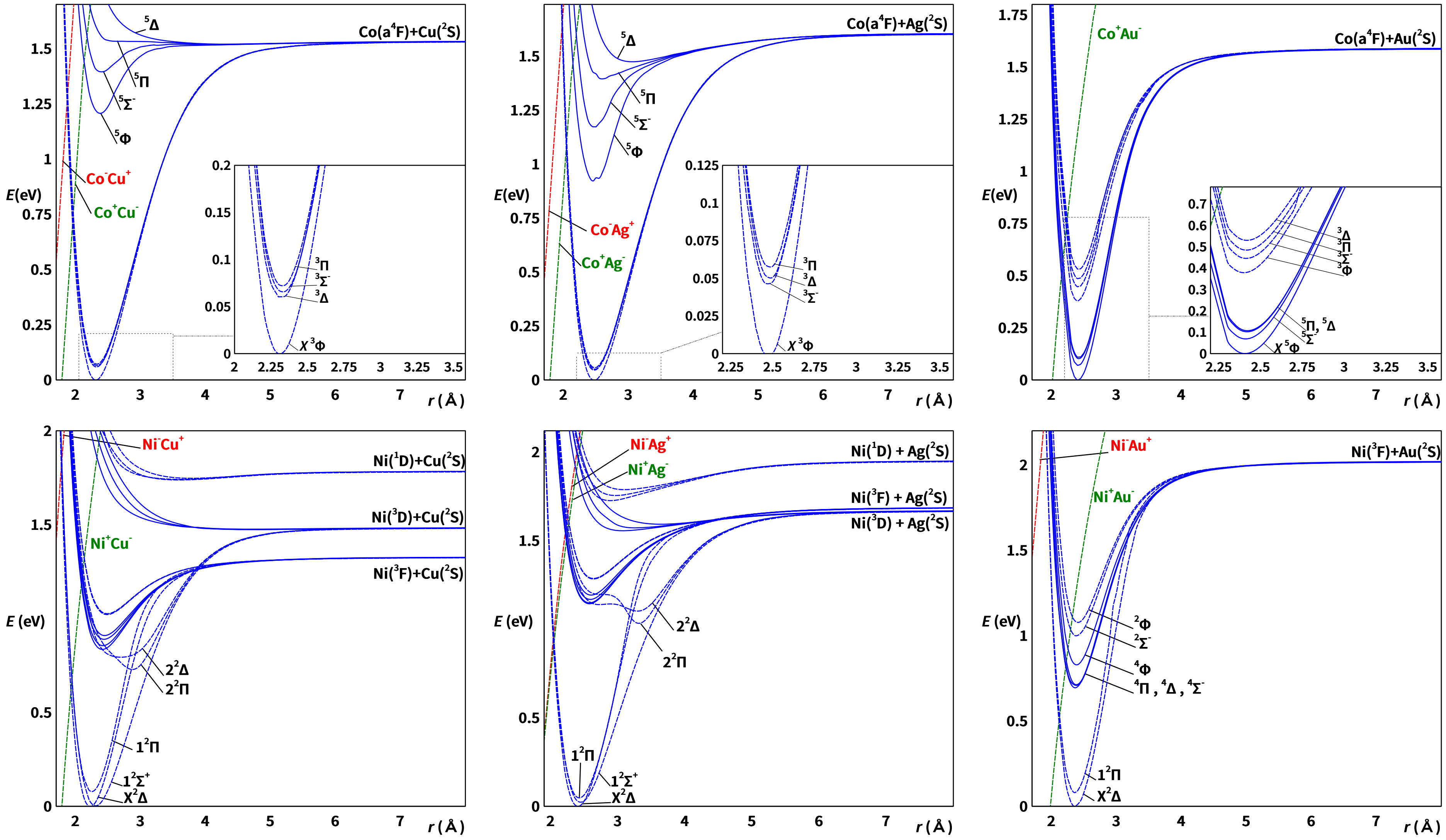

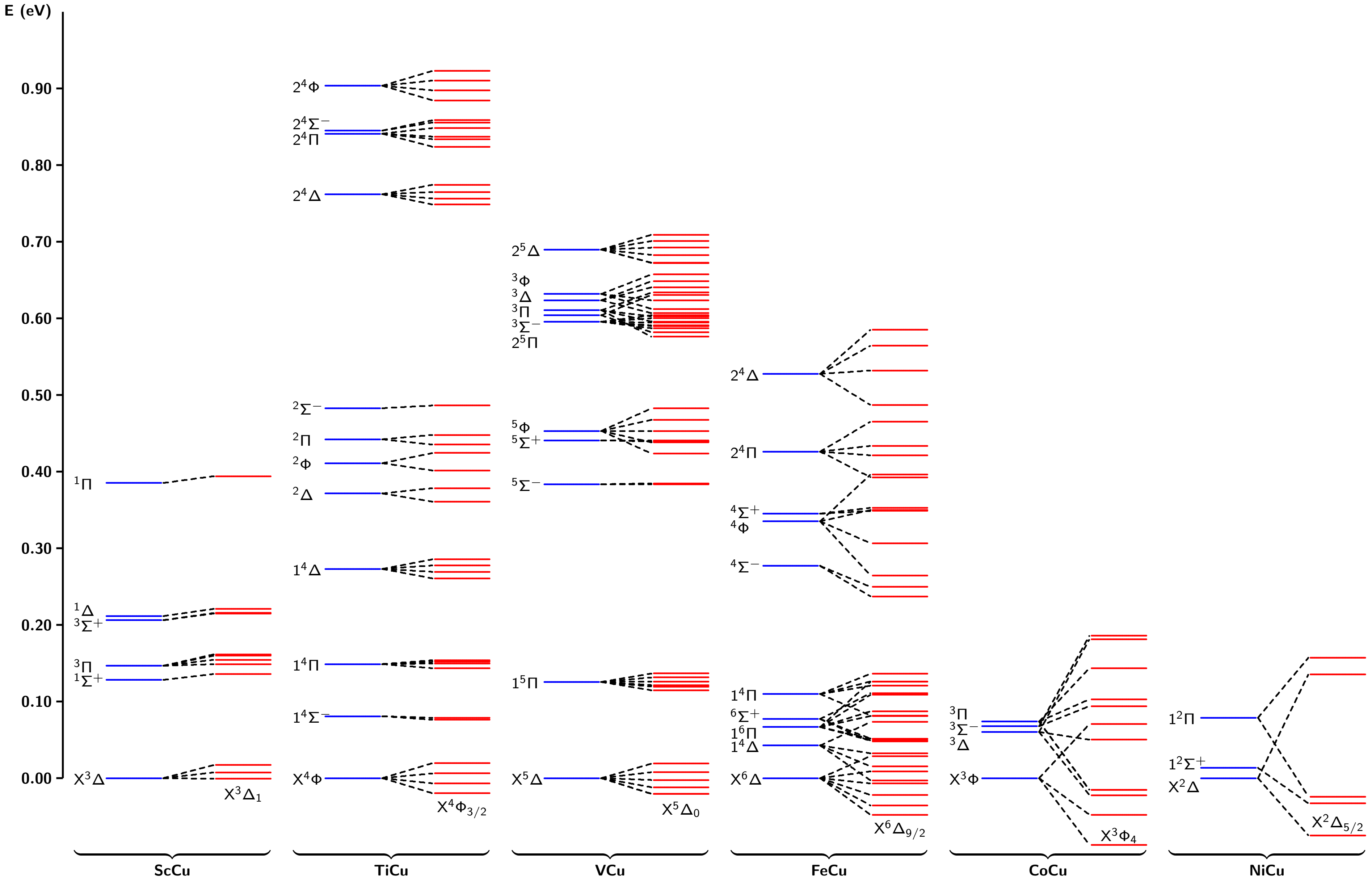

Figure B.5: The splitting from ΛS to Ω terms of the diatomic molecules *A*Cu around the respective ground state bond lengths. The energies of the ΛS ground states are chosen to be zero. For CrCu ($X^6\Sigma^+$, $^8\Sigma^+$, $2^6\Sigma^+$, $^4\Sigma^+$) and MnCu ($X^7\Sigma^+$ and $1^5\Sigma^+$) spin-orbit splittings were predicted to be negligibly *small*.

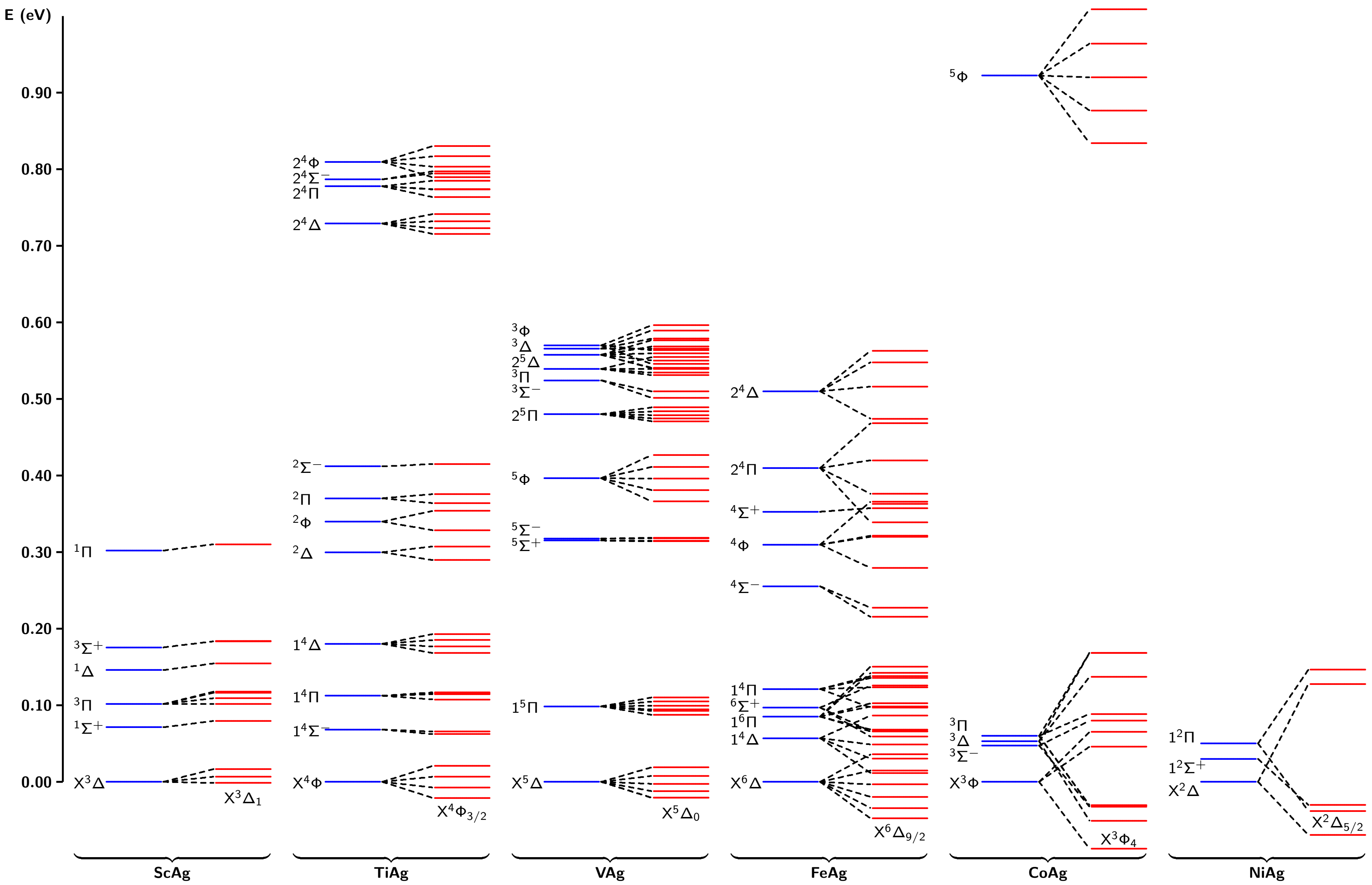

Figure B.6: The splitting from ΛS to Ω terms of the diatomic molecules AAg around the respective ground state bond lengths. The energies of the ΛS ground states are chosen to be zero. For CrAg ($X^6\Sigma^+$, $^8\Sigma^+$, $2^6\Sigma^+$, $^4\Sigma^+$) and MnAg ($X^7\Sigma^+$ and $1^5\Sigma^+$) spin-orbit splittings were obtained to be negligibly *small*.

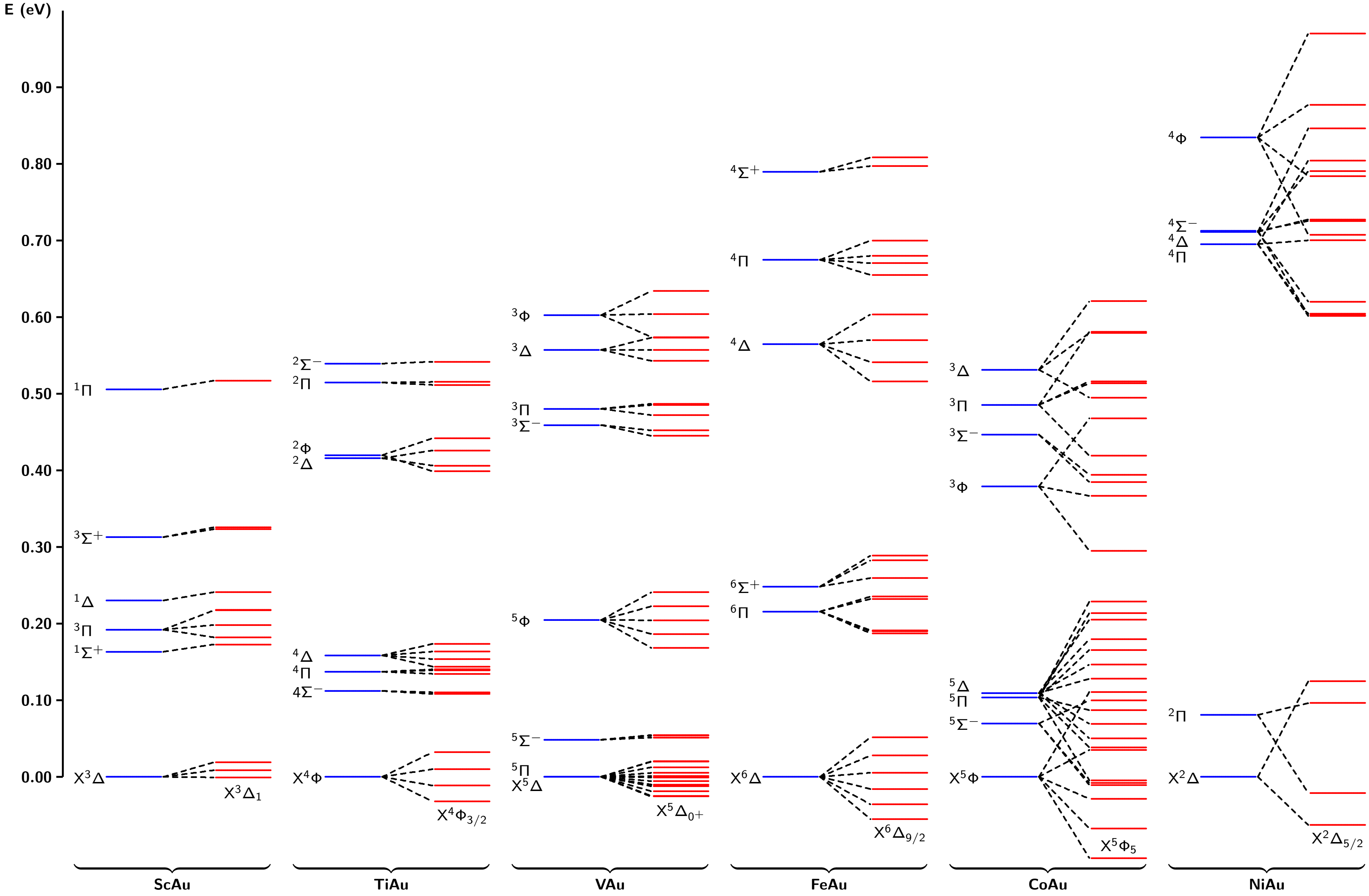

Figure B.7: The splitting from ΛS to Ω terms of the diatomic molecules *A*Au around the respective ground state bond lengths. The energies of the ΛS ground states are chosen to be zero. For CrAu ($X^6\Sigma^+$ and $^8\Sigma^+$) and MnAu ($X^7\Sigma^+$ and $1^5\Sigma^+$) spin-orbit splittings were calculated to be negligibly *small*.

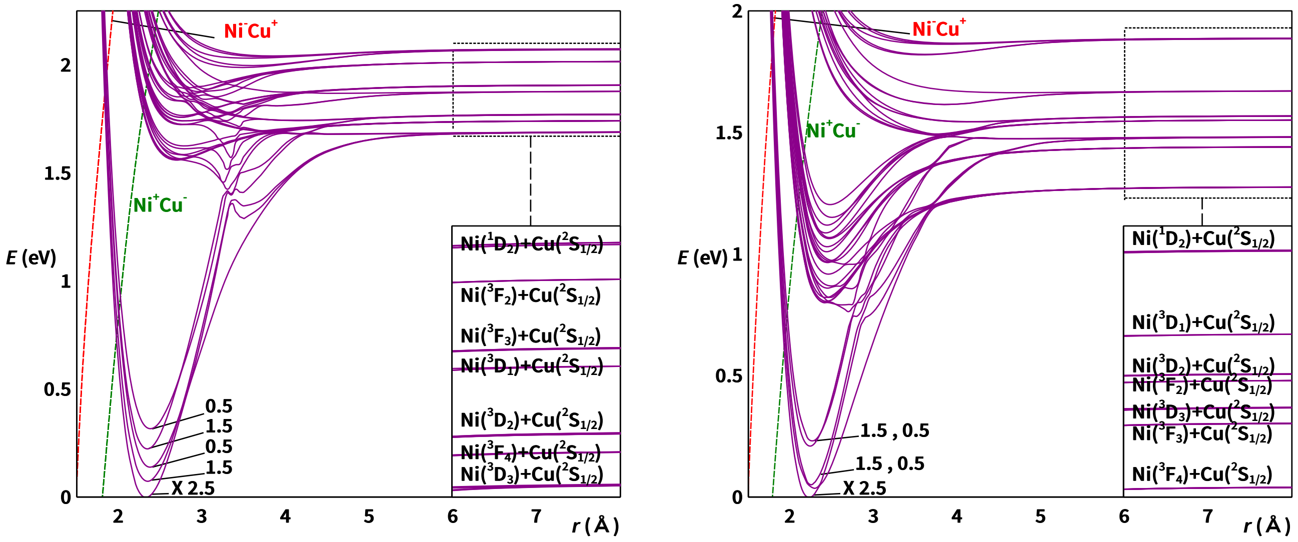

Figure B.8: Spin-orbit coupled potential energy curves of the ground and low-lying excited Ω terms of NiCu obtained at the MRCI[(11)E,(7)O] (left) and MRCI[(10+11)E,(5+7)O] (right) levels of theory.

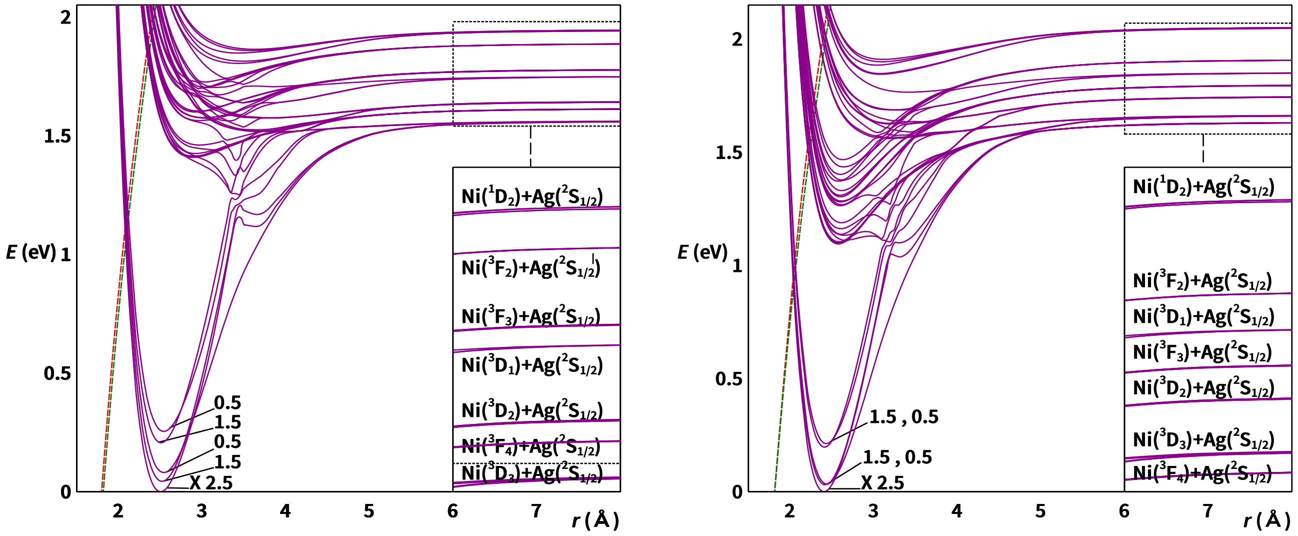

Figure B.9: Spin-orbit coupled potential energy curves of the ground and low-lying excited Ω terms of NiAg obtained at the MRCI[(11)E,(7)O] (left) and MRCI[(10+11)E,(5+7)O] (right) levels of theory.

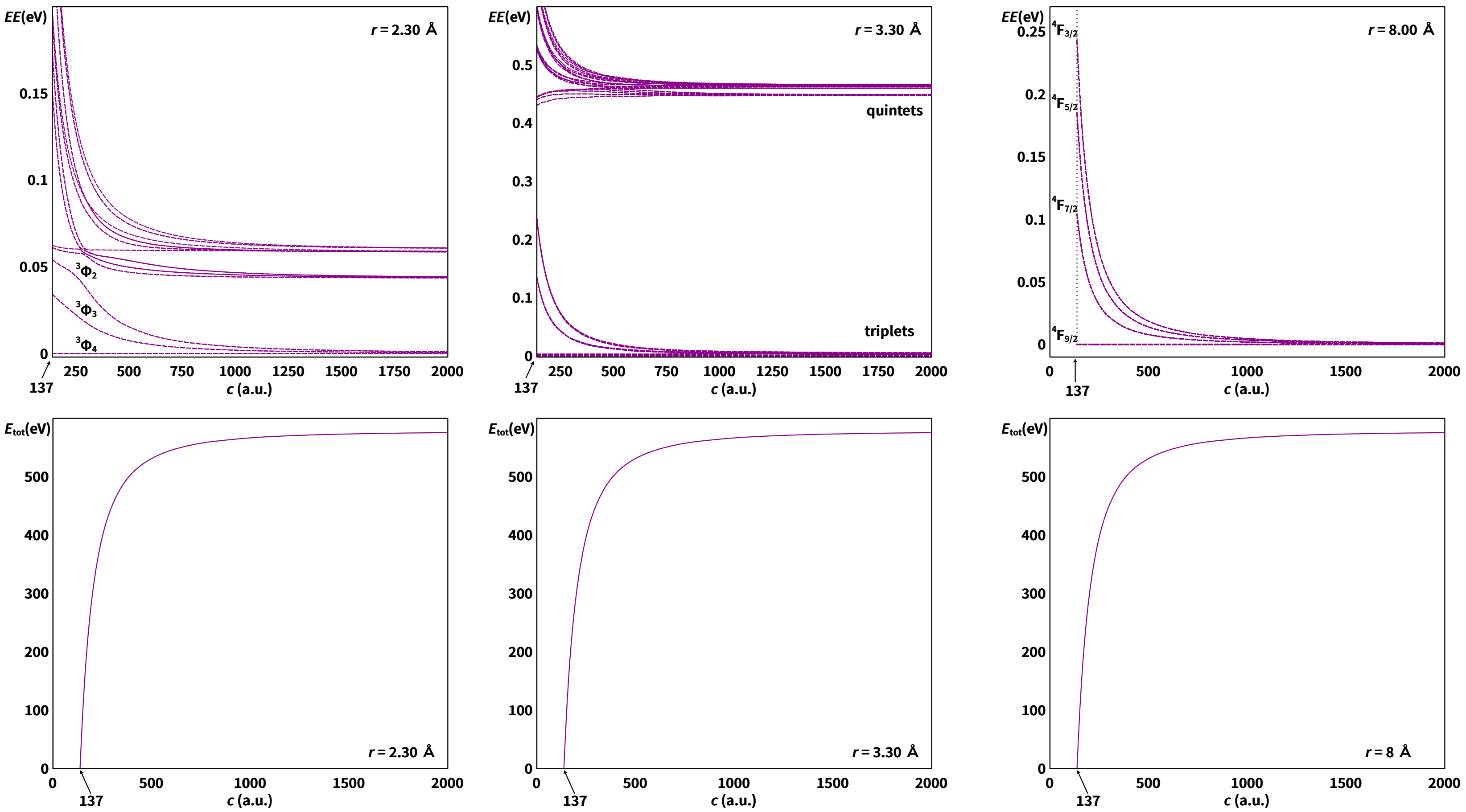

Figure B.10: Above: Vertical excitation energies (EE) of the low-lying terms of CoCu as a function of c at r = 2.30, 3.30, and 8.00 Å calculated at DKH-CASSCF. The energy of the lowest Ω term is chosen to be the zero. Below: The corresponding total energy (E_{tot}) of the lowest Ω term as a function of c. The energy at the relativistic limit ($c = 137.0359895$) is chosen to be the zero.

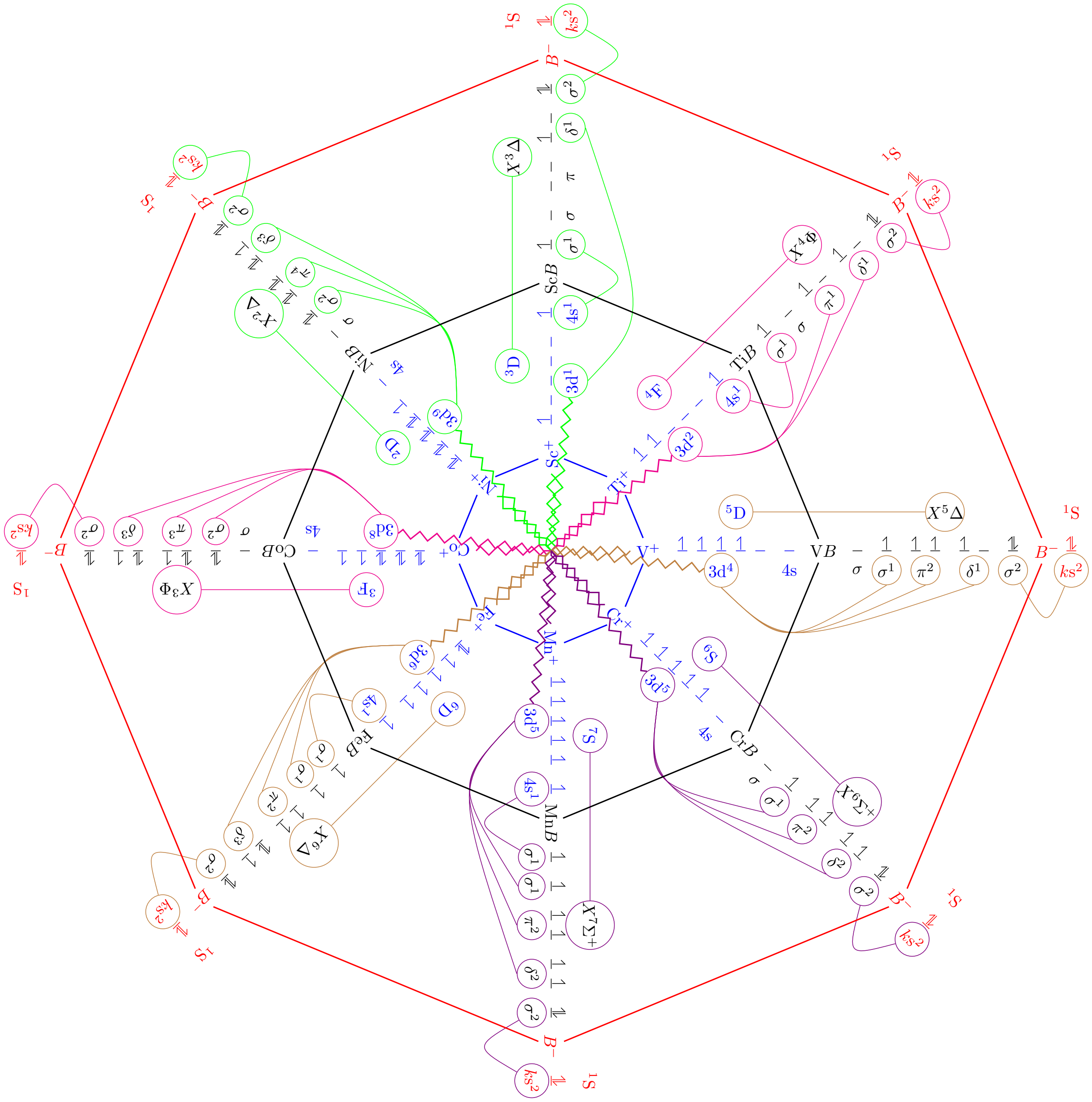
ScB
TiB
VB
CrB
MnB
FeB
CoB
NiB
Sc+
Ti+
V+
Cr+
Mn+
Fe+
Co+
Ni+
B−
1S
ks2
X3Δ
X4Φ
X5Δ
X6Σ+
X7Σ+
X6Δ
X3Φ
X2Δ
3D
4F
5D
6S
7S
6D
3F
2D
3d1
3d2
3d4
3d5
3d6
3d8
3d9
4s1
4s
σ
π
δ
σ1
σ2
π1
π2
π3
π4
δ1
δ2
δ3

Figure B.11: Octagonal representation of the ground state configurations and terms for the ion-pair $A^+ + B^-$ and the diatomic molecules AB and the binary relation observed between them.

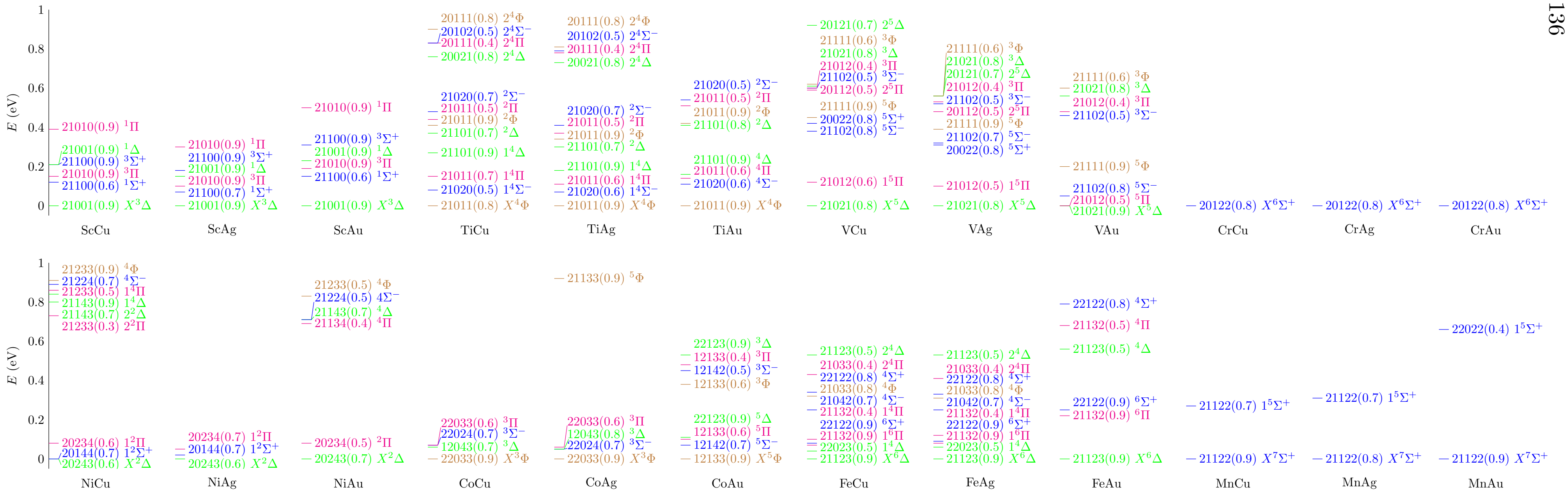

Figure B.12: Electronic configurations dominating the low-lying states of the diatomic molecules AB obtained at the DKH-MRCI(+Q) level of theory. The occupations of the active/outer-valence orbitals sσdσ^*sσ^*dπ^*dδ^* are given for the dominant configurations with weights in parenthesis.

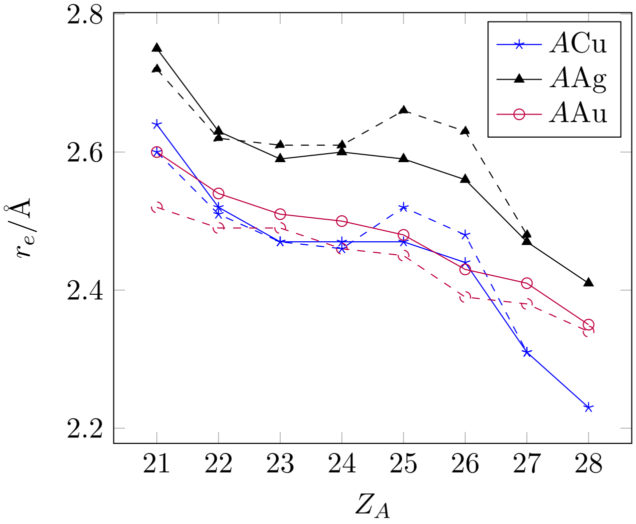

Figure B.13: Ground state bond lengths (r_e) of the diatomic molecules AB (A = Sc-Ni, B = Cu/Ag/Au), obtained at the DKH-MRCI(+Q) level of theory. Dashed lines correspond to the calculations considering outer-core correlation effects.

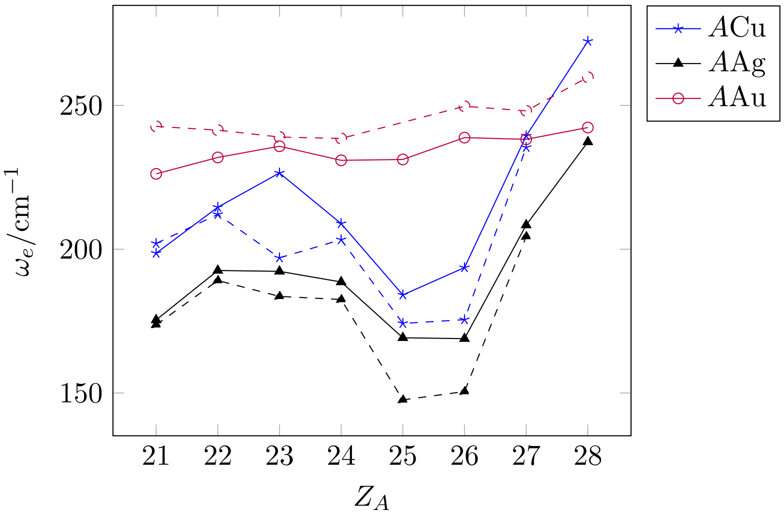

Figure B.14: Ground state harmonic frequency (ω_e) of the diatomic molecules AB (A = Sc-Ni, B = Cu/Ag/Au), obtained at the DKH-MRCI(+Q) level of theory. Dashed lines correspond to the calculations considering outer-core correlation effects.

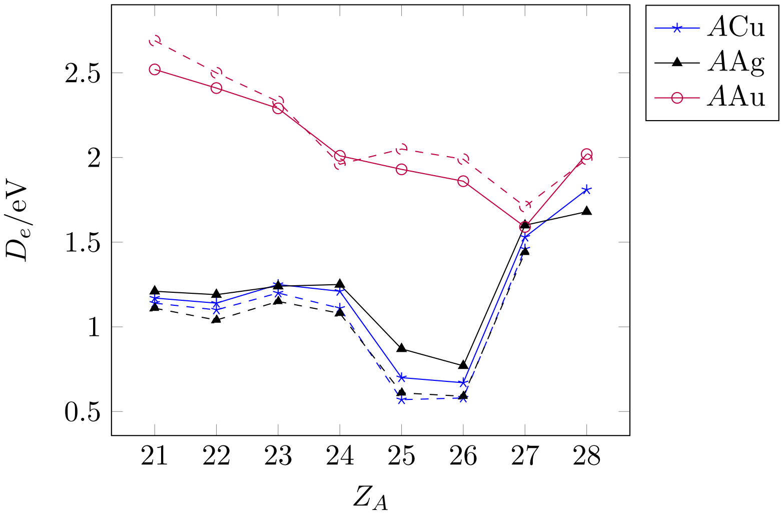

Figure B.15: Ground state dissociation energies (D_e) of the diatomic molecules AB (A = Sc-Ni, B = Cu/Ag/Au), obtained at the DKH-MRCI(+Q) level of theory. Dashed lines correspond to the calculations considering outer-core correlation effects.

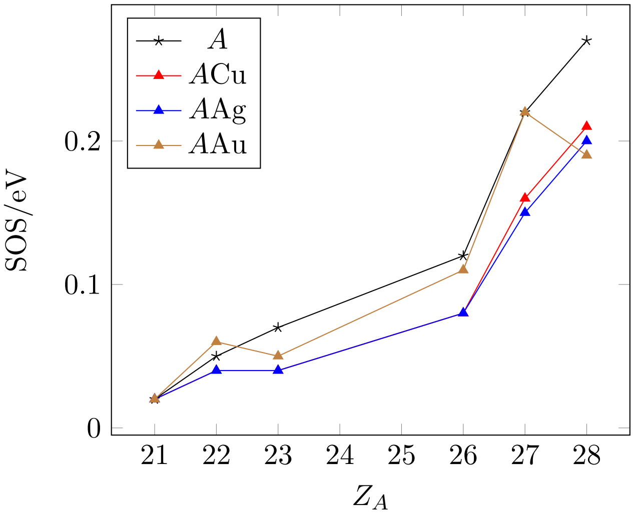

Figure B.16: Ground state spin-orbit splitting (SOS) for the atoms A and the diatomic molecules AB (A = Sc-Ni, B = Cu/Ag/Au).

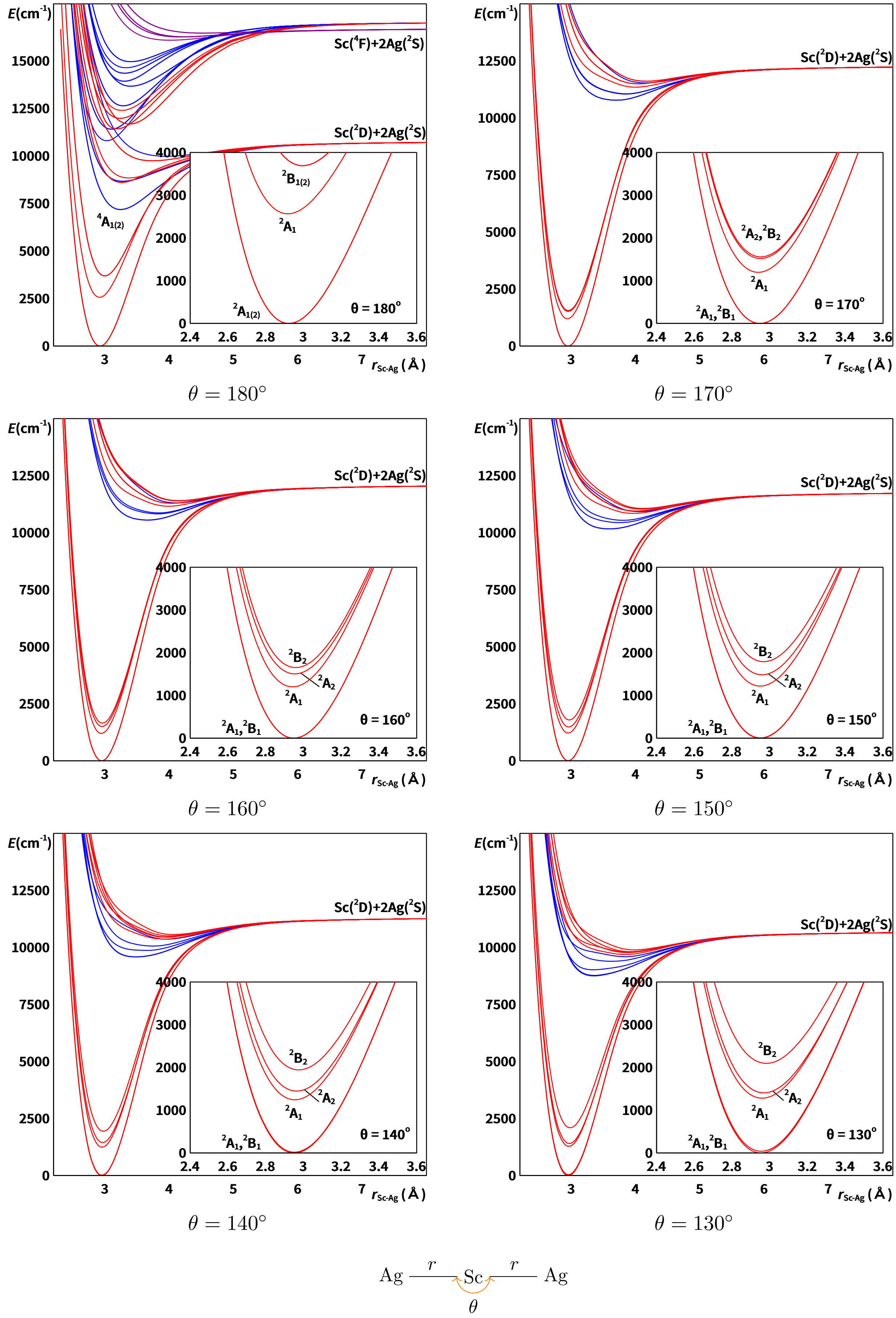

$\theta = 180°$ $\theta = 170°$

$\theta = 160°$ $\theta = 150°$

$\theta = 140°$ $\theta = 130°$

Figure B.17: $E(\theta, r; {}^{2S+1}\Gamma)$ for AgScAg obtained at SA-CASSCF(3/5,7/8). Zero of energy corresponds to the lowest total energy for the associated angle.

Continued on next page

Continued from previous page

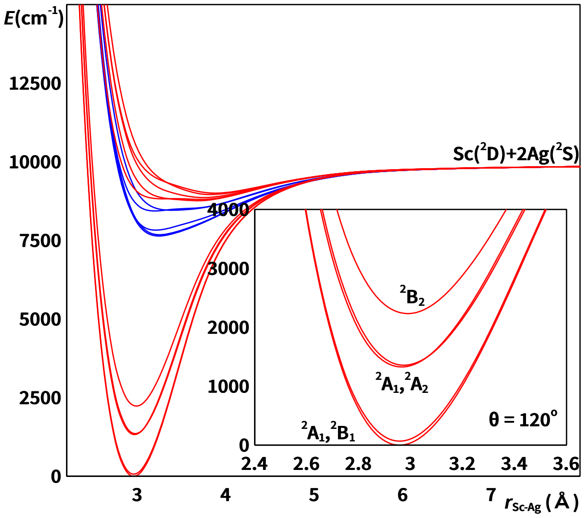

$\theta = 120°$

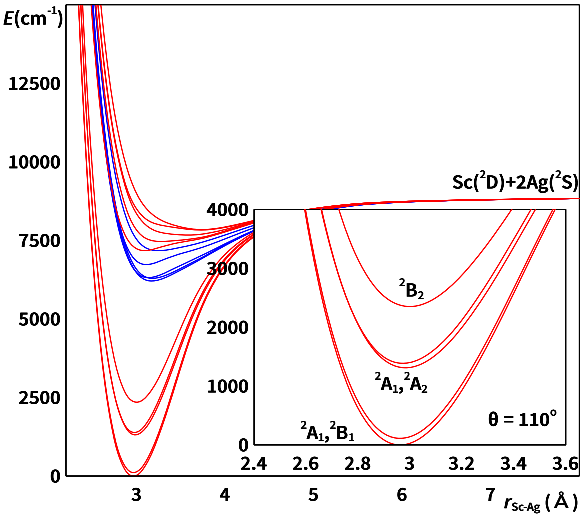

$\theta = 110°$

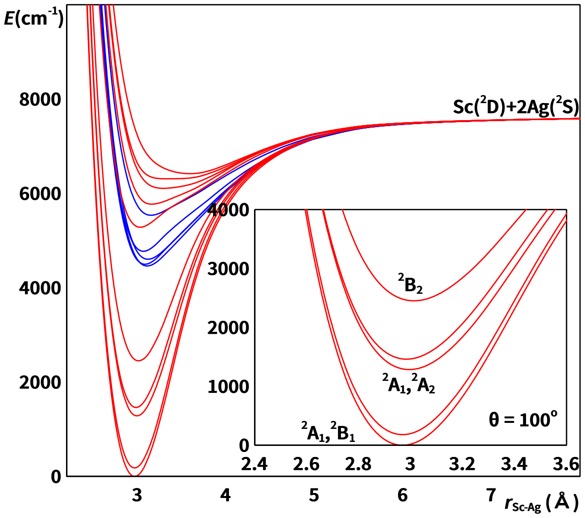

$\theta = 100°$

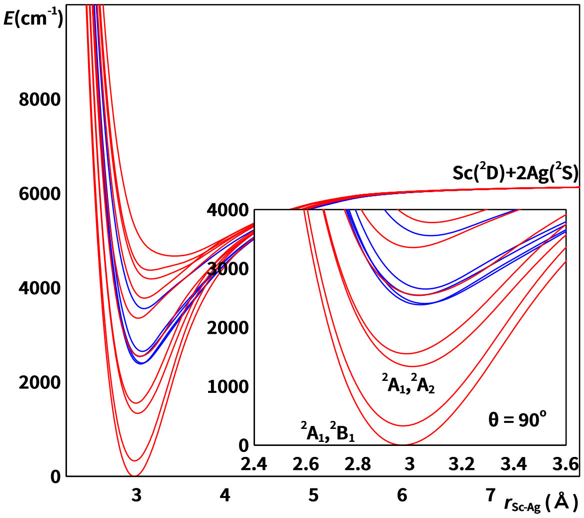

$\theta = 90°$

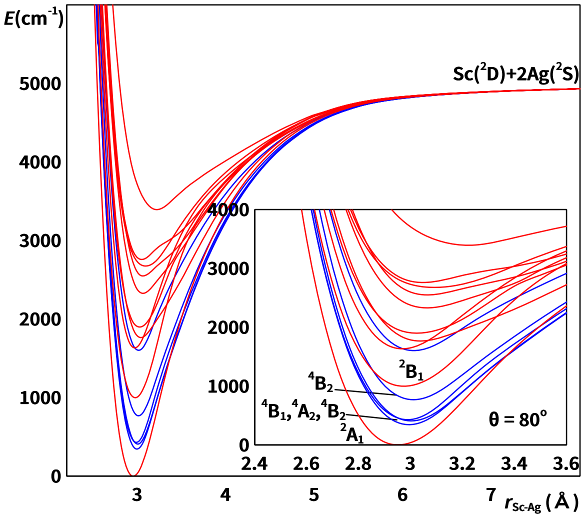

$\theta = 80°$

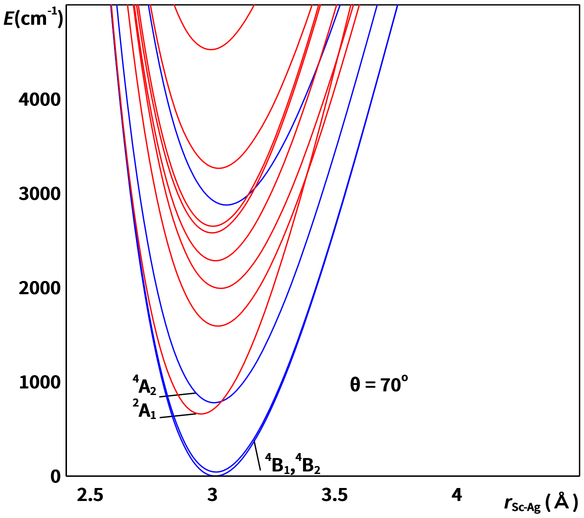

$\theta = 70°$

Continued on next page

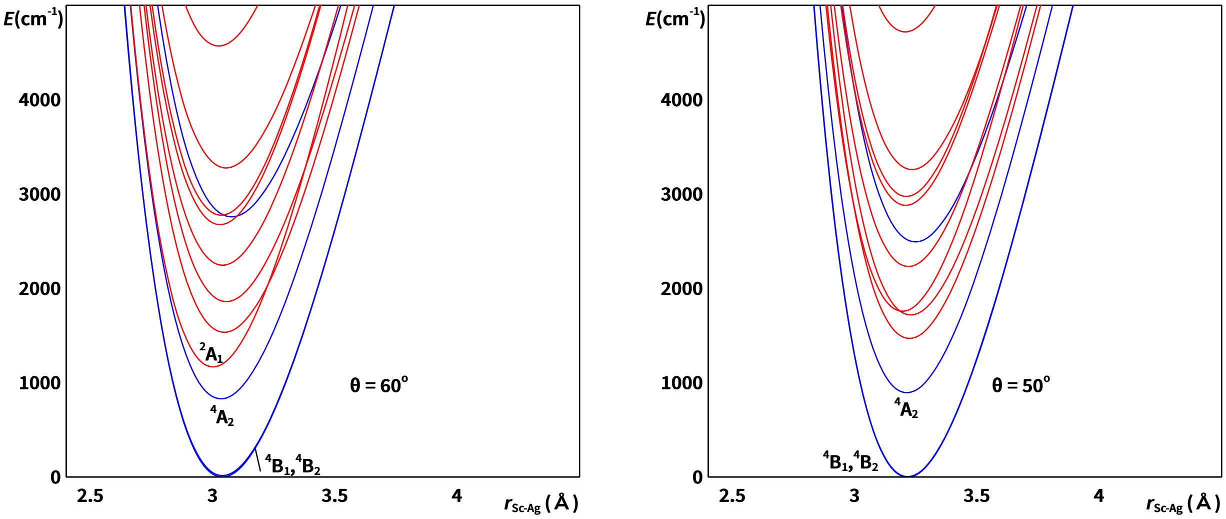

$\theta = 60°$

$\theta = 50°$

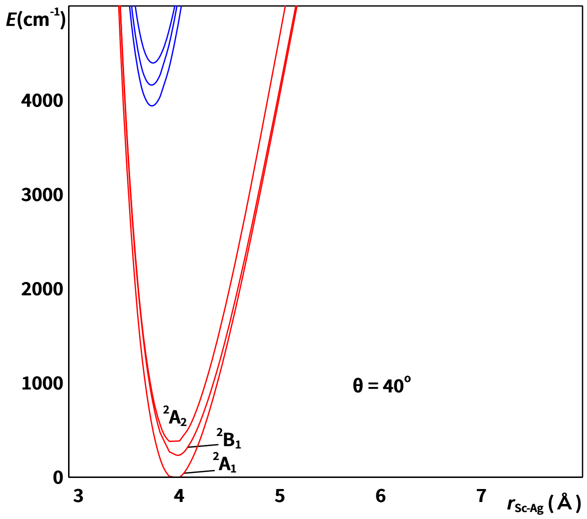

$\theta = 40°$

Continued from previous page

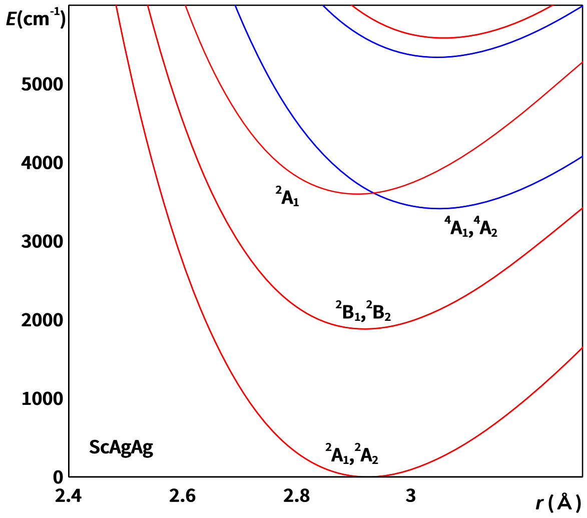

$\mathrm{Sc}\ \overset{r}{\text{———}}\ \mathrm{Ag}\ \overset{r}{\text{———}}\ \mathrm{Ag}$

Figure B.18: $E(r;{}^{2S+1}\Lambda)$ for ScAgAg obtained at the SA-CASSCF(5,8).

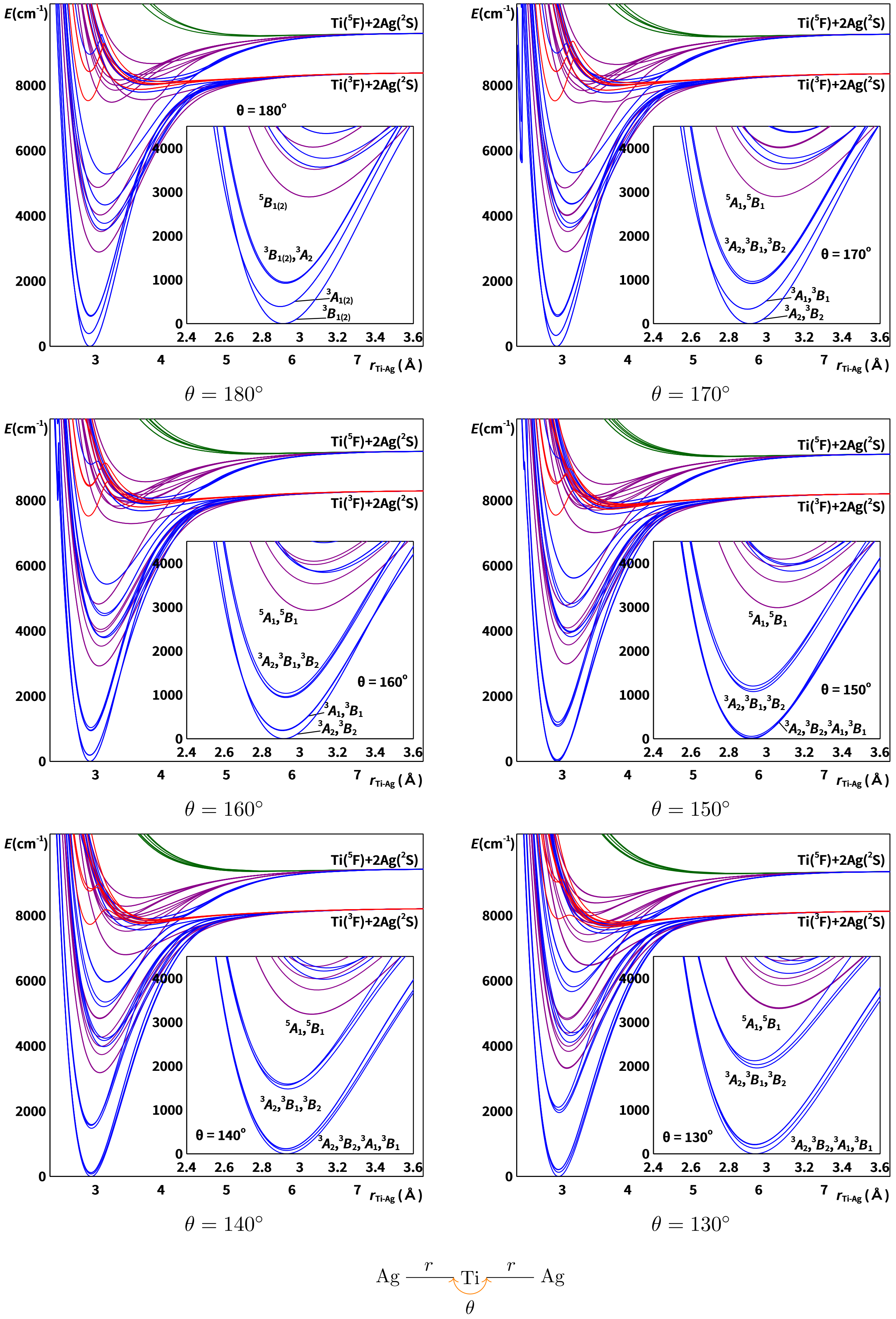

$\theta = 180°$ $\theta = 170°$

$\theta = 160°$ $\theta = 150°$

$\theta = 140°$ $\theta = 130°$

Figure B.19: $E(\theta, r; {}^{2S+1}\Gamma)$ for AgTiAg obtained at the SA-CASSCF(6,8). Zero of energy corresponds to the lowest total energy for the associated angle.

Continued on next page

Continued from previous page

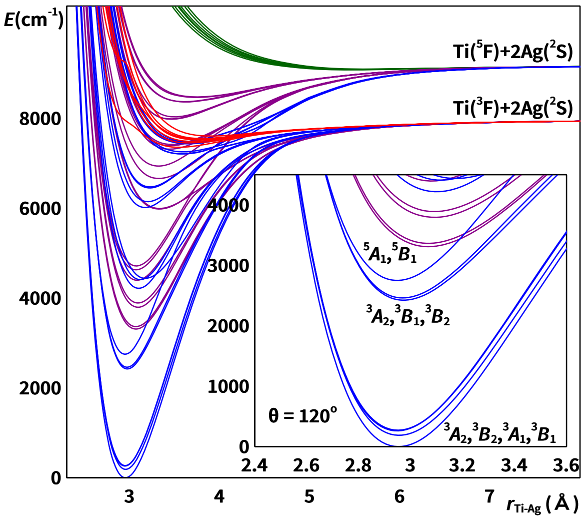

$\theta = 120°$

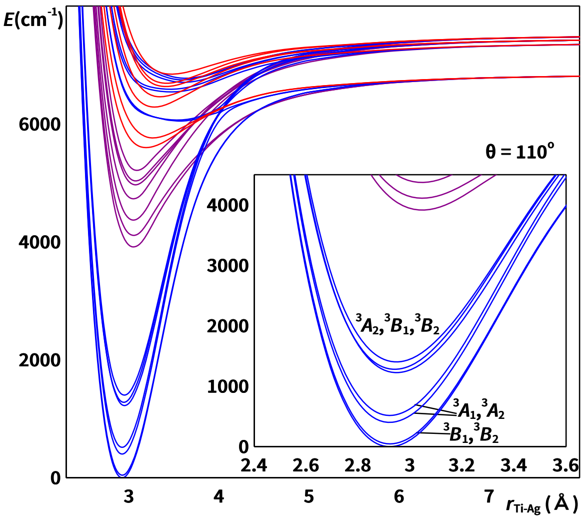

$\theta = 110°$

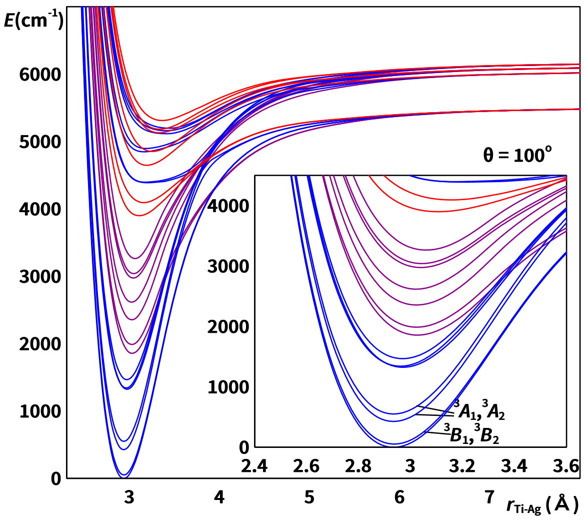

$\theta = 100°$

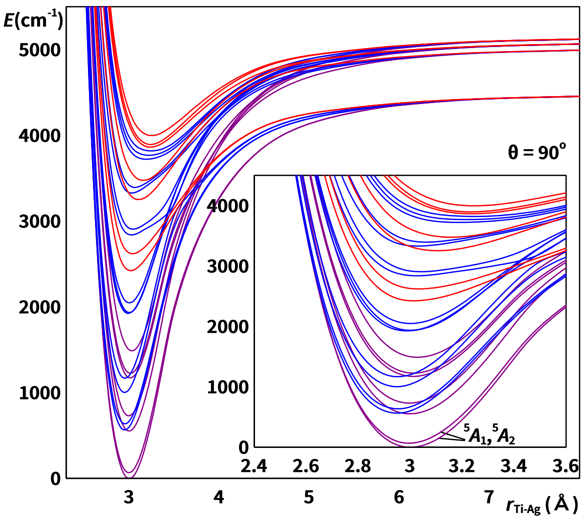

$\theta = 90°$

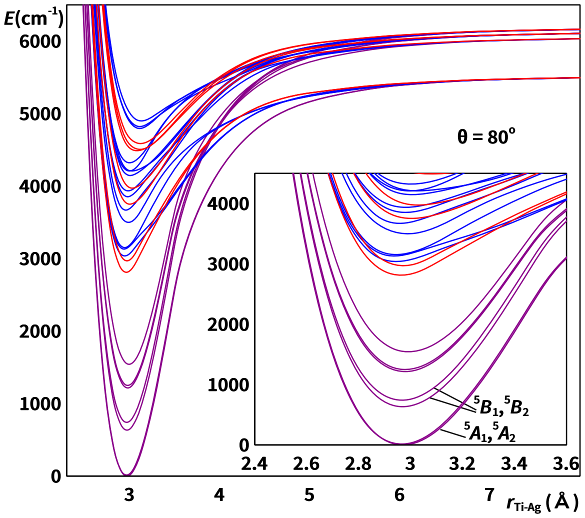

$\theta = 80°$

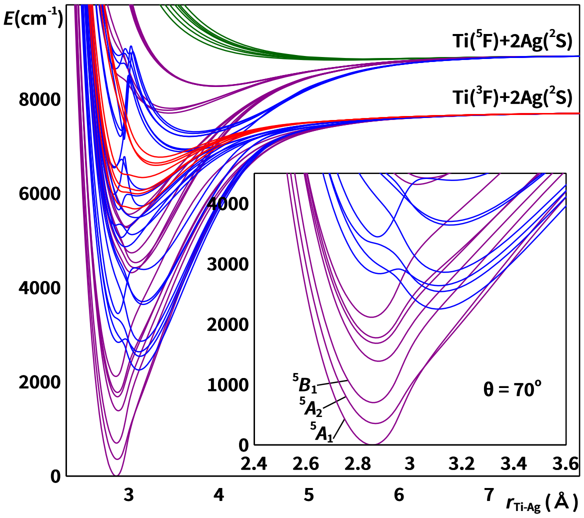

$\theta = 70°$

Continued on next page

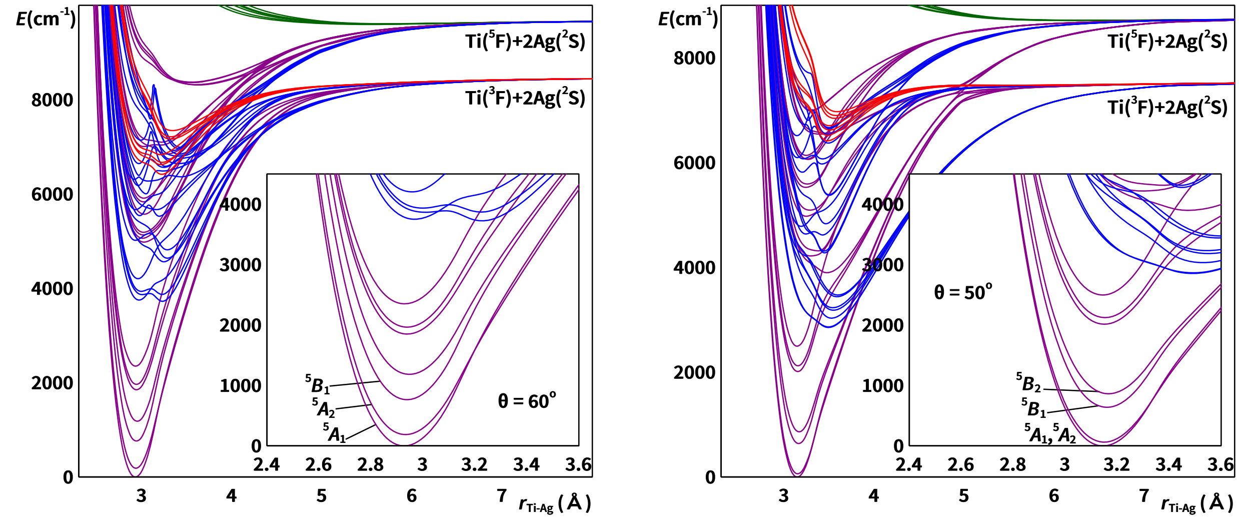

$\theta = 60°$ $\theta = 50°$

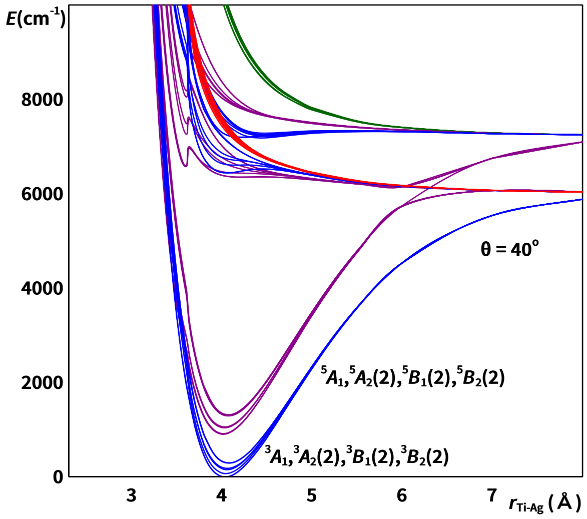

$\theta = 40°$

Continued from previous page

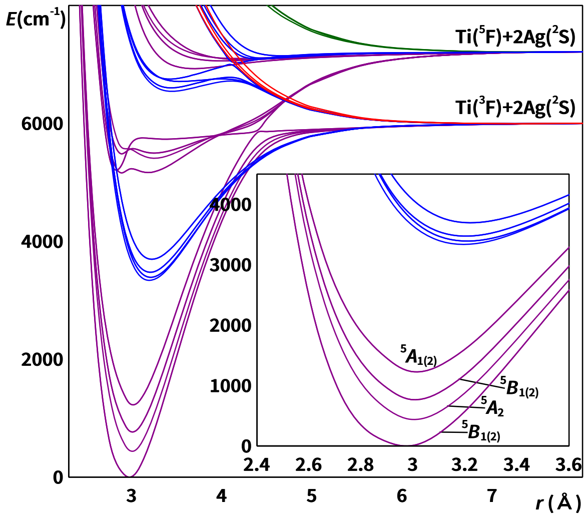

$$\mathrm{Ti}\overset{r}{\text{———}}\mathrm{Ag}\overset{r}{\text{———}}\mathrm{Ag}$$

Figure B.20: $E(r;{}^{2S+1}\Lambda)$ for the TiAgAg obtained at the SA-CASSCF(6,8).

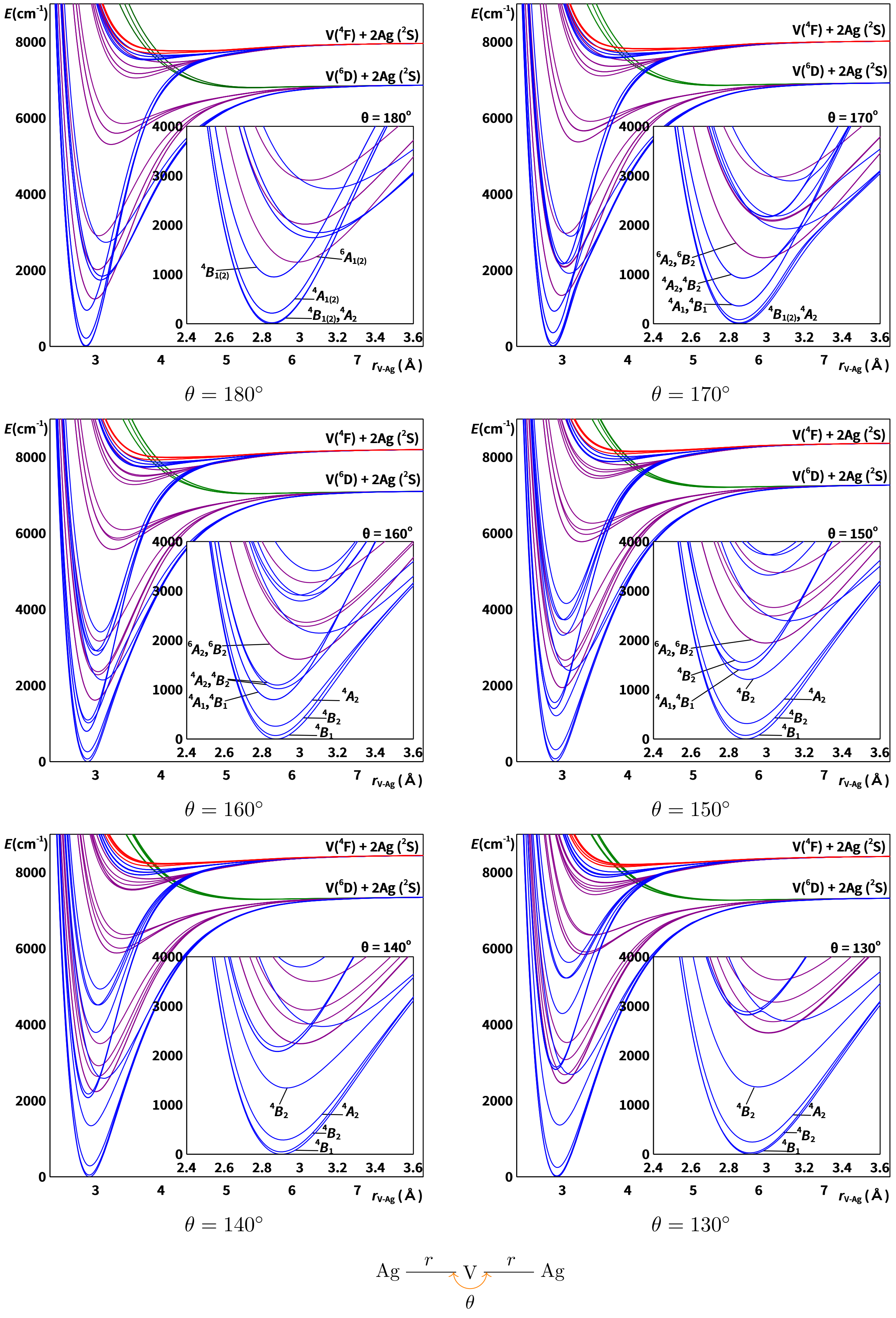

$\theta = 180^\circ$ $\theta = 170^\circ$

$\theta = 160^\circ$ $\theta = 150^\circ$

$\theta = 140^\circ$ $\theta = 130^\circ$

Figure B.21: $E(\theta, r; {}^{2S+1}\Gamma)$ for AgVAg obtained at the SA-CASSCF(7,8). Zero of energy corresponds to the lowest total energy for the associated angle.

Continued on next page

Continued from previous page

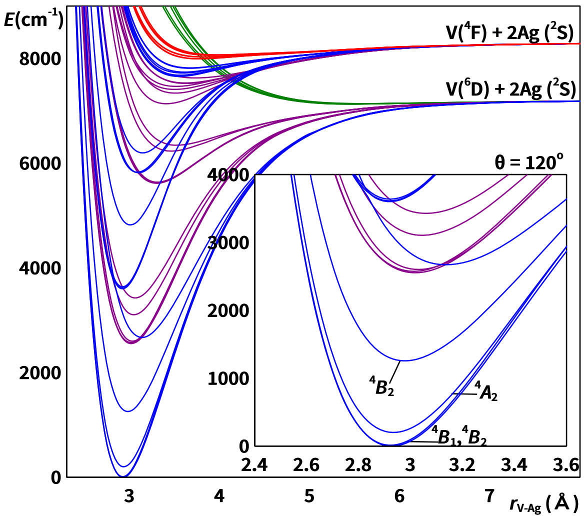

$\theta = 120°$

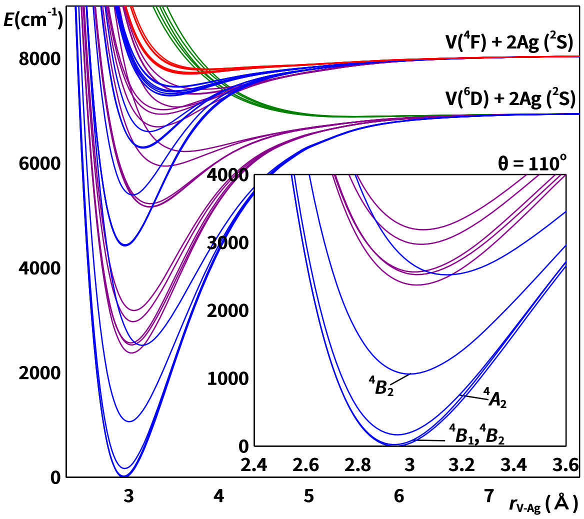

$\theta = 110°$

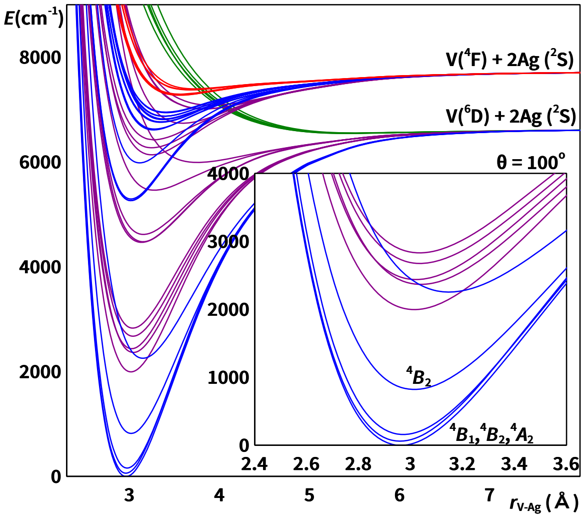

$\theta = 100°$

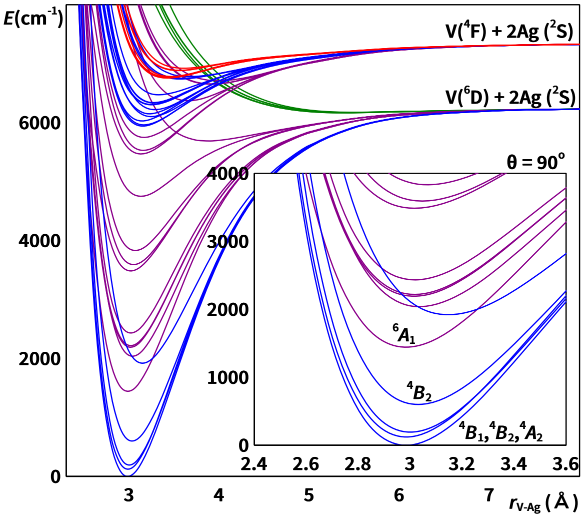

$\theta = 90°$

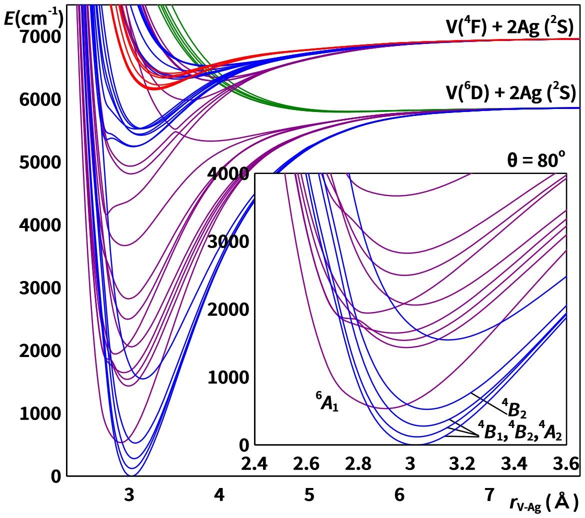

$\theta = 80°$

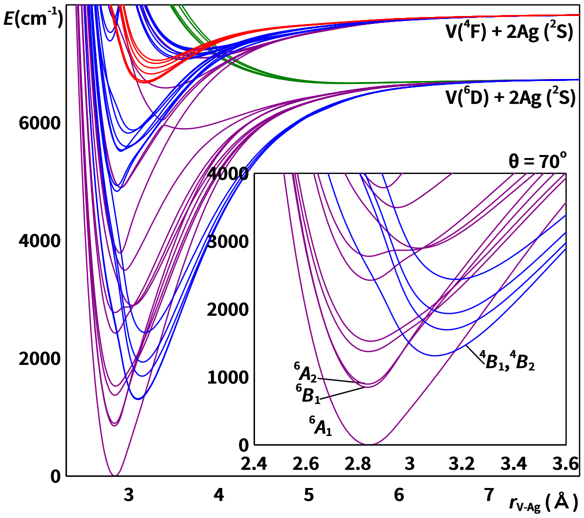

$\theta = 70°$

Continued on next page

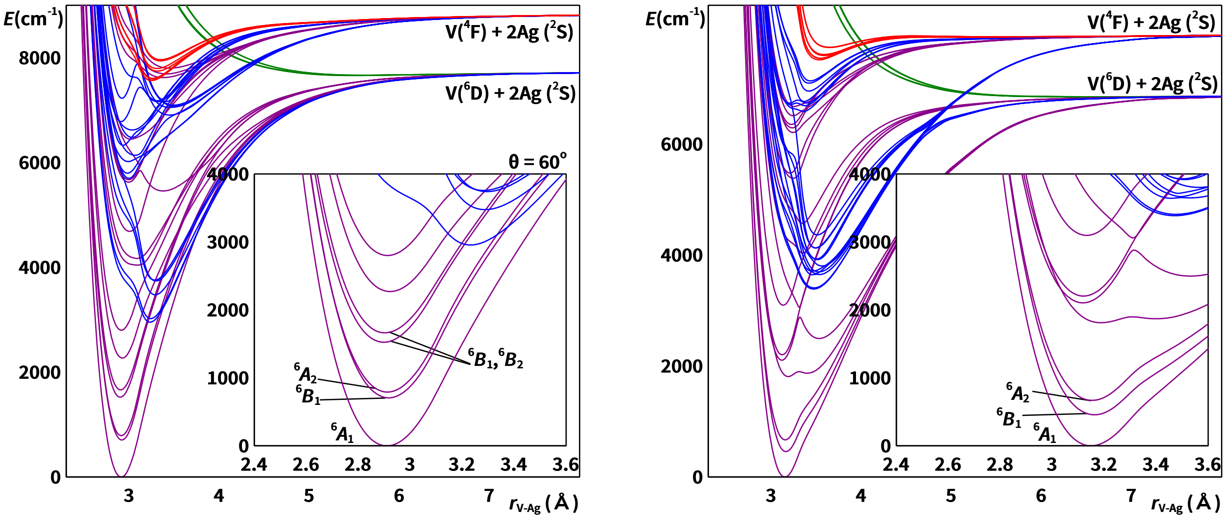

$\theta = 60°$ $\theta = 50°$

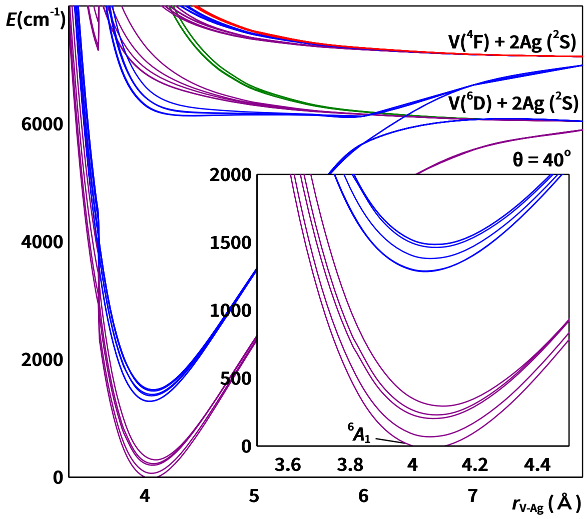

$\theta = 40°$

Continued from previous page

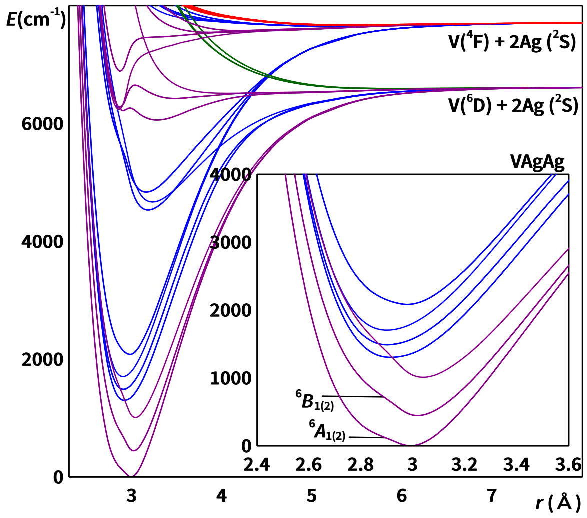

$\mathrm{V} \overset{r}{\text{———}} \mathrm{Ag} \overset{r}{\text{———}} \mathrm{Ag}$

Figure B.22: $E(r; {}^{2S+1}\Lambda)$ for VAgAg obtained at the SA-CASSCF(7,8).

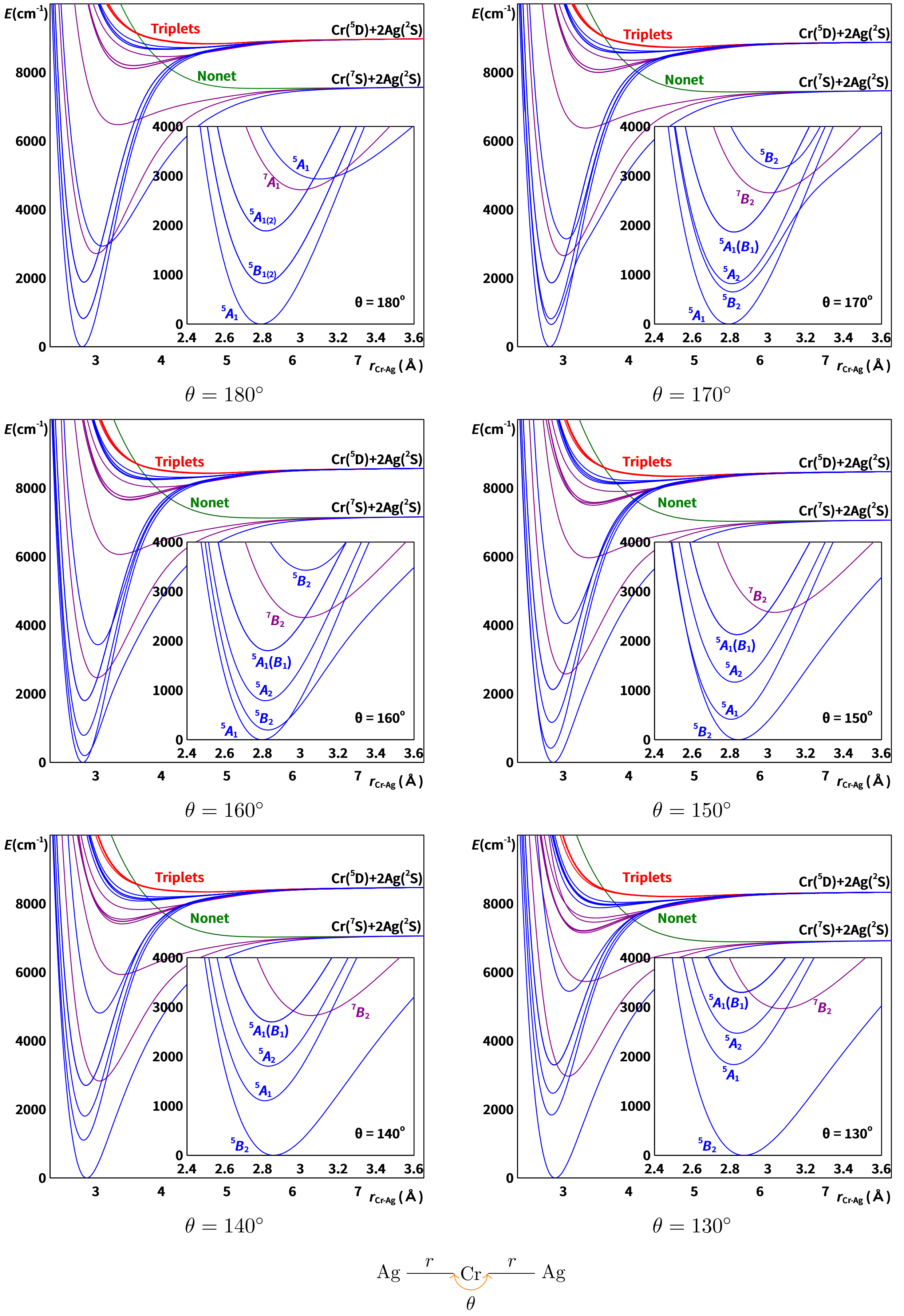

$\theta = 180°$ $\theta = 170°$

$\theta = 160°$ $\theta = 150°$

$\theta = 140°$ $\theta = 130°$

Figure B.23: $E(\theta, r; {}^{2S+1}\Gamma)$ for AgCrAg obtained at the SA-CASSCF(8,8). Zero of energy corresponds to the lowest total energy for the associated angle.

Continued on next page

Continued from previous page

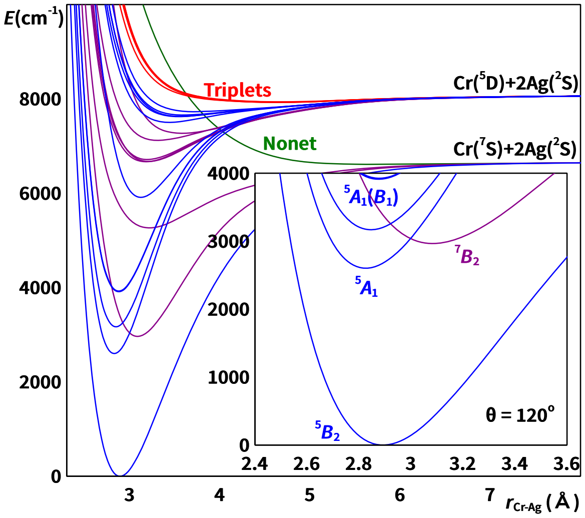

$\theta = 120°$

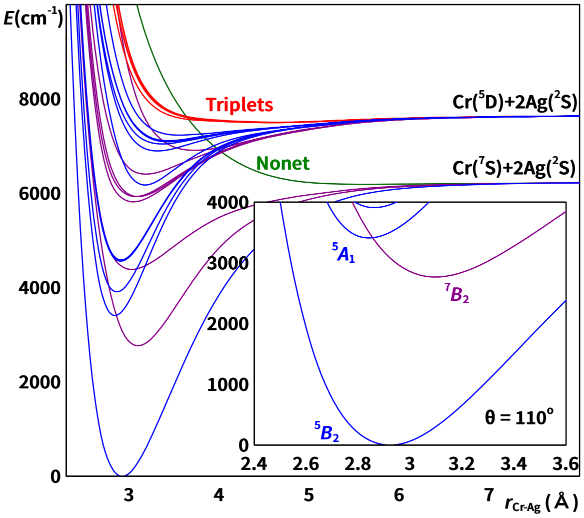

$\theta = 110°$

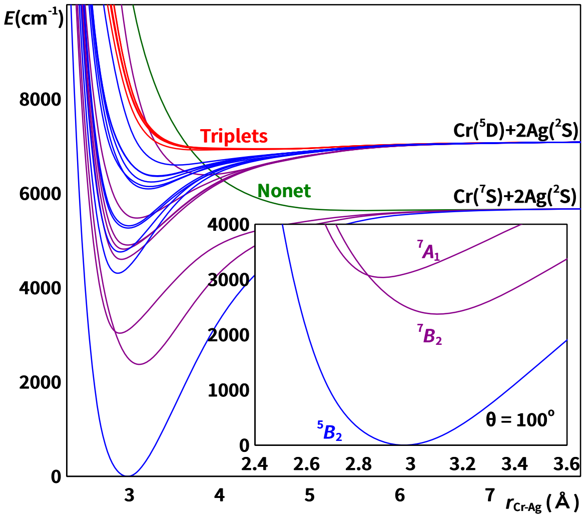

$\theta = 100°$

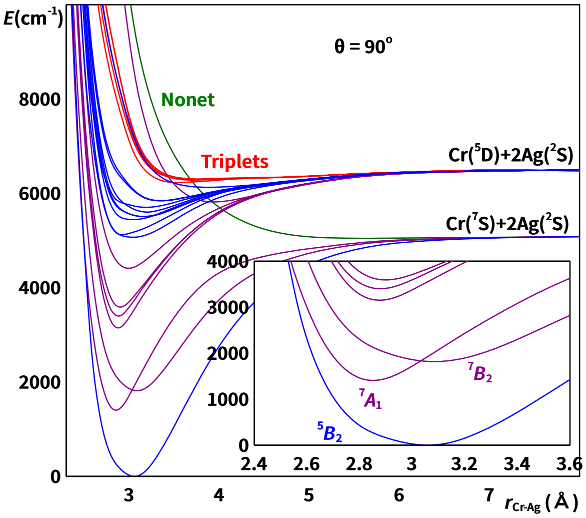

$\theta = 90°$

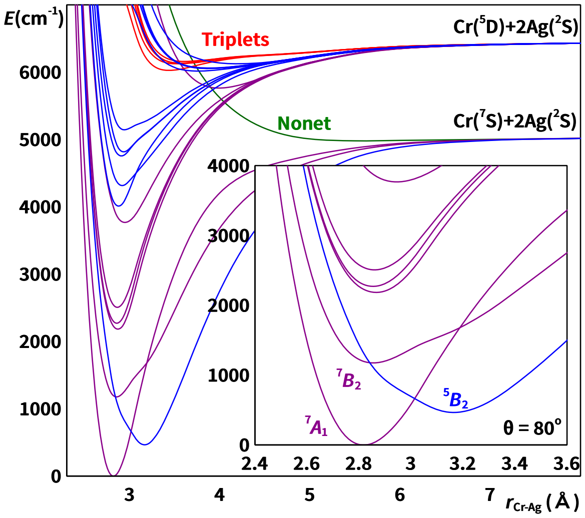

$\theta = 80°$

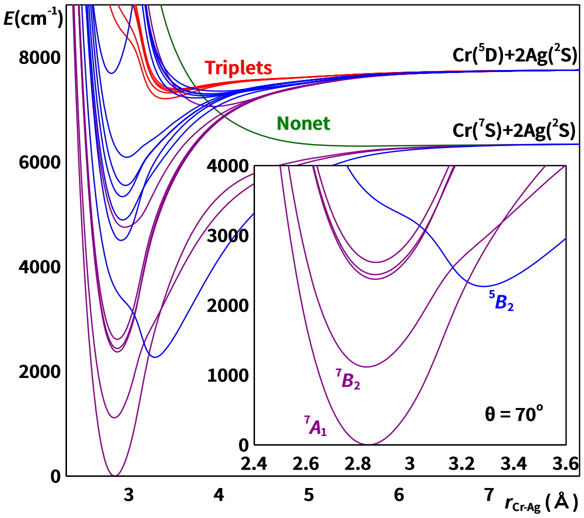

$\theta = 70°$

Continued on next page

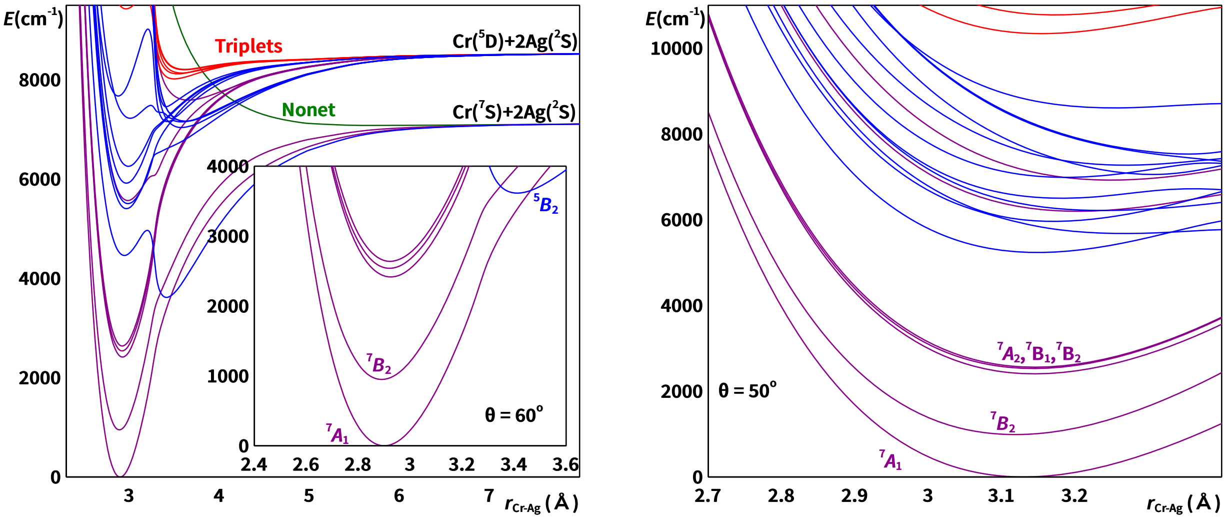

$\theta = 60°$ $\theta = 50°$

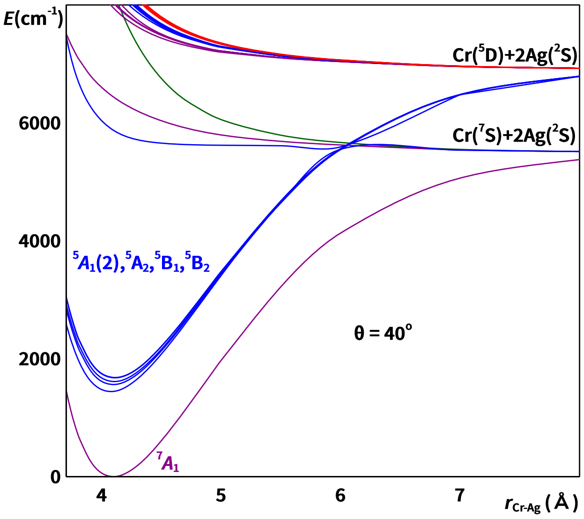

$\theta = 40°$

Continued from previous page

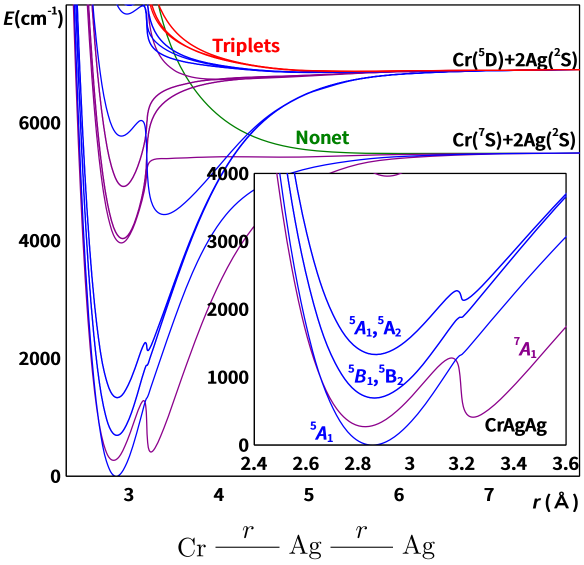

Figure B.24: $E(r; {}^{2S+1}\Lambda)$ for CrAgAg obtained at the SA-CASSCF(8,8).

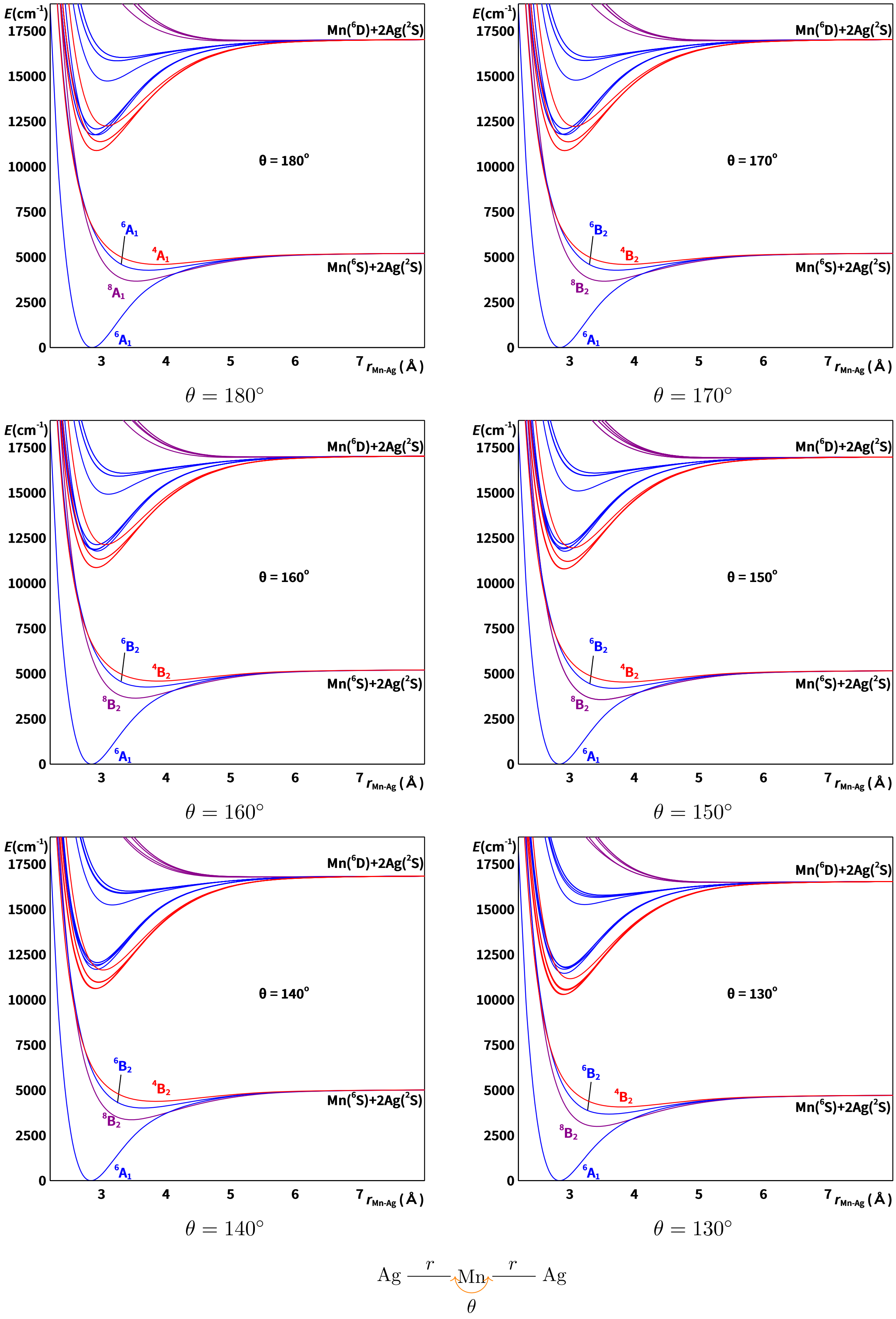

$\theta = 180^\circ$

$\theta = 170^\circ$

$\theta = 160^\circ$

$\theta = 150^\circ$

$\theta = 140^\circ$

$\theta = 130^\circ$

Figure B.25: $E(\theta, r; {}^{2S+1}\Gamma)$ for AgMnAg obtained at the SA-CASSCF(9,8). Zero of energy corresponds to the lowest total energy for the associated angle.

Continued on next page

Continued from previous page

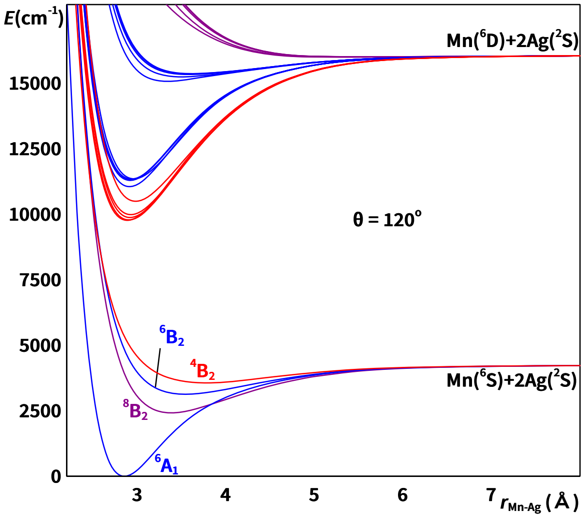

$\theta = 120°$

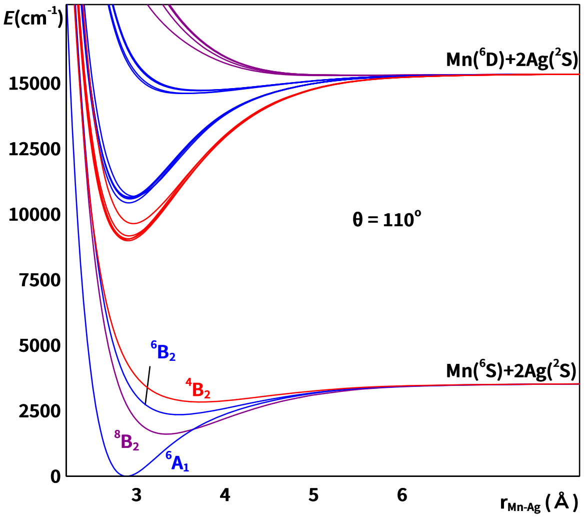

$\theta = 110°$

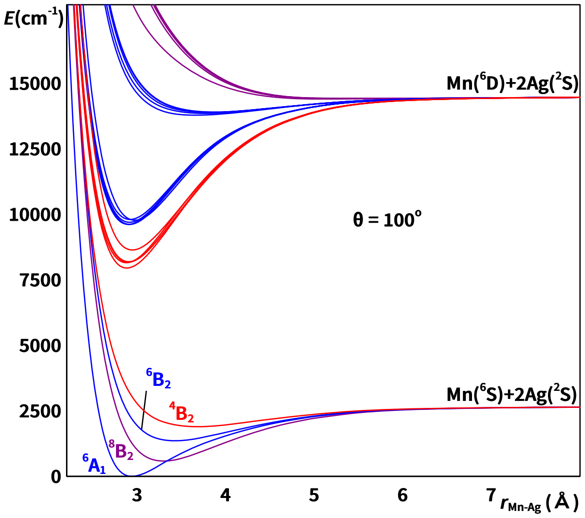

$\theta = 100°$

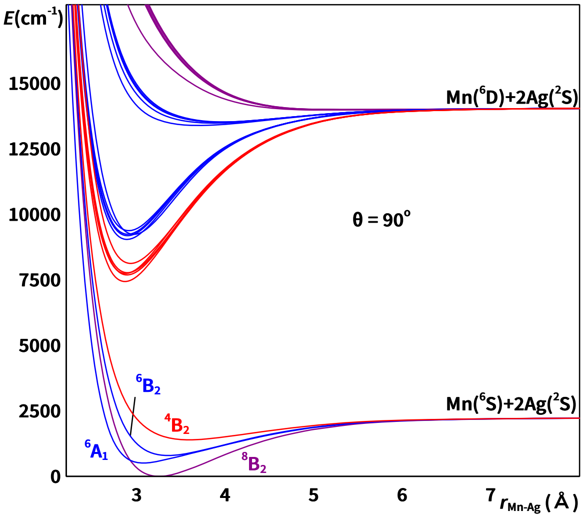

$\theta = 90°$

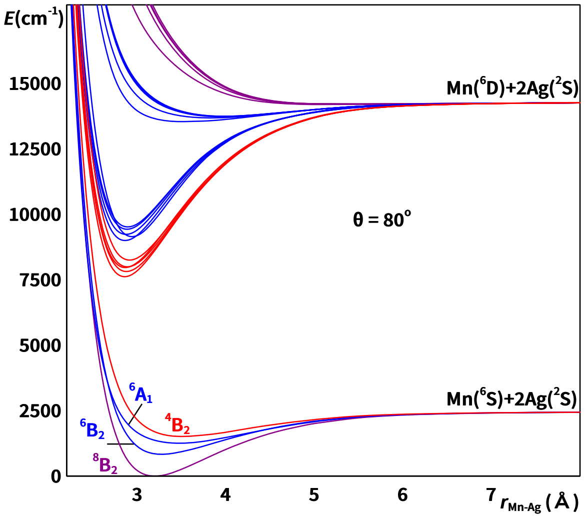

$\theta = 80°$

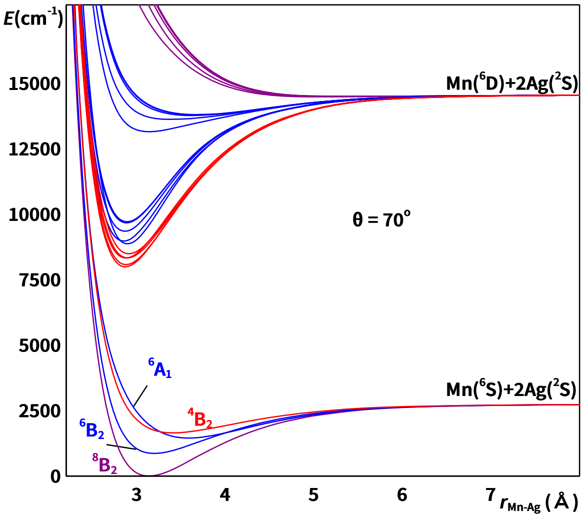

$\theta = 70°$

Continued on next page

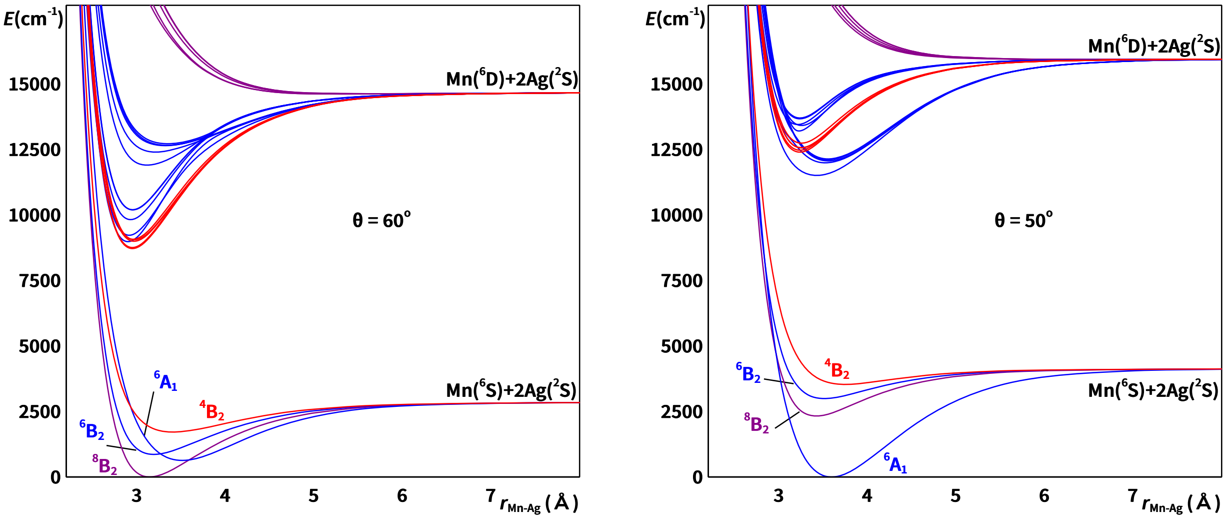

$\theta = 60°$ $\theta = 50°$

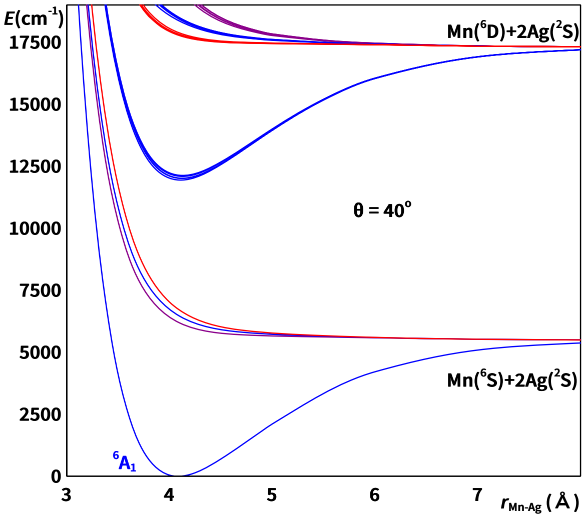

$\theta = 40°$

Continued from previous page

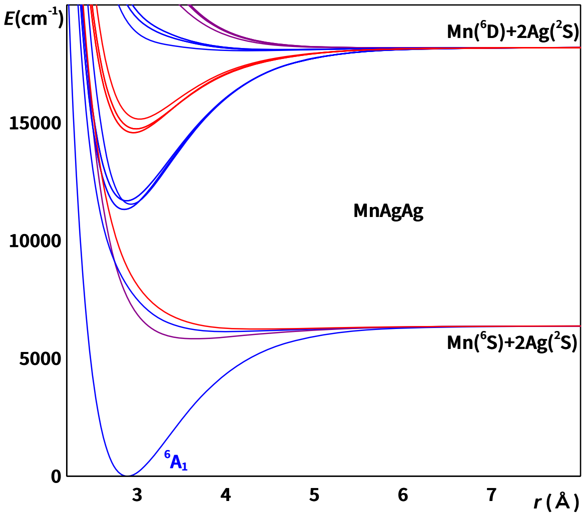

$\text{Mn} \overset{r}{\text{———}} \text{Ag} \overset{r}{\text{———}} \text{Ag}$

Figure B.26: $E(r; {}^{2S+1}\Lambda)$ for MnAgAg obtained at the SA-CASSCF(9,8).

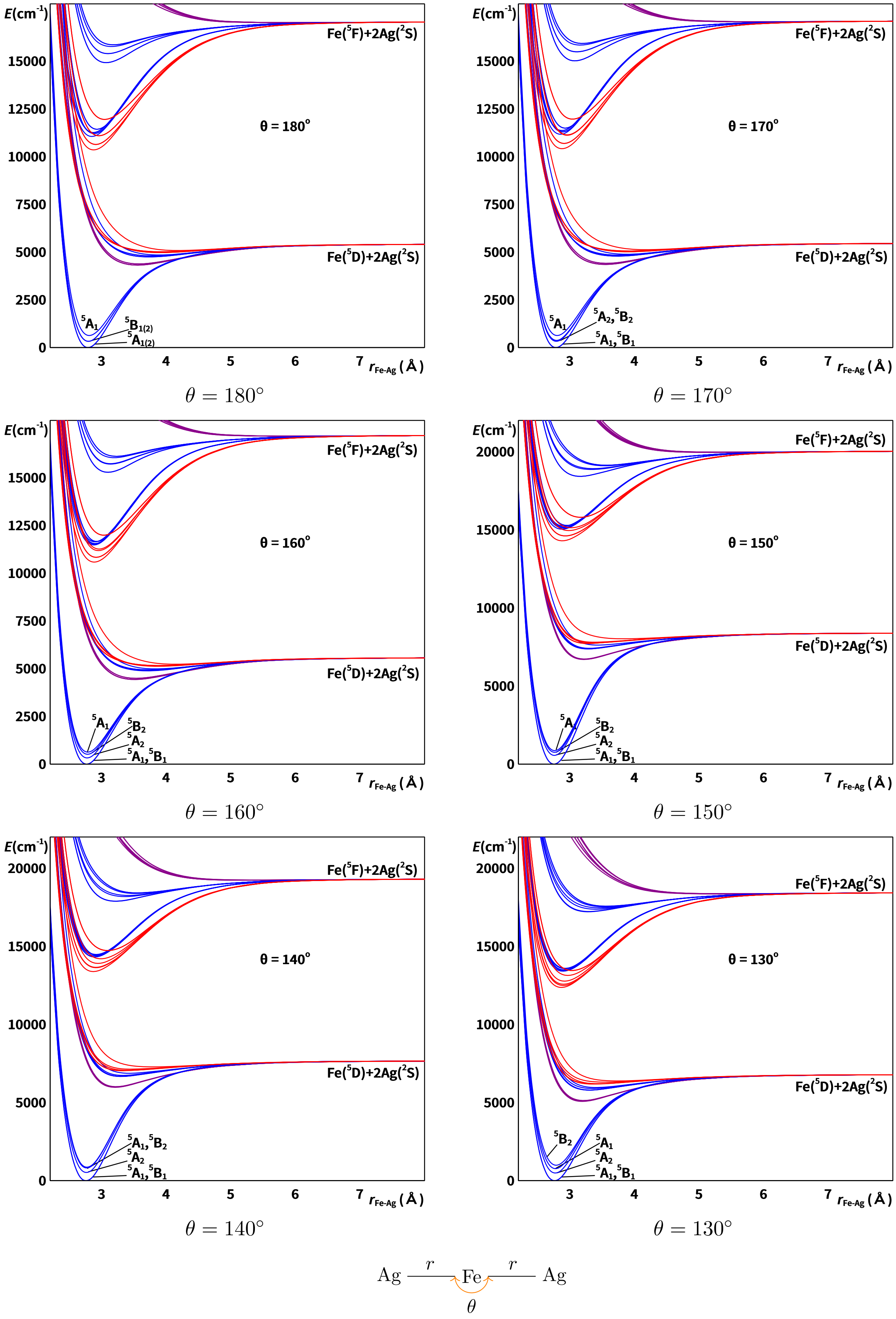

$\theta = 180^\circ$

$\theta = 170^\circ$

$\theta = 160^\circ$

$\theta = 150^\circ$

$\theta = 140^\circ$

$\theta = 130^\circ$

Figure B.27: $E(\theta, r; {}^{2S+1}\Gamma)$ for AgFeAg obtained at the SA-CASSCF(10,8). Zero of energy corresponds to the lowest total energy for the associated angle.

Continued on next page

Continued from previous page

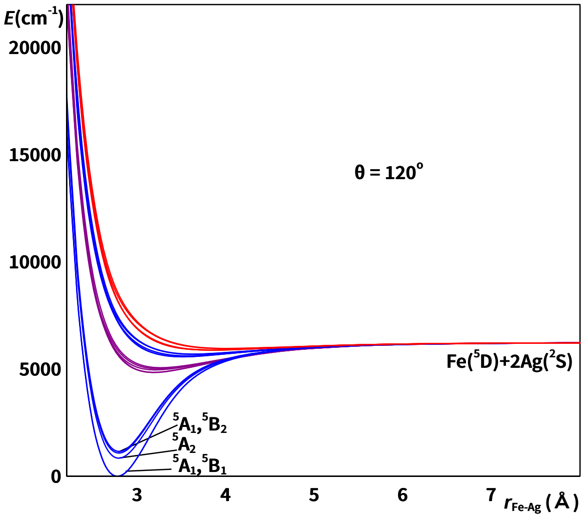

$\theta = 120°$

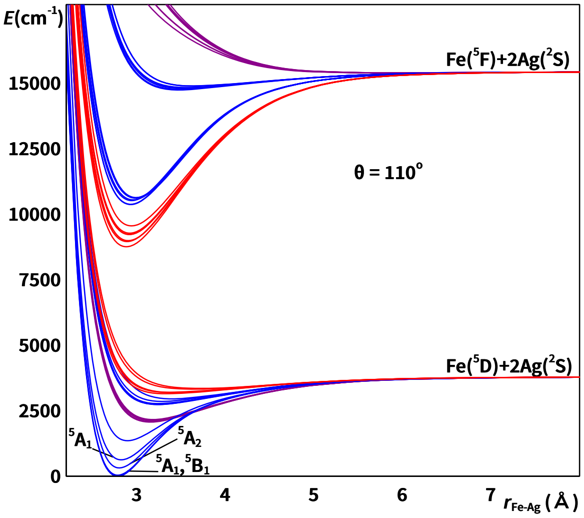

$\theta = 110°$

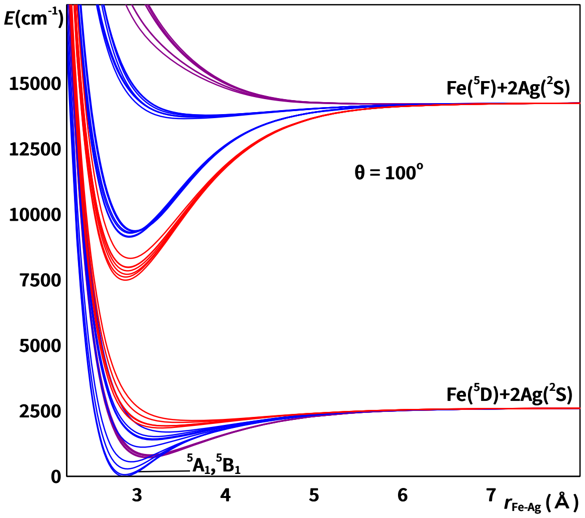

$\theta = 100°$

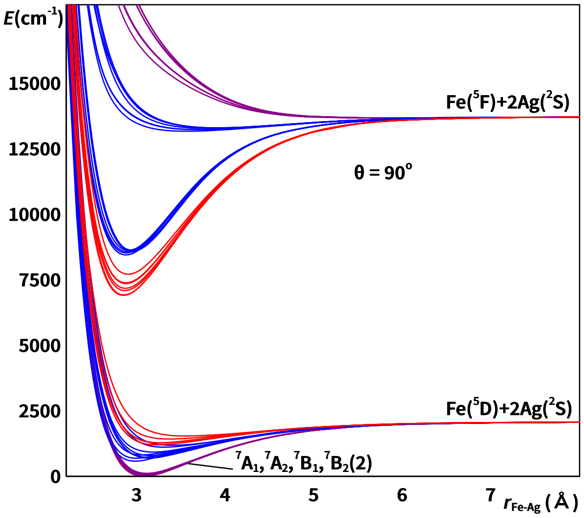

$\theta = 90°$

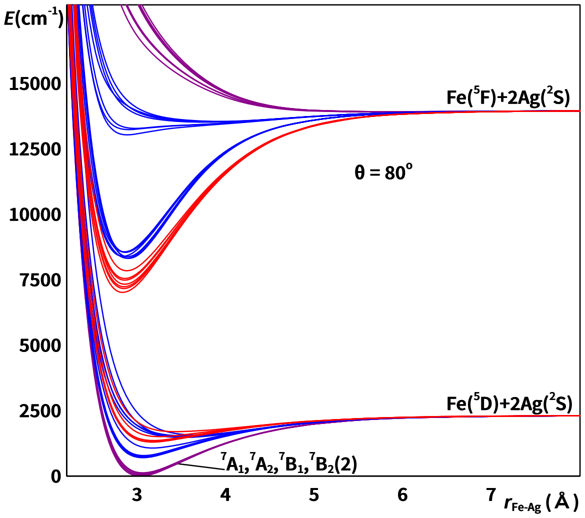

$\theta = 80°$

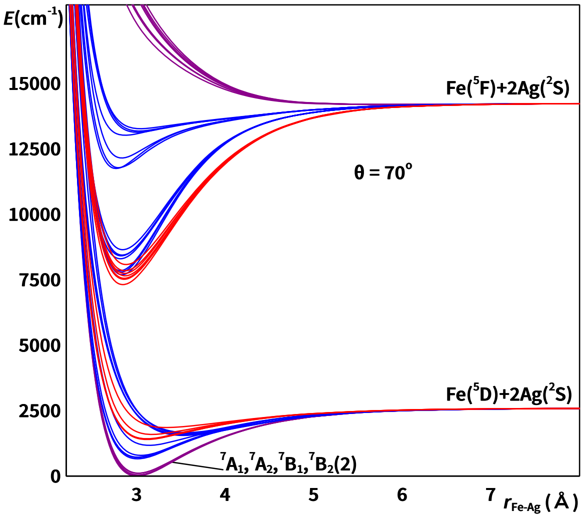

$\theta = 70°$

Continued on next page

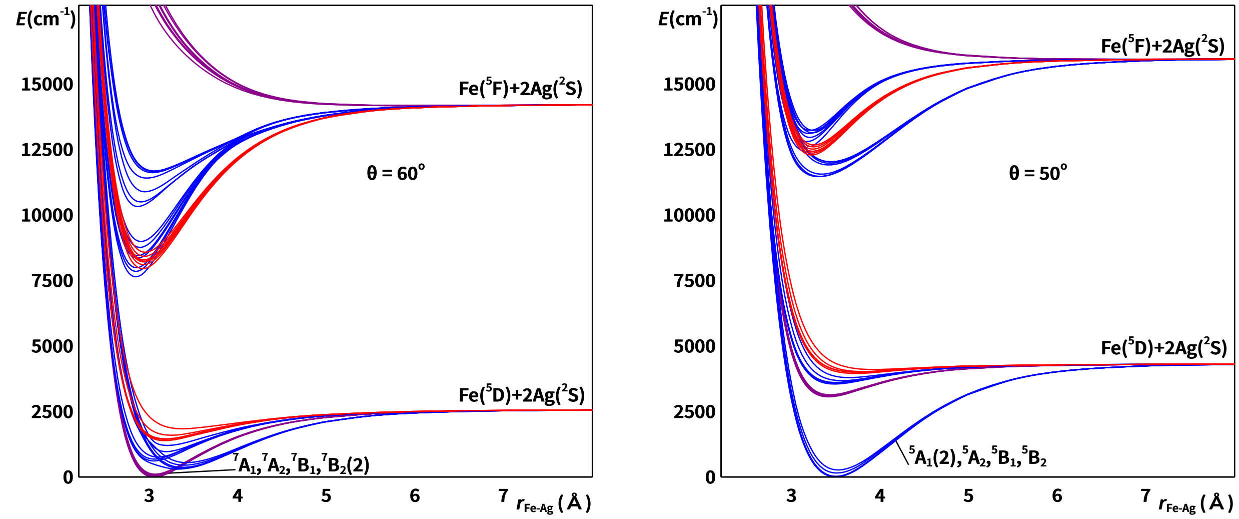

$\theta = 60°$ $\theta = 50°$

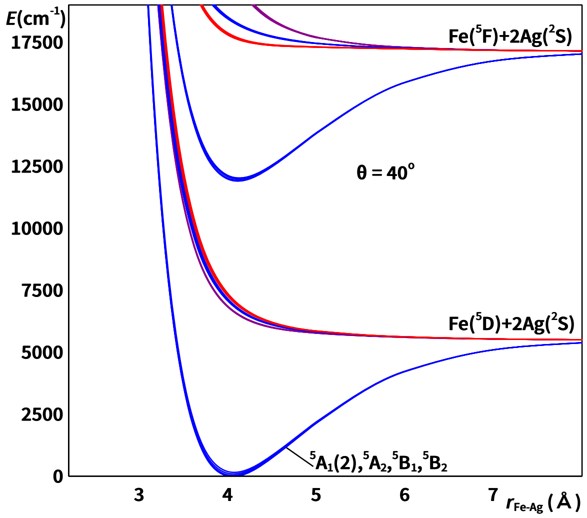

$\theta = 40°$

Continued from previous page

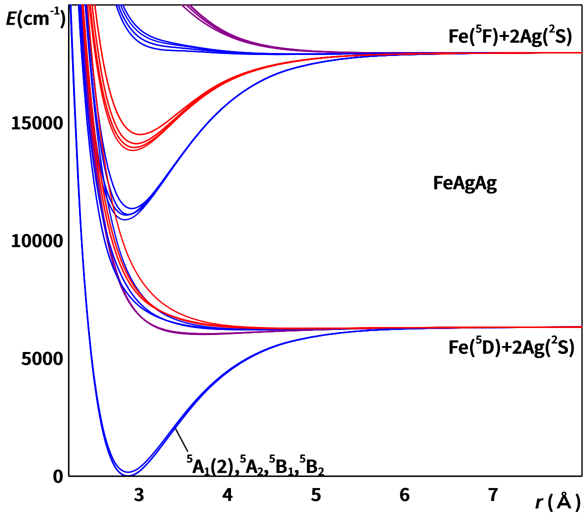

$\mathrm{Fe} \overset{r}{\text{———}} \mathrm{Ag} \overset{r}{\text{———}} \mathrm{Ag}$

Figure B.28: $E(r; {}^{2S+1}\Lambda)$ for FeAgAg obtained at the SA-CASSCF(10,8).

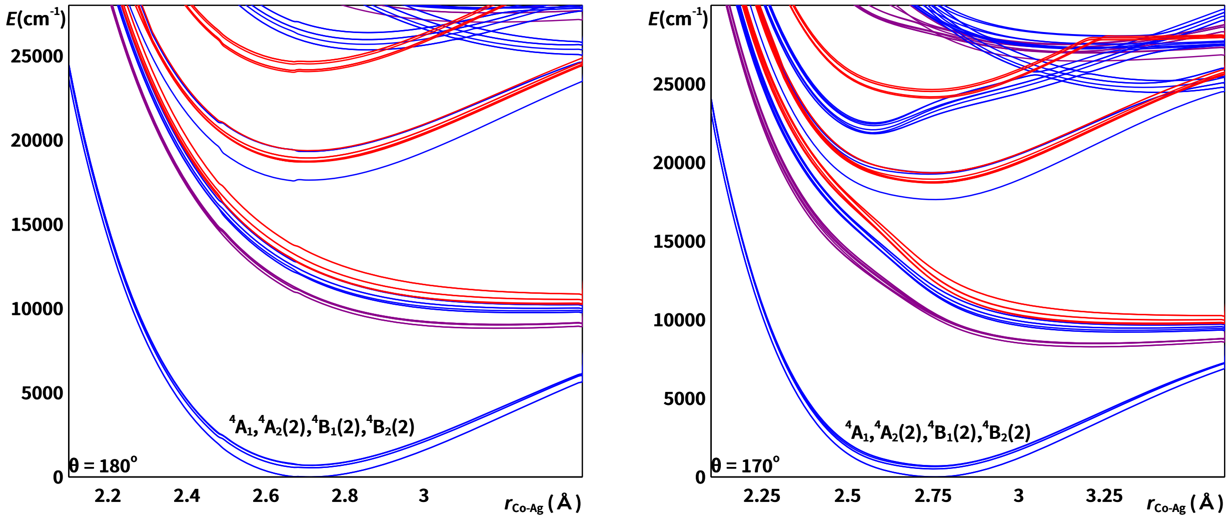

$\theta = 180°$ $\theta = 170°$

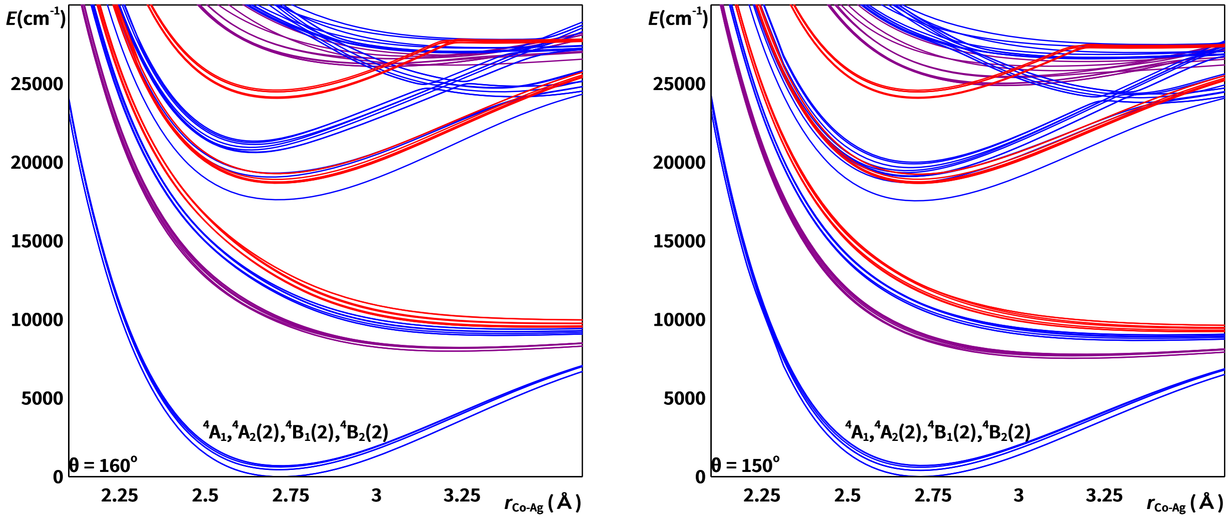

$\theta = 160°$ $\theta = 150°$

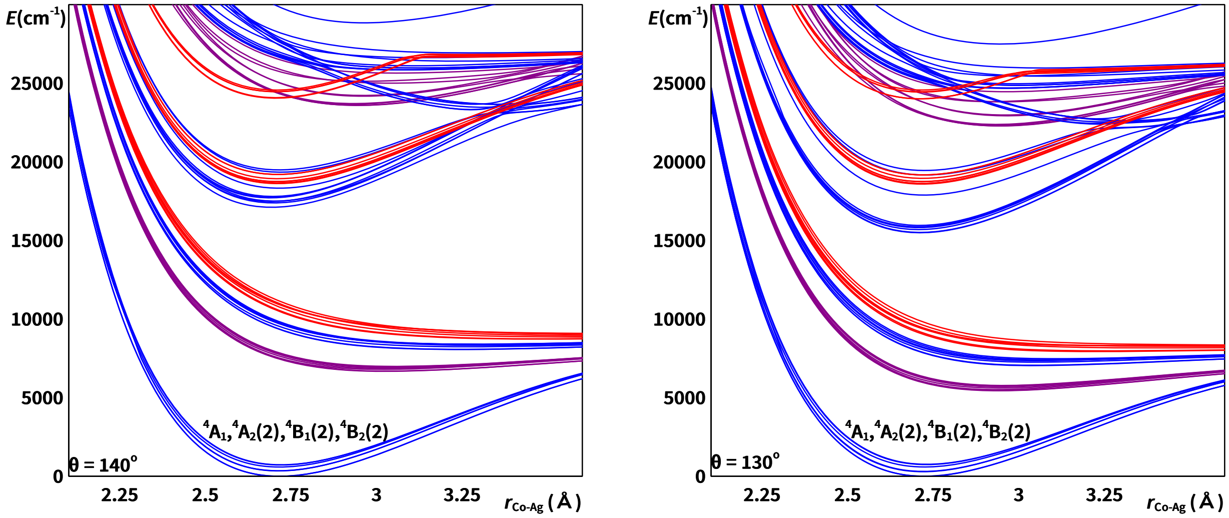

$\theta = 140°$ $\theta = 130°$

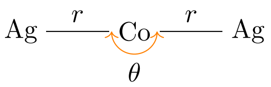

Figure B.29: $E(\theta, r; {}^{2S+1}\Gamma)$ for AgCoAg obtained at the SA-CASSCF(11,8). Zero of energy corresponds to the lowest total energy for the associated angle.

Continued on next page

Continued from previous page

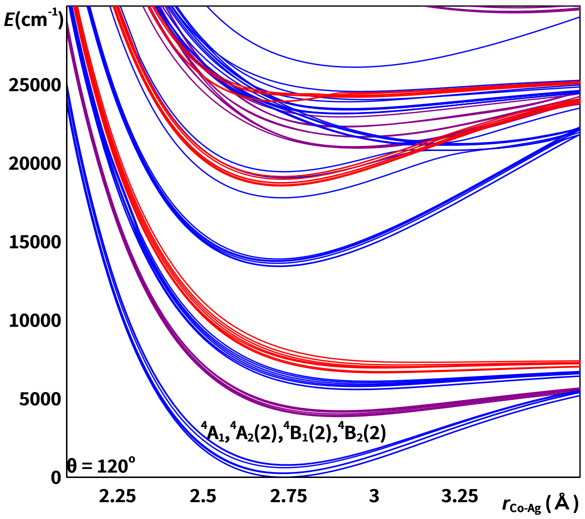

$\theta = 120°$

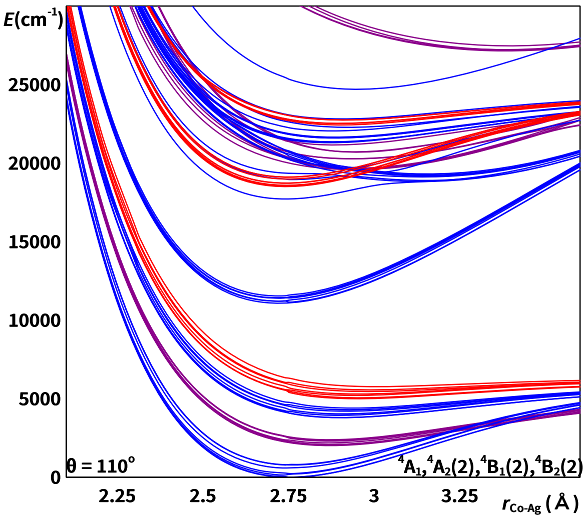

$\theta = 110°$

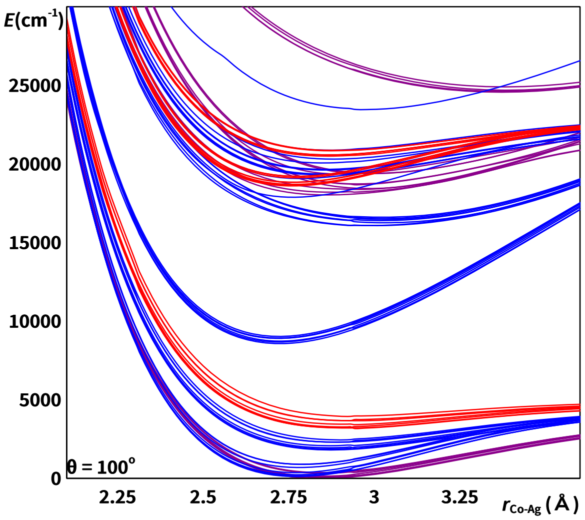

$\theta = 100°$

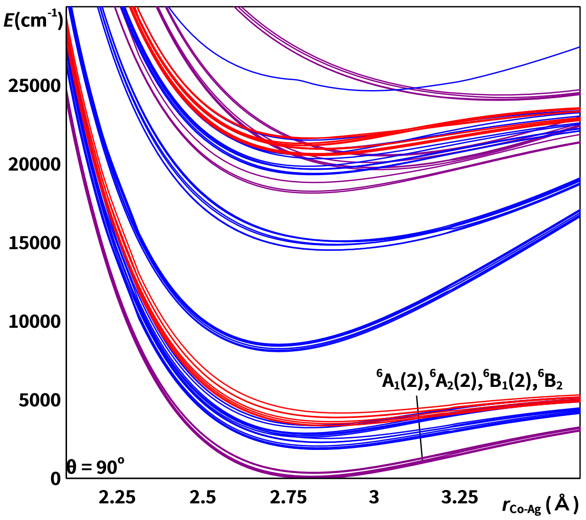

$\theta = 90°$

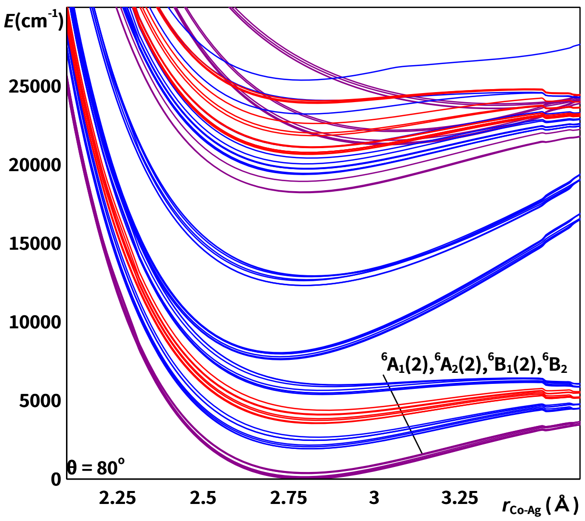

$\theta = 80°$

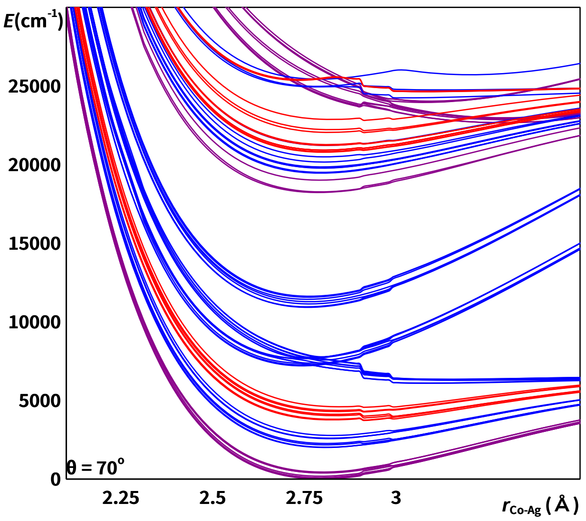

$\theta = 70°$

Continued on next page

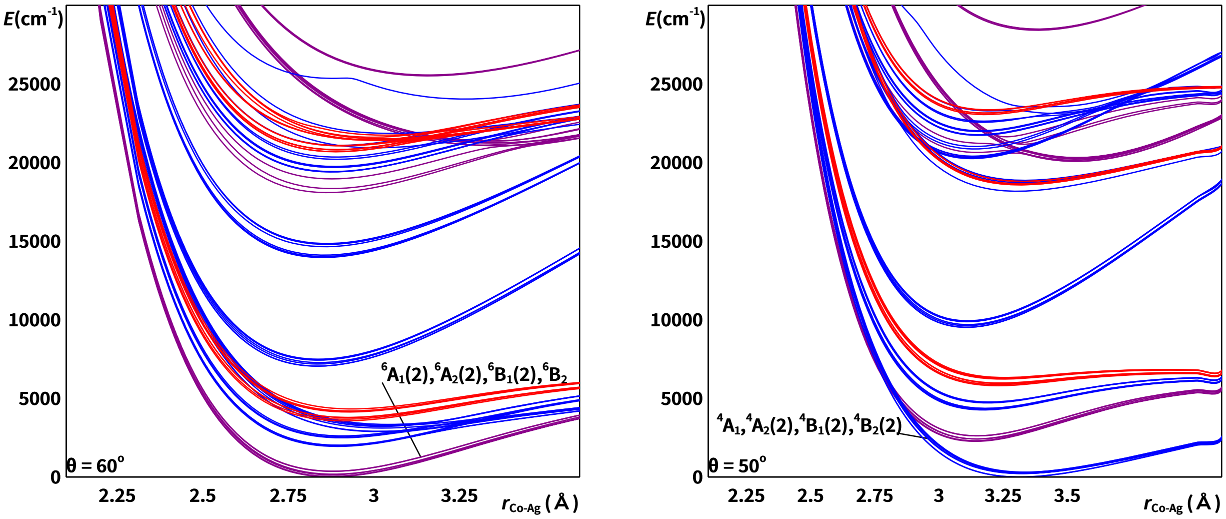

$\theta = 60°$ $\theta = 50°$

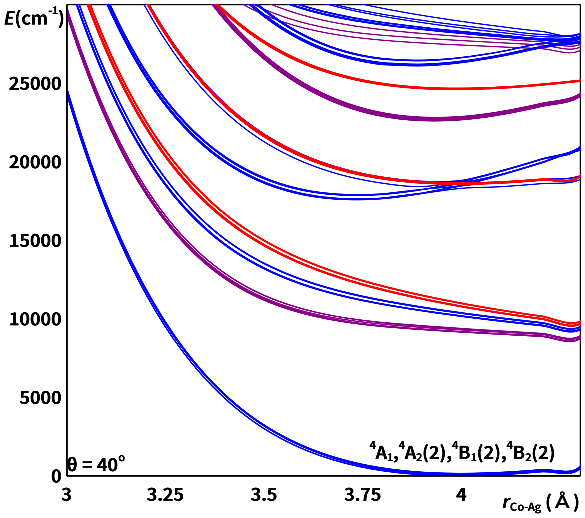

$\theta = 40°$

Continued from previous page

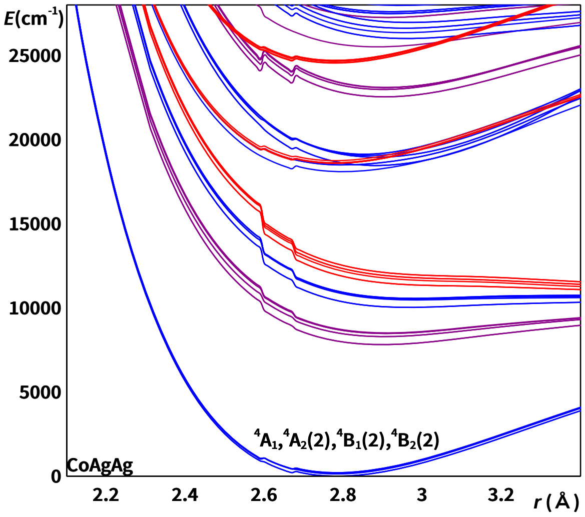

$\mathrm{Co} \overset{r}{\text{———}} \mathrm{Ag} \overset{r}{\text{———}} \mathrm{Ag}$

Figure B.30: $E(r; {}^{2S+1}\Lambda)$ for CoAgAg obtained at the SA-CASSCF(11,8).

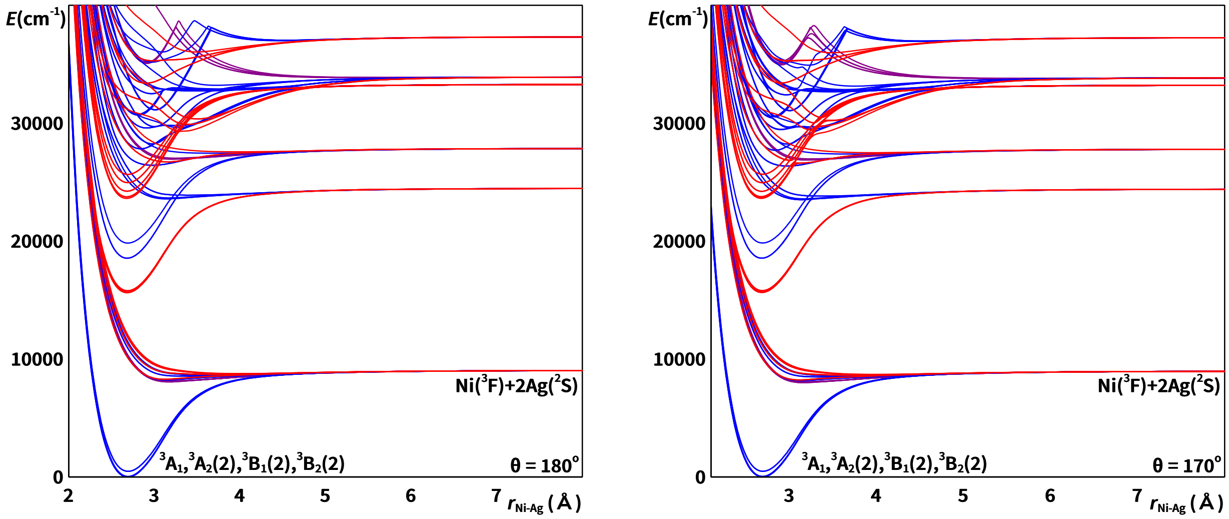

$\theta = 180°$ $\theta = 170°$

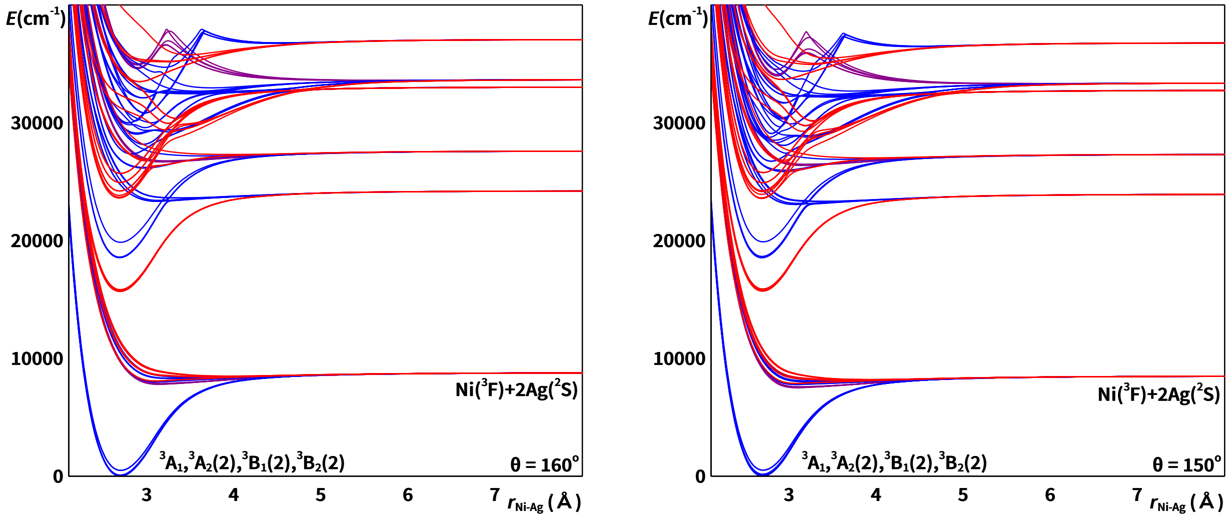

$\theta = 160°$ $\theta = 150°$

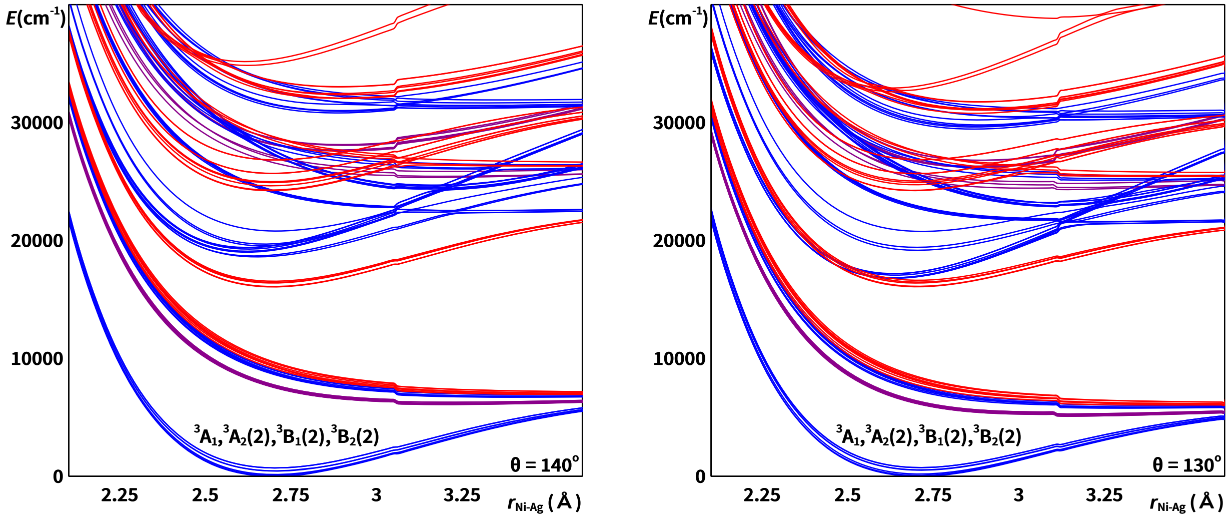

$\theta = 140°$ $\theta = 130°$

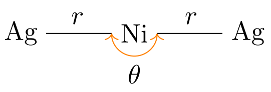

Figure B.31: $E(\theta, r; {}^{2S+1}\Gamma)$ for AgNiAg obtained at the SA-CASSCF(12,8). Zero of energy corresponds to the lowest total energy for the associated angle.

Continued on next page

Continued from previous page

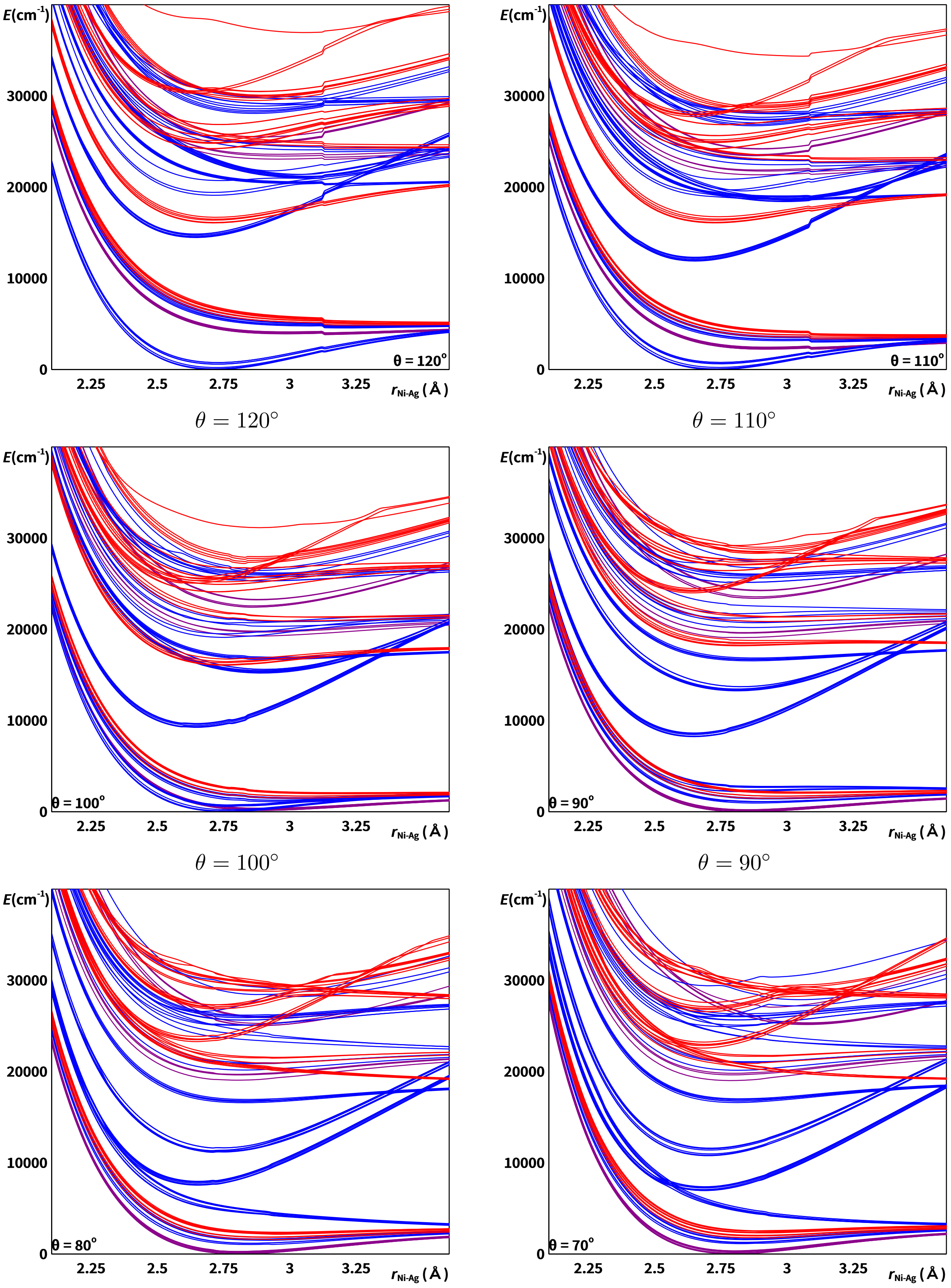

$\theta = 120^\circ$ $\theta = 110^\circ$

$\theta = 100^\circ$ $\theta = 90^\circ$

$\theta = 80^\circ$ $\theta = 70^\circ$

Continued on next page

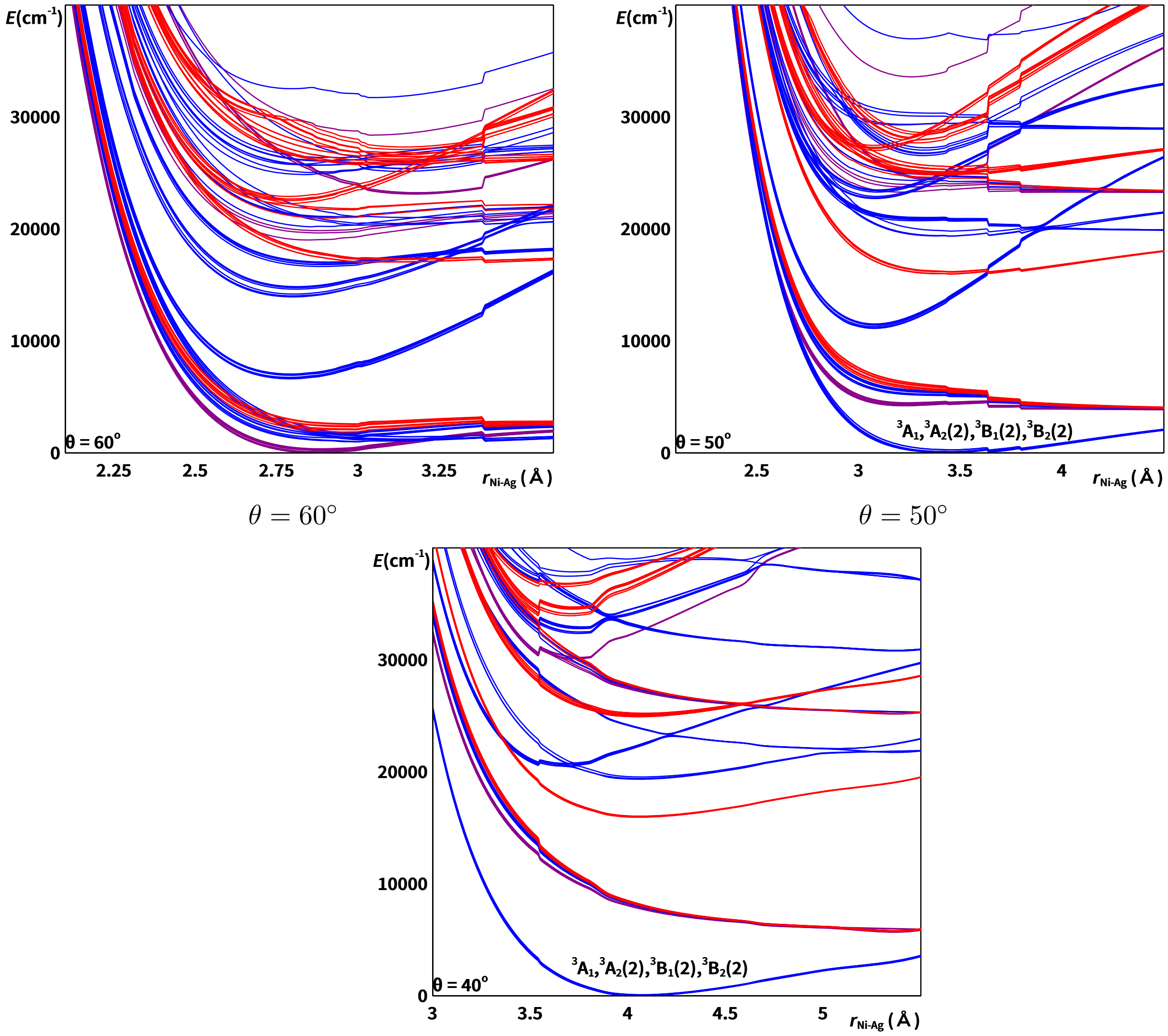

$\theta = 60°$ $\theta = 50°$

$\theta = 40°$

Continued from previous page

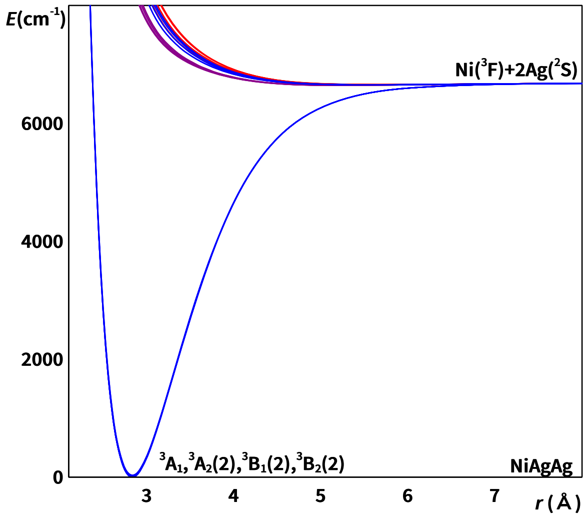

$\mathrm{Ni} \overset{r}{\text{———}} \mathrm{Ag} \overset{r}{\text{———}} \mathrm{Ag}$

Figure B.32: $E(r; {}^{2S+1}\Lambda)$ for NiAgAg obtained at the SA-CASSCF(12,8).

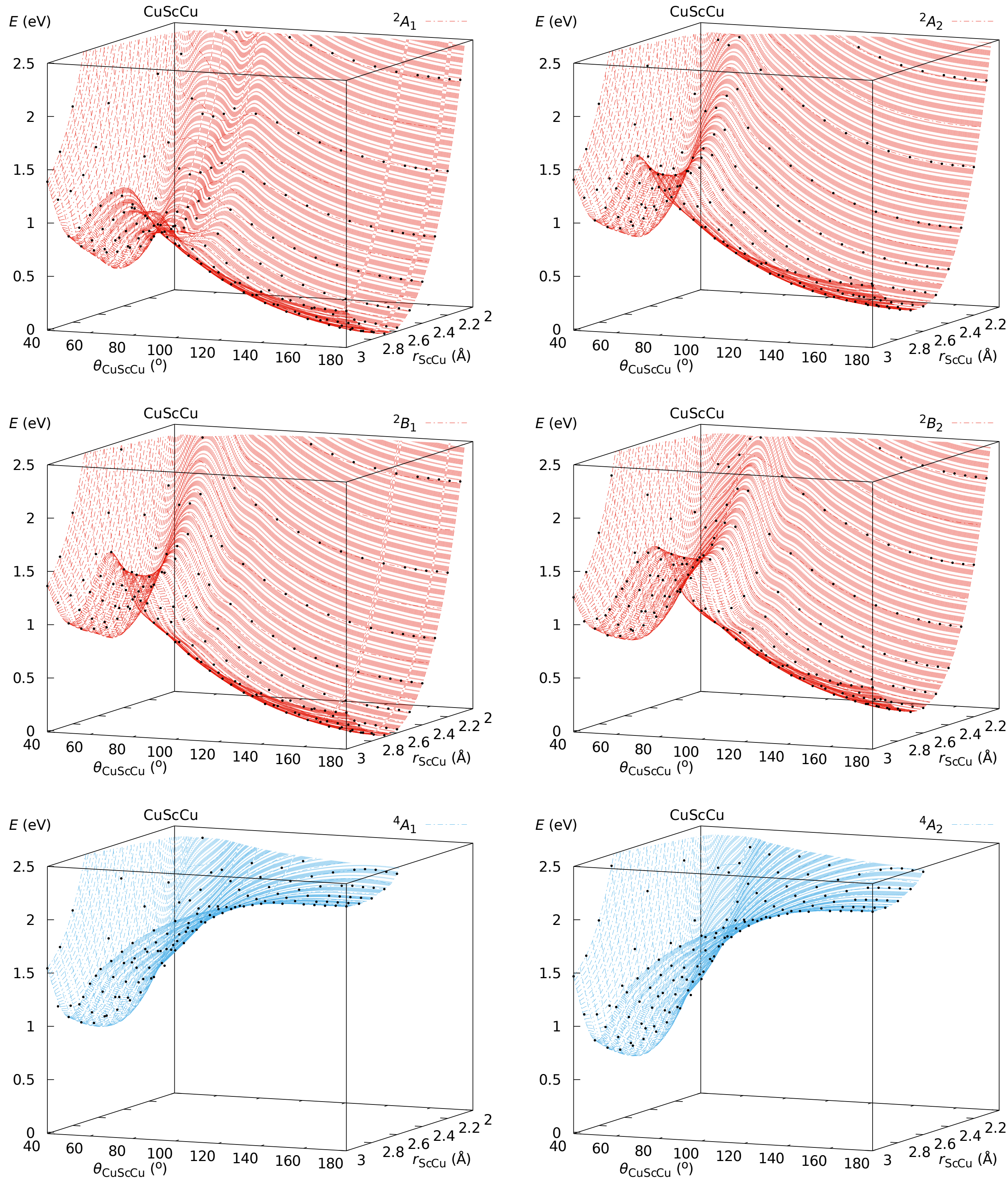

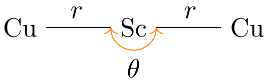

$40° \leq \theta \leq 180°, 2\ \text{Å} \leq r \leq 3\ \text{Å}, {}^{2,4}\{A_1 \oplus B_1 \oplus B_2 \oplus A_2\}$

Figure B.33: PESs, $E(\theta, r; {}^{2S+1}\Gamma)$, of CuScCu obtained at DKH-MRCI[(20+5)E,(10+8)O]. *Ab initio* points are indicated in black.

Continued on next page

Continued from previous page

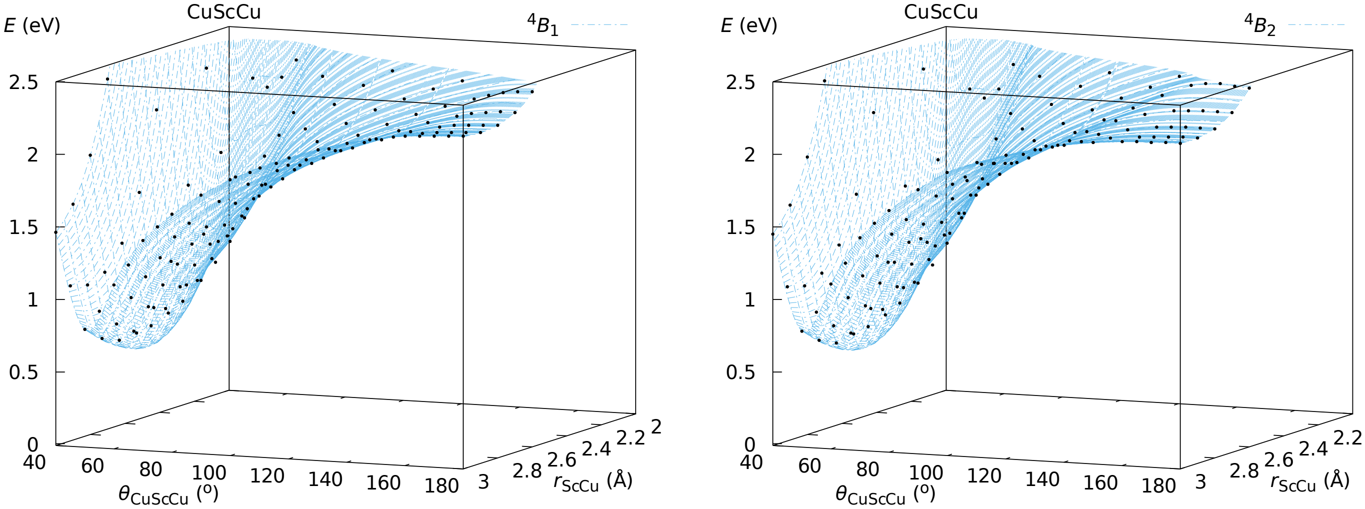

* * *

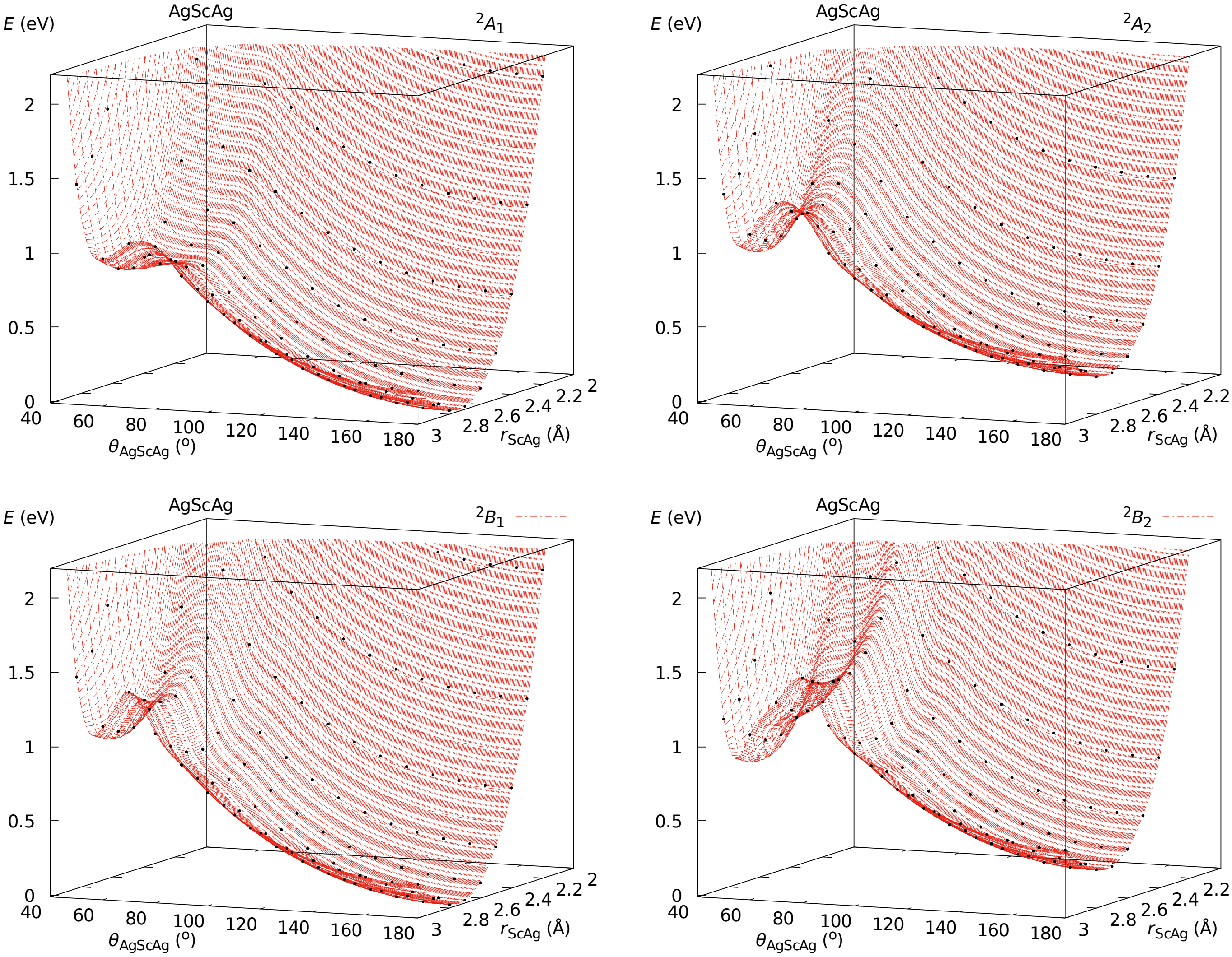

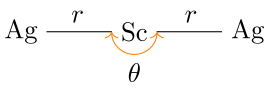

$40° \leq \theta \leq 180°, 2\ \text{Å} \leq r \leq 3\ \text{Å}, {}^{2,4}\{A_1 \oplus B_1 \oplus B_2 \oplus A_2\}$

Figure B.34: PESs, $E(\theta, r; {}^{2S+1}\Gamma)$, of AgScAg obtained at DKH-MRCI[(20+5)E,(10+8)O]. *Ab initio* points are indicated in black.

Continued on next page

Continued from previous page

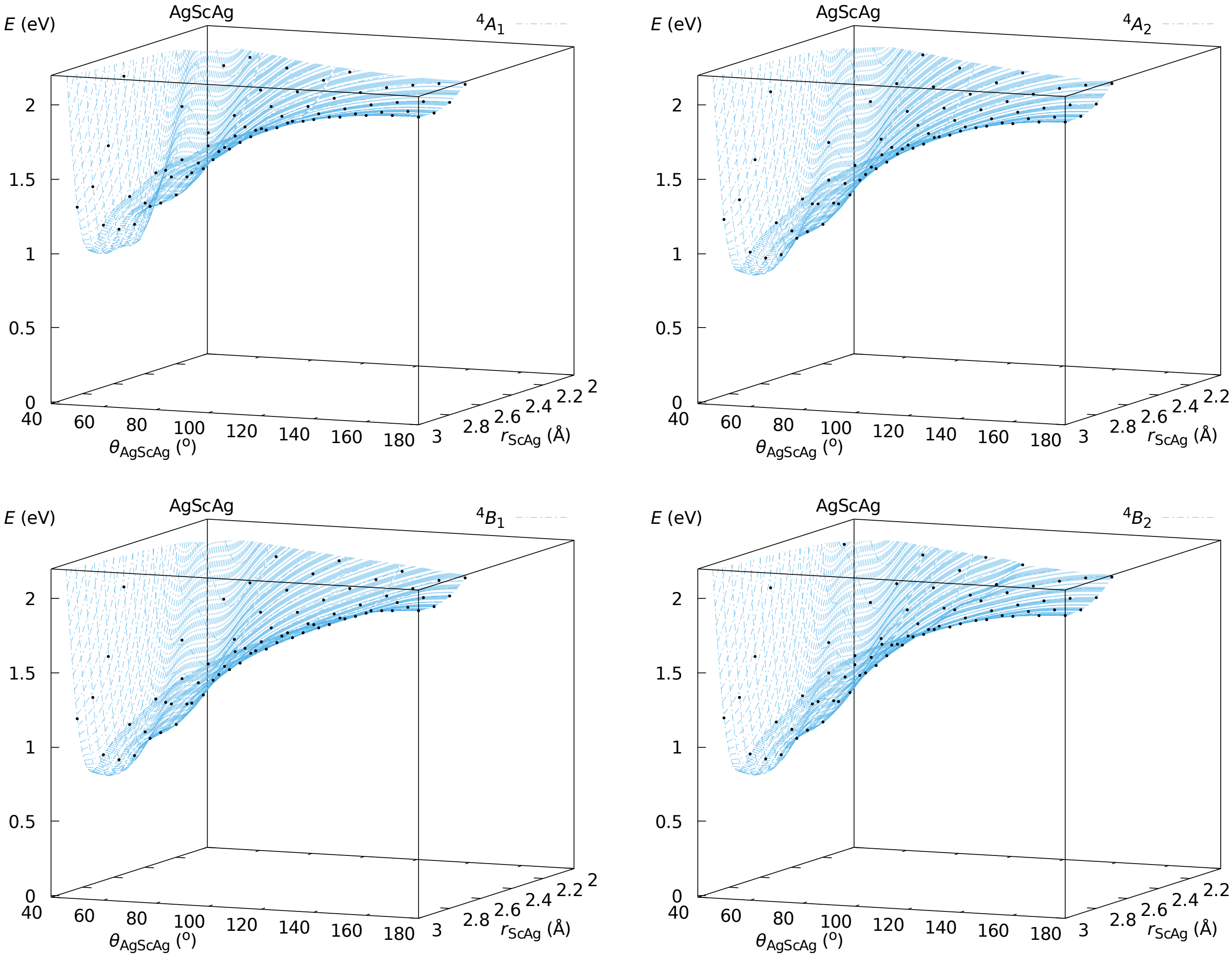

* * *

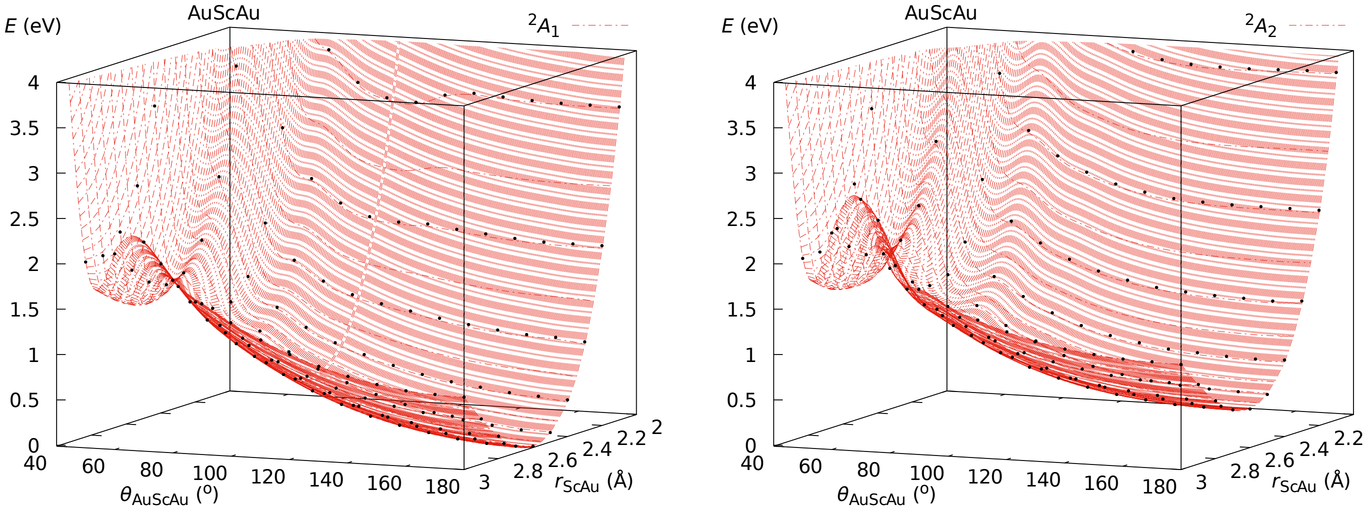

$$\mathrm{Au}\ \overset{r}{\text{——}}\ \underset{\theta}{\mathrm{Sc}}\ \overset{r}{\text{——}}\ \mathrm{Au} \qquad 40^\circ \le \theta \le 180^\circ, 2\ \text{Å} \le r \le 3\ \text{Å}, {}^{2,4}\{A_1 \oplus B_1 \oplus B_2 \oplus A_2\}$$

Figure B.35: PESs, $E(\theta, r; {}^{2S+1}\Gamma)$, of AuScAu obtained at DKH-MRCI[(20+5)E,(10+8)O]. *Ab initio* points are indicated in black.

Continued on next page

Continued from previous page

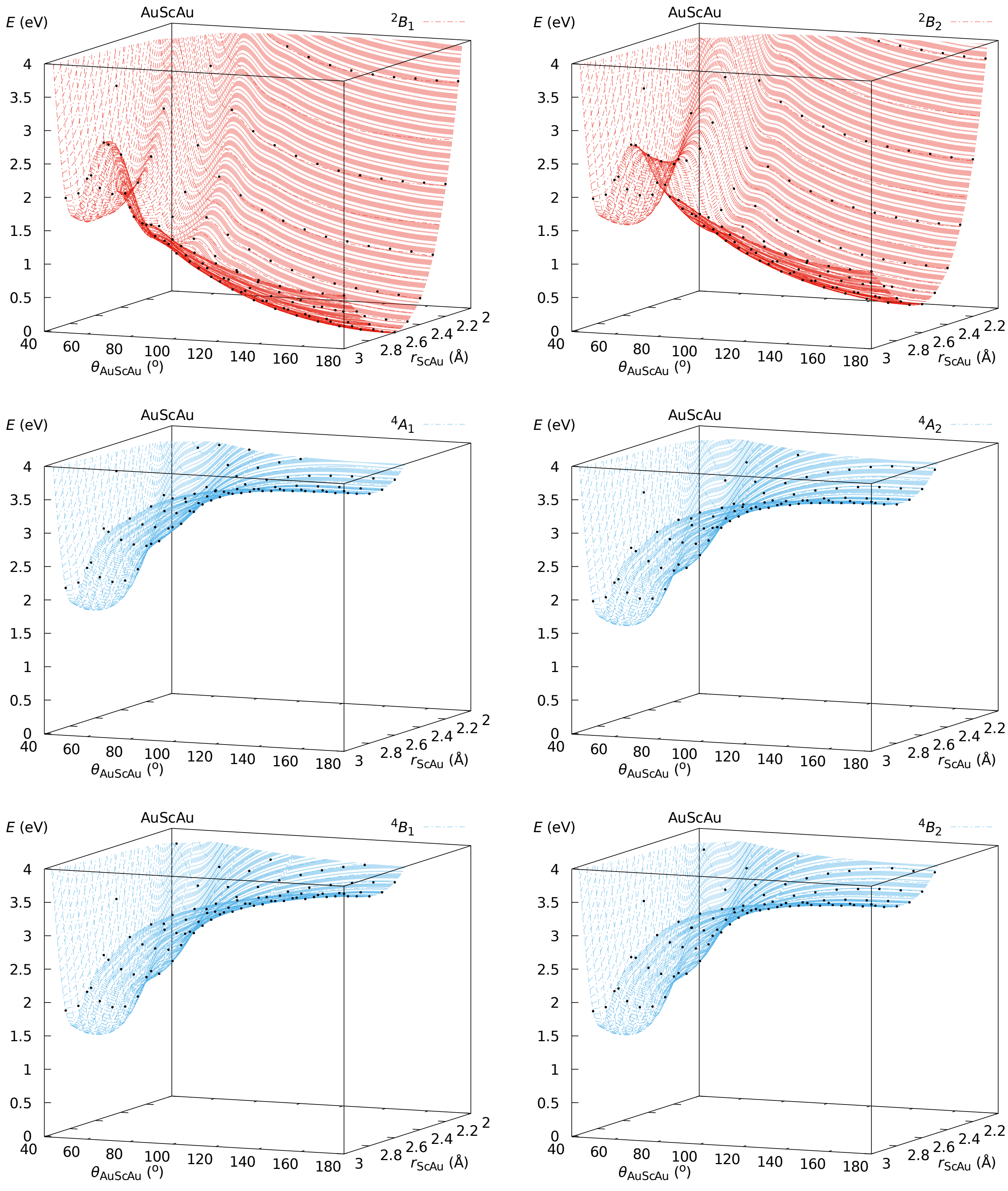

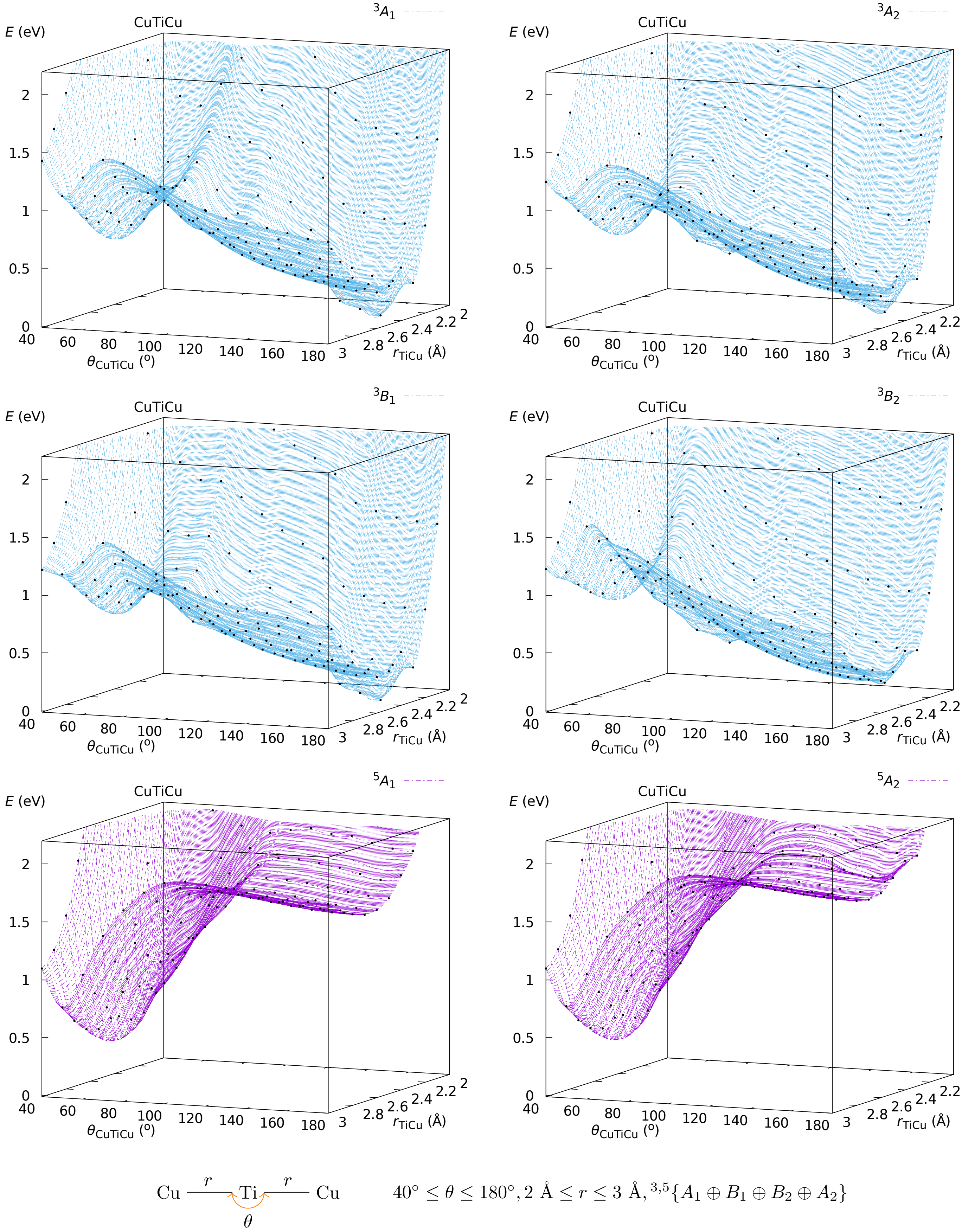

$40° \leq \theta \leq 180°, 2\ \text{Å} \leq r \leq 3\ \text{Å}, {}^{3,5}\{A_1 \oplus B_1 \oplus B_2 \oplus A_2\}$

Figure B.36: PESs, $E(\theta, r; {}^{2S+1}\Gamma)$, of CuTiCu obtained at the DKH-MRCI[(20+6)E,(10+8)O] level of theory. *Ab initio* points are indicated in black.

Continued on next page

Continued from previous page

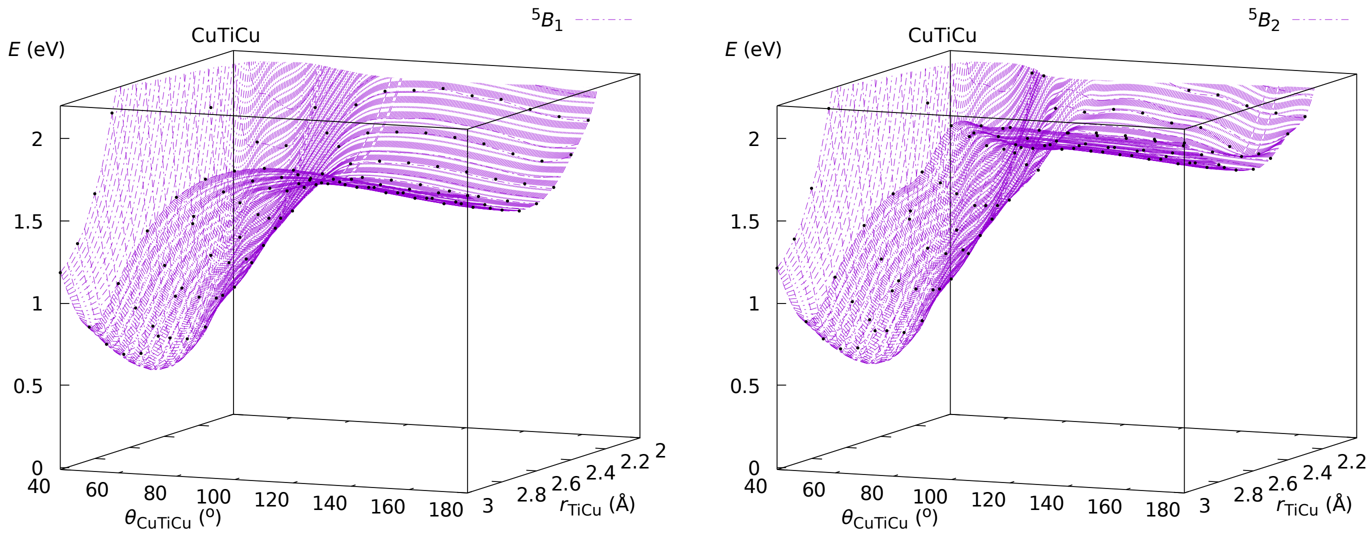

* * *

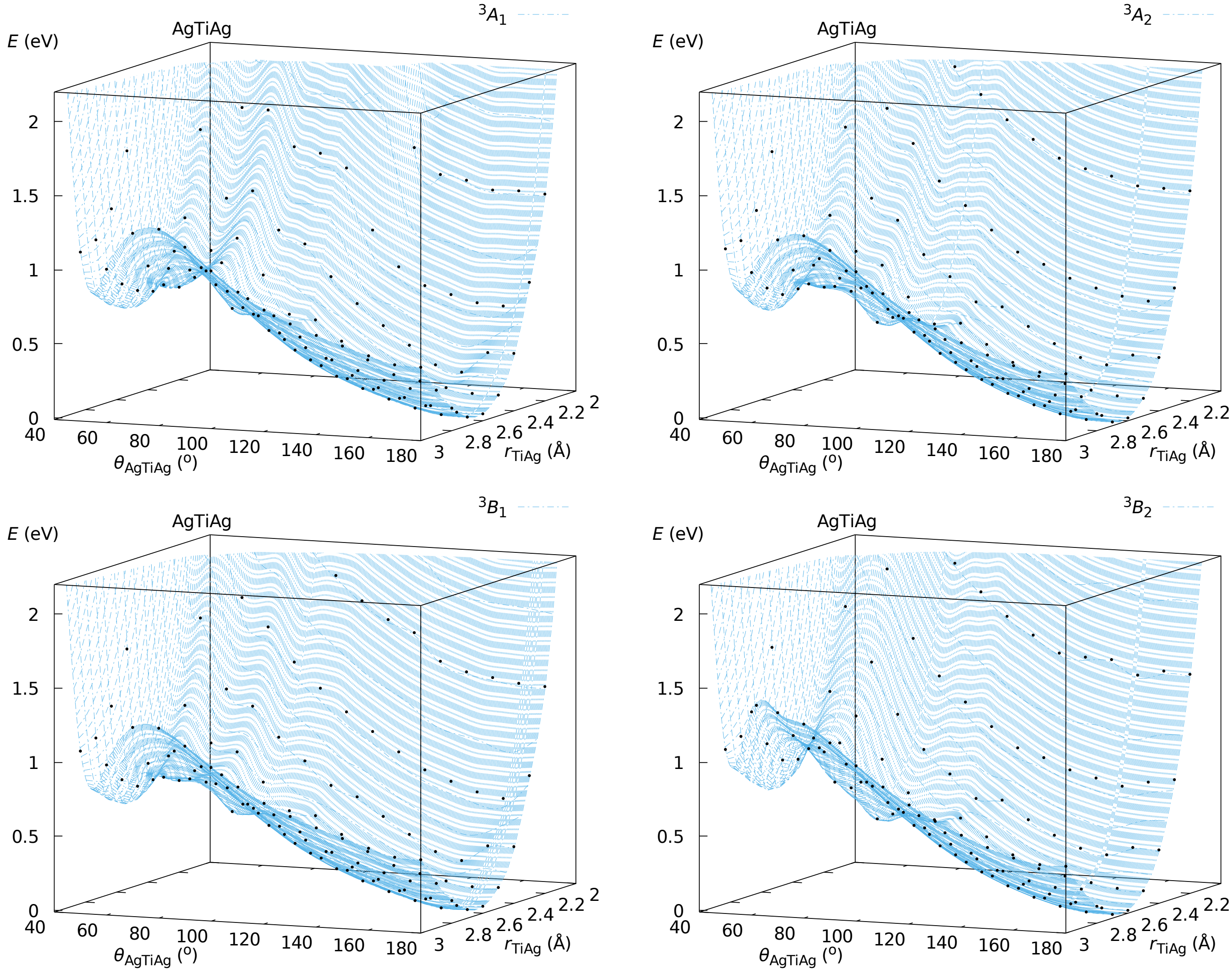

$\mathrm{Ag}\overset{r}{\text{———}}\underset{\theta}{\mathrm{Ti}}\overset{r}{\text{———}}\mathrm{Ag}$ $40^\circ \leq \theta \leq 180^\circ, 2\ \text{Å} \leq r \leq 3\ \text{Å}, {}^{3,5}\{A_1 \oplus B_1 \oplus B_2 \oplus A_2\}$

Figure B.37: PESs, $E(\theta, r; {}^{2S+1}\Gamma)$, of AgTiAg obtained at the DKH-MRCI[(20+6)E,(10+8)O] level of theory. *Ab initio* points are indicated in black.

Continued on next page

Continued from previous page

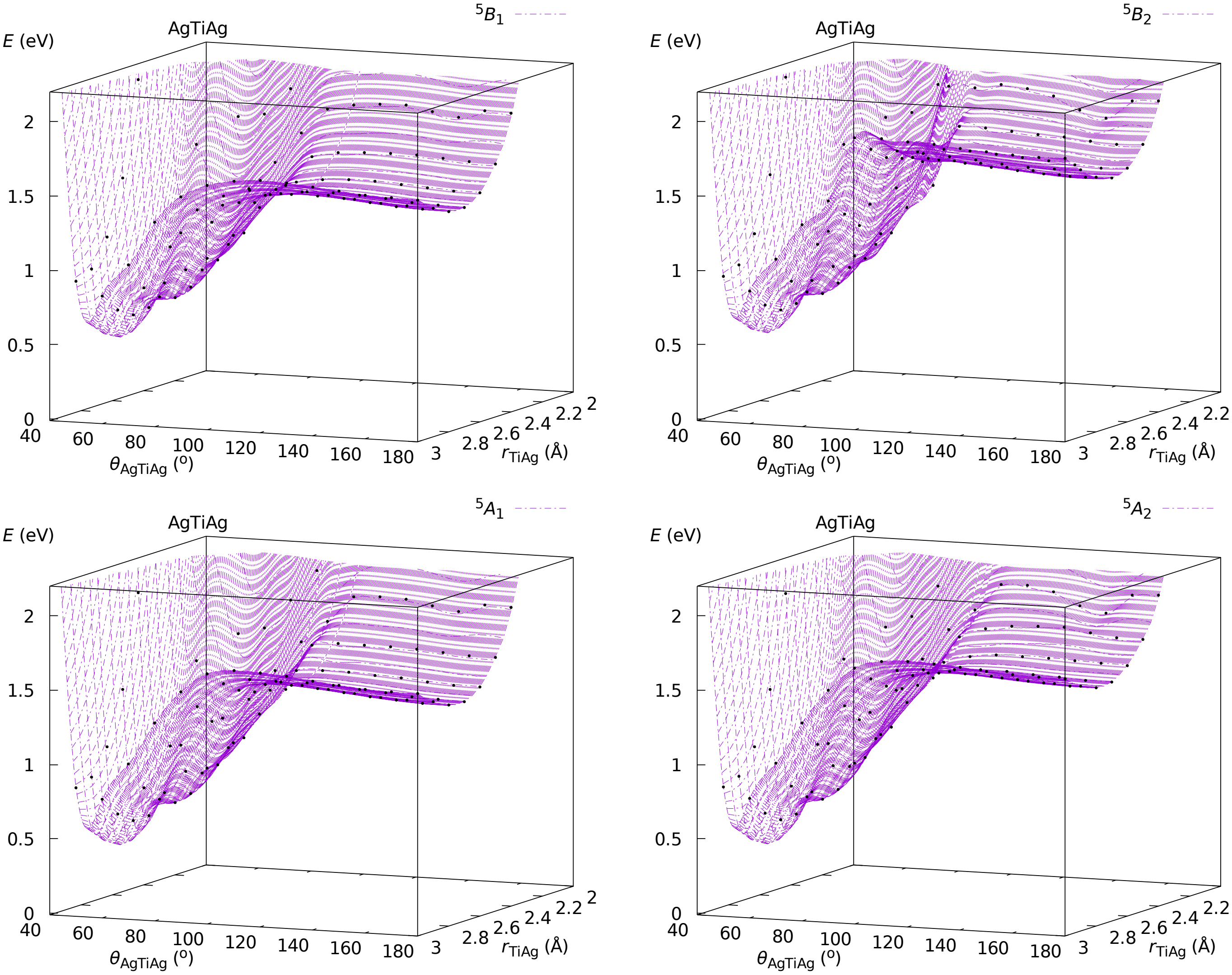

* * *

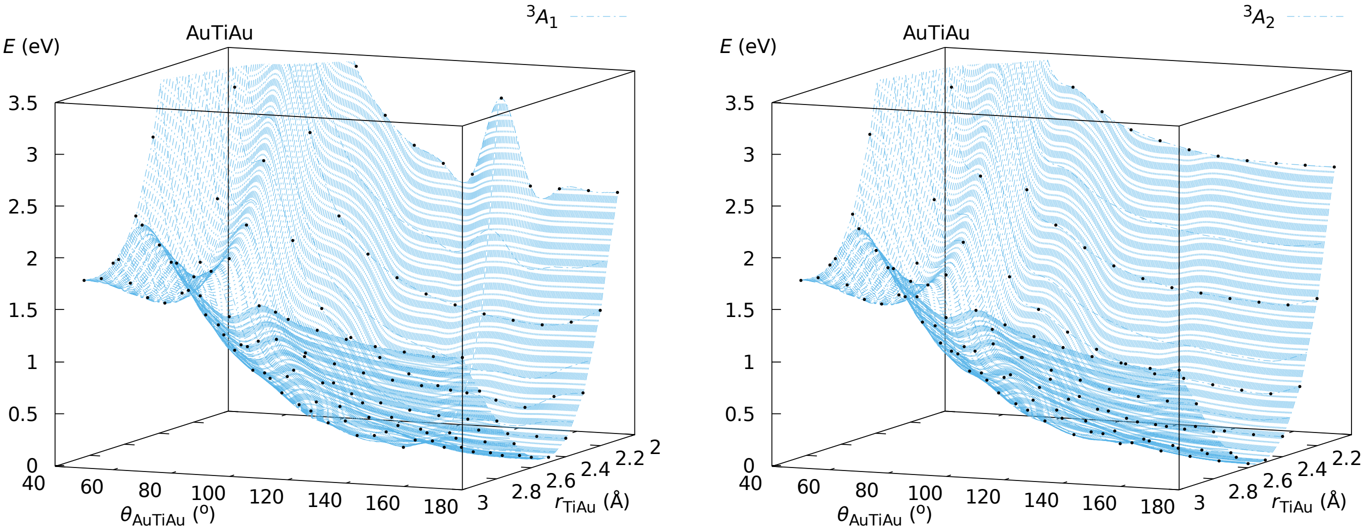

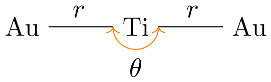

$40° \leq \theta \leq 180°, 2\ \text{Å} \leq r \leq 3\ \text{Å}, {}^{3,5}\{A_1 \oplus B_1 \oplus B_2 \oplus A_2\}$

Figure B.38: PESs, $E(\theta, r; {}^{2S+1}\Gamma)$, of AuTiAu obtained at the DKH-MRCI[(20+6)E,(10+8)O] level of theory. *Ab initio* points are indicated in black.

Continued on next page

Continued from previous page

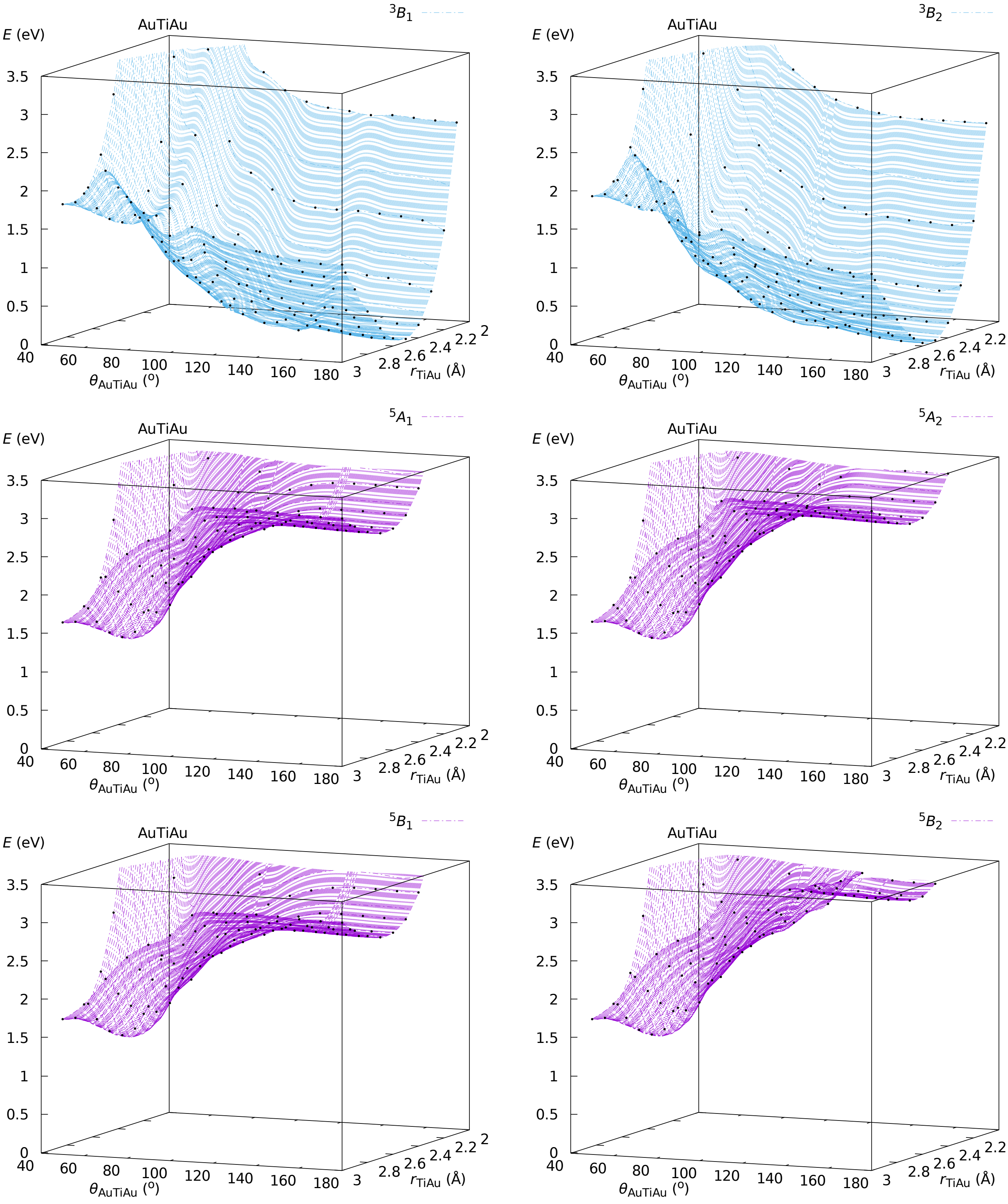

* * *

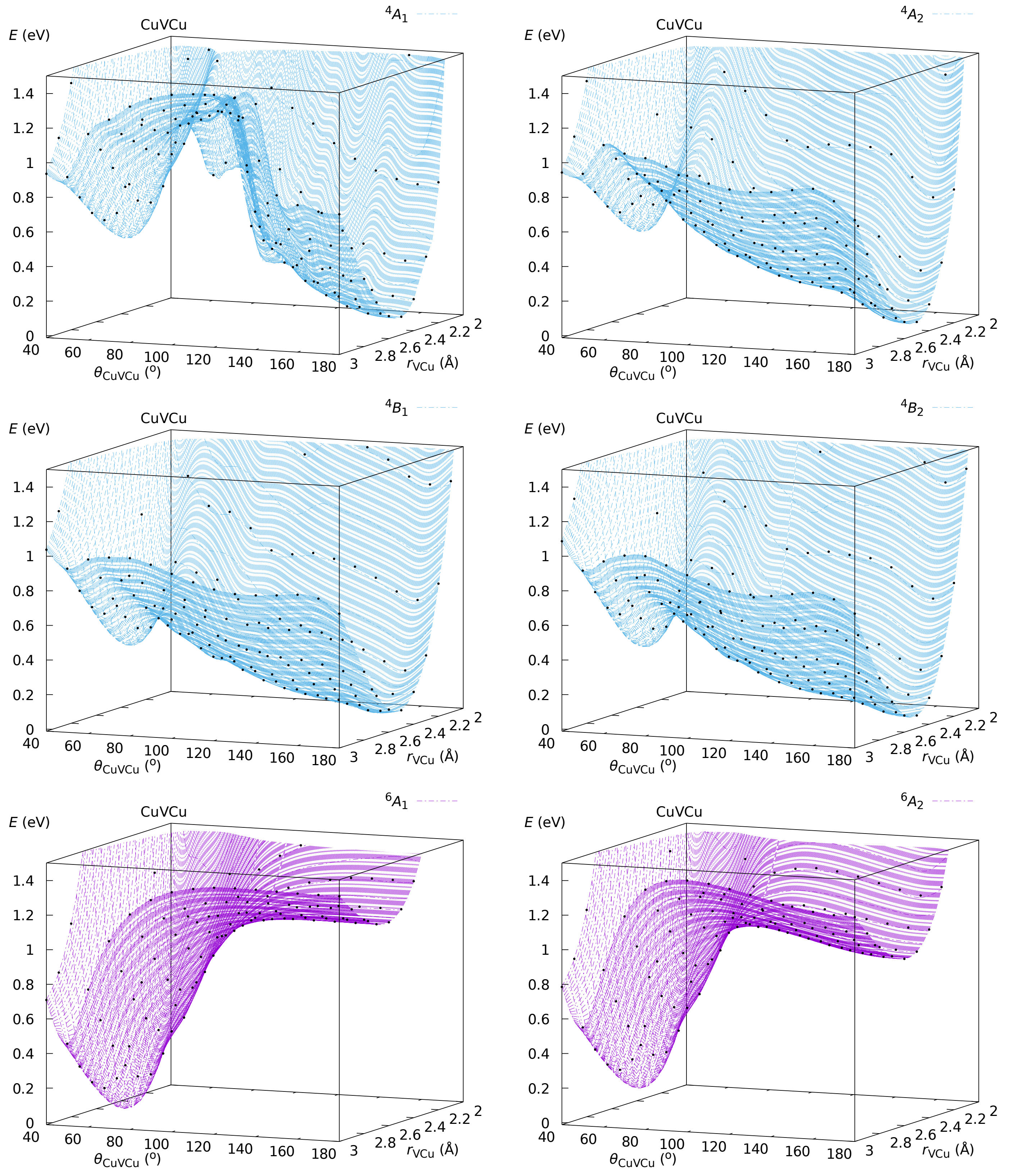

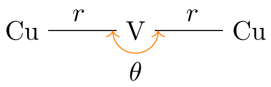

$40° \leq \theta \leq 180°, 2\ \text{Å} \leq r \leq 3\ \text{Å}, {}^{4,6}\{A_1 \oplus B_1 \oplus B_2 \oplus A_2\}$

Figure B.39: PESs, $E(\theta, r; {}^{2S+1}\Gamma)$, of CuVCu obtained at the DKH-MRCI[(20+7)E,(10+8)O] level of theory. *Ab initio* points are indicated in black.

Continued on next page

Continued from previous page

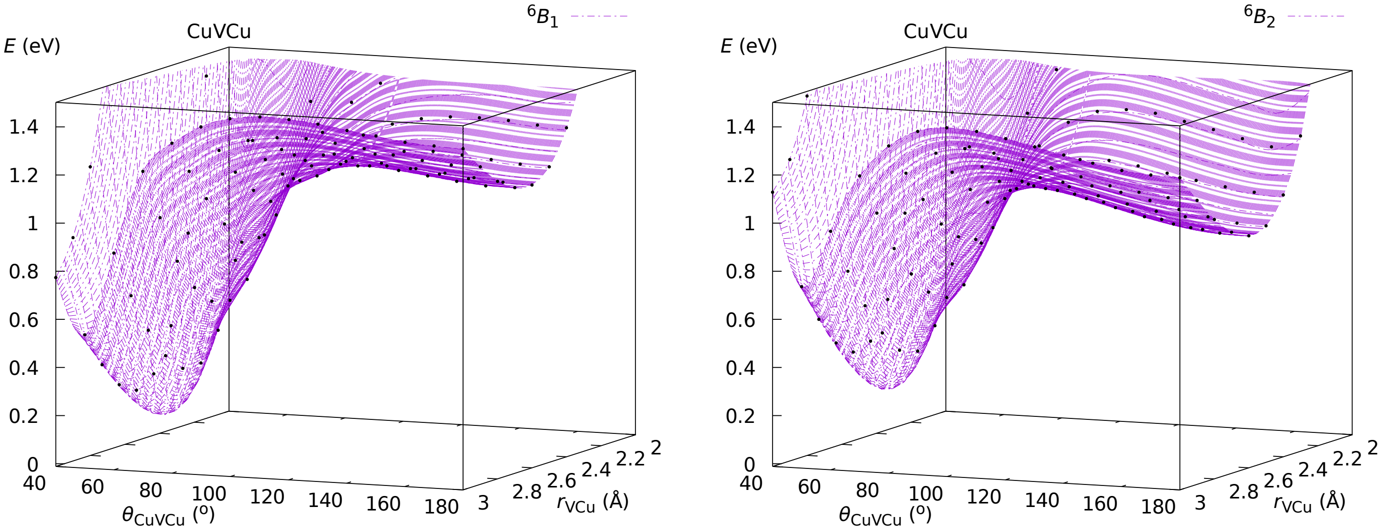

* * *

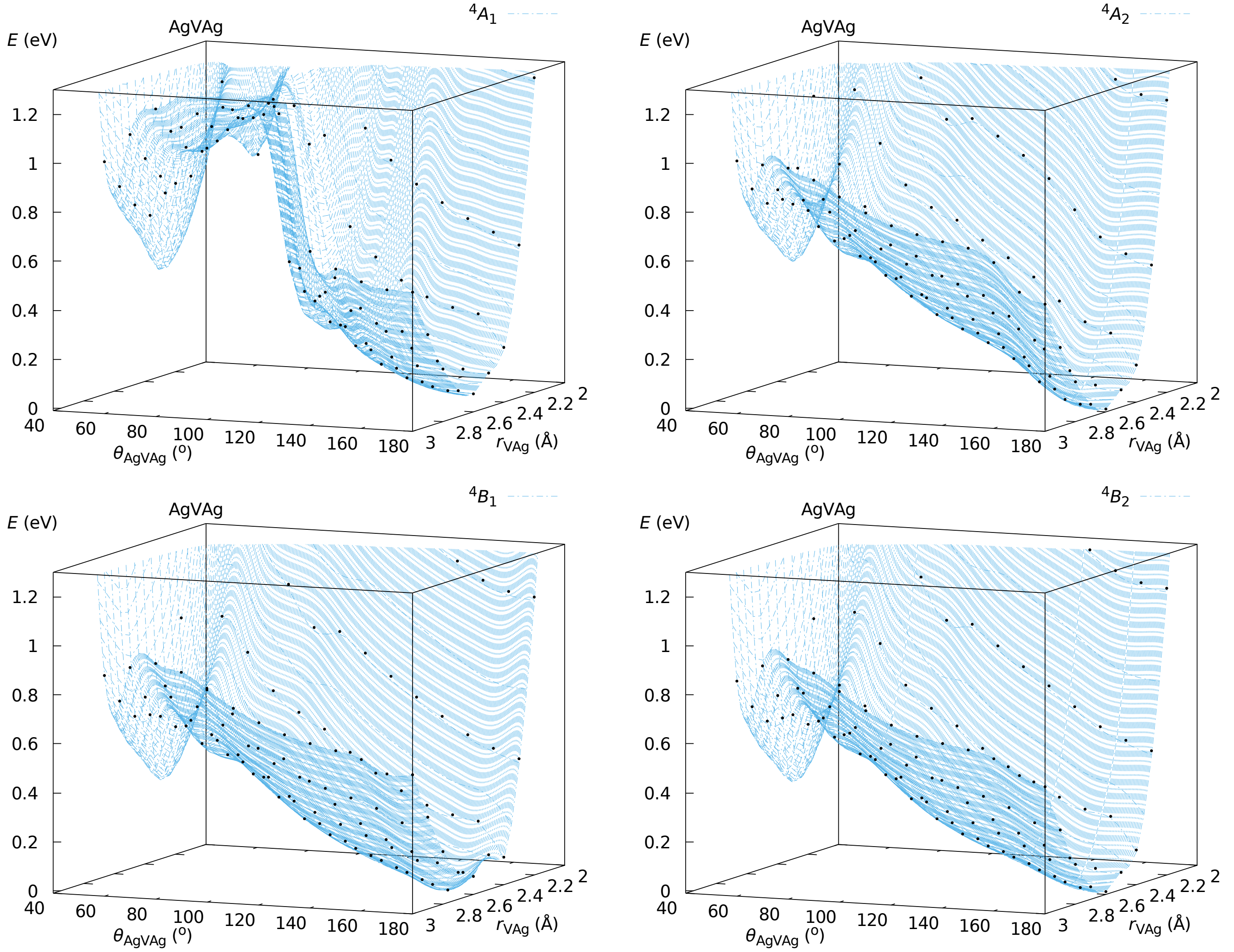

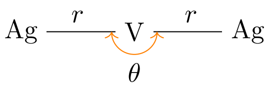

$40^\circ \le \theta \le 180^\circ, 2\ \text{Å} \le r \le 3\ \text{Å}, {}^{4,6}\{A_1 \oplus B_1 \oplus B_2 \oplus A_2\}$

Figure B.40: PESs, $E(\theta, r; {}^{2S+1}\Gamma)$, of AgVAg obtained at the DKH-MRCI[(20+7)E,(10+8)O] level of theory. *Ab initio* points are indicated in black.

Continued on next page

Continued from previous page

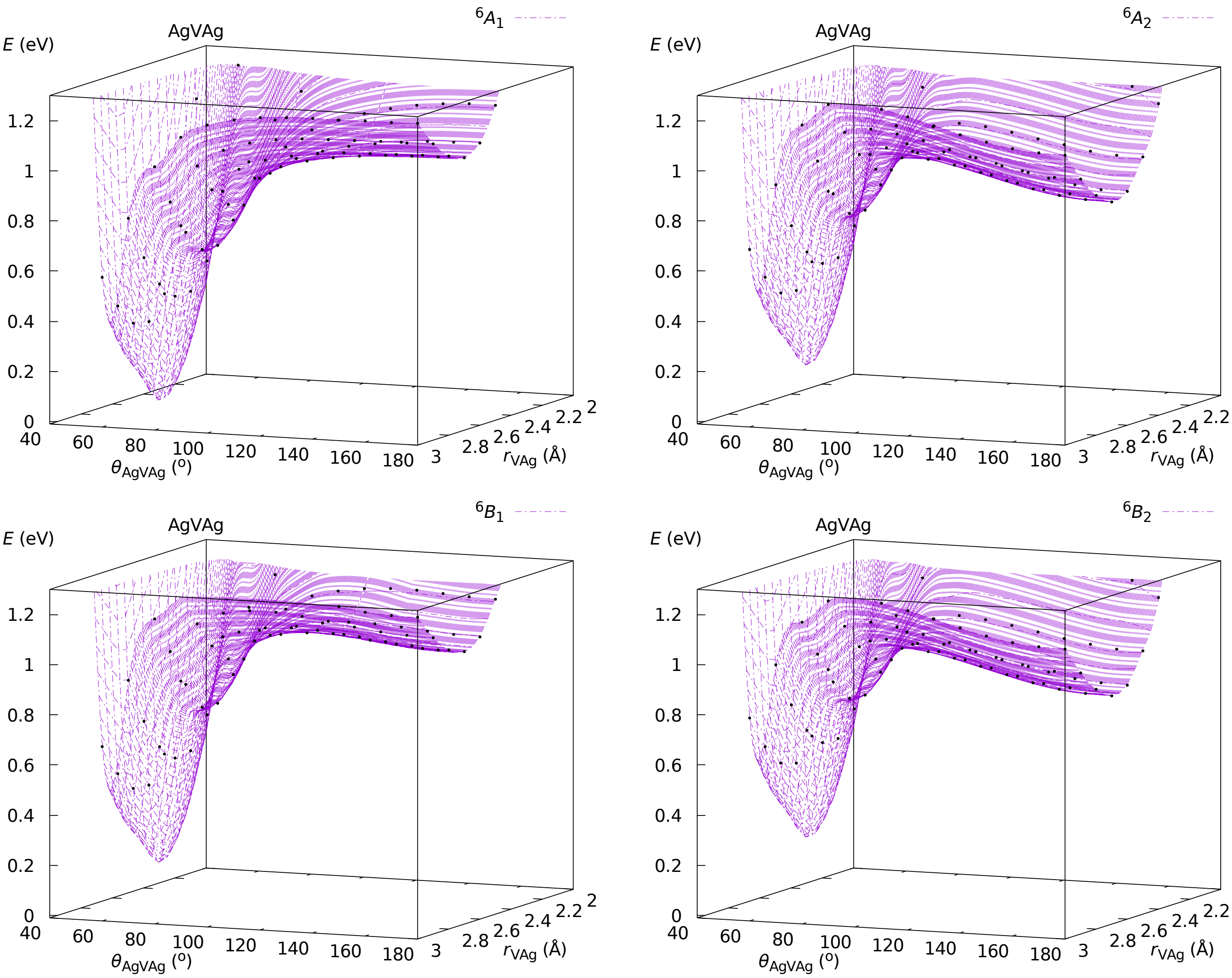

* * *

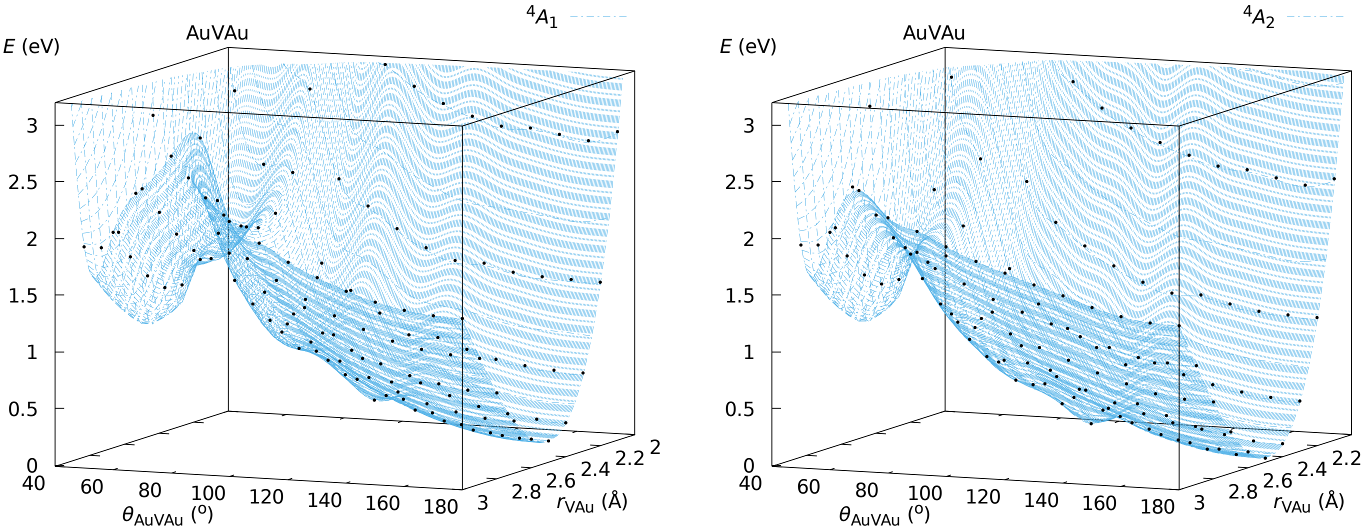

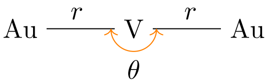

$40^\circ \leq \theta \leq 180^\circ, 2\ \text{Å} \leq r \leq 3\ \text{Å}, {}^{4,6}\{A_1 \oplus B_1 \oplus B_2 \oplus A_2\}$

Figure B.41: PESs, $E(\theta, r; {}^{2S+1}\Gamma)$, of AuVAu obtained at the DKH-MRCI[(20+7)E,(10+8)O] level of theory. *Ab initio* points are indicated in black.

Continued on next page

Continued from previous page

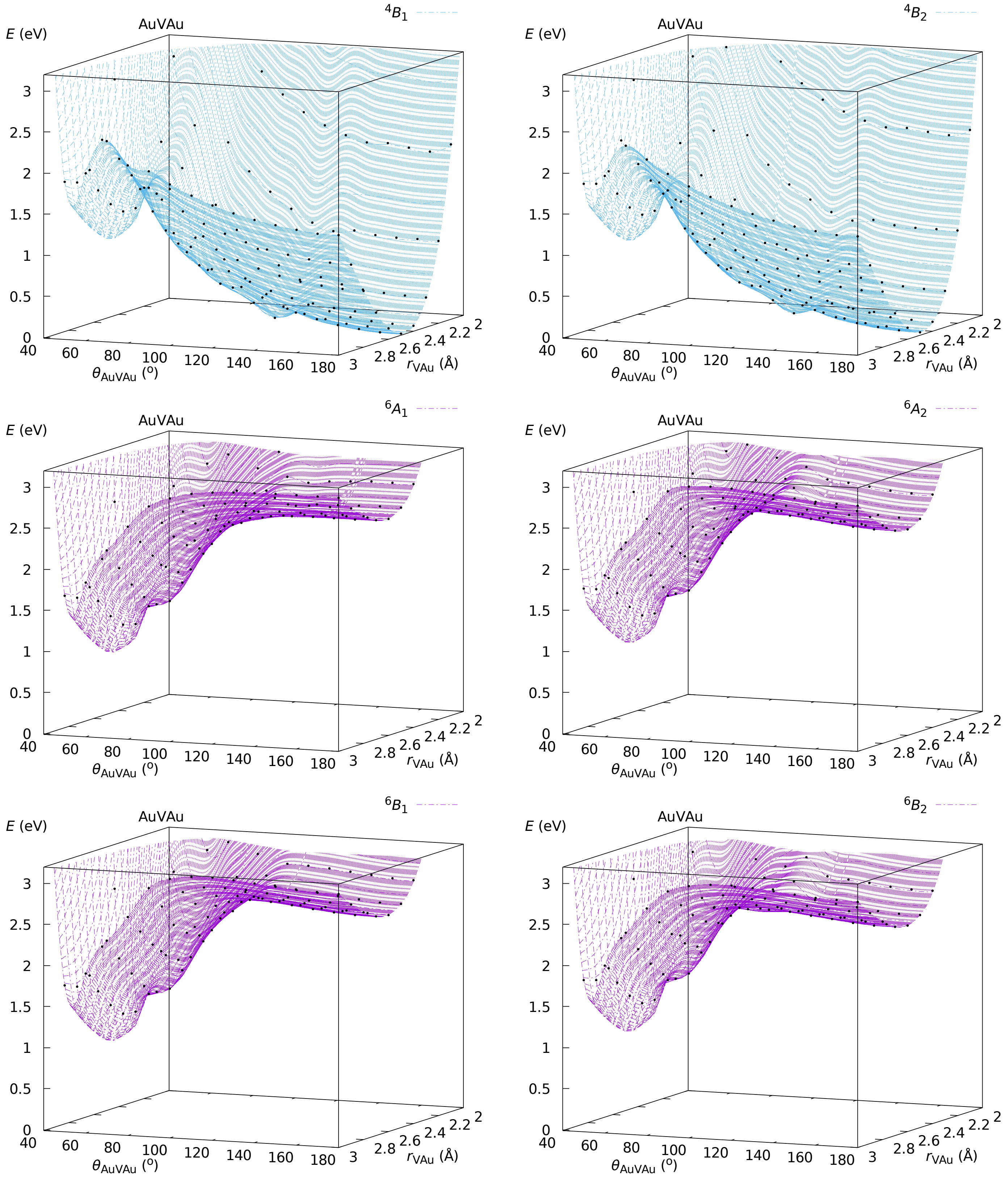

* * *

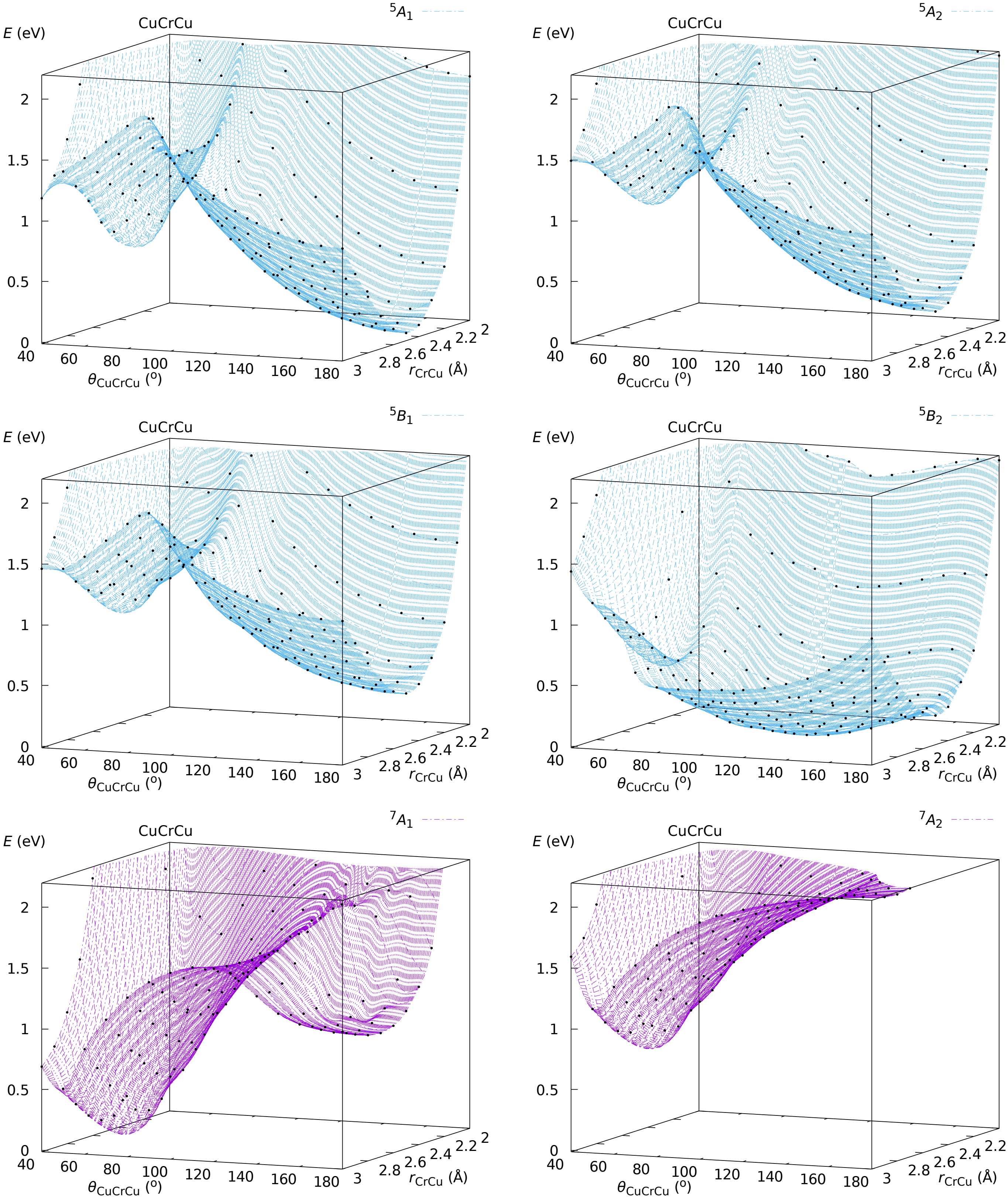

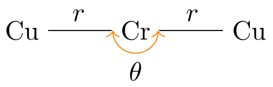

$40^\circ \leq \theta \leq 180^\circ, 2$ Å $\leq r \leq 3$ Å, $^{5,7}\{A_1 \oplus B_1 \oplus B_2 \oplus A_2\}$

Figure B.42: PESs, $E(\theta, r; {}^{2S+1}\Gamma)$, of CuCrCu obtained at the DKH-MRCI[(20+8)E,(10+8)O] level of theory. *Ab initio* points are indicated in black.

Continued on next page

Continued from previous page

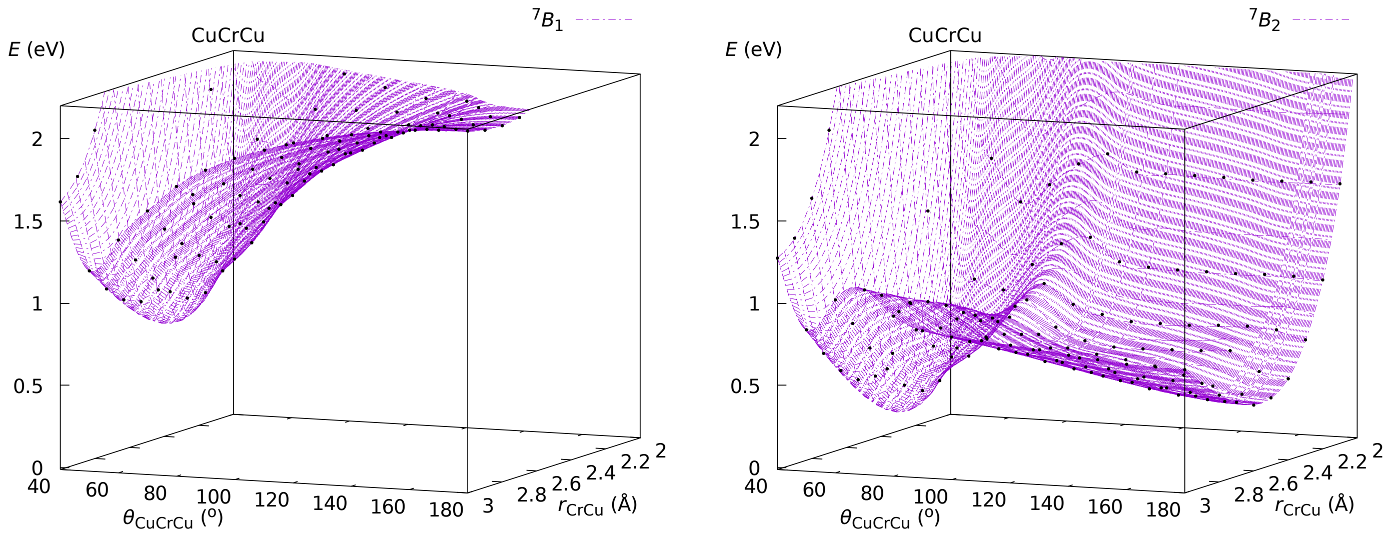

* * *

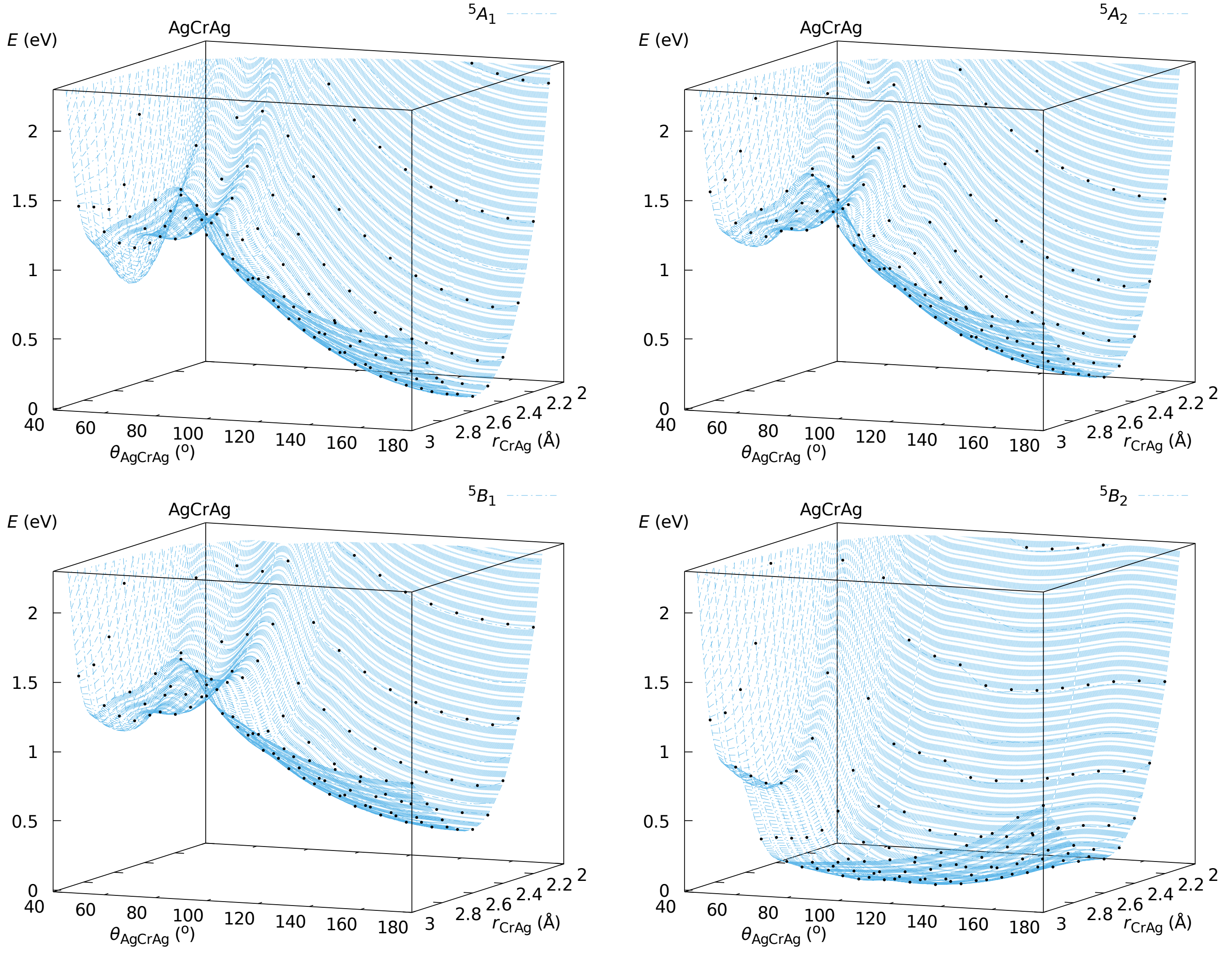

$\mathrm{Ag} \overset{r}{\text{——}} \underset{\theta}{\mathrm{Cr}} \overset{r}{\text{——}} \mathrm{Ag}$ $40^\circ \leq \theta \leq 180^\circ, 2\ \text{Å} \leq r \leq 3\ \text{Å}, {}^{5,7}\{A_1 \oplus B_1 \oplus B_2 \oplus A_2\}$

Figure B.43: PESs, $E(\theta, r; {}^{2S+1}\Gamma)$, of AgCrAg obtained at the DKH-MRCI[(20+8)E,(10+8)O] level of theory. *Ab initio* points are indicated in black.

Continued on next page

Continued from previous page

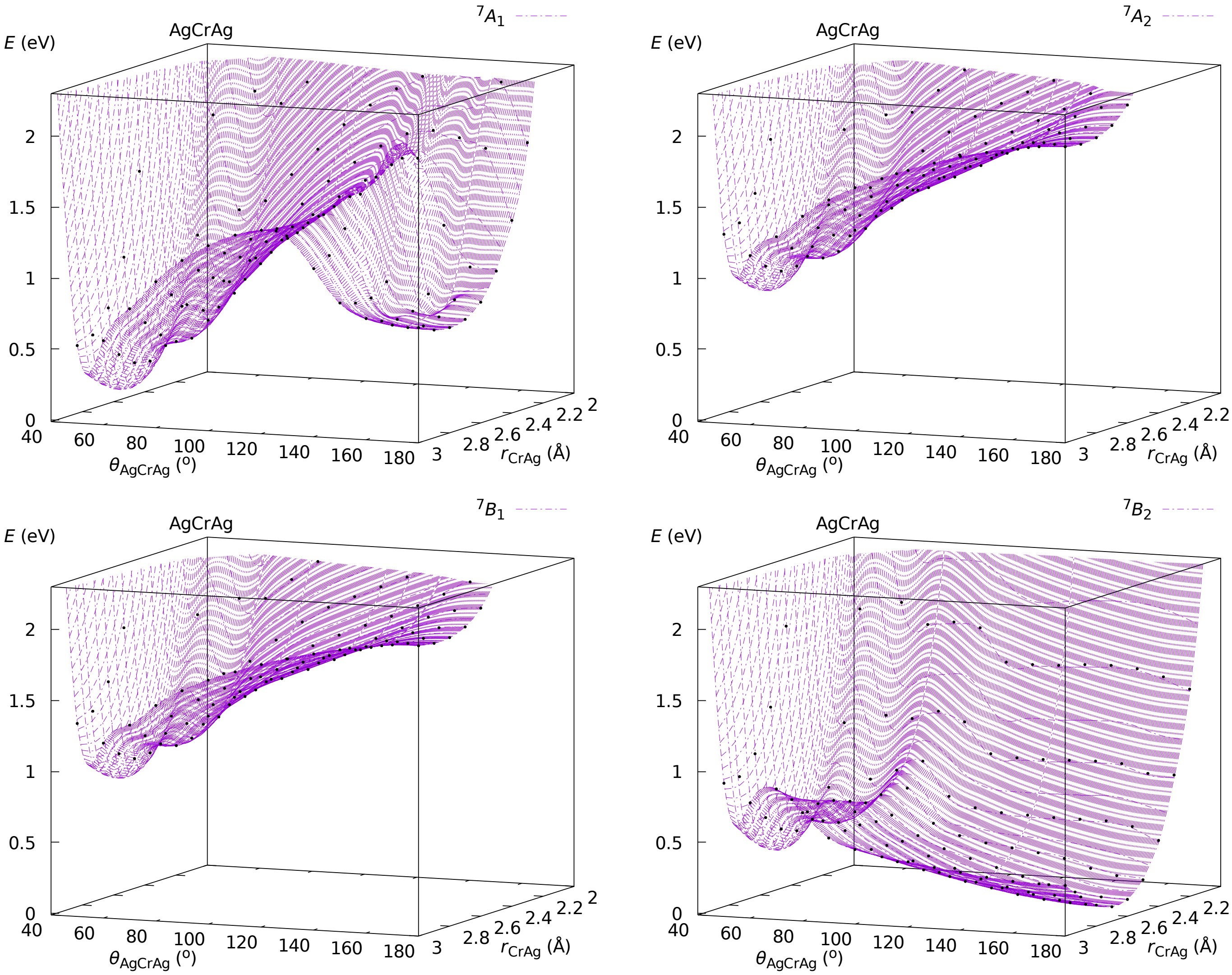

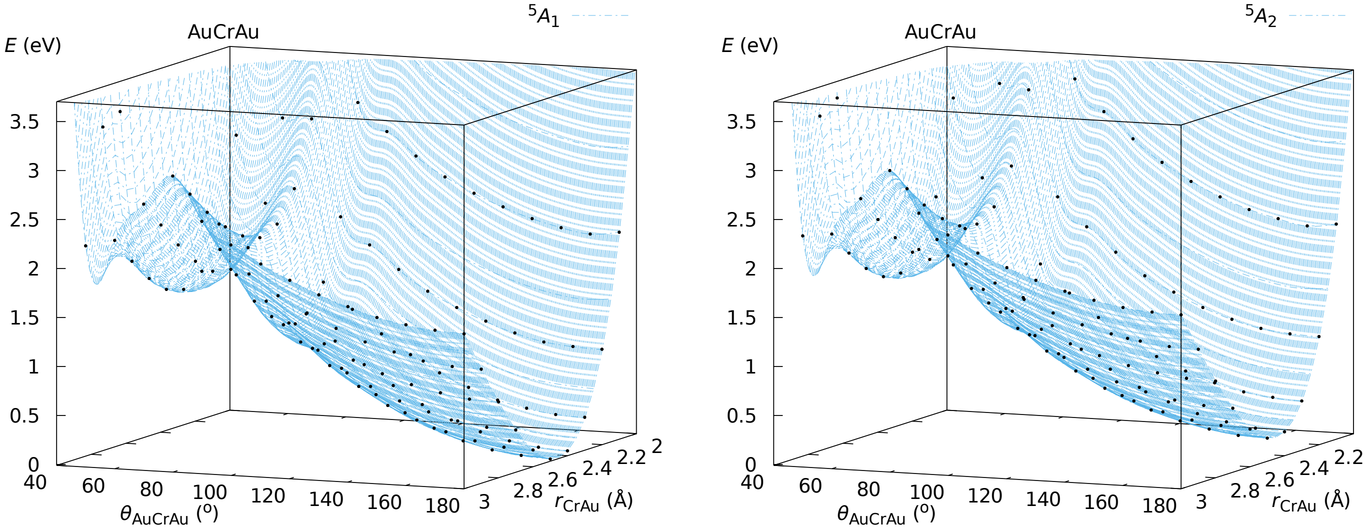

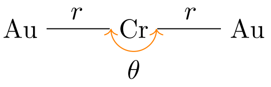

$40° \leq \theta \leq 180°, 2$ Å $\leq r \leq 3$ Å, $^{5,7}\{A_1 \oplus B_1 \oplus B_2 \oplus A_2\}$

Figure B.44: PESs, $E(\theta, r; {}^{2S+1}\Gamma)$, of AuCrAu obtained at the DKH-MRCI[(20+8)E,(10+8)O] level of theory. *Ab initio* points are indicated in black.

Continued on next page

Continued from previous page

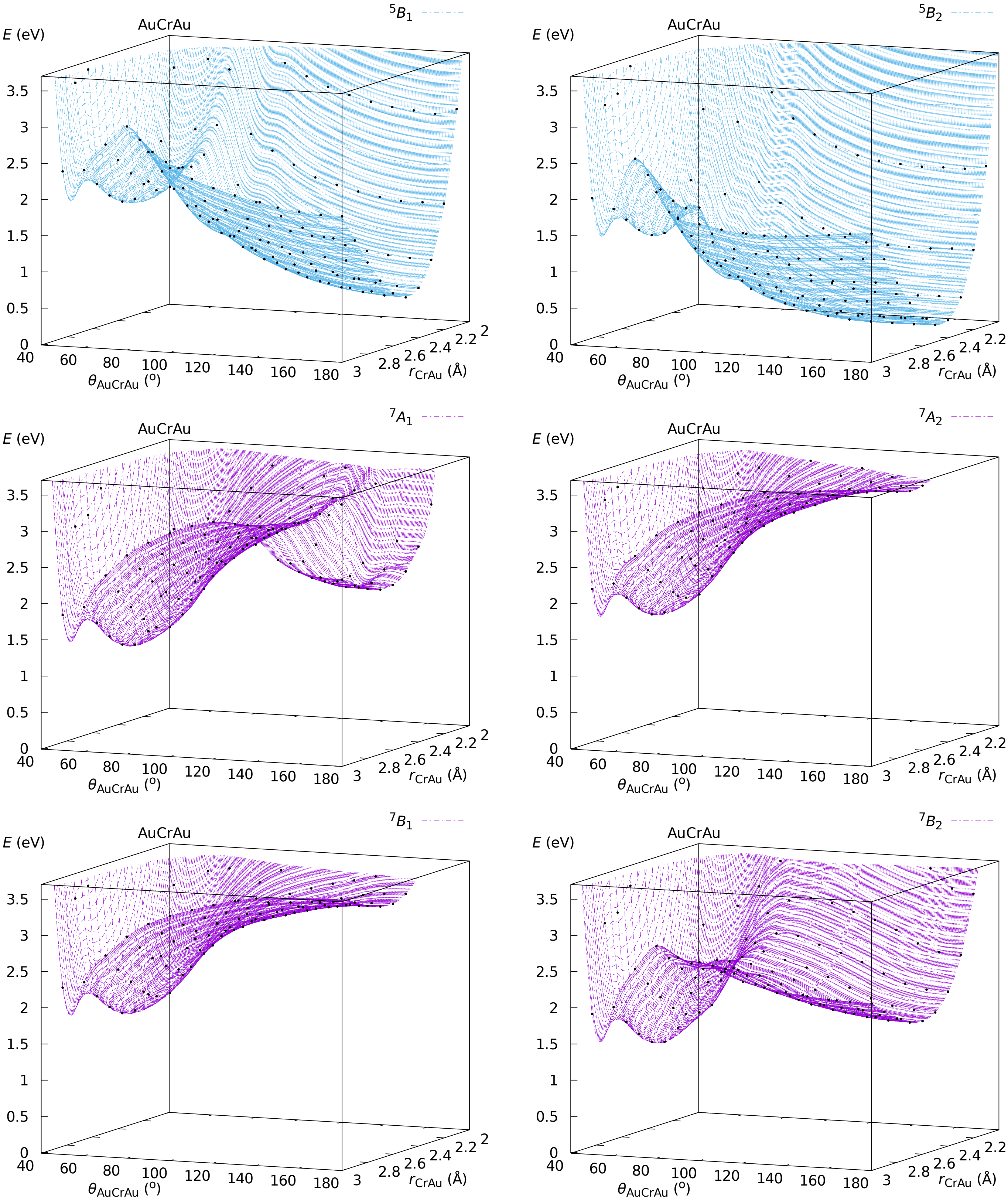

◆

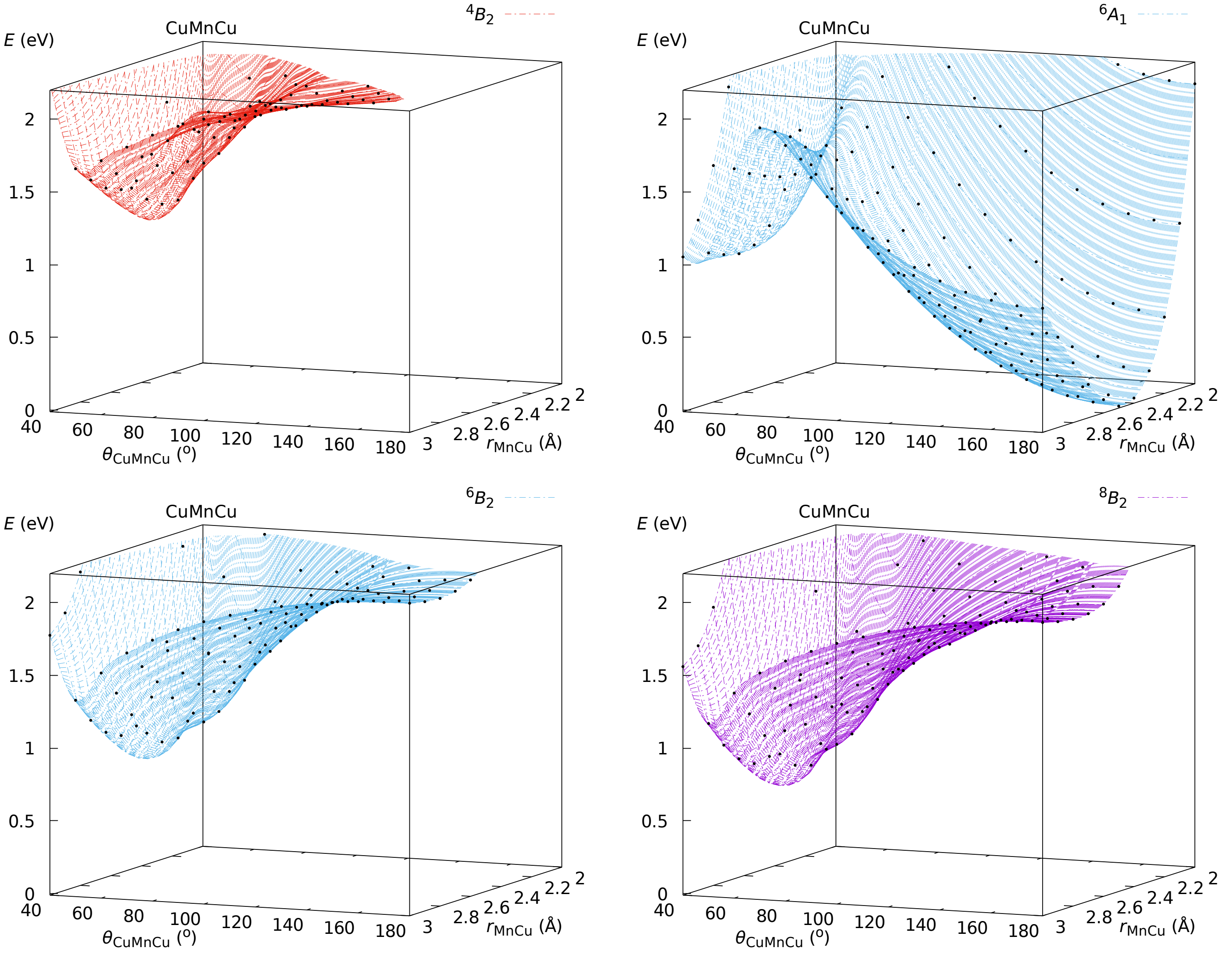

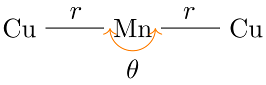

$40° \leq \theta \leq 180°, 2\ \text{Å} \leq r \leq 3\ \text{Å}, {}^4B_2 \oplus {}^6A_1 \oplus {}^6B_2 \oplus {}^8B_2$

Figure B.45: PESs, $E(\theta, r; {}^{2S+1}\Gamma)$, of CuMnCu obtained at the DKH-MRCI[(20+9)E,(10+8)O] level of theory. *Ab initio* points are indicated in black.

* * *

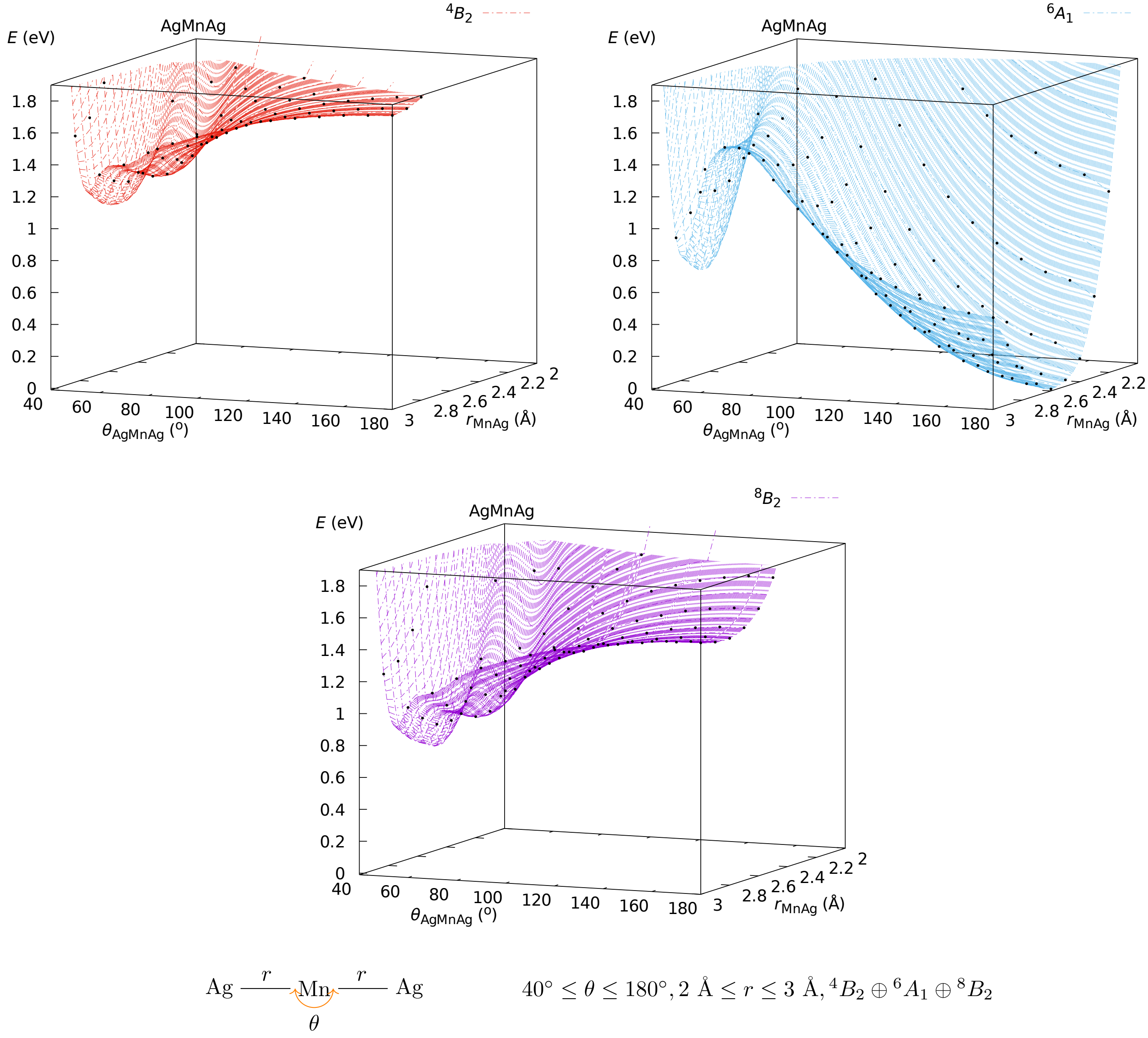

$40° \leq \theta \leq 180°, 2$ Å $\leq r \leq 3$ Å$, {}^4B_2 \oplus {}^6A_1 \oplus {}^8B_2$

Figure B.46: PESs, $E(\theta, r; {}^{2S+1}\Gamma)$, of AgMnAg obtained at the DKH-MRCI[(20+9)E,(10+8)O] level of theory. *Ab initio* points are indicated in black.

* * *

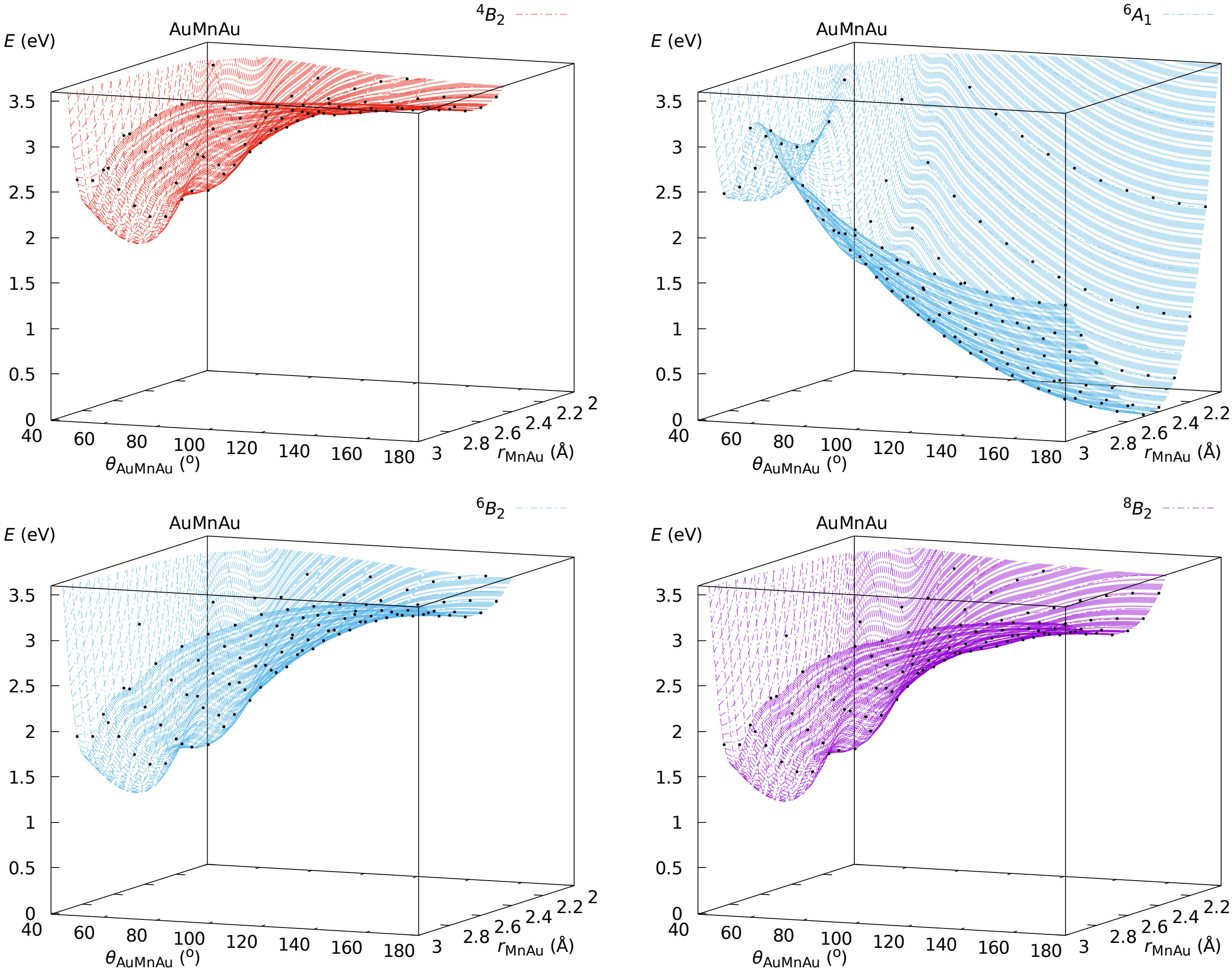

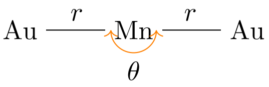

$40° \leq \theta \leq 180°, 2\ \text{Å} \leq r \leq 3\ \text{Å}, {}^4B_2 \oplus {}^6A_1 \oplus {}^6B_2 \oplus {}^8B_2$

Figure B.47: PESs, $E(\theta, r; {}^{2S+1}\Gamma)$, of AuMnAu obtained at the DKH-MRCI[(20+9)E,(10+8)O] level of theory. *Ab initio* points are indicated in black.

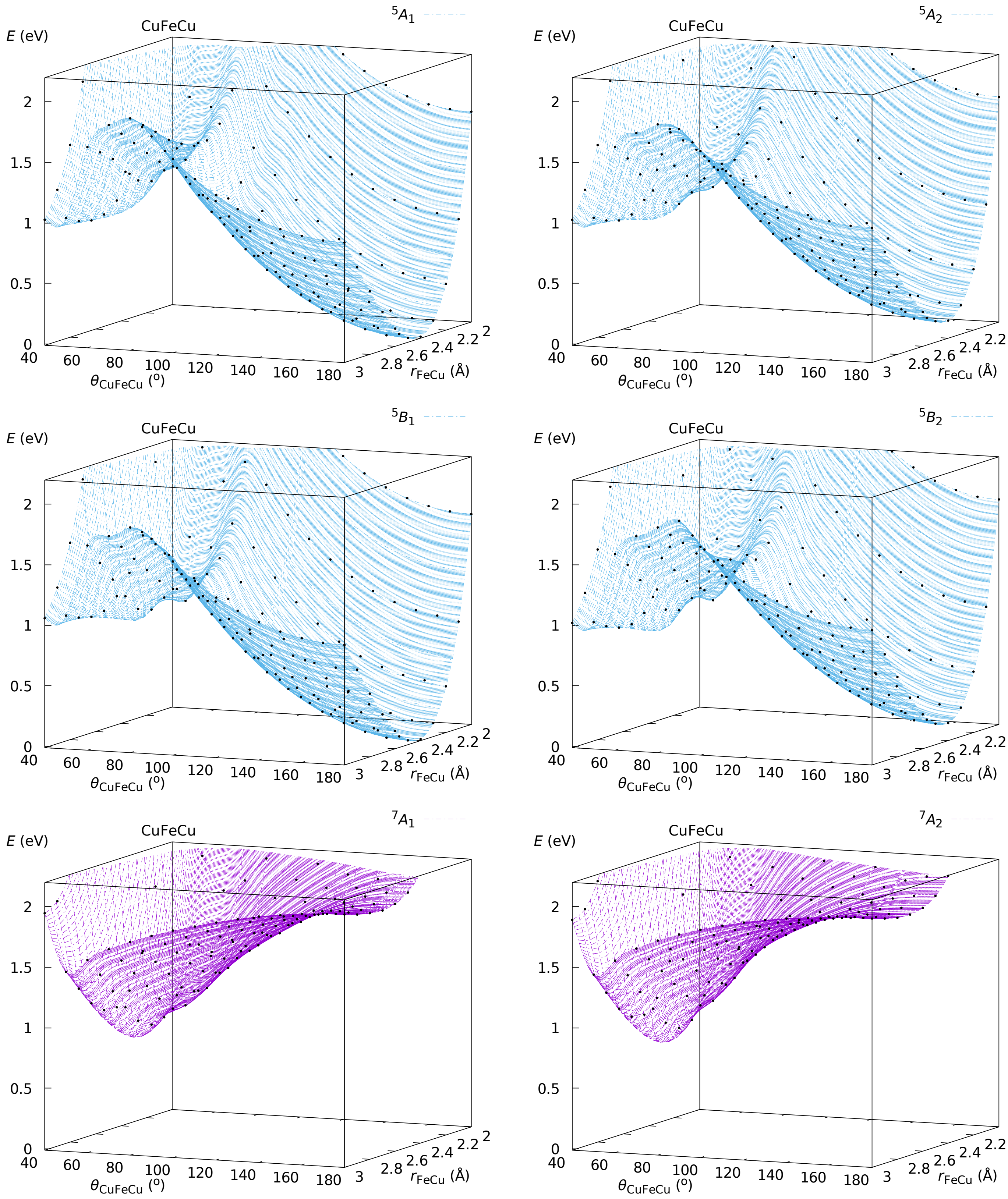

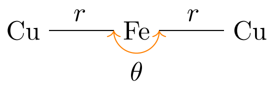

$40° \leq \theta \leq 180°, 2$ Å $\leq r \leq 3$ Å, $^{5,7}\{A_1 \oplus B_1 \oplus B_2 \oplus A_2\}$

Figure B.48: PESs, $E(\theta, r; {}^{2S+1}\Gamma)$, of CuFeCu obtained at the DKH-MRCI[(20+10)E,(10+8)O] level of theory. *Ab initio* points are indicated in black.

Continued on next page

Continued from previous page

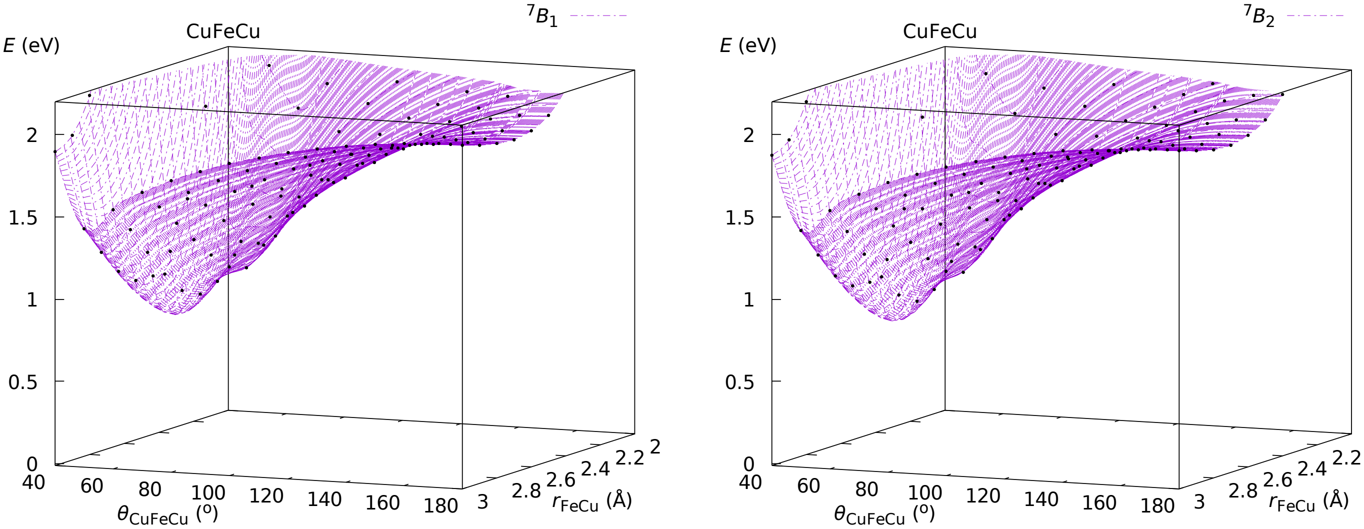

* * *

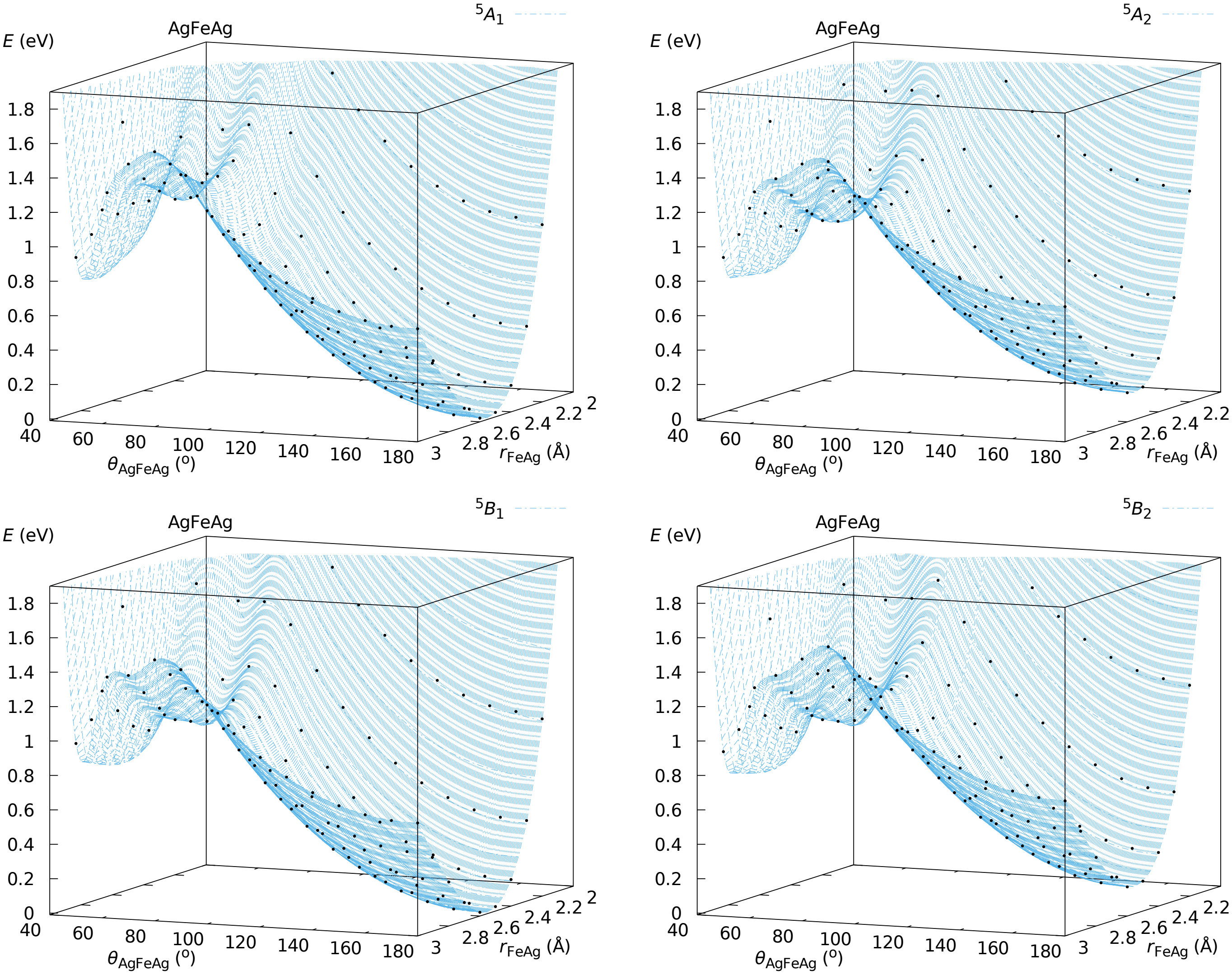

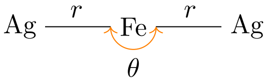

$40° \leq \theta \leq 180°, 2\text{ Å} \leq r \leq 3\text{ Å}, {}^{5,7}\{A_1 \oplus B_1 \oplus B_2 \oplus A_2\}$

Figure B.49: PESs, $E(\theta, r; {}^{2S+1}\Gamma)$, of AgFeAg obtained at the DKH-MRCI[(20+10)E,(10+8)O] level of theory. *Ab initio* points are indicated in black.

Continued on next page

Continued from previous page

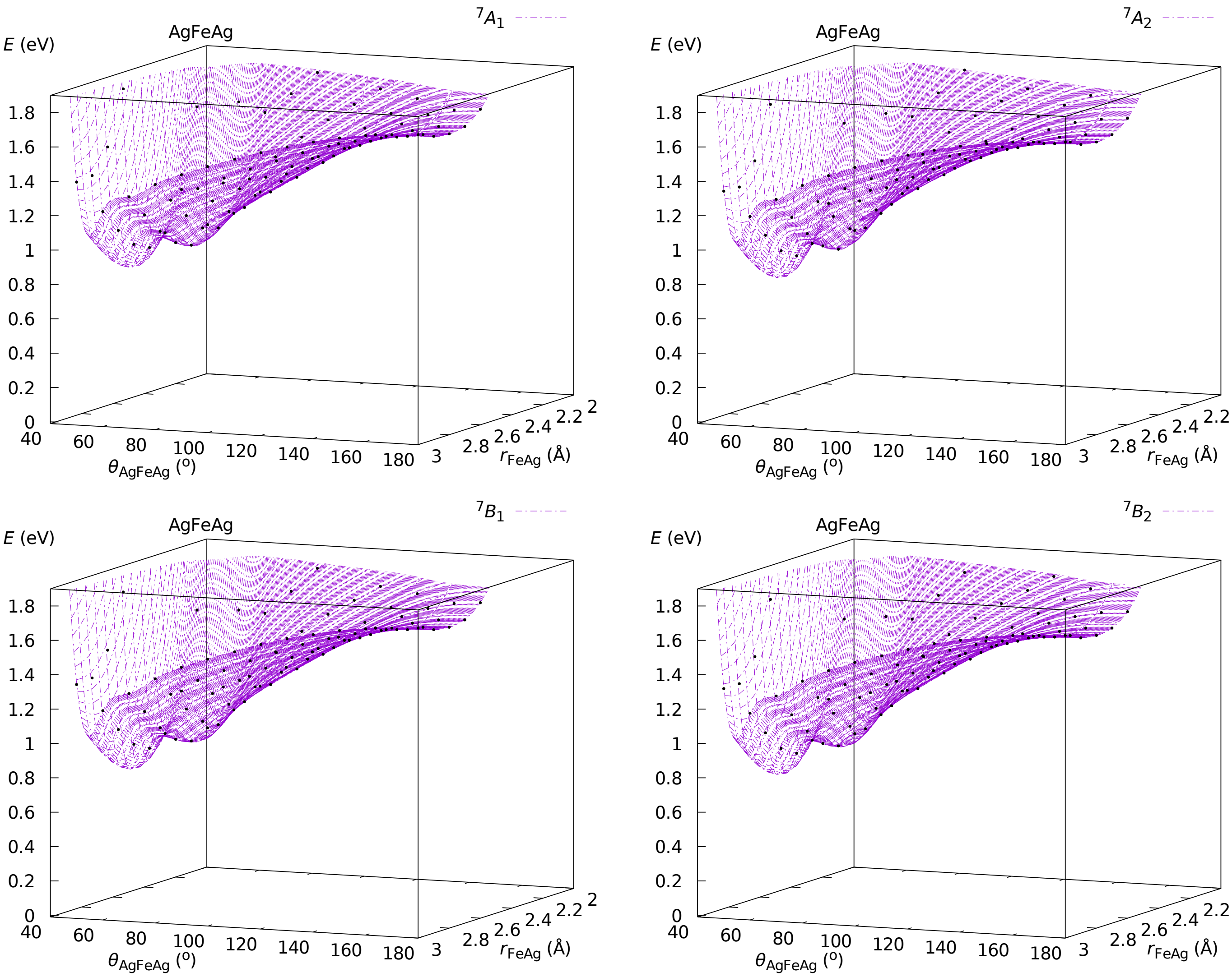

* * *

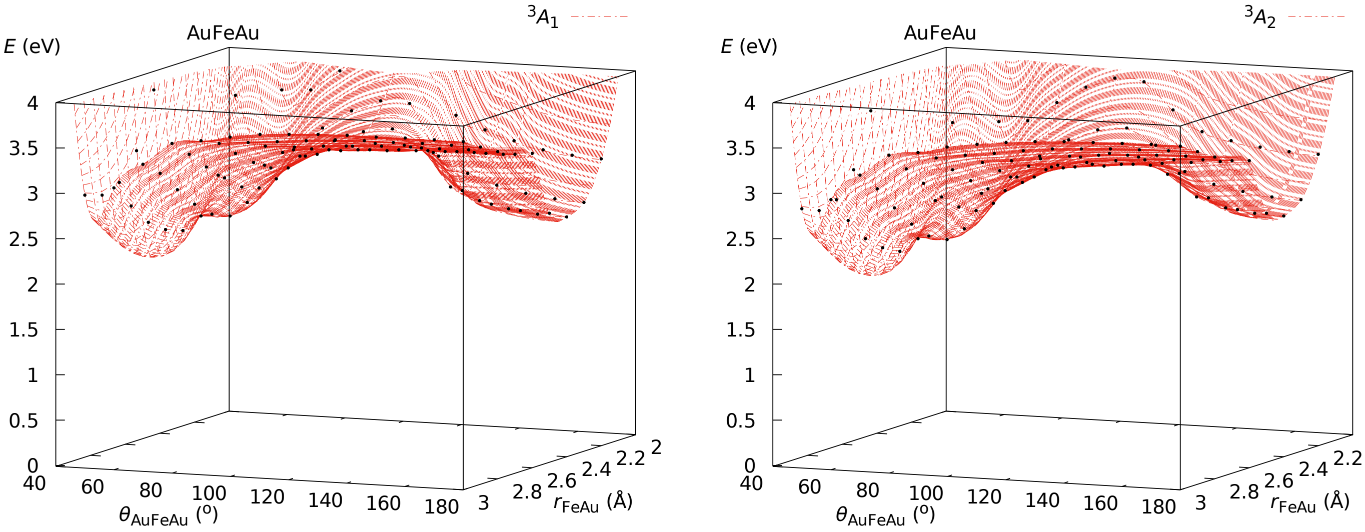

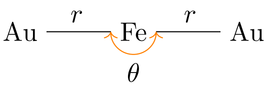

$40^\circ \le \theta \le 180^\circ, 2\ \text{Å} \le r \le 3\ \text{Å}, {}^{3,5,7}\{A_1 \oplus B_1 \oplus B_2 \oplus A_2\}$

Figure B.50: PESs, $E(\theta, r; {}^{2S+1}\Gamma)$, of AuFeAu obtained at the DKH-MRCI[(20+10)E,(10+8)O] level of theory. *Ab initio* points are indicated in black.

Continued on next page

Continued from previous page

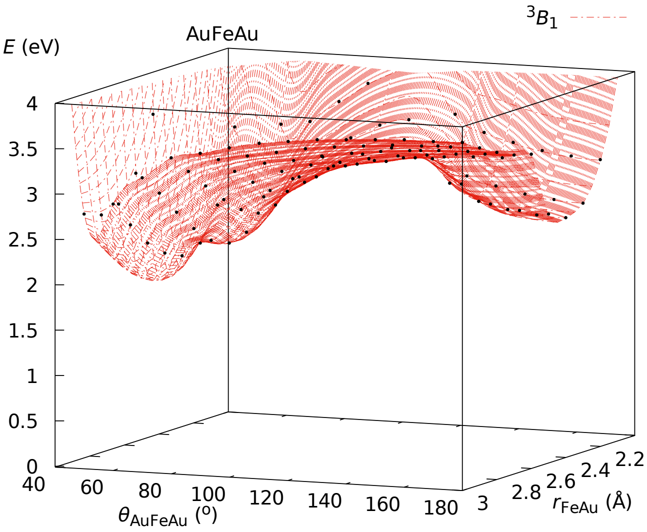

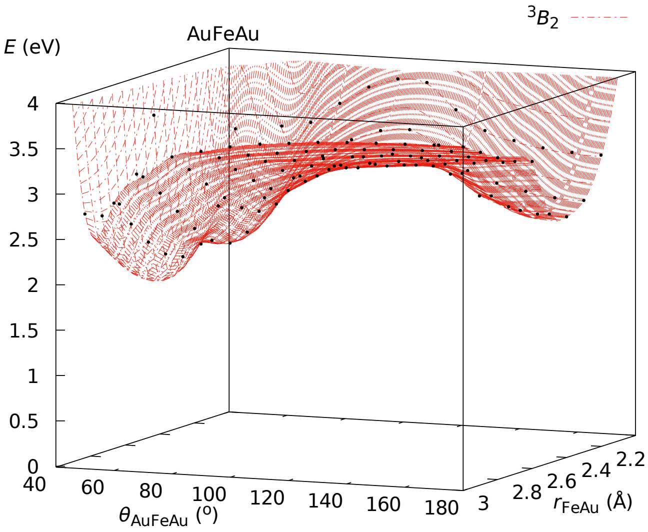

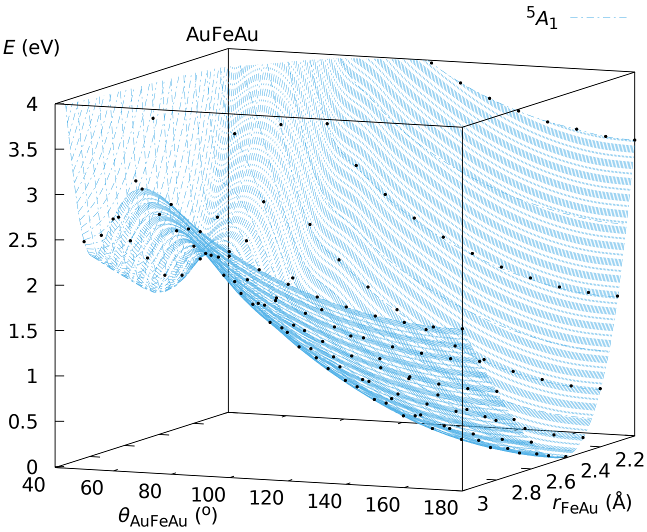

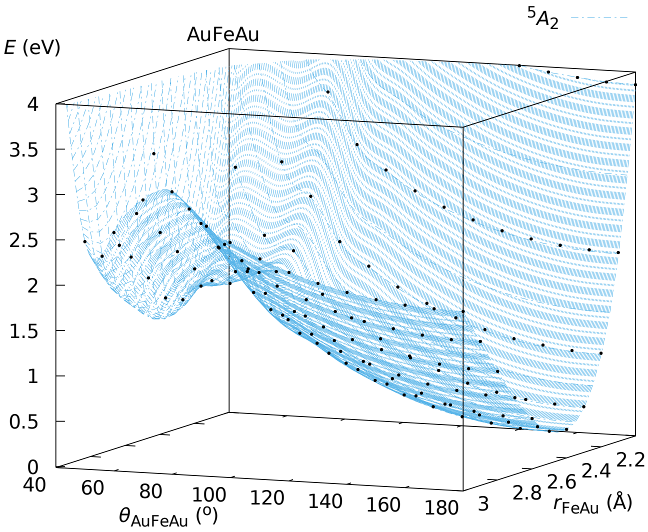

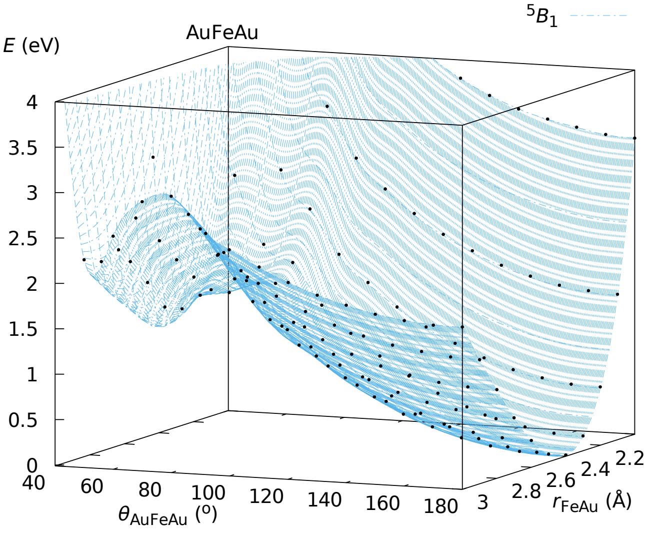

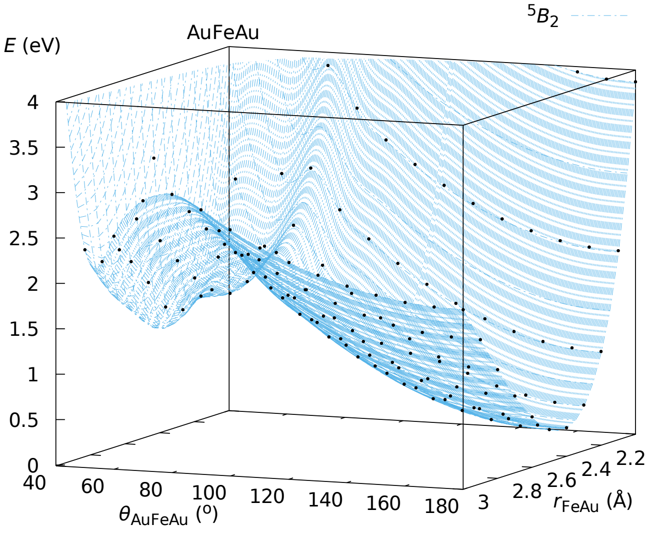

Continued on next page

Continued from previous page

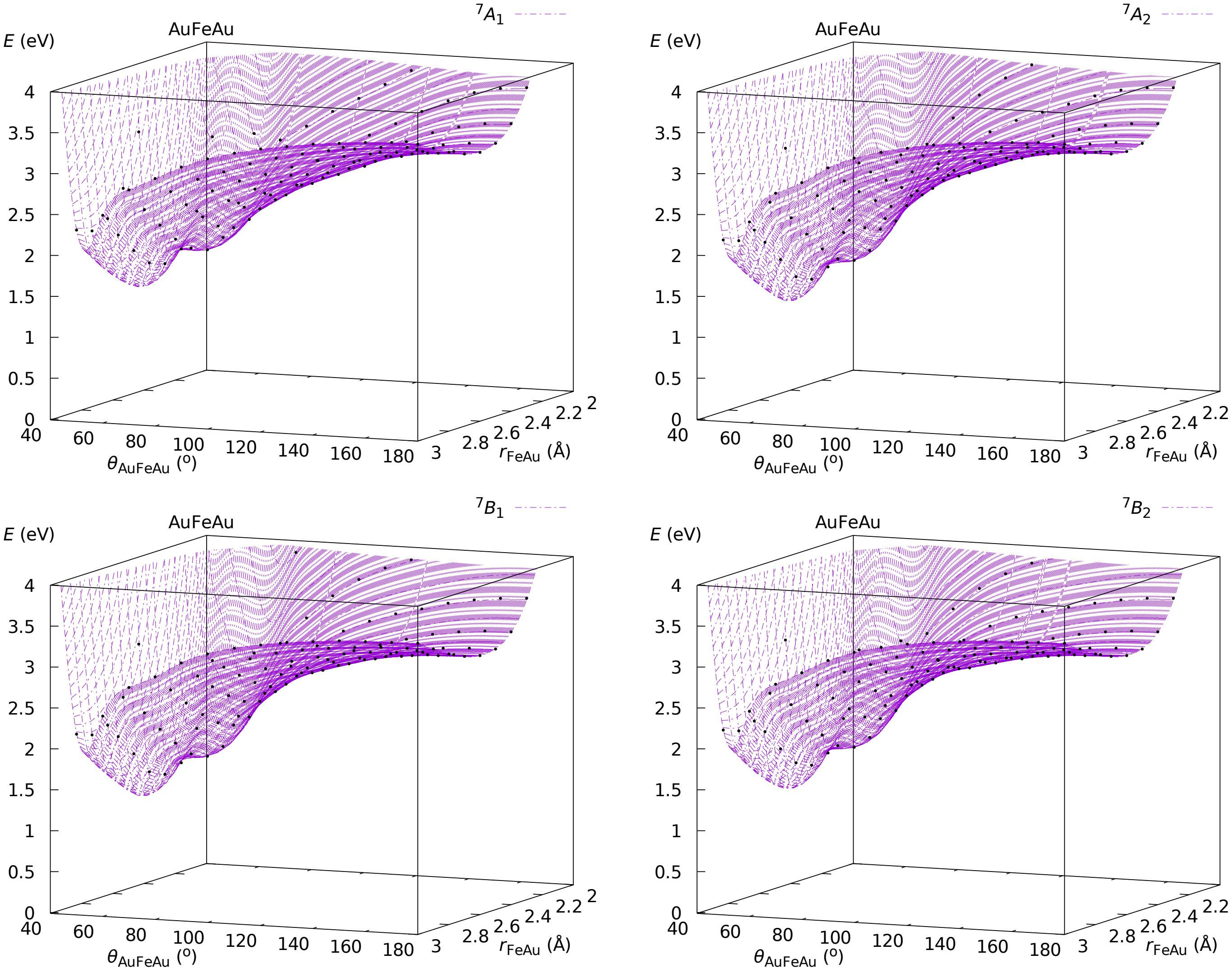

* * *

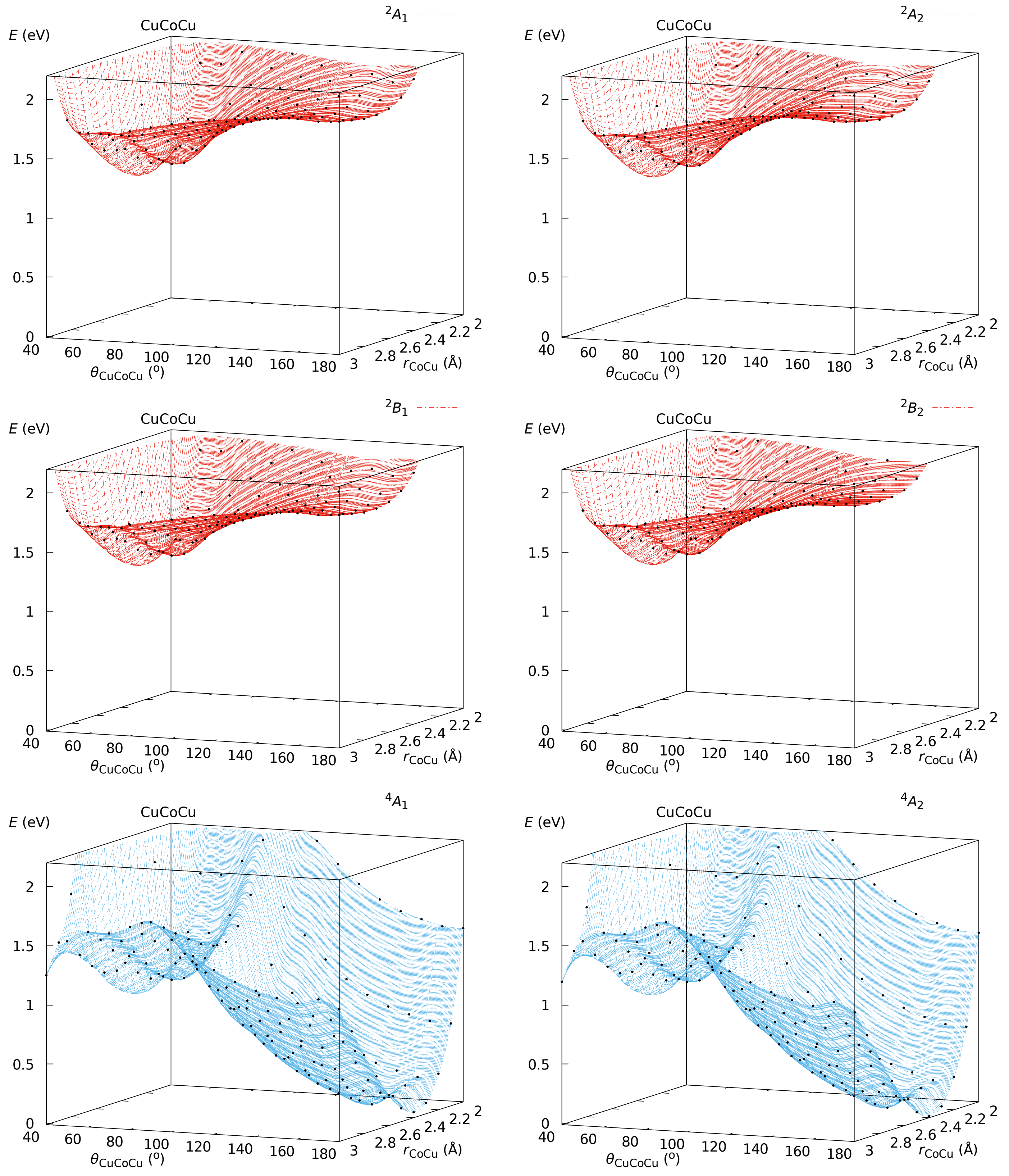

$\mathrm{Cu}\overset{r}{\text{——}}\underset{\theta}{\mathrm{Co}}\overset{r}{\text{——}}\mathrm{Cu}$ $\quad 40^\circ \leq \theta \leq 180^\circ, 2\ \text{Å} \leq r \leq 3\ \text{Å}, {}^{2,4,6}\{A_1 \oplus B_1 \oplus B_2 \oplus A_2\}$

Figure B.51: PESs, $E(\theta, r; {}^{2S+1}\Gamma)$, of CuCoCu obtained at the DKH-MRCI[(20+11)E,(10+8)O] level of theory. *Ab initio* points are indicated in black.

Continued on next page

Continued from previous page

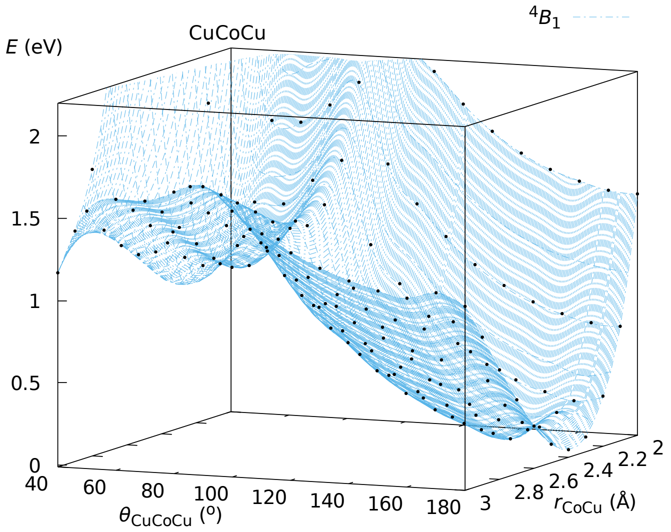

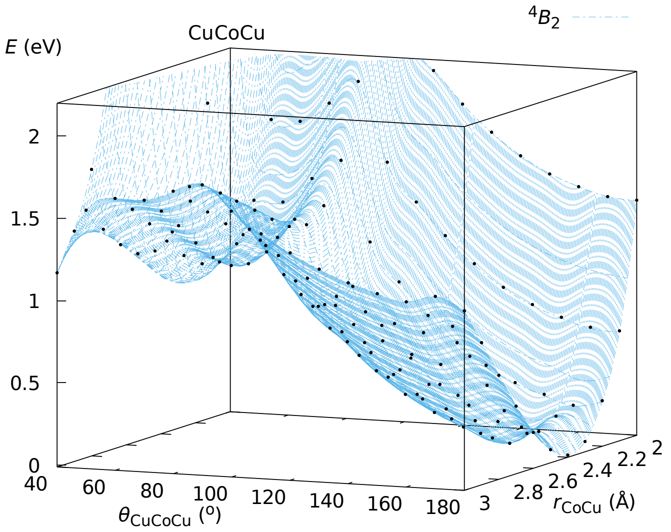

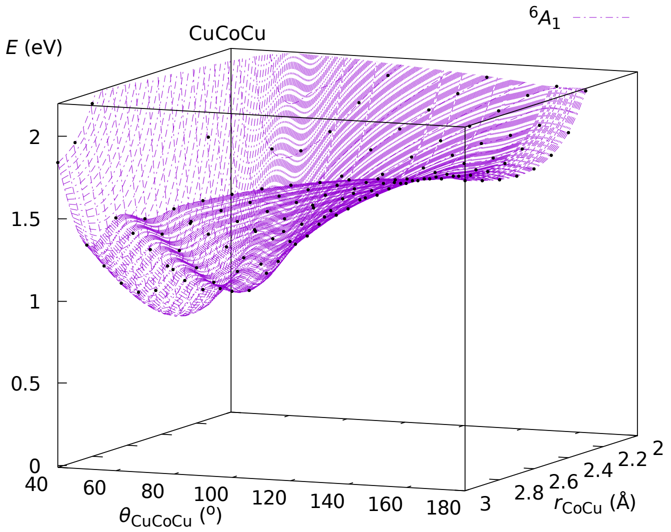

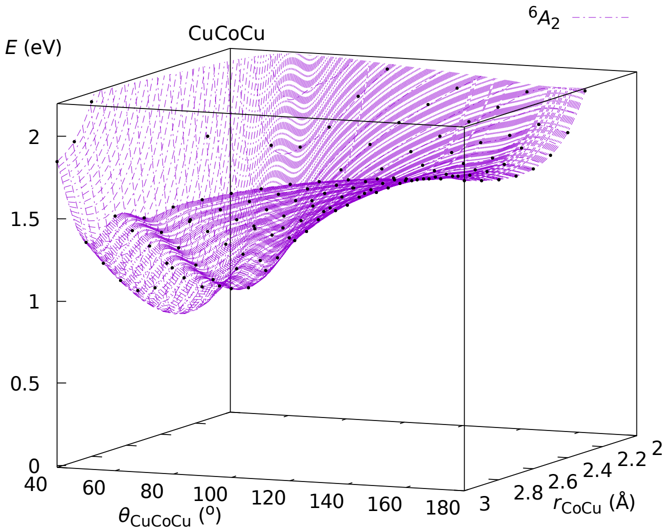

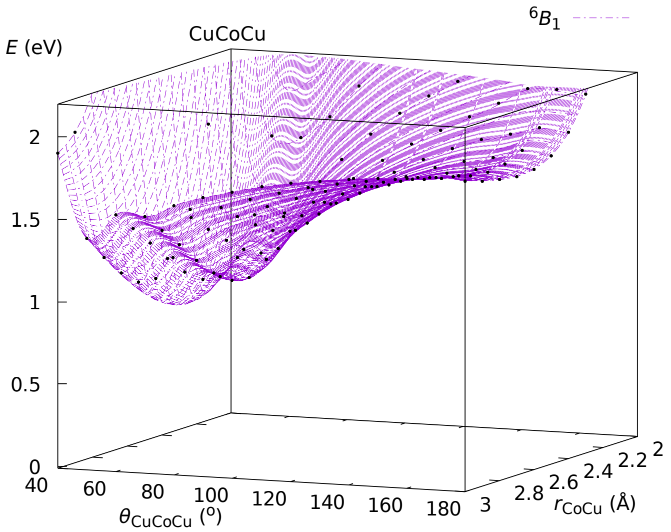

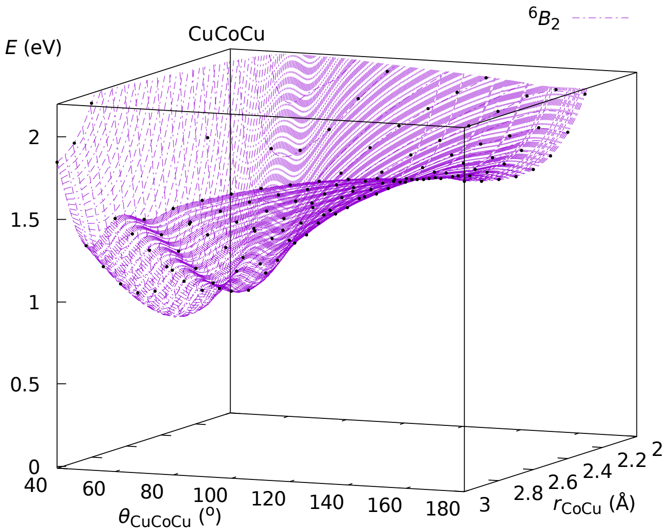

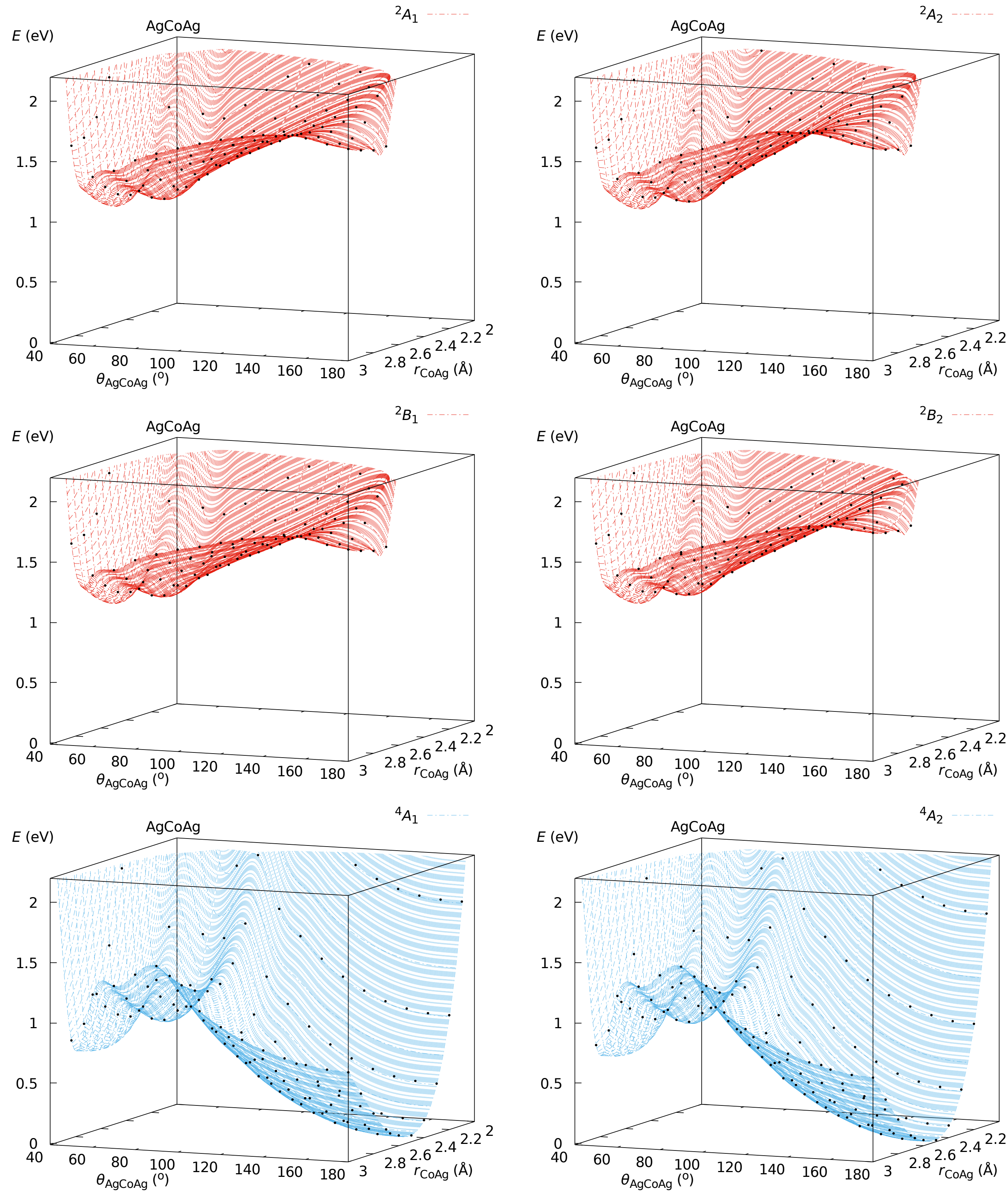

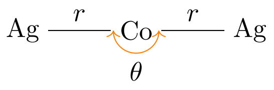

$40° \leq \theta \leq 180°, 2\ \text{Å} \leq r \leq 3\ \text{Å}, {}^{2,4,6}\{A_1 \oplus B_1 \oplus B_2 \oplus A_2\}$

Figure B.52: PESs, $E(\theta, r; {}^{2S+1}\Gamma)$, of AgCoAg obtained at the DKH-MRCI[(20+11)E,(10+8)O] level of theory. *Ab initio* points are indicated in black.

Continued on next page

Continued from previous page

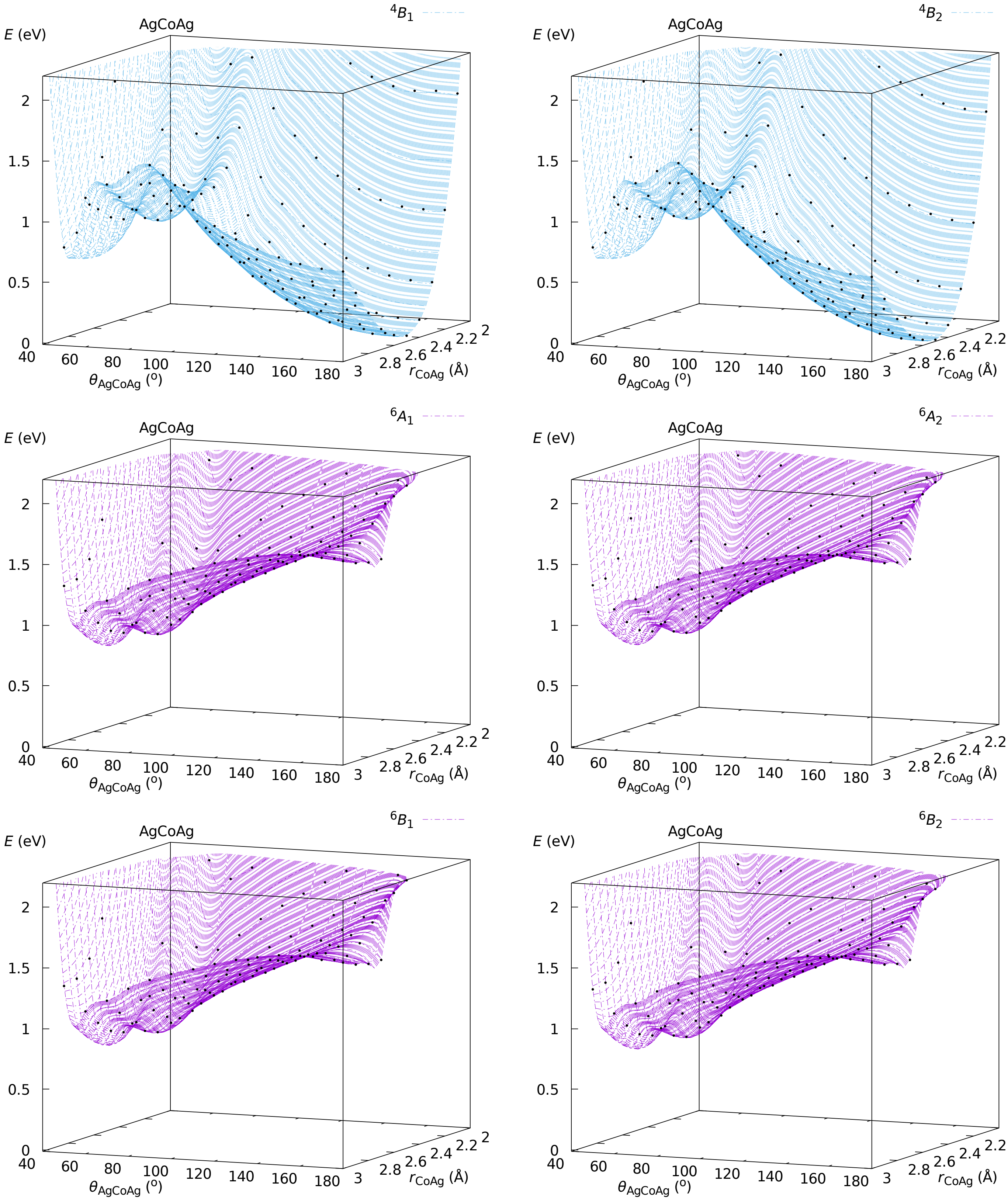

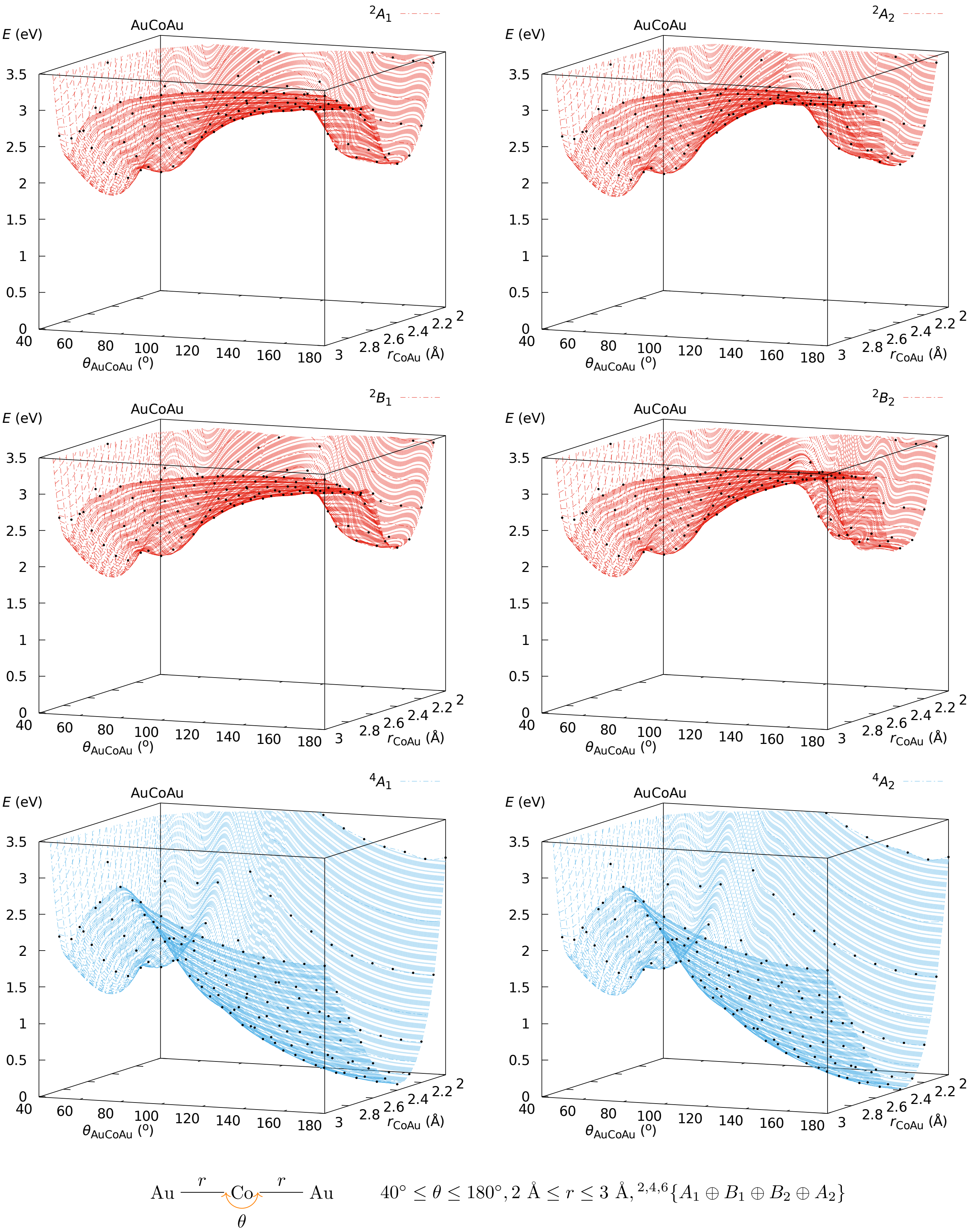

$40° \leq \theta \leq 180°, 2\ \text{Å} \leq r \leq 3\ \text{Å}, {}^{2,4,6}\{A_1 \oplus B_1 \oplus B_2 \oplus A_2\}$

Figure B.53: PESs, $E(\theta, r; {}^{2S+1}\Gamma)$, of AuCoAu obtained at the DKH-MRCI[(20+11)E,(10+8)O] level of theory. *Ab initio* points are indicated in black.

Continued on next page

Continued from previous page

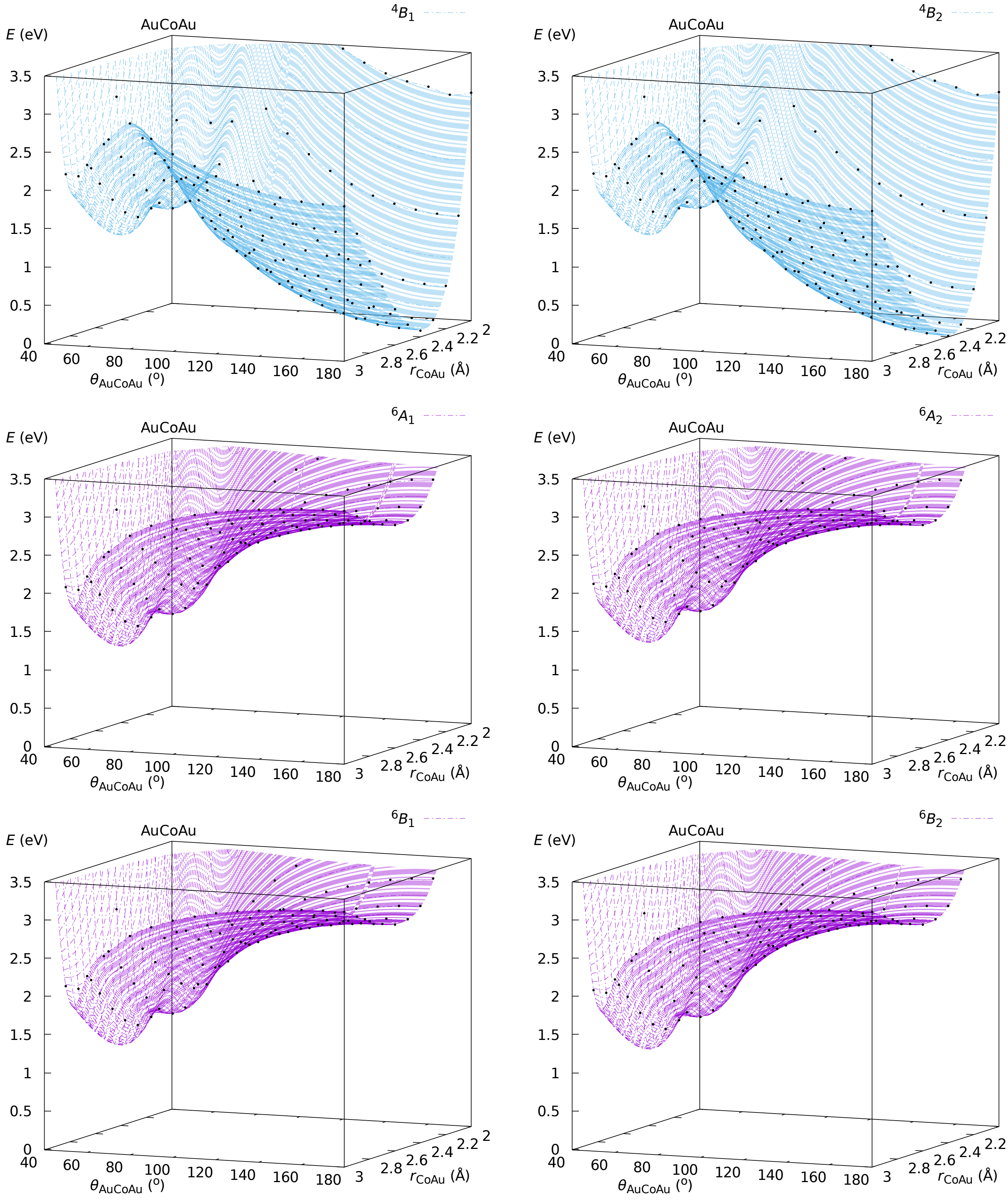

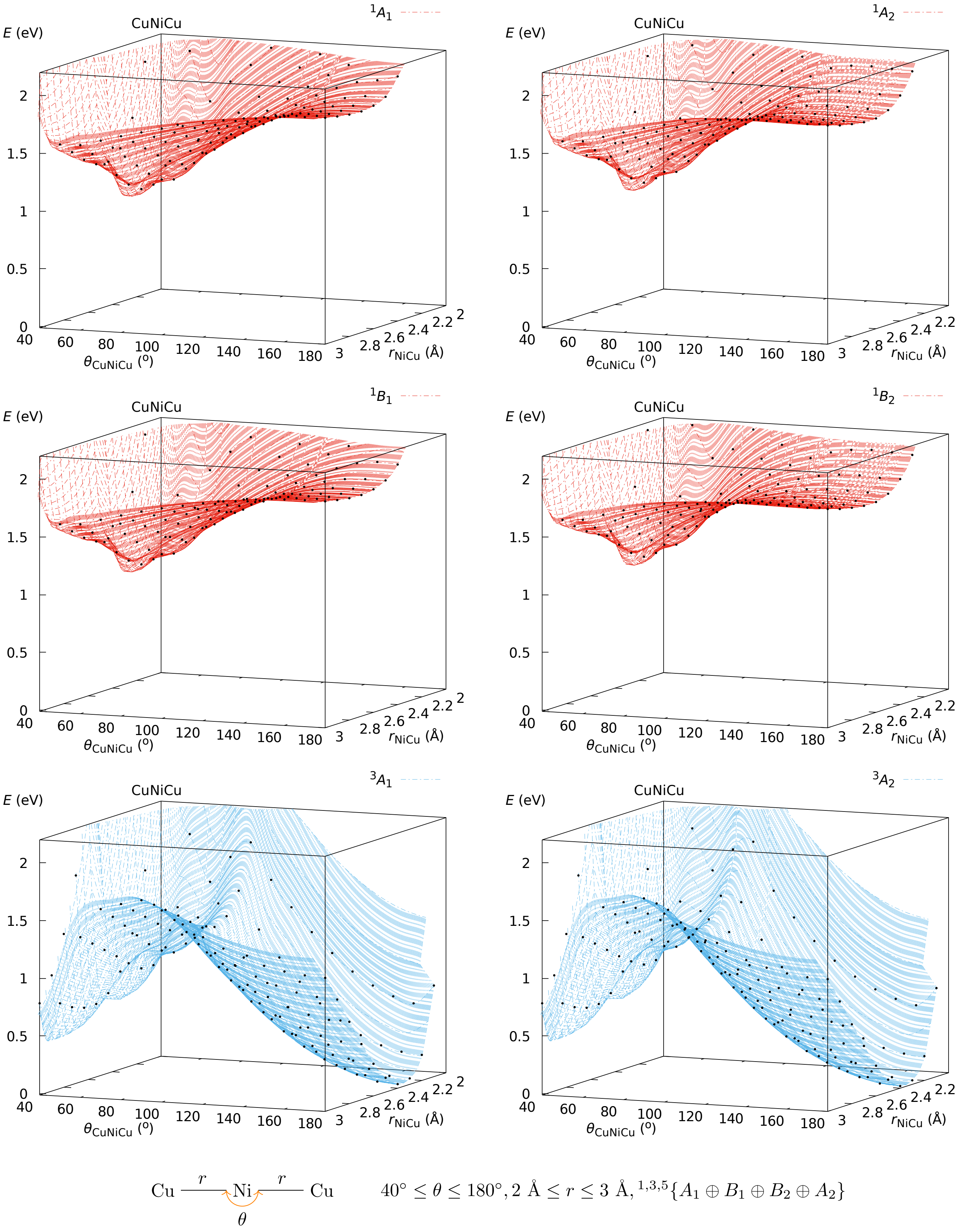

Figure B.54: PESs, $E(\theta, r; {}^{2S+1}\Gamma)$, of CuNiCu obtained at the DKH-MRCI[(20+12)E,(10+8)O] level of theory. *Ab initio* points are indicated in black.

Continued on next page

Continued from previous page

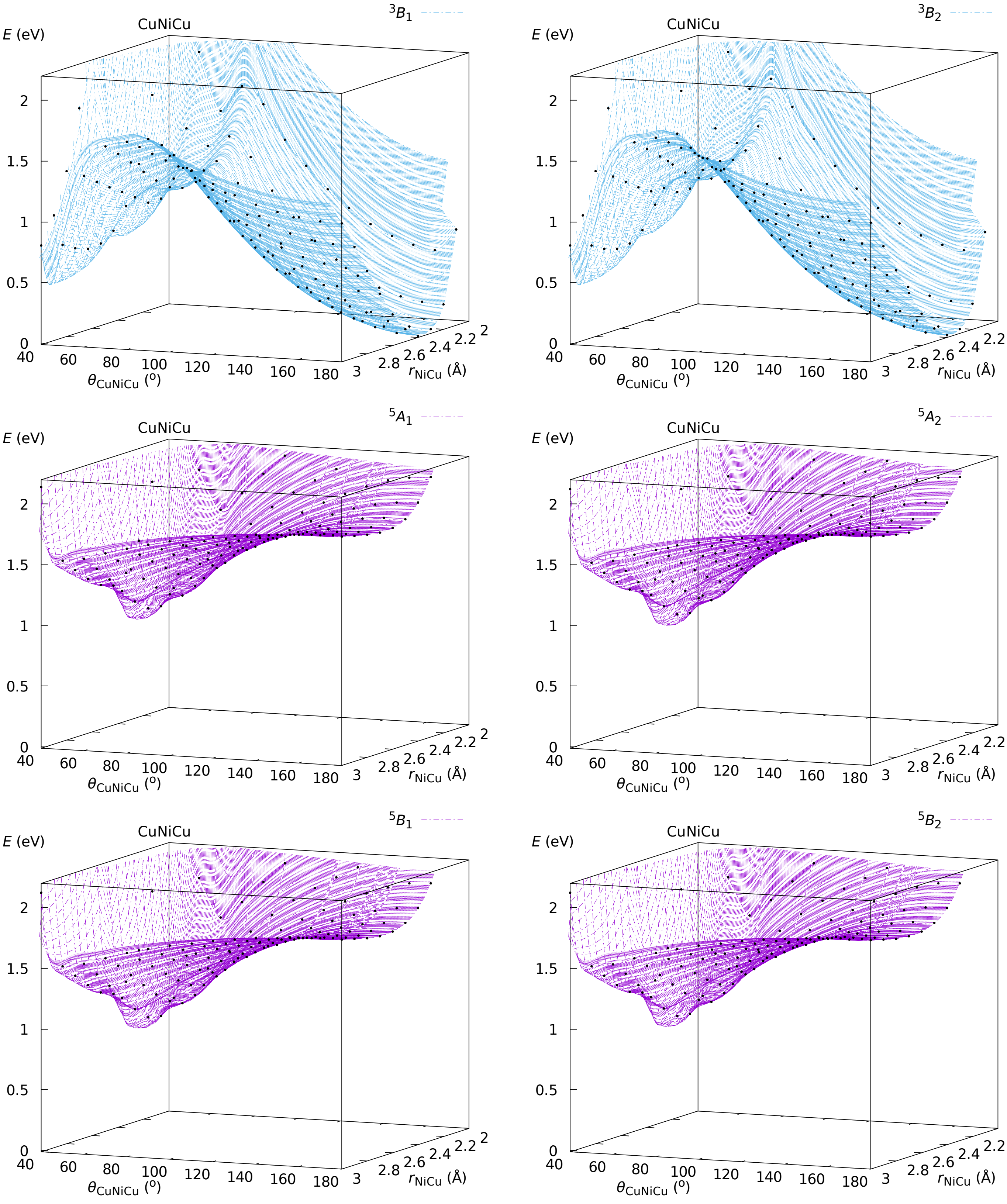

* * *

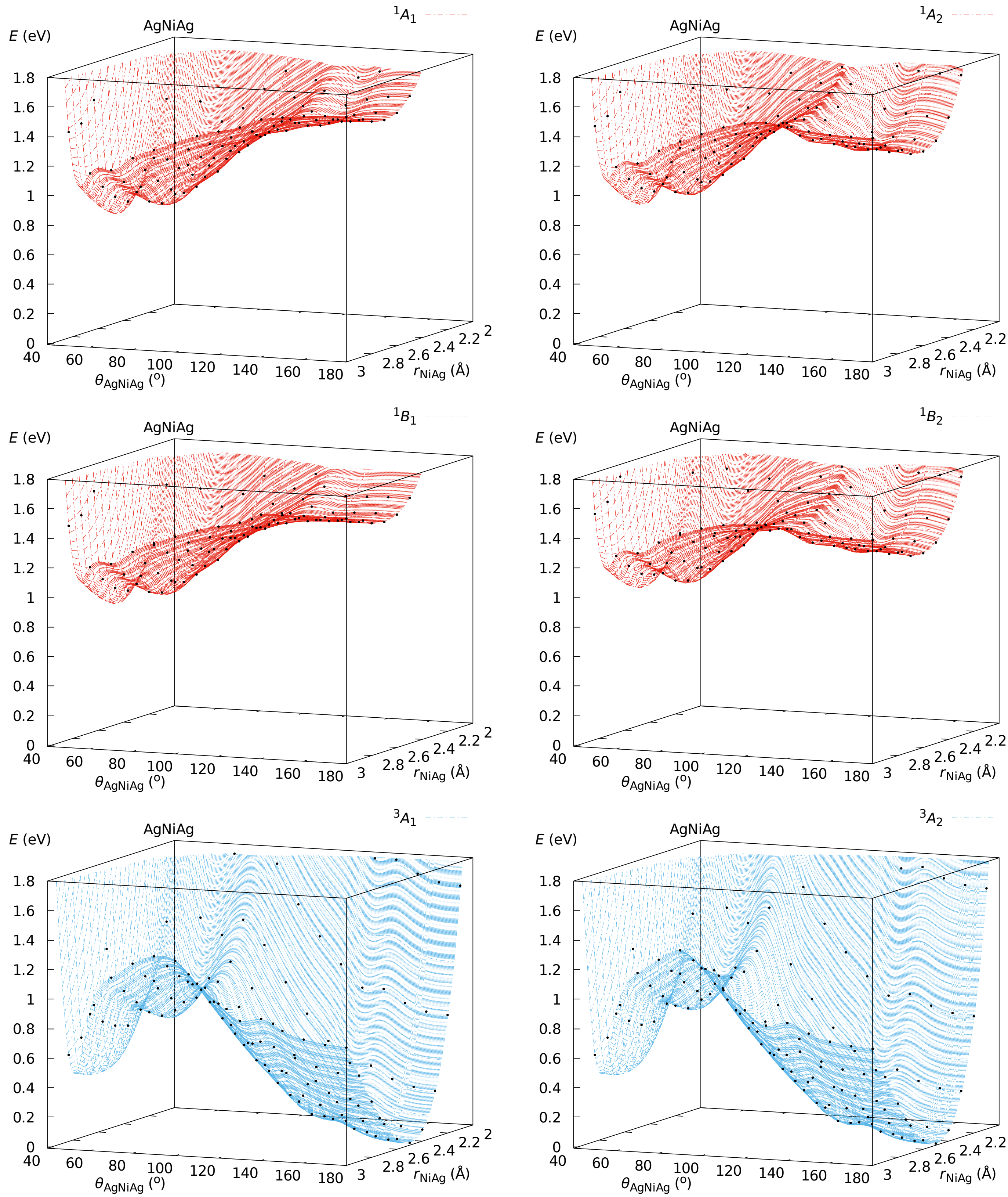

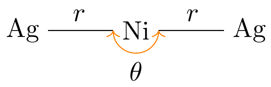

$40° \leq \theta \leq 180°, 2 \text{ Å} \leq r \leq 3 \text{ Å}, {}^{1,3,5}\{A_1 \oplus B_1 \oplus B_2 \oplus A_2\}$

Figure B.55: PESs, $E(\theta, r; {}^{2S+1}\Gamma)$, of AgNiAg obtained at the DKH-MRCI[(20+12)E,(10+8)O] level of theory. *Ab initio* points are indicated in black.

Continued on next page

Continued from previous page

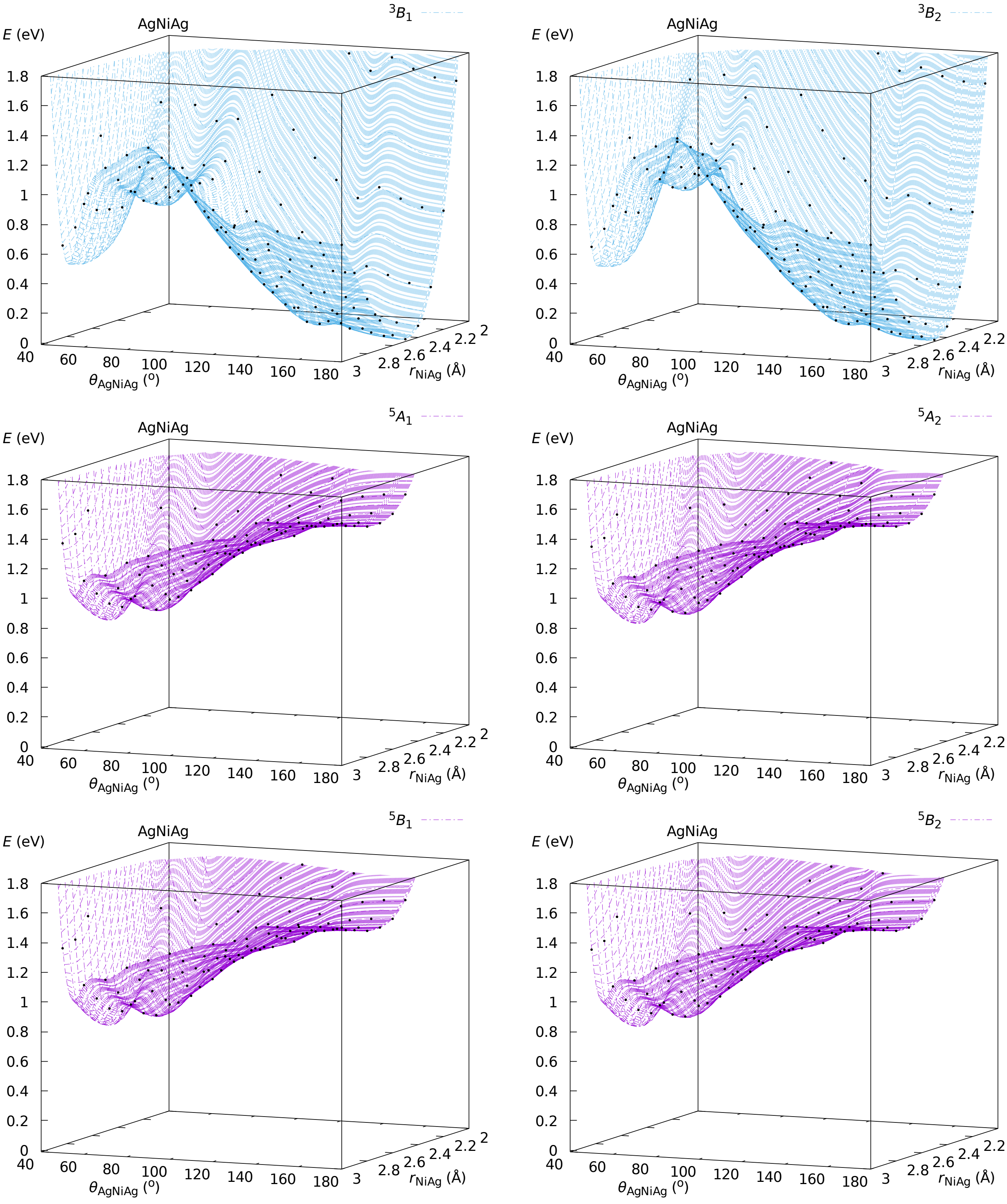

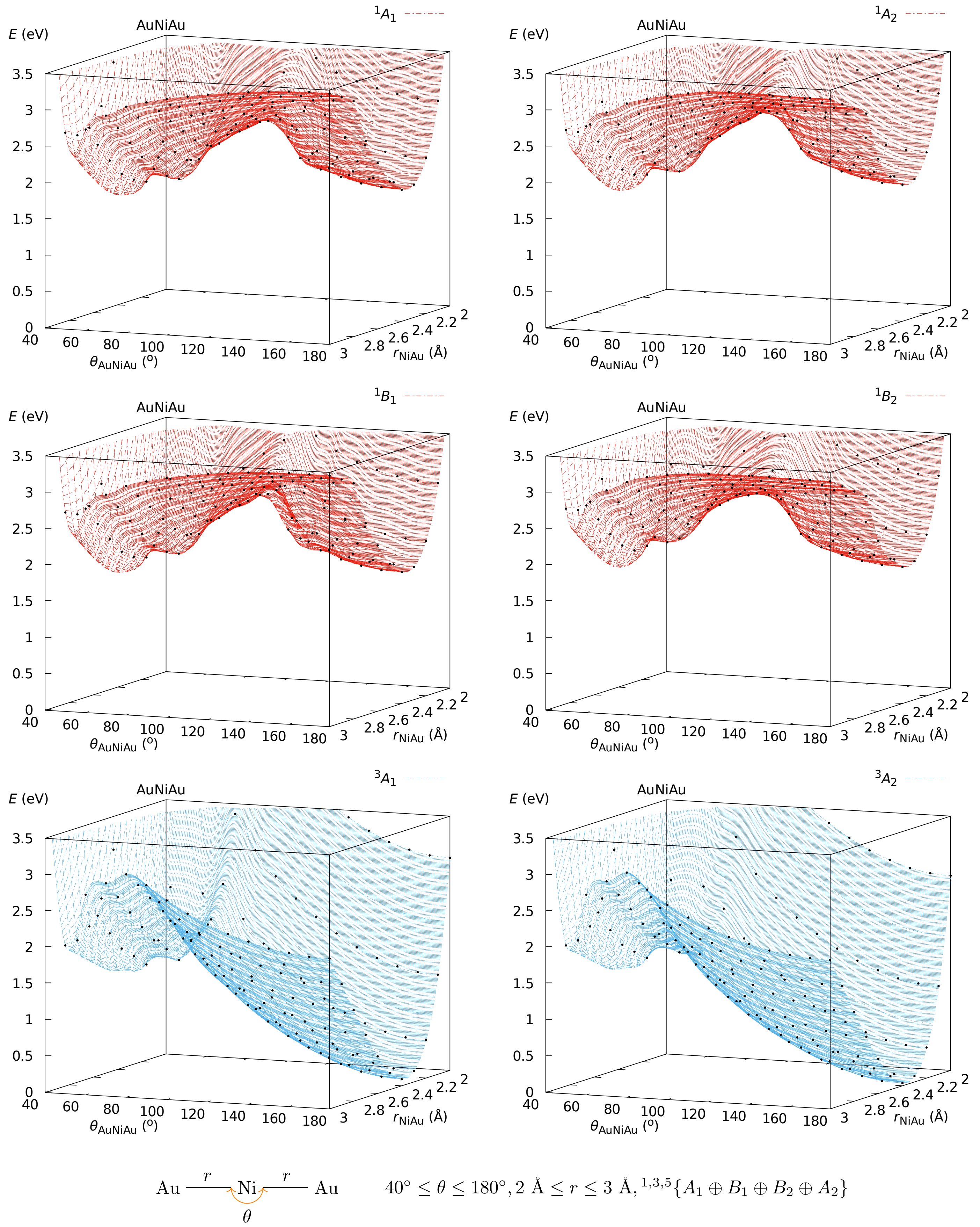

$40° \leq \theta \leq 180°, 2$ Å $\leq r \leq 3$ Å, $^{1,3,5}\{A_1 \oplus B_1 \oplus B_2 \oplus A_2\}$

Figure B.56: PESs, $E(\theta, r; {}^{2S+1}\Gamma)$, of AuNiAu obtained at the DKH-MRCI[(20+12)E,(10+8)O] level of theory. *Ab initio* points are indicated in black.

Continued on next page

Continued from previous page

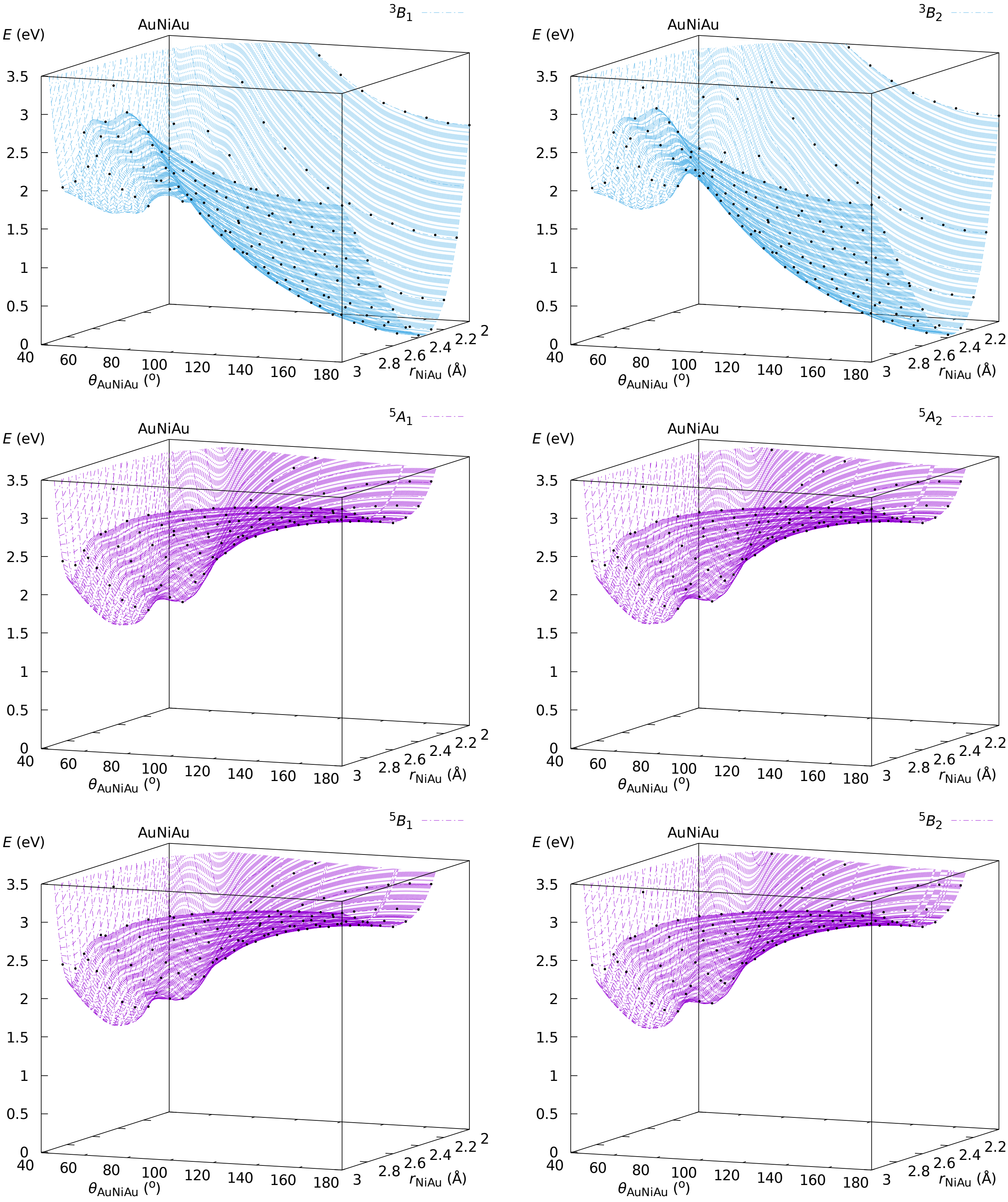

* * *

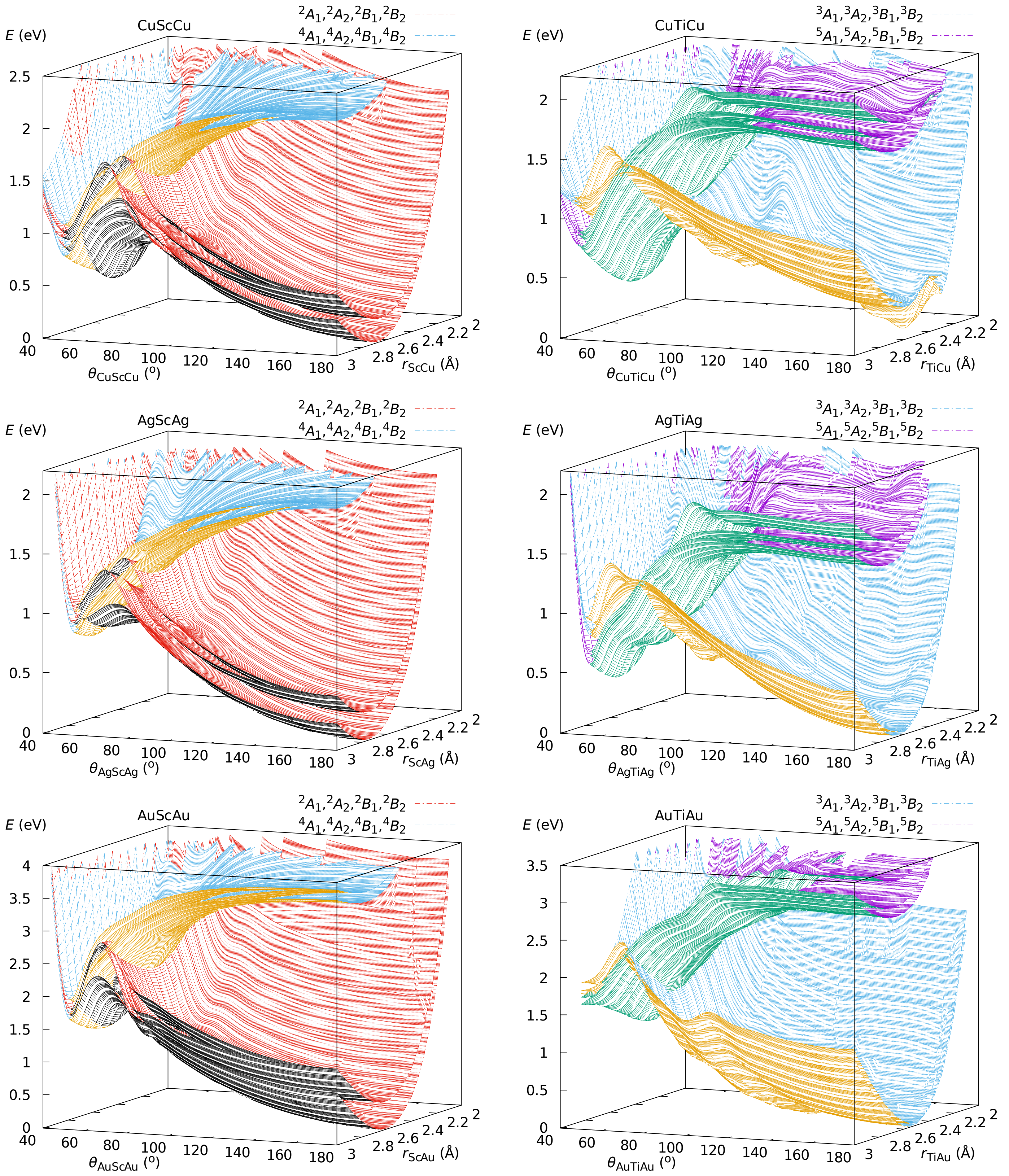

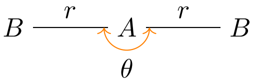

$40° \le \theta \le 180°, 2\ \text{Å} \le r \le 3\ \text{Å}, {}^{2S+1}\{A_1 \oplus B_1 \oplus B_2 \oplus A_2\}$

Figure B.57: PESs, $E(\theta, r; {}^{2S+1}\Gamma)$, of BAB obtained at the DKH-MRCI level of theory. *Continued on next page*

Continued from previous page

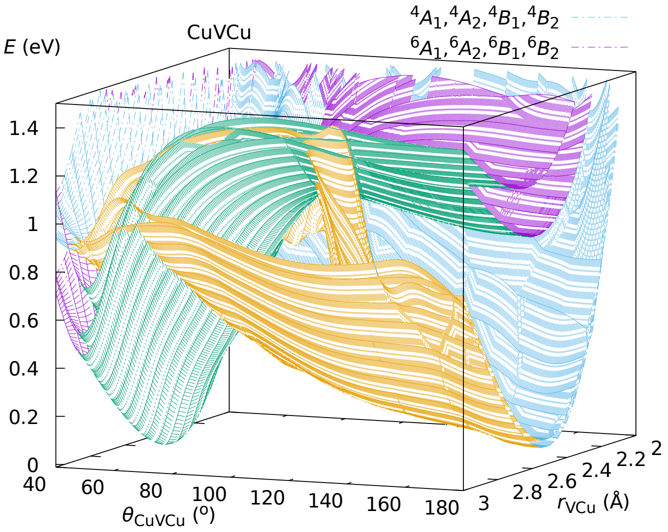

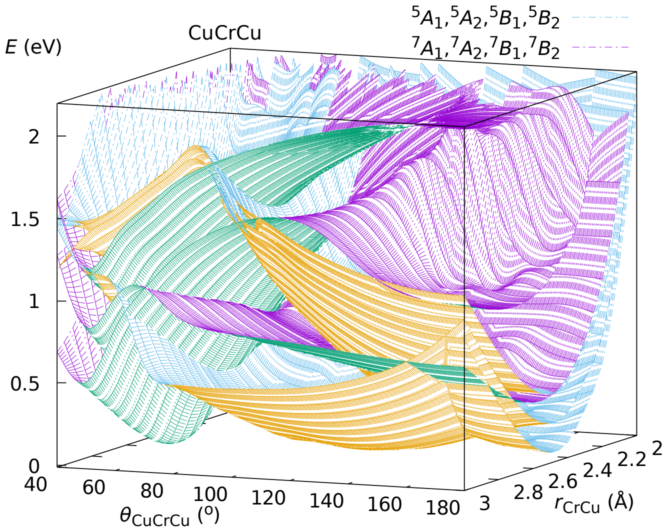

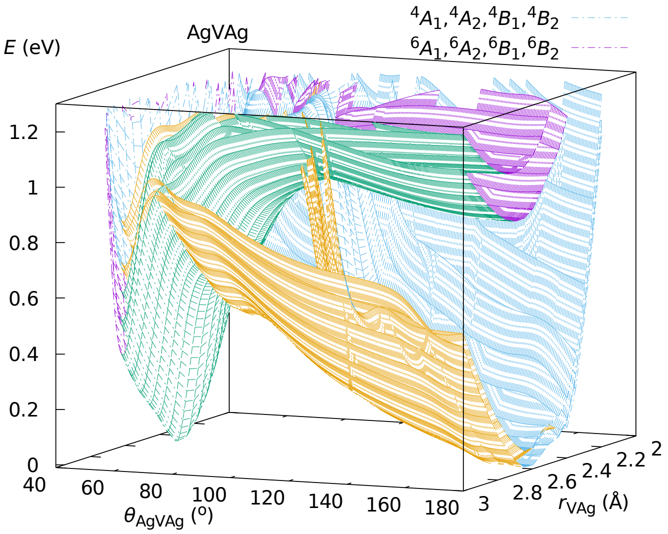

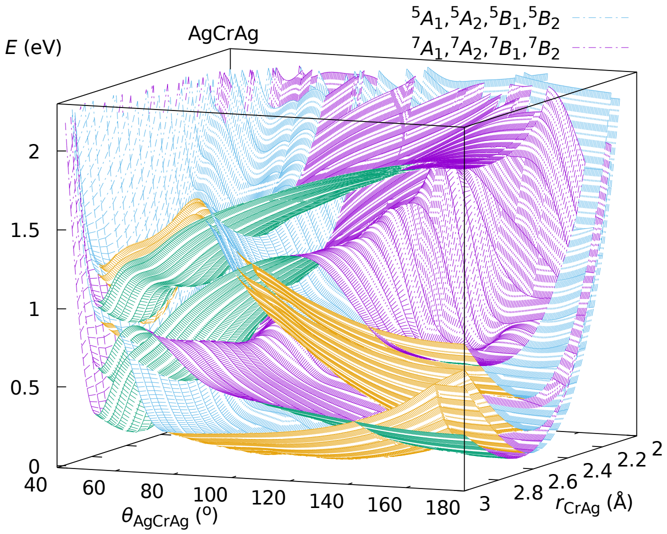

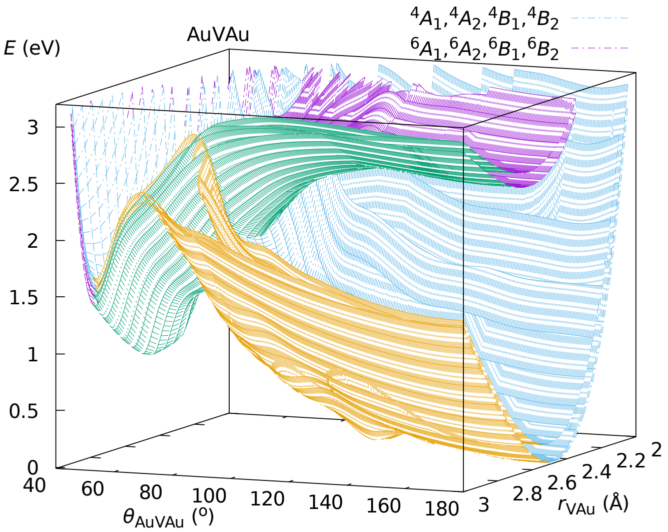

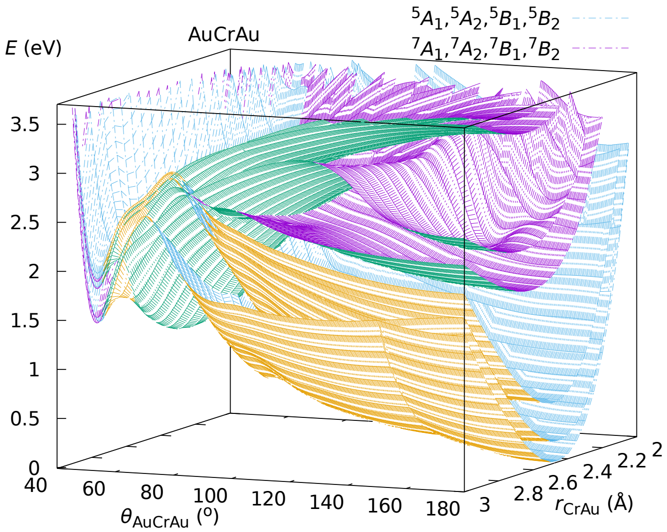

Continued on next page

Continued from previous page

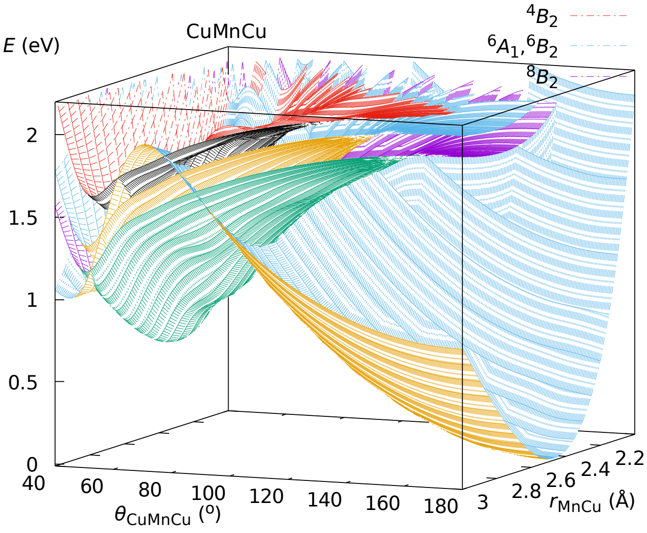

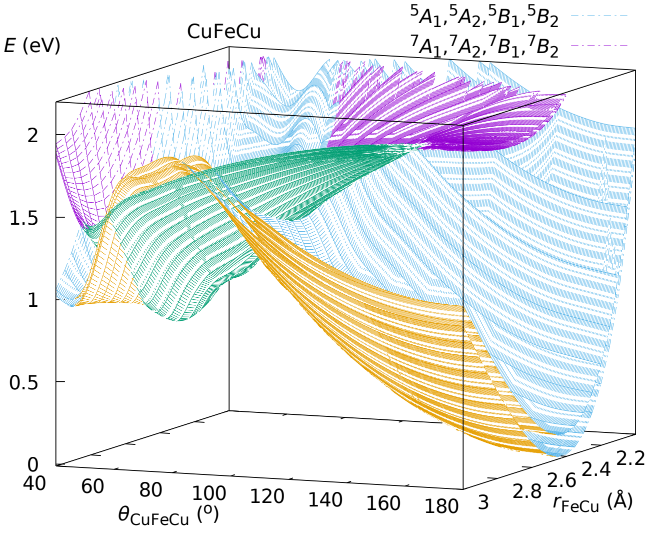

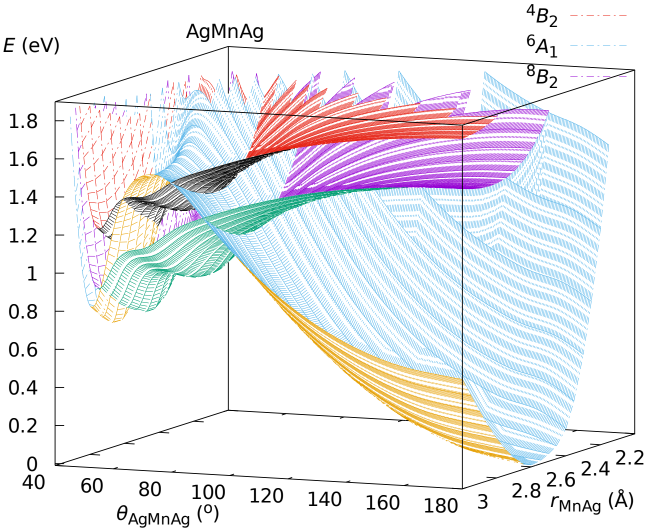

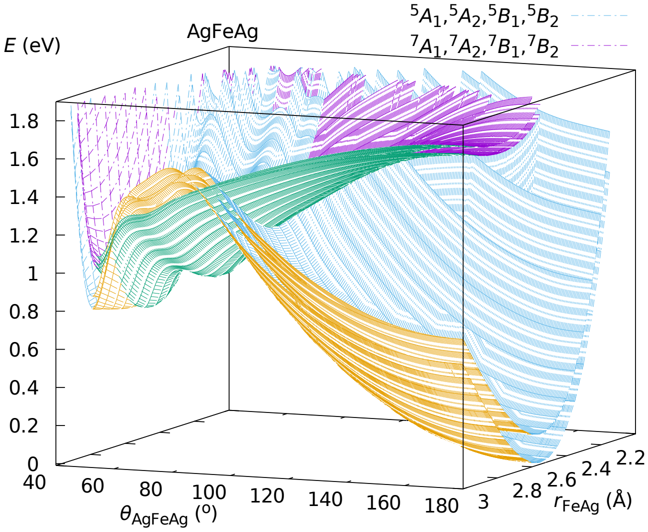

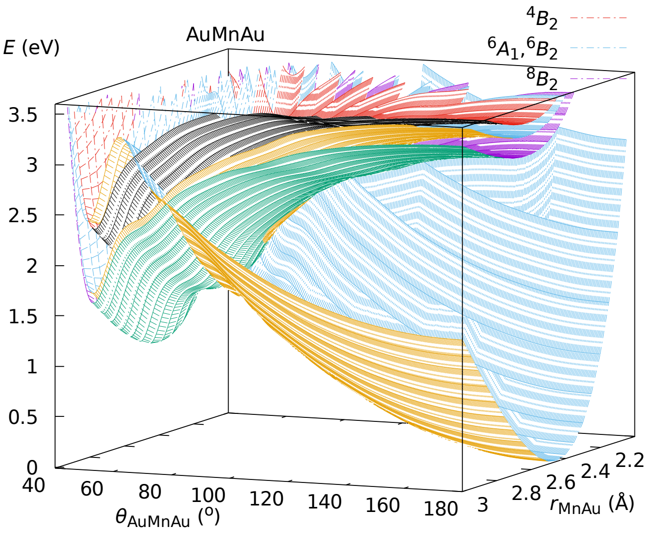

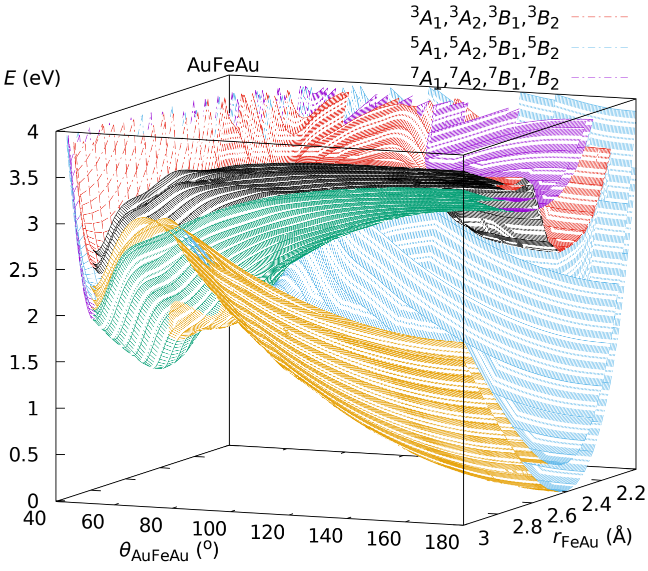

Continued on next page

Continued from previous page

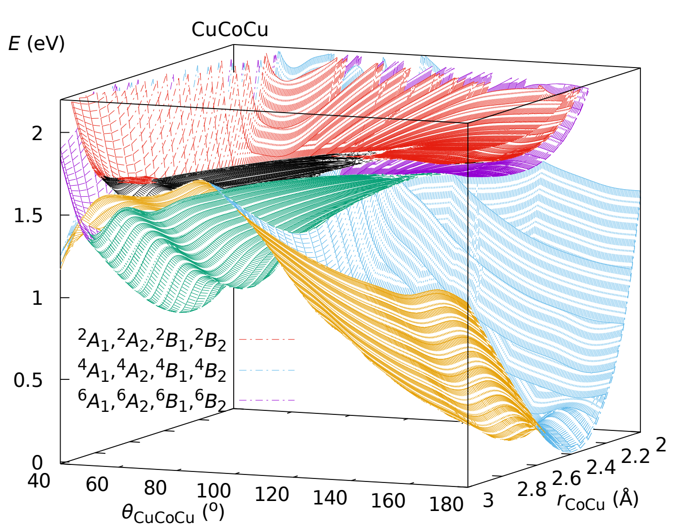

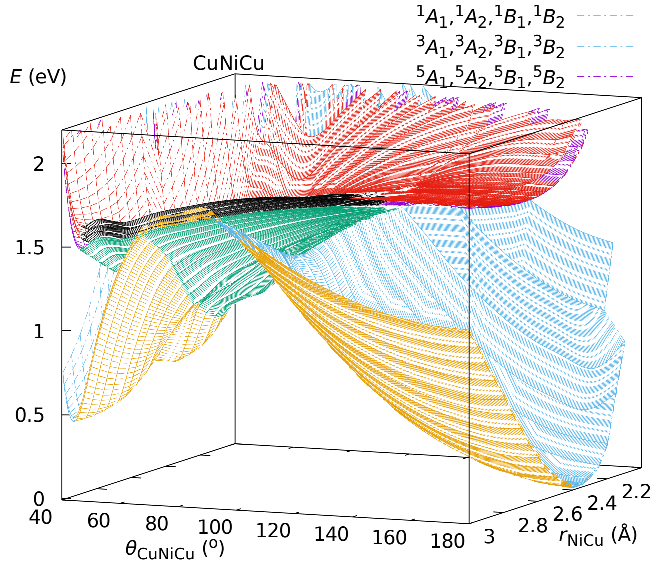

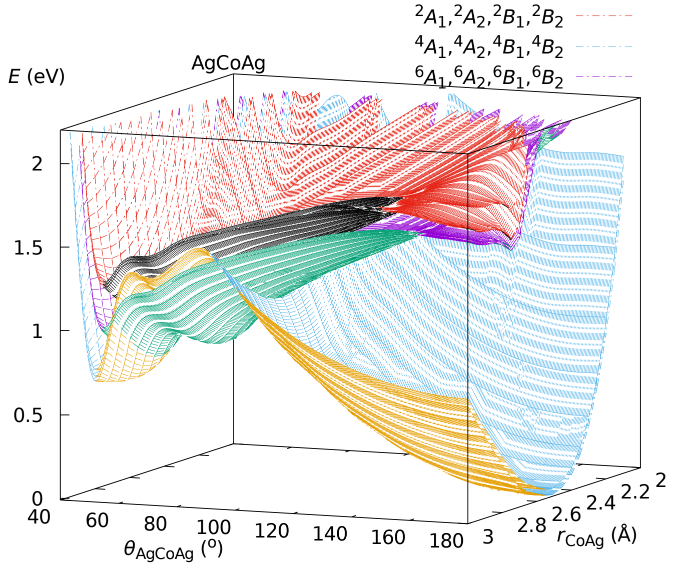

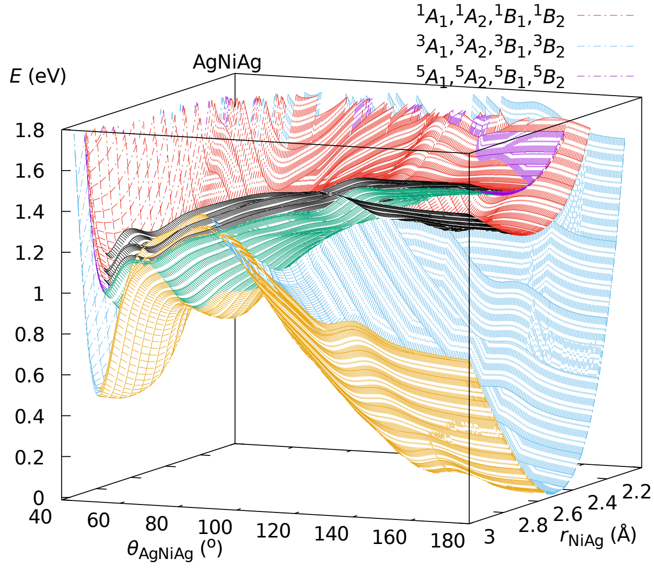

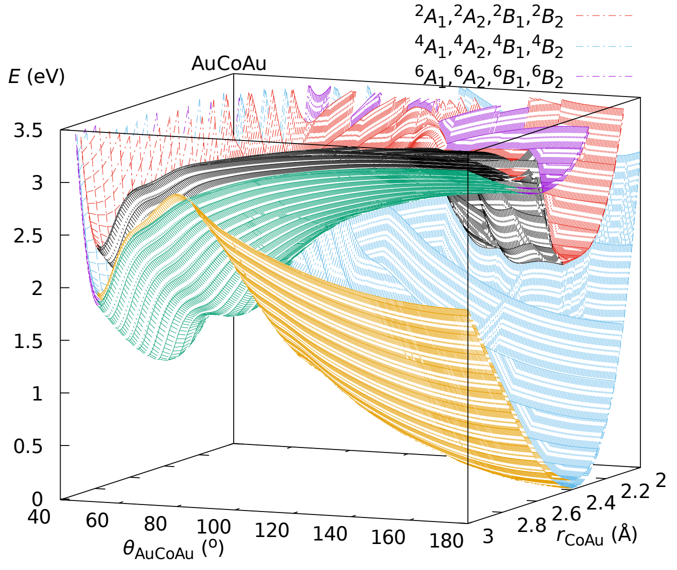

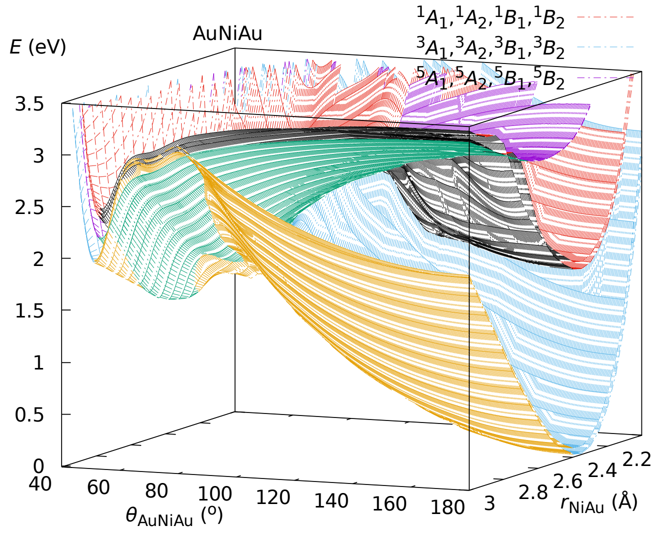

Notice that the iso-energy contours (figures B.58-B.80) are overall drawn with the incremental level of 0.02 eV, one in every three levels is tagged with energies. One can therefore, darting a glance over the levels, approximately locate the minima and their electronic energies with respect to the ground state of the given system.

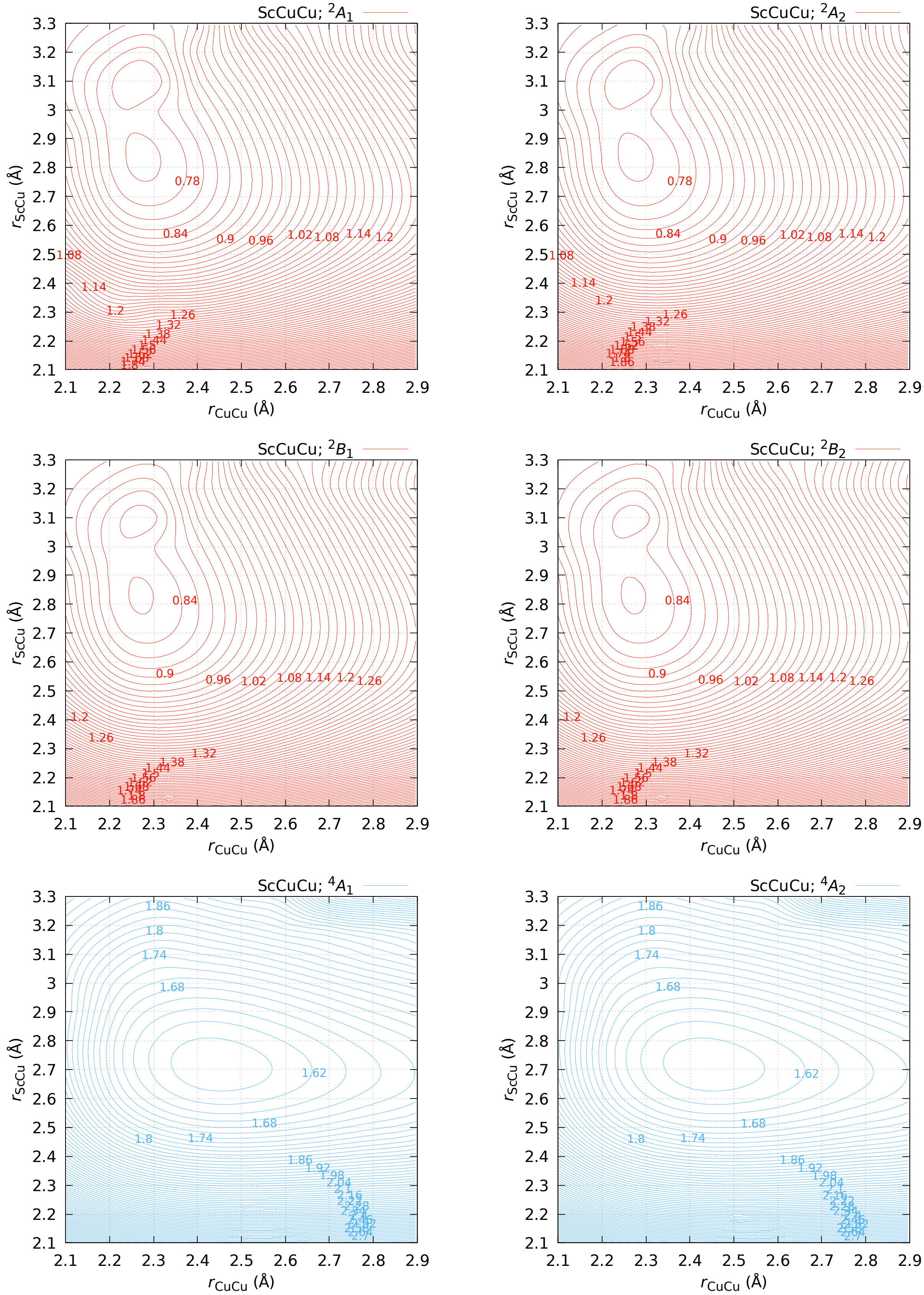

Figure B.58: Potential energy surfaces, $E(r_{\mathrm{ScCu}}, r_{\mathrm{CuCu}}; {}^{2,4}\Lambda)$, of the linear ScCuCu structure obtained at DKH-MRCI[(20+5)E,(10+8)O]. *Ab initio* points are indicated with the intersections of the grid lines. Iso-energies are in eV and relative to the $\tilde{X}^2\Delta_g$ ground state.

Continued on next page

Continued from previous page

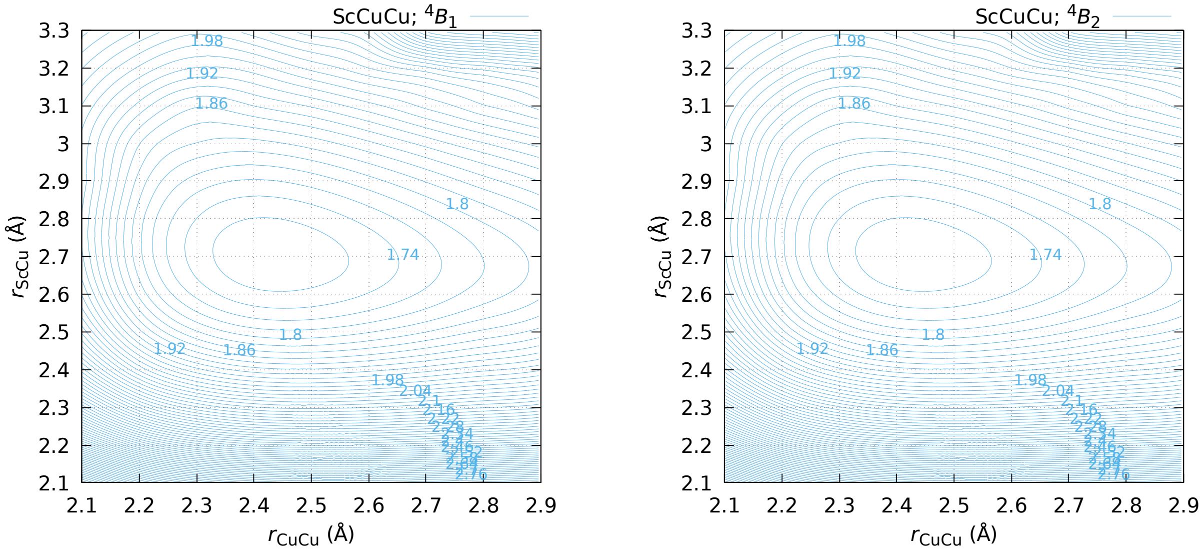

* * *

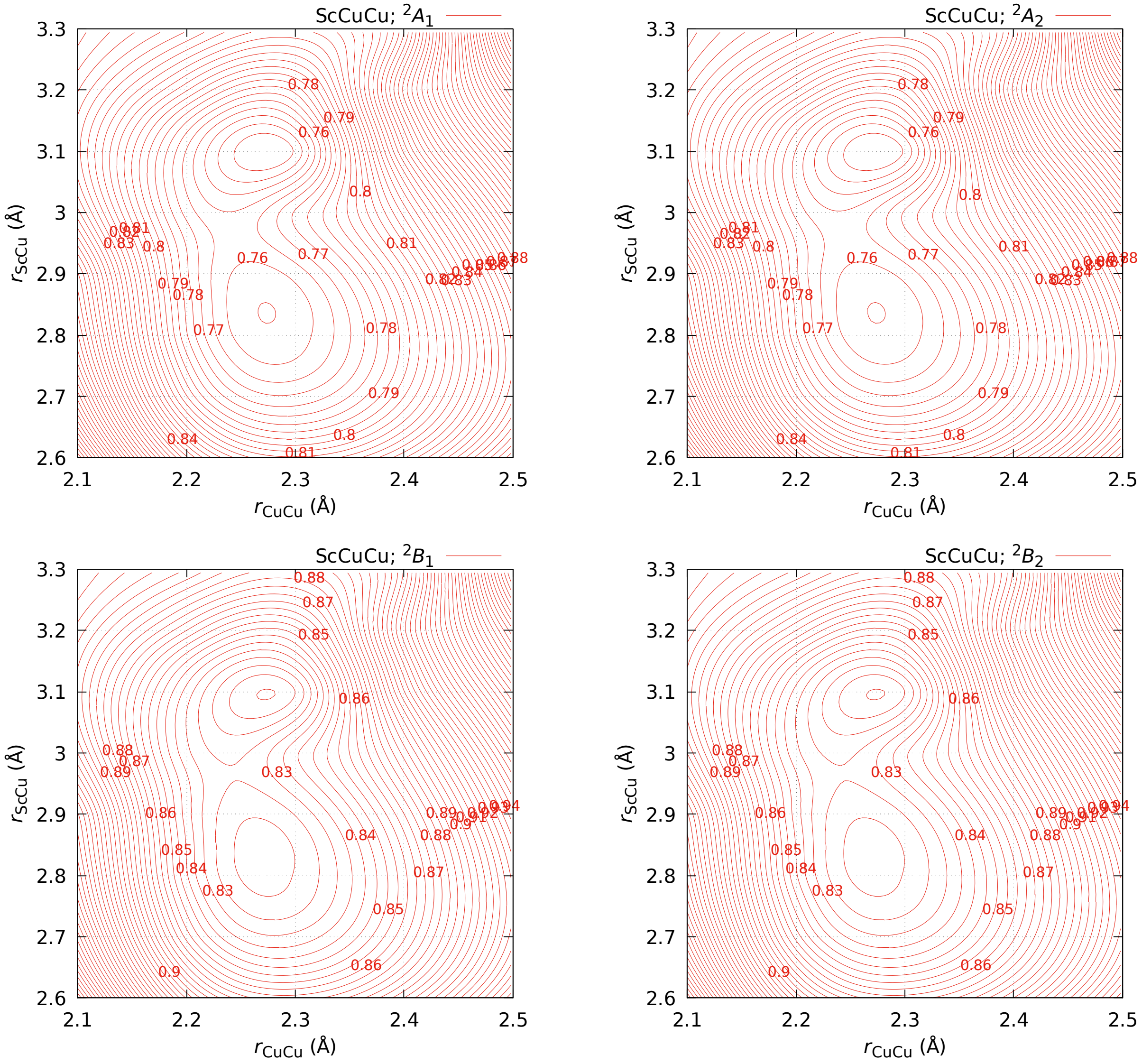

Figure B.59: A closer look at the doublet states of the linear ScCuCu structure obtained at DKH-MRCI[(20+5)E,(10+8)O]. *Ab initio* points are indicated with the intersections of the grid lines. Iso-energies are in eV and relative to the $\tilde{X}^2\Delta_g$ ground state.

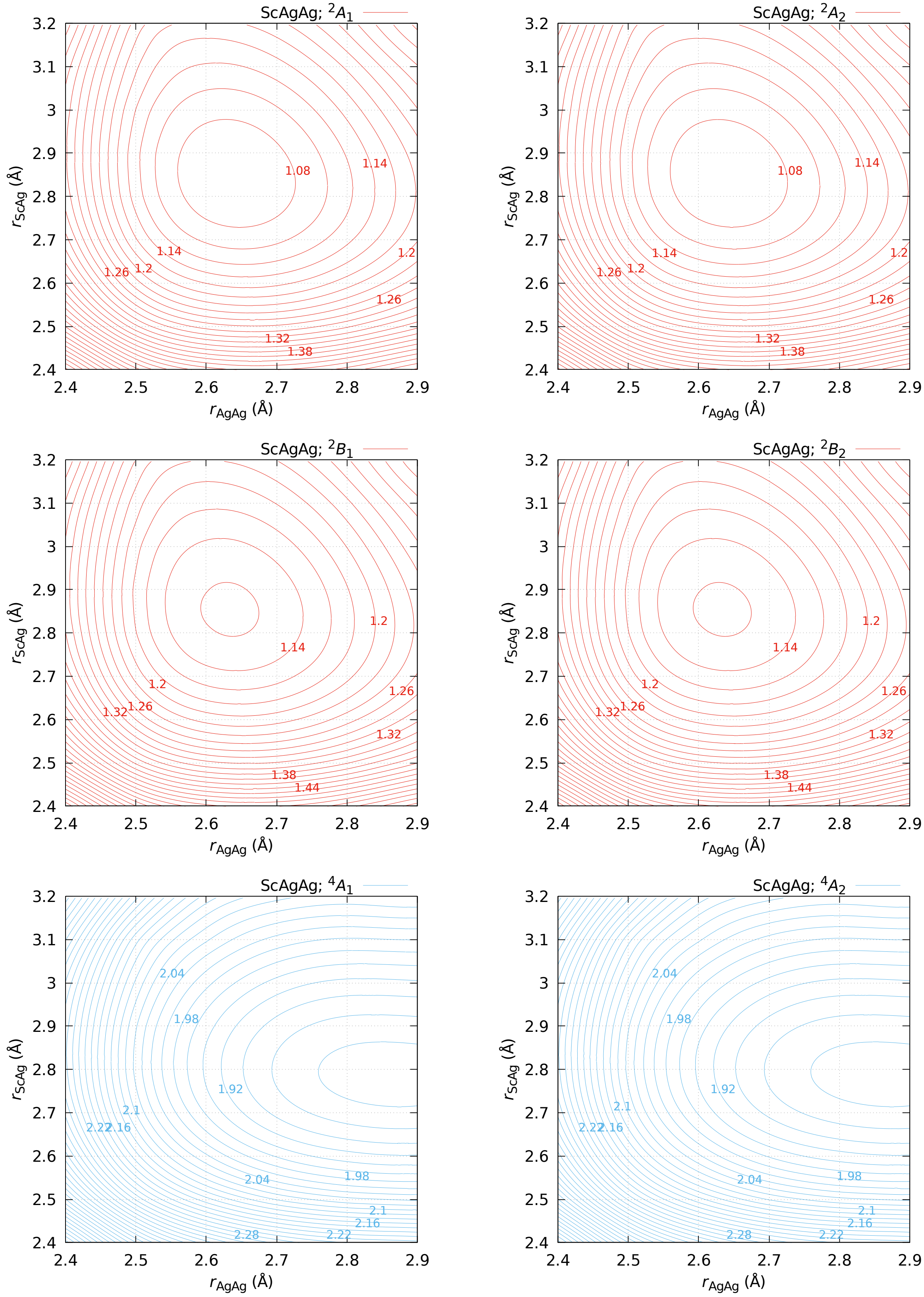

Figure B.60: Potential energy surfaces, $E(r_{\text{ScAg}}, r_{\text{AgAg}}; {}^{2,4}\Lambda)$, of the linear ScAgAg structure obtained at DKH-MRCI[(20+5)E,(10+8)O]. *Ab initio* points are indicated with the intersections of the grid lines. Iso-energies are in eV and relative to the $\tilde{X}^2\Delta_g$ ground state.

Continued on next page

Continued from previous page

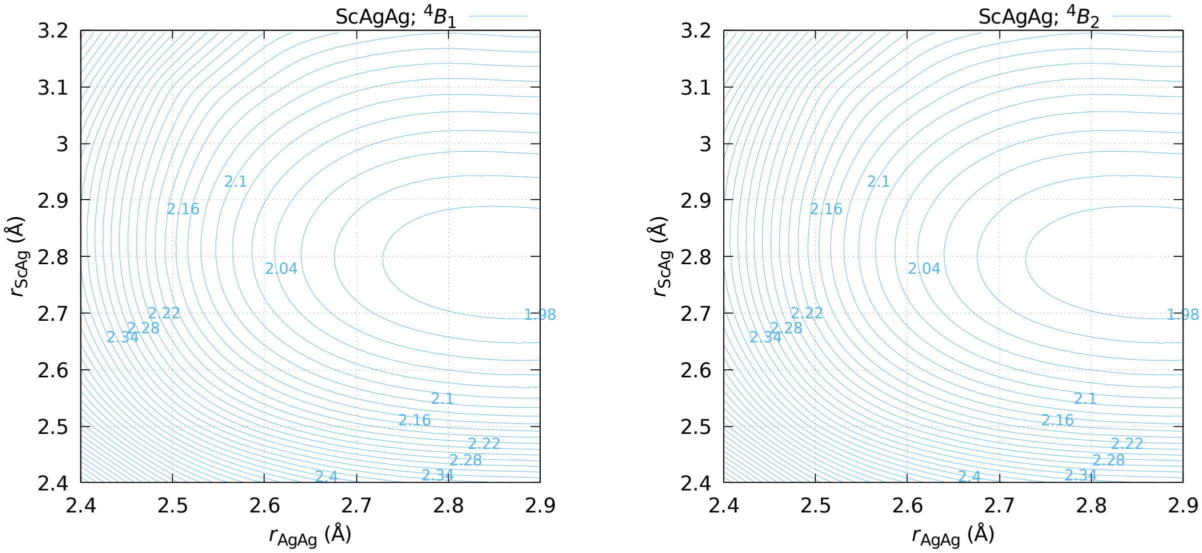

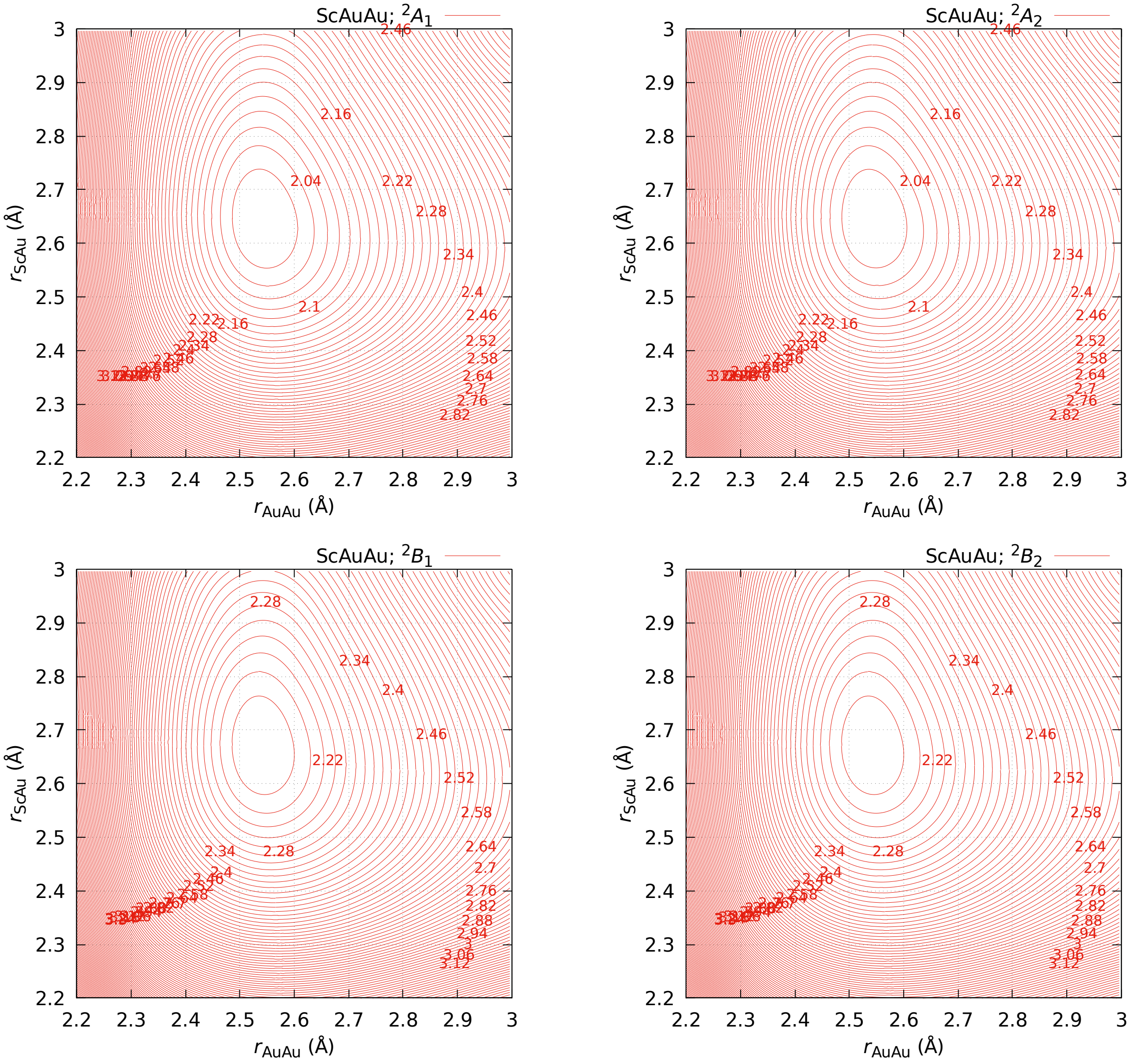

Figure B.61: Potential energy surfaces, $E(r_{\mathrm{ScAu}}, r_{\mathrm{AuAu}}; {}^{2,4}\Lambda)$, of the linear ScAuAu structure obtained at DKH-MRCI[(20+5)E,(10+8)O]. *Ab initio* points are indicated with the intersections of the grid lines. Iso-energies are in eV and relative to the $\tilde{X}^2\Delta_g$ ground state.

Continued on next page

Continued from previous page

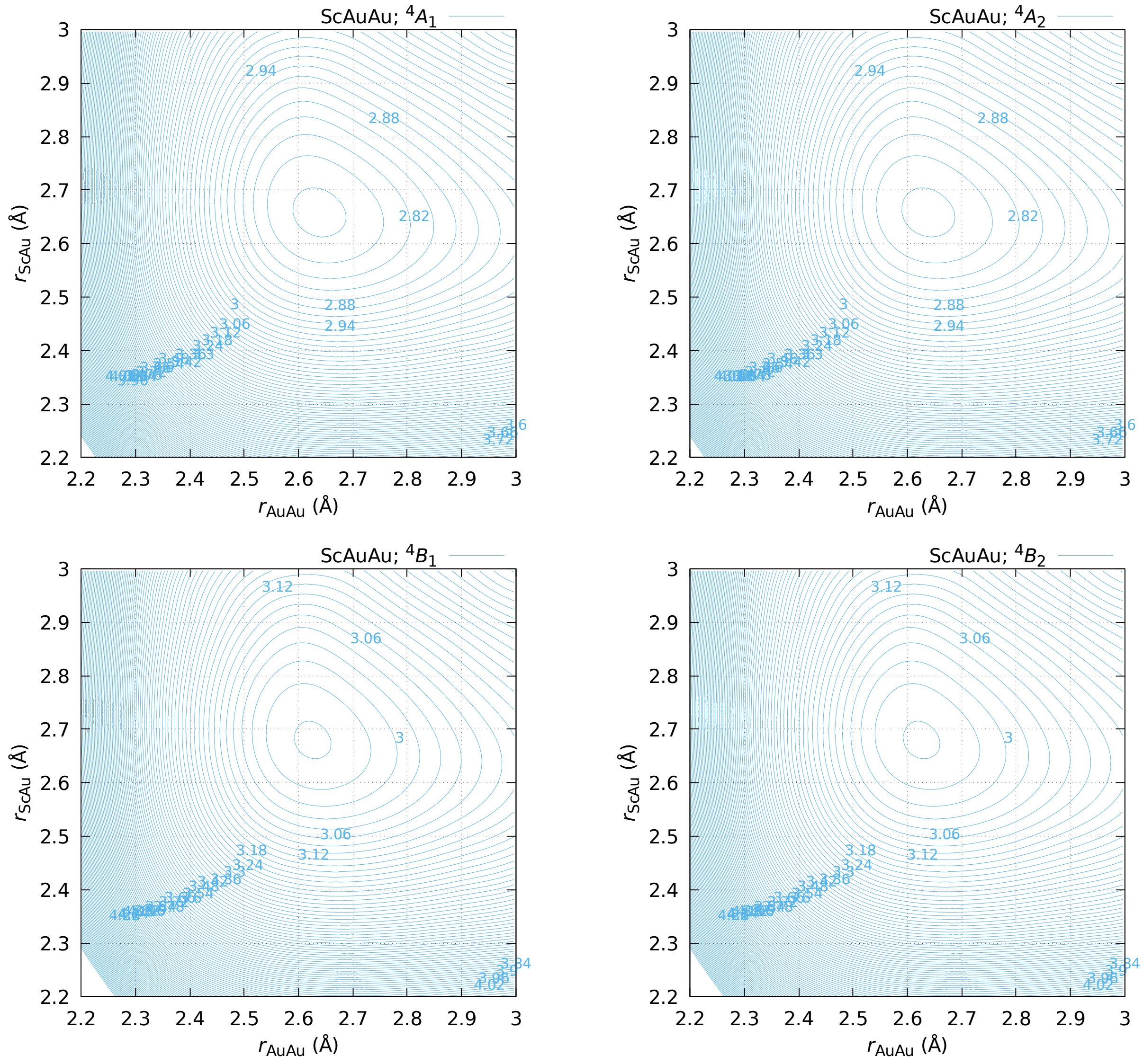

* * *

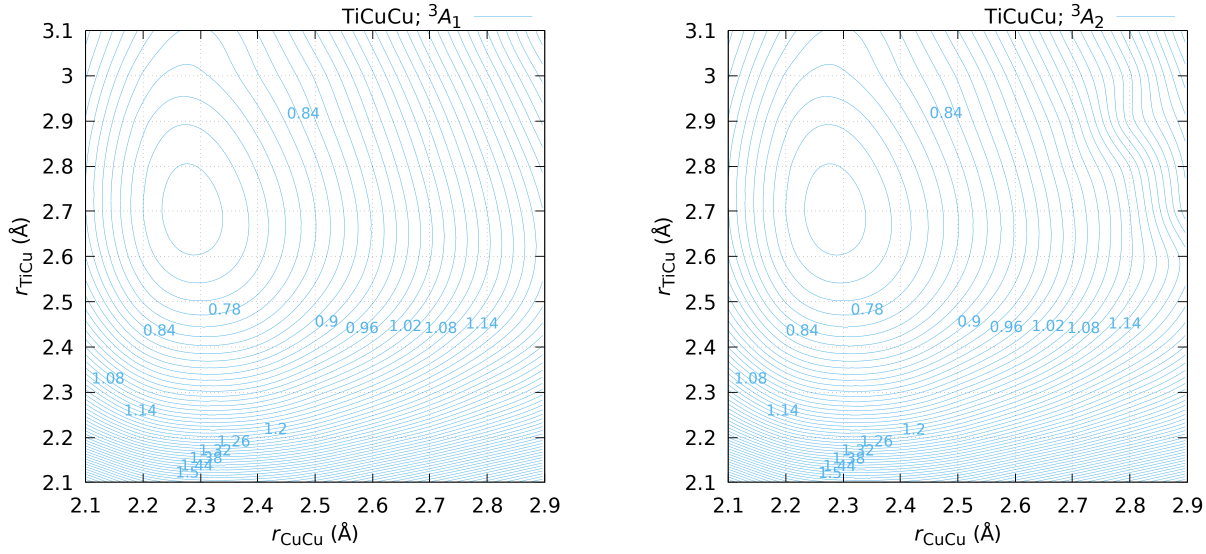

Figure B.62: Potential energy surfaces, $E(r_{\mathrm{TiCu}}, r_{\mathrm{CuCu}}; {}^{3,5}\Lambda)$, of the linear TiCuCu structure obtained at DKH-MRCI[(20+6)E,(10+8)O]. *Ab initio* points are indicated with the intersections of grid lines. Iso-energies are in eV and relative to the lowest state.

Continued on next page

Continued from previous page

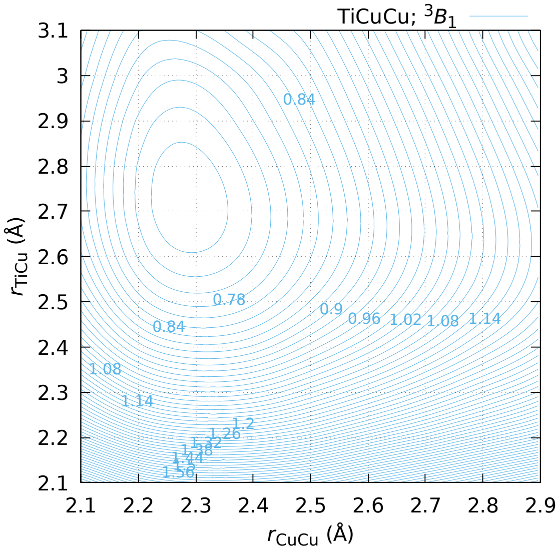

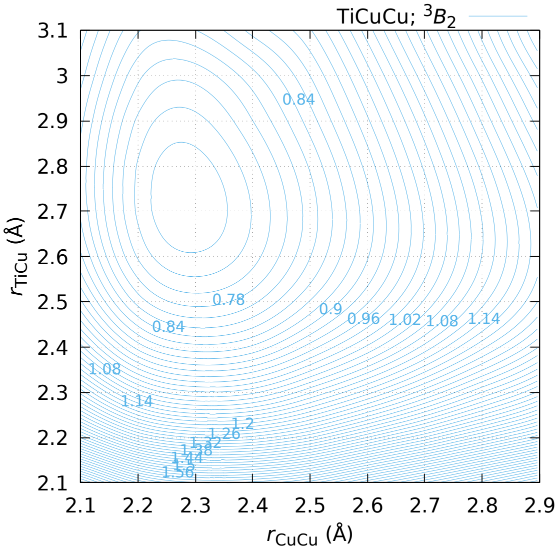

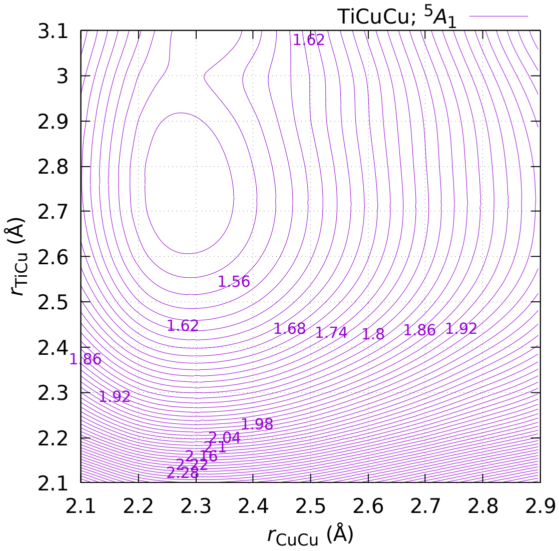

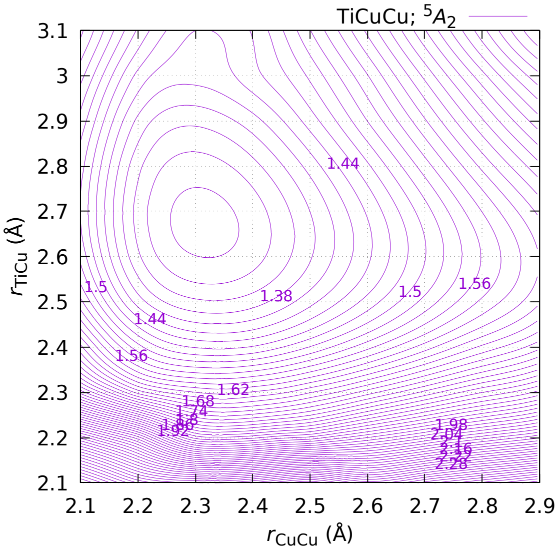

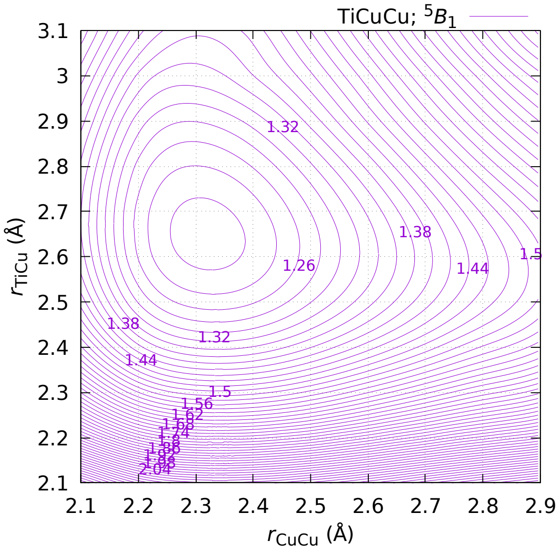

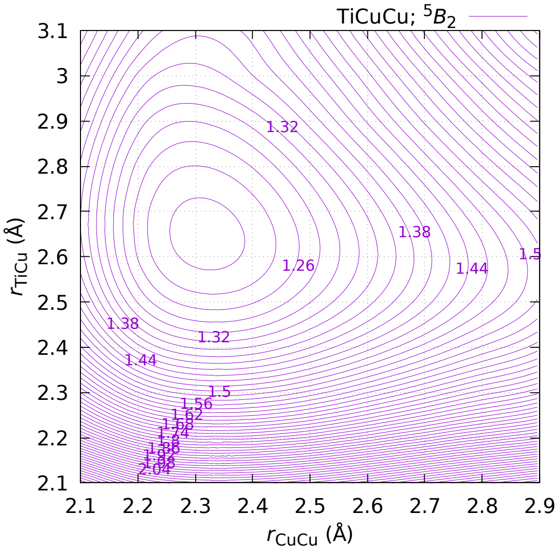

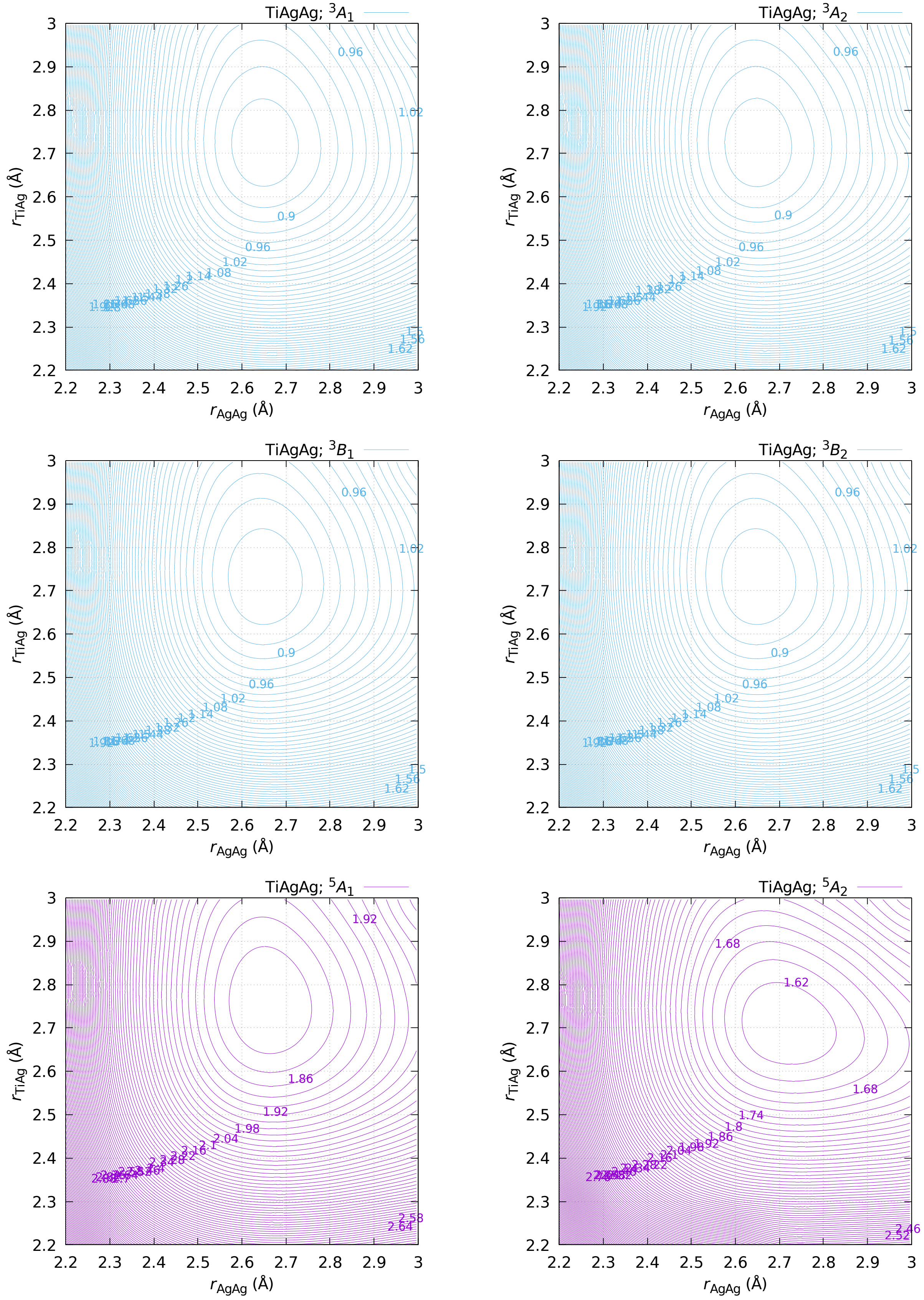

Figure B.63: Potential energy surfaces, $E(r_{\text{TiAg}}, r_{\text{AgAg}};\, ^{3,5}\Lambda)$, of the linear TiAgAg structure obtained at DKH-MRCI[(20+6)E,(10+8)O]. *Ab initio* points are indicated with the intersections of grid lines. Iso-energies are in eV and relative to the $\tilde{X}^3\Phi_g$ ground state.

Continued on next page

Continued from previous page

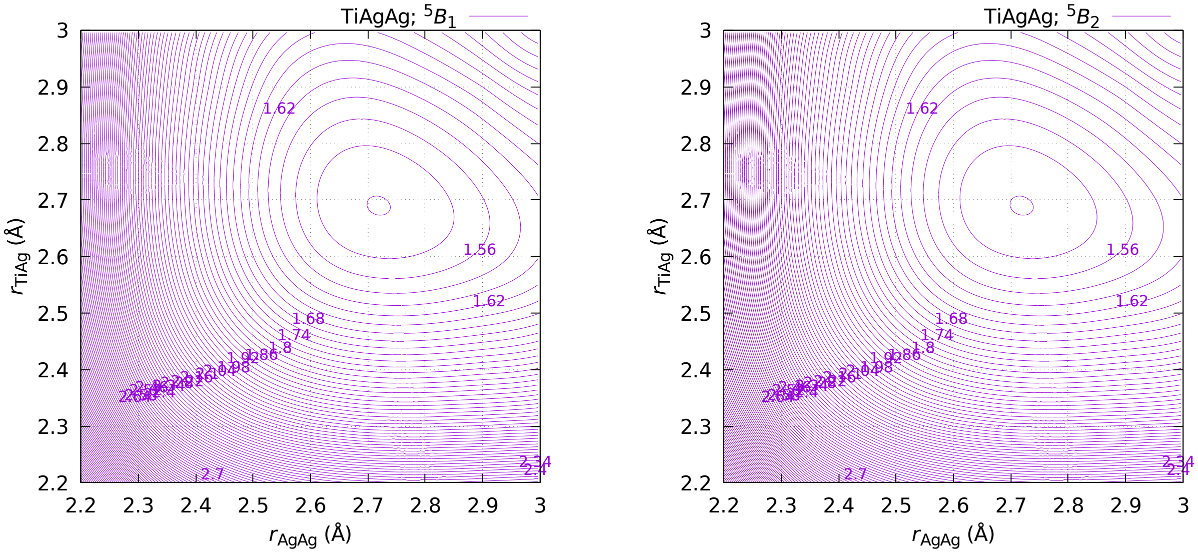

* * *

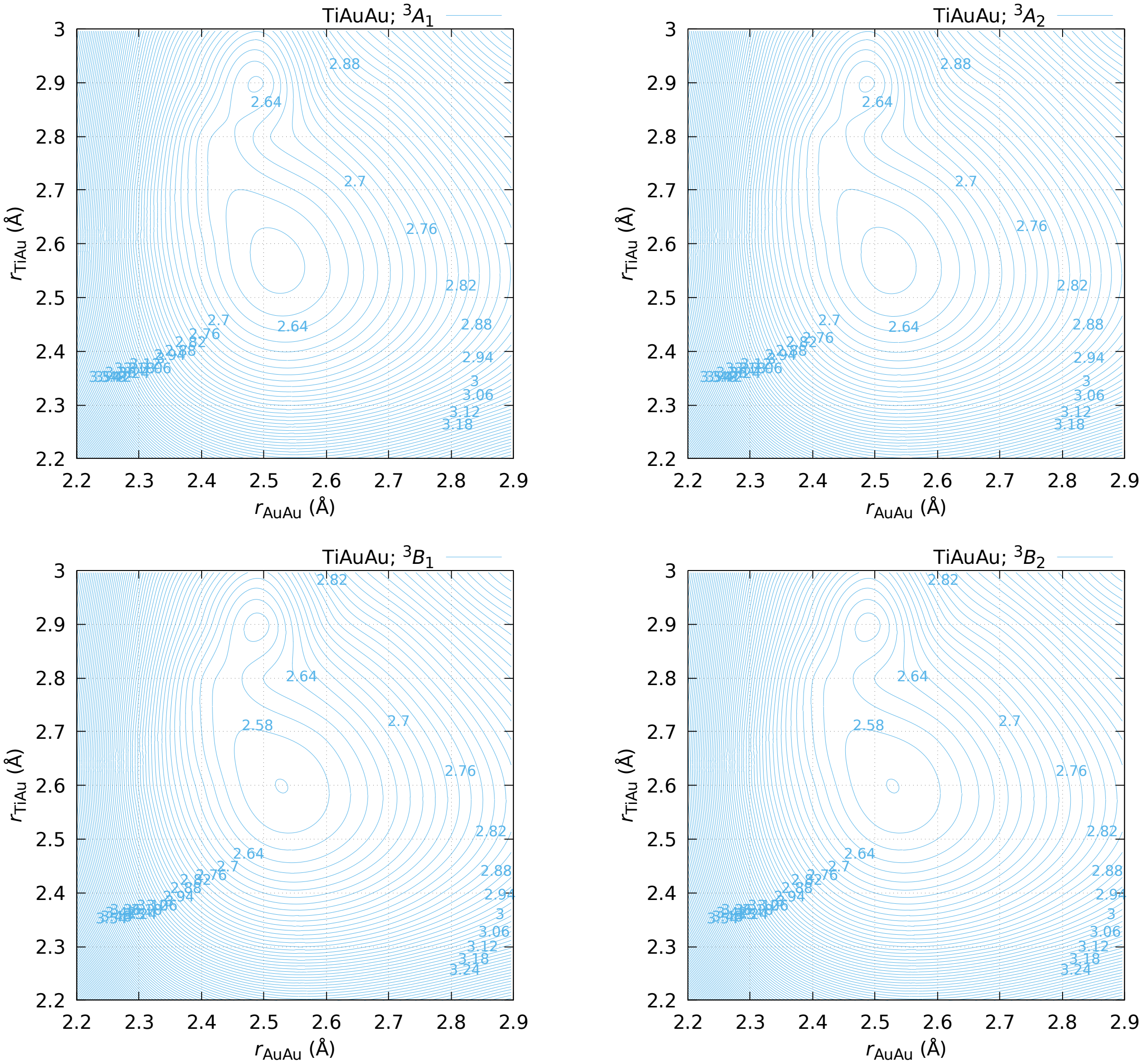

Figure B.64: Potential energy surfaces, $E(r_{\mathrm{TiAu}}, r_{\mathrm{AuAu}}; {}^{3,5}\Lambda)$, of the linear TiAuAu structure obtained at DKH-MRCI[(20+6)E,(10+8)O]. *Ab initio* points are indicated with the intersections of grid lines. Iso-energies are in eV and relative to the $\tilde{X}^3\Phi_g$ ground state.

Continued on next page

Continued from previous page

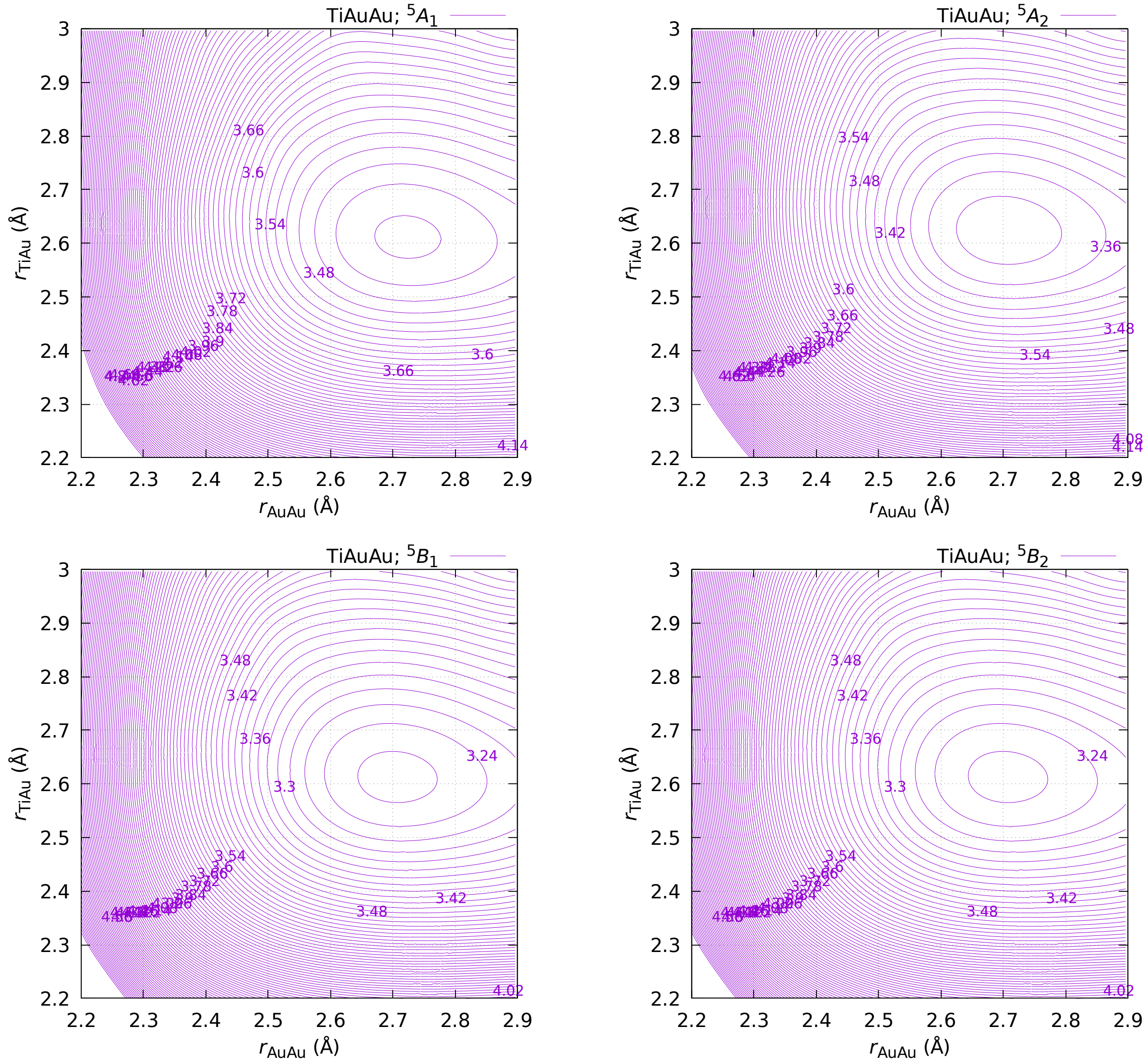

* * *

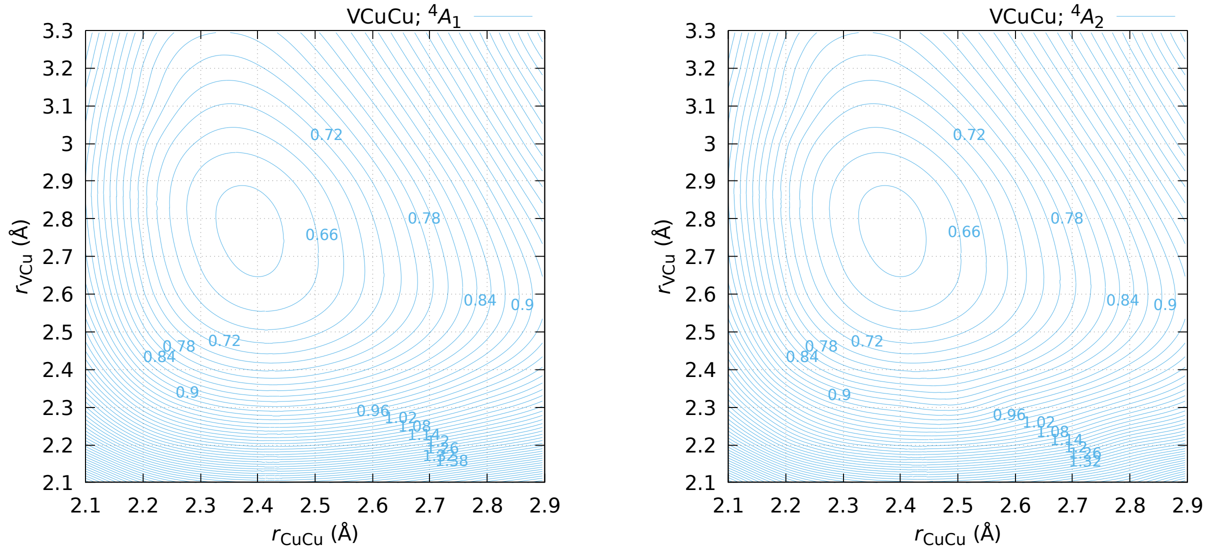

Figure B.65: Potential energy surfaces, $E(r_{\mathrm{VCu}}, r_{\mathrm{CuCu}}; {}^{4,6}\Lambda)$, of the linear VCuCu structure obtained at DKH-MRCI[(20+7)E,(10+8)O]. *Ab initio* points are indicated with the intersections of grid lines. Iso-energies are in eV and relative to the lowest state.

Continued on next page

Continued from previous page

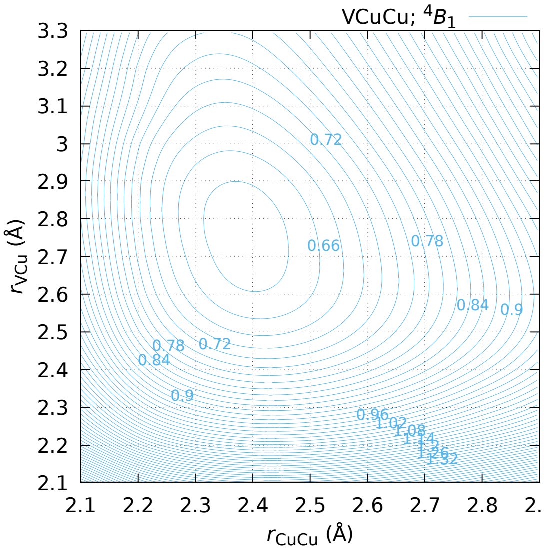

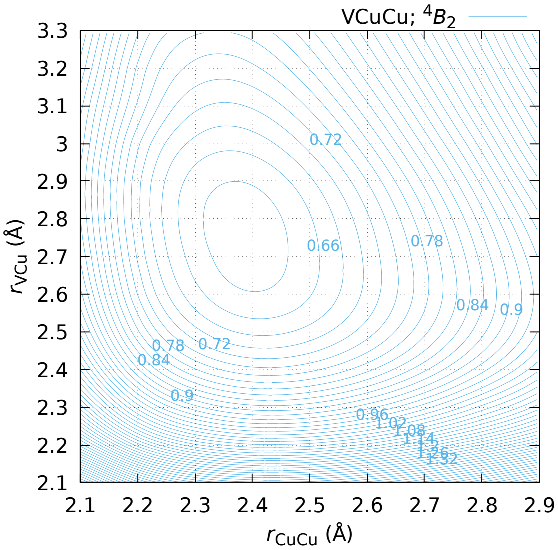

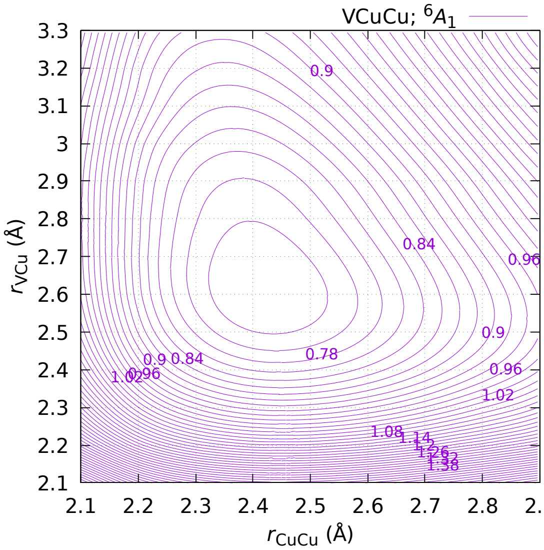

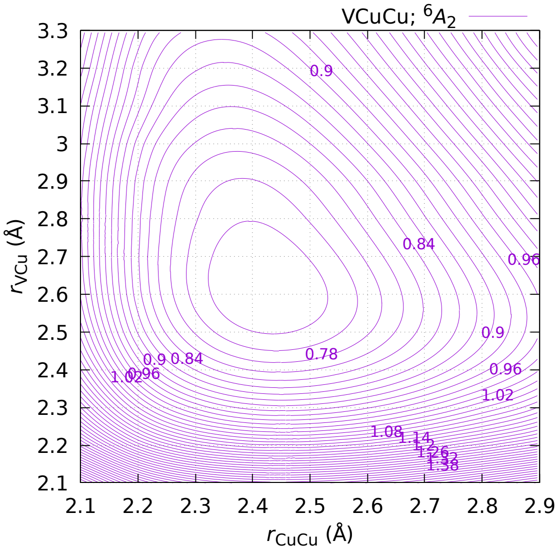

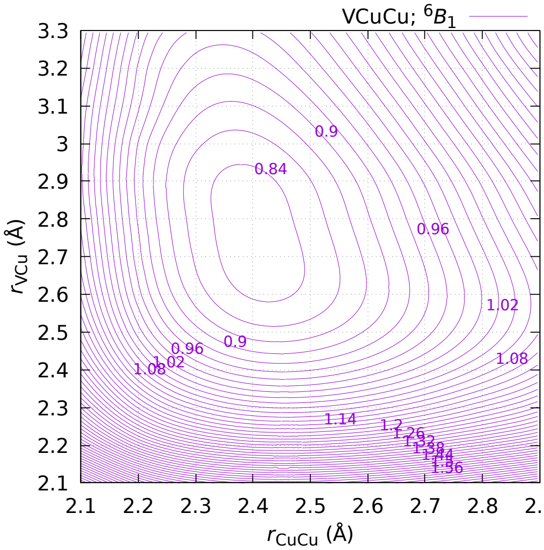

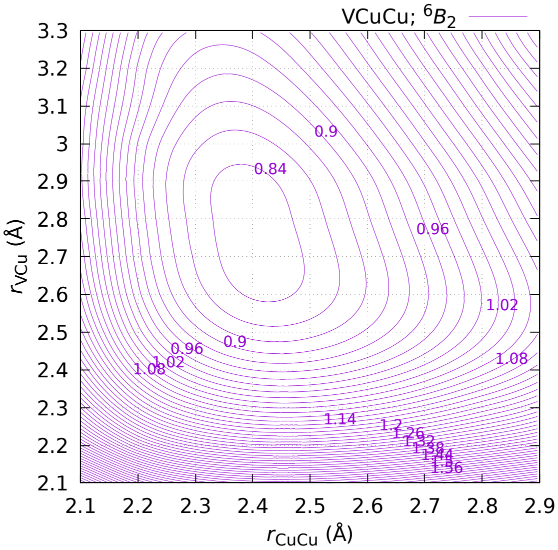

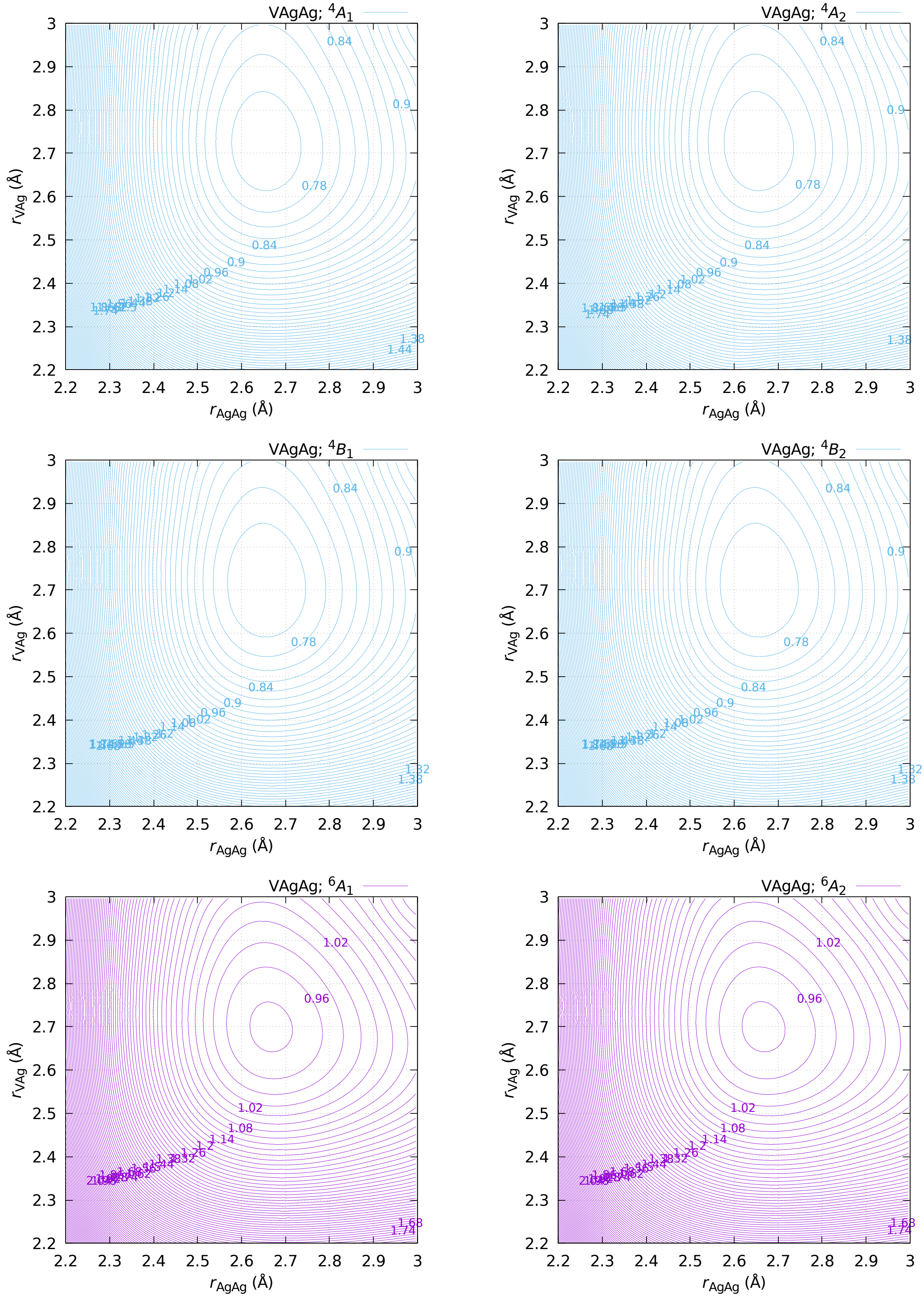

Figure B.66: Potential energy surfaces, $E(r_{\mathrm{VAg}}, r_{\mathrm{AgAg}}; {}^{4,6}\Lambda)$, of the linear VAgAg structure obtained at DKH-MRCI[(20+7)E,(10+8)O]. *Ab initio* points are indicated with the intersections of grid lines. Iso-energies are in eV and relative to the lowest state.

Continued on next page

Continued from previous page

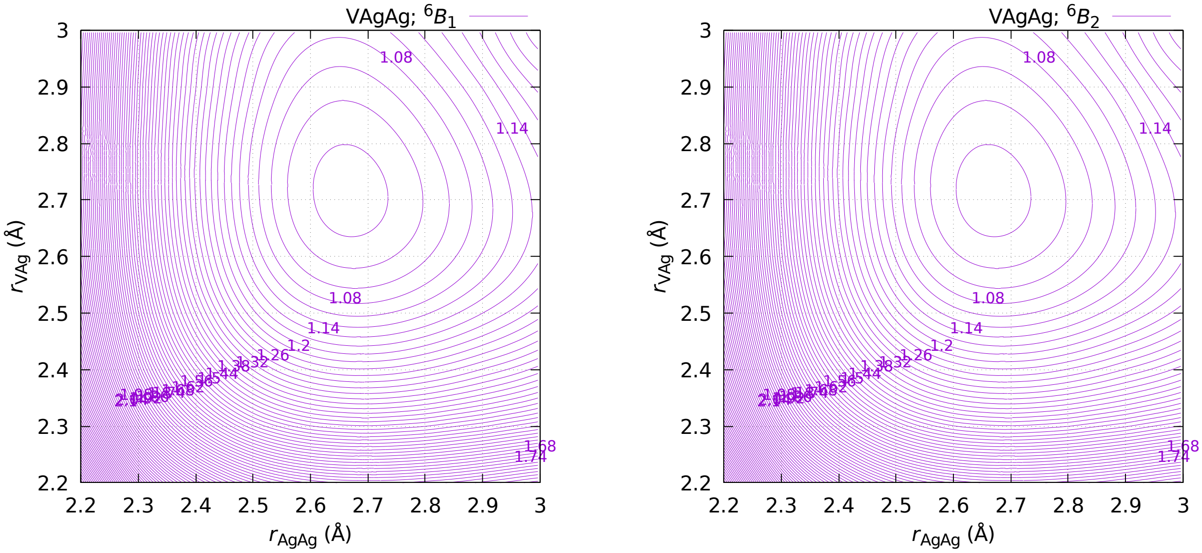

* * *

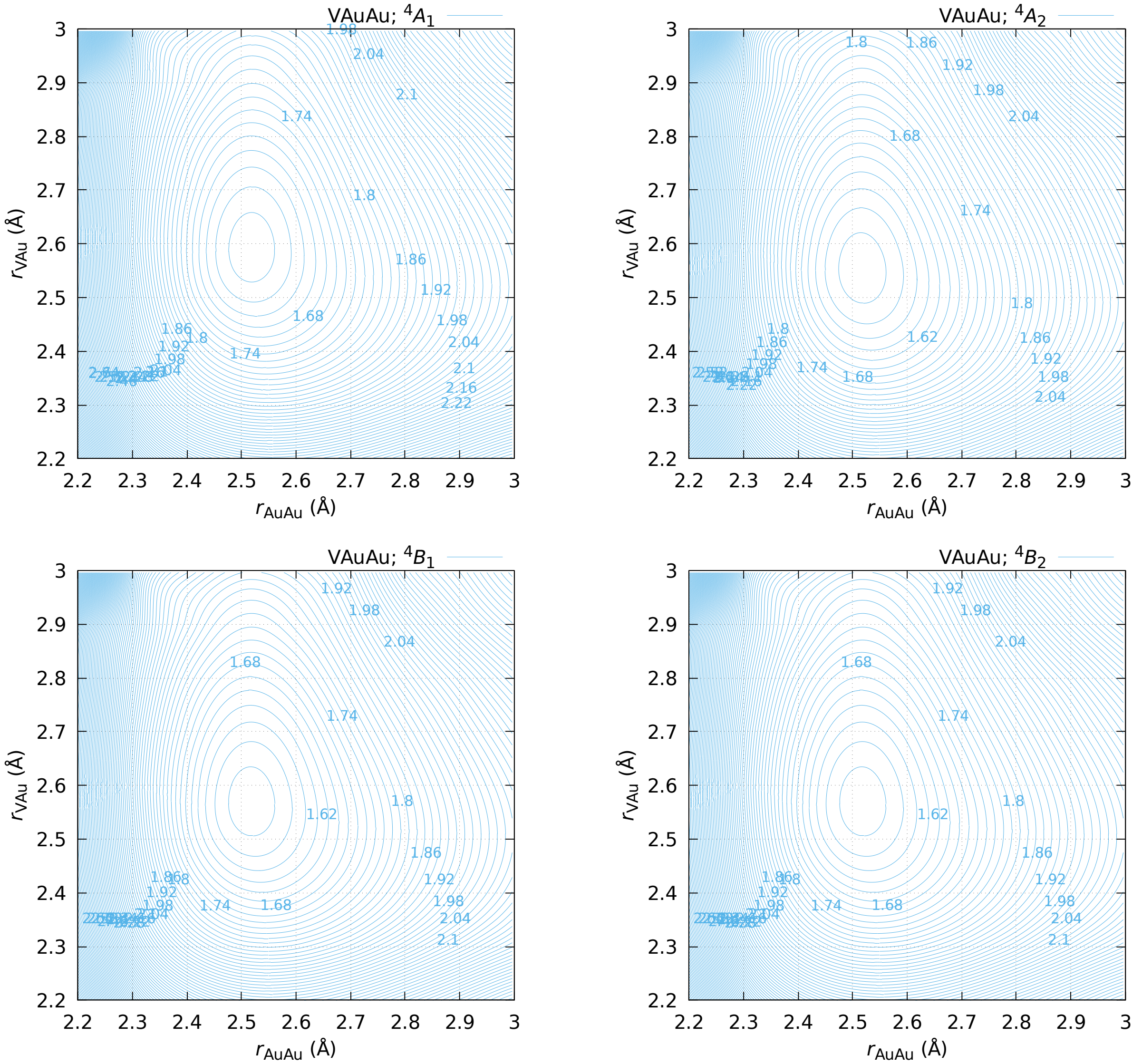

Figure B.67: Potential energy surfaces, $E(r_{\text{VAu}}, r_{\text{AuAu}}; {}^{4,6}\Lambda)$, of the linear VAuAu structure obtained at DKH-MRCI[(20+7)E,(10+8)O]. *Ab initio* points are indicated with the intersections of grid lines. Iso-energies are in eV and relative to the $\tilde{X}^4\Lambda^{(-)}$ ground state.

Continued on next page

Continued from previous page

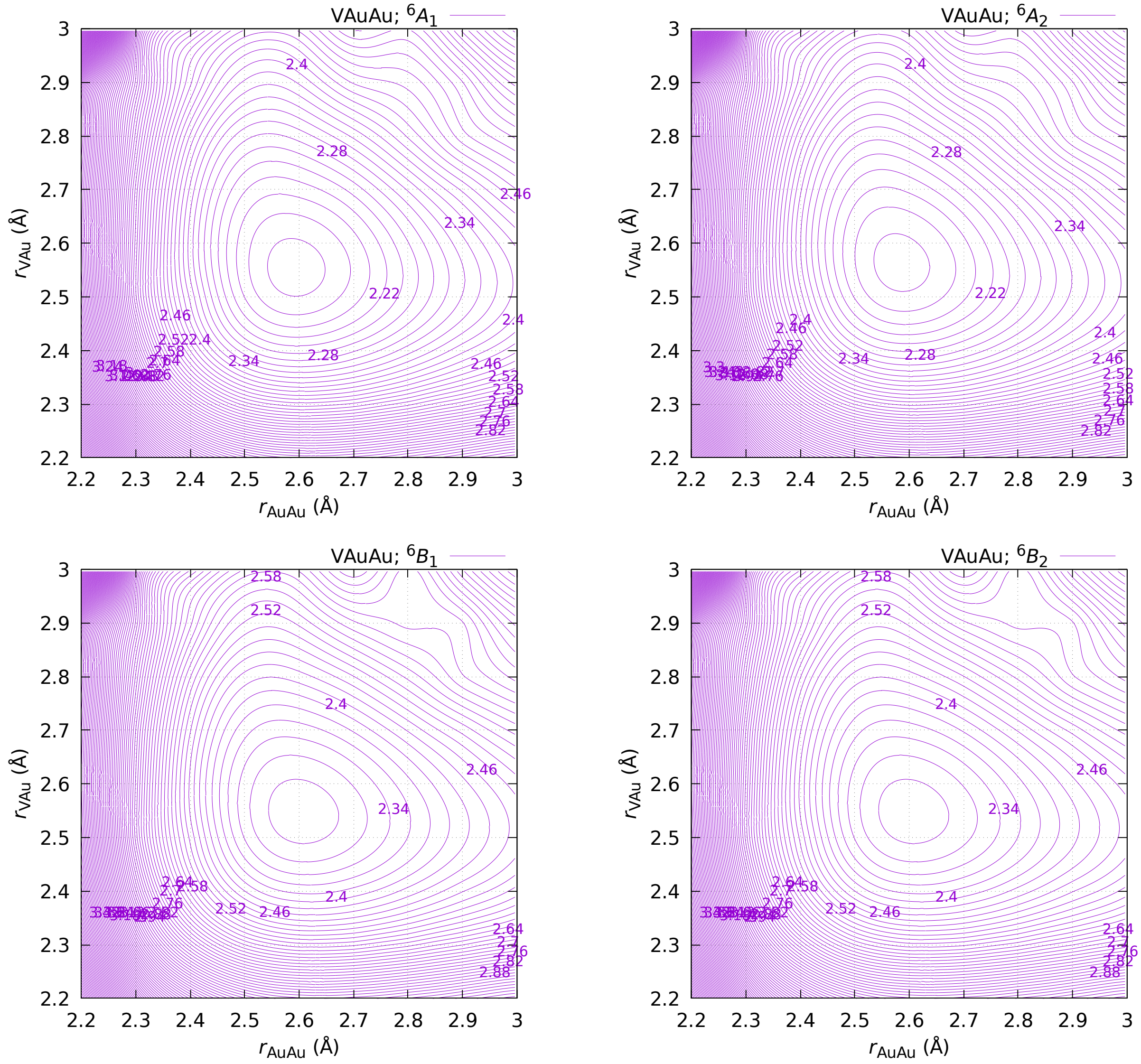

* * *

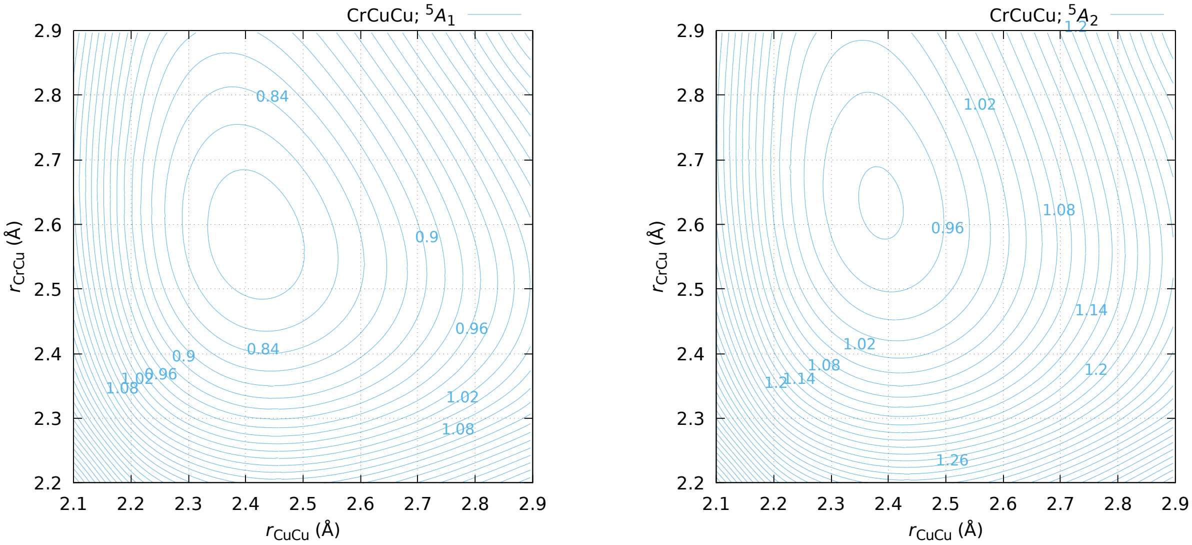

Figure B.68: Potential energy surfaces, $E(r_{\mathrm{CrCu}}, r_{\mathrm{CuCu}}; {}^{5,7}\Lambda)$, of the linear CrCuCu structure obtained at DKH-MRCI[(20+8)E,(10+8)O]. *Ab initio* points are indicated with the intersections of grid lines. Iso-energies are in eV and relative to the $\tilde{x}^7\Sigma^+$ state.

Continued on next page

Continued from previous page

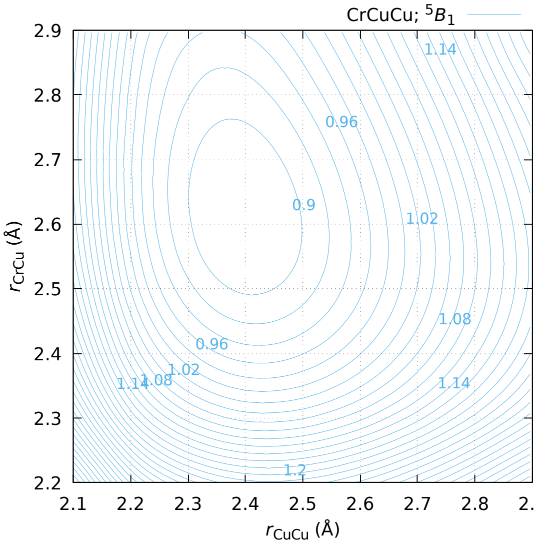

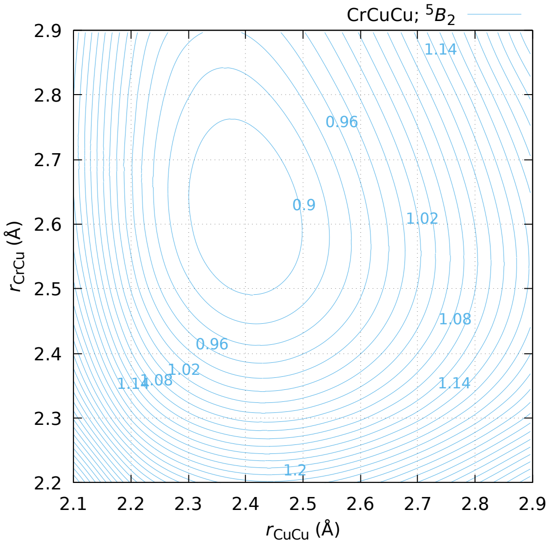

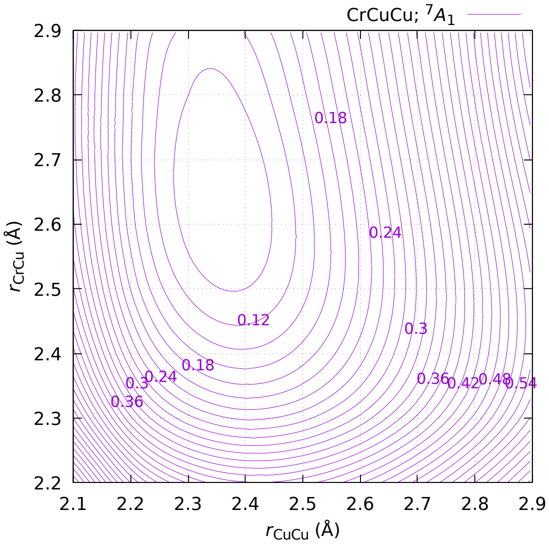

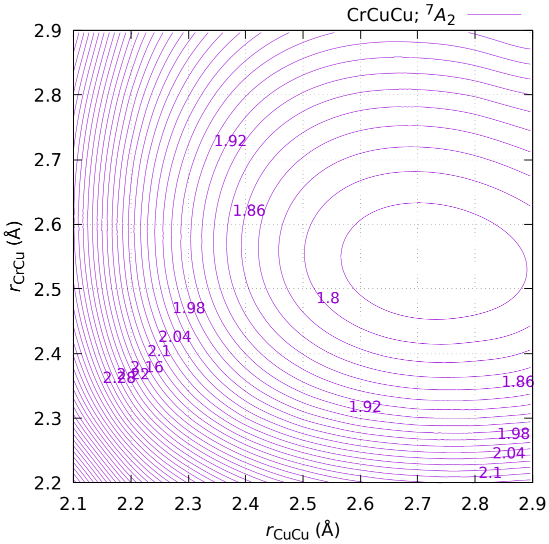

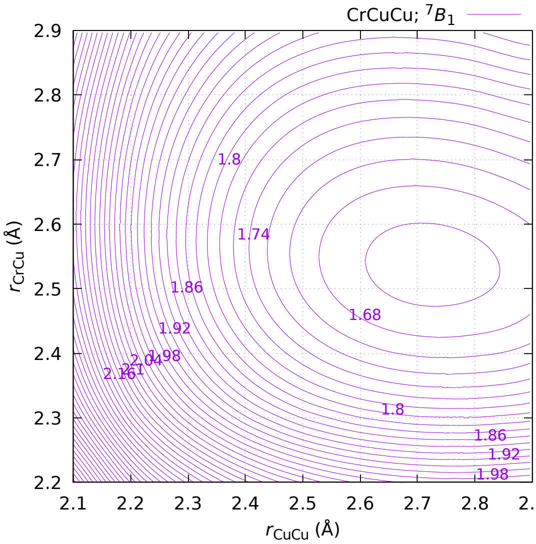

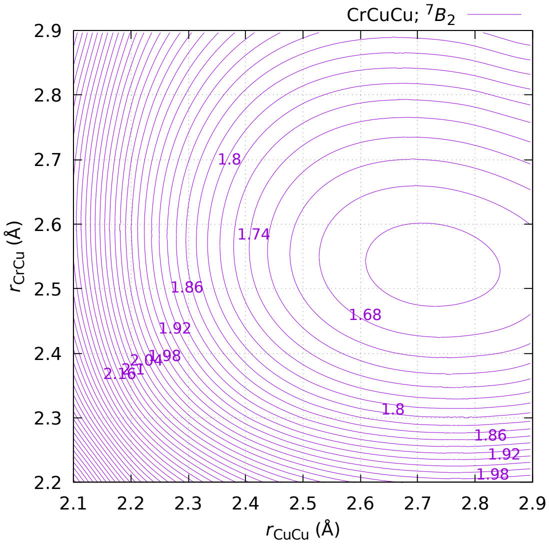

Continued from previous page

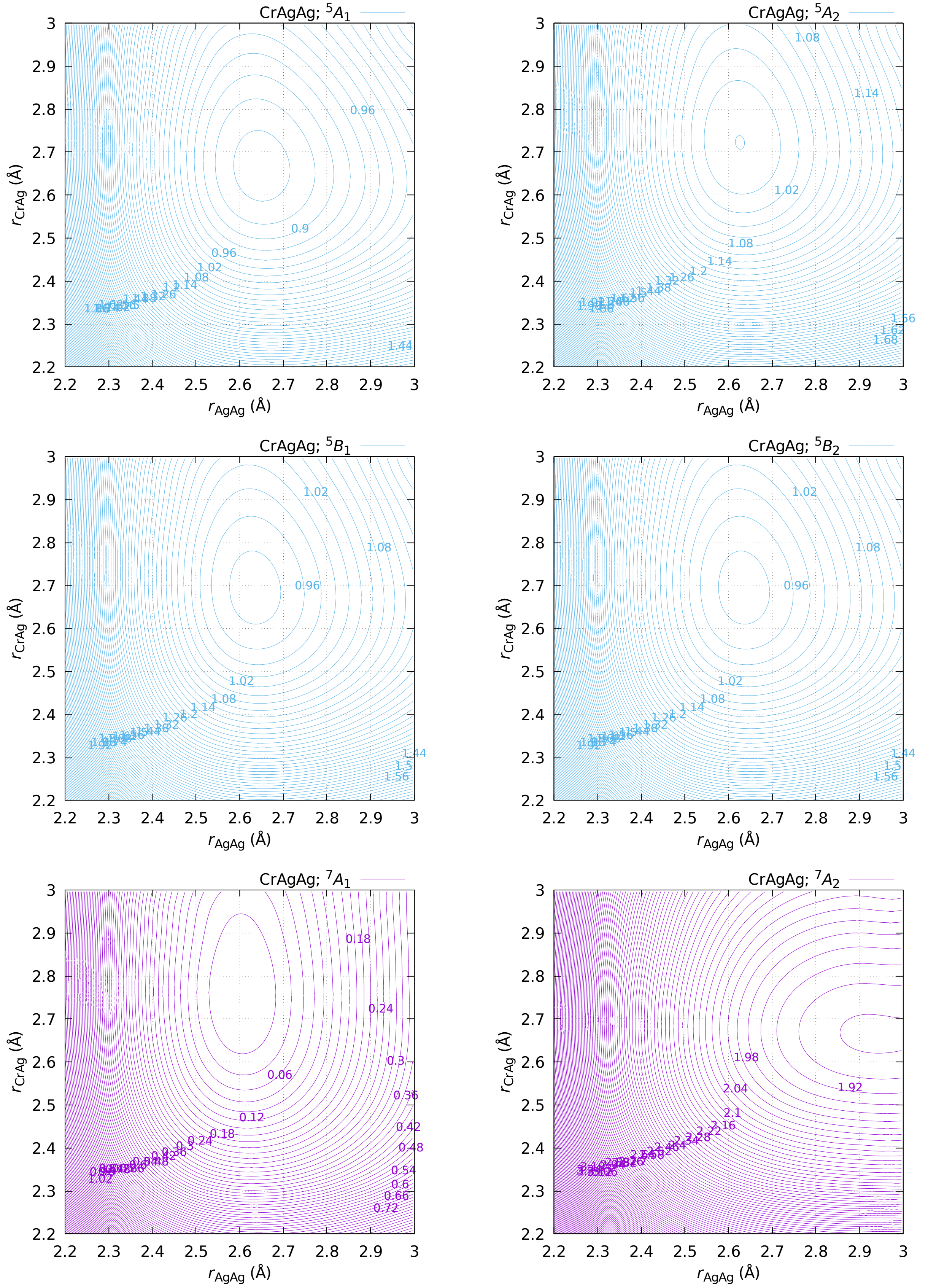

Figure B.69: Potential energy surfaces, $E(r_{\mathrm{CrAg}}, r_{\mathrm{AgAg}}; {}^{5,7}\Lambda)$, of the linear CrAgAg structure obtained at DKH-MRCI[(20+8)E,(10+8)O]. *Ab initio* points are indicated with the intersections of grid lines. Iso-energies are in eV and relative to the $\tilde{x}^7\Sigma^+$ state.

Continued on next page

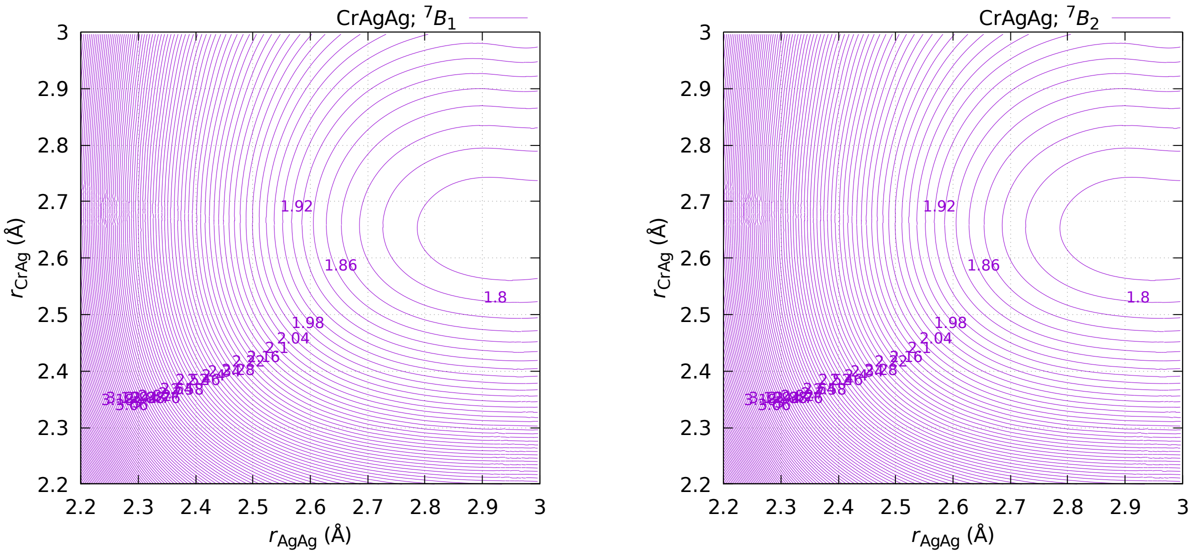

* * *

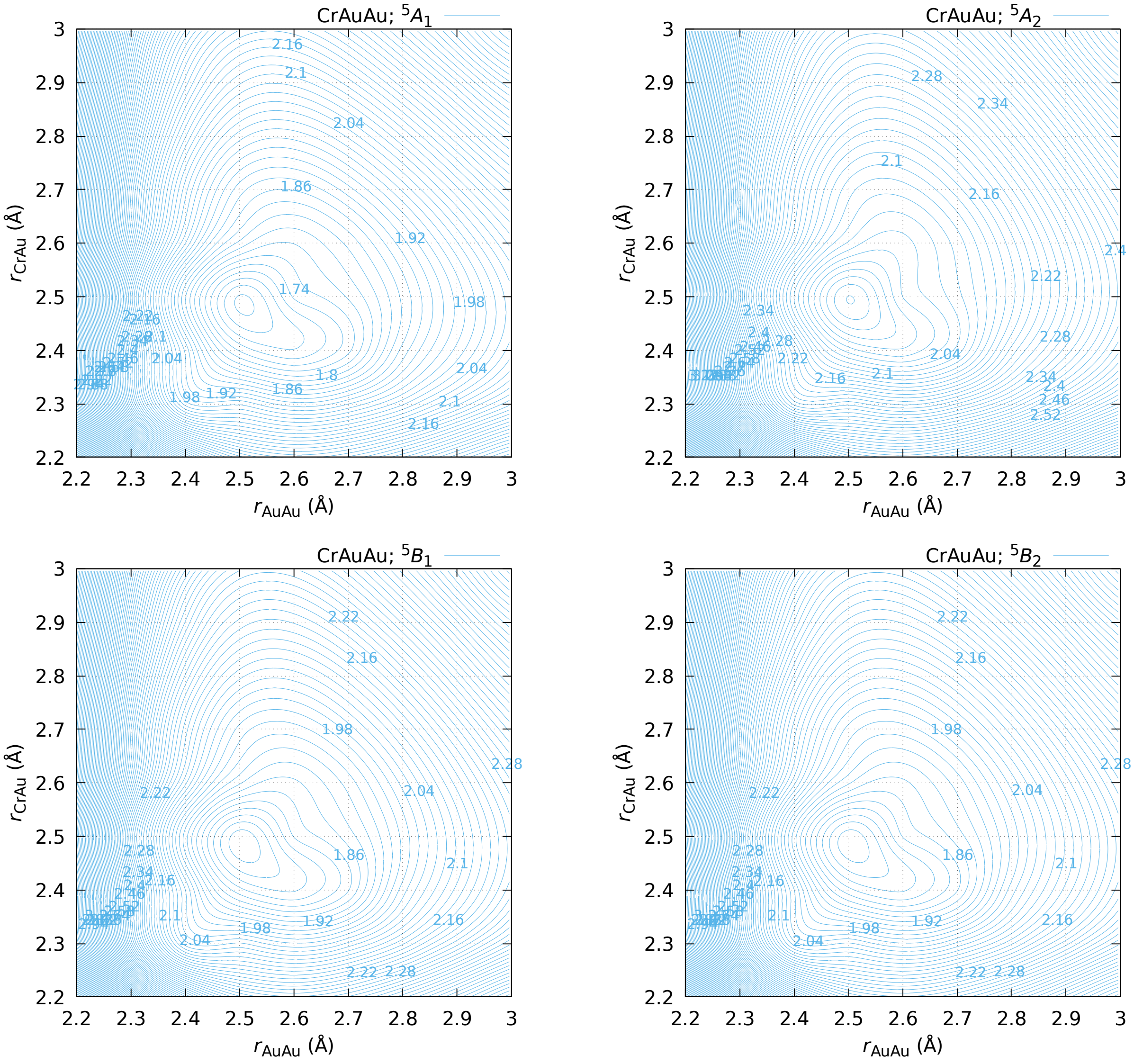

Figure B.70: Potential energy surfaces, $E(r_{\text{CrAu}}, r_{\text{AuAu}}; {}^{5,7}\Lambda)$, of the linear CrAuAu structure obtained at DKH-MRCI[(20+8)E,(10+8)O]. *Ab initio* points are indicated with the intersections of grid lines. Iso-energies are in eV and relative to the $\tilde{X}^5\Sigma_g^+$ ground state.

Continued on next page

Continued from previous page

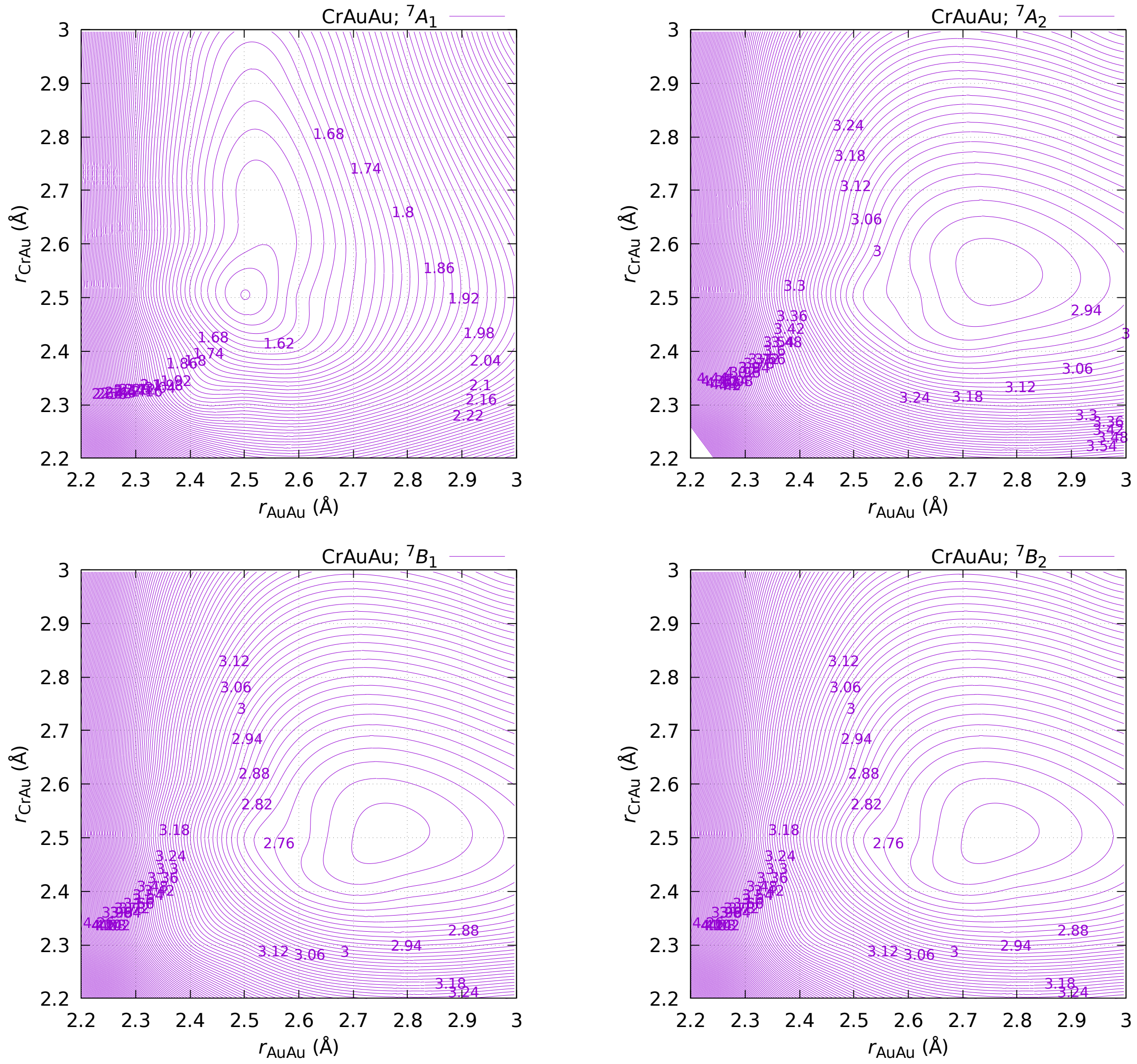

* * *

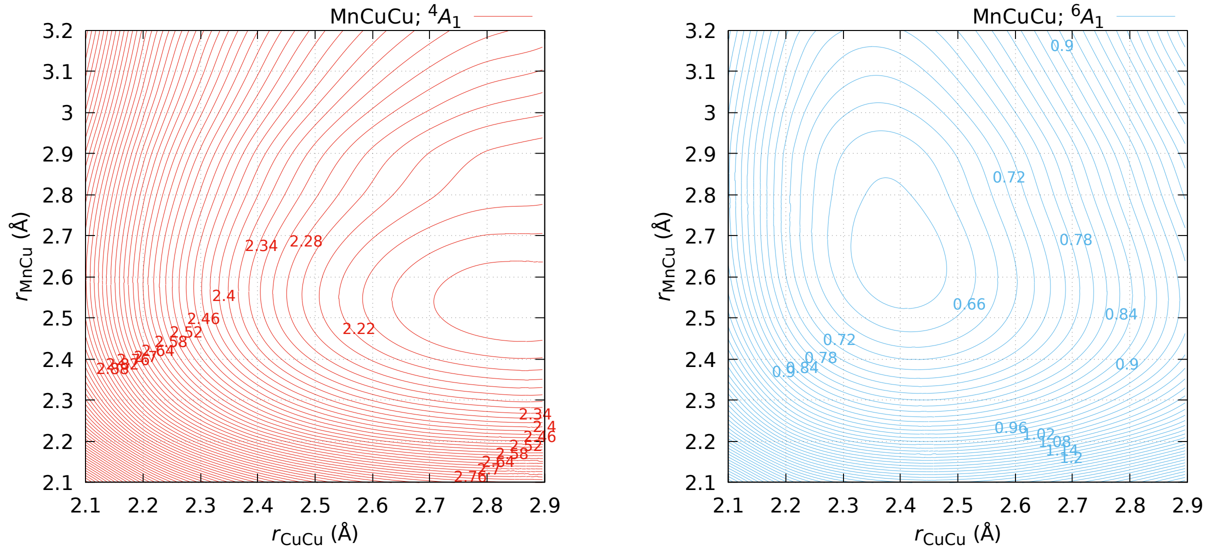

Figure B.71: Potential energy surfaces, $E(r_{\mathrm{MnCu}}, r_{\mathrm{CuCu}}; {}^{4,6,8}\Lambda)$, of the linear MnCuCu structure obtained at DKH-MRCI[(20+9)E,(10+8)O]. *Ab initio* points are indicated with the intersections of grid lines. Iso-energies are in eV and relative to the $\tilde{X}^6\Sigma_g^+$ ground state.

Continued on next page

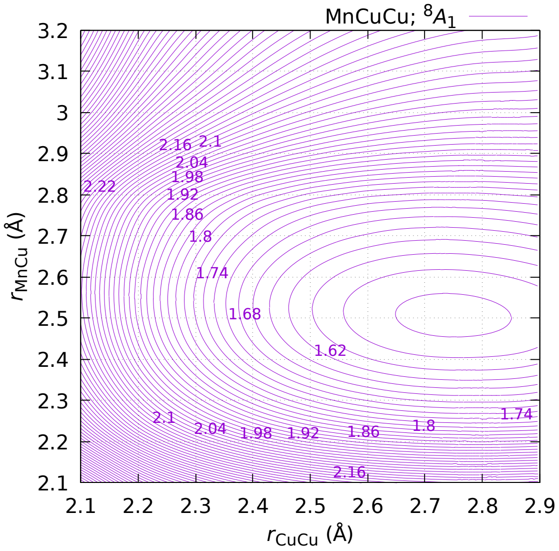

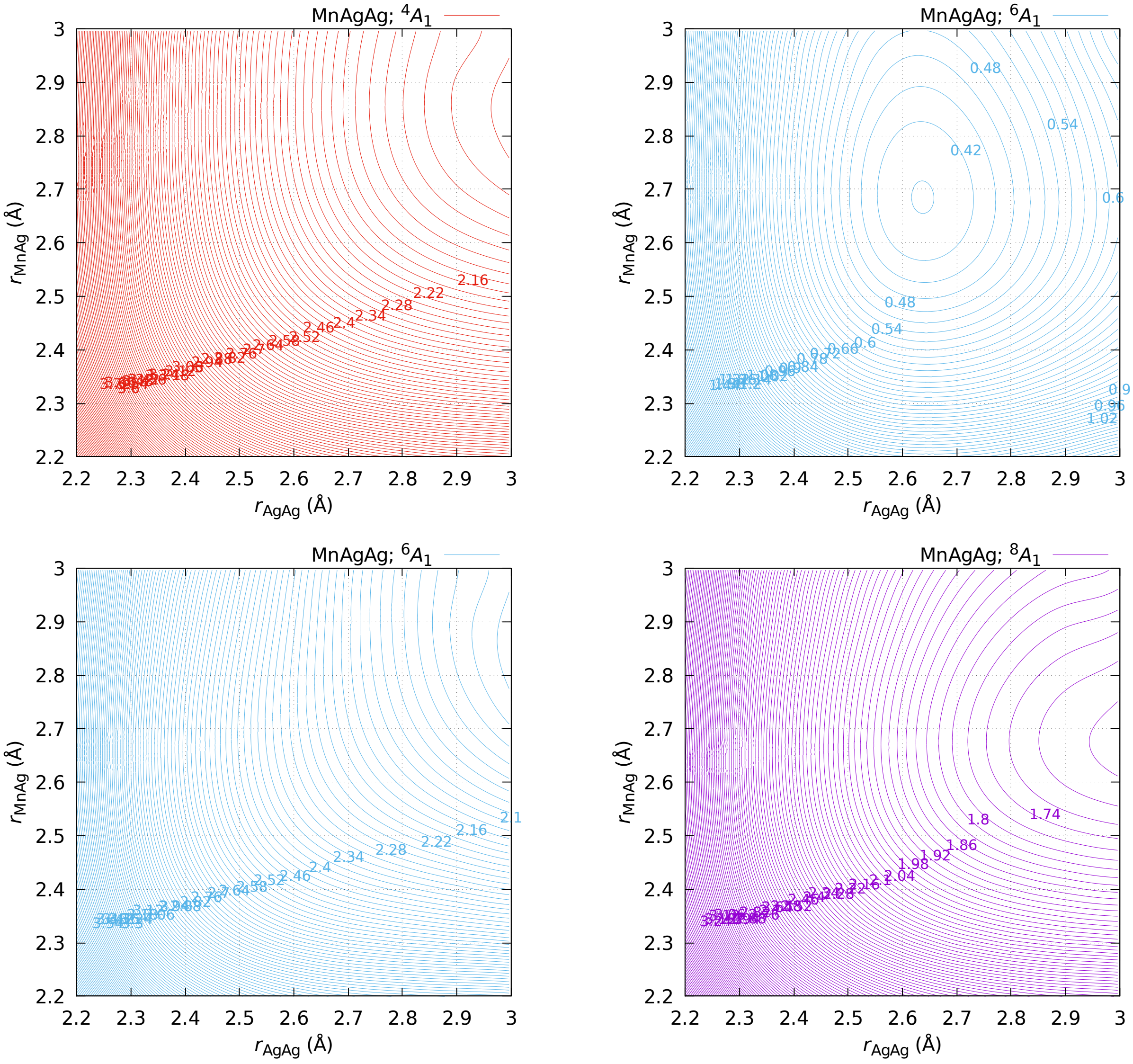

Figure B.72: Potential energy surfaces, $E(r_{\mathrm{MnAg}}, r_{\mathrm{AgAg}}; {}^{4,6,8}\Lambda)$, of the linear MnAgAg structure obtained at DKH-MRCI[(20+9)E,(10+8)O]. *Ab initio* points are indicated with the intersections of grid lines. Iso-energies are in eV and relative to the $\tilde{X}^6\Sigma_g^+$ ground state.

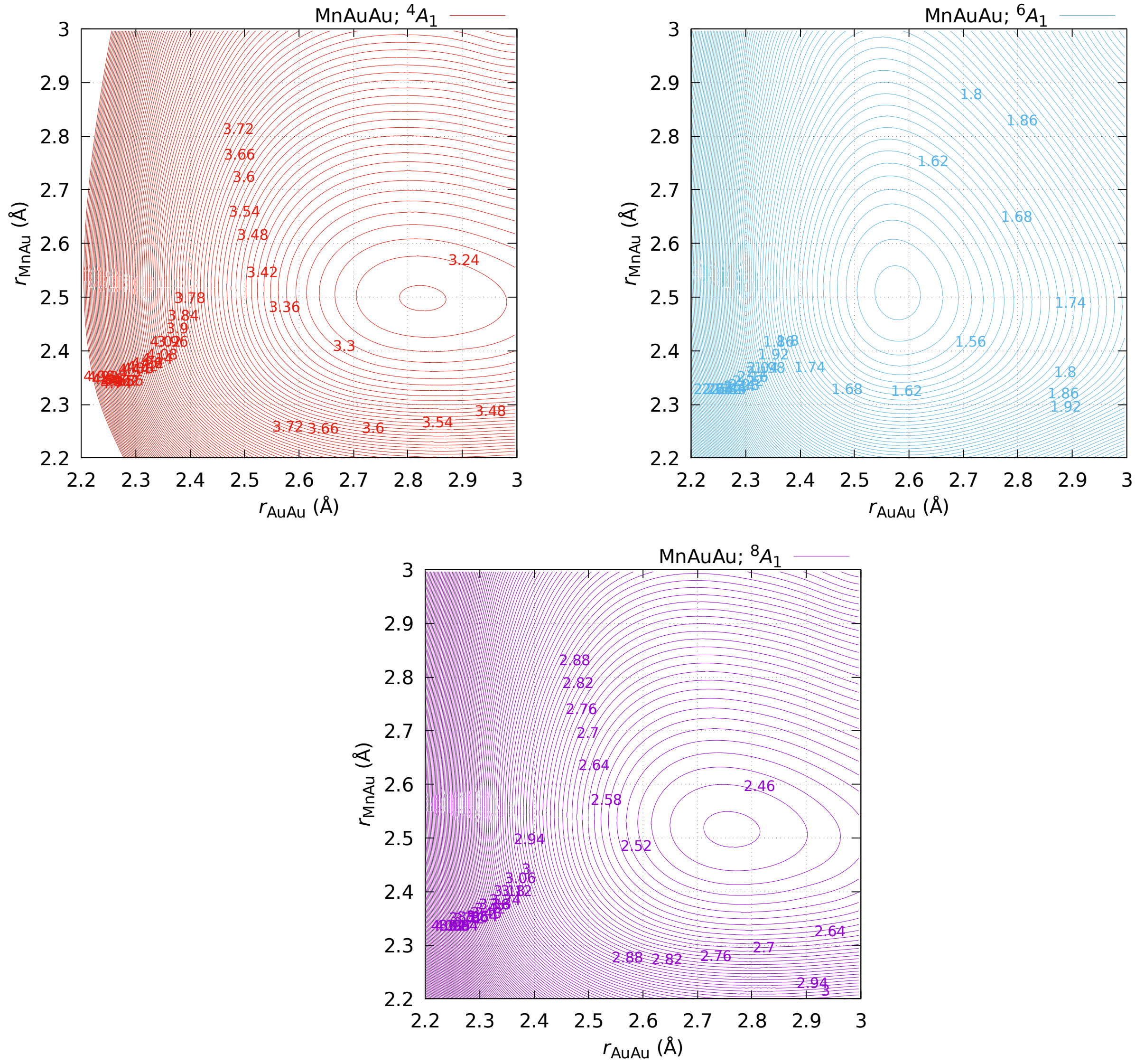

Figure B.73: Potential energy surfaces, $E(r_{\mathrm{MnAu}}, r_{\mathrm{AuAu}}; {}^{4,6,8}\Lambda)$, of the linear MnAuAu structure obtained at DKH-MRCI[(20+9)E,(10+8)O]. *Ab initio* points are indicated with the intersections of grid lines. Iso-energies are in eV and relative to the $\tilde{X}^6\Sigma_g^+$ ground state.

* * *

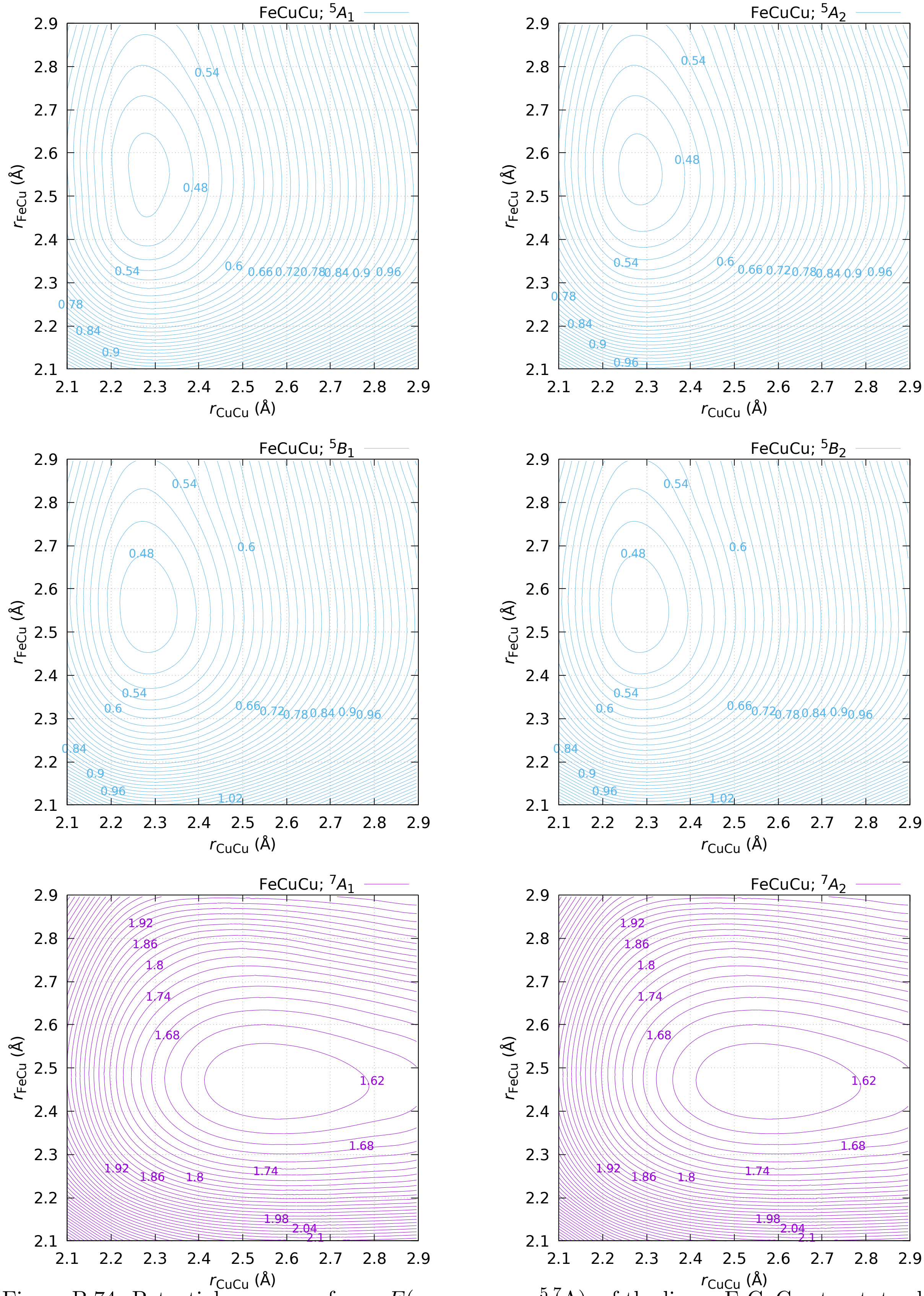

Figure B.74: Potential energy surfaces, $E(r_{\mathrm{FeCu}}, r_{\mathrm{CuCu}}; {}^{5,7}\Lambda)$, of the linear FeCuCu structute obtained at DKH-MRCI[(20+10)E,(10+8)O]. *Ab initio* points are indicated with the intersections of grid lines. Iso-energies are in eV and relative to the $\tilde{X}^5\Delta_g$ ground state.

Continued on next page

Continued from previous page

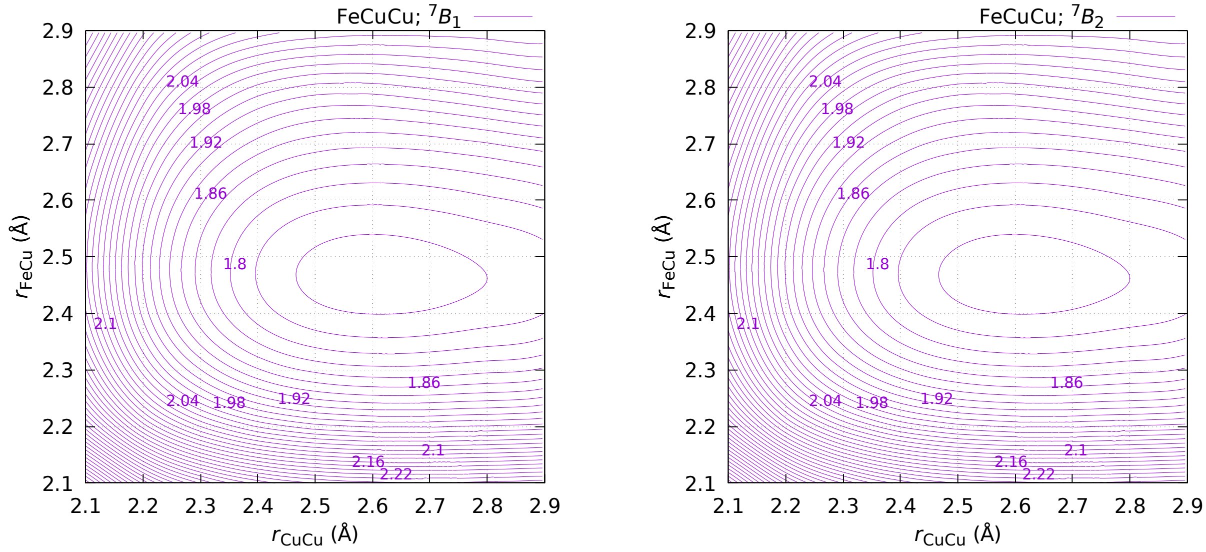

◆

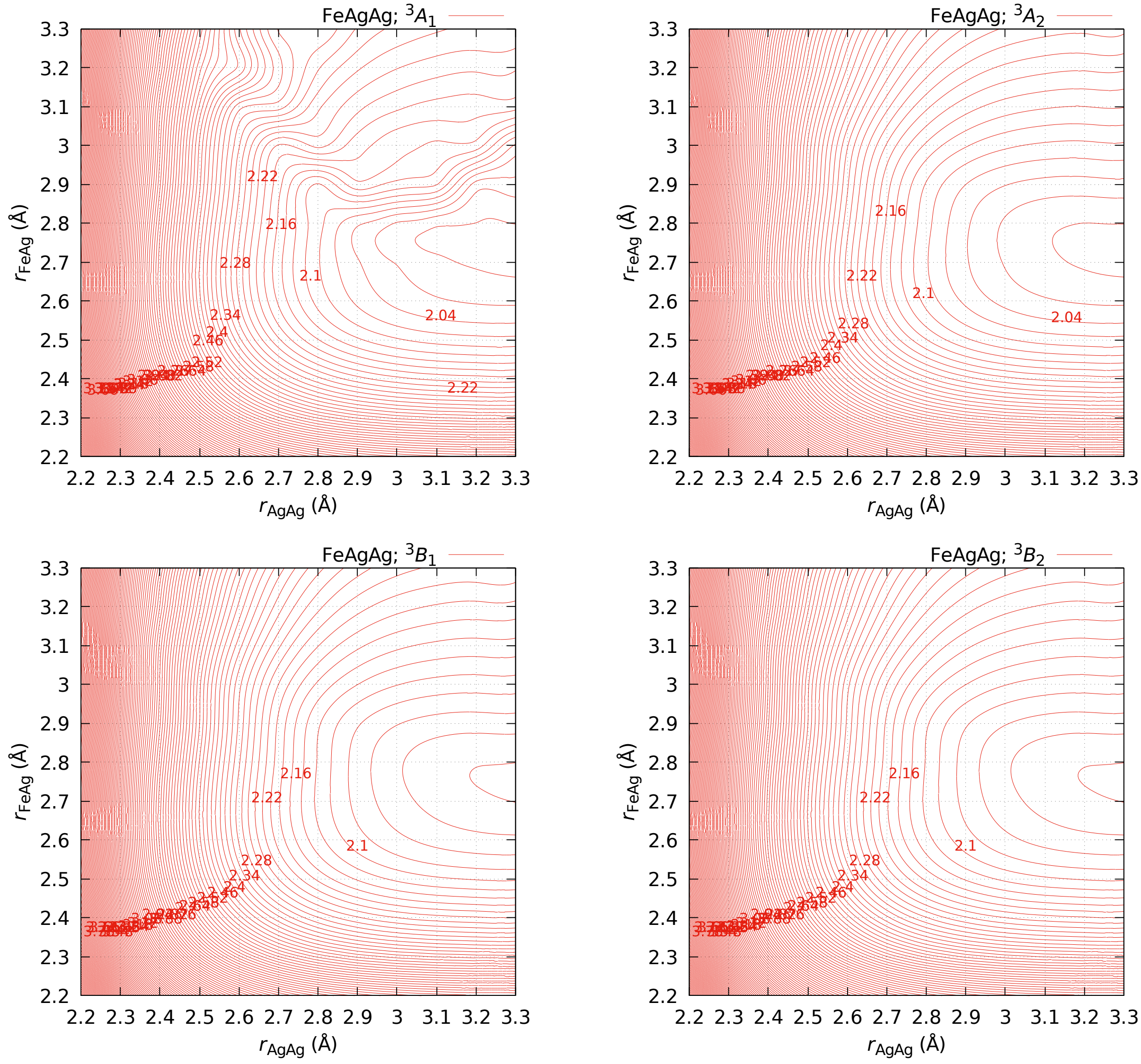

Figure B.75: Potential energy surfaces, $E(r_{\rm FeAg}, r_{\rm AgAg}; {}^{3,5,7}\Lambda)$, of the linear FeAgAg structure obtained at DKH-MRCI[(20+10)E,(10+8)O]. Iso-energies are in eV and relative to the $\tilde{X}^5\Delta_g$ ground state.

Continued on next page

Continued from previous page

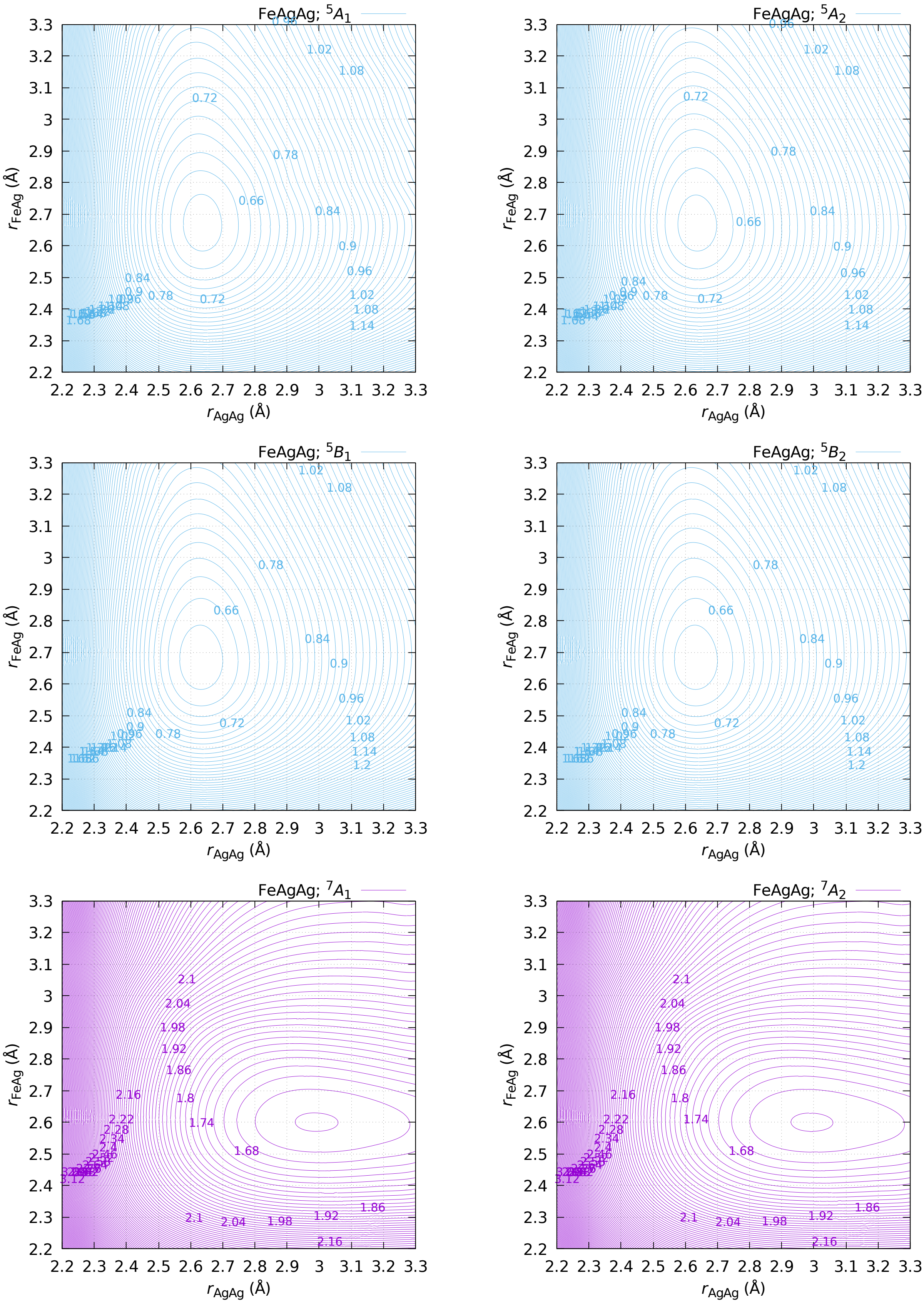

Continued on next page

Continued from previous page

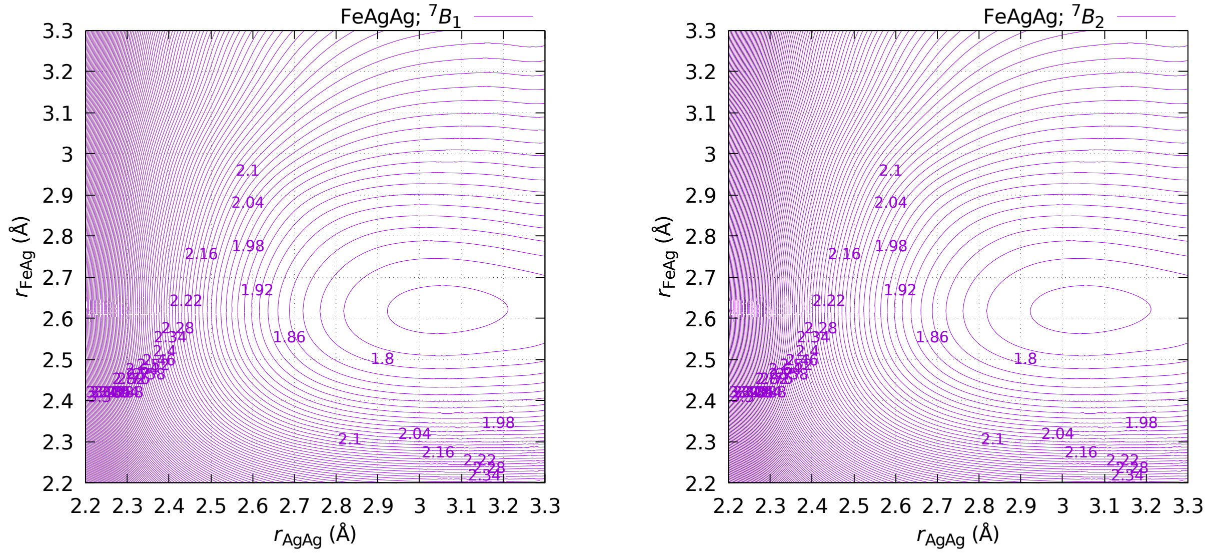

* * *

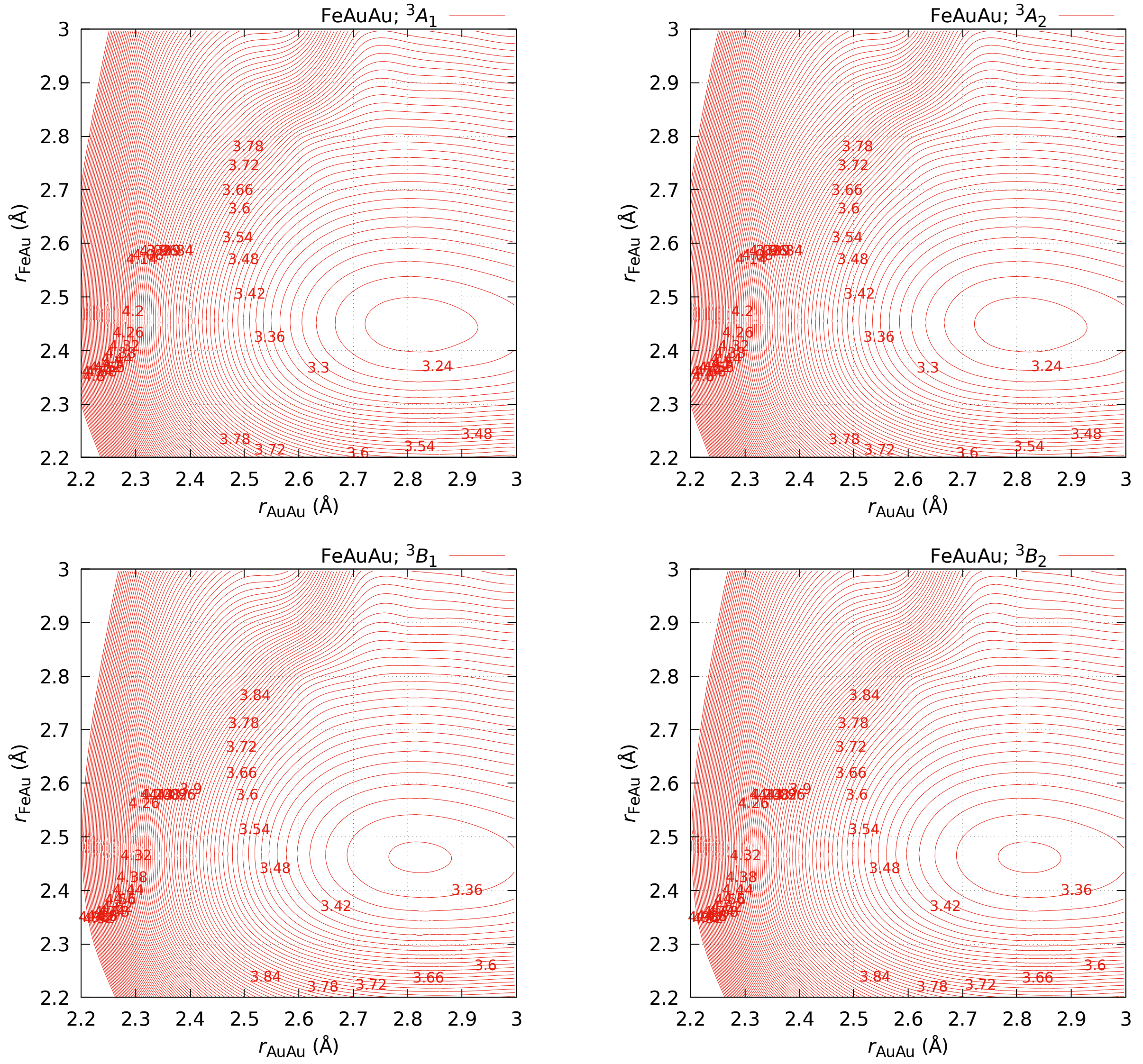

Figure B.76: Potential energy surfaces, $E(r_{\mathrm{FeAu}}, r_{\mathrm{AuAu}}; {}^{3,5,7}\Lambda)$, of the linear FeAuAu structure obtained at DKH-MRCI[(20+10)E,(10+8)O]. Iso-energies are in eV and relative to the $\tilde{X}^5\Delta_g$ ground state.

Continued on next page

Continued from previous page

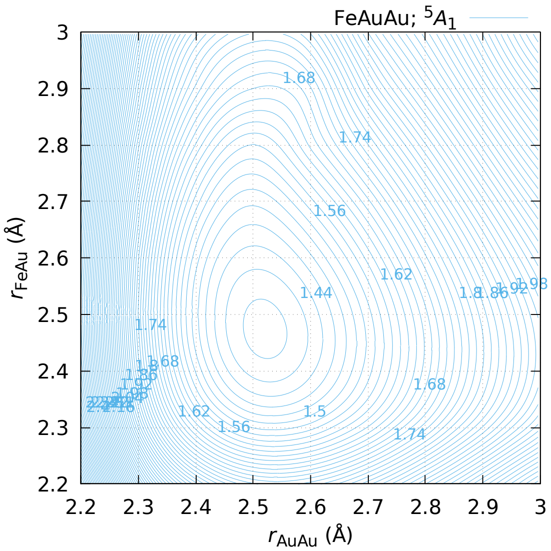

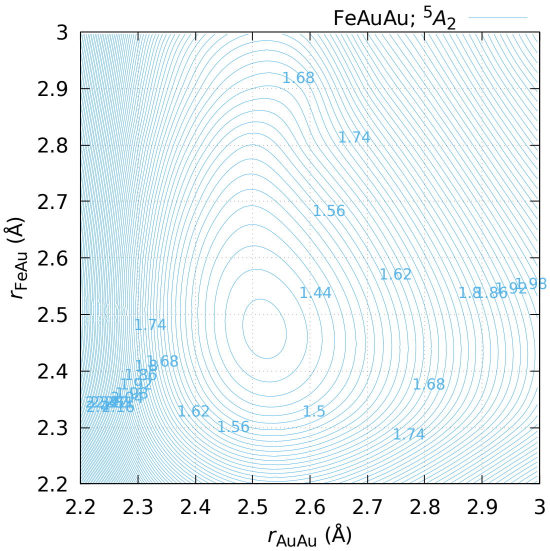

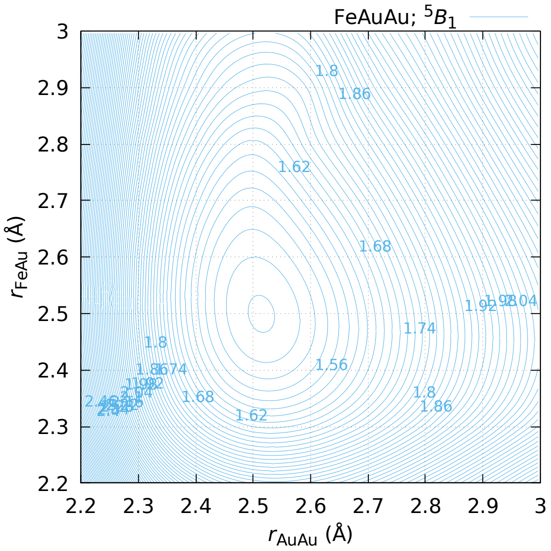

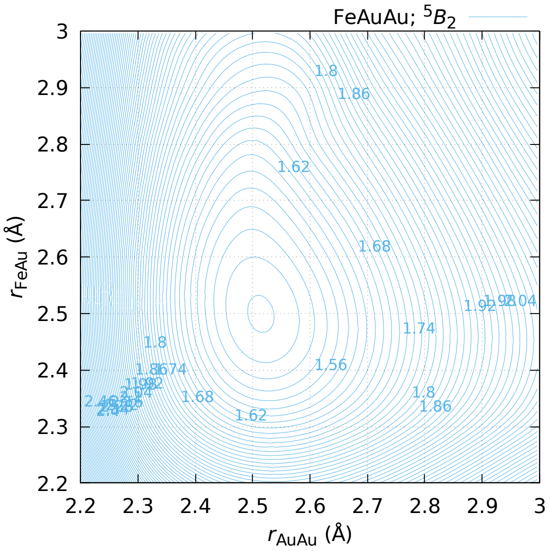

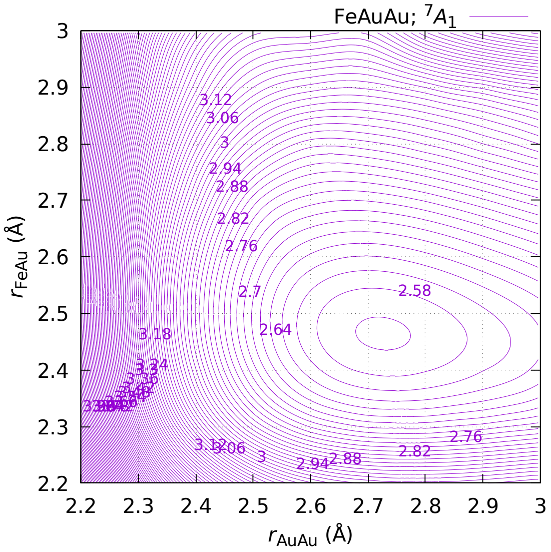

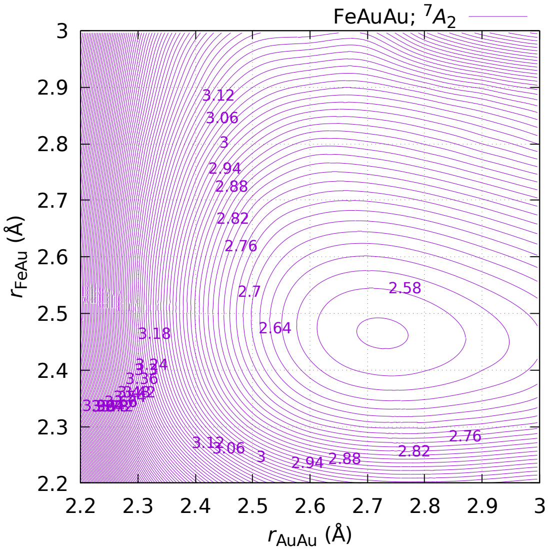

Continued on next page

Continued from previous page

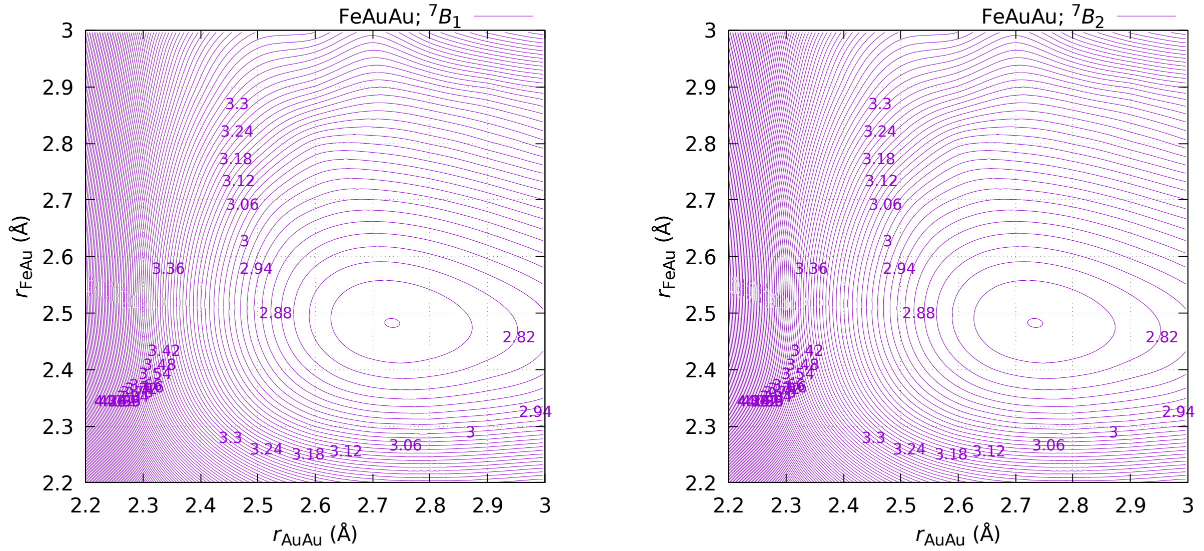

* * *

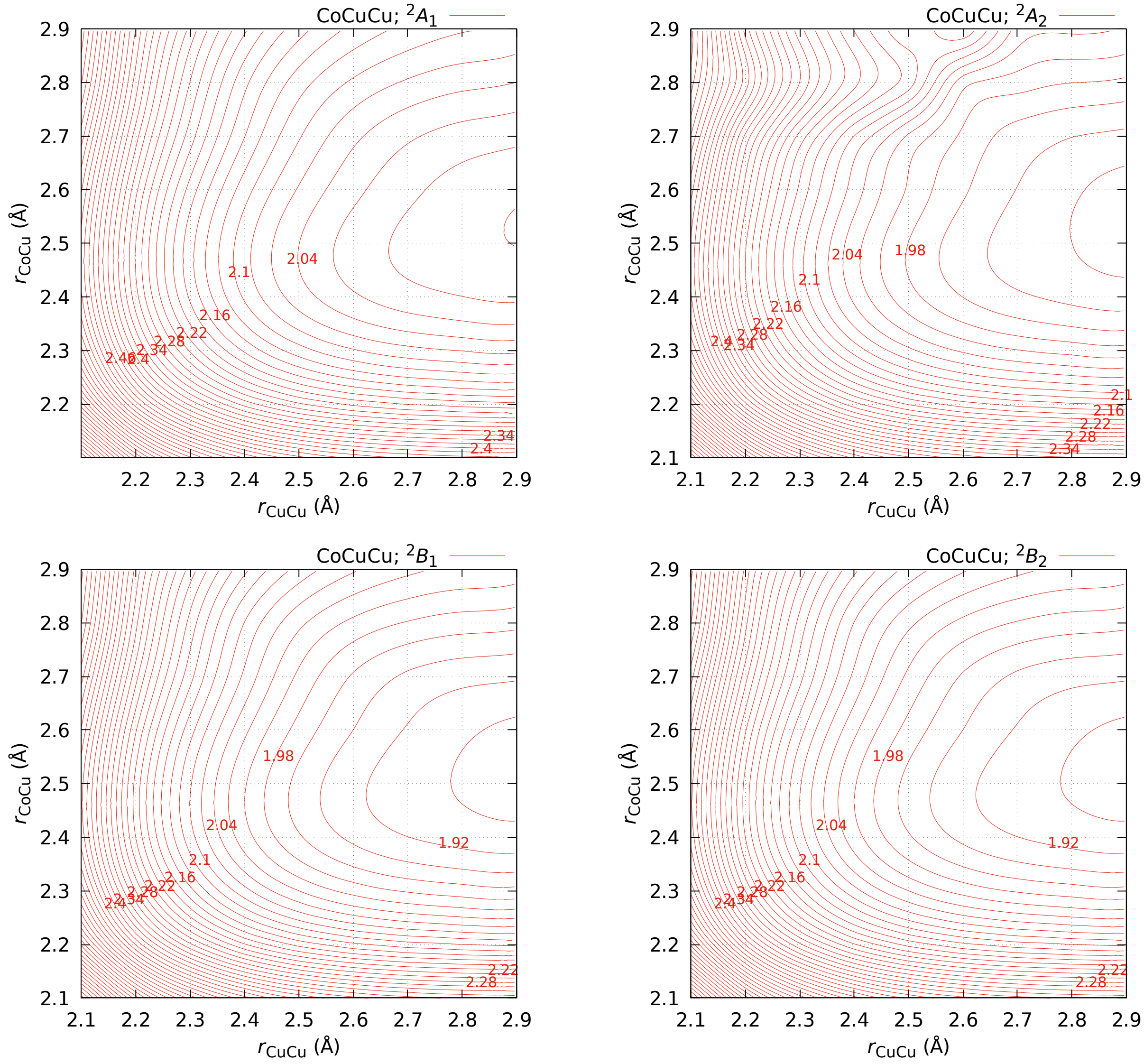

Figure B.77: Potential energy surfaces, $E(r_{\text{CoCu}}, r_{\text{CuCu}}; {}^{2,4,6}\Lambda)$, of CoCuCu ($C_{\infty v}$) obtained at DKH-MRCI[(20+11)E,(10+8)O]. Iso-energies are in eV and relative to the $\tilde{X}\,^4\Phi_g$ ground state.

Continued on next page

Continued from previous page

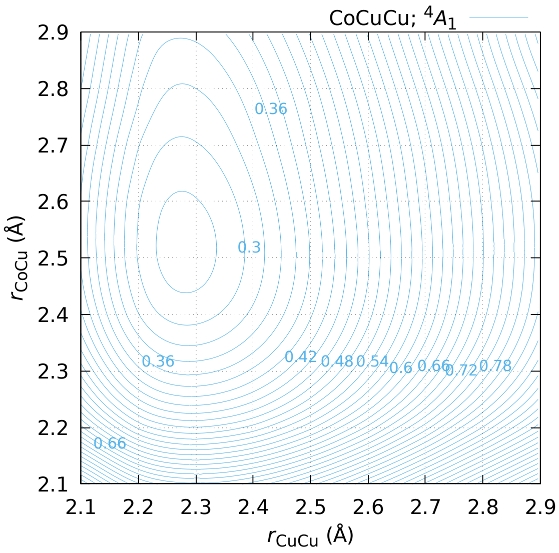

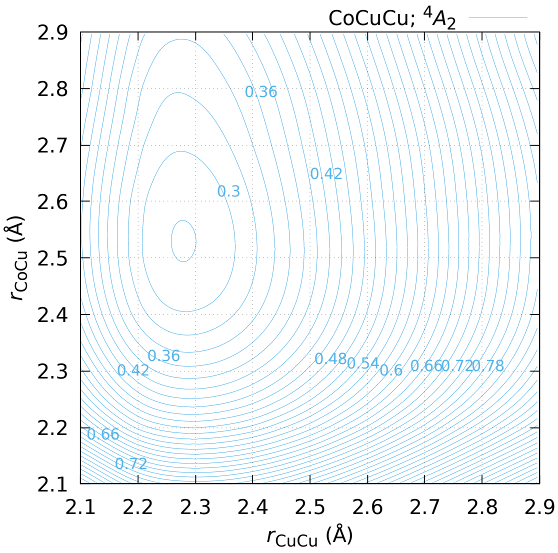

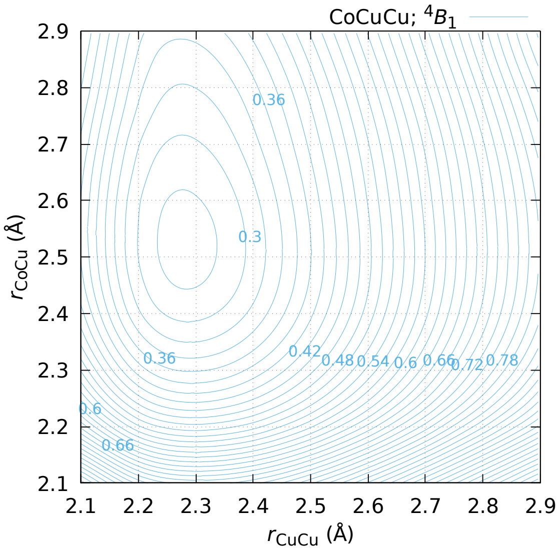

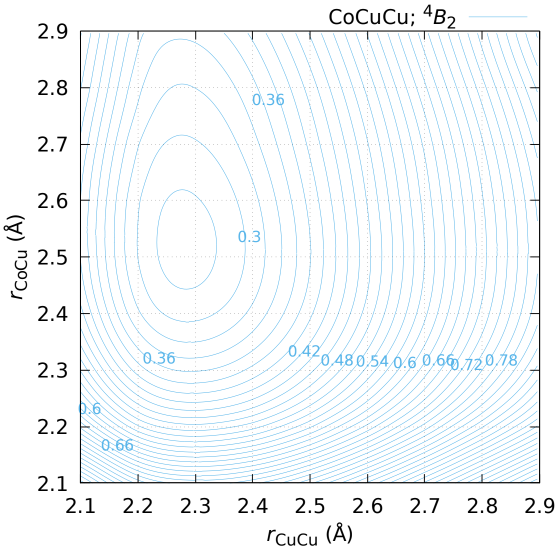

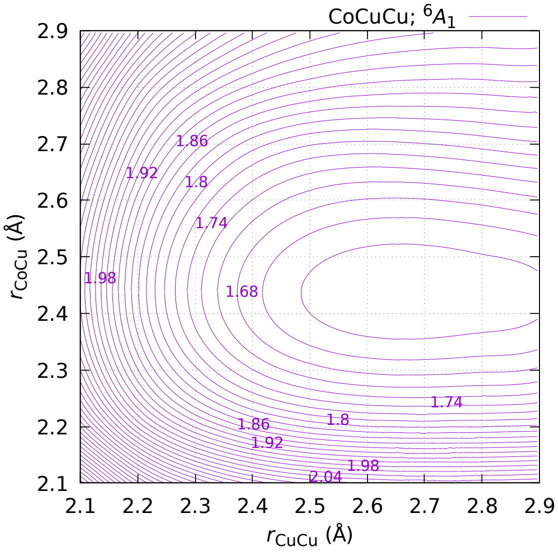

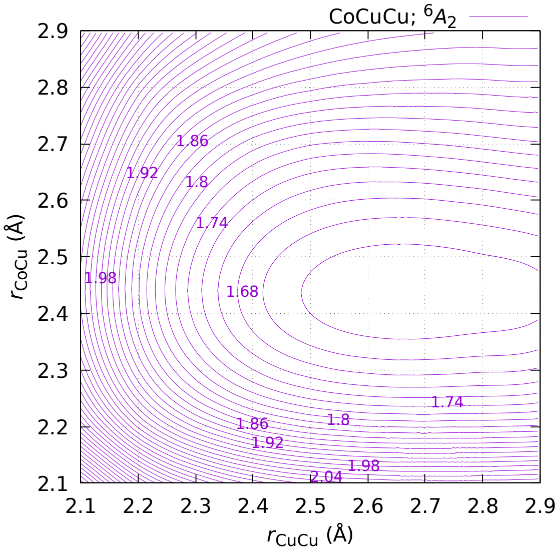

Continued on next page

Continued from previous page

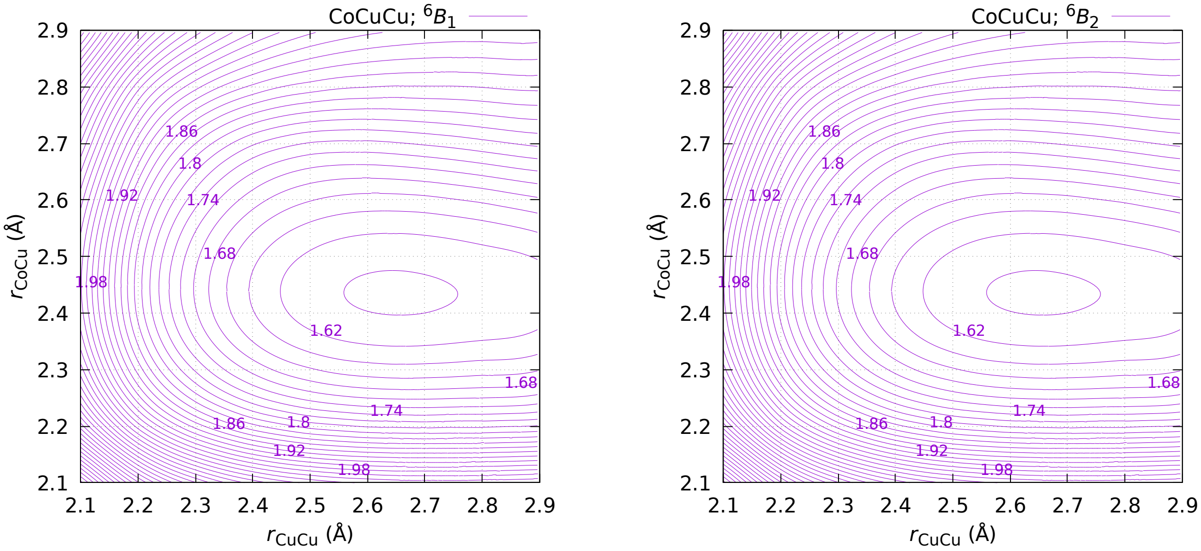

* * *

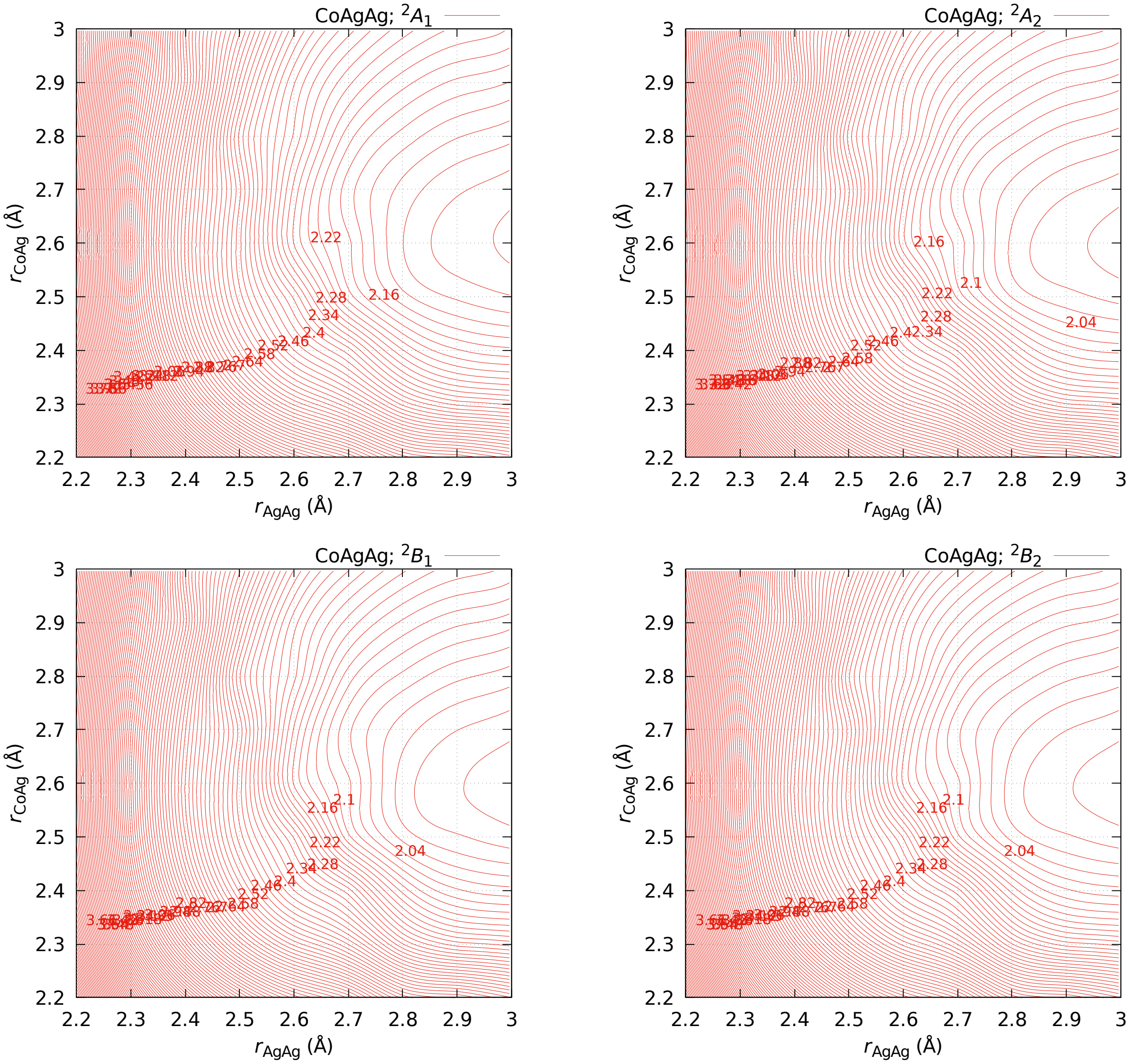

Figure B.78: Potential energy surfaces, $E(r_{\text{CoAg}}, r_{\text{AgAg}}; {}^{2,4,6}\Lambda)$, of CoAgAg ($C_{\infty v}$) obtained at DKH-MRCI[(20+11)E,(10+8)O]. Iso-energies are in eV and relative to the $\tilde{X}^4\Lambda_g^{(-)}$.

Continued on next page

Continued from previous page

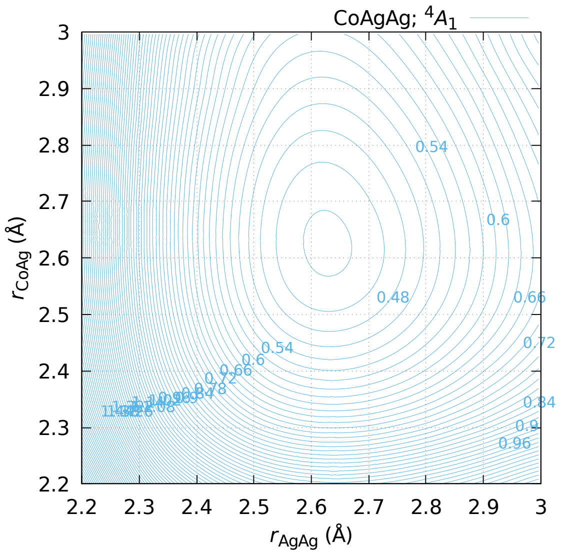

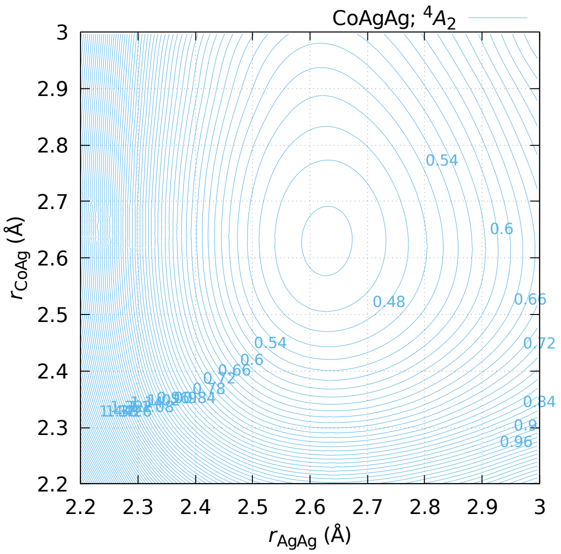

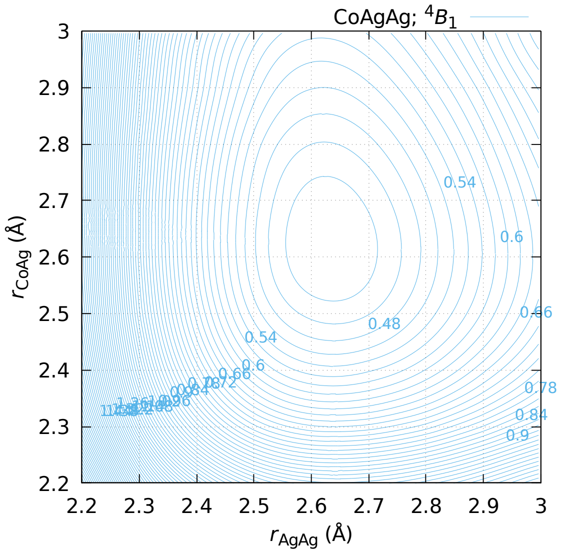

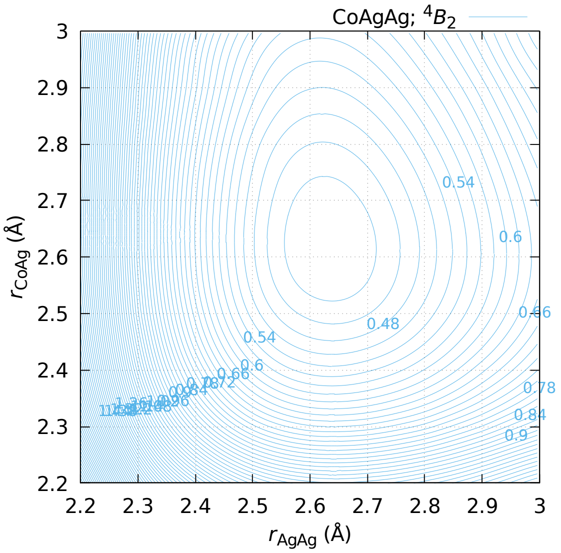

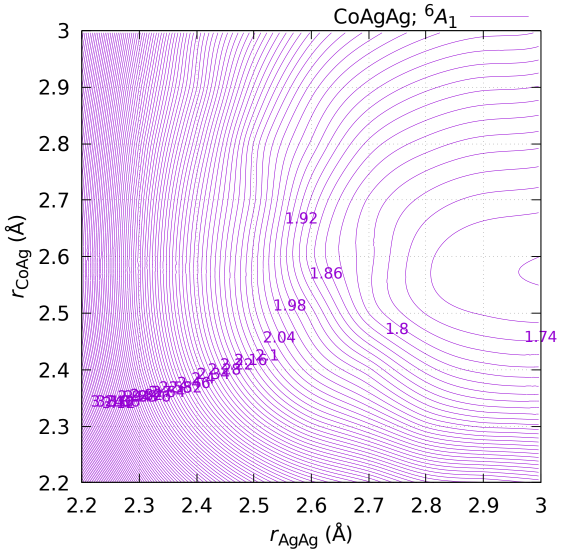

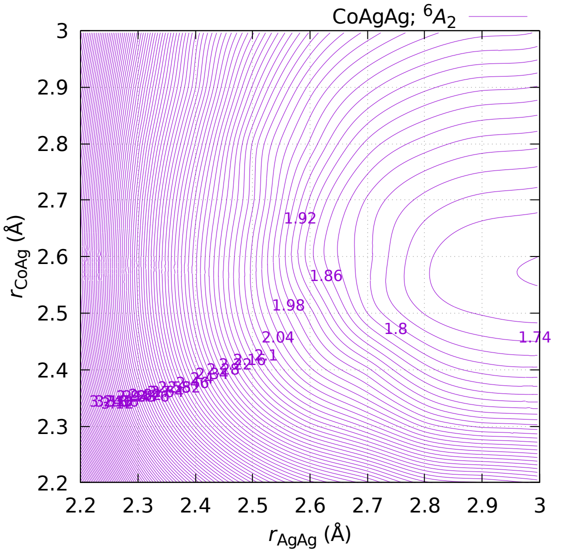

Continued on next page

Continued from previous page

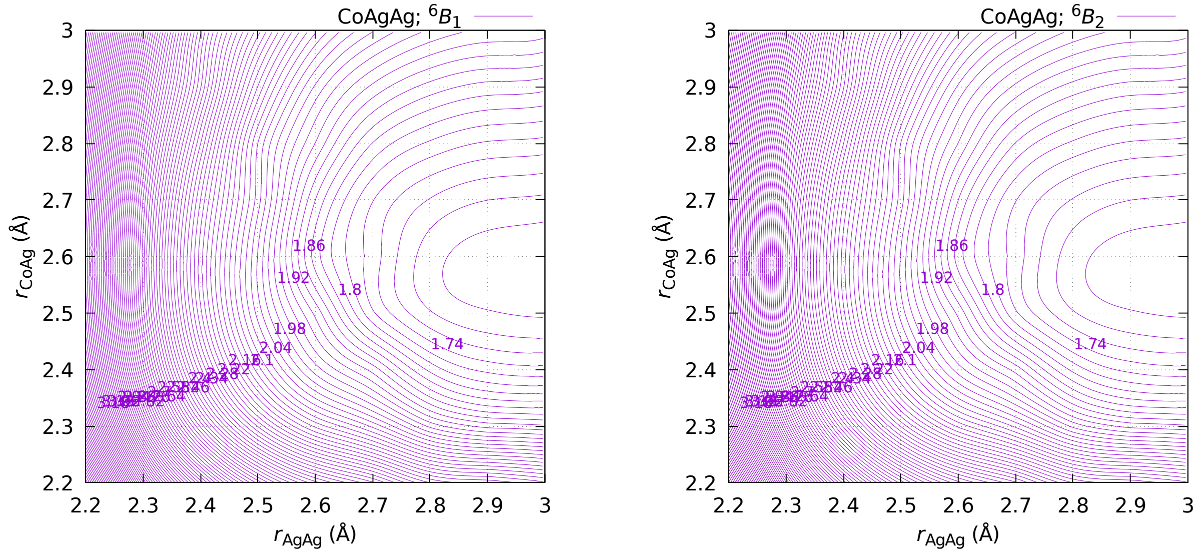

* * *

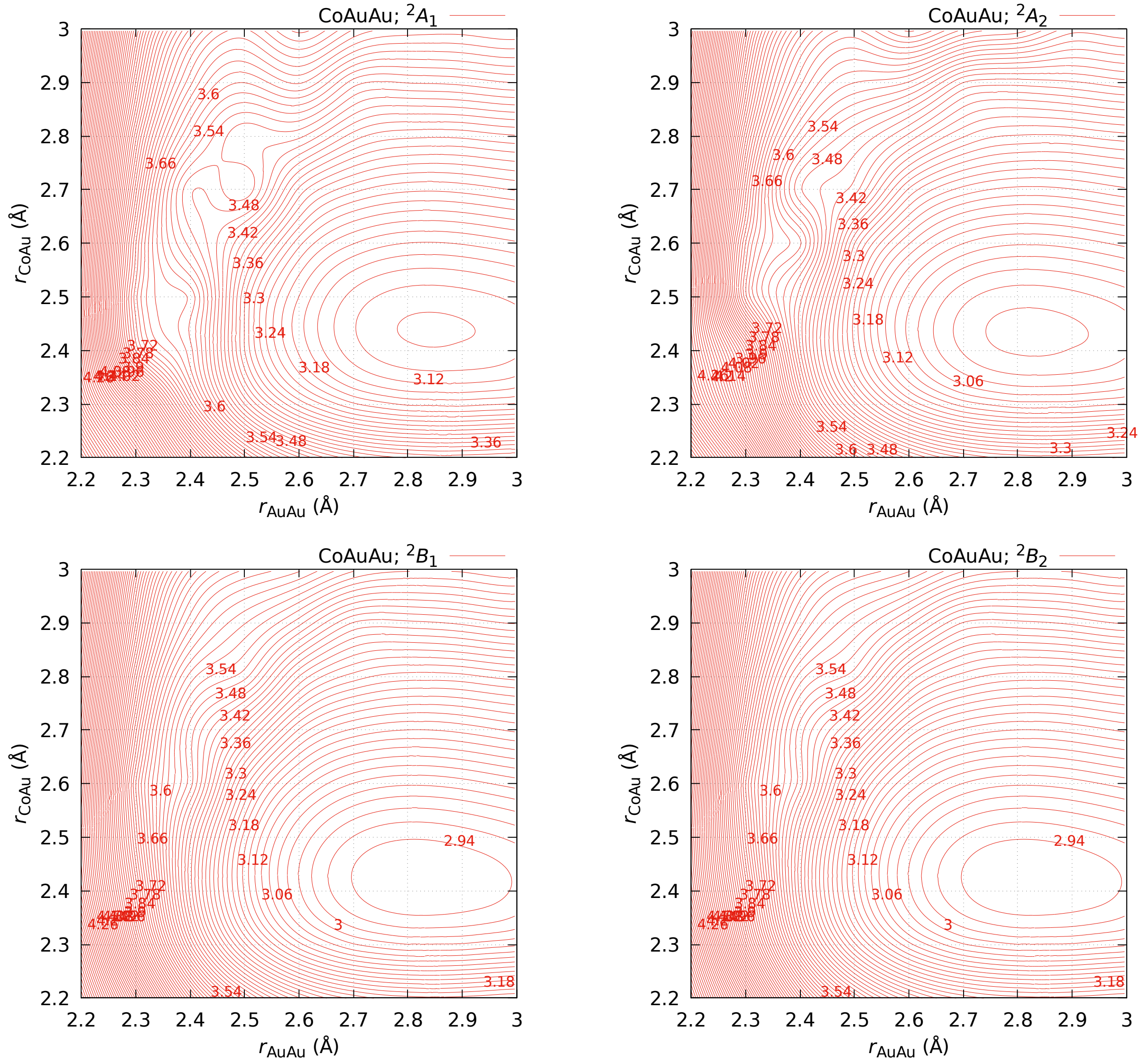

Figure B.79: Potential energy surfaces, $E(r_{\mathrm{CoAu}}, r_{\mathrm{AuAu}}; {}^{2,4,6}\Lambda)$, of CoAuAu ($C_{\infty v}$) obtained at DKH-MRCI[(20+11)E,(10+8)O]. Iso-energies are in eV and relative to the $\tilde{X}^4\Lambda_g^{(-)}$ ground state.

Continued on next page

Continued from previous page

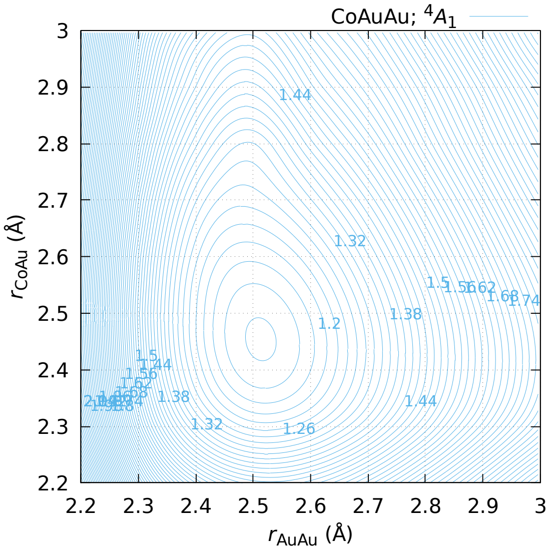

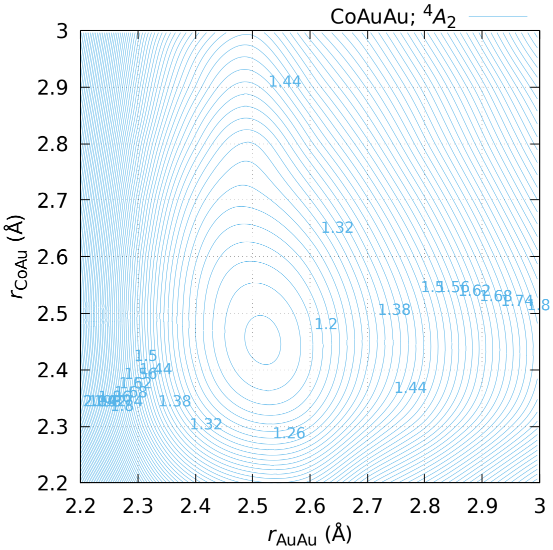

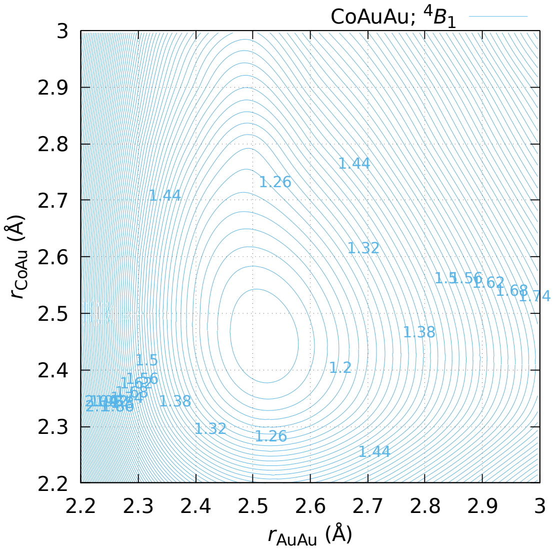

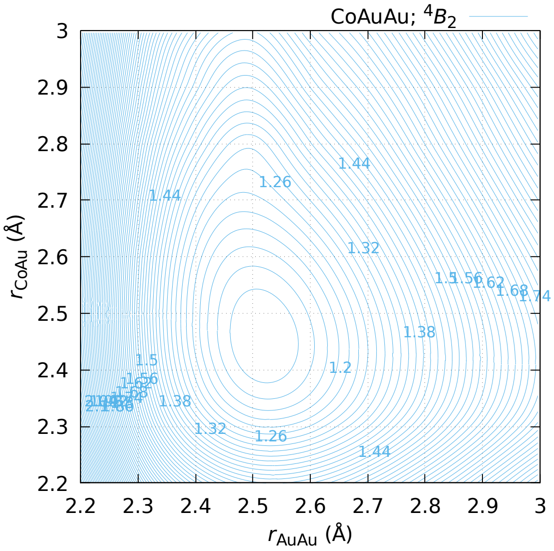

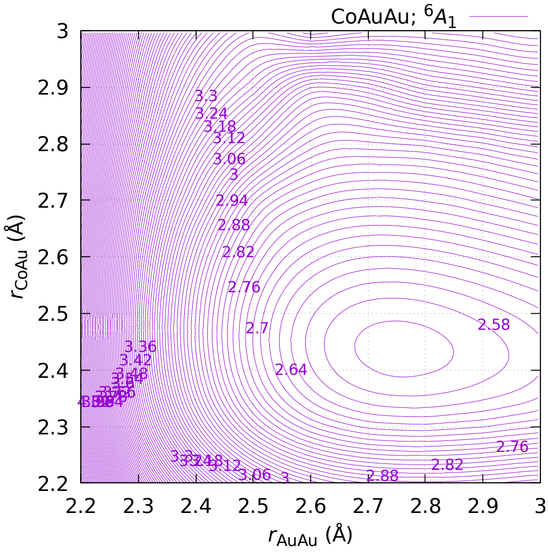

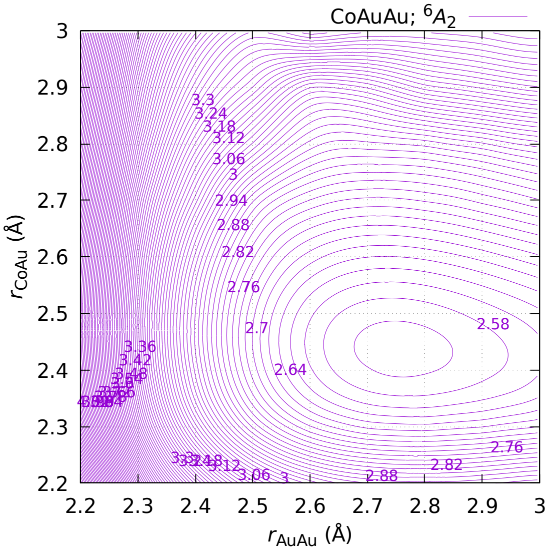

Continued on next page

Continued from previous page

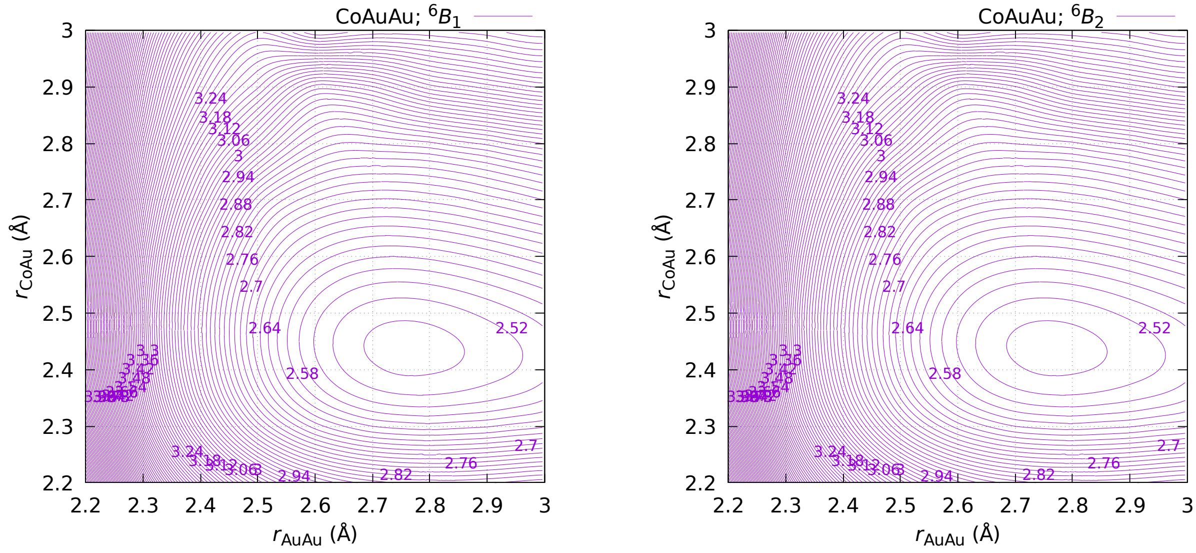

* * *

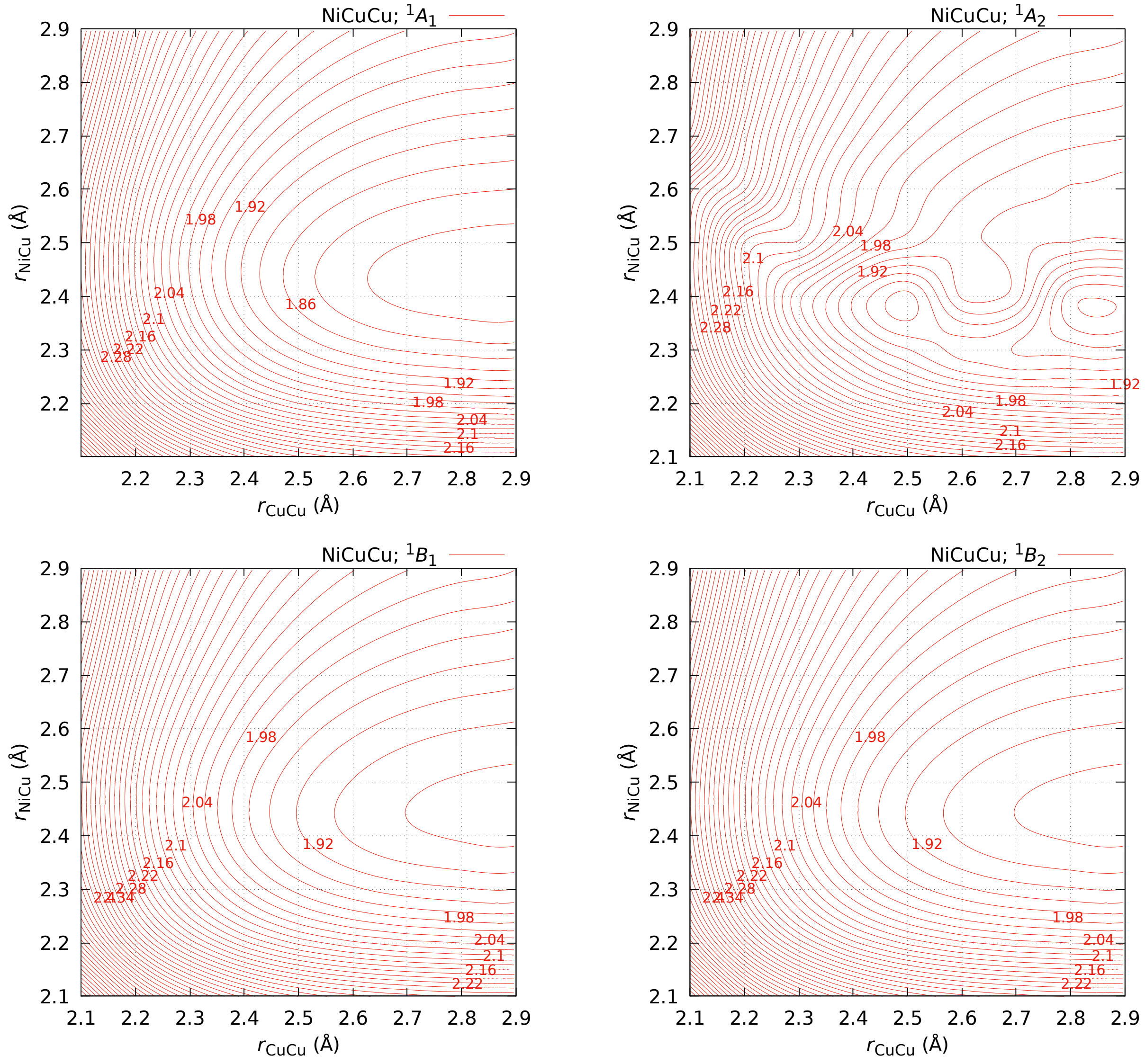

Figure B.80: Potential energy surfaces, $E(r_{\mathrm{NiCu}}, r_{\mathrm{CuCu}};\, ^{1,3,5}\Lambda)$, of the linear NiCuCu structure obtained at DKH-MRCI[(20+12)E,(10+8)O]. Iso-energies are in eV and relative to the $\tilde{X}^3\Lambda_g^{(-)}$ ground state.

Continued on next page

Continued from previous page

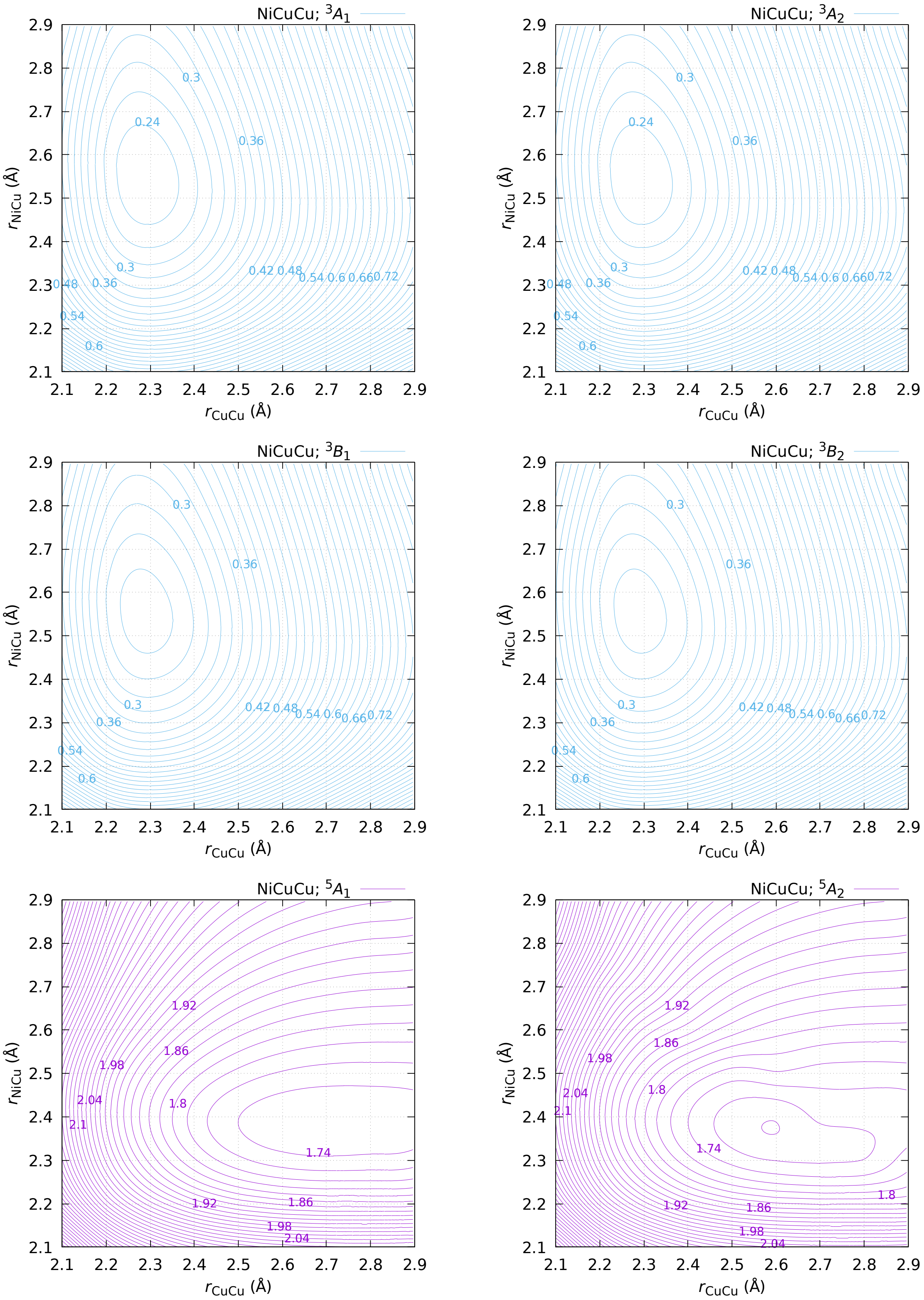

Continued on next page

Continued from previous page

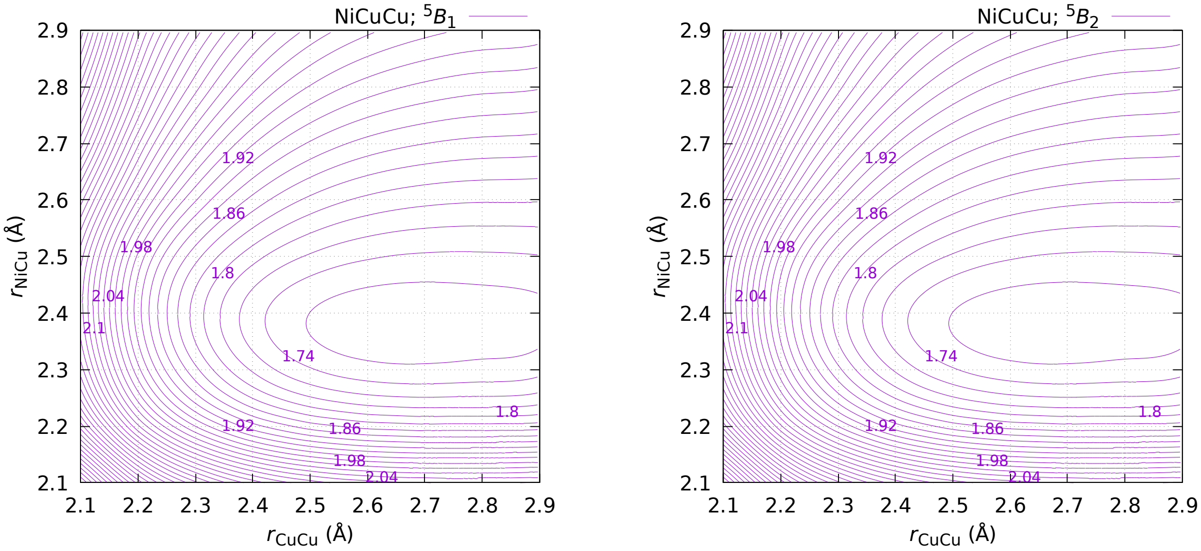

* * *

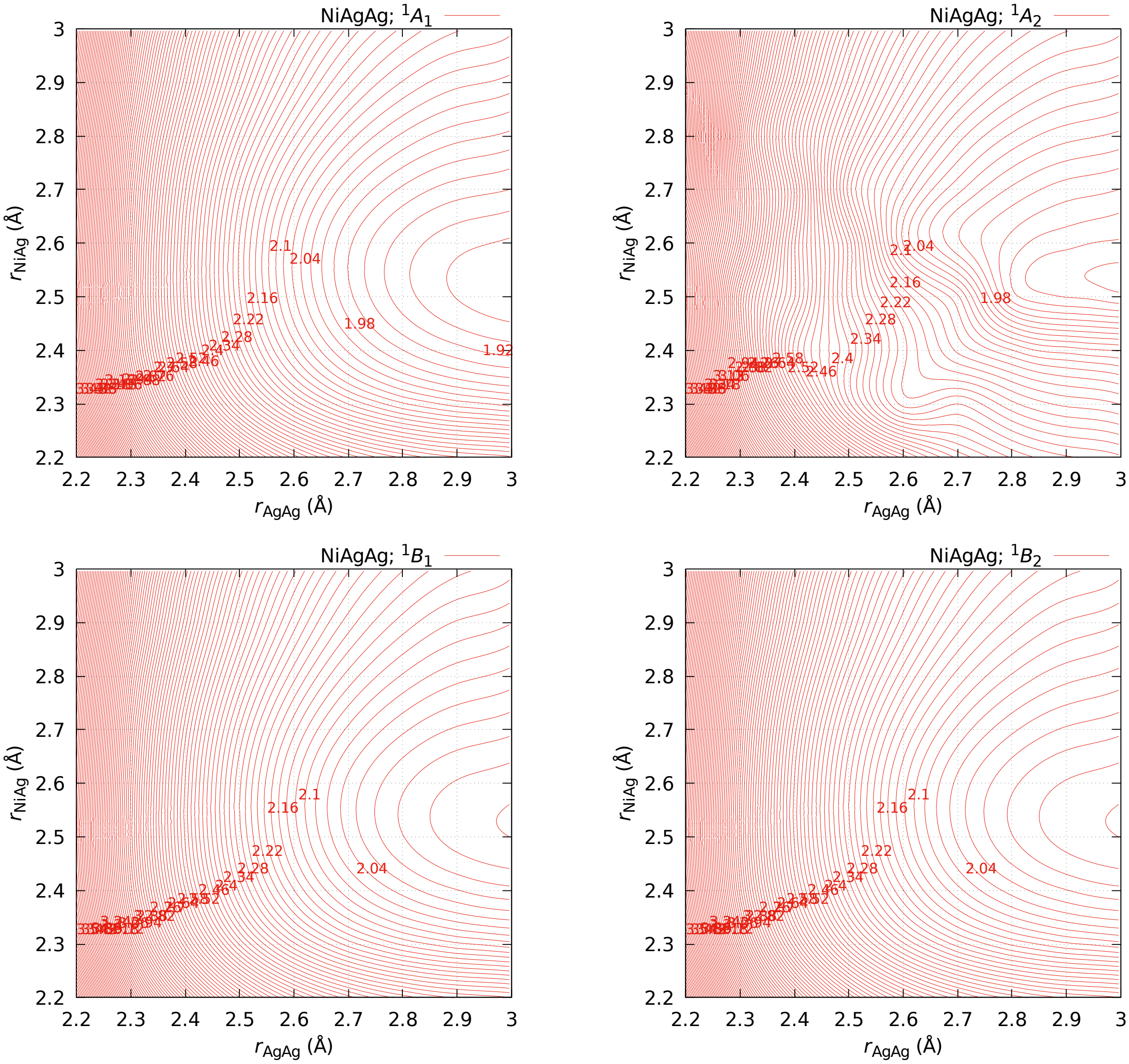

Figure B.81: Potential energy surfaces, $E(r_{\mathrm{NiAg}}, r_{\mathrm{AgAg}}; {}^{1,3,5}\Lambda)$, of the linear NiAgAg structure obtained at DKH-MRCI[(20+12)E,(10+8)O]. Iso-energies are in eV and relative to the $\tilde{X}^3\Lambda_g^{(-)}$ ground state.

Continued on next page

Continued from previous page

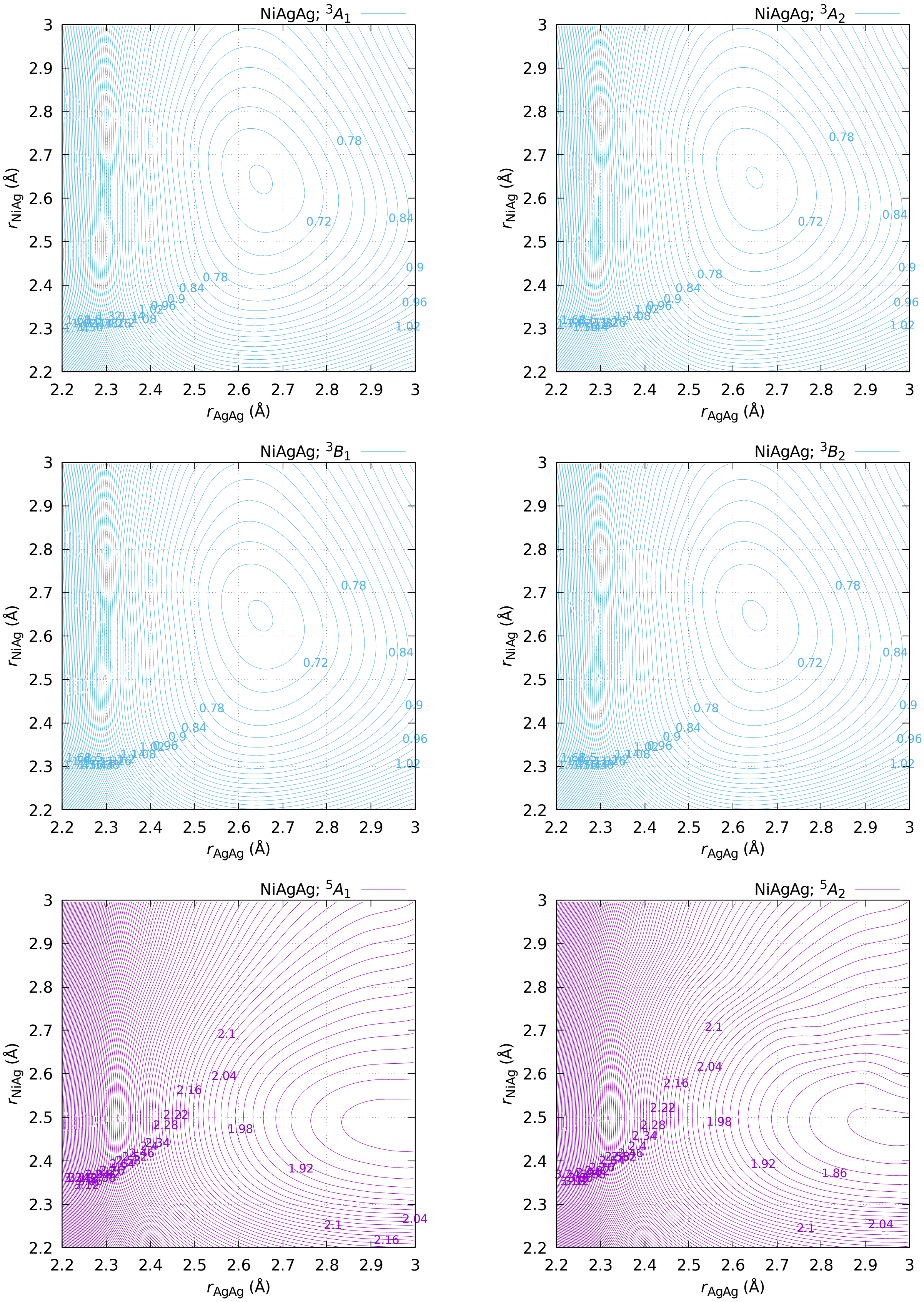

Continued on next page

Continued from previous page

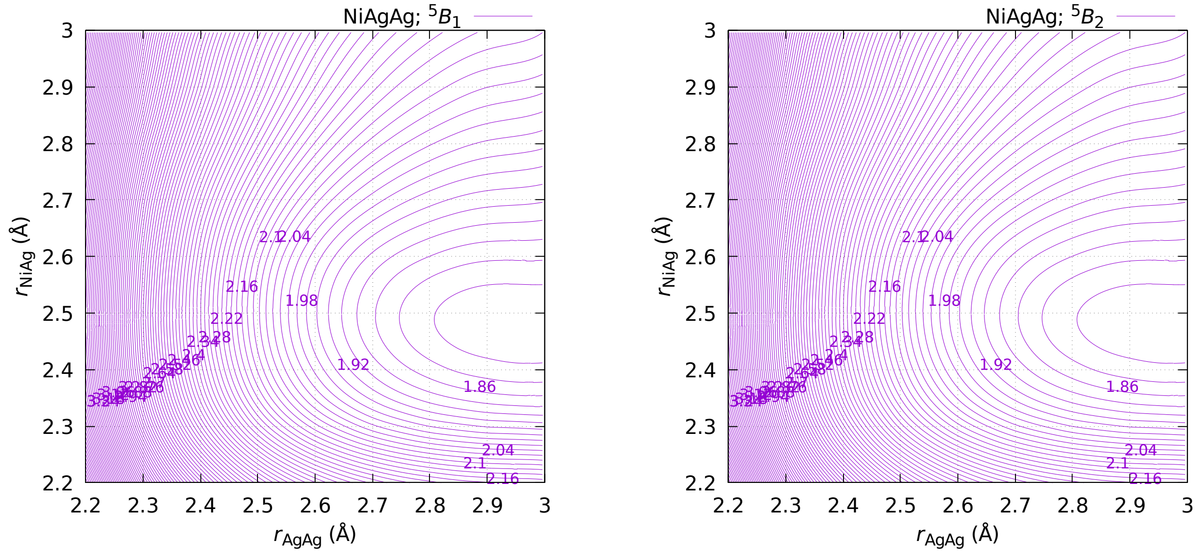

* * *

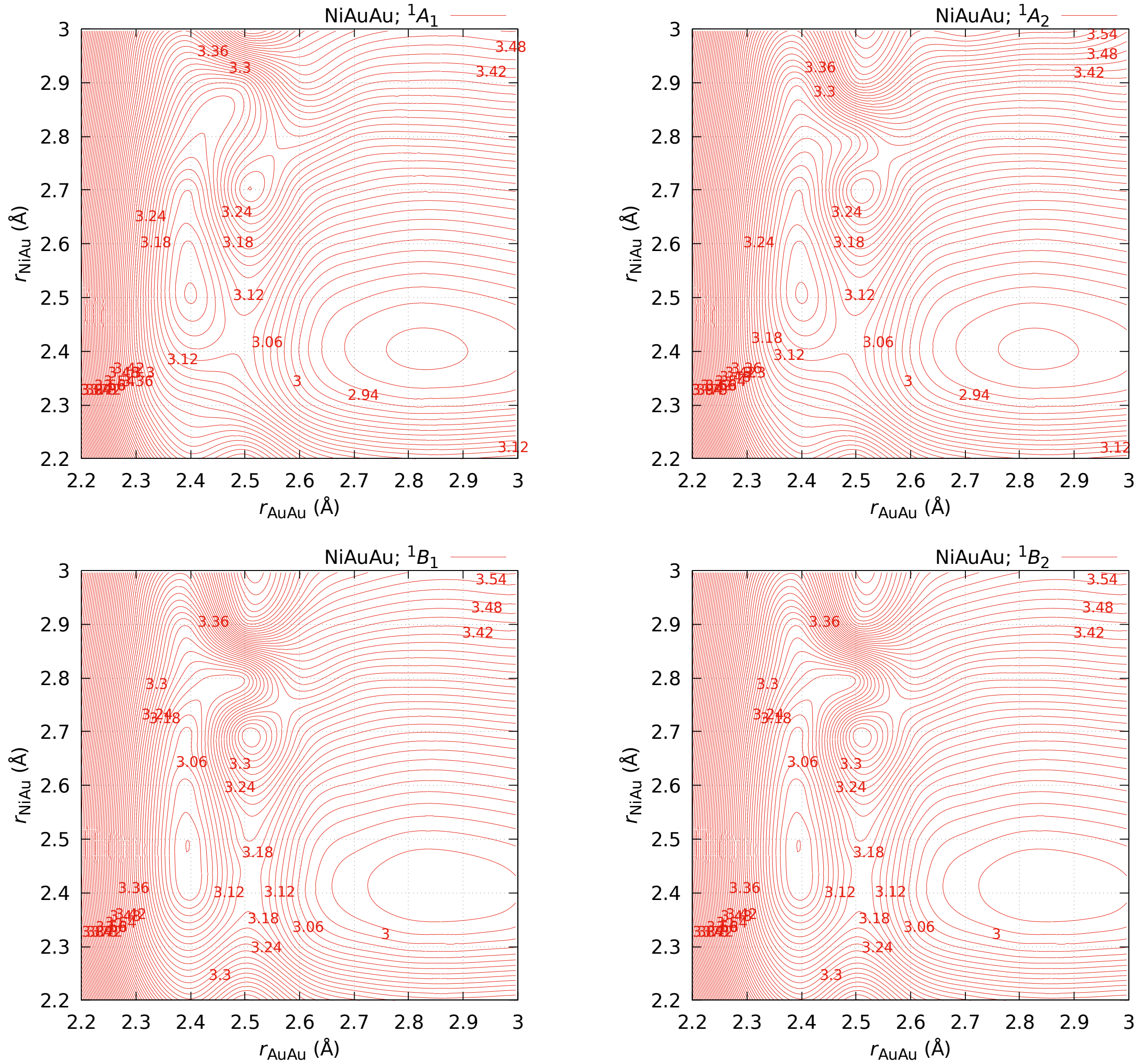

Figure B.82: Potential energy surfaces, $E(r_{\mathrm{NiAu}}, r_{\mathrm{AuAu}}; {}^{1,3,5}\Lambda)$, of the linear NiAuAu structure obtained at DKH-MRCI[(20+12)E,(10+8)O]. Iso-energies are in eV and relative to the $\tilde{X}^3\Lambda_g^{(-)}$ ground state.

Continued on next page

Continued from previous page

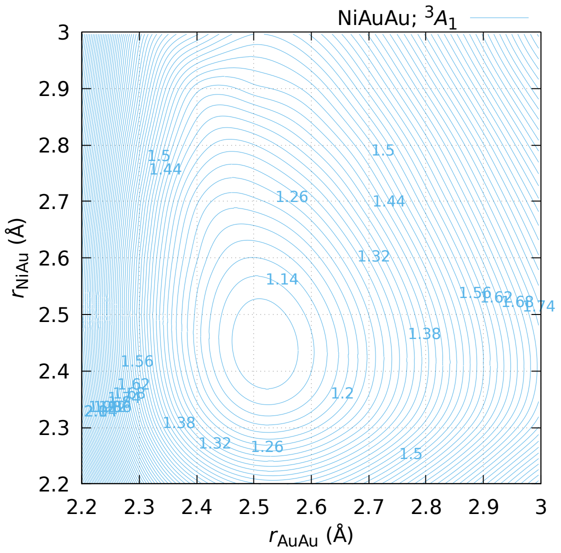

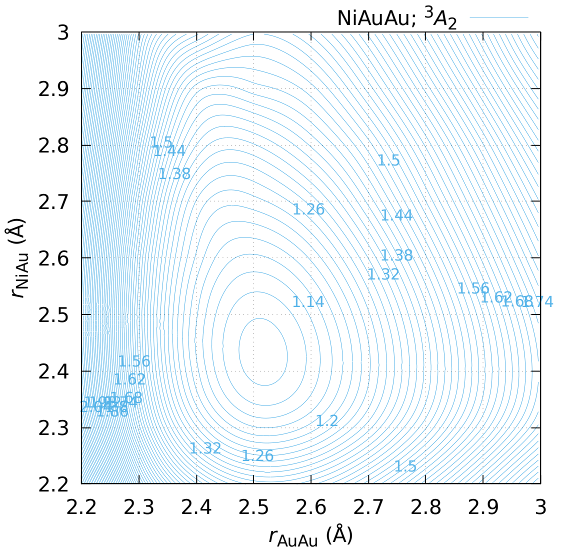

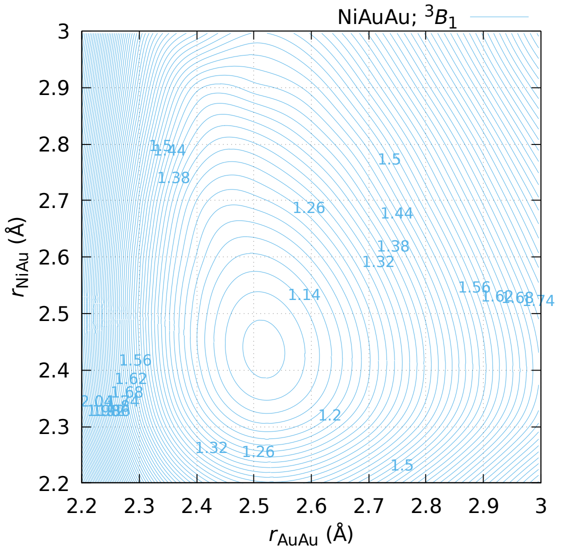

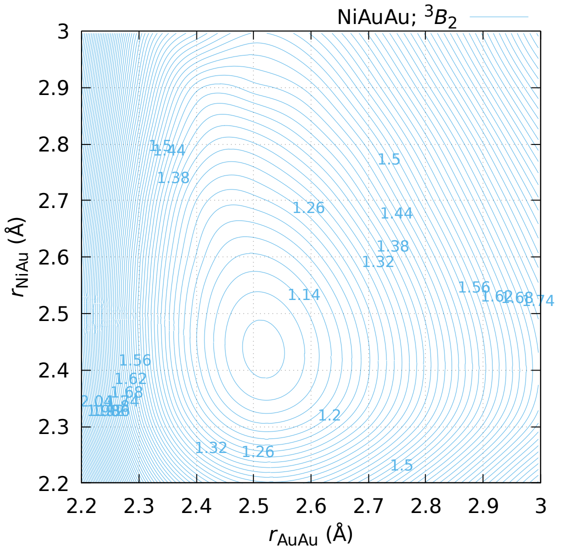

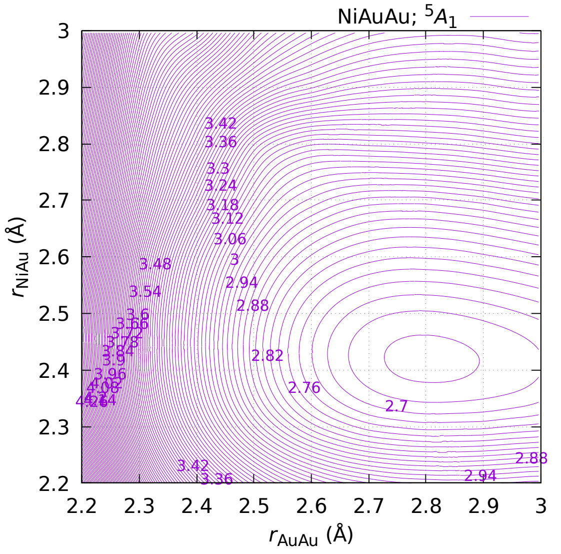

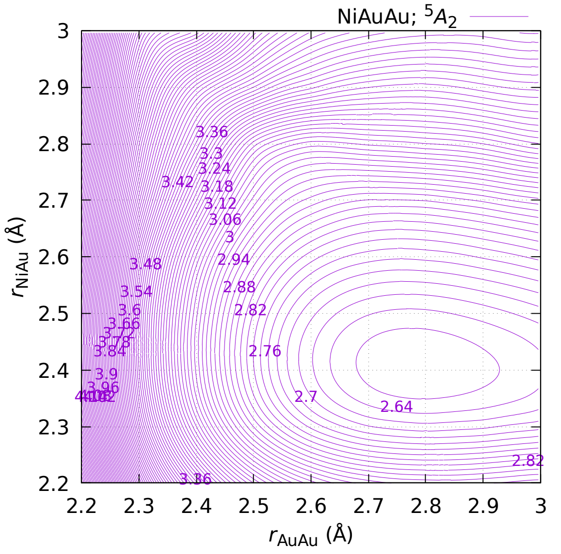

Continued on next page

Continued from previous page

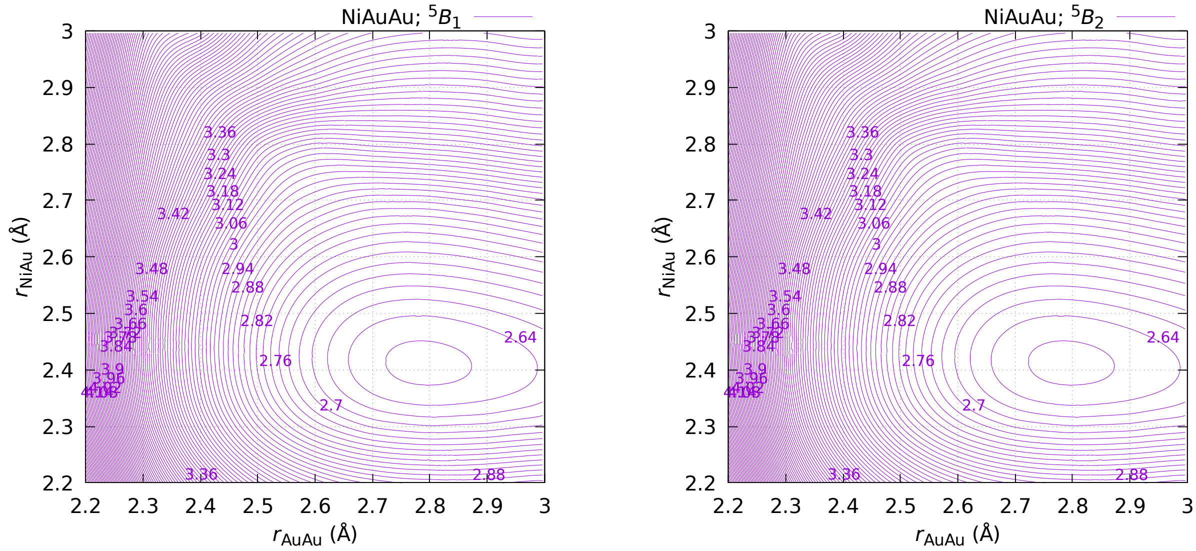

* * *

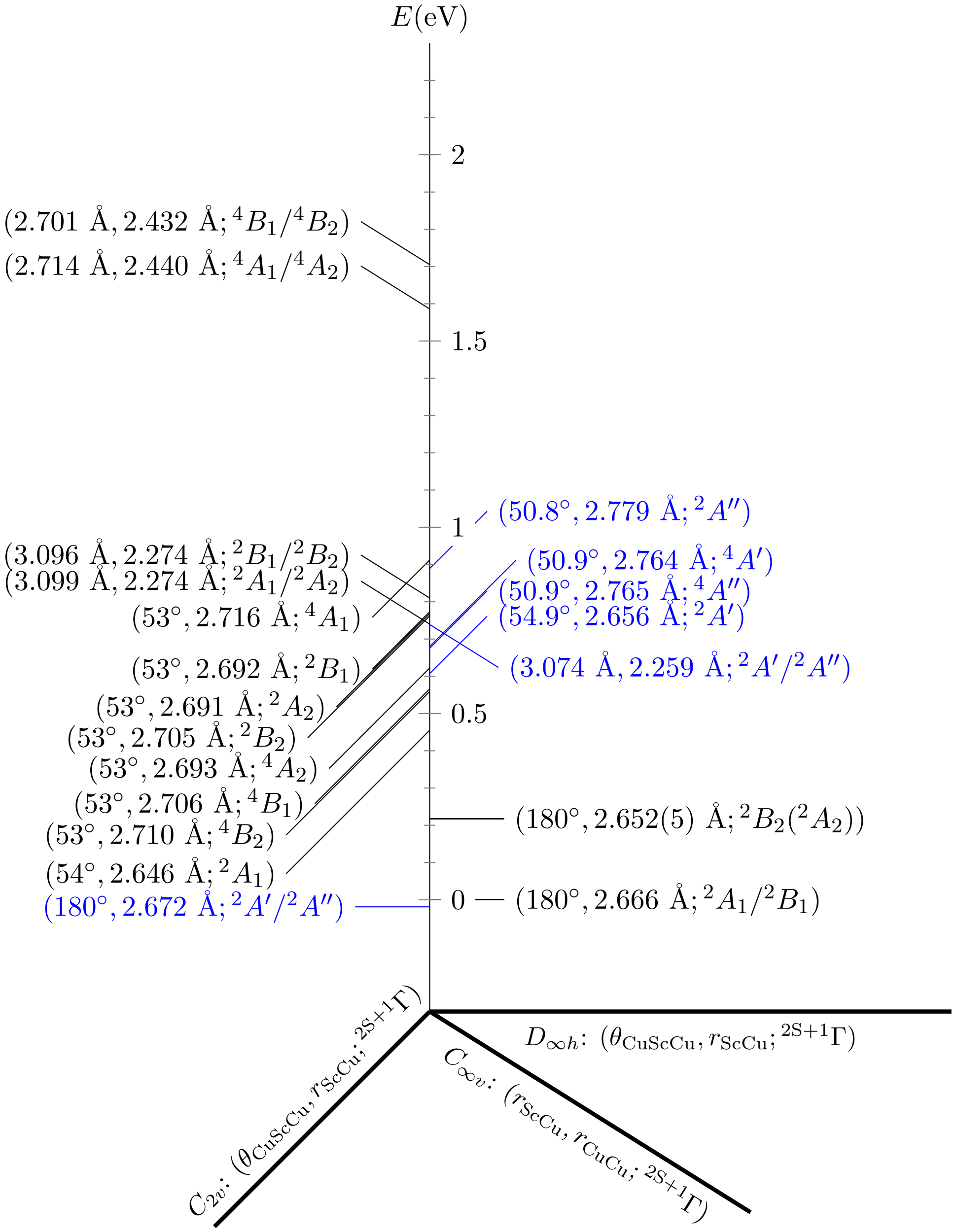

Figure B.83: Low-lying ΓS states of **ScCu$_2$** within the symmetries $D_{\infty h}$, $C_{\infty v}$, and C_{2v} obtained at the MRCI[(20+5)E,(10+8)O] level of theory. Potential minima are shown in black and optimised minima in blue.

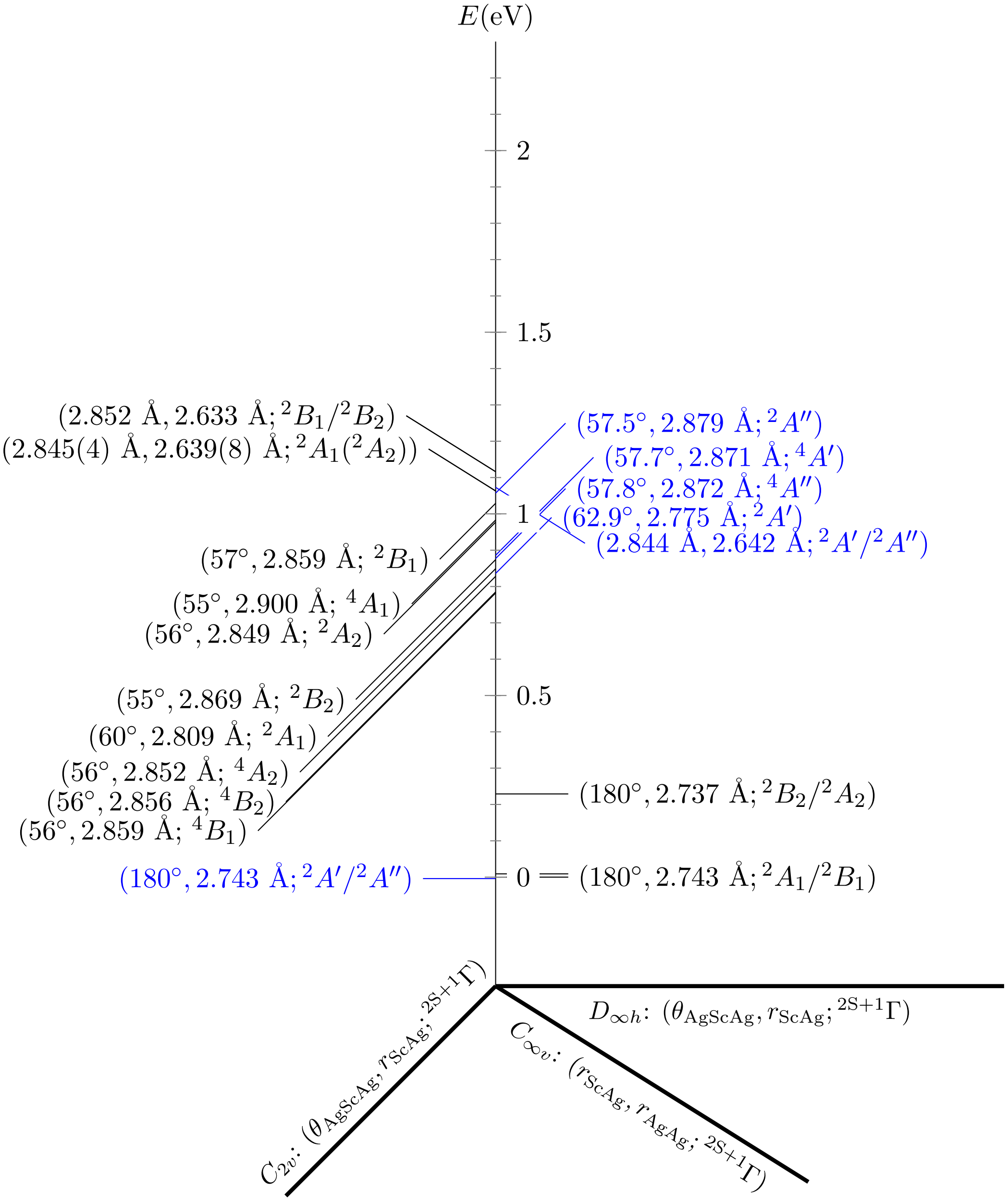
E(eV)
2
1.5
1
0.5
0
$(2.852$ Å$, 2.633$ Å$; {}^2B_1/{}^2B_2)$
$(2.845(4)$ Å$, 2.639(8)$ Å$; {}^2A_1({}^2A_2))$
$(57.5°, 2.879$ Å$; {}^2A'')$
$(57.7°, 2.871$ Å$; {}^4A')$
$(57.8°, 2.872$ Å$; {}^4A'')$
$(62.9°, 2.775$ Å$; {}^2A')$
$(2.844$ Å$, 2.642$ Å$; {}^2A'/{}^2A'')$
$(57°, 2.859$ Å$; {}^2B_1)$
$(55°, 2.900$ Å$; {}^4A_1)$
$(56°, 2.849$ Å$; {}^2A_2)$
$(55°, 2.869$ Å$; {}^2B_2)$
$(60°, 2.809$ Å$; {}^2A_1)$
$(56°, 2.852$ Å$; {}^4A_2)$
$(56°, 2.856$ Å$; {}^4B_2)$
$(56°, 2.859$ Å$; {}^4B_1)$
$(180°, 2.737$ Å$; {}^2B_2/{}^2A_2)$
$(180°, 2.743$ Å$; {}^2A'/{}^2A'')$
$(180°, 2.743$ Å$; {}^2A_1/{}^2B_1)$
$D_{\infty h}$: $(\theta_{\mathrm{AgScAg}}, r_{\mathrm{ScAg}}; {}^{2S+1}\Gamma)$
$C_{\infty v}$: $(r_{\mathrm{ScAg}}, r_{\mathrm{AgAg}}; {}^{2S+1}\Gamma)$
C_{2v}: $(\theta_{\mathrm{AgScAg}}, r_{\mathrm{ScAg}}; {}^{2S+1}\Gamma)$

Figure B.84: Low-lying ΓS states of **ScAg$_2$** within the symmetries $D_{\infty h}$, $C_{\infty v}$, and C_{2v} obtained at the MRCI[(20+5)E,(10+8)O] level of theory. Potential minima are shown in black and optimised minima in blue. Note that here the ground state has the A_1 and B_1 components, while in the CASSCF potentials with $\theta = 180°$ (figure B.17) it has A_1 and A_2. This is due to the change of principal axis in the calculations.

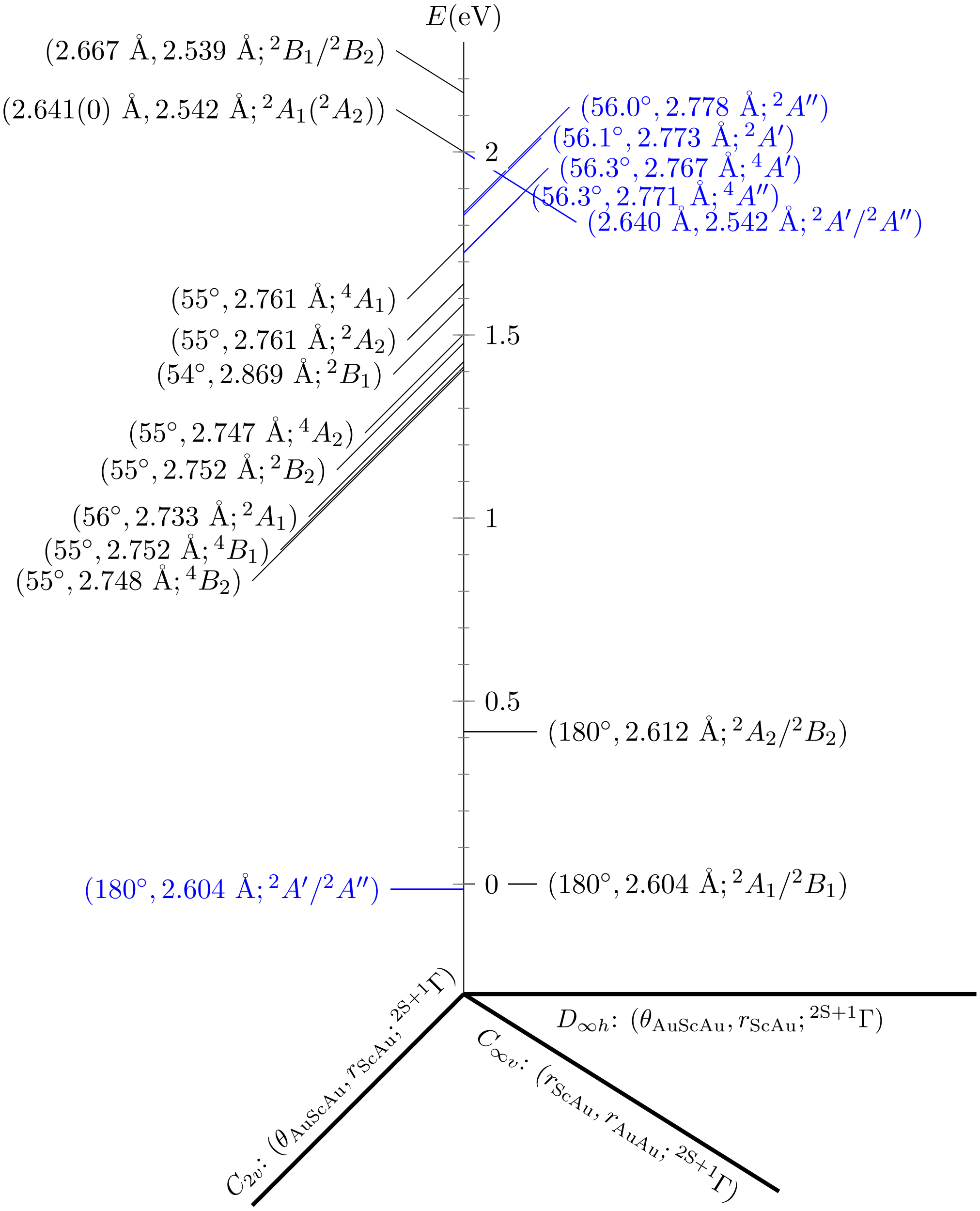
E(eV)
2
1.5
1
0.5
0
(2.667 Å, 2.539 Å; $^2B_1/^2B_2$)
(2.641(0) Å, 2.542 Å; $^2A_1(^2A_2)$)
(56.0°, 2.778 Å; $^2A''$)
(56.1°, 2.773 Å; $^2A'$)
(56.3°, 2.767 Å; $^4A'$)
(56.3°, 2.771 Å; $^4A''$)
(2.640 Å, 2.542 Å; $^2A'/^2A''$)
(55°, 2.761 Å; $^4A_1$)
(55°, 2.761 Å; $^2A_2$)
(54°, 2.869 Å; $^2B_1$)
(55°, 2.747 Å; $^4A_2$)
(55°, 2.752 Å; $^2B_2$)
(56°, 2.733 Å; $^2A_1$)
(55°, 2.752 Å; $^4B_1$)
(55°, 2.748 Å; $^4B_2$)
(180°, 2.612 Å; $^2A_2/^2B_2$)
(180°, 2.604 Å; $^2A'/^2A''$)
(180°, 2.604 Å; $^2A_1/^2B_1$)
$D_{\infty h}$: ($\theta_{\mathrm{AuScAu}}, r_{\mathrm{ScAu}}; {}^{2S+1}\Gamma$)
$C_{\infty v}$: ($r_{\mathrm{ScAu}}, r_{\mathrm{AuAu}}; {}^{2S+1}\Gamma$)
C_{2v}: ($\theta_{\mathrm{AuScAu}}, r_{\mathrm{ScAu}}; {}^{2S+1}\Gamma$)

Figure B.85: Low-lying ΓS states of **ScAu₂** within the symmetries $D_{\infty h}$, $C_{\infty v}$, and C_{2v} obtained at the MRCI[(20+5)E,(10+8)O] level of theory. Potential minima are shown in black and optimised minima in blue.

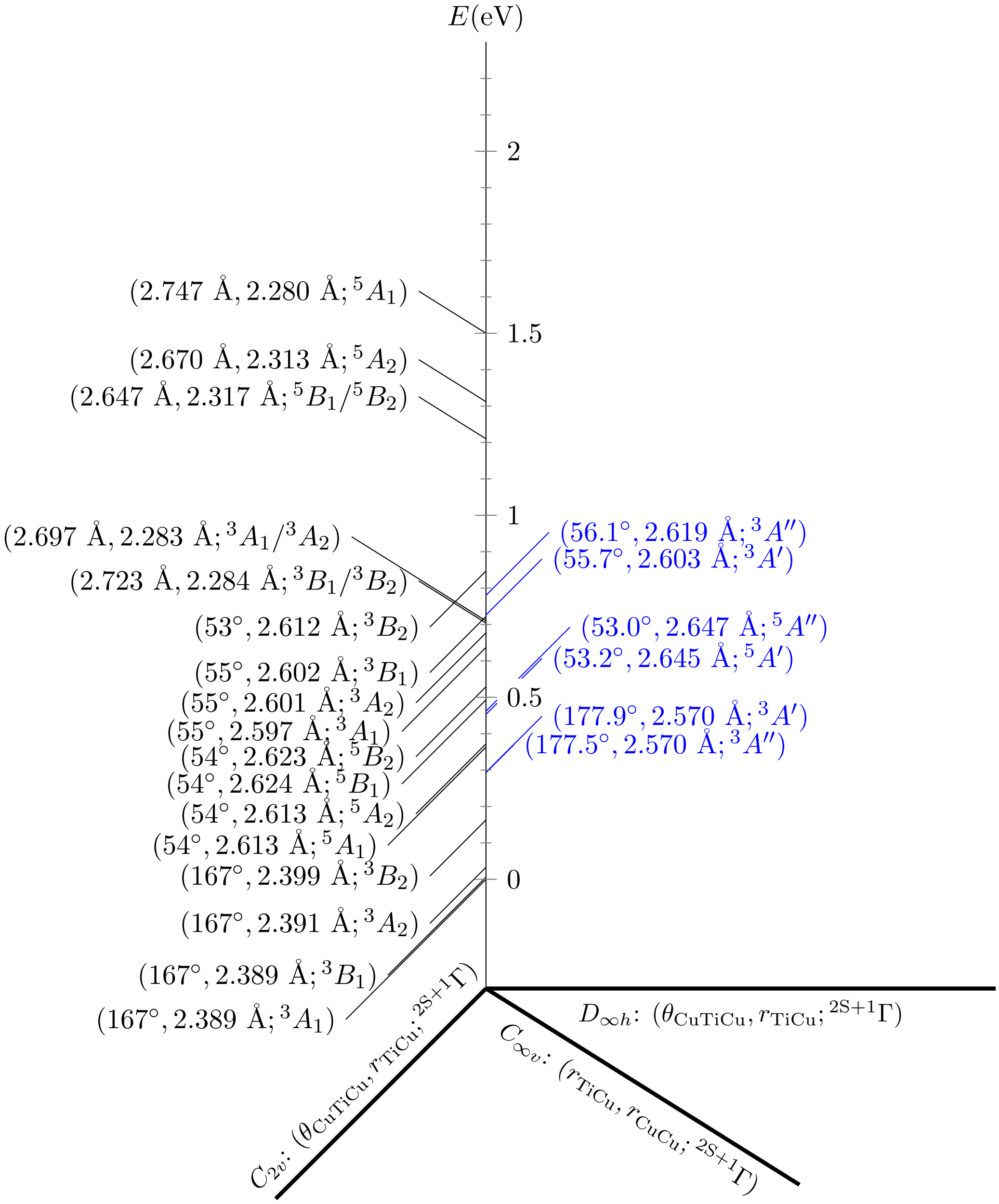

Figure B.86: Low-lying ΓS states of **TiCu$_2$** within the symmetries $D_{\infty h}$, $C_{\infty v}$, and C_{2v} obtained at the MRCI[(20+6)E,(10+8)O] level of theory. Potential minima are shown in black and optimised minima in blue.

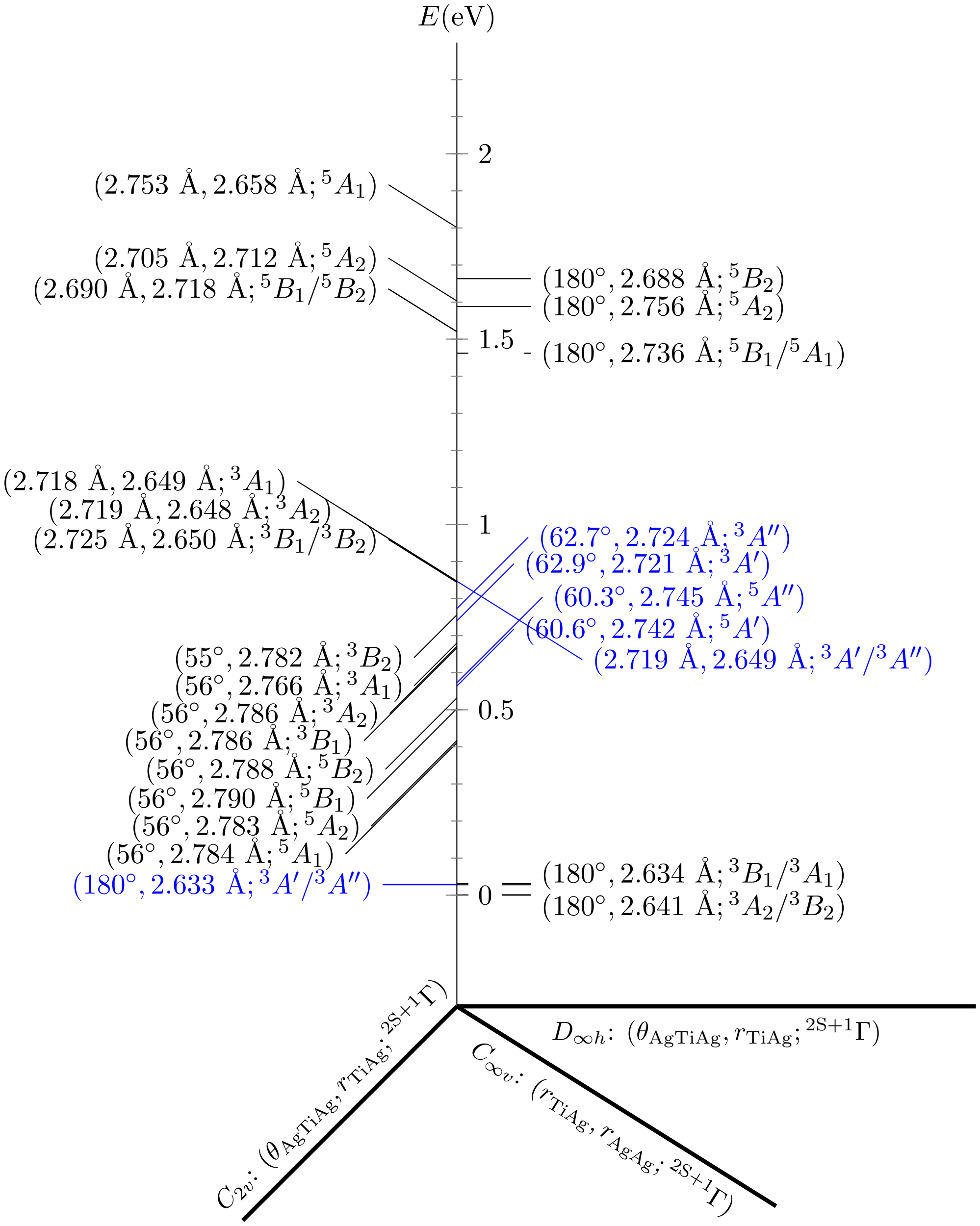
E(eV)
2
1.5
1
0.5
0
(2.753 Å, 2.658 Å; $^5A_1$)
(2.705 Å, 2.712 Å; $^5A_2$)
(2.690 Å, 2.718 Å; $^5B_1/^5B_2$)
(180°, 2.688 Å; $^5B_2$)
(180°, 2.756 Å; $^5A_2$)
(180°, 2.736 Å; $^5B_1/^5A_1$)
(2.718 Å, 2.649 Å; $^3A_1$)
(2.719 Å, 2.648 Å; $^3A_2$)
(2.725 Å, 2.650 Å; $^3B_1/^3B_2$)
(62.7°, 2.724 Å; $^3A''$)
(62.9°, 2.721 Å; $^3A'$)
(60.3°, 2.745 Å; $^5A''$)
(60.6°, 2.742 Å; $^5A'$)
(2.719 Å, 2.649 Å; $^3A'/^3A''$)
(55°, 2.782 Å; $^3B_2$)
(56°, 2.766 Å; $^3A_1$)
(56°, 2.786 Å; $^3A_2$)
(56°, 2.786 Å; $^3B_1$)
(56°, 2.788 Å; $^5B_2$)
(56°, 2.790 Å; $^5B_1$)
(56°, 2.783 Å; $^5A_2$)
(56°, 2.784 Å; $^5A_1$)
(180°, 2.633 Å; $^3A'/^3A''$)
(180°, 2.634 Å; $^3B_1/^3A_1$)
(180°, 2.641 Å; $^3A_2/^3B_2$)
$D_{\infty h}$: ($\theta_{\mathrm{AgTiAg}}, r_{\mathrm{TiAg}}; {}^{2S+1}\Gamma$)
$C_{\infty v}$: ($r_{\mathrm{TiAg}}, r_{\mathrm{AgAg}}; {}^{2S+1}\Gamma$)
C_{2v}: ($\theta_{\mathrm{AgTiAg}}, r_{\mathrm{TiAg}}; {}^{2S+1}\Gamma$)

Figure B.87: Low-lying ΓS states of **TiAg$_2$** within the symmetries $D_{\infty h}$, $C_{\infty v}$, and C_{2v} obtained at the MRCI[(20+6)E,(10+8)O] level of theory. Potential minima are shown in black and optimised minima in blue.

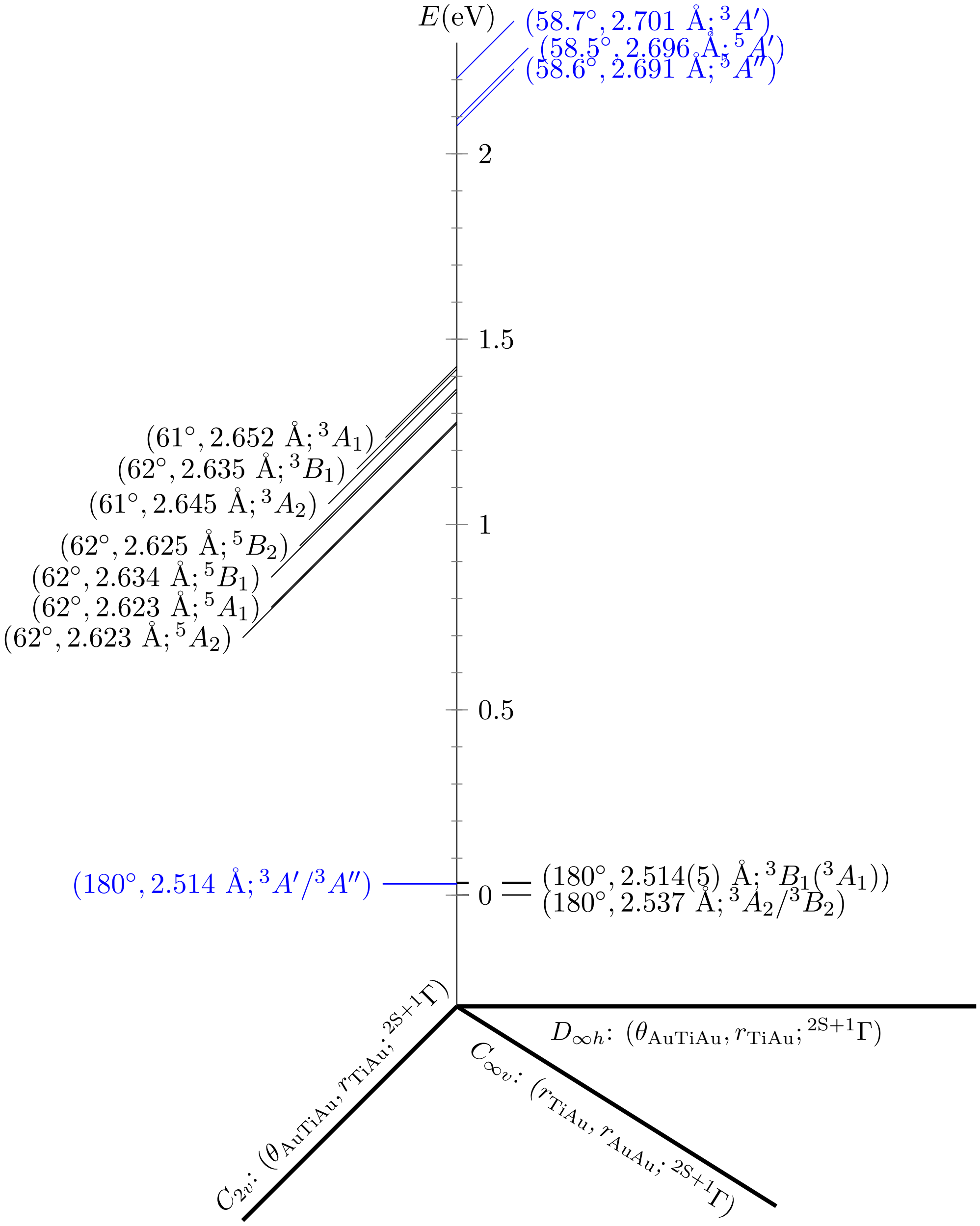

Figure B.88: Low-lying ΓS states of $\mathbf{TiAu_2}$ within the symmetries $D_{\infty h}$, $C_{\infty v}$, and C_{2v} obtained at the MRCI[(20+6)E,(10+8)O] level of theory. Potential minima are shown in black and optimised minima in blue.

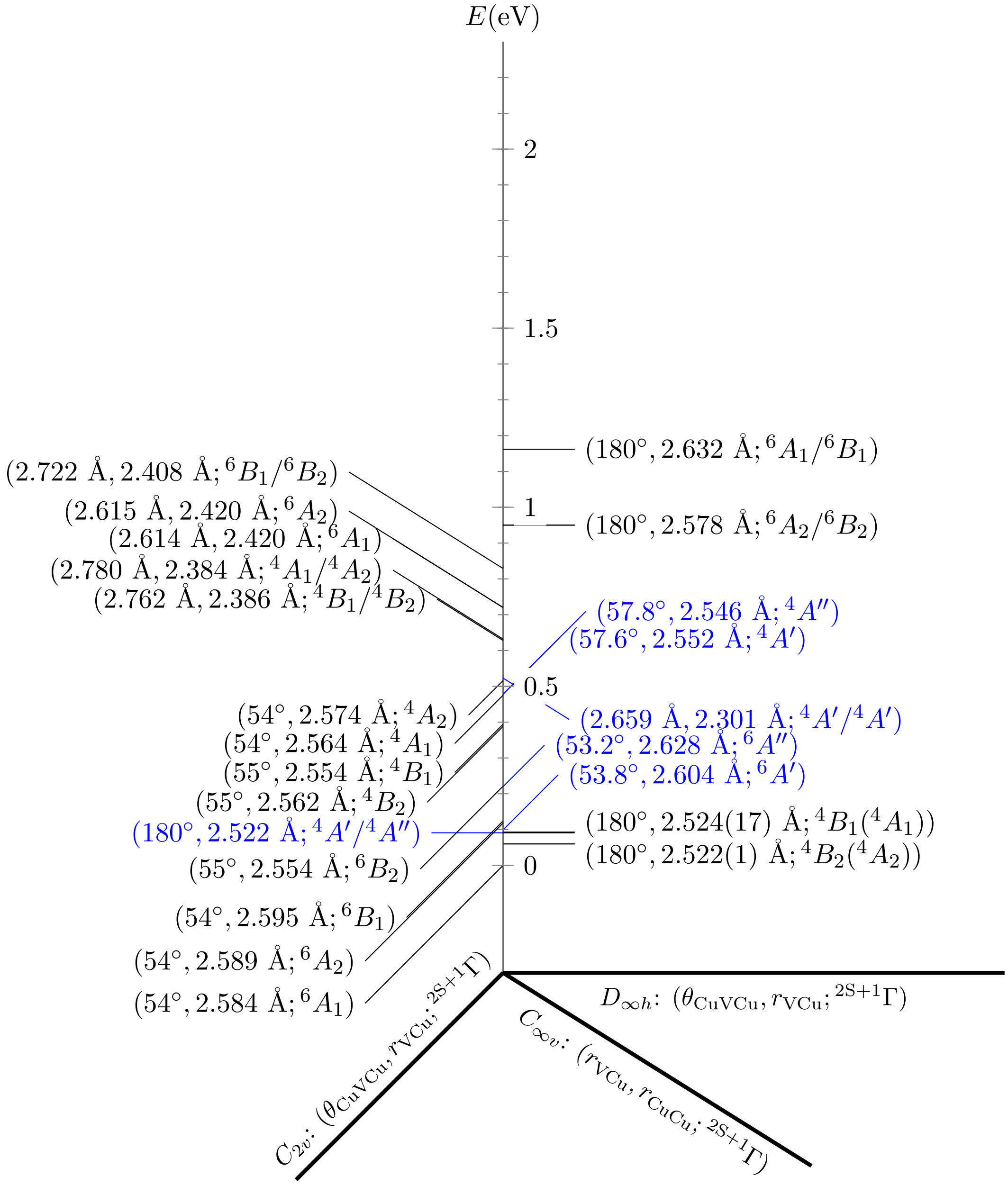

Figure B.89: Low-lying ΓS states of **VCu₂** within the symmetries $D_{\infty h}$, $C_{\infty v}$, and C_{2v} obtained at the MRCI[(20+7)E,(10+8)O] level of theory. Potential minima are shown in black and optimised minima in blue.

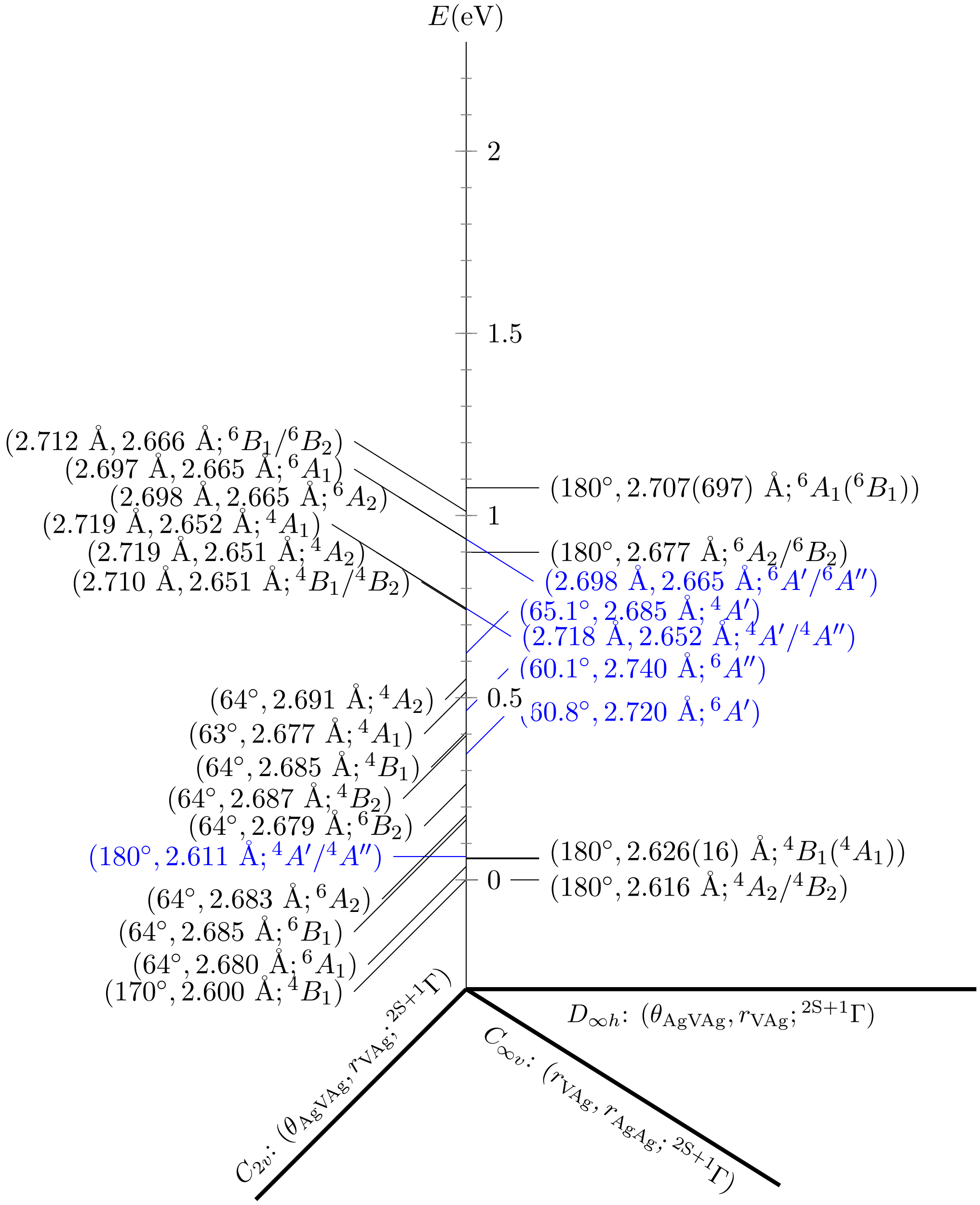
E(eV)
2
1.5
1
0.5
0
(2.712 Å, 2.666 Å; $^6B_1/^6B_2$)
(2.697 Å, 2.665 Å; $^6A_1$)
(2.698 Å, 2.665 Å; $^6A_2$)
(2.719 Å, 2.652 Å; $^4A_1$)
(2.719 Å, 2.651 Å; $^4A_2$)
(2.710 Å, 2.651 Å; $^4B_1/^4B_2$)
(64°, 2.691 Å; $^4A_2$)
(63°, 2.677 Å; $^4A_1$)
(64°, 2.685 Å; $^4B_1$)
(64°, 2.687 Å; $^4B_2$)
(64°, 2.679 Å; $^6B_2$)
(180°, 2.611 Å; $^4A'/^4A''$)
(64°, 2.683 Å; $^6A_2$)
(64°, 2.685 Å; $^6B_1$)
(64°, 2.680 Å; $^6A_1$)
(170°, 2.600 Å; $^4B_1$)
(180°, 2.707(697) Å; $^6A_1(^6B_1)$)
(180°, 2.677 Å; $^6A_2/^6B_2$)
(2.698 Å, 2.665 Å; $^6A'/^6A''$)
(65.1°, 2.685 Å; $^4A'$)
(2.718 Å, 2.652 Å; $^4A'/^4A''$)
(60.1°, 2.740 Å; $^6A''$)
(60.8°, 2.720 Å; $^6A'$)
(180°, 2.626(16) Å; $^4B_1(^4A_1)$)
(180°, 2.616 Å; $^4A_2/^4B_2$)
$D_{\infty h}$: $(\theta_{\mathrm{AgVAg}}, r_{\mathrm{VAg}}; {}^{2S+1}\Gamma)$
$C_{\infty v}$: $(r_{\mathrm{VAg}}, r_{\mathrm{AgAg}}; {}^{2S+1}\Gamma)$
C_{2v}: $(\theta_{\mathrm{AgVAg}}, r_{\mathrm{VAg}}; {}^{2S+1}\Gamma)$

Figure B.90: Low-lying ΓS states of $\mathbf{VAg_2}$ within the symmetries $D_{\infty h}$, $C_{\infty v}$, and C_{2v} obtained at the MRCI[(20+7)E,(10+8)O] level of theory. Potential minima are shown in black and optimised minima in blue.

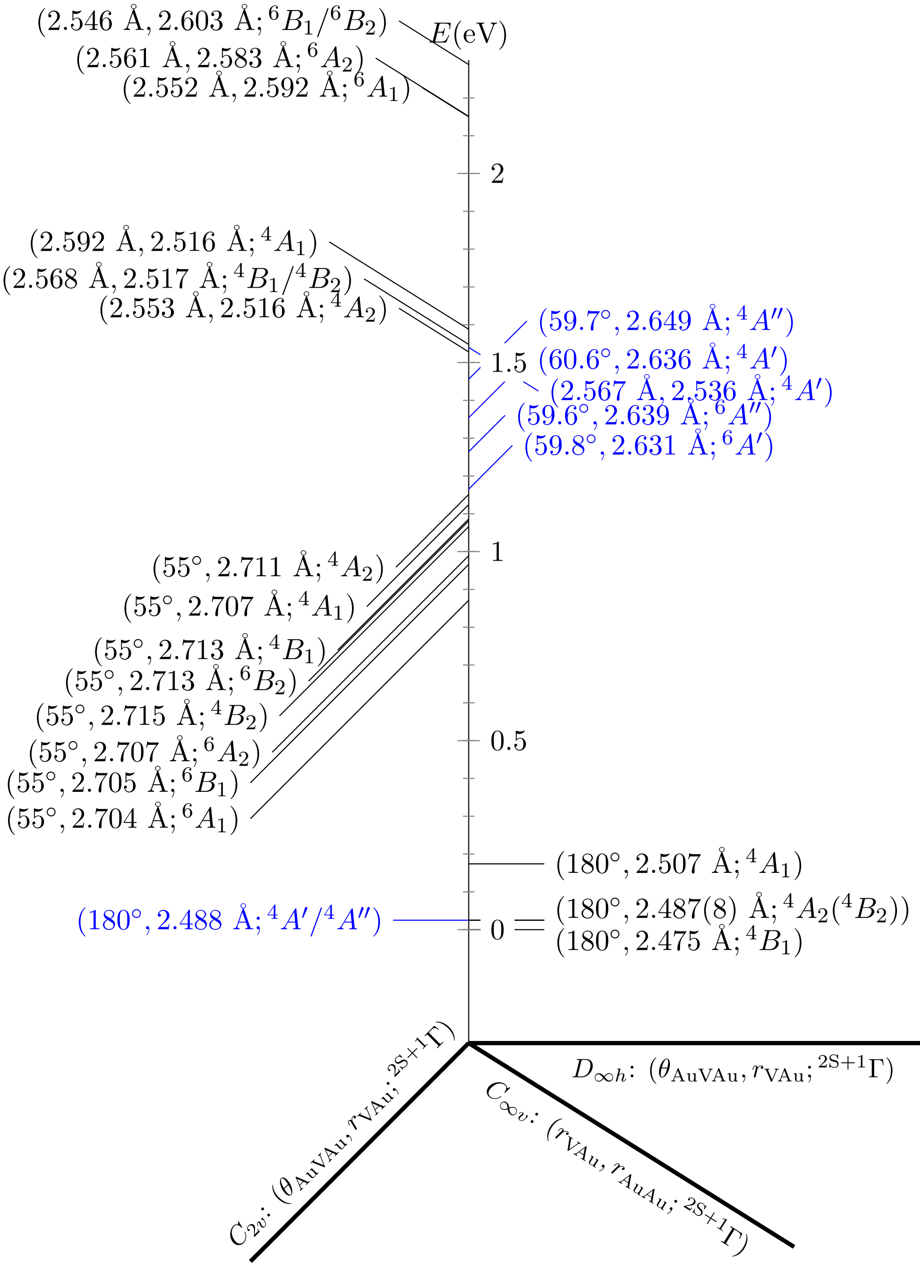

(2.546 Å, 2.603 Å; $^6B_1/^6B_2$)
E(eV)
(2.561 Å, 2.583 Å; $^6A_2$)
(2.552 Å, 2.592 Å; $^6A_1$)
2
(2.592 Å, 2.516 Å; $^4A_1$)
(2.568 Å, 2.517 Å; $^4B_1/^4B_2$)
(2.553 Å, 2.516 Å; $^4A_2$)
(59.7°, 2.649 Å; $^4A''$)
1.5
(60.6°, 2.636 Å; $^4A'$)
(2.567 Å, 2.536 Å; $^4A'$)
(59.6°, 2.639 Å; $^6A''$)
(59.8°, 2.631 Å; $^6A'$)
1
(55°, 2.711 Å; $^4A_2$)
(55°, 2.707 Å; $^4A_1$)
(55°, 2.713 Å; $^4B_1$)
(55°, 2.713 Å; $^6B_2$)
(55°, 2.715 Å; $^4B_2$)
0.5
(55°, 2.707 Å; $^6A_2$)
(55°, 2.705 Å; $^6B_1$)
(55°, 2.704 Å; $^6A_1$)
(180°, 2.507 Å; $^4A_1$)
(180°, 2.488 Å; $^4A'/^4A''$)
(180°, 2.487(8) Å; $^4A_2$($^4B_2$))
0
(180°, 2.475 Å; $^4B_1$)
C_{2v}: ($\theta_{\mathrm{AuVAu}}, r_{\mathrm{VAu}}; {}^{2\mathrm{S}+1}\Gamma$)
$D_{\infty h}$: ($\theta_{\mathrm{AuVAu}}, r_{\mathrm{VAu}}; {}^{2\mathrm{S}+1}\Gamma$)
$C_{\infty v}$: ($r_{\mathrm{VAu}}, r_{\mathrm{AuAu}}; {}^{2\mathrm{S}+1}\Gamma$)

Figure B.91: Low-lying ΓS states of **VAu$_2$** within the symmetries $D_{\infty h}$, $C_{\infty v}$, and C_{2v} obtained at the MRCI[(20+7)E,(10+8)O] level of theory. Potential minima are shown in black and optimised minima in blue.

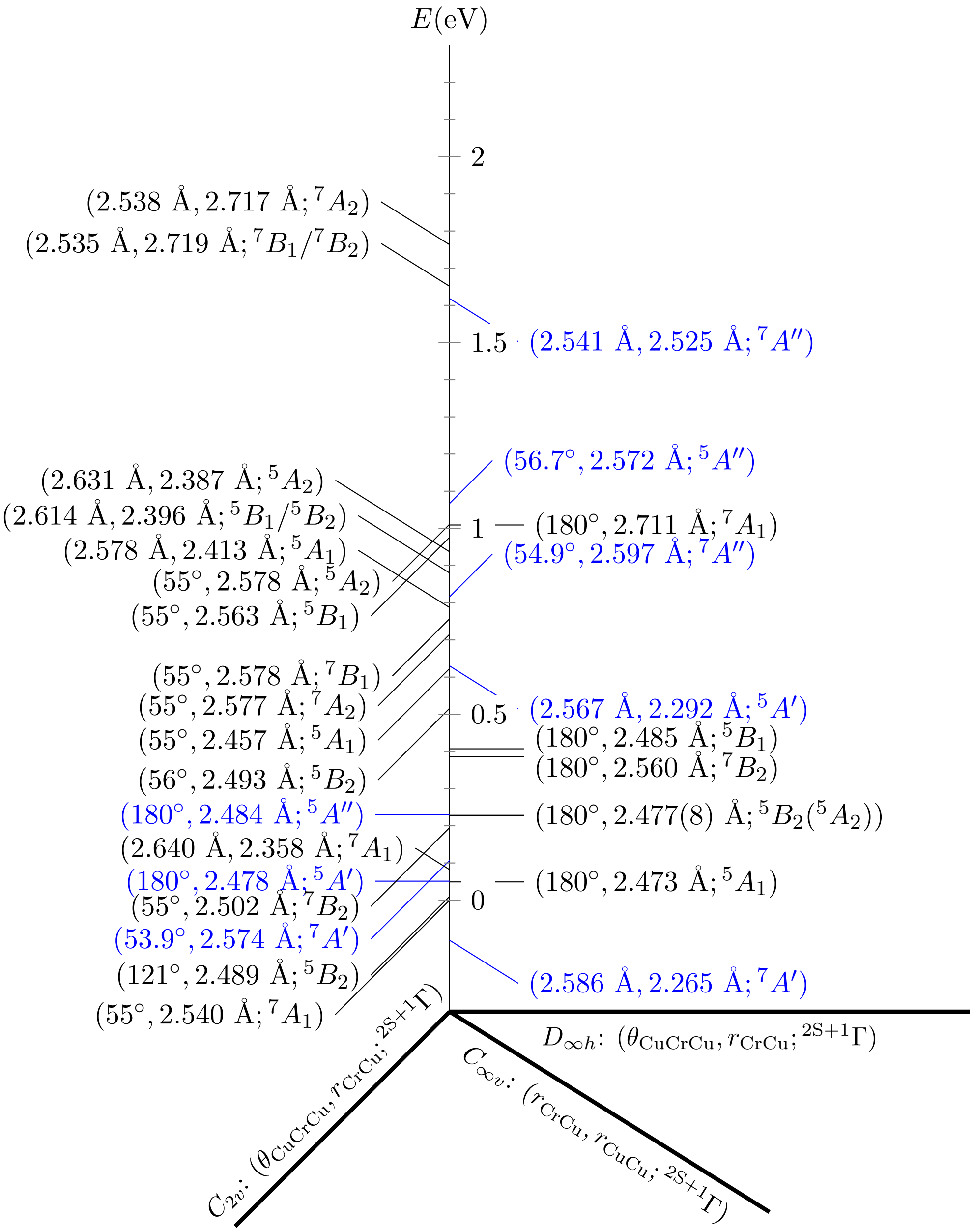
E(eV)
2
1.5
1
0.5
0
(2.538 Å, 2.717 Å; $^7A_2$)
(2.535 Å, 2.719 Å; $^7B_1/^7B_2$)
(2.541 Å, 2.525 Å; $^7A''$)
(56.7°, 2.572 Å; $^5A''$)
(2.631 Å, 2.387 Å; $^5A_2$)
(2.614 Å, 2.396 Å; $^5B_1/^5B_2$)
(180°, 2.711 Å; $^7A_1$)
(2.578 Å, 2.413 Å; $^5A_1$)
(54.9°, 2.597 Å; $^7A''$)
(55°, 2.578 Å; $^5A_2$)
(55°, 2.563 Å; $^5B_1$)
(55°, 2.578 Å; $^7B_1$)
(55°, 2.577 Å; $^7A_2$)
(2.567 Å, 2.292 Å; $^5A'$)
(55°, 2.457 Å; $^5A_1$)
(180°, 2.485 Å; $^5B_1$)
(180°, 2.560 Å; $^7B_2$)
(56°, 2.493 Å; $^5B_2$)
(180°, 2.484 Å; $^5A''$)
(180°, 2.477(8) Å; $^5B_2(^5A_2)$)
(2.640 Å, 2.358 Å; $^7A_1$)
(180°, 2.478 Å; $^5A'$)
(180°, 2.473 Å; $^5A_1$)
(55°, 2.502 Å; $^7B_2$)
(53.9°, 2.574 Å; $^7A'$)
(121°, 2.489 Å; $^5B_2$)
(2.586 Å, 2.265 Å; $^7A'$)
(55°, 2.540 Å; $^7A_1$)
$D_{\infty h}$: ($\theta_{\mathrm{CuCrCu}}, r_{\mathrm{CrCu}}; {}^{2S+1}\Gamma$)
$C_{\infty v}$: ($r_{\mathrm{CrCu}}, r_{\mathrm{CuCu}}; {}^{2S+1}\Gamma$)
C_{2v}: ($\theta_{\mathrm{CuCrCu}}, r_{\mathrm{CrCu}}; {}^{2S+1}\Gamma$)

Figure B.92: Low-lying ΓS states of **CrCu$_2$** within the symmetries $D_{\infty h}$, $C_{\infty v}$, and C_{2v} obtained at the MRCI[(20+8)E,(10+8)O] level of theory. Potential minima are shown in black and optimised minima in blue.

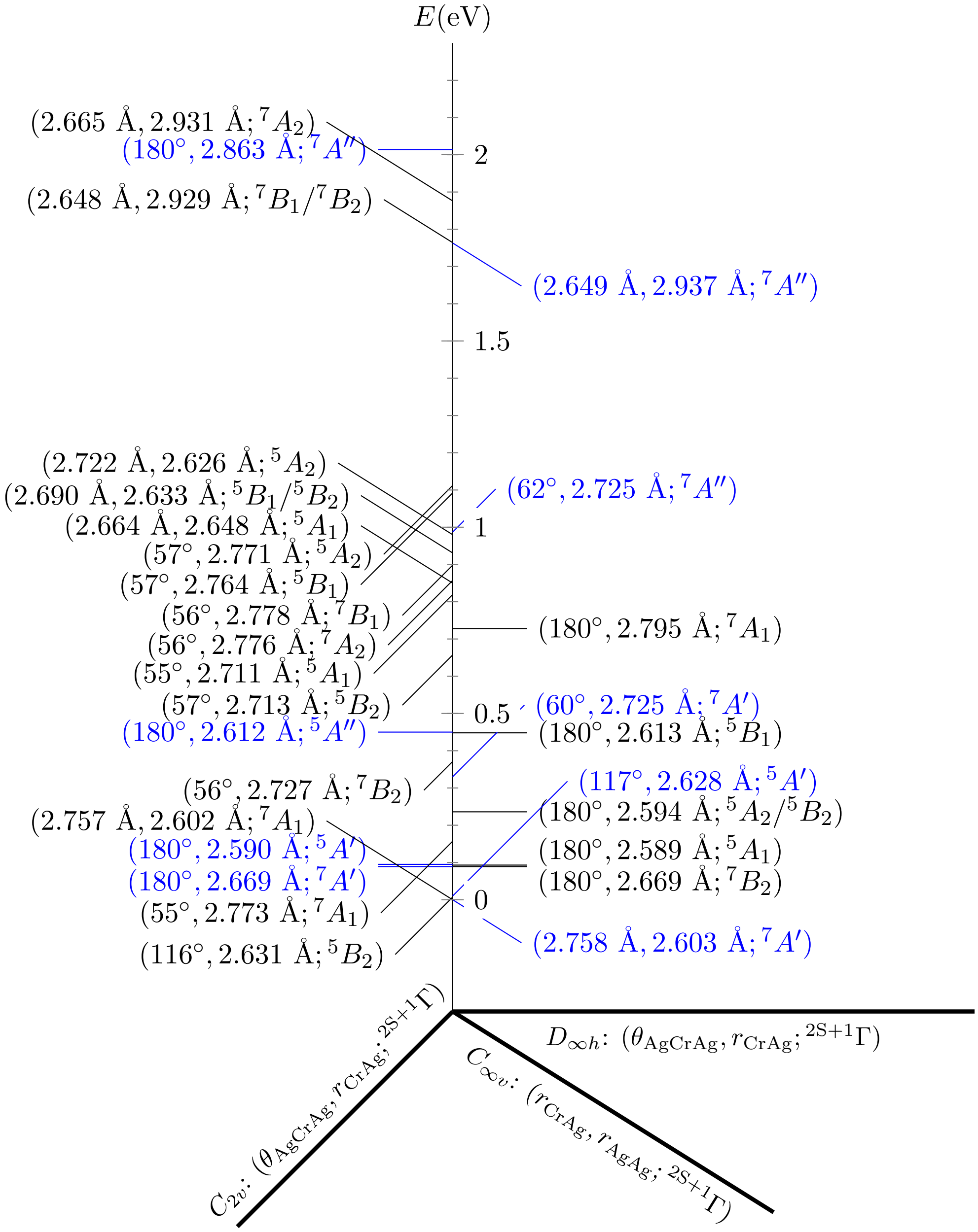

Figure B.93: Low-lying ΓS states of **CrAg$_2$** within the symmetries $D_{\infty h}$, $C_{\infty v}$, and C_{2v} obtained at the MRCI[(20+8)E,(10+8)O] level of theory. Potential minima are shown in black and optimised minima in blue.

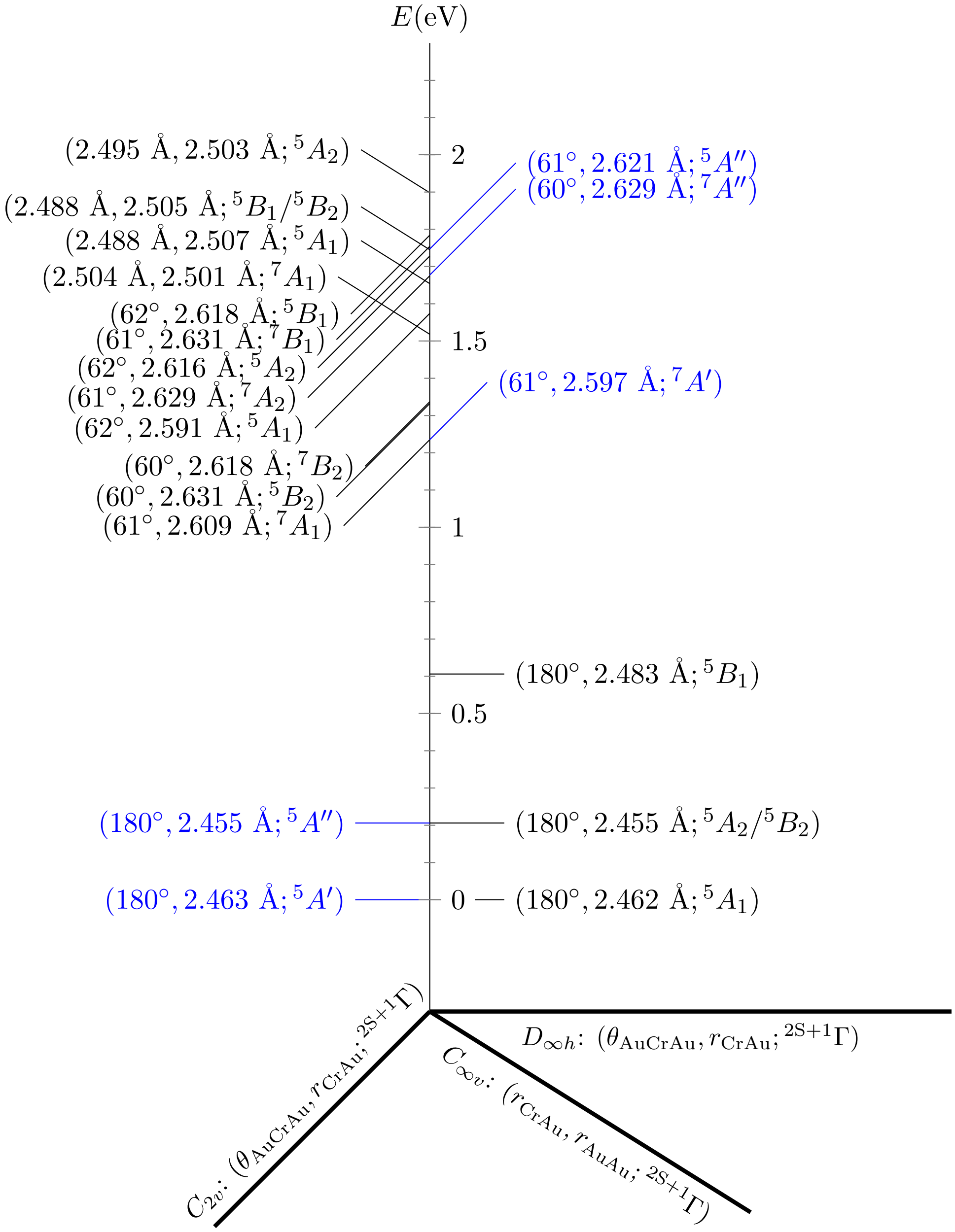
E(eV)
2
1.5
1
0.5
0
(2.495 Å, 2.503 Å; $^5A_2$)
(2.488 Å, 2.505 Å; $^5B_1/^5B_2$)
(2.488 Å, 2.507 Å; $^5A_1$)
(2.504 Å, 2.501 Å; $^7A_1$)
(62°, 2.618 Å; $^5B_1$)
(61°, 2.631 Å; $^7B_1$)
(62°, 2.616 Å; $^5A_2$)
(61°, 2.629 Å; $^7A_2$)
(62°, 2.591 Å; $^5A_1$)
(60°, 2.618 Å; $^7B_2$)
(60°, 2.631 Å; $^5B_2$)
(61°, 2.609 Å; $^7A_1$)
(61°, 2.621 Å; $^5A''$)
(60°, 2.629 Å; $^7A''$)
(61°, 2.597 Å; $^7A'$)
(180°, 2.483 Å; $^5B_1$)
(180°, 2.455 Å; $^5A''$)
(180°, 2.455 Å; $^5A_2/^5B_2$)
(180°, 2.463 Å; $^5A'$)
(180°, 2.462 Å; $^5A_1$)
$D_{\infty h}$: ($\theta_{\mathrm{AuCrAu}}, r_{\mathrm{CrAu}}; {}^{2S+1}\Gamma$)
$C_{\infty v}$: ($r_{\mathrm{CrAu}}, r_{\mathrm{AuAu}}; {}^{2S+1}\Gamma$)
C_{2v}: ($\theta_{\mathrm{AuCrAu}}, r_{\mathrm{CrAu}}; {}^{2S+1}\Gamma$)

Figure B.94: Low-lying ΓS states of **CrAu$_2$** within the symmetries $D_{\infty h}$, $C_{\infty v}$, and C_{2v} obtained at the MRCI[(20+8)E,(10+8)O] level of theory. Potential minima are shown in black and optimised minima in blue.

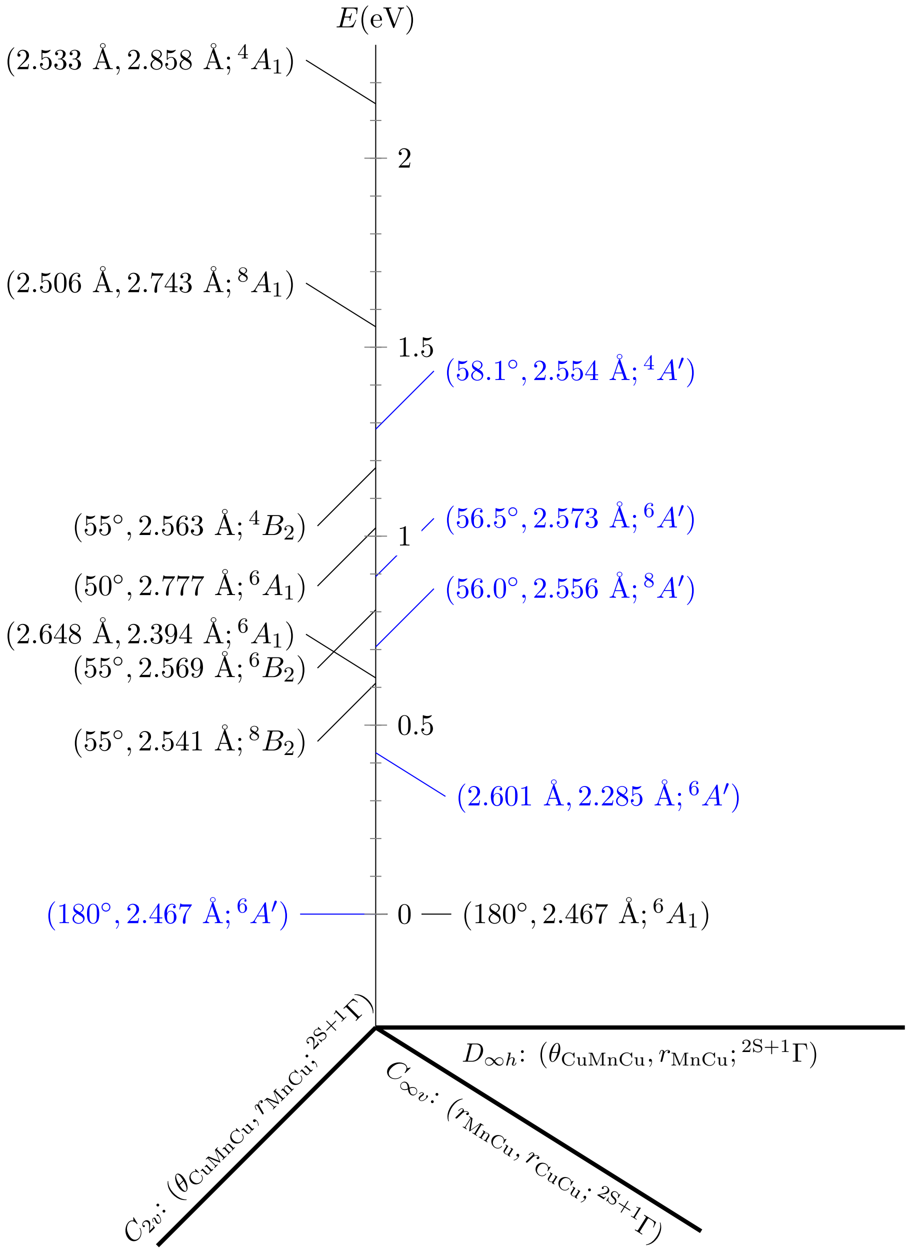

Figure B.95: Low-lying ΓS states of **MnCu$_2$** within the symmetries $D_{\infty h}$, $C_{\infty v}$, and C_{2v} obtained at the MRCI[(20+9)E,(10+8)O] level of theory. Potential minima are shown in black and optimised minima in blue.

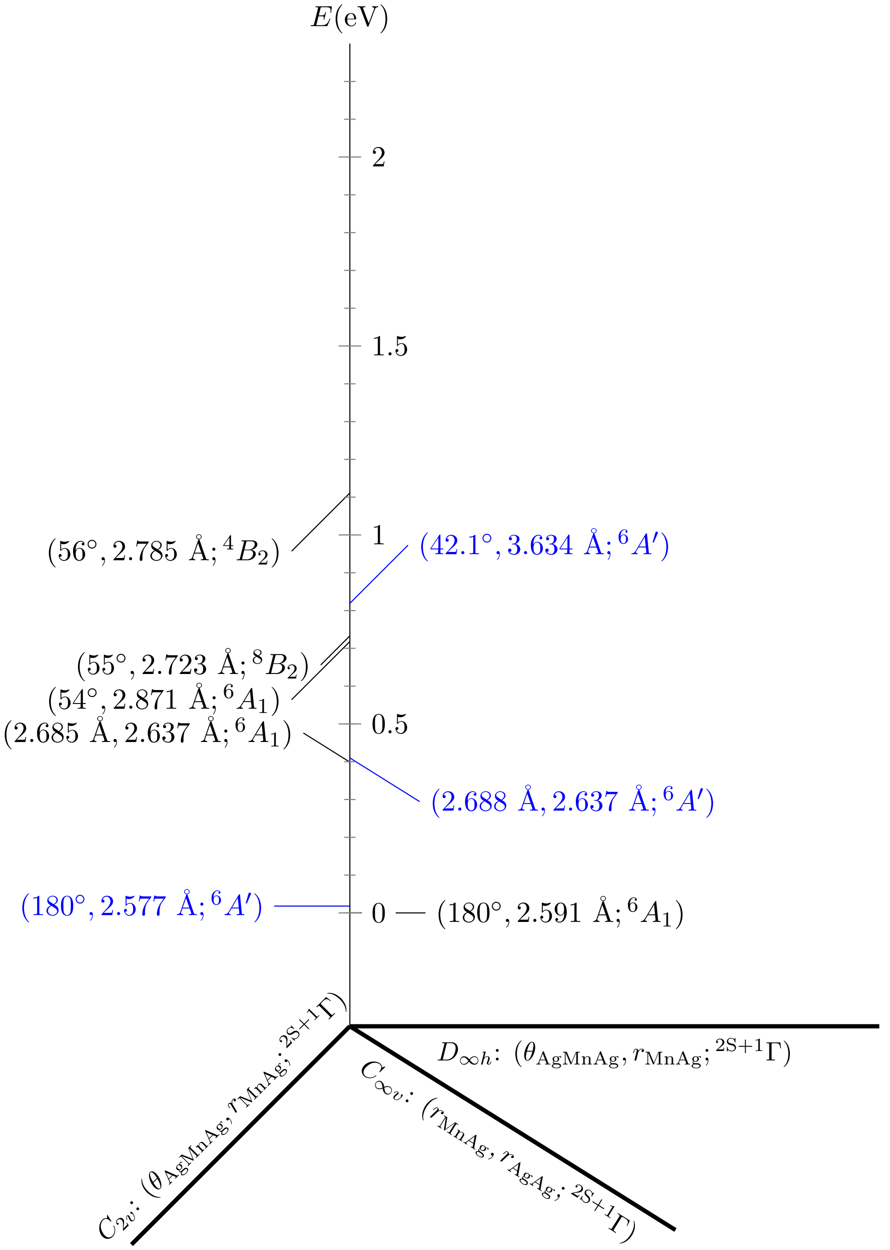
E(eV)
2
1.5
1
0.5
0
(56°, 2.785 Å; ⁴B₂)
(42.1°, 3.634 Å; ⁶A′)
(55°, 2.723 Å; ⁸B₂)
(54°, 2.871 Å; ⁶A₁)
(2.685 Å, 2.637 Å; ⁶A₁)
(2.688 Å, 2.637 Å; ⁶A′)
(180°, 2.577 Å; ⁶A′)
(180°, 2.591 Å; ⁶A₁)
D∞h: (θAgMnAg, rMnAg; 2S+1Γ)
C∞v: (rMnAg, rAgAg; 2S+1Γ)
C2v: (θAgMnAg, rMnAg; 2S+1Γ)

Figure B.96: Low-lying ΓS states of **MnAg$_2$** within the symmetries $D_{\infty h}$, $C_{\infty v}$, and C_{2v} obtained at the MRCI[(20+9)E,(10+8)O] level of theory. Potential minima are shown in black and optimised minima in blue.

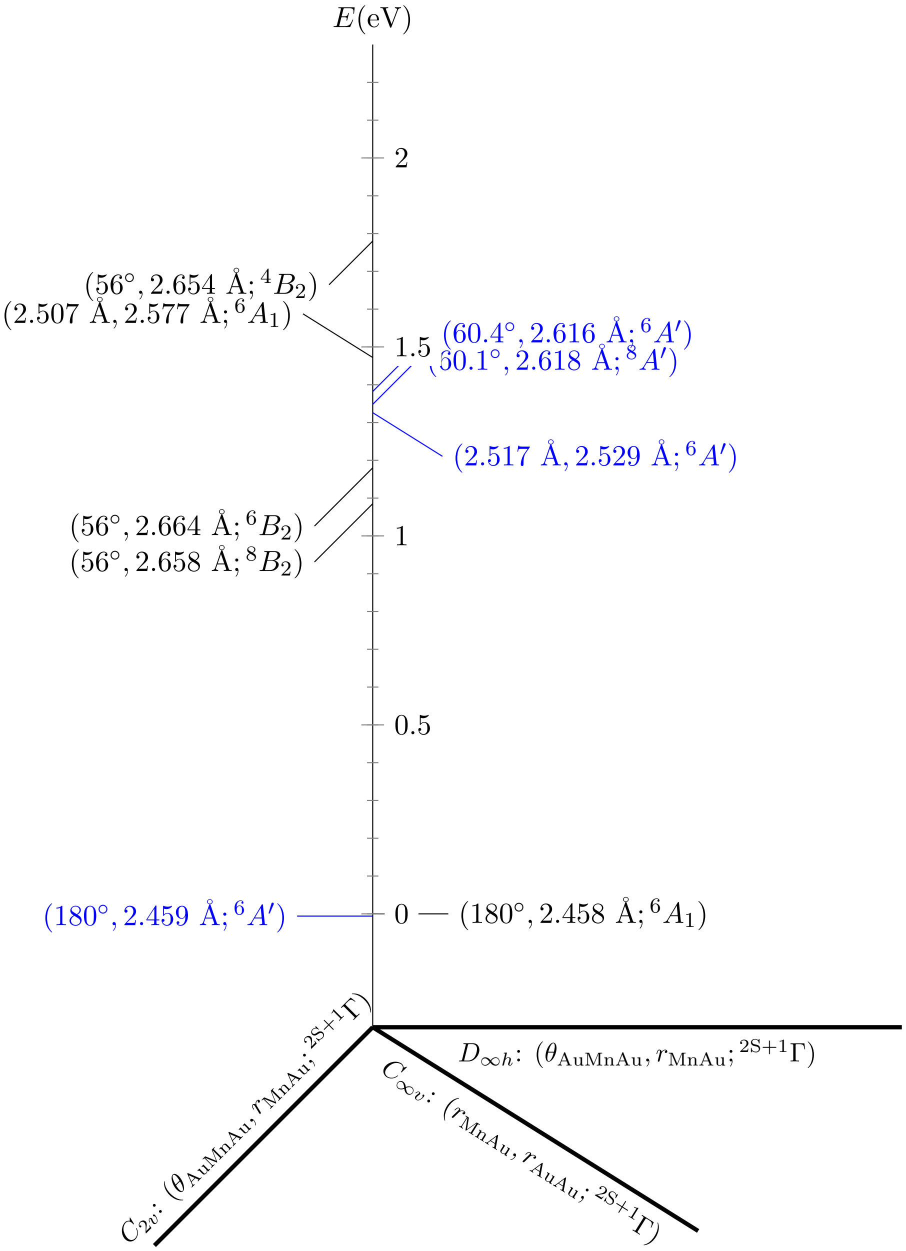
E(eV)
2
1.5
1
0.5
0
$(56°, 2.654\ \text{Å}; {}^4B_2)$
$(2.507\ \text{Å}, 2.577\ \text{Å}; {}^6A_1)$
$(60.4°, 2.616\ \text{Å}; {}^6A')$
$(60.1°, 2.618\ \text{Å}; {}^8A')$
$(2.517\ \text{Å}, 2.529\ \text{Å}; {}^6A')$
$(56°, 2.664\ \text{Å}; {}^6B_2)$
$(56°, 2.658\ \text{Å}; {}^8B_2)$
$(180°, 2.459\ \text{Å}; {}^6A')$
$(180°, 2.458\ \text{Å}; {}^6A_1)$
$D_{\infty h}$: $(\theta_{\text{AuMnAu}}, r_{\text{MnAu}}; {}^{2S+1}\Gamma)$
$C_{\infty v}$: $(r_{\text{MnAu}}, r_{\text{AuAu}}; {}^{2S+1}\Gamma)$
C_{2v}: $(\theta_{\text{AuMnAu}}, r_{\text{MnAu}}; {}^{2S+1}\Gamma)$

Figure B.97: Low-lying ΓS states of **MnAu₂** within the symmetries $D_{\infty h}$, $C_{\infty v}$, and C_{2v} obtained at the MRCI[(20+9)E,(10+8)O] level of theory. Potential minima are shown in black and optimised minima in blue.

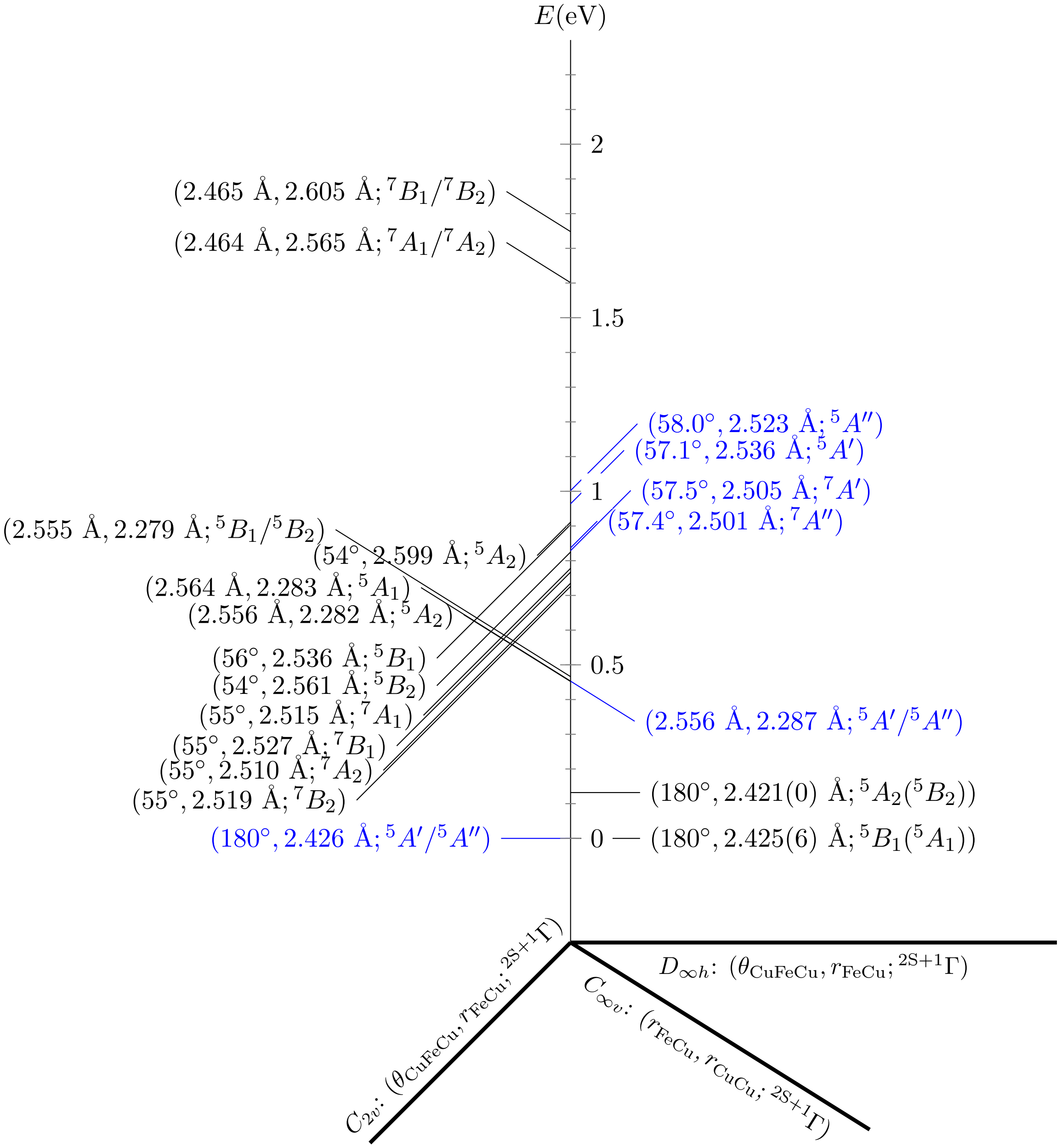

Figure B.98: Low-lying ΓS states of **FeCu₂** within the symmetries $D_{\infty h}$, $C_{\infty v}$, and C_{2v} obtained at the MRCI[(20+10)E,(10+8)O] level of theory. Potential minima are shown in black and optimised minima in blue.

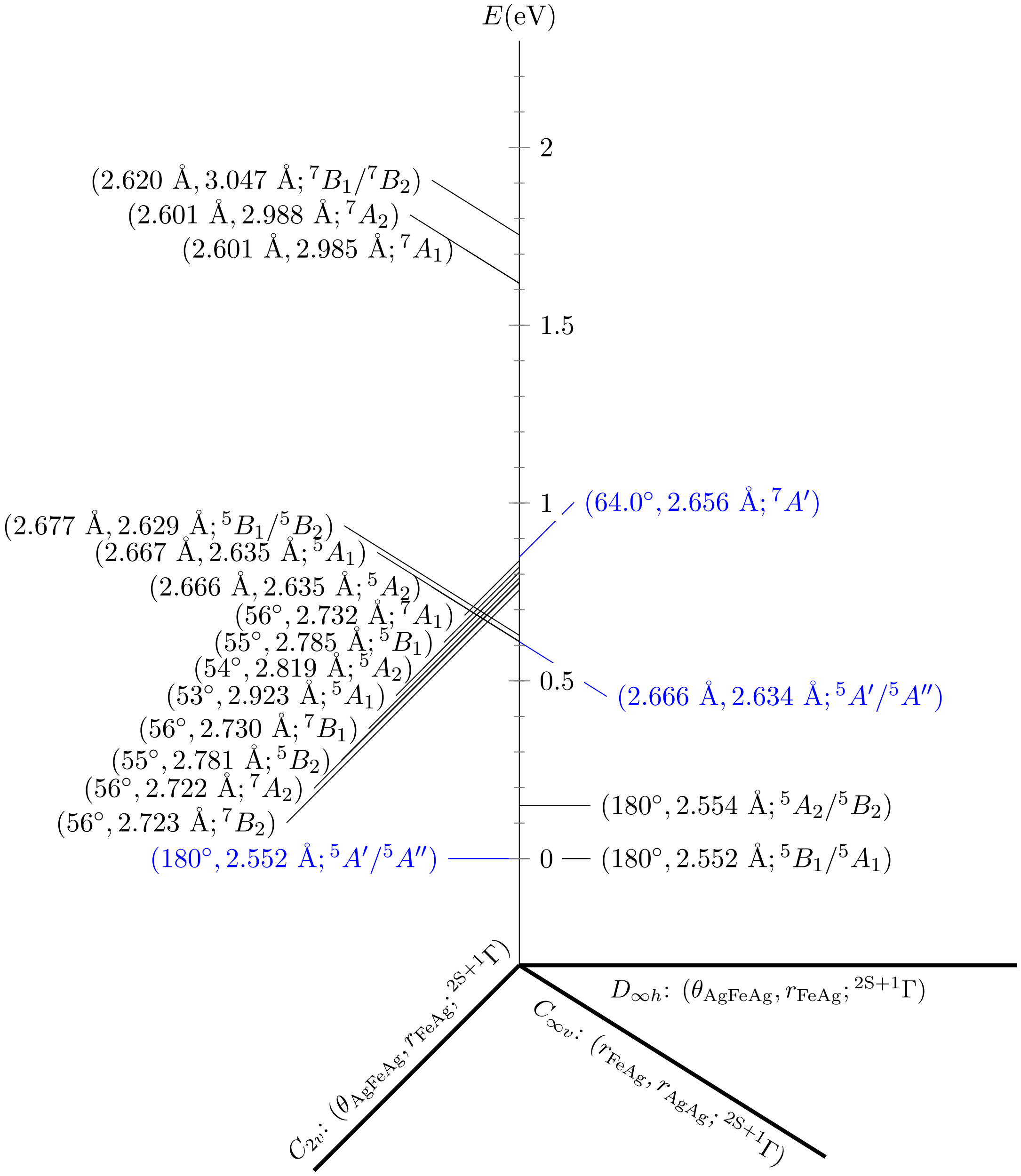

Figure B.99: Low-lying ΓS states of $\mathbf{FeAg_2}$ within the symmetries $D_{\infty h}$, $C_{\infty v}$, and C_{2v} obtained at the MRCI[(20+10)E,(10+8)O] level of theory. Potential minima are shown in black and optimised minima in blue.

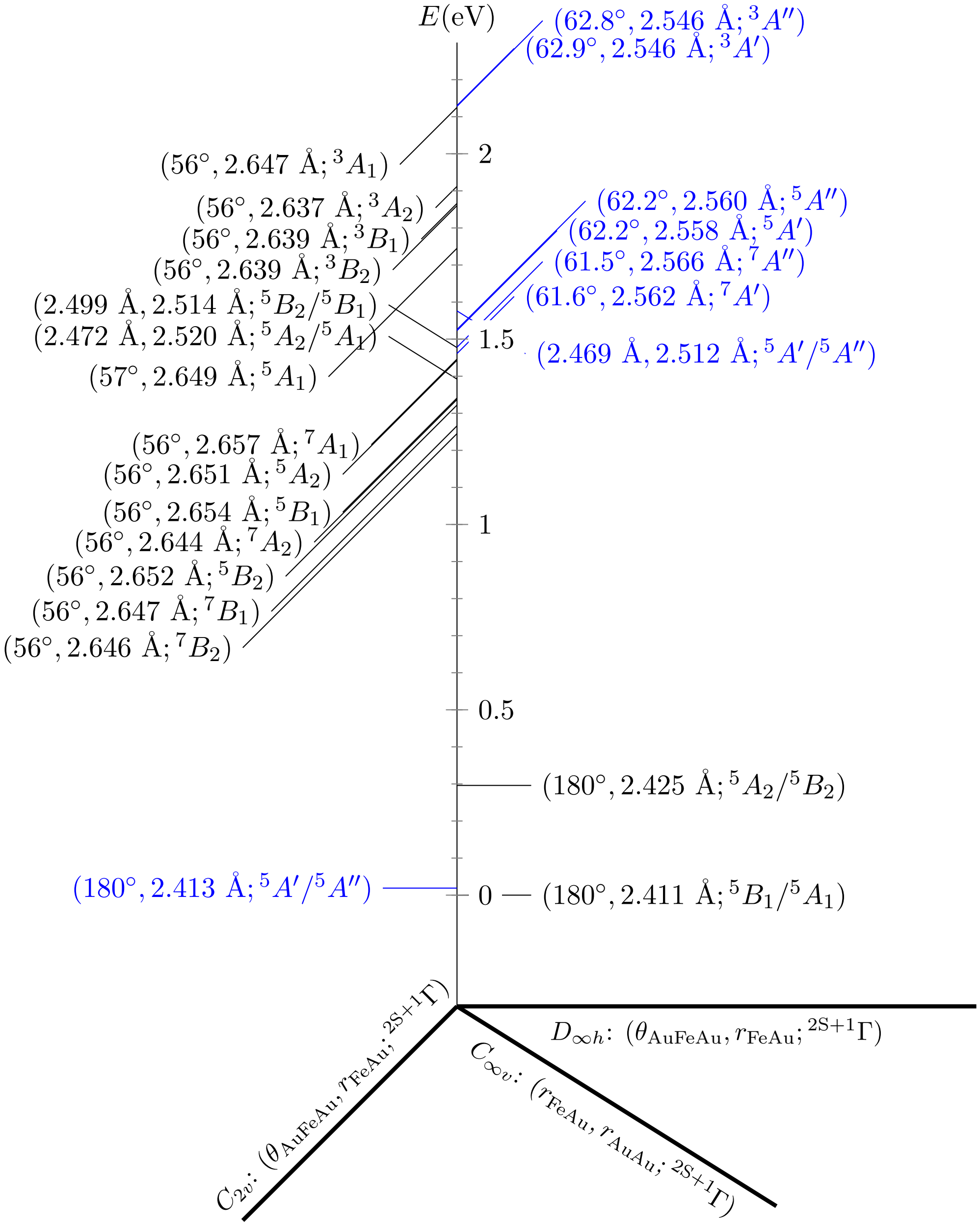
E(eV)
$(62.8°, 2.546$ Å$; {}^3A'')$
$(62.9°, 2.546$ Å$; {}^3A')$
$(56°, 2.647$ Å$; {}^3A_1)$
2
$(56°, 2.637$ Å$; {}^3A_2)$
$(56°, 2.639$ Å$; {}^3B_1)$
$(56°, 2.639$ Å$; {}^3B_2)$
$(62.2°, 2.560$ Å$; {}^5A'')$
$(62.2°, 2.558$ Å$; {}^5A')$
$(61.5°, 2.566$ Å$; {}^7A'')$
$(61.6°, 2.562$ Å$; {}^7A')$
$(2.499$ Å$, 2.514$ Å$; {}^5B_2/{}^5B_1)$
$(2.472$ Å$, 2.520$ Å$; {}^5A_2/{}^5A_1)$
1.5
$(2.469$ Å$, 2.512$ Å$; {}^5A'/{}^5A'')$
$(57°, 2.649$ Å$; {}^5A_1)$
$(56°, 2.657$ Å$; {}^7A_1)$
$(56°, 2.651$ Å$; {}^5A_2)$
$(56°, 2.654$ Å$; {}^5B_1)$
1
$(56°, 2.644$ Å$; {}^7A_2)$
$(56°, 2.652$ Å$; {}^5B_2)$
$(56°, 2.647$ Å$; {}^7B_1)$
$(56°, 2.646$ Å$; {}^7B_2)$
0.5
$(180°, 2.425$ Å$; {}^5A_2/{}^5B_2)$
$(180°, 2.413$ Å$; {}^5A'/{}^5A'')$
0
$(180°, 2.411$ Å$; {}^5B_1/{}^5A_1)$
$D_{\infty h}$: $(\theta_{\mathrm{AuFeAu}}, r_{\mathrm{FeAu}}; {}^{2S+1}\Gamma)$
$C_{\infty v}$: $(r_{\mathrm{FeAu}}, r_{\mathrm{AuAu}}; {}^{2S+1}\Gamma)$
C_{2v}: $(\theta_{\mathrm{AuFeAu}}, r_{\mathrm{FeAu}}; {}^{2S+1}\Gamma)$

Figure B.100: Low-lying ΓS states of **FeAu$_2$** within the symmetries $D_{\infty h}$, $C_{\infty v}$, and C_{2v} obtained at the MRCI[(20+10)E,(10+8)O] level of theory. Potential minima are shown in black and optimised minima in blue.

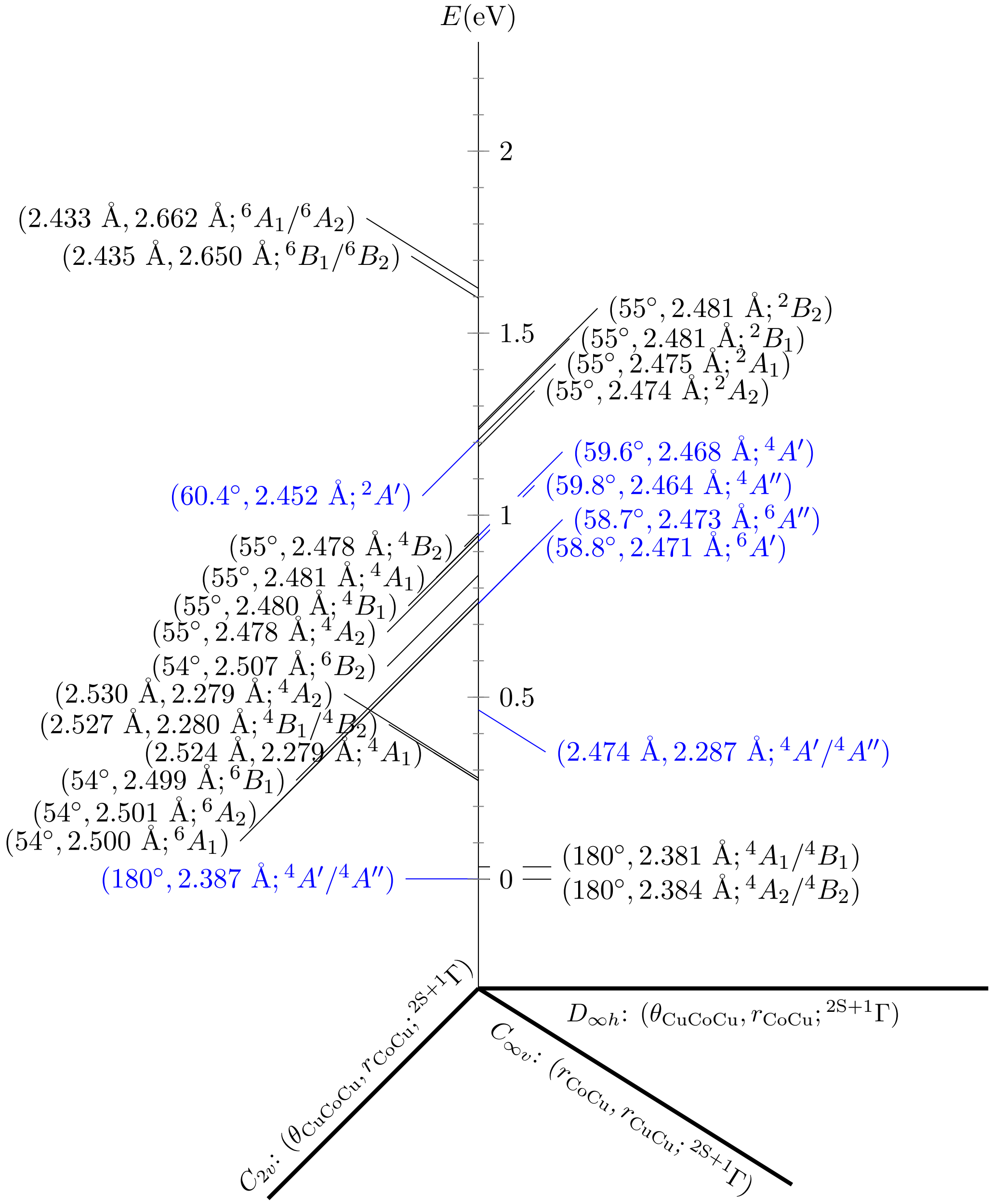
E(eV)
2
1.5
1
0.5
0
(2.433 Å, 2.662 Å; $^6A_1/^6A_2$)
(2.435 Å, 2.650 Å; $^6B_1/^6B_2$)
(55°, 2.481 Å; $^2B_2$)
(55°, 2.481 Å; $^2B_1$)
(55°, 2.475 Å; $^2A_1$)
(55°, 2.474 Å; $^2A_2$)
(59.6°, 2.468 Å; $^4A'$)
(60.4°, 2.452 Å; $^2A'$)
(59.8°, 2.464 Å; $^4A''$)
(58.7°, 2.473 Å; $^6A''$)
(55°, 2.478 Å; $^4B_2$)
(58.8°, 2.471 Å; $^6A'$)
(55°, 2.481 Å; $^4A_1$)
(55°, 2.480 Å; $^4B_1$)
(55°, 2.478 Å; $^4A_2$)
(54°, 2.507 Å; $^6B_2$)
(2.530 Å, 2.279 Å; $^4A_2$)
(2.527 Å, 2.280 Å; $^4B_1/^4B_2$)
(2.474 Å, 2.287 Å; $^4A'/^4A''$)
(2.524 Å, 2.279 Å; $^4A_1$)
(54°, 2.499 Å; $^6B_1$)
(54°, 2.501 Å; $^6A_2$)
(54°, 2.500 Å; $^6A_1$)
(180°, 2.381 Å; $^4A_1/^4B_1$)
(180°, 2.387 Å; $^4A'/^4A''$)
(180°, 2.384 Å; $^4A_2/^4B_2$)
$D_{\infty h}$: ($\theta_{\mathrm{CuCoCu}}, r_{\mathrm{CoCu}}; {}^{2\mathrm{S}+1}\Gamma$)
$C_{\infty v}$: ($r_{\mathrm{CoCu}}, r_{\mathrm{CuCu}}; {}^{2\mathrm{S}+1}\Gamma$)
C_{2v}: ($\theta_{\mathrm{CuCoCu}}, r_{\mathrm{CoCu}}; {}^{2\mathrm{S}+1}\Gamma$)

Figure B.101: Low-lying ΓS states of **CoCu₂** within the symmetries $D_{\infty h}$, $C_{\infty v}$, and C_{2v} obtained at the MRCI[(20+11)E,(10+8)O] level of theory. Potential minima are shown in black and optimised minima in blue.

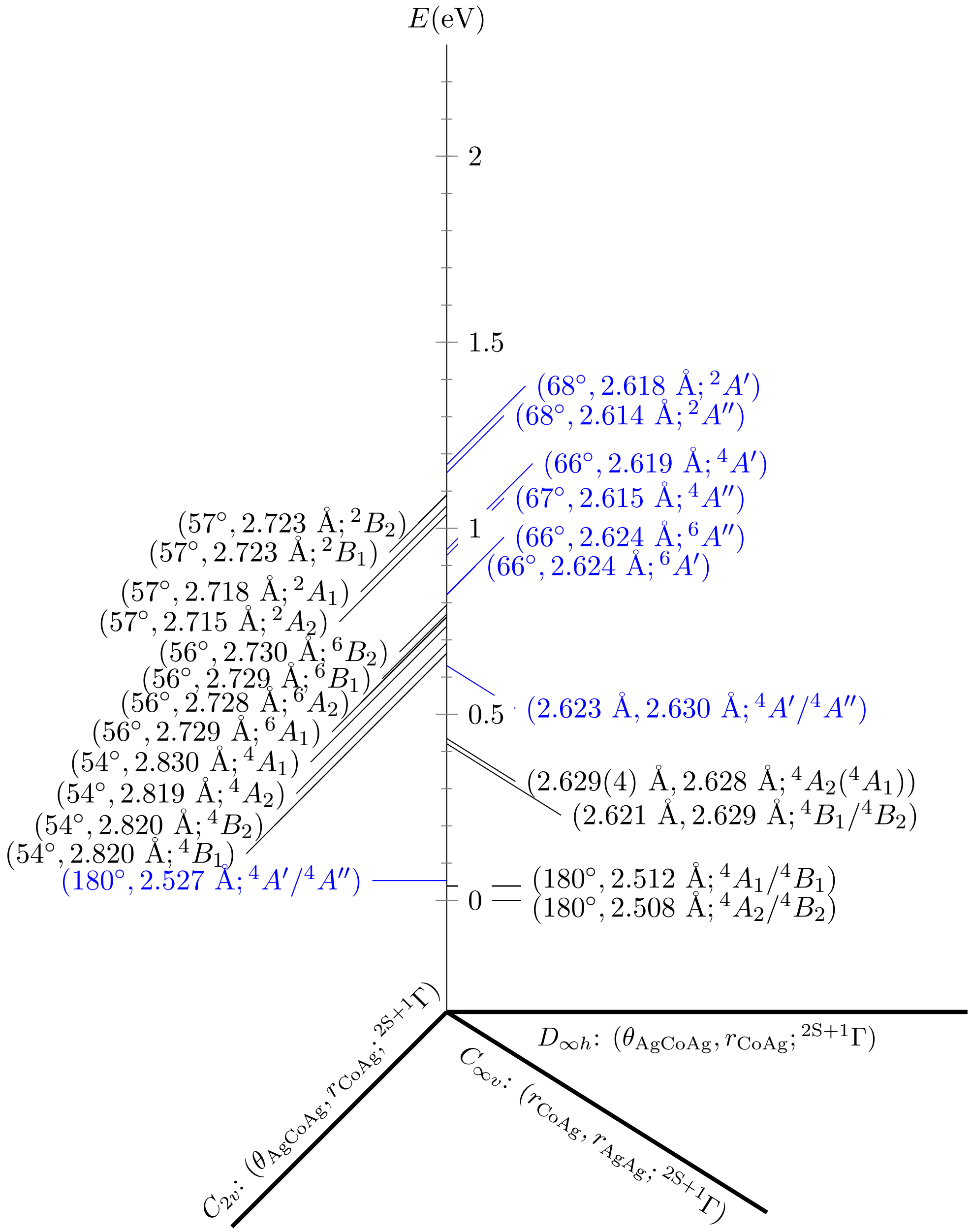

Figure B.102: Low-lying ΓS states of **CoAg$_2$** within the symmetries $D_{\infty h}$, $C_{\infty v}$, and C_{2v} obtained at the MRCI[(20+11)E,(10+8)O] level of theory. Potential minima are shown in black and optimised minima in blue.

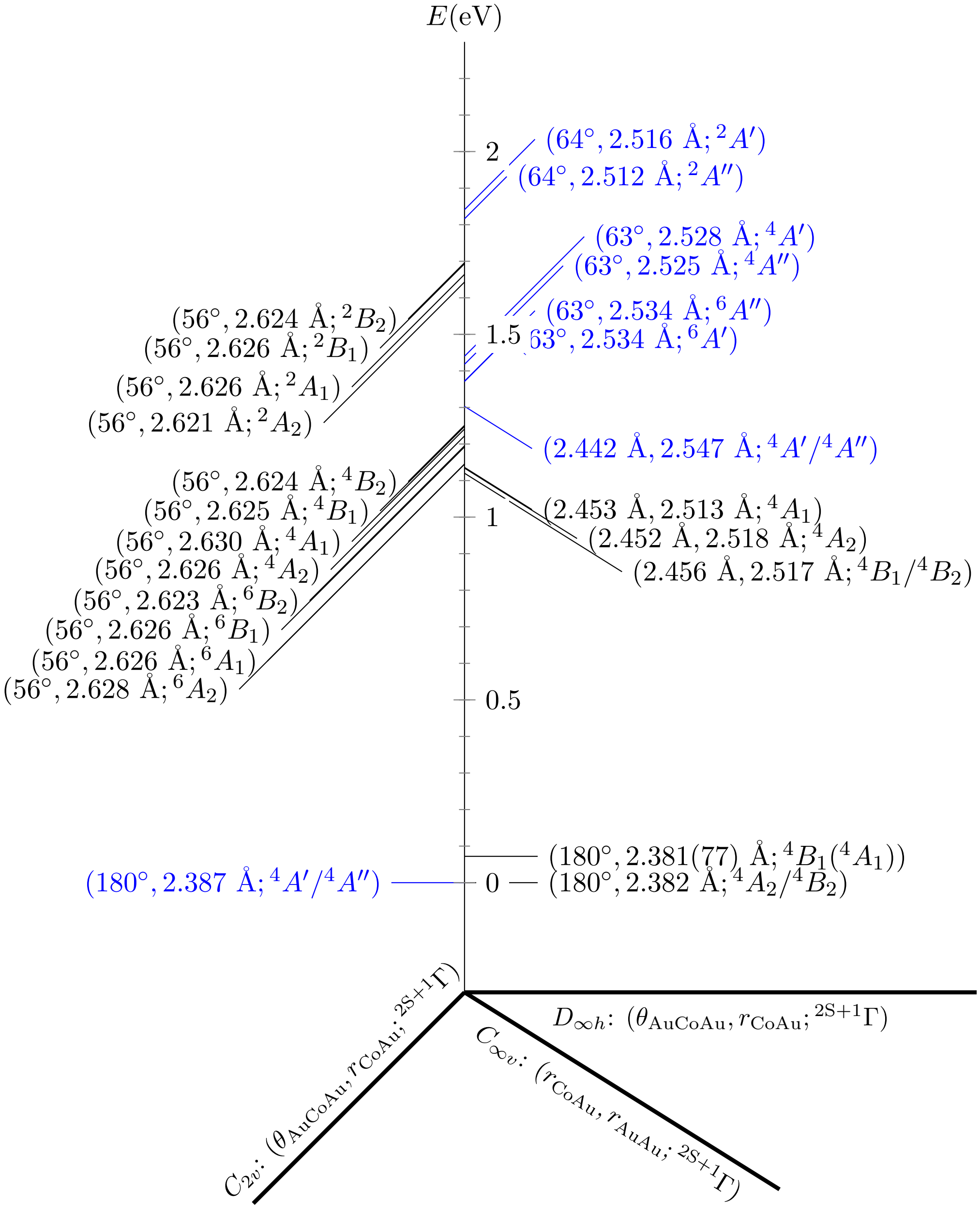

Figure B.103: Low-lying ΓS states of **CoAu$_2$** within the symmetries $D_{\infty h}$, $C_{\infty v}$, and C_{2v} obtained at the MRCI[(20+11)E,(10+8)O] level of theory. Potential minima are shown in black and optimised minima in blue.

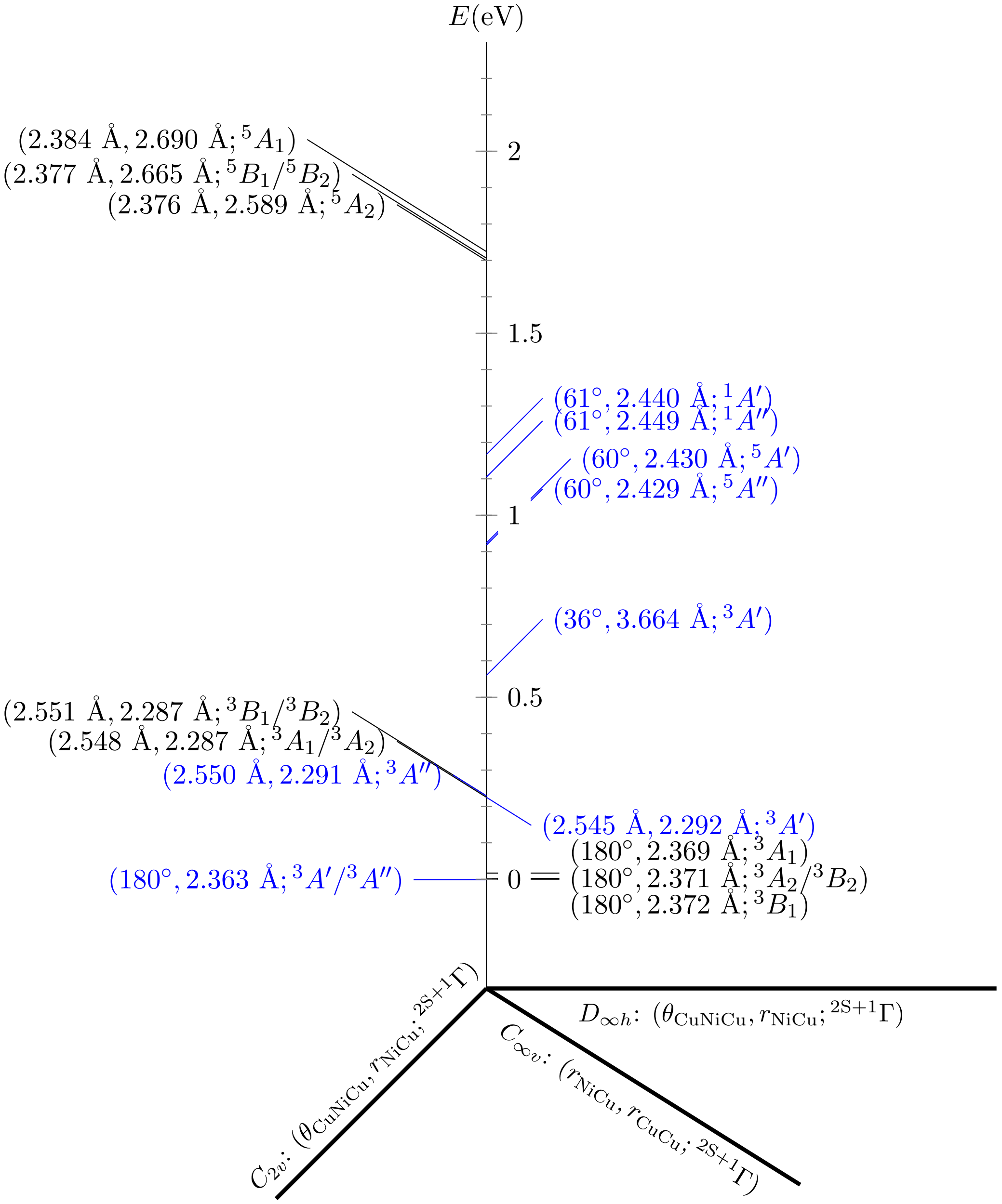
E(eV)
2
1.5
1
0.5
0
(2.384 Å, 2.690 Å; $^5A_1$)
(2.377 Å, 2.665 Å; $^5B_1/^5B_2$)
(2.376 Å, 2.589 Å; $^5A_2$)
(61°, 2.440 Å; $^1A'$)
(61°, 2.449 Å; $^1A''$)
(60°, 2.430 Å; $^5A'$)
(60°, 2.429 Å; $^5A''$)
(36°, 3.664 Å; $^3A'$)
(2.551 Å, 2.287 Å; $^3B_1/^3B_2$)
(2.548 Å, 2.287 Å; $^3A_1/^3A_2$)
(2.550 Å, 2.291 Å; $^3A''$)
(2.545 Å, 2.292 Å; $^3A'$)
(180°, 2.369 Å; $^3A_1$)
(180°, 2.371 Å; $^3A_2/^3B_2$)
(180°, 2.372 Å; $^3B_1$)
(180°, 2.363 Å; $^3A'/^3A''$)
$D_{\infty h}$: ($\theta_{\text{CuNiCu}}, r_{\text{NiCu}}; {}^{2S+1}\Gamma$)
$C_{\infty v}$: ($r_{\text{NiCu}}, r_{\text{CuCu}}; {}^{2S+1}\Gamma$)
C_{2v}: ($\theta_{\text{CuNiCu}}, r_{\text{NiCu}}; {}^{2S+1}\Gamma$)

Figure B.104: Low-lying ΓS states of **NiCu₂** within the symmetries $D_{\infty h}$, $C_{\infty v}$, and C_{2v} obtained at the MRCI[(20+12)E,(10+8)O] level of theory. Potential minima are shown in black and optimised minima in blue.

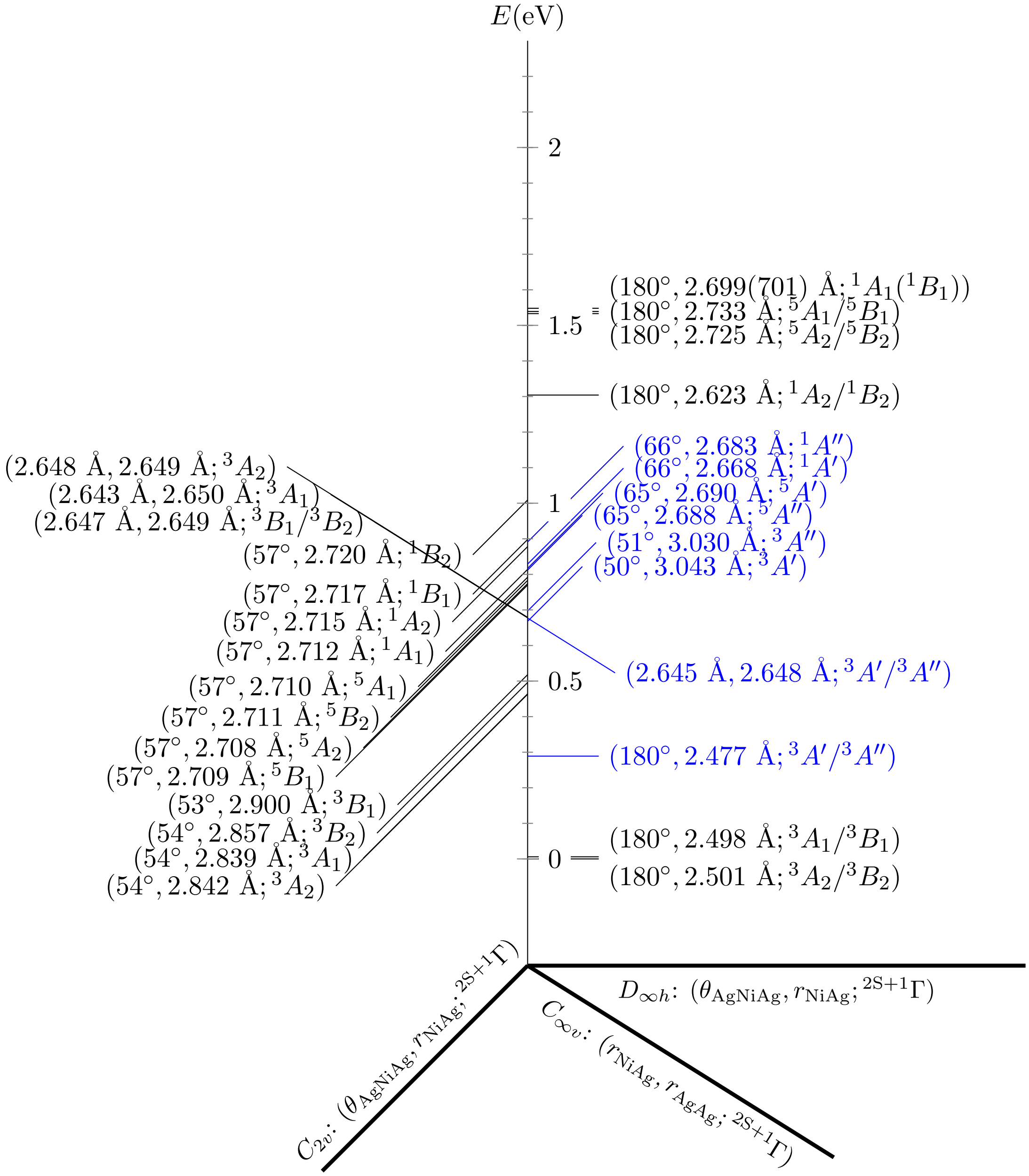

Figure B.105: Low-lying ΓS states of **NiAg$_2$** within the symmetries $D_{\infty h}$, $C_{\infty v}$, and C_{2v} obtained at the MRCI[(20+12)E,(10+8)O] level of theory. Potential minima are shown in black and optimised minima in blue.

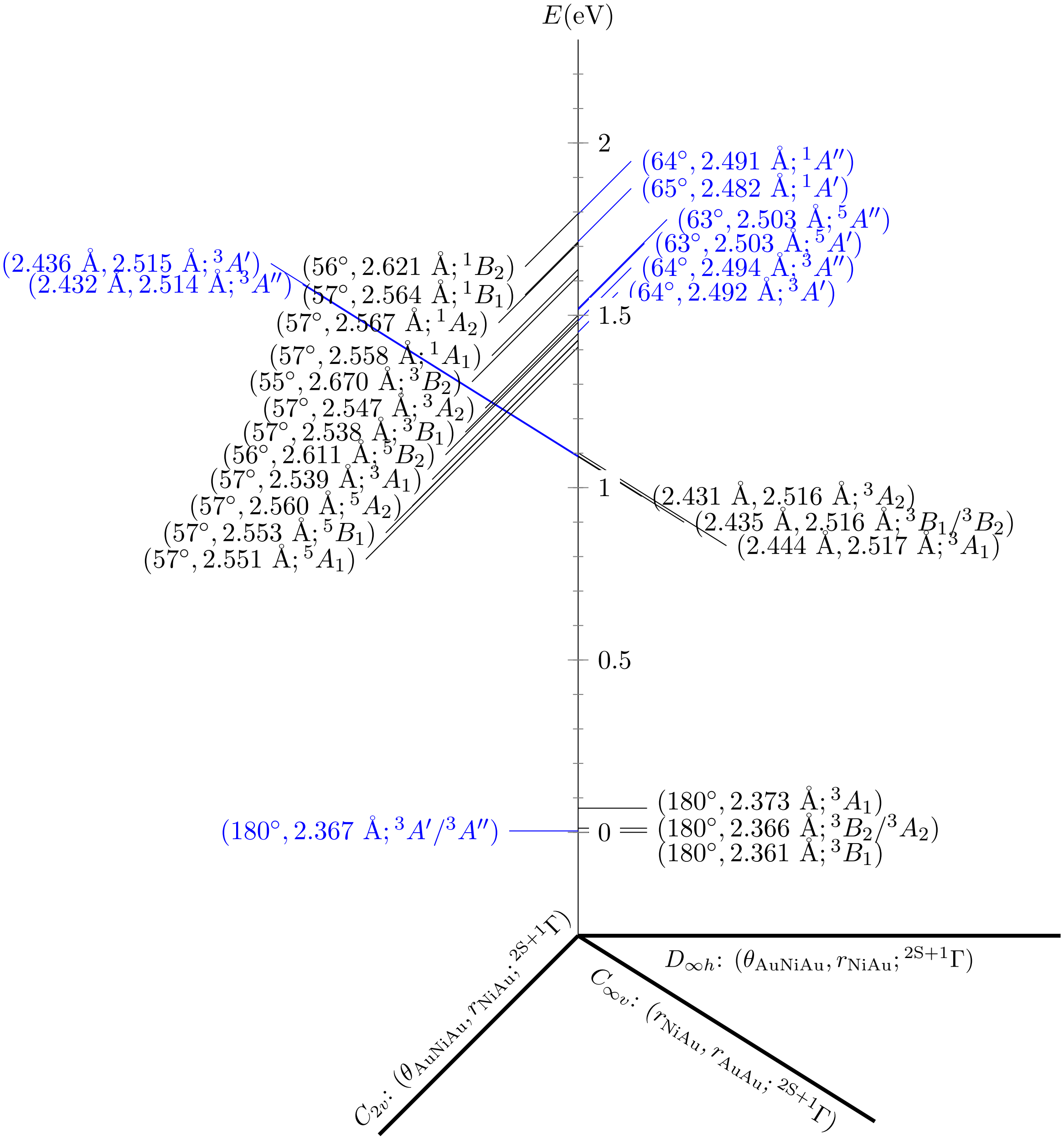
E(eV)
2
1.5
1
0.5
0
$(64°, 2.491\ \text{Å}; {}^1A'')$
$(65°, 2.482\ \text{Å}; {}^1A')$
$(63°, 2.503\ \text{Å}; {}^5A'')$
$(63°, 2.503\ \text{Å}; {}^5A')$
$(64°, 2.494\ \text{Å}; {}^3A'')$
$(64°, 2.492\ \text{Å}; {}^3A')$
$(2.436\ \text{Å}, 2.515\ \text{Å}; {}^3A')$
$(2.432\ \text{Å}, 2.514\ \text{Å}; {}^3A'')$
$(56°, 2.621\ \text{Å}; {}^1B_2)$
$(57°, 2.564\ \text{Å}; {}^1B_1)$
$(57°, 2.567\ \text{Å}; {}^1A_2)$
$(57°, 2.558\ \text{Å}; {}^1A_1)$
$(55°, 2.670\ \text{Å}; {}^3B_2)$
$(57°, 2.547\ \text{Å}; {}^3A_2)$
$(57°, 2.538\ \text{Å}; {}^3B_1)$
$(56°, 2.611\ \text{Å}; {}^5B_2)$
$(57°, 2.539\ \text{Å}; {}^3A_1)$
$(57°, 2.560\ \text{Å}; {}^5A_2)$
$(57°, 2.553\ \text{Å}; {}^5B_1)$
$(57°, 2.551\ \text{Å}; {}^5A_1)$
$(2.431\ \text{Å}, 2.516\ \text{Å}; {}^3A_2)$
$(2.435\ \text{Å}, 2.516\ \text{Å}; {}^3B_1/{}^3B_2)$
$(2.444\ \text{Å}, 2.517\ \text{Å}; {}^3A_1)$
$(180°, 2.373\ \text{Å}; {}^3A_1)$
$(180°, 2.366\ \text{Å}; {}^3B_2/{}^3A_2)$
$(180°, 2.361\ \text{Å}; {}^3B_1)$
$(180°, 2.367\ \text{Å}; {}^3A'/{}^3A'')$
$D_{\infty h}$: $(\theta_{\text{AuNiAu}}, r_{\text{NiAu}}; {}^{2S+1}\Gamma)$
$C_{\infty v}$: $(r_{\text{NiAu}}, r_{\text{AuAu}}; {}^{2S+1}\Gamma)$
C_{2v}: $(\theta_{\text{AuNiAu}}, r_{\text{NiAu}}; {}^{2S+1}\Gamma)$

Figure B.106: Low-lying ΓS states of **NiAu$_2$** within the symmetries $D_{\infty h}$, $C_{\infty v}$, and C_{2v} obtained at the MRCI[(20+12)E,(10+8)O] level of theory. Potential minima are shown in black and optimised minima in blue.

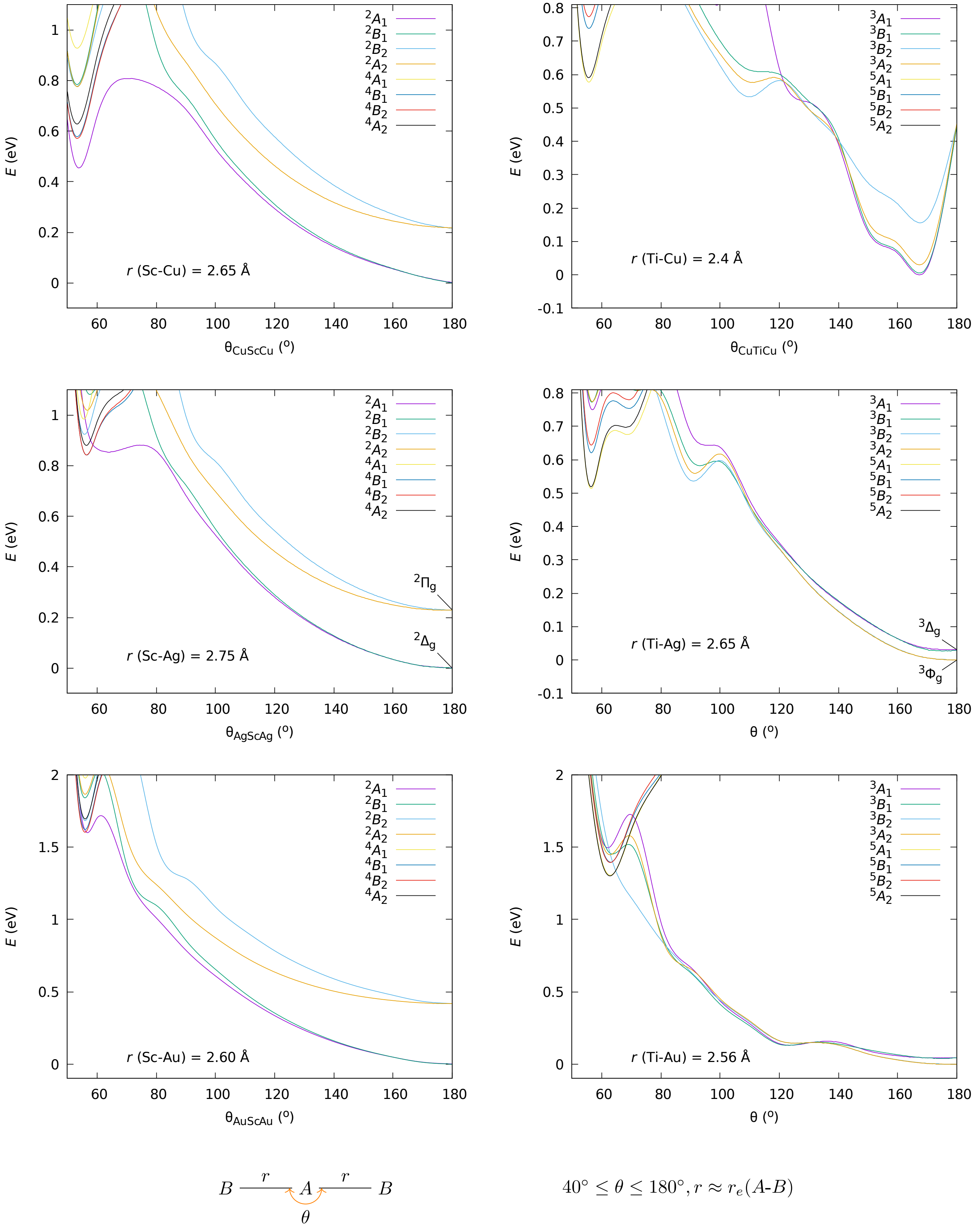

$40^\circ \leq \theta \leq 180^\circ, r \approx r_e(A\text{-}B)$

Figure B.107: Cuts along PESs, $E(\theta, r \approx r_e; {}^{2S+1}\Gamma)$, obtained at the DKH-MRCI level of theory.

Continued on next page

Continued from previous page

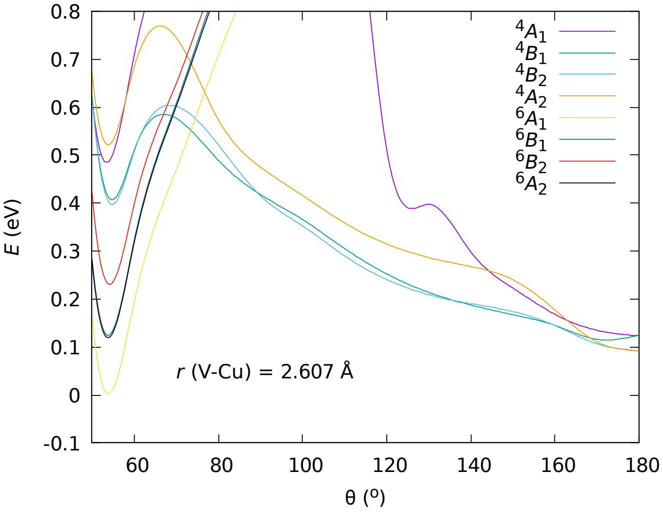

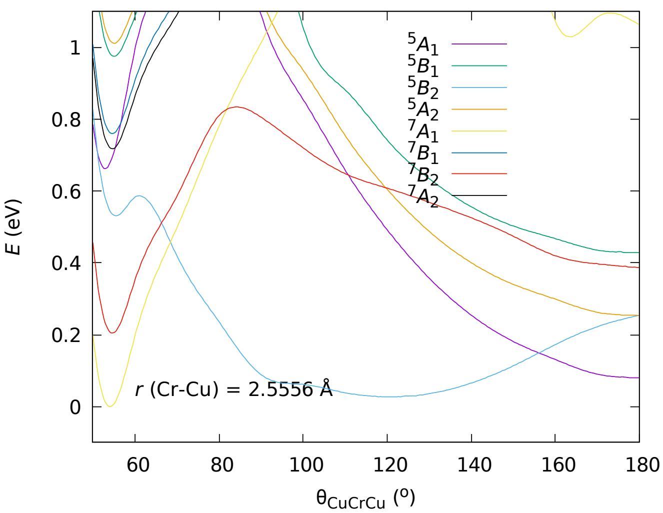

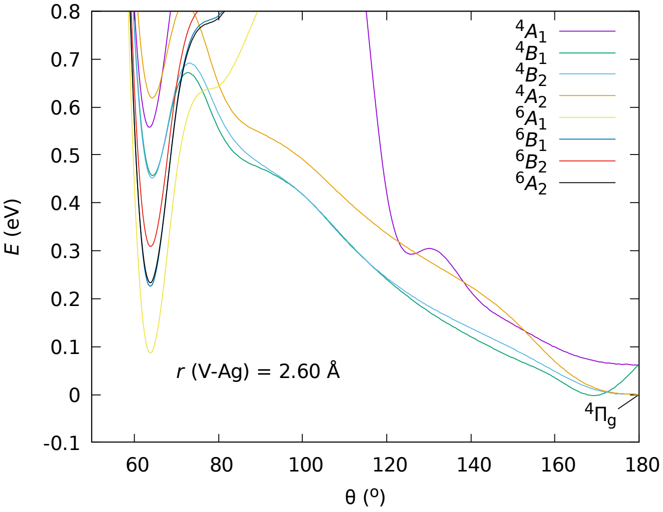

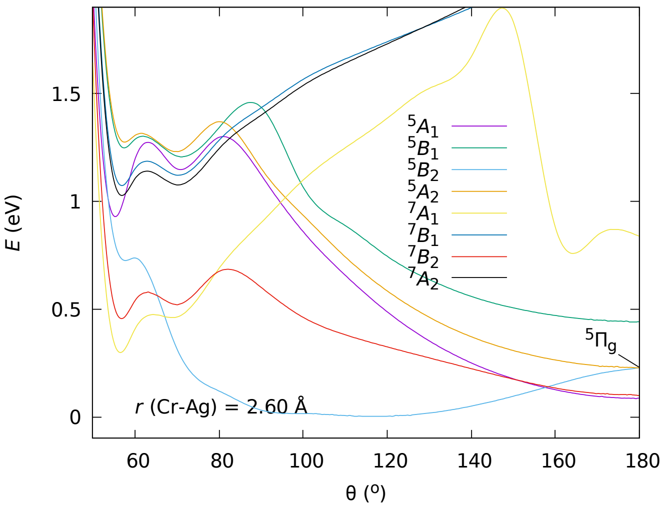

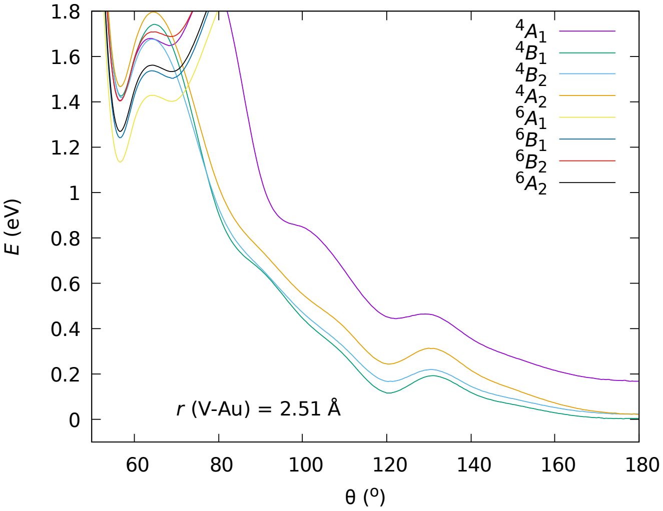

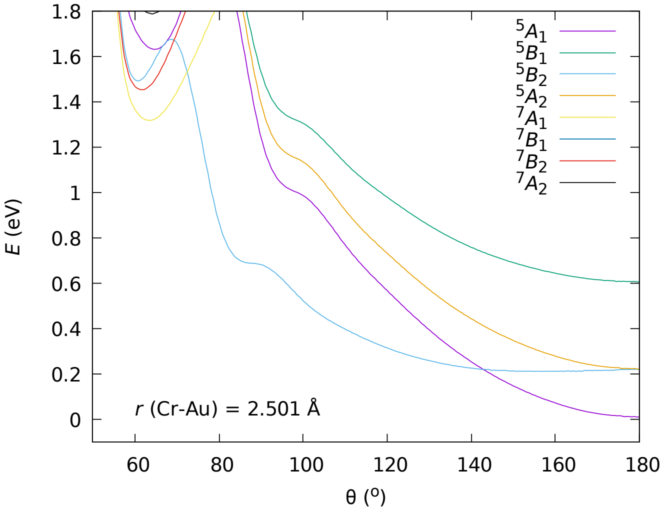

Continued on next page

Continued from previous page

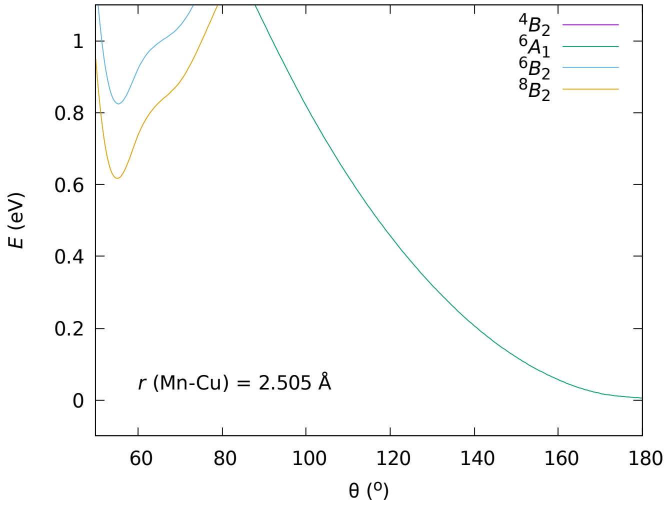

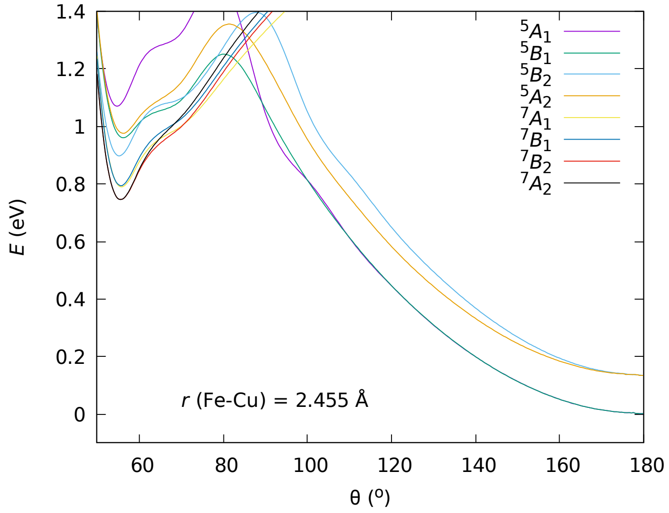

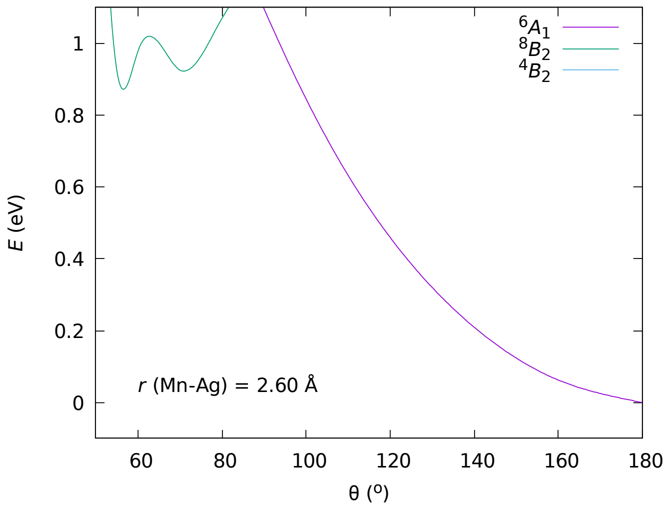

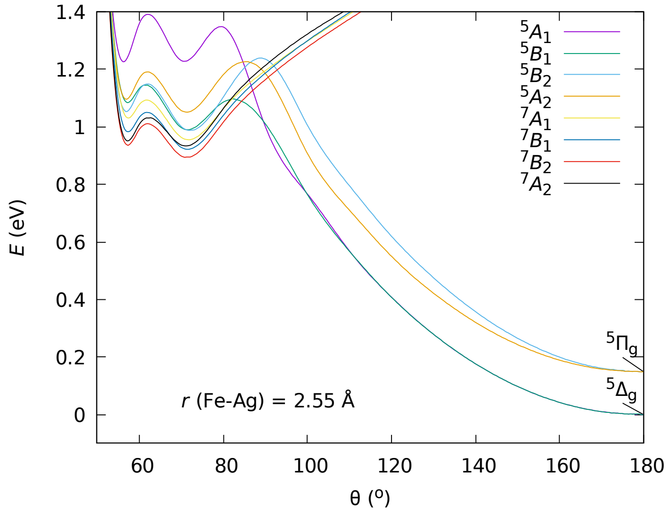

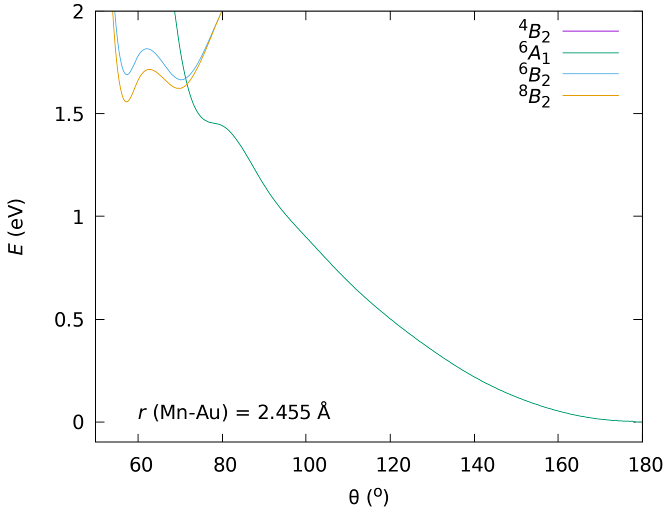

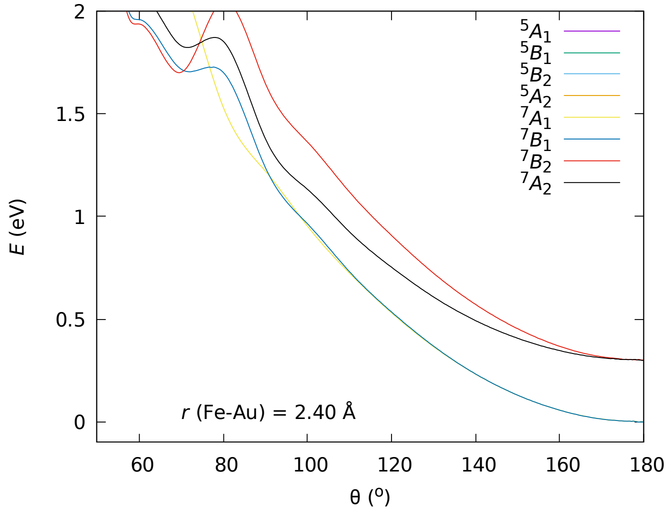

Continued on next page

Continued from previous page

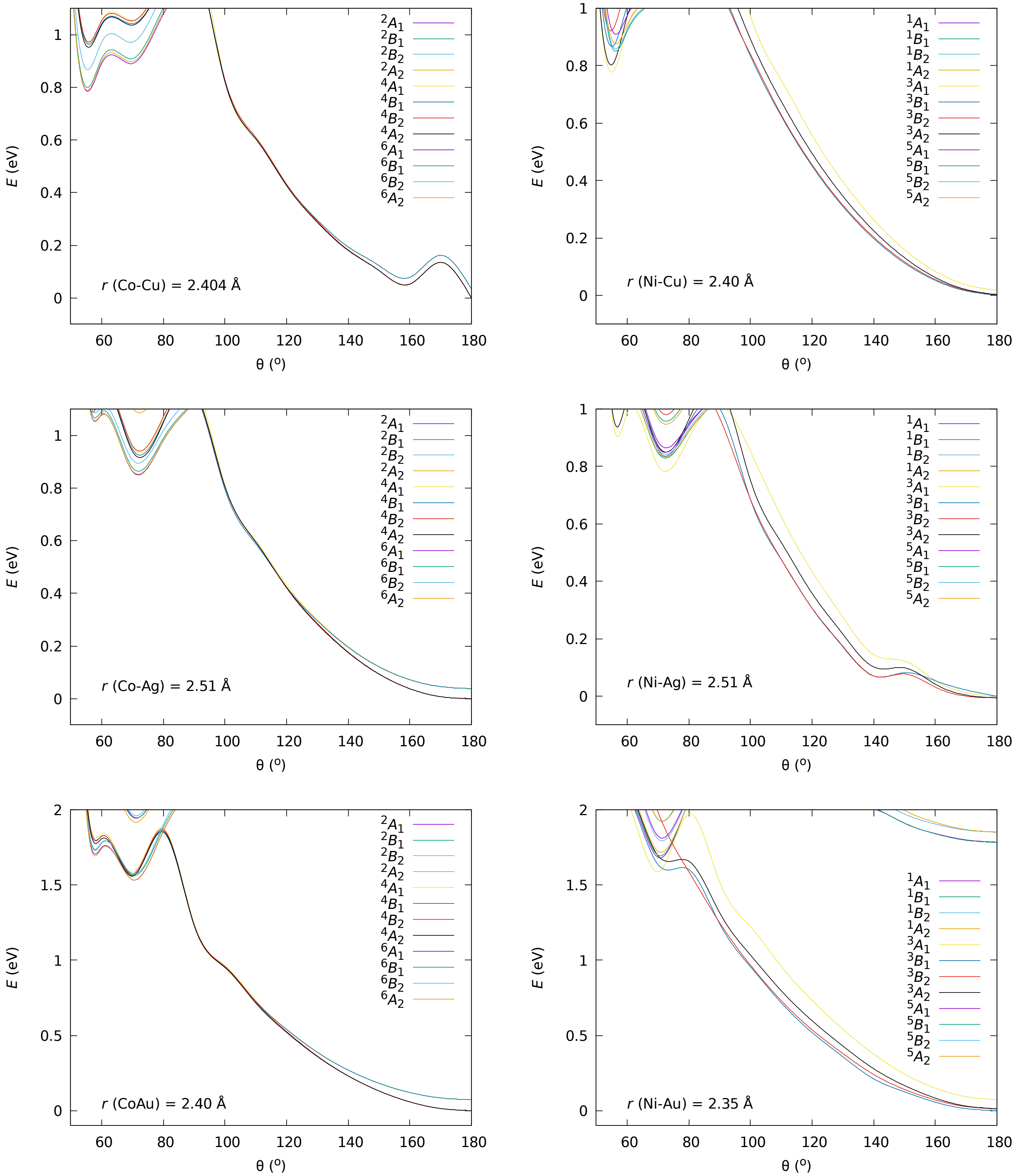

Continued on next page

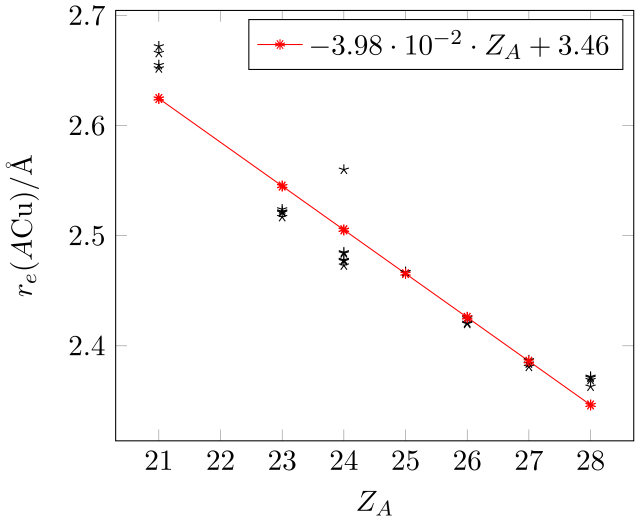

Figure B.108: Equilibrium A-Cu internuclear distances $r_e(A\mathrm{Cu})$ of the low-lying states of the linear $D_{\infty h}$ CuACu structures (A = Sc-Ni), obtained at the DKH-MRCI(+Q) level of theory.

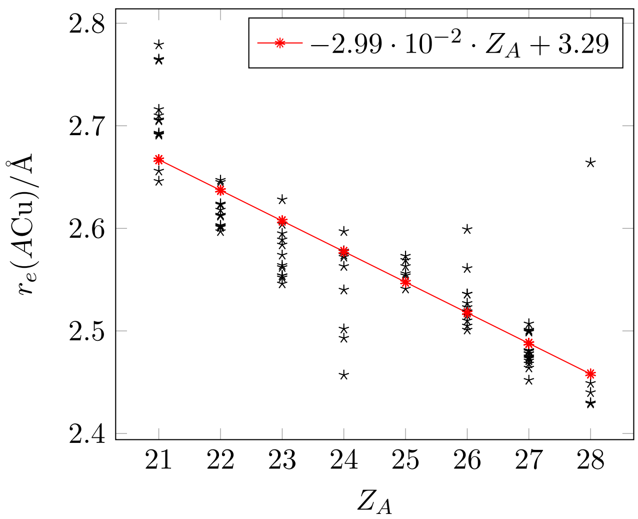

Figure B.109: Equilibrium A-Cu internuclear distances $r_e(A\mathrm{Cu})$ of the low-lying states of the bent C_{2v} CuACu structures (A = Sc-Ni), obtained at the DKH-MRCI(+Q) level of theory.

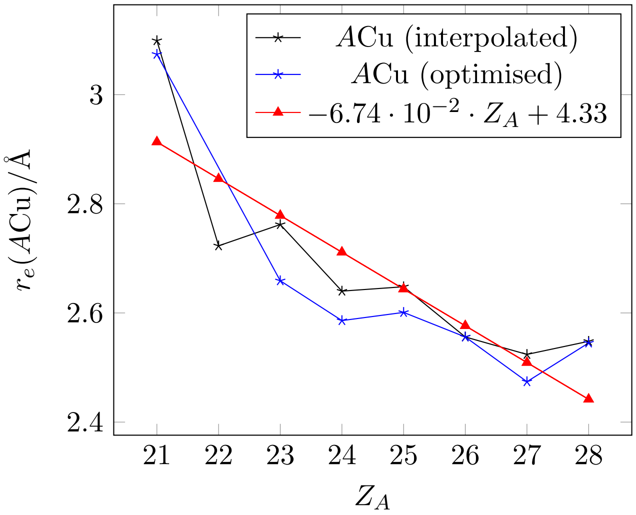

Figure B.110: Lowest state equilibrium A-Cu bond lengths $r_e(A\mathrm{Cu})$ of the linear ACuCu ($C_{\infty v}$) structures ($A = $ Sc-Ni), obtained at the DKH-MRCI(+Q) level of theory.

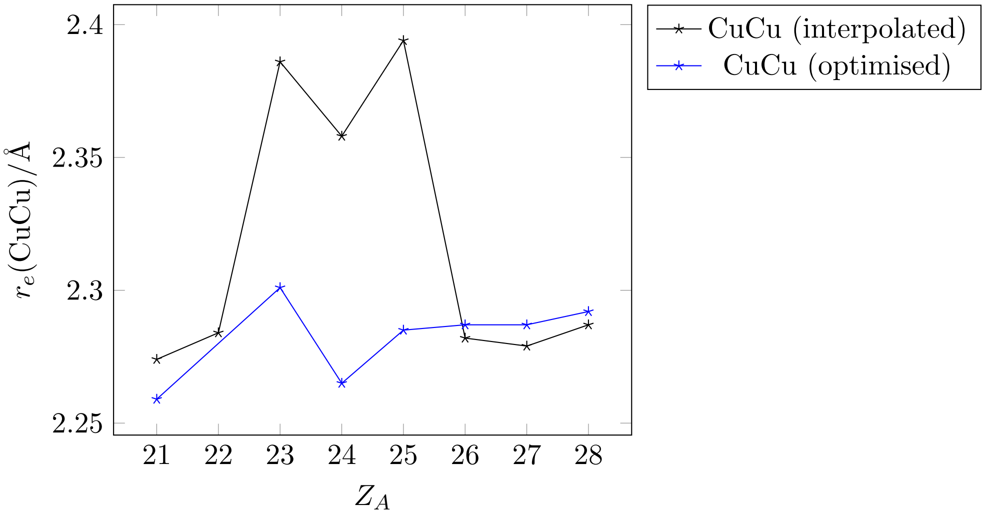

Figure B.111: Lowest state Cu-Cu bond lengths $r_e(\mathrm{CuCu})$ of the linear $C_{\infty v}$ ACuCu structures ($A = $ Sc-Ni), obtained at the DKH-MRCI(+Q) level of theory.

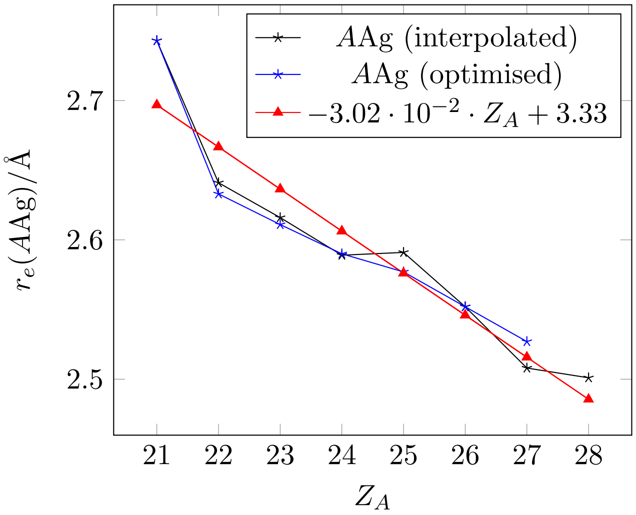

Figure B.112: Lowest state A-Ag bond lengths $r_e(A\text{Ag})$ of the linear $D_{\infty h}$ AgAAg structures ($A = $ Sc-Ni), obtained at the DKH-MRCI(+Q) level of theory.

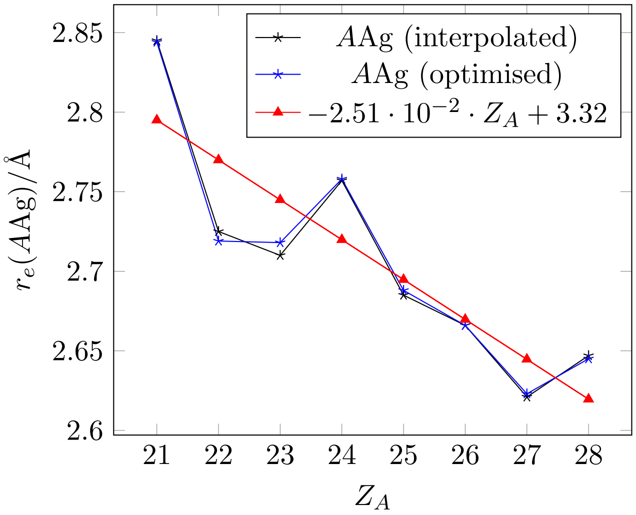

Figure B.113: Lowest state equilibrium A-Ag bond lengths $r_e(A\text{Ag})$ of the linear $C_{\infty v}$ AAgAg structures ($A = $ Sc-Ni), obtained at the DKH-MRCI(+Q) level of theory.

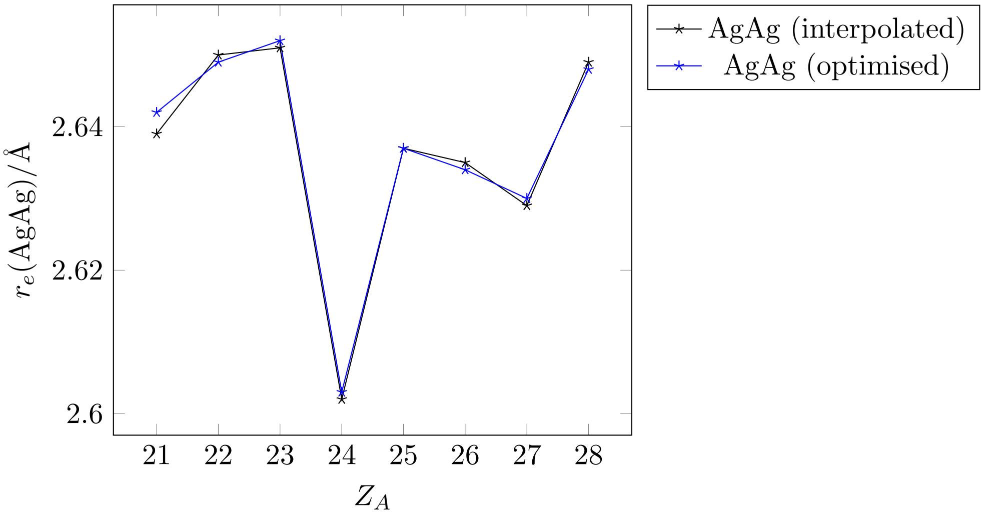

Figure B.114: Lowest state Ag-Ag bond lengths of the linear $C_{\infty v}$ AAgAg structures ($A =$ Sc-Ni), obtained at the DKH-MRCI(+Q) level of theory.

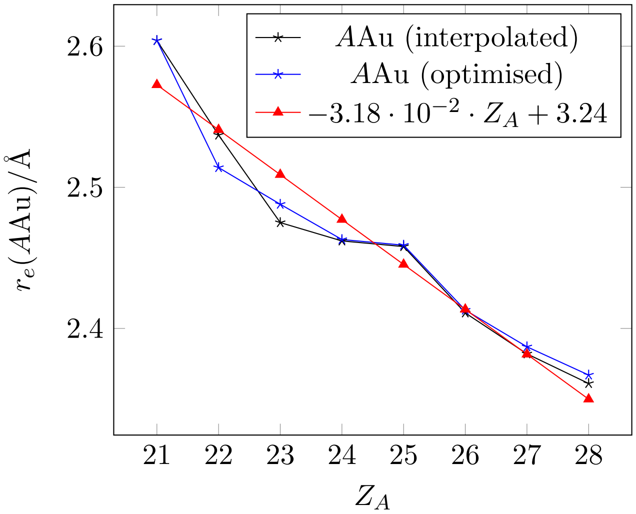

Figure B.115: Lowest state equilibrium A-Au bond lengths $r_e(A\mathrm{Au})$ of the linear $D_{\infty h}$ AuAAu structures ($A =$ Sc-Ni), obtained at the DKH-MRCI(+Q) level of theory.

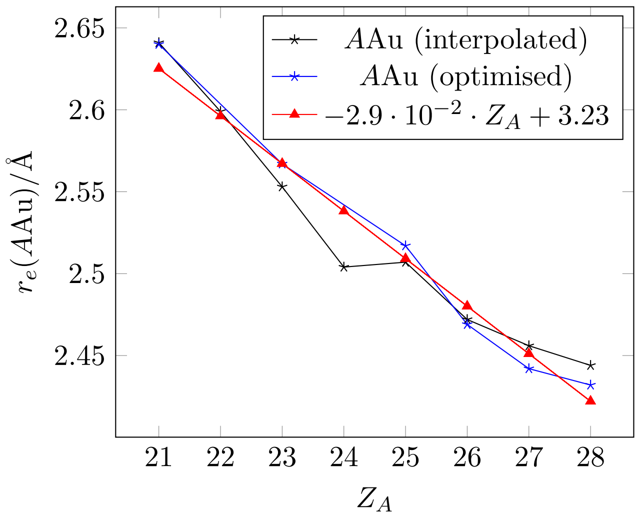

Figure B.116: Lowest state equilibrium A-Au bond lengths $r_e(A\mathrm{Au})$ of the linear $C_{\infty v}$ AAuAu structures ($A = $ Sc-Ni), obtained at the DKH-MRCI(+Q) level of theory.

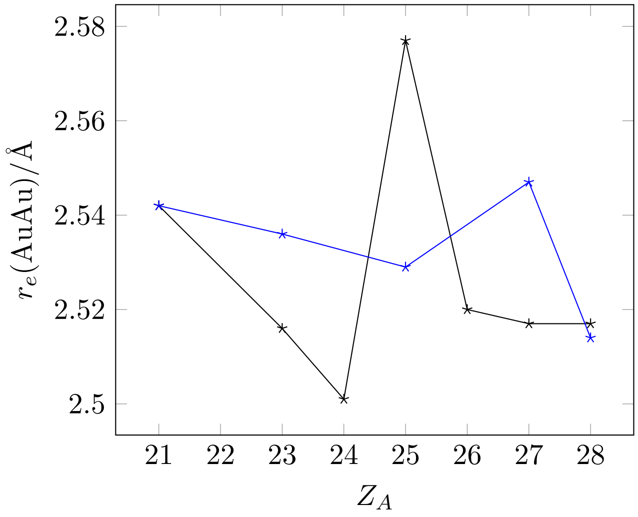

Figure B.117: Lowest state Au-Au bond lengths $r_e(\mathrm{AuAu})$ of the linear $C_{\infty v}$ AAuAu structures ($A = $ Sc-Ni), obtained at the DKH-MRCI(+Q) level of theory.